Multi-objective Optimisation Metrics for Combining Seismic and Production Data in Automated Reservoir History Matching

Onwunyili Christian Chime

Submitted for the degree of Doctor of Philosophy

Heriot-Watt University

Institute of Petroleum Engineering

School of Energy, Geoscience, Infrastructure and Society

June 2018

ABSTRACT

Information from the time-lapse (4D) seismic data can be integrated with those from producing wells to calibrate reservoir models. 4D seismic data provides valuable information at high spatial resolution while the information provided by the production data are at high temporal resolution. However, combining the two data sources can be challenging as they are often conflicting. In addition, information from production wells themselves are often correlated and can also be conflicting especially in reservoirs of complex geology. This study will examine alternative approaches to integrating data of different sources in the automatic history matching loop. The study will focus on using multiple-objective methods in history matching to identify those that are most appropriate for the data available.

The problem of identifying suitable metrics for comparing data is investigated in the context of data assimilation, formulation of objective functions, optimisation methods and parameterisation scheme. Traditional data assimilation based on global misfit functions or weighted multi-objective functions create bias which result in predictions from some areas of the model having a good fit to the data and others having very poor fit. The key to rectifying the bias was found in the approaches proposed in this study which are based on the concept of dominance. A new set of algorithms called the Dynamic Screening of Fronts in Multiobjective Optimisation (DSFMO) has been developed which enables the handling of many objectives in multi-objective fashion.

With DSFMO approach, several options for selecting models for next iteration are studied and their performance appraised using different analytical functions of many objectives and parameters. The proposed approaches are also tested and validated by applying them to some synthetic reservoir models. DSFMO is then implemented in resolving the problem of many conflicting objectives in the seismic and production history matching of the Statoil Norne Field. Compared to the traditional stochastic approaches, results show that DSFMO yield better data-fitting models that reflect the uncertainty in model predictions.

We also investigated the use of experimental design techniques in calibrating proxy models and suggested ways of improving the quality of proxy models in history matching. We thereafter proposed a proxy-based approach for model appraisal and uncertainty assessment in Bayesian context. We found that Markov Chain Monte Carlo resampling with the proxy model takes minutes instead of hours.

DEDICATION

This thesis is dedicated
to my lovely children,
Zitel and
Koby

ACKNOWLEDGEMENTS

Firstly, I would like to express my sincere gratitude to my supervisor, Dr Karl D. Stephen, for his continuous support from day one of my Ph.D research. His patience, motivation, and immense knowledge of optimisation guided me to the successful completion of this thesis.

I would also like to thank my examining committee, Prof. Patrick Corbett and Dr. Carolina Coll, for their time in evaluating the thesis, and for their insightful comments.

My sincere thanks also go to Statoil, operators of Norne Field for providing the real field data and for granting me the permission to publish the results of Norne Field history matching.

Appreciations to my sponsor, the Commonwealth Scholarship Commission in the UK (CSC), for funding of this work, and to Schlumberger Geoquest for the use of Eclipse 100 software. Malcolm Sambridge is appreciated for use of the Neighbourhood Algorithm and the Neighbourhood Bayesian Inference Algorithm

Thanks to the Institute of Petroleum Engineering at Heriot Watt University for providing the required facilities and for creating a comfortable work environment.

Special thanks to the smiling faces of my children, Zitel and Koby, which kept me going in the most challenging times. To God be the glory.

ACADEMIC REGISTRY
Research Thesis Submission

Name*:*	Onwunyili Christian Chime		
School:	Energy, Geoscience, Infrastructure and Society (EGIS)		
Version: *(i.e. First, Resubmission, Final)*	Final	Degree Sought:	PhD in Petroleum Engineering

Declaration

In accordance with the appropriate regulations I hereby submit my thesis and I declare that:

1) the thesis embodies the results of my own work and has been composed by myself
2) where appropriate, I have made acknowledgement of the work of others and have made reference to work carried out in collaboration with other persons
3) the thesis is the correct version of the thesis for submission and is the same version as any electronic versions submitted*.
4) my thesis for the award referred to, deposited in the Heriot-Watt University Library, should be made available for loan or photocopying and be available via the Institutional Repository, subject to such conditions as the Librarian may require
5) I understand that as a student of the University I am required to abide by the Regulations of the University and to conform to its discipline.
6) I confirm that the thesis has been verified against plagiarism via an approved plagiarism detection application e.g. Turnitin.

* *Please note that it is the responsibility of the candidate to ensure that the correct version of the thesis is submitted.*

Signature of Candidate*:*		Date:	26/06/2018

Submission

Submitted By *(name in capitals):*	ONWUNYILI Christian Chime
Signature of Individual Submitting:	
Date Submitted:	26/06/2018

For Completion in the Student Service Centre (SSC)

Received in the SSC by *(name in capitals):*			
1.1 Method of Submission *(Handed in to SSC; posted through internal/external mail):*			
1.2 E-thesis Submitted (**mandatory for final theses)**			
Signature:		Date:	

TABLE OF CONTENTS

LISTS OF TABLES

LISTS OF FIGURES

Glossary

$\in_{k,d}$ noise in the measured data
$\in_{k,m}$model error
$\mu_n(t)$ mean of a normally distributed time dependent reservoir observable
σ_d standard deviation of the data error
$\sigma_n(t)$ standard deviation of a normally distributed time dependent reservoir observable
μ shear modulus
$\mu(x, y, z, t)$ mean of a normally distributed time-space dependent reservoir observable
AI Acoustic Impedance
ASHM Automated Seismic History Matching
AVO Amplitude versus offset
AVO amplitude versus offset
BBD Box-Behnken Design
c_1, c_2 tuning parameters of *PSO*
CCD Central Composite Design
C_D data covariance matrix
CDF cumulative density function
c_h the upper sealing of the learning factors in PSO
CI Coloured Inversion
C_p Correlation matrix,
DE Differential Evolution
do observed data
DOD D-optimal Design
DOPS Pareto-based multi-objective optimisation with production and seismic data treated as two separate functions
DSFMO Dynamic Screening of Front in Multi-Objective Optimisation
DSFMOGA Dynamic Screening of Front in Multi-Objective Optimisation with genetic algorithm
DSFMONA Dynamic Screening of Front in Multi-Objective Optimisation with the neighbourhood algorithm
ED experimental design
EnKF Ensemble Kalman Filter
EOR Enhanced Oil Recovery
Fm Formation
FOPR field oil production rate
FOPT Field Oil Production Total
FWPR field water production rate
FWPT Field Water Production Total
g(m) model prediction
GA Genetic Algorithm
GI Genetic inversion
GOR Gas Oil Ratio
GOR Gas Oil Ratio
GP-SR Genetic Programming Based Symbolic Regression
HMC Hamiltonian Monte Carlo
Ip P-wave impedance
Is S-wave impedance
K bulk modulus
kro oil relative permeability
krw water relative permeability
LDM Local Dissimilarity Map

LHD Latin Hypercube Design
m vector of model parameters
MAE Mean Absolute Error
MAP maximum a posteriori estimate
MC Monte Carlo
MCMC Markov Chain Monte Carlo
MOP multi-objective optimisation using only production data
MOPS multi-objective optimisation using production and seismic data
m_p vector of prior model parameters
MPI Message Passing Interface
MSE mean square error
MULTREGT Transmissibility multiplier between regions
MULTZ Transmissibility multiplier in vertical direction
NA Neighbourhood Algorithm
NABayes Neighbourhood Algorithm Bayesian Inference
N_d number of data or measurements
NRMS normalised *RMS*
NTG Net-to-Gross
O(m) Objective function given a model, *m*
OGOC original gas–oil contact
OOWC original oil–water contact
OPR Oil Production Rates
OWC Oil Water Contact
P^{creep} creep mutation
PDF Probability distribution function
P_{eff} Effective Pressure
PEM Petro-Elastic Model
PF Pareto Front
P^{jump} jump mutation
POWC produced oil–water contact
PPD Posterior Probability Density
PSO Particle Swarm Optimisation
QRNG quasi random number generator
r_1, r_2 random functions used in *PSO*
RFT Repeat Formation Tester
RI recursive inversion
RML Randomized Maximum Likelihood
RMS root mean square
RSM response surface methodology
RST Reservoir Saturation Tool
SA Simulated Annealing
SAS Saleev-Antonov-Sobol
S_g gas saturation
SHM Seismic History Matching
SIS Sequential indicator simulation
S_o oil saturation
SOP single objective optimisation using production data only
SOPS Single sum-objective optimisation using production and seismic data
SOS single objective optimisation using seismic data only
SSI Sparse Spike Inversion
stdev Standard deviation
S_w water saturation

S_w water saturation
V-Cell voronoi cell
Vp P-wave velocity
vp velocity of particle in *PSO*
Vs S-wave velocity
V_{sh} shale volume
w[i] inertia time variant constant applied to *ith* particle in *PSO*
WAG Water Alternating Gas
WBHP Well Bottom Hole Flowing Pressure
w_d angular frequency of damped oscillation in PSO
WOPR well oil production rates
WPR Water Production Rates
WWPR well water production rates
xp position of particle in *PSO*
x_{pgb} global best position of particle in *PSO*
x_{plb} local best position of particle in *PSO*
δ damping ratio of oscillation in PSO
ρ density
$\sigma(x, y, z, t)$ stdev of a normally distributed time-space dependent reservoir observable

PUBLICATIONS

Onwunyili, C.C., and Stephen, K.D., 2018. A Fast Approach to Ensemble Appraisal and Reservoir Performance Predictions. 80th EAGE Conference and Exhibition 2018 held in Copenhagen, 11-14 June 2018.

Publications in Preparation:

1. Improving Model Predictive Powers in Proxy-Assisted History Matching

2. Proxy-Assisted Multiple Realisation Appraisal and Probabilistic Production Forecasting

3. Multi-objective optimisation metrics for integrating seismic and production data in automated reservoir history matching

4. Dynamic Screening of Fronts in Multi-Objective History Matching of Norne Field

Chapter 1 – Introduction

1.1 Background and Context: Developments in History Matching

Obtaining the most accurate and reliable reservoir-simulation model is a necessary step in any reservoir management project aimed at optimising production and maximising profit. Field development decisions are made based on the models, and probabilistic forecasting is made much easier if multiple history-matched reservoir models are available.

The process of reservoir model building involves the integration of various uncertain data classified as either static data (examples: geological data, petrophysical logs, core data, pre-production seismic data) or dynamic data (examples: well test data, production logs, fluid flow rates and ratios, reservoir pressures, time lapse seismic data). After building the base case reservoir model based on the available data, the model parameters need to be calibrated further (by adjusting model parameters such as porosity, permeability, porosity, net-to-gross, barriers and fault transmissibility etc. within a given uncertainty bound), as more information (especially in the form of dynamic data) are gathered, so as to give predictions that will closely match what is/are observed or measured. The process involves the assimilation of the observed data in a model updating workflow known as history matching. After proper calibration, the reservoir-simulation model becomes very useful for predictions and decision making for future field development.

The development of history matching techniques dates back to the 1960's when the traditional manual history matching was the only technique available (Jens-Petter, 2006). Although the manual method is still in use today, there has been a shift to automated history matching in recent years. The new technology that replaces manual history represents a very important progress in field management. In the manual approach, all models' files are prepared manually, and the simulation runs are launched in succession, followed by visual comparison of line plots. This process is time consuming, assimilates very limited data and is very subjective as the reservoir engineer, given the limited time resources, is forced to opt for a single 'best' model as the solution. History matching is an inverse problem and is non-unique, however, like the mathematical under-determined problem, with more unknowns than equations. This implies that multiple solution models can give the same reservoir response as the measured data, and none contains the true model parameters and may therefore be unreliable for forecasting. The result of typical history matching is a handful of different calibrated models representing several possible combinations of parameters. Therefore, by using only one single model determined

through a trial and error approach, as in the case of the manual deterministic history matching method, for prediction purposes will further increase the risk and uncertainty in decision-making. Another factor is that it is not easy to manually adjust a large number of parameters simultaneously considering the complex nature of reservoir model behaviour and parameters interdependency (for example, Arwini and Stephen, 2011).

Another development in the techniques of history matching that followed the manual approach was the use of proxy models. It was a useful adaption of the manual history matching method in which a number of manually updated models were launched in an independent simulation runs. The reservoir responses of the models were then represented by polynomial proxy through regression and used for further predictions and uncertainty assessment. Although the use of proxy models speeds up calculations, it has its pitfalls - it is not suitable for complex reservoirs and for reservoirs requiring the updating of many parameters as its quality decreases with increasing complexity and as the number of parameters increases (Jens-Petter, 2006).

The commonly used technique today for history matching is the automatic stochastic optimisation which allows multiple independent simulations to run in parallel and searches the solution space more efficiently. This approach has been reported to be very successful and may be preferred to the proxy model because it is more efficient in higher model dimensions and reflects the nonlinear parameter interactions and dependencies that proxy models fail to include (Jens-Petter, 2006). With this approach, we can only hope to generate thousands of multiple realisation of the solution models and with their predictions we define the uncertainty envelope, but this does not reduce the non-uniqueness in the solutions of the history matching problem.

Efforts to reduce the non-uniqueness, reduce the parameter uncertainty and increase prediction accuracy led to the introduction of time lapse seismic data as a constraint, in addition to the conventional production data, in history matching. Ideally, as pointed out in Huang *et al.* (1997), the reservoir-simulation model needs to concurrently honour all available data including static (geological and geophysical data) and dynamic (time-lapse and production data), to be relied on for predicting reservoir responses.

Recent efforts to use production data and 4D seismic data as history-matching constraints have focused on automatic history matching in fully integrated workflows. The difference in the workflows are typically marked by the type of optimisation algorithm used, often categorised into: (i) Deterministic (or gradient-based), (ii) Stochastic Optimisation

methods and (iii) Probabilistic data assimilation. The optimation methods are discussed later under section 2.2.4 in Chapter 2.

Figure 1.1 shows a general history matching workflow integrating both time lapse seismic data and production data for upating a geologic model.

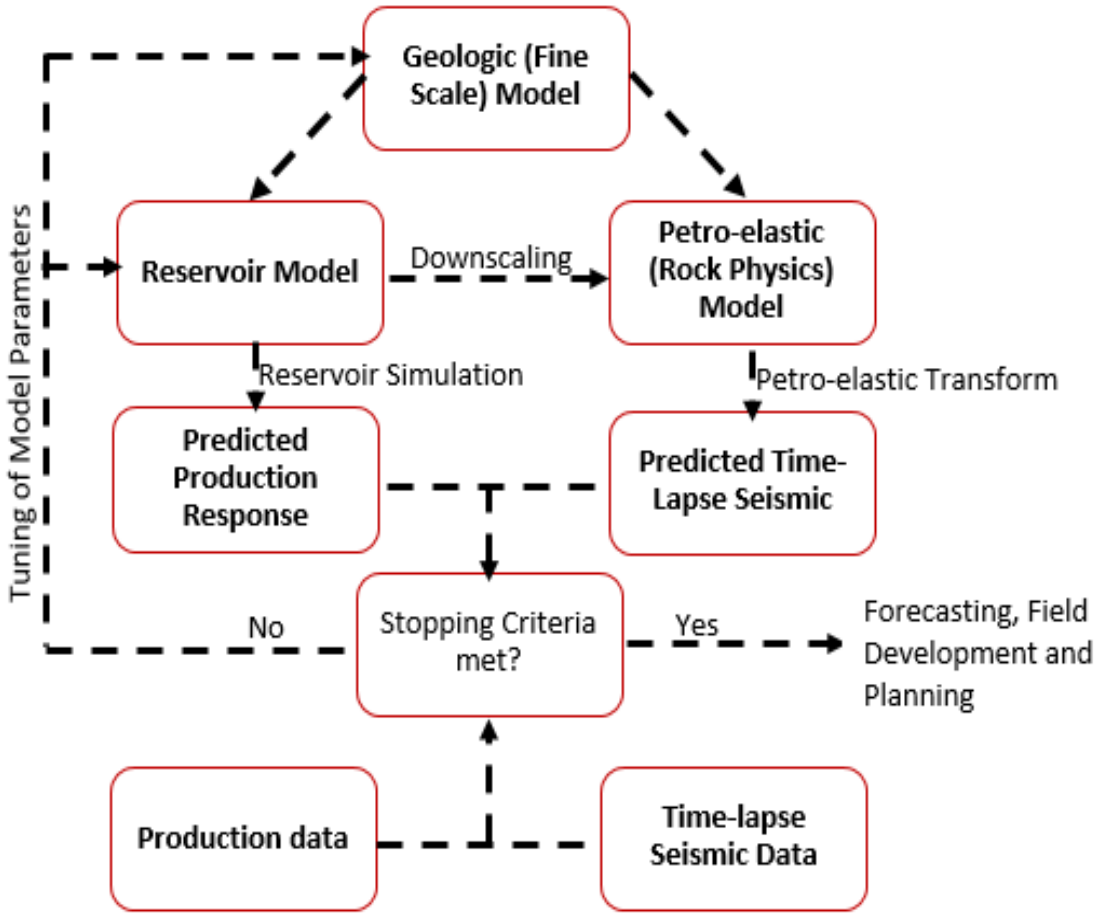

Figure 1.1 General History Matching workflow: easy to draw but 'Herculean' in implementation

The workflow depicts the 4D Seismic history matching in which the measured production and time-lapse seismic data are used simulataneosly to compare the predicted production and seismic data. Both predicted data are generated from the reservoir model upscaled from the fine scale geologic model. Production data is predicted through numerical reservoir simulation while the time-lapse seismic is predicted through petro-elastic transform. Multiple models are generated as the optimisation algorithm aims to explore the entire model space in search of models that minimise the misfit between the predicted and measured data. After some iteration steps, depending on the stopping criteria, the accepted reservoir models may be used for forecasting, field development and planning.

1.2 Time Lapse Seismic Tool in History Matching

As a reservoir-surveillance tool, time-lapse seismic application entails the interpretation of data from repeated seismic surveys acquired at different times during field development to extract useful information for monitoring changes in reservoir fluid saturation, pressure, and other properties that change due to production activity. Time lapse seismic data carry a lot more spatial information, which the well data lack, and therefore provide useful information on the reservoir heterogeneities that control the production behaviour of a field. Time lapse seismic data are fundamentally based in geophysiscs but has found wide applications in reservoir monitoring including: monitoring of fluid movements in different production scenarios (examples: waterflooding, gas injection, gas exsolution), monitoring pressure changes as a result of production activity (for example: in depleting reservoirs, near injection wells), monitoring various kinds of EOR processes (for example: steam floods), finding the location of trapped hydrocarbons for infill drilling, and as history-matching constraints for calibrating reservoir simulation models. Johnston (2013) sums up the role and value of time-lapse seismic method as follows: "Your company is offered a tool that can tell you whether a field is performing according to plan and that can help you locate undrained hydrocarbons, optimize infill-well and workover opportunities, manage injection and offtake, and help ensure maximum recovery. The cost is less than that of drilling a single well. Would you purchase that tool? Chances are that you will." The application of the seismic technology is, however, not simple being faced with issues such as the repeatability or similarity of the different seismic surveys, the degree of responsiveness of seismic signals to production changes (detectability), interpretation and integration of information derived from time lapse data with various geologic and production data at appropriate scale.

As attractive and promising as quantitative seismic history matching might be, its implementation is not an easy task, and it is faced with a number of challenges and questions discussed in Johnston (2013). The challenges include:

1) How do we define the objective function in a multi-objective optimisation constrained by both production and seismic data (data of differing scales)?
2) Which seismic domain (reflectivity, impedance, or saturation and pressure domain) is the most appropriate for comparing predicted/simulated 4D seismic with the measured 4D seismic?
3) At what scale should the comparison be made? (Should we upscale the seismic properties to coarse simulation grid to enable comparison between the predicted and observed, or should the reservoir properties in the simulation-model grid be downscaled?),

4) What if the original geologic model was not conditioned by the baseline 3D seismic data, and as a result the initial simulation model is inconsistent with the information derived from the baseline survey?
5) How accurate is the petro-elastic model used to estimate the 4D seismic attributes (example: acoustic impedance) from the simulated reservoir properties (saturation and pressure) or used to invert the 4D seismic data to the reservoir simulation properties?
6) What is the best optimisation algorithm to use in matching a large data like time –lapse data to prevent the misfit function (or objective function) from being trapped in a local minimum?

1.3 Research Objectives

From the foregoing discussions, it is obvious that the progression in time-lapse seismic interpretation, from qualitative to quantitative methods, have been faced with numerous challenges making the incorporation of seismic data in automatic history matching a difficult task. The benefits of time lapse technology as a reservoir-surveillance tool is, however, too significant to be ignored: it is useful in boosting reserves and ultimate recovery, helping in optimisation of field-development plans by locating undrained hydrocarbons, choosing the optimal infill-well locations, updating reservoir model parameters, identifying compartmentalisation, mapping fluid flow-paths. Consequently, seismic history matching has become a continually evolving topic for both the industry and the academia, with special focus on several of the challenges that must be addressed before automating the incorporation. It is the purpose of this work to add to the database of knowledge in the field of seismic history matching by critically looking at some of the challenges and demonstrating ways of tackling them using the available resources including a synthetic field study and the Norne Field data: focusing on using multiple-objective methods in history matching to identify those that are most appropriate for the data available. We therefore outline the main objectives of this work as follows:

1. To examine the relative nature of time lapse seismic and study approaches to data calibration to ensure integration at the appropriate scales
2. To study the differences in information and constraints provided by production and seismic data, and the nature of conflict arising when the two datasets of different scales are incorporated simultaneously in the history matching workflow.
3. Identify and apply the most appropriate multiple-objective method in history matching to resolve the challenges posed by the conflicting objectives (production data misfit and seismic data misfit).

4. To investigate the applicability of proxy models in seismic history matching and its potential in reducing the high cost of computation which characterises the stochastic approach to history matching problems.
5. To develop an approach for facilitating the appraisal of stochastic history matching results to evaluate for measures of resolution and trade-off in the reservoir model parameters, and estimate uncertainty in simulation-model predictions.
6. To appraise the performances of different optimisation algorithms in searching the model space during history matching with the available data and investigate what the best posterior probability should be as the solution to the history matching problem.
7. To identify and implement a parameterisation scheme that preserves the geological consistency while searching for the best data fitting models.
8. To test and implement the approaches developed in this work in the history matching of the Norne Field.

We plan to accomplish the afore-mentioned objectives in an automated seismic history matching workflow which bridges the gap between geophysics and reservoir simulation in an iterative loop comprised of reservoir flow simulation, petro-elastic transform and seismic modelling. However, prior to the incorporation of the various data into the automated workflow data preparation will include: seismic signal post-processing and seismic inversion (with sub-processes such as petro-physical logs editing and calibration, seismic well-tie, velocity models and domain-conversion), and calculation of other relevant seismic attributes.

1.4 Outline of the Thesis

The rest of this thesis is organised in eight chapters briefly reviewed as follows:

History Matching is formulated as an inverse problem, and for that reason, **Chapter 2** introduces the basic concepts of inverse theory and the elements of a generalised seismic history matching workflow including; the forward problem, parameterisation, objective function, optimization algorithm, seismic modelling and seismic inversion. An extensive review of the literature highlighting the challenges and problems faced in seismic history matching as well as the progress made so far in addressing the problems are also presented in this chapter.

Chapter 3 identifies seismic history matching as a reservoir parameters estimation problem and describes the methodology and approach adopted in this work for matching production data only, seismic data only and for matching both data in an automated workflow. Experiments designed to test some hypothesis in this work requires development of software tools which adopts, and modifies where necessary, some

standard and conventional techniques and algorithm to fit the experimentation purpose. The elements of seismic history matching workflow are described thoroughly in the context of the adopted methodology. Discussions are also made on model and data error, convergence and stopping criteria, and the method for normalisation of seismic attributes.

Chapter 4 is a critical review on the use of proxy representation of response surface *in lieu* of reservoir simulator for history matching. The chapter examines experimental design methods and explores ways to improve the quality of proxy models in a proxy-assisted history matching study**.** Here it is demonstrated that the use of GA-based symbolic regression can give some high-quality quadratic polynomial proxy model to represent the reservoir response surface. Non-domination sorting of the objectives in the entire model space is used to assess the quality of solutions to the synthetic history matching problem in case studies involving different experimental design techniques.

Our approach and methodology to speeding up history matching and appraisal are tested and validated in **Chapter 5** using a synthetic field for which the true solutions of seismic history matching are known *ab inito*. The chapter presents an approach for adequate appraisal of history matching results. The ensemble of models generated in some history matching cases are subjected to an appraisal process to make inferences within the Bayesian network. It is demonstrated how proxy models can speed up the appraisal process and enable exhaustive search of the model space. Statistical measures of trade of trade-off in model parameters and data resolution are computed, and the constraints provided by production and seismic data are compared to assess the value of information provided by data in the history matching cases. In addition, a novel approach for uncertainty quantification and probabilistic forecasting is demonstrated here

In Chapter 6, the Norne Field development plans are reviewed in view of applying our methodology to a real field case. In this chapter, a quality check of all the datasets provided for the field is done and the results of seismic signal post-processing, inversion and other derived seismic attributes are presented. Scenario-based synthetic seismic modelling on Norne Field is reviewed for the response of the Norne Field time lapse data to changes in reservoir properties to ascertain the level of detectability of production-induced changes in Norne Field seismic and to make the right choice of seismic attributes for history matching. An extensive review of previous history matching studies on Norne Field is presented and key uncertainties in the field identified through sensitivity analysis.

Chapter 7 focuses on defining the objective function of history matching for proper integration of data at the appropriate scale in seismic history matching, and for adequate data assimilation in the multiple-objective optimisation. Options for selection of models during optimisation are investigated using a suite of algorithms based on dominance. The capability of the algorithms is tested using several analytical functions and synthetic reservoir models.

Chapter 8 is on implementation of the techniques developed in the thesis for updating the Norne Field reservoir using seismic and production data. The emphasis here is on the use of multi-objective optimisation to resolve then the very challenging Norne Field history matching and uncertainty quantification.

Finally, **Chapter 9** contains the summary reflecting the most important results of the work and the conclusions drawn from analysing the results. Recommendations are also made for further studies.

Chapter 2– Review of Inverse Theory and Seismic History Matching

2.1 Overview History Matching; an Inverse Problem

The estimation of reservoir parameters, especially the petro-physical properties of the reservoir, is done by history matching some observable parameters such as production and 4D seismic data.

Reservoir is a physical system and as Tarantola (1987) identifies, there are three steps involved in scientific study of a physical system:

- Parameterization: identifying the minimum set of model parameters whose values completely characterise the physical system from a given perspective.
- Mathematical/ Forward modelling: using physical laws to make predictions on the measured values of some observable parameters, and
- Inverse Problem modelling: using the actual measured values of the observable parameters to estimate the values of the variables that describe the physical system.

Oliver *et al* (2008) states the inverse problem as: "determine plausible values of model parameters given inexact (uncertain) data and an assumed theoretical model relating the observed data to the model". In order to solve the inverse problem for petroleum reservoir parameter estimation, the problem is often formulated with the following elements:

- The forward problem
- Parameterisation
- Objective function
- Optimization Algorithm

The mathematical model, or the forward problem, is formulated to predict the reservoir response (in terms of rates, volumes, fractions of volumes, pressures and so on) for any given set of model parameters. The difference between a predicted response and the corresponding measured value is called the residual or misfit. The aim of history matching is to optimise or minimise the objective function which is a sum of weighted residuals through a series of iterations. At each iteration a different set of model parameters are chosen for the prediction using an optimization algorithm. The optimization algorithm is designed to minimise or optimise the objective function in search for the 'best models'.

2.2 Formulation of an Inverse Problem

A typical approach in framing the inverse problem for fitting the reservoir models to the measurable quantities and estimating the model parameters considers the viewpoints expressed in Tarantola (1987) and Oliver *et al*. (2008). Generally, history matching is ill-posed and requires the determination of infinitely large model parameters using the observables which are often 'polluted' due to noise in measurements – *data error*. The model should then be reparameterised to reduce the parameters and a good metric should therefore account for model errors and data errors. The solution to the history matching problem lise in the posterior probability density function (PPD) which is very difficult to construct in full. Notwithstanding, a good formulation should be such to approximate the PPD as much as possible.

2.2.1 The forward problem

One of the challenging features of the inverse problems in reservoir engineering is that the petroleum reservoirs are heterogeneous porous media; and the nonlinear relationship between the observables and parameters is highly complex and difficult to compute. In the forward problem, the parameters of the reservoir (for example: permeability, porosity, fault transmissivity) are given, and a deterministic method is available for evaluating the response such as rates, volumes, seismic amplitudes, saturation and pressures. The mathematical model varies in complexity depending on the problem and is typically represented by a complex differential equation whose solution could be analytical or numerical. Because reservoir saturation and pressure are functions of location, reservoir parameters, fluid properties and time, it is impractical to find an analytical solution to the complex differential equations that define fluid flow in oil and gas reservoir. Although the analytical techniques are still very useful especially for preliminary analysis in new field developments with very sparse data, a robust solution to the complexities of parameter estimation problem is provided through numerical reservoir simulators, for instance ECLIPSE 100. In this case the reservoir is discretised into several gridblocks to capture as much heterogeneity and spatial information as possible. Within each gridblock, the simulation assumes that the reservoir properties are constant. The reservoir simulator then solves the forward problem by evaluating a system of finite-difference equations which approximates a series of partial differential equations in a heterogeneous porous medium.

For matching seismic data, a Petro-Elastic Model (PEM) can be used to convert changes in fluid saturations and pressures from the simulation into predicted impedance or other

elastic properties for each simulation cell. A PEM is derived based on some laboratory work on core data, and ultimately it may be tested and calibrated by using petrophysical data from the logs. The output of the petro-elastic model will be elastic properties of the reservoir which will be used to generate the seismic data in the impedance domain or in the amplitude domain. Working in the amplitude domain requires some additional steps such as grid regularisation (refinement of the reservoir model grid to be in the same scale as observed seismic data) in order to match the output of PEM in reservoir model scale to seismic scale. In addition, amplitude domain requires additional computations relating to the convolution of reflectivity data with wavelets. The domain of comparison in this thesis is the impedance domain. The petro-elastic model is usually generated from empirical equations derived for particular fields and some equations for fluid substitution such as the Gassmann (1951) equation are commonly used.

2.2.2 Parameterisation

A parameterisation scheme is a way of updating all possible variables in a model through the modification of only a few (Oliver and Chen, 2011).

Construction of a computer model of a petroleum reservoir involves integrating various inaccurate information about rock and fluid properties in an array of thousands of cells with each cell having a distinct set of parameters such as porosity, permeability and saturation depending on reservoir heterogeneity. Each piece of information in the cells of the model can be potentially modified during history matching to improve the flow and/or seismic predictions of the model. The implication is that the number of cell attributes to be adjusted in a history matching problem becomes exceedingly large whereas the number of independent observed data for constraining the attributes are very limited, resulting in a very ill-posed history matching problem. The difficulty in having an ill-posed problem is not only in the fact that it is difficult to solve but in that there is an infinite number of solutions that are non-unique, and thus despite giving a good match the history data, there will always be some elements of doubt over the predictions made with any of such model solutions. Choosing the appropriate parameters to adjust and the number of parameters to consider is a critical step in history matching. Apart from rendering an unstable solution, increasing the number parameters also implies increasing computational cost. On the other hand, if the choice of parameters is wrong or the number of parameters (and the range of the parameters) chosen is inadequate, the results of the history matching can be unreliable, and the predictive power of a history-matched reservoir model is reduced or lost completely.

One technique for tackling the non-uniqueness problem is linear regularisation or the constrained linear inversion method which is related to the Levenberg–Marquardt algorithm and applies a filter to give preference to a solution with desirable properties and confine the range of solutions to those in agreement to the imposed criteria such as the smoothness or solutions with smaller Euclidean norm (Tikhonov and Arsenin, 1977). Jafarpour *et al.*, (2010) adapted the approach of Tikhonov & Arsenin (1977) by minimization of a least-squares objective function augmented by an L1-norm of truncated low-frequency discrete cosine transform coefficients to promote solutions that are sparse in the transform domain. Although linear regularisation may be an exceptional generic method for regularization of ill-posed problems in statistics or machine learning, the regularisation term does not carry the prior geological information required to screen the reservoir model solutions in a more technical fashion. Besides, some optimisation methods based on constrained linear inversion may lack the capability of working in high dimensional spaces, and may still need the number of parameters to be reduced through parameterisation. The choice of initial reservoir parameterization can be subjective, can be based on experience, or based on the results of well test, seismic, geological and petrophysical interpretations. Some properties such as porosity, permeability, net-to-gross, structural boundaries and elastic properties of the rock do not vary significantly with time and are regarded as static properties. On the other hand, the properties such as saturation and pressure which vary with time (producing history) are referred to as dynamic properties.

A sensitivity study of the reservoir simulation response to the parameters can serve as a guide to screening of the parameters and subsequent re-parameterisation. Usually, parameters are screened based on how sensitive the objective function is with respect to them, so that those parameters that have the most influence on the objective function or the misfit function are selected for updating during history matching. Nevertheless, the choice of parameters is dependent on the quantity being predicted for which we want to match with the observed data. For instance, relative permeabilities and end-point scaling may be the choice when matching water cut (or phase flows in general), strength of aquifer and absolute permeabilities for reservoir pressures and the stratigraphic barriers and faults to match complex flow patterns. Some uncertain parameters, such as rock and fluid compressibility, elastic moduli of rocks, the fluid contacts, barrier / fault transmissibility multipliers, size and strength of the aquifer, capillary pressure, relative permeability, fluid densities and viscosities, are referred to as regional parameters and are not directly assigned to the spatial grid blocks. The regional parameters may either be

controlling the whole simulation model or some regions of it and so do not need to be reparameterised. However, rock properties such as permeability, net-to -gross and porosity are grid cell properties and because we deal with thousands of grid cells, these parameters need to be reparameterised before history matching.

Parameterisation, or reparameterisation, has been considered in different ways by many authors. A parameterisation scheme called zonation method (Jacquard and Jain, 1965; Jahns. 1966) involves subdividing the reservoir into a number of homogenous regions with constant properties which are then used as the history matching parameters. The traditional zonation approach allows reservoir zonation to be carried out before optimisation of the zone parameters but once the optimisation commences the zonation cannot be changed but only the properties in the zones can be updated. Although the zonation method results in fast initial reduction of misfit between the model predictions and the corresponding measured data, its major limitation lies in the fact that the resulting model solution(s) will be too coarse and may not capture the heterogeneity of the reservoir properly. An improvement on this has been made on some modern approaches such as the gradzone technique and adaptive multiscale methods. In the gradzone scheme (Bissel, 1994) information contained in the current sensitivity matrix and the current correlation patterns of the parameters are used to make changes to the zonation before the next optimisation step. Likewise, in the multi-scale adaptive approach the parameterisation is not prefixed prior to history matching. Instead, a hierarchical search for the correct parameterization is performed at the various steps of history matching based on information derived from the measured data (Yoon *et al*, 1999; Grimstad *et al*, 2003). In other parameterisation schemes, researchers have placed focus on honouring the prior geostatistical constraint while updating the reservoir model parameters by using parameterisation methods like pilot points with Kriging (De Marseily *et al*. 1984), gradual deformation (Rogerro and Hu, 1998, Hu *et al*., 2001, Le Ravalec-Dupin *et al*, 2000) kernel principal component analysis (Sarma *et al.*, 2007) and probability perturbation (Hoffman and Caers, 2005). Some other researchers have made efforts towards finding the key parts of the reservoir which need updating by using some complementary techniques such as the streamline reservoir simulation (Milliken *et al.*, 2001; Agarwal and Blunt, 2003; Maschio and Schiozer, 2004; Singh *et al.*,2014), the adjoint approach (Chen *et al*. 1974; Chavent *et al*. 1975), the data-sensitivity matrix (Rodrigues, 2006), the principal component Analysis (Gavalas *et al*, 1976; Chen *et al.*, 2014), or just choosing only the reservoir region around the wells for updating (Solorzano *et al*. 1973). In streamline simulation, for instance, the prime parameters to be updated during history

matching are the properties of the grid cells along the injector-producer streamline trajectories.

Generally, parameterisation brings in additional modelling error especially in highly heterogeneous reservoirs. If we decide not to parameterise and use the grid block method and consider all grid block properties as independent parameters as done in Dadashpour *et al*. (2007), we are practically faced not only with the problem of large number of unknowns but also with that of significant spatial discontinuities in the reservoir model (Floris *et al*. 2001).

2.2.3 Objective Function

The production and seismic data is incorporated into the history matching workflows through the objective function or misfit. The objective function is a measure of the mismatch between the measured production data to the simulated ones and/or the measured 4D seismic attributes to the simulated ones. In the automated history matching, the optimisation algorithm is used to find better data-fitting models by minimizing the objective function. In joint inversion of production and time lapse seismic data, the effectiveness of data assimilation is dependent on how the differences between measured data and simulated responses are formulated. Measured seismic and production are data of different sources, at different scales and precision, and so, integrating the information coming from both data has been one of the most challenging issues in seismic history matching.

Several forms of objective functions exist in the literature, typically formulated as the squares of the residuals which can be sum-of-squares, least-square and weighted least-square. For any given model, *m*, the misfit of the model prediction, *g(m)*, and the observed data, *do*, can be formulated as a general L2 norm which also considers the noise statistics. Tarantola (2005) defines the general L2 norm of the objective function as:

$$O(m) = (g(m) - d_o)^T C_D^{-1}(g(m) - d_o) + (m - m_p)^T C_p^{-1}(m - m_p) \quad (2.1)$$

Where the covariance matrix C_D is included to reflect the data and modelling error and and C_p is the correlation matrix, m_p is the prior solution. The least-square formulation is popularly used and is known to be suitable for comparing the predicted and observed production data. On the other hand, some researchers believed that the least-square metric was not relevant for evaluating the seismic misfit (Aanonsen *et al*., 2003; Roggero *et al*., 2012). This is because seismic data is obtained at every location in the grid while production data are localized at wells. Tillier *et al*. (2012) suggested a different metric,

called Local Dissimilarity Map (LDM), for evaluating the mismatch in seismic data. The LDM is based on Hausdorff metric which measures the local dissimilarities between the two grids. The method requires filtration and classification of observed and simulated data so that the grids are converted into binary images to identify the presence or absence of a seismic feature. The global dissimilarity between the simulated and observed seismic was computed as the sum of the squared local dissimilarities over the entire grid and then incorporated into the objective function. Le Ravalec *et al*. (2012) showed the robustness of this approach in seismic history matching of a North Sea field. In a similar approach, Obidegwu (2015) used the Hamming distance between simulated and observed binary images of gas distribution to evaluate the objective function in seismic history matching of a United Kingdom Continental Shelf (UKCS) field.

In this work, we use a sum of squares misfit discussed under section 3.6 in Chapter 3. With the multi-objective formulation discussed in section 3.8, (and more extensively in Chapter 7), the seismic and production misfits are formulated as separate sum of squares functions and are handled in multi-objective fashion

2.2.4 Optimisation Methods

In history matching, the role of minimisation of the objective function is performed by an optimisation algorithm. As introduced in Chapter 1, the optimisation algorithm can be any of the three types: (i) Deterministic (or gradient-based), (ii) Stochastic Optimisation methods and (iii) Probabilistic data assimilation. The choice of the optimisation method to adopt considers the exploitative and /or exploratory natures of the different algorithms (Sambridge and Mosegaard, 2002). Generally, the gradient based methods are more exploitative, being faster in updating of models and in convergence, but are liable to be trapped at local optimum. Gradient-based optimization methods were adopted by Gosselin *et al.* (2003), Mezghani *et al*. (2004), Dong and Oliver (2005), Dadashpour *et al.* (2007) and Rwechungura *et al.* (2011) etc. in integrated workflows of seismic and production history-matching of reservoir models. Gradient-based algorithms or deterministic algorithms, such as Steepest Descent, Gauss-Newton and Levenberg-Marquardt algorithms, converge faster to a solution than stochastic algorithms but the single solution provided is determined by the nearest local optimum to the initial guess.

On the other hand, the stochastic–based global methods are more explorative as they give more extensive search of the parameter space and are more suited for finding global solution and for uncertainty analysis. Stochastic optimization methods are known to generate numerous reservoir models or realisations that honour the historical data and are

more suitable in tackling the non-uniqueness of history matching. An example of stochastic optimisation is found in Stephen *et al.* (2006) where multiple models of different reservoir parameter values were generated at each iteration during seismic and production history matching. As the iteration continued, the model probabilities were updated within a Bayesian framework and were then used in guiding the sampling of the model space. The main challenge in applying global algorithms or the stochastic methods is the computational time as expensive and time-consuming simulations should be run on a large number of models. In this research, three different stochastic optimisation methods are used: Neighbourhood Algorithm, Genetic Algorithm and Particle Swarm Optimisation (see section 3.7 in Chapter 3 for dscription of the methods). Our methods of speeding up simulation includes proxy modelling (developed in Chapter 4) and parallel computations (implemented in Chapter 7 and 8).

Like the stochastic optimisation methods, the probabilistic data assimilation generates multiple history matched models but does not perturb the model parameters directly. Instead, it perturbs the models' probabilities while searching for better data-fitting models. Examples of the algorithms in this category include: the Ensemble Kalman Filter (EnKF), the Randomized Maximum Likelihood (RML). EnKF is based on a sequential data assimilating scheme and rely on the Gaussian assumption to generate a posterior ensemble that gives an estimate of uncertainty (Nevadal *et al*., 2005; Gu and Oliver, 2005; Liu and Oliver, 2005; Haugen *et al*., 2006; Li and Reynolds, 2007; Gu and Oliver, 2007; Chen *et al*., 2009). Randomised Maximum Likelihood is a generalization to nonlinear models of Gaussian posterior for sampling the posterior in Bayesian history matching via minimization of a stochastic non-linear objective function (Khaninezhad and Jafarpour, 2013; Chen *et al.*, 2017; Fan *et al.*, 2017)

2.3 Automatic Seismic History Matching (SHM)

Integrating the time lapse information from seismic into the reservoir model presents a challenge in any reservoir management project in which quantitative reservoir model updating is required. To meet the challenge, an automatic iterative workflow in a closed-loop reservoir management is applied. Figure 2.1 shows an integrated workflow, implemented in Stephen (2006), Stephen (2007), Arwini and Stephen (2011) for assimilation of 4D seismic data and production data in history matching and forecasting. Basically, the model parameters are updated in iterative loop using an optimization algorithm to minimize an objective function defined as the weighted sum of the production mismatch and seismic mismatch.

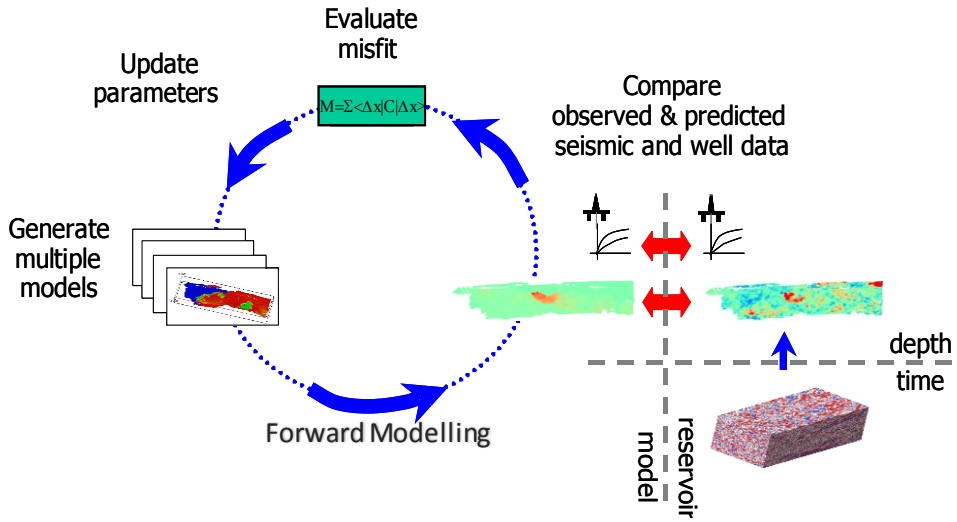

Figure 2.1. Automated Seismic History Matching workflow [Stephen et al. (2006); Stephen et al. (2007)]

Recent efforts to use production data and 4D seismic data as history-match constraints have focused on automatic history matching in fully integrated workflows. For example, Stephen *et al*. (2005) generated multiple models of different reservoir parameter values at each iteration during seismic and production history matching. As the iteration continued, the model probabilities were updated within a Bayesian framework and then used in guiding the sampling of the model space. Gosselin *et al*. (2003), Dadashpour *et al*. (2007) and Rwechungura *et al*. (2011) adopted a gradient-based method for optimization in integrated seismic and production history-matching. Other efforts to use computer-aided seismic and production history matching include Mezghani *et al*. (2004), Jin *et al*. (2011), Aanonsen *et al*. (2009), Fahimuddin *et al*. (2010), Rogerro *et al*. (2007), Skjervheim *et al*. (2005) and so on.

Generally, the seismic history matching workflow starts with a base case reservoir simulation model and follows the iterative optimisation procedure described in Stephen *et al*, 2006, and outlined as follows:

i. Perturb the reservoir model parameters of interest
ii. Simulate reservoir fluid dynamics on the perturbed reservoir model using either black oil model simulator or compositional model simulator to predict saturation and pressure responses
iii. Create synthetic time lapse seismic attribute from the simulation output. Here, the predicted saturation and pressures together with properties such as porosity and solution GOR are used to generate seismic attributes (examples: acoustic

impedance (AI), time traces) at each chosen time of survey through petro-elastic transform (using rock physics model).

iv. Create average maps or volumes of the synthetic attribute and the differences of the maps at different times give the respective time-lapse attribute change. The maps are typically depth-averages of the seismic attribute data volumes evaluated within the reservoir window.

v. Calculate the mismatch between predicted and measured time-lapse attribute as well as the predicted and measured production data using the objective function

vi. Update the model probability (within a Bayesian framework) and use that to guide further perturbations or the sampling of the model space, according to the optimisation algorithm used

vii. Repeat step 'i.' to 'vi.' until the stopping criteria is met.

2.4 Challenges in Automatic Seismic History Matching

Automatic Seismic History Matching is not an easy task as there are many challenges that must be addressed in its implementation. The challenges are embodied in the various elements of the workflow which include objective function, the domain of production and seismic data to compare, upscaling of the seismic attributes to the simulation grid scale or the downscaling of the simulation data to the seismic scale, estimation of data and modelling errors, and computing time and cost.

Because 4D seismic data is prone to non-repeatable noise and errors, the objective function as the weighted sum of seismic misfit and production misfit needs to be defined properly. There must be reliable and objective ways of defining the metric for the mismatch between the model and the different data domains. The current practice is to adjust the weights in the objective function to balance the relative influence of production and seismic data depending on each data set's quality.

Secondly, there is the popular question: which domain is the most appropriate for the comparison of simulated and observed 4D seismic? It is relatively common in recent literature to compare the reservoir simulation results and 4D seismic in the domain of petro-elastic properties such as impedance (Waggoner *et al*, 2002; Gosselin *et al*., 2003; Aanonsen *et al*, 2003; Mezghani *et al*, 2004; El Quair *et al*, 2005; Stephen *et al*, 2006; Roggero *et al*, 2007; Fahimuddin *et al*, 2010). However, the comparison can be in one of several different domains (examples in Figure 2.2).

Sagitov *et al*. (2012) considered different domains and observes that the misfit surfaces are different when performing seismic history matching in different domains. They underlined the need for accurate comparison of predicted and observed 4D seismic data in tackling the non-uniqueness of the inverse problem, and concluded that the use of equivalent domains for observed and predicted data gives a more unique misfit response and better result. Perhaps the impedance domain is considered by many researchers as the best 4D attribute to use because it can be obtained through the well-developed seismic inversion techniques and rock physics modelling. Johnston (2013) points out that the choice of impedance domain avoids the need to calculate the synthetic seismic volume through the error-prone convolutional model at each iteration during the optimization of the objective function. A less common approach is to invert the observed seismic data to pressures and saturations which are compared with the pressures and saturations from reservoirs simulation (Landro *et al*, 2001, Dadashpour *et al*., 2006, Floricich *et al*., 2005). However, like Gosselin *et al*. (2003) implies, the process is considered difficult and it brings its own errors. Whatever domain one chooses to adopt comes with its advantages and disadvantages. If one starts from the simulation model and generate synthetic seismic traces, the main sources of uncertainties come from the petro-elastic model (PEM) and seismic modelling. Seismic modelling can be highly time-consuming especially when full wave simulation is adopted as opposed to the less CPU intensive convolution methods. If one decides to start from measured 4D seismic data to invert for pressure and saturation, the major uncertainties will arise from the process of seismic inversion used to calculate the attributes, and either from calibration issues when empirical inversion is used in place of the more robust rock physics or from the PEM itself (Stephen *et al*., 2006; MacBeth, 2007). The foregoing notwithstanding, the optimum domain for the seismic comparison is still a topic of research.

Furthermore, regardless of which domain adopted for comparison in the objective function, the fit or misfit between the simulated seismic and observed seismic depends largely on the accuracy of the petro-elastic model (PEM). The petro-elastic modelling errors affects the impedance values estimated from the simulation properties like pressure and saturation, and on the other hand, the pressure and saturation values estimated from the inversion of 4D seismic data. Roggero at al. (2007) points to the sensitivity of the pressure effects around the water-injector wells to petro-elastic model and the huge impact that PEM has on the misfit between the simulated and observed seismic.

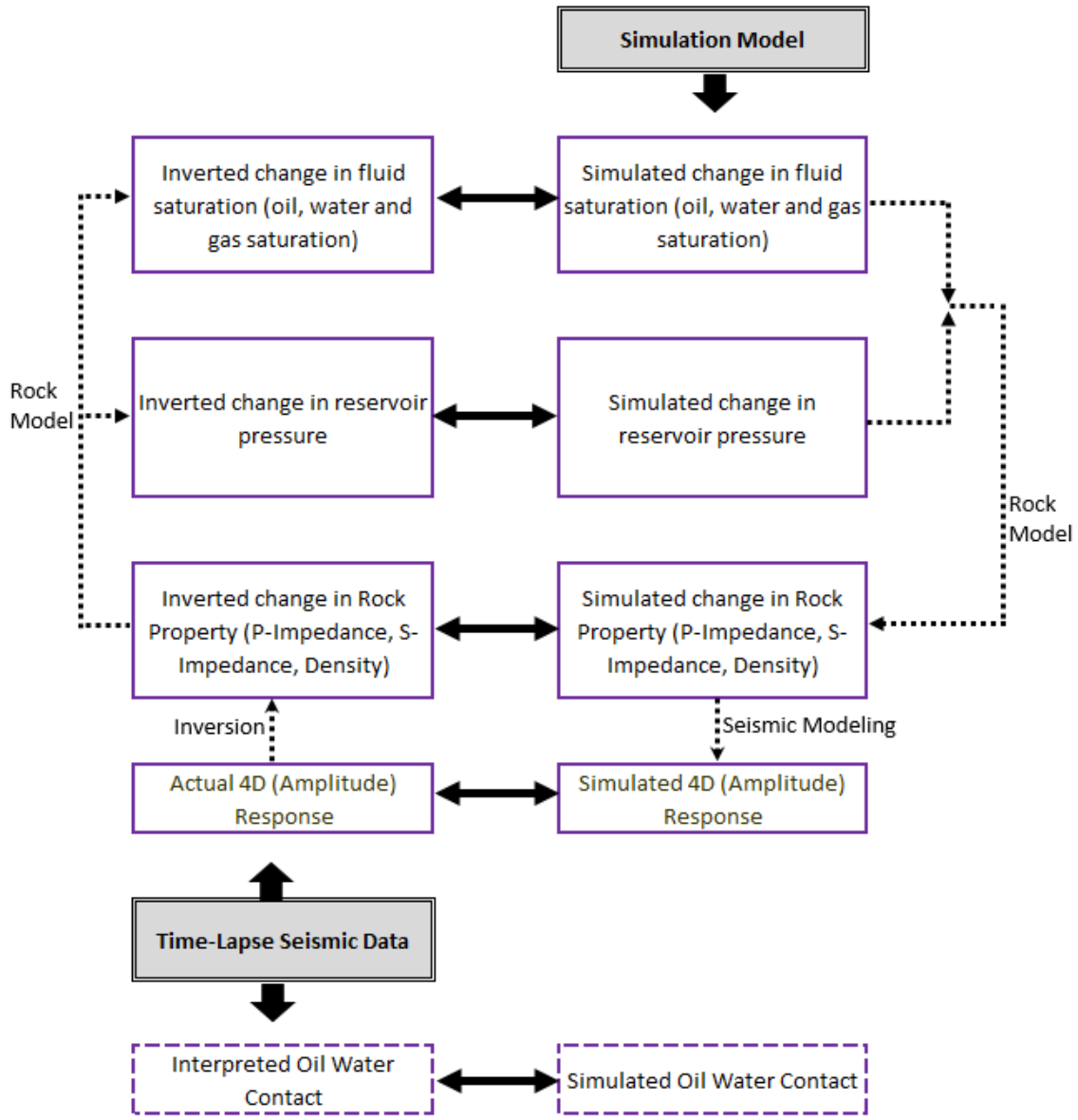

Figure 2.1 Examples of domains for 4D seismic comparison

Another challenge is that of scale. The seismic history matching procedure is carried out in the domain of the simulation grid, so the time lapse information contained in the attribute map need be resampled into the simulation grid. Ullmann *et al*. (2011) is of the opinion that effort is wasted in using 4D seismic data in computer-aided history matching if the original simulation model happens not to be consistent with the information from the original 3D seismic. Upscaled simulation models predict smooth saturation profiles which might not give accurate predictions of the seismic response (Sengupta *et al*., 2003). As a result, a downscaling process from the simulation grid to a finer geologic grid is required to properly model the 4D seismic from simulation. The techniques currently in use for downscaling vary in complexity and sophistication. Mezghani *et al* (2004) use a simple method which subsamples the simulation grid but ignores fine-scale heterogeneity. Castro *et al*. (2006) adopts a flow-based approach to downscaling coarse

grid saturations by reconstructing the fine scale saturation from the local boundary conditions determined from the global coarse scale. Enchery *et al*. (2007) proposes a technique for downscaling pressures and saturations from the simulation scale to geological scale which considers mass conservation as well as subsampling of the simulation grid in trying to capture some fine scale heterogeneity. The challenges presented by downscaling is avoided by Stephen *et al*. (2005) by constructing the geologic and simulation models at the same grid. The predicted impedance is usually obtained at a coarser simulation grid scale compared to the observed seismic scale in the finer seismic grid. To enable comparison, Stephen *et al*. (2005) opted to keep the observed impedance data as intact as possible and downscale the predicted impedance through interpolation. More so, calibration and normalization of seismic data may be required for unbiased quantitative comparison to the predictions of the models (Kazemi *et al*., 2011). The forgoing implies that the introduction of seismic data into the history matching workflow may give additional model and data errors which are difficult to estimate. The errors give rise to a non-zero minimum misfit and affects the accuracy of history matching and predictions.

Seismic history matching is a multi-objective optimisation problem, so the history matching procedure consists of minimizing a misfit function which is a weighted sum of production misfit and seismic misfit. The weights in the misfit function determines the influence that each of the production and seismic data will have in the optimisation process, and choosing the correct weight to create the right balance is a challenge – and because it is user-defined, has largely been subjective. In a Gulf of Mexico time-lapse project, Waggoner *et al.* (2002) chose the weights biased in favour of seismic data in consideration of the high-quality time lapse seismic and to better match the reservoir drainage which was governed more by lateral heterogeneity.

The choice of optimization algorithm is also a challenge in automatic seismic and production history matching. As one tries to match the enormous data, especially while using gradient-based approaches, the simulation can be trapped in a local minimum and may not be able to explore the parameter space adequately. Stochastic methods avoid the local minima, explores the parameter space better, generate multiple models but are more CPU intensive.

Despite the challenges in application, the time-lapse seismic measurements as a concept and technology has evolved through the ages starting from the discussions in 1980s of its potentials in petro-elastic modelling literatures (Nur, 1982; Nur and Wang, 1990) and its pioneering pilot tests in

thermal recovery projects (Pullin *et al*, 1987; Greaves and Fulp, 1987) through the 1990s when the applicability of the tool was demonstrated and economic viability proved for conventional oil reservoirs using legacy data not designed specifically for time lapse interpretation. In the late 90's dedicated time-lapse acquisition commenced (Lumley *et al*., 1994; Jack, 1997). The dedicated 4D seismic shooting proved to improve the repeatability and has led companies into installing permanent seabed cables for seismic monitoring taking advantages of multiple repeated surveys, though its cost-effectiveness had not yet been ascertained (Watts, 2011). The application of the tool has since then been growing and has matured to the extent to be regarded as a reliable reservoir monitoring tool for monitoring fluid contact movement (Wences *et al*., 2004), for qualitative interpretation and manual reservoir-simulation model updates as discussed in Blonk *et al.* (1998), Yilmaz (2001), Staples *et al*. (2005), Calvert (2005), Zachariassen *et al*. (2006), Castro *et al* (2009), Seldal *et al*. (2009), Johnston (2013) etc. and for quantitative assisted/automated history matching as implemented in Gosselin *et al* (2003), Mezghani *et al*. (2004), Stephen *et al*. (2006), Roggero *et al*, (2007), Obidegwu *et al*. (2015), Ray and Landa (2017), Trani *et al.* (2017) etc.

2.5 Time Lapse Prediction Theory

Interpretation practices for time lapse seismic rely on differences in seismic images of same subsurface target in producing field shot at different times to show production-induced changes. Changes in the state of the reservoir during production such as fluid-saturation changes, pressure or stress changes, change in temperature and change in porosity result in changes in elastic properties of the subsurface rocks (velocity and density) leading to changes in seismic response. These changes can be detected on the differences of the seismic vintages (Figure 2.3). The first seismic survey shot before production starts is called a baseline survey, and the subsequent surveys are called monitor surveys as they are acquired for reservoir monitoring.

Prediction of time-lapse response requires that changes in seismic response resulting from production changes be modelled using the reservoir rock physics, otherwise called petro-elastic model (PEM). In this section, we intend to discuss as briefly as possible the theoretical background for linking the production-induced changes in the reservoir with the seismic properties of the reservoir rocks, but we also note that besides production effects, there are other factors that affect the elastic properties of reservoir rocks (Table 2.1).

One of the most important tasks in any time lapse project is to achieve the highest level of repeatability in the seismic vintages. Repeatability is a measure of the similarity between the seismic vintages, and a primary goal of 4D acquisition and processing is to

maximise repeatability (Johnston, 2013). Ideally one would hope that perfect repeatability is achieved so that in taking the differences of the seismic changes the effects caused by all the non-production related factors (listed in Table 2.1) cancel out leaving us with only the anomalies or signal reflection production-induced effects only.

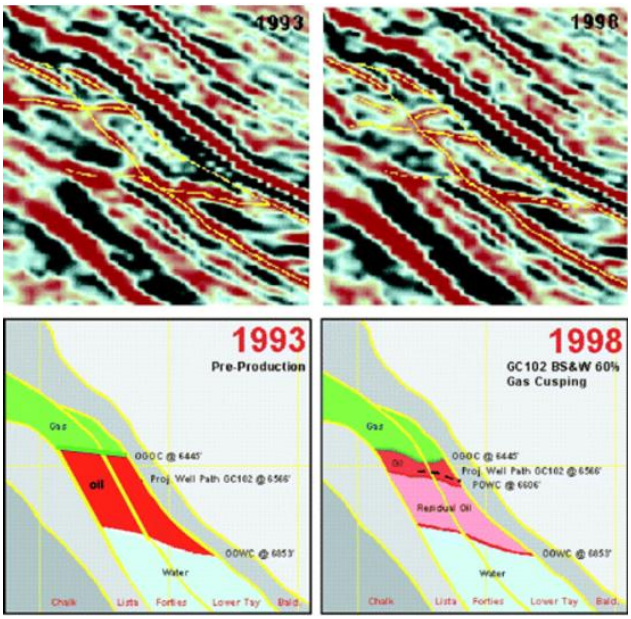

Figure 2.2 Examples of time lapse changes. Observed events include the weakening of the original oil–water contact (OOWC) and original gas–oil contact (OGOC), the downward movement of the OGOC and the appearance of an intra-reservoir seismic event representing the produced oil–water contact (POWC) on the right-hand seismic section. After Kloosterman et al. (2003)

Table 2.1 Factors affecting the elastic properties of reservoir rocks, ordered from top to bottom in increasing importance. In Johnston (2013) after Wang (2001)

Rock Properties	**Reservoir Fluid**	**Environment**
Compaction	Viscosity	Frequency
Consolidation history	Density	Stress History
Age	Wettability	Depositional Environment
Cementation	Fluid Composition	Temperature
Texture	Phase	Reservoir Process
Bulk Density	Fluid Type	Production History
Clay Content	Gas/Oil, Gas/Water values	Layer Geometry
Anisotropy	Saturation	Reservoir Pressure
Fractures		
Porosity		
Lithology		
Pore Shape		

Seismic Waves and Rock Physics

At its most fundamental level, time lapse seismic is simply an image of pressure and saturation changes due to production of hydrocarbons, recorded as changes in seismic amplitude and travel time which will be captured in the seismic rock physics model in terms of the seismic wave velocity. There are two kinds of seismic waves in reservoir rocks: compressional, or P-waves and shear, or S-waves, and their respective velocities (P-wave velocity *Vp*, , S-wave velocity *Vs*) and impedances (P-wave impedance *Ip*, S-wave impedance *Is*) are defined in terms of the bulk modulus *K*, shear modulus μ, and density ρ as follows.

$$V_p = \sqrt{\frac{K + \frac{4\mu}{3}}{\rho}} \tag{2.2}$$

$$V_s = \sqrt{\frac{\mu}{\rho}} \tag{2.3}$$

$$I_p = \rho V_p \tag{2.4}$$

$$I_s = \rho V_s \tag{2.5}$$

Impedance contrasts occur in the subsurface at the plane interface between two thick elastic layers (for example gas-water interface, oil-water interface, shale-sand interface etc) forming 'elastic' boundaries at which reflection of seismic waves occur. It is this reflection that is recorded at the surface during seismic acquisition. For seismic wave traveling from a thick elastic medium 1 to medium 2, the normal incidence reflectivity, R_{12}, is defined as (Mavko *et al., 2009*):

$$R_{12} = \frac{\rho_2 V_{p_2} - \rho_1 V_{p_1}}{\rho_2 V_{p_2} + \rho_1 V_{p_1}} \tag{2.6}$$

The modelling of seismic gathers is fundamentally the convolution of the reflectivity and a wavelet (Figure 2.4) which in its simplest form is the 1D convolutional model (Yilmaz, 2001) given as follows:

$$s(t) = w(t) \otimes R(t) + \epsilon(t), \tag{2.7}$$

where $s(t)$ is the seismic trace, $w(t)$ is the seismic wavelet, $R(t)$ is the reflectivity, $\epsilon(t)$ is a random noise, and $\otimes$ is the convolution operator.

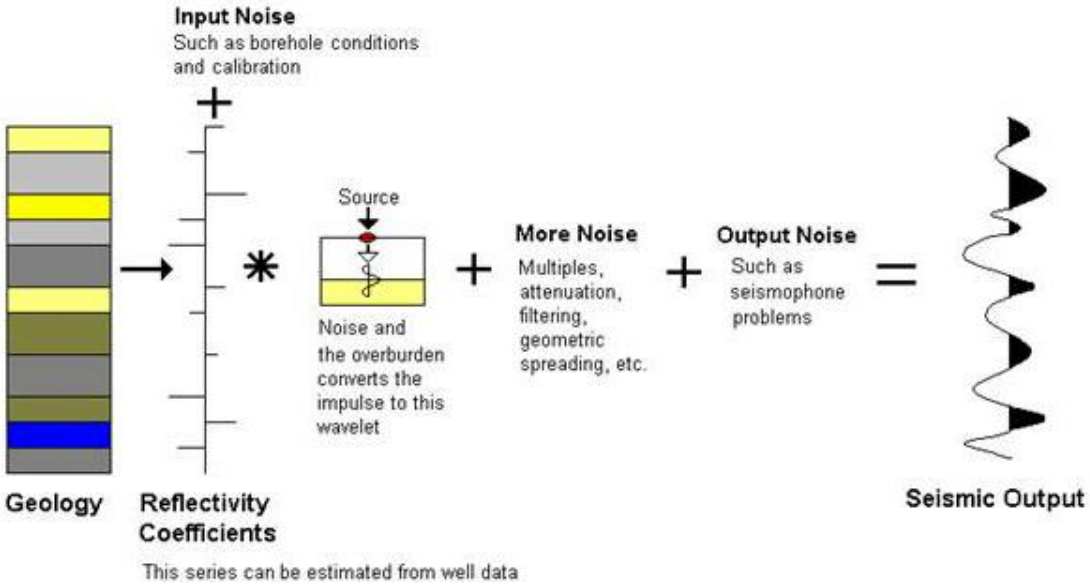

Figure 2.3 The convolution model: seismic trace is equal to wavelet convolved with reflectivity with noise added. After Walden and White (1998)

Time Lapse Effect from Saturation Change

One form of the Gassmann's equation (Gassmann, 1951) for calculating the saturated bulk modulus of a rock at a given reservoir condition and fluid type is:

$$K_{sat}^{r} = K_{dry}^{r} + \frac{\left(1 - \frac{K_{dry}^{r}}{K_{gr}^{r}}\right)^{2}}{\frac{\emptyset}{K_f} + \frac{1-\emptyset}{K_{gr}^{r}} - \frac{K_{dry}^{r}}{{K_{gr}^{r}}^{2}}} \tag{2.8}$$

Where $\emptyset$ is the porosity and K_{dry}, K_{sat}, K_{gr} and K_f are the bulk moduli of the dry-rock-frame, saturated rock, mineral matrix and pore fluid respectively. The subscript r identifies rock type (sand or shale). The effective fluid bulk modulus is given by Reuss average, often referred to as Wood's equation, as a saturation weighted harmonic average of the different phases in rock pore space:

$$\frac{1}{K_f} = \frac{S_w}{K_w} + \frac{S_o}{K_o} + \frac{S_g}{K_g} \tag{2.9}$$

where S_g, S_o, and S_w are values of the gas, oil and water saturations in the cell respectively, and K_g, K_o, and K_w are values of the gas, oil and water bulk moduli respectively. Shear modulus is independent of the pore fluid saturation, so that:

$$\mu_{sat}^{r} = \mu_{dry}^{r} \tag{2.10}$$

where μ_{sat}^{r} is the fluid-saturated shear moduli.

The density of the saturated rock can be simply computed with the volume averaging equation (mass balance).

$$\rho_{sat} = (1 - \emptyset)\rho_{dry} + \emptyset\rho_f \tag{2.11}$$

$$\rho_f = S_w\rho_w + S_o\rho_o + S_g\rho_g \tag{2.12}$$

where $\rho_{sat}, \rho_{dry}, \rho_f, \rho_w, \rho_o, and\ \rho_g$ are the densities of saturated rock, dry rock, fluid mixture, water, oil, and gas respectively. *Sw*, *So*, *Sg*, *Kw*, *Ko* and *Kg* may be obtained using Batzle and Wang (1992). Some assumptions implicit in the Gassmann's equation are discussed in Kuster and Toksöz (1974), Wang (2001), Mavko *et al*. (2009), Grechka (2009). The major implication of the assumptions is that the bulk modulus calculated using Gassmann equation is usually lower than those measured in the ultrasonic laboratory or measured with a sonic-logging tool. Wang (2000) extensively compares the wave velocities calculated using Gassmann equation to those measured in the laboratory and noted the dependency of the results on the pore aspect-ratio. He revealed that the Gassmann-predicted velocities matches laboratory-measured seismic velocities in unconsolidated clean sands and sandstones (with high aspect ratio/ high interconnectivity) at high effective pressures but not for rocks of low aspect-ratio where significant wave dispersion occurs at very low frequencies, and the disparity in results widen when the rocks are saturated with high-viscosity fluids. Wang (2000) concluded that rocks with pores of low aspect-ratio gives velocities measured at seismic frequencies to be greater than Gassmann-calculated velocities but less than laboratory-measured velocities. On the other hand, comparison of fluid displacement effect on seismic properties shows that the laboratory-measured velocities matches the Gassmann-predicted velocities for compressional waves in sands, sandstones and dolomites, but for shear velocities the predictions using Gassmann equation gives slightly greater fluid effect than the laboratory measured (Figure 2.5). The Gassmann-predicted and the laboratory-measured effects of fluid displacement (in Figure 2.5a) are roughly in agreement and it might be safe to conclude that they can be directly applied to time lapse studies and interpretation. The explanation to the observed match between the predicted and the measured is that fluid displacement conforms to a large extent with the Gassmann assumptions, as only the fluids in large pores that are highly connected gets swept by the displacement process

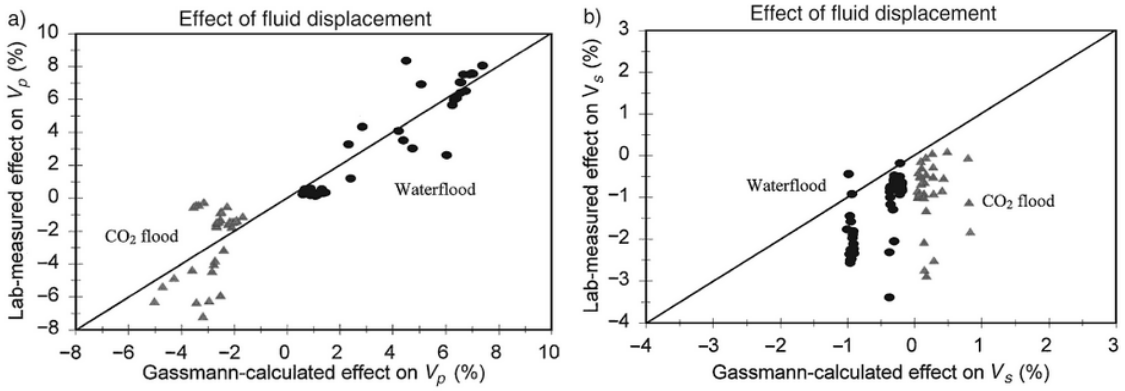

Figure 2.5 Comparison of the Gassmann-predicted effects of fluid displacement on seismic properties to Laboratory-measured effects using two displacement scenarios (waterflooding and CO_2 flooding) for a) Compressional wave velocity, V_p b) Shear wave velocity, V_s in sands, sandstones and dolomites. The waterflooded sandstones and sands are shown in solid circles while the CO_2-flooded dolomites are shown in grey-shaded triangles. (Wang, 2000)

.

There are many other models for fluid substitution reviewed in Mavko *et al* (2009) including the Biot theory (Biot, 1956) which extends the Gassmann equation to the full frequency range. With Biot theory, unfortunately, the difference in seismic velocity predicted between nil and infinite frequencies is in most cases less than 3% for most reservoir rocks (Winkler, 1985; Nur and Wang, 1990). Consequently, Gassmann's equation, instead of the full frequency Biot's theory, is still the popular model for fluid substitution (Wang, 2000).

If the Gassmann assumptions are taken to be valid, then the equation predicts the changes in the acoustic velocity of different homogeneous fluid systems as shown in Figure 2.6. Contrast in fluid compressibility (or moduli) and density influences the level of the dependence of the acoustic velocity on the fluid saturation, and for gas/water system, the contrasts in moduli and density is much more pronounced resulting in high sensitivity of velocity to gas saturation. At first, as the gas saturation increases, the P-wave velocity decreases drastically because the moduli of gas K_g dominates the calculation of K_f (using Equation 2.8) even at a small amount of gas in water. After a few percentage points of gas saturation, at the limit as K_f approaches K_g, velocity begins to increase as the gas saturation increases as the effect of decrease in density of the rock dominates the effect of moduli in Equation 2.1. As the P-wave impedance is the product of density and velocity, it continues to decrease with increasing gas saturation. In the case of normal light oil/water systems, velocity decreases with increasing oil saturation though not drastically as in the case of gas/water system (because the contrast in moduli and density is less in oil/water system than in gas/water system). And for heavy oils, where the moduli

and density are approximately equal, velocity is almost insensitive to the oil saturation change.

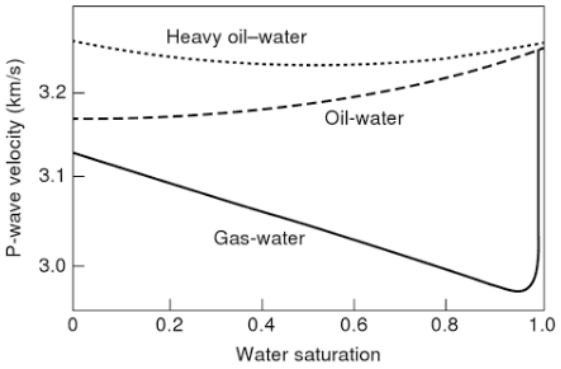

Figure 2.6 Changes in P-wave velocity predicted using Gassmann equations for three different homogeneous fluid systems of contrasting moduli and density. After Johnston (2013)

In order to apply the fluid substitution (Equation 2.7) practically, the acoustic properties of reservoir fluids (bulk modulus and density need to be known or determined as they are affected by production-induced changes in composition, pressure and temperature. Fortunately, there are some reliable empirical relations developed through a combination of the knowledge of equations of state, laws of thermodynamics, laboratory measurements and correlations based on laboratory data in Batzle and Wang (1992), Han and Batzle (2000), Han *et al* (2008) which are widely used in the industry for seismic modelling. The dependencies of the acoustic properties of fluid on production-induced effects are illustrated in Figures 2.7 - 2.10, and summarised in Table 2.2.

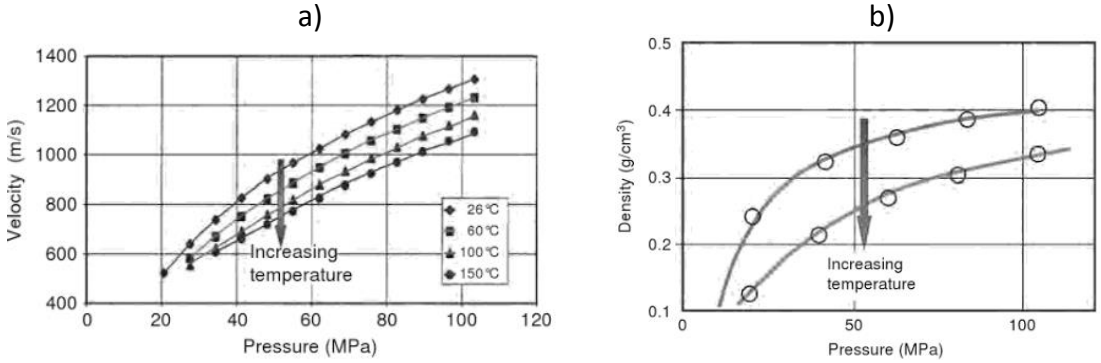

Figure 2.7 Dependency of reservoir gas acoustic properties on pressure at different temperatures, plotted for a) Acoustic velocity and b) Density of gas. After Han and Batzle in Johnston (2013)

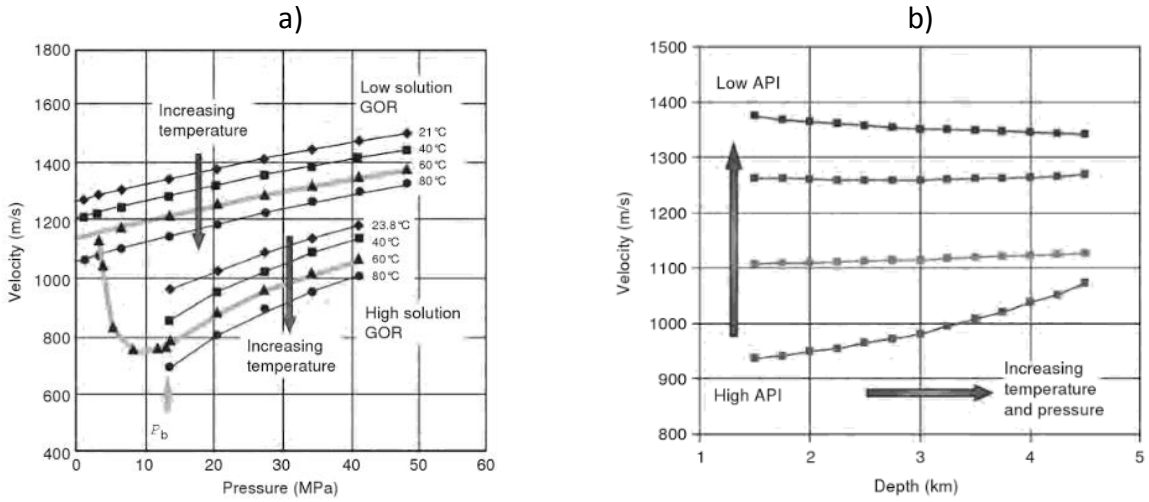

Figure 2.8 Dependency of reservoir oil acoustic velocity on a) pressure and temperature plotted for dead oil (oil of low solution GOR) and live oil (oil of high solution GOR): As the pressure falls below the bubble point of the live oil (P_b = 13MPa illustrated for live oil at 60ºC), ex-solution of gas occurs leading to increase in acoustic velocity towards that of dead oil, b) depth and composition: pressure and temperature increase with depth, and low gravity oil velocity is affected more by temperature variation while low gravity oil velocity is affected more by variations in pressure. After Han and Batzle in Johnston (2013)

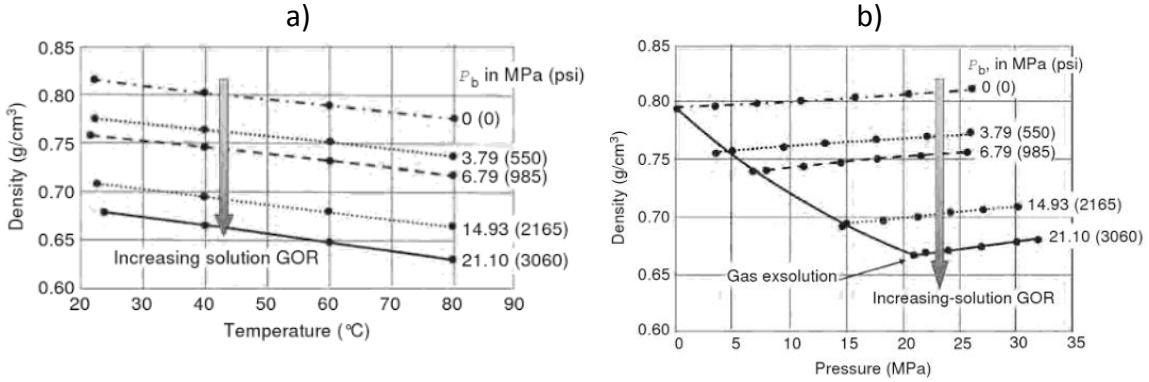

Figure 2.9 Dependency of density of reservoir oil for different solution GORs (high solution GOR corresponds to high bubble point) on a) Temperature: As the temperature increases, or /and as the solution GOR increases, the density decreases and b) Pressure: below bubble point gas ex-solution results in increase in density of oil. After Han and Batzle in Johnston (2013).

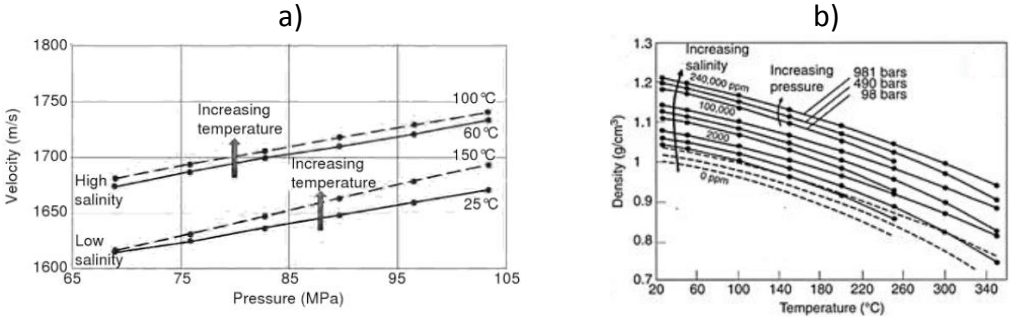

Figure 2.10 Dependency of reservoir brine (saline water) acoustic properties on pressure at different temperatures, plotted for a) Acoustic velocity in the high salinity case and in the case of low salinity: increase in temperature results in slight

increase in velocity and b) Density of brine: temperature variation affects the brine density more than pressure. After Han and Batzle in Johnston (2013)

Table 2.2 The effect of increasing values of reservoir pressure, temperature and fluid composition on acoustic properties of the fluid. After Johnston (2013)

Fluid Properties	P-Wave Velocity	Density
1) Reservoir Gas		
Increasing Pressure	Increase	Increase
Increasing Temperature	Decrease	Decrease
Increasing Gas Gravity	Increase	Decrease
2) Reservoir Oil		
Increasing Pressure	Increase	Increase
Increasing Temperature	Decrease	Decrease
Increasing Solution GOR	Decrease	Decrease
API Gravity	Decrease	Decrease
3) Brine		
Increasing Salinity	Increase	Increase
Increasing Pressure	Increase	Increase
Increasing Temperature	Slight Increase	Decrease

The effect of mineralogy and porosity

It is not completely true that time-lapse seismic technique cancels out the geology (Johnston, 2013) as the degree of changes in elastic properties induced by changes in fluid saturation and pressure is also dependent on lithology, porosity and clay content of the reservoir rock, which may give rise to a geologic overprint on the time lapse signal. The dependency of elastic properties (P-wave velocity) of clastic sedimentary rocks on porosity and shale volume (V_{sh}) is demonstrated in Figure 2.11, where p-wave velocity decreases as porosity increases for clean sands, and for this particular case p-wave velocity decreases as V_{sh} increases (which is expected in North Sea where high porosity, unconsolidated Tertiary or younger shales are dominant).

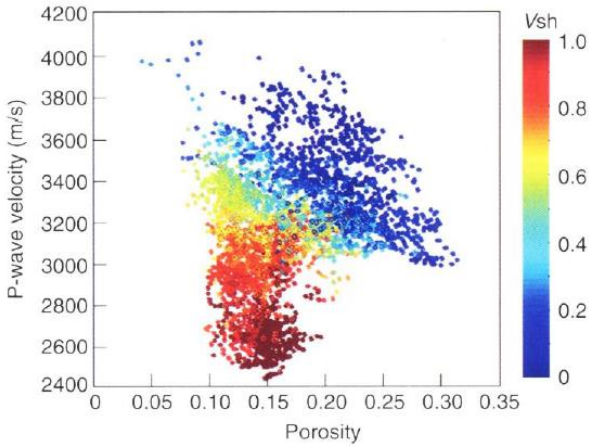

Figure 2.11 Dependence of P-wave velocity on porosity for different values of shale volume plotted for a North Sea well log data. For clean sandstones (blue points), velocity decreases as volume fraction of shale increases. After Johnston (2013)

Pressure Dependence of the dry bulk modulus

Apart from affecting the fluid acoustic properties (velocity and density) and gas saturation, changes in reservoir pressure may result in changes in the reservoir-rock framework thereby affecting the porosity and the dry bulk and shear moduli of the rock. There are many ways of predicting the pressure dependence of an acoustic property (dry bulk or shear modulus or velocity) including methods based on theoretical physics (Kuster and Toksoz, 1974, Nur and Dvorkin, 1996), methods based on empirical measurements (eg. in Eberhart-Phillips *et al*., 1989). Velocity measurements may be done in the laboratory using dry core samples (to avoid dispersion effects), then saturating them for fluid substitution using Gassmann equation, and ultimately fitting a function (Equation 2.13) to the velocity vs differential pressure data, or to the dry bulk modulus versus differential pressure data, which typically follows exponential trend (Figure 2.12)

$$V_p = V_{inf}\left(1 - Ae^{\frac{-P_{eff}}{P_c}}\right) \tag{2.13}$$

Where the constants V_{inf}, A and P_c are determined from the curve fitting. We use a variant of the above equation to determine dry bulk modulus in this work.

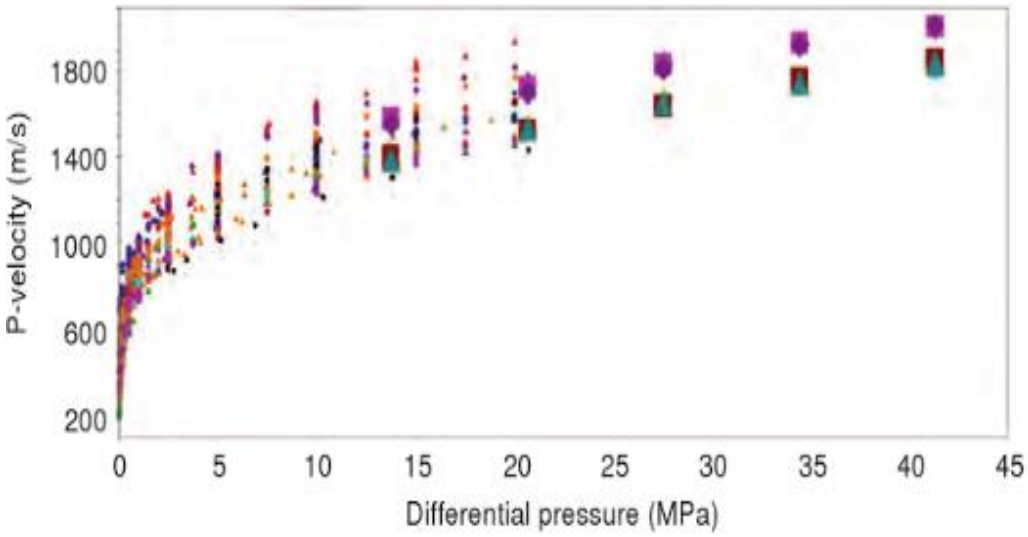

Figure 2.12 Pressure Dependence of P-wave Velocity for dry, clean, unconsolidated sands showing similar trends from several experiments. After Johnston (2013)

2.6 Time Lapse Seismic Modelling

In time lapse projects, seismic response studies are typically aimed at assessing the time lapse signal over a wide range (or full range, if possible) of changes in rock properties, saturation, and pressure.

In this work, seismic modelling finds application in the seismic response studies to predict the seismic response for different reservoir properties and production scenarios which is

then compared to the observed/measured seismic data in order to interpret the observed changes in the time lapse seismic. A detailed review of methods for modelling seismic response can be found in Margrave and Manning (2004), but a brief overview of practical methods of seismic modelling is given in this section for the case of one-dimensional modelling (using well log data) and 3-dimensional modelling (using simulation to seismic modelling). Modelling the 4D seismic signal is then based on differencing modelled signals of individual surveys as in the case of observed data: surveys are acquired independently (Sagitov and Stephen, 2014).

2.6.1 Well Log to Seismic

Johnston (2013) points out the two approaches to time lapse modelling using well logs: 1) Differencing the seismic-gather models predicted with well logs, 2) Applying systematic changes to the reservoir properties.

In approach '1', the well reflectivity is computed from the sonic and density logs (refer to Equation 2.4) and convolved with a wavelet (Equation 2.7) to produce the well synthetic seismic. The wavelet is obtained through standard seismic-well tie process and by spectral smoothing over a certain frequency (say 10 Hz) and averaging over a range of seismic traces. Johnston (2013) demonstrates the value that could be gained from seismic-gather models derived from well logs noting that the results could suggest alternative interpretation approaches to facilitate time lapse detectability: For example, the use of 3NMO-corrected seismic-gather models in the case of Figure 2.13 could help one decide on interpreting far-angle partial stacks, rather than near-angle stacks or full-angle stacks because far-angle stacks might yield a more detectable time-lapse signal (higher change in amplitudes). The red vertical bar in Figure 2.13 denotes the reservoir sand window while the red well-log curve is the original p-wave velocity log. Here it is the relative change in the amplitude that matters and Class III AVO response is not needed for a strong time-lapse signal. The amplitude colours observed below the reservoir are the results of time-shift (arrival time differences) caused by the change in velocity within the reservoir. For the upper reservoir sand, whereas the baseline survey (original well log) exhibits a class IIP AVO (Amplitude versus offset) response, the monitor show class I, while the difference reveals increase in amplitude increasing as offset increases.

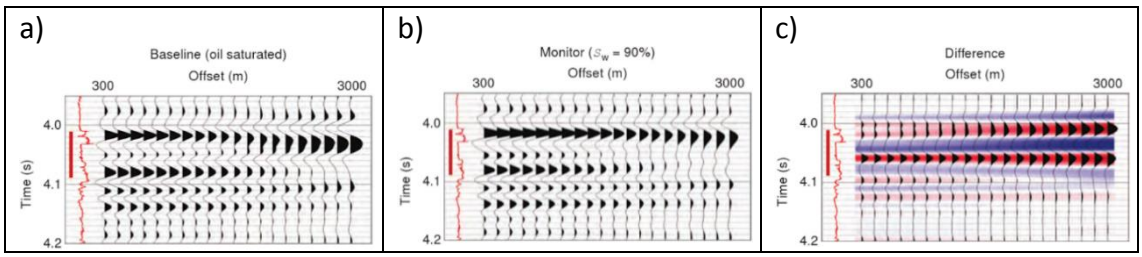

Figure 2.13 Normal-Moveout-corrected Seismic-gather modelled from well logs for a) baseline survey (oil saturated reservoir) b) Monitor Survey (10% oil saturation) c) The difference (monitor minus baseline) showing increase in amplitude with increasing offset. After Johnston (2013)

The second approach is exemplified by deriving the synthetic seismic traces from the same well logs (as in approach '1' above) through the application of systematic changes in: i.) water saturation over the entire reservoir interval (Figure 2.14 a), ii.) Vertical water sweep (Figure 2.14 b). The seismic differences relative to the first trace in Figure 2.12 a) and Figure 2.14 c are also shown respectively to highlight the importance of seismic response study in determining the degree of saturation change required to observe a time lapse signal (Figure 2.14 c), and the importance in determining the minimum sweep required to detect time lapse signal (Figure 2.14 d).

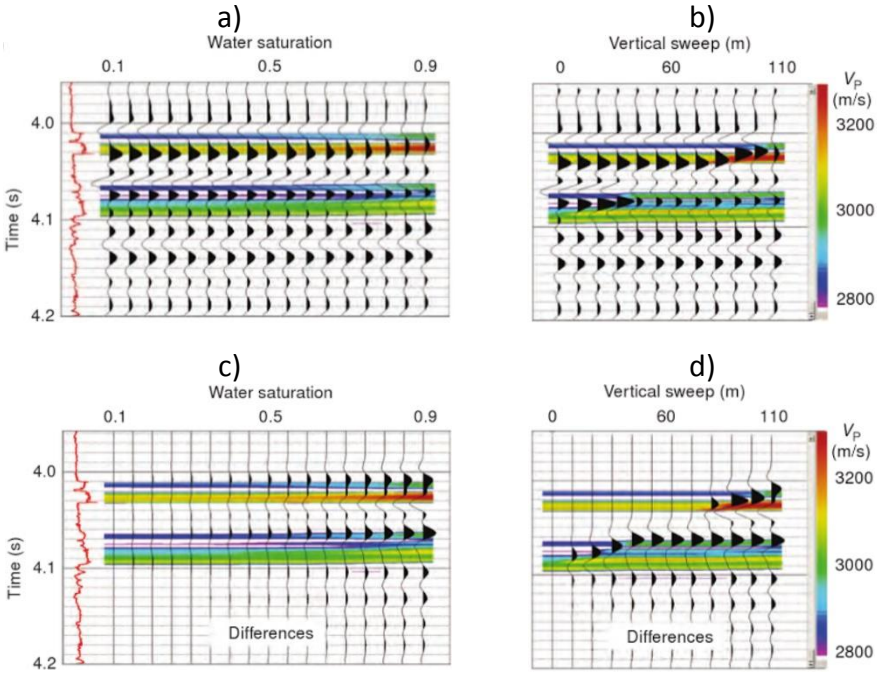

Figure 2.14 Synthetic seismic traces derived from the same well logs in Figure 2.11 with systematic changes in saturation and sweep, and coloured by P-wave velocity in the background a) increasing water saturation in the entire reservoir sands, b) increasing vertical sweep, c) amplitude differences relative to the first trace in part a) (Note: the first trace is at initial water saturation Sw = Swirr= 10%), d) amplitude differences relative to the first trace in part b) (Note: the first trace is at initial water sweep = 0 m). After Johnston (2013).

2.6.2 Reservoir Simulation to Seismic (Sim-to-Seis)

Sim-to-Seis process involves running the flow simulation in time to predict saturation and pressure changes, due to production activities, which in turn can be converted to seismic attributes of interest via petroelatic transform. In other words, the process relates the properties that describe the geologic model (porosity, facies etc) and the reservoir simulation model (saturation, pressure etc) to the elastic properties of the reservoir (P-wave velocity, S-wave velocity, and density), using petroelastic model (Johnston, 2013). This method is preferable to well-log based time-lapse modelling because it offers scenarios to address lateral-sweep interpretation which cannot be done with the well-logs. However, the results of Sim-to-Seis model is as good as the reservoir model, and we recognise that both the geologic and simulation models are wrong but remain the most useful information to start with. Detailed descrption of the steps in Sim-to-Seis approach to time-lapse modelling is given in Johnston (2013). Acoustic changes (ie. changes in density and velocity) can be modelled, or obtained from the reservoir flow simulation, and convolved with the wavelet to give the time lapse change

Time lapse seismic response studies could suggest the 'best' interpretation approach that enhances detectability. It is mostly believed that interpretation based on full-stack difference data is the most appropriate for time lapse amplitude interpretation because it has greater S/N (Signal-to-Noise) ratios than partial-stack data. However, Johnston (2013) points to the benefits of partial-angle stacks in elastic inversion of time lapse seismic, noting that full-stack data is not a good representation of zero-offset response (even in the case of saturation dominated changes which is driven primarily by changes in P-wave impedance), and so the inverted full-stack difference data (or quadrature-phase data) is best suited for qualitative interpretation of acoustic change (impedance change).

2.6.3 Seismic Inversion Methods

Several workflows have been adopted in performing time-lapse inversion, including: i.) those based on taking the difference of baseline and monitor impedances derived from independent inversions of the baseline and monitor seismic vintages (see Sarkar *et al*, 2003), ii.) those based on coupled inversion of the baseline and monitor seismic data, in which case a baseline impedance model obtained from the inversion of the baseline data is used as an initial model to constrain the inversion of the monitor seismic data (see Sarkar *et al*, 2003), and iii.) those based on inversion of an already differenced seismic data (see Sarkar *et al*, 2003 and El Ouair., 2005). The different inversion methods are broadly categorised in Figure 2.15, while a generalised workflow for integrating seismic

data and well log data during seismic inversion is shown in Figure 2.16. No matter the workflow adopted, the implementation requires an inversion algorithm, and there are two main issues of importance in calculating a subsurface impedance model from the seismic data: i.) the frequency in seismic data is typically limited in the range 10 Hz to 80 Hz (it is bandlimited) and therefore lacks the original low and high frequency data which the well log data has., ii.) the impedance model solution from seismic inversion is non-unique.

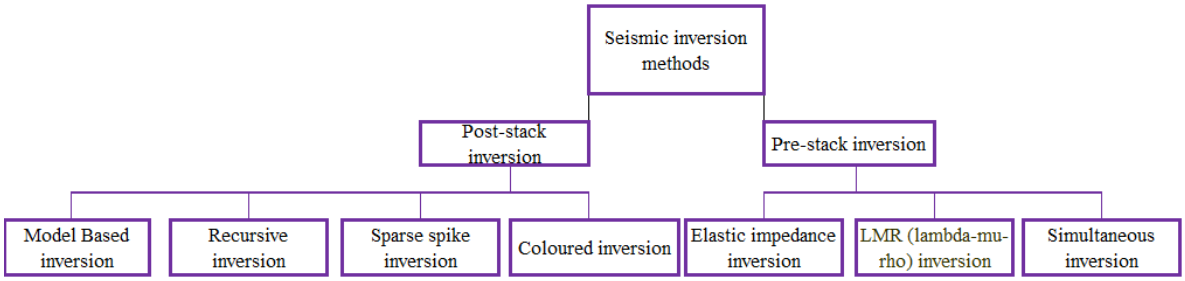

Figure 2.15 Seismic inversion methods

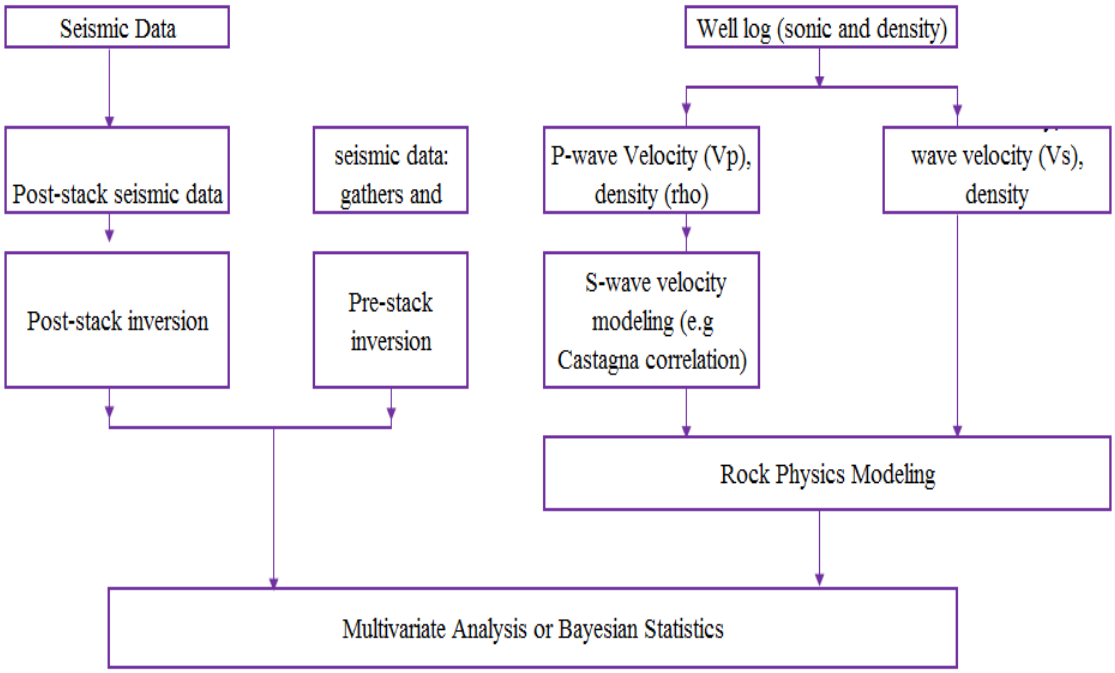

Figure 2.16 Generalised workflow for integrating seismic and well log data in seismic inversion

Because seismic data is bandlimited, it is missing information that should be contained in a high frequency data as well as the information in low frequency data. It is important to recover the missing frequencies as much as possible during inversion, and since log data contains frequencies higher and lower than that of seismic data, it is a good idea to use the log data in constraining the inversion. The use of frequencies higher than the frequency in the seismic data may, however, introduce too much model constraint (or

influence) on inversion that cannot be validated by the true seismic data. Inversion techniques estimate the values of impedance from seismic data by removing the wavelet that originated from the seismic acquisition and processing. Treated as a bandpass filter, the wavelet is scaled by well control to restore the missing low frequency component. A good practice will be to honour the well log data for the low frequency band, and honour the layered geology (for high frequency band) and select the model that gives the least number of layers: sparse reflectivity assumes that the earth model consists of a number of homogeneous layers.

An algorithm used in seismic inversion can either yield deterministic result or stochastic result depending on whether it yields a single solution (deterministic) or many realisations of the model solution (stochastic). Some inversion algorithms are called Model-Based as they use the convolutional model theory or any other seismic forward modelling technique to predict the model seismic response which is then compared with the observed seismic data iteratively to obtain a good match. Yet there are some other algorithms built to estimate the subsurface impedance model directly from the seismic trace by: i.) integration of seismic traces in a process called recursive method, ii.) coloured inversion. The output of an inversion process can be in absolute properties (example: absolute impedance estimated through a broad-band process), or it can be in the form of relative properties (for example, relative impedance calculated in a bandlimited inversion process). For more detailed review of different kinds of inversion methods see Russell and Hampson, 1991; and/or Curia, 2009. Inversion can be pre-stack or post-stack depending on the input seismic data. A brief description of each of the different inversion methods follows.

2.6.3.1 Model-Based Inversion (MBI)

MBI starts with the geological or earth model (example: initial impedance model derived from well logs) which is then perturbed until the error between the synthetic seismic created by the perturbed model and the real seismic data is minimised. The mathematical basis for the inversion is to minimise the function below (Geoview HRS-9, 2014):

$$J = w_1(S - W * R) + w_2(M - H * R) \qquad (2.14)$$

Where: S = the seismic trace

W = the wavelet

R = the final reflectivity

M= the initial guess model impedance

H = the integration operator which convolves with the final reflectivity to produce the final impedance

Equation 2.14 is a multi-objective function with conflicting objectives and the weights, w_1 and w_2, are included to determine how the objectives are balanced. The higher the values of w_1 the more the solution models the seismic trace, and the higher the values of w_2 the more the model solution is forced to honour the initial impedance model.

The general work flow for MBI is outlined in the following steps (Maurya and Sarker, 2016):

i. AI values are calculated at well locations using density and P-wave velocity logs (sonic logs).
ii. Horizons are picked in the seismic section to serve as a control in interpolating impedance values in locations between the wells, and also to provide structural information for model between the wells
iii. The initial AI model is obtained by populating the entire seismic grid with values of impedance calculated through interpolation along horizons and between the well locations
iv. The initial impedance model is divided into layers or blocks of appropriate size (as the blocking interval becomes smaller, the resolution increases but the run time tends to increase proportionally; and block size should not be too small compared to the width of the main lobe of the seismic wavelet (Geoview HRS-9, 2014))
v. Statistical wavelet is extracted from the seismic section.
vi. The wavelet is convolved with the reflectivity (obtained from the layered impedance model) to create the synthetic seismic trace.
vii. Least squares optimization is applied to minimize the objective function (Equation 2.13) which is a metric for difference between the observed and synthetic seismic.
viii. Optimisation is done by modifying the block size and amplitude and repeating step vi (iteratively) until the difference between the synthetic trace and the observed trace is minimised.

2.6.3.2 Bandlimited or Recursive Inversion (RI)

The classical RI was the first type of inversion technique developed to estimate the AI, and is based on recursive calculations using the general impedance-reflectivity equation below for a total *i* layers of impedance (Lindseth, 1979):

$$Z_j = Z_1 * \prod_{J=2}^{i} \frac{1 + R_j}{1 - R_j} \quad (2.15)$$

where R_i is the reflection coefficient at the j-th interface with P-wave impedance Z_j, and Z_1 is the impedance of the first layer.

In this case, each layer's impedance is a function of all the reflection coefficients of the layers above it, and minor errors in those reflection coefficients can cumulatively produce significant errors in the calculated impedance. The cumulative error manifests as long wavelength trends attributable to the lack of low frequency information in the seismic trace (Geoview HRS-9, 2014). "The low frequency component should be extracted from well logs and added to the inversion results", Sagitov and Stephen (2014) points out.

Moreover, Equation 2.15 is valid if a wave normal incidence is assumed, and the seismic trace is a convolutional model so that reflection coefficients can be estimated from the trace by deconvolution. To illustrate the difference in the output from model-based and bandlimited inversion, Russel and Hampson (2006) compared the result of inversion by recursive method and model-based inversion and found that the model-based results were more representative of the geology than the bandlimited results.

2.6.3.3 Coloured Inversion (CI)

Developed by Lancaster and Whitcombe (2000), CI technique is similar to bandlimited inversion but very fast, and does not need a good initial model or a wavelet; rather, it applies an operator in the frequency domain to a seismic trace to transform the seismic trace into impedance. The process involves deriving the frequency spectrum of the AI from well log data and using the derived spectrum to compute the spectrum of the operator. The phase of the operator which is -90^0 allows its integration with the reflectivity series to estimate the impedances. The results of CI is relative AI with + and - values, not the absolute AI of other inversion methods (Geoview, HRS-9, 2014)

The Procedure for fast-track CI is described in Lancaster and Whitcombe (2000) and in Geoview, HRS-9 (2014), and is outlined as follows:

i. The AI data is gathered for all the wells in the field (or all nearby wells) and the impedance and frequency values are plotted on a log-log scale or semi-log scale (Figure 2.17a and b)

ii. A regression line (straight line is fitted through the data to represent the impedance spectrum.

iii. The average seismic spectrum is calculated from the seismic traces around the wells.

iv. The two spectra (impedance spectrum and amplitude spectrum) are used to calculate the coloured amplitude spectrum as below:

$$CIA_f = \frac{Z_f}{\overline{S_f}} \qquad 2.16$$

Where CIA_f is the coloured amplitude spectrum in frequency domain, Z_f is the AI spectrum in frequency domain, and $\overline{S_f}$ is the average seismic spectrum also in frequency domain

v. The calculated coloured amplitude spectrum is combined with the 90° phase shift to create the CI Operator

vi. This operator is convoluted with the seismic traces, to transform the seismic spectrum to the impedance spectrum, resulting in relative AI values.

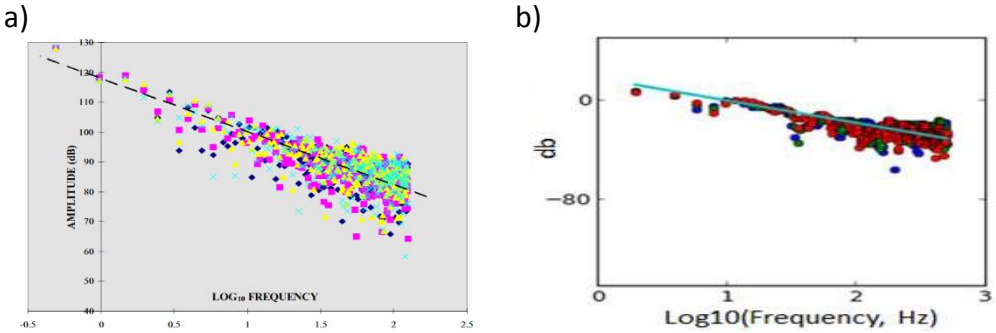

Figure 2.17 Estimating α-values from the spectrum of impedance logs : a) for a real North sea field (After Lancaster and Whitcombe, 2000), b) a synthetic field (After Sagitov and Stephen, 2014).

CI process is a direct transform of the seismic data using a single convolution which implies that the information in the AI domain comes directly from the seismic. The CI result should therefore be viewed as a base case for application of subsequent more sophisticated techniques that utilise constraints and/or initial models such as the model-based inversion.

2.6.3.4 Sparse Spike Inversion (SSI)

As stated in Li (2001), the goal of SSI is to obtain a high-resolution impedance profile from low resolution or band limited seismic data. The inversion technique is designed to meet sparse reflectivity, which assumes that the earth model consists of a number of homogeneous layers, and the model that gives the least number of layers should be

chosen. The resulting high-resolution impedance possesses a broad band of spectrum, displays a blocky structure in time or depth domain, directly relates to the petrophysical properties of rock formation (thus, lithology), and therefore is more suitable for the interpretation work than the original seismic data.

Maurya and Sarker (2016) compared the results of inversion of post-stack seismic data from the Blackfoot Field, in Canada, using the different inversion techniques described so far, including MBI, RI, CI, SSI (Figure 2.18). The results show that all the methods give good and consistent results, and all resolved the low-impedance zones corresponding to the target gas sand within a channel. However, Maurya and Sarker (2016) showed that the MBI yielded the model with the highest correlation coefficient and least RMS error indicating that it is the best inversion technique for Blackfoot Field seismic data.

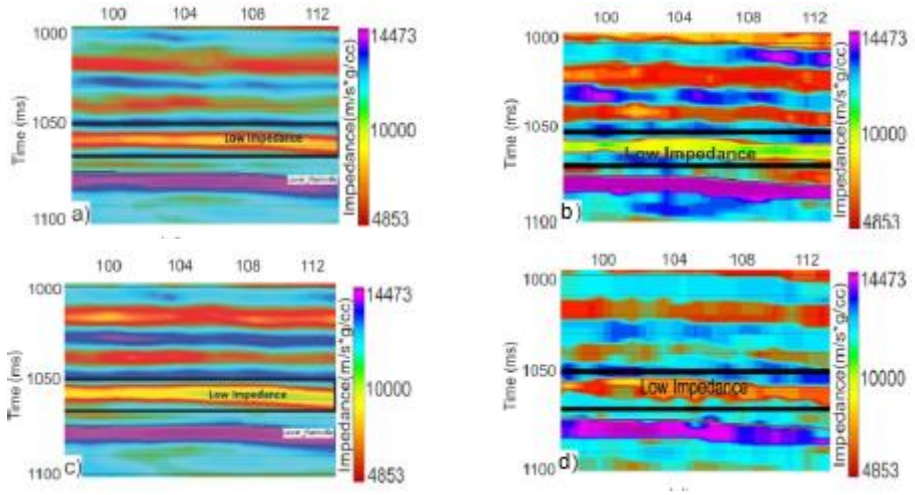

Figure 2.18 Cross-section of inverted impedance for Blackfoot field using a) Model-Based Inversion, b) RI, c) Linear programming SSI and d) CI. The low impedance zone (near 1060ms) highlighted by the rectangle is well-resolved by each of the inversion method, and confirm the presence of reservoir in the channel area at 1060-1065ms time.

2.6.3.5 Neural Network & Genetic inversion (NNGI)

Genetic inversion (GI) combines multi-layer neural networks and genetic inversion algorithm to derive an AI inversion volume given a volume of seismic amplitude cube and well logs. Unlike the methods described previously most of which are based on strong and constraining prior information that are difficult to acquire, the required inputs in the case of NNGI are limited to the seismic amplitude, and the well logs. Typically, AI logs are derived from the respective sonic logs and bulk density logs (AI Log = P-wave velocity log * Bulk Density Logs) of selected wells and are used as training data. This method therefore requires no input wavelet and does not require any initial property

modelling unlike many other poststack inversion methods. It also generates results quicker compared to the other methods.

GI is an advancement on the traditional artificial neural network for property modelling, in that it is still based on the neural network process but combines it with the genetic algorithm to generate a nonlinear multitrace operator. To produce the multitrace operator, a subvolume, or entire volume, of the input seismic is trained against well data (the impedance logs at the well locations). The multitrace operator is then used to invert the seismic data and predict the impedance log responses that best fit to the given well data (Figures. 2.19).

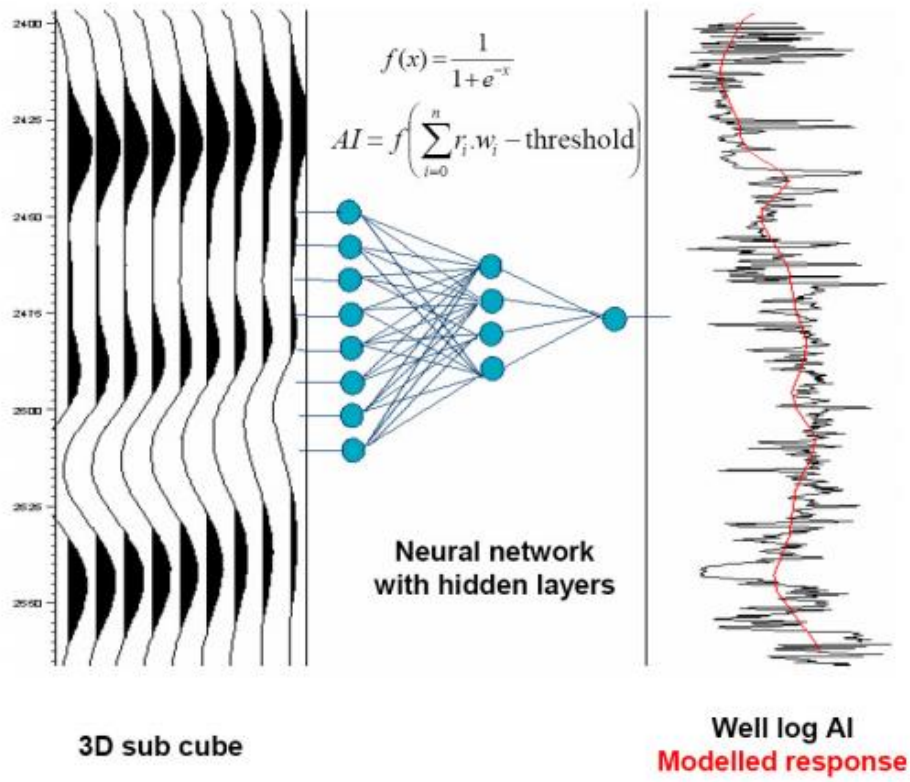

Figure 2.19. Linking the seismic traces and AI Logs through Artificial Neural Networks. After Veeken et al., 2009

To some extent the workflow of GI compares well with that of CI, with notable difference. CI uses a linear algorithm (Lancaster and Whitcombe 2000). The linear mode computes a series of weights derived by a curve fitting procedure that utilizes a least-squares minimization, while in the non-linear mode a neural network is trained, using the selected attributes as inputs. The more complex GI scheme generates improved results, because it better honours subtle changes in the input dataset (Veeken *et al*, 2009). This phenomenon has been demonstrated already by Hampson *et al*. (2001), who pioneered the neural network application for seismic reservoir characterization purposes. Hampson *et al*

(2001) shows how a combination of seismic attributes is used to create a function that links the seismic to the petrophysical property in order to match the given well data (e.g., Hampson *et al*., 2001). The complexity of this multi-attribute method is that it is difficult to define attributes that should be used and the combination varies from volume to volume. It is also difficult to control the prediction quality and there is a chance of neural net overtraining and especially overfitting when the training set is "memorized" in the network (Veeken *et al*., 2009). GI requires a single seismic cube (e.g. poststack migrated true amplitude or AI) and a set of wells with a petrophysical property which has some relation to seismic (e.g., porosity, velocity, bulk modulus).

2.6.3.6 Stochastic Inversion (SI)

Stochastic inversion methods have been developed to generate multiple high-frequency realisation of rock properties from seismic data (Francis, 2002), to overcome the band-limited solution from deterministic inversion (Oldenburg *et al*., 1983). Stochastic inversion was introduced by Haas and Dubrule (1994) using Sequential Gaussian Simulation (SGS), and a fast approach to stochastic inversion was developed by Buland and Omre (2003) using Gaussian PDF. A combination of the two methods (SGS approach and Gaussian PDF) can be found in Doyen (2007), Escobar *et al*., (2007).

The fundamental difference between deterministic and stochastic inversion is that while deterministic inversion techniques produce a single "best" solution, stochastic inversion methods produce multiple realisations of plausible solutions. The deterministic method handles inversion as a least-squares regression problem, while in stochastic inversion, the least-squares inversion technique is extended by formulating the problem using a Gaussian probability density function, PDF (Tarantola, 1987). The SI allows sampling of various scenarios of the input distributions (ie. from the PDF of V_p, V_s and ρ) using the Monte Carlo (MC) or Markov Chain Monte Carlo (MCMC) approach. The input distributions are derived from well log analysis to define the mean and standard deviations of the various inputs (although V_s and ρ can be set as functions of V_p using, for example, Castagna's correlation and Gardiners equation respectively).

The probabilities of the multiple realisations from this approach can be calculated using Bayesian statistics to give probabilistic impedance. In Figure 2.20, the P-impedance results from deterministic inversion are compared to the P10, P50 and P90 P-impedance estimates from probabilistic/ stochastic inversion. The deterministic and P50 probabilistic results are similar at the upper gas reservoir, indicated by the arrows, but different at the lower gas reservoir. The differences in the lower gas reservoir is attributed to the methods

of handling the low frequency inputs as well as layer sampling which differ in the two inversion algorithms (Dennis and John, 2010): the low frequency model input in deterministic inversion is derived from interpolation between well control, while in stochastic/probabilistic inversion the input model is defined by the mean P-impedance and its standard deviation derived from the distributions of the input properties.

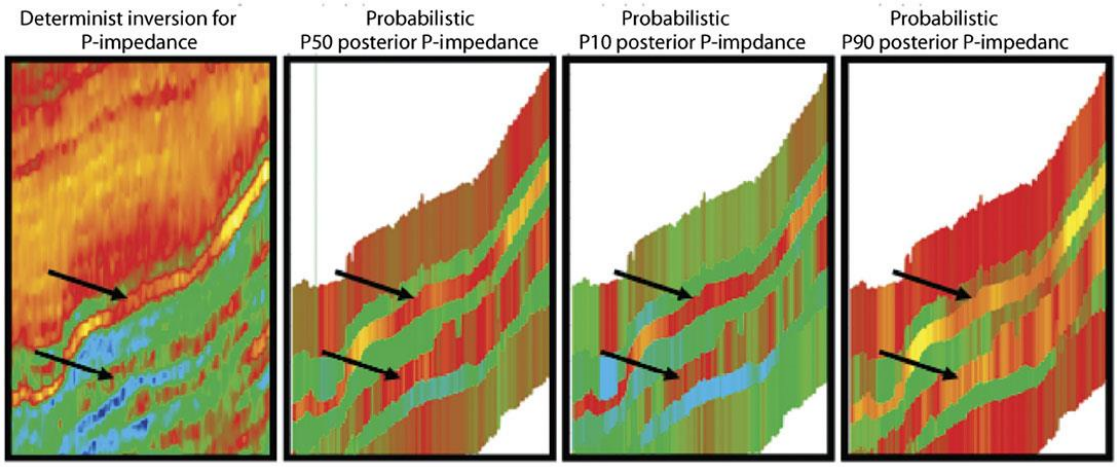

Figure 2.20. P-impedance results from deterministic inversion compared to the probabilistic P-impedance. The arrows indicate two separate gas reservoirs. After Dennis and John, 2010

Chapter 3–Parameter Estimation through Seismic History Matching: The Methodology

Overview

This chapter will describe the automatic history matching workflow, the concepts and methods that have been adopted in this work for history matching using seismic and production historical data. Generally, a good approach to solving inverse problems using history matching should have the essential elements introduced in Chapter 2 of this thesis. The elements which include the forward problem, parameterisation, objective function and optimization algorithms were described briefly in the previous chapter but will be treated in more detail here in the context of the methodology applied in this work. Some results obtained from history matching a synthetic reservoir are presented to set the tone for subsequent works.

3.1 Introduction

In presenting the workflow adopted in this work, this chapter is organised to describe:

- The scheme adopted for parameterisation:
  i. Parameter screening and sensitivity analysis
  ii. Facies Update
  iii. The pilot point method and Kriging
- The reservoir flow dynamics used in generating responses for several combination of parameters
- The rock physics behind the transformation of the rock properties and reservoir dynamic properties to synthetic 4D seismic data.
- The global objective function, and its multi-objective components, adopted in comparing the reservoir response for each combination of parameters and the corresponding history data
- The optimisation algorithm adopted in this work
  i. The Neighbourhood Algorithm (NA)
  ii. The Genetic Algorithm (GA)
  iii. Particle Swarm Optimisation (PSO)

3.2 The Parameterisation Scheme

Information provided by the geology as well as the depletion mechanism play part in the decision to select the likely important parameters to be included in the parameter updating

scheme and/or the locations in the reservoir where modifications in parameters may be needed in the course of history matching. The range of these uncertain parameters is also guided by prior knowledge of geology and drainage mechanisms. This work seeks to adopt some reliable ways of selecting and combining the parameters, which can be applied to any field, so as to reduce the number of simulation runs required for the automatic history matching work efficiently. Two different parameter updating schemes are adopted in this work: single parameter update and the pilot point scheme. The descriptions of the schemes follow.

3.2.1 Single Variable Parameterisation Scheme

This method enables the updates of property multipliers (e.g vertical transmissibility multiplier: MULTZ) directly set up as variables in the input simulation model. The parameterisation scheme enables the replacement of the constants in the reservoir model data file with values selected from the specified parameter range. A single variable is either assigned to cells, layers or regions in the reservoir grid having distinctive properties. There may be as many single variables as the number of sub-volumes of distinct properties but reparameterisation should aim to reduce the number as much as possible and still maintain the overall reservoir characteristics. Each single parameter represents the multiplier of the property of the cells it identifies and can be sampled linearly or on the log scale during history matching. The same multiplier, and hence single parameter, can be assigned to multiple variables or variable combinations if necessary. With this set-up, parameters assigned to MULTZ, for example, can be changed and perturbed giving significant flexibility to automatic history matching. Parameter distributions over all or part of the reservoir model can be changed while other parameterisation techniques such as the use of fault multipliers, rock physics parameters etc. can still be applied in modifying heterogeneity distribution

3.2.2 Pilot Point (PP) Scheme

The pilot point method, which is one of the first geostatistical parameterisation techniques sometimes referred to as Master Location Method, was originally developed by de Marsily *et al*. (1984) as a technique for reducing the number of parameters in reservoir characterisation using kriging for interpolation of permeability at locations between the pilot point locations at which the permeability is estimated by an inversion method. Developed by Georges Matheron (Matheron, 1971), kriging-based interpolation is a spatial statistics tool which relies on covariance function and assumes the guess of the

random property field to be known field. The pilot point method was originally used in interpreting well interference test data giving the best estimate that was mostly a smooth surface. In a similar technique, Brèfort and Pelcè (1990), estimated property fields in a problem involving a highly compressible gas field. LaVenue and Pickens (1992) in calibrating a groundwater flow model to measured head and permeability, made some additions to the pilot point method so that the locations of the pilot points were calculated automatically. The method was modified further by Rama Rao *et al*. (1995) who proposed a method for placing the pilot point automatically at locations deemed most useful for minimising the mismatch in the pressure data. Equally probable realisations of the permeability field were produced by first generating the property field that was conditioned to measured permeability and then using pilot point method to produce a smooth correction of the permeability field that also gives the least misfit to the pressure data. The technique was also used by Gomez-Hernandez *et al*. (1997) for permeability field calibration to pressure history data. Stephen *et al*, (2006) used the pilot points for the Schiehallion model history matching by placing the points according to the anticipated sensitivity to permeability of the observed 4D anomalies. The points were adjusted during history matching as the sensitivity to the data was observed to be greater around a certain injector well.

Kriging techniques have since been extended to take different forms; some details of different types of Kriging methods can be found in Doyen (2007). Sagitov and Stephen (2013) investigated the problem of the optimal model complexity in the context of choosing appropriate parameterisation scheme for adequate integration of spatial information from seismic. The pilot point scheme was found to give a smooth property field, and is important in increasing the flexibility of parameterisation so as to avoid bias in model predictions that might be created when the parameterisation scheme is based on geobodies/objects extracted from seismic interpretation. Sagitov and Stephen (2013) made a strong case for the pilot- point method by concluding that it removes the strong controlling effect of the prior knowledge for the real scale of dynamic constraint to be felt, creating a balance between the prior knowledge in a parameterisation and its flexibility to calibration with dynamic data. To choose the pilot point locations, the suggested practice is to find out those parameters in certain locations in the reservoir for which the data is most sensitive to: in general, pilot points are selected at locations interpreted to have large uncertainties in reservoir properties. In a history matching study with the model of Nelson field, Kazemi and Stephen (2011) considered two approaches to placement of pilot points. In the first case, which was found to be better, major flow

paths in the reservoir were determined using streamline analysis and then the pilot points were placed to control the flow paths. In the second case, the misfits at well locations were looked at and pilot points were then placed around the wells with the highest misfits. Other applications of the pilot point method include Landa and Horne (1997), Bissell *et al*. (1997), Roggero (1997) Backer *et al*. (2001), Floris *et al*. (2001), Arenas *et al*. (2001) etc.

To reduce the number of parameters in this work, application of the pilot-point method modifies poorly defined properties such as net:gross, transmissibility and vertical and horizontal permeability at a few locations from which they are interpolated in the entire grids representing the reservoir. The values of the parameters or their modifiers at the pilot points are regarded as the unknowns which are progressively modified and updated to minimise the misfit between the simulated response and measured response.

3.2.3 Synthetic Benchmark SGS model

We show an example of the pilot point parameterisation scheme in a benchmark synthetic reservoir model called SGS. This SGS model is also used in various synthetic history matching studies in this thesis. The reservoir model is a bounded fault block and is characterised by 25 x 25 x 4 cells (Figure 3.1), each measuring 100m x 100m x 7m. The cells are populated with Net:Gross, porosity and permeability values using Sequential Gaussian Simulation (for details see Stephen 2007). In Figure 3.2, the relative permeability curves, K_{rw} (for water) and K_{ro} (for oil) are shown as functions of the water saturation, S_w. A single horizontal producer well is supported by a vertical injector at a distance of 1600m. The field produces 18,000 STB/day of liquid (the pressure limit is never reached) and the injector is on pressure control and the field remains above bubble point. The STOIIP in the model is 109.8×10^6 STB and Recovery Factor after 2976 days is typically around 30%. The seismic prediction for the model uses the petro-elastic model presented by Stephen *et al*. 2006 and predicted AIs are used as synthetic observation data.

The reservoir parameters are perturbed and updated in a pilot point parameterisation scheme (de Marseily 1984). We can choose to modify the multipliers of properties such as the transmissibility, NTG, permeability at the six pilot point locations in the reservoir simulation model. The pilot points, as identified with pink dots in Figure 3.1, are placed on a lattice of 5 x 5 x 1 nodes which lies on top of the simulation grid. The nodes are 5 cells apart in each direction and the separation corresponds to the variogram range of the underlying permeability field. The pilot points are indexed accordingly using (i,j) lattice co-ordinates. These parameters are labelled from 1 to 6 in the figure to illustrate how pilot

points are chosen. The pilot point corner points are indexed from starting at the simulation grid origin (1,1) but the origin may be shifted if desired by the pilot point separation. It is also possible to set any of the pilot points on any fixed multiplier value (example is when hard data is available which is typically the case at the wells so that interpolation and propagation for the parameter values in the neighbouring cells will be conditioned to both the new values at the pilot point and the fixed values at the wells). The multipliers are interpolated using Kriging with an appropriate variogram range equal to the size of the separation of the pilot points to avoid any interference between the pilot points. We populate the initial ensemble of models by randomly sampling a six-dimensional parameter space such that the multipliers of the pilot points can vary within the specified parameter limits.

Although one can sample on the linear scale, sampling on the log (base 10) scale is preferable when changing pilot points to avoid bias in sampling by the optimisation algorithm. For instance, in linear sampling with limits of 0.1 to 10, the optimisation algorithm (for example, NA code) will be skewed towards sampling between 1 and 10 and few values will be sampled between 0.1 and 1. Separate pilot points may be assigned to net-to-gross, horizontal permeability (or the transmissibility or the multipliers of the horizontal permeability) and/or vertical permeability etc. giving up to three separate pilot point multiplier fields.

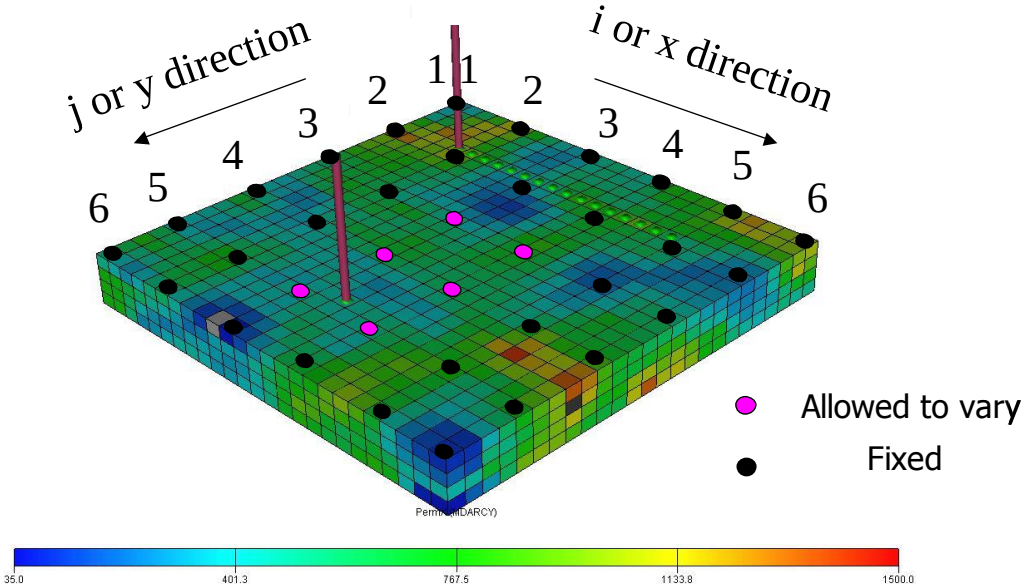

Figure 3.1 Simple 25 x 25 x 4 model used in the synthetic seismic history matching study

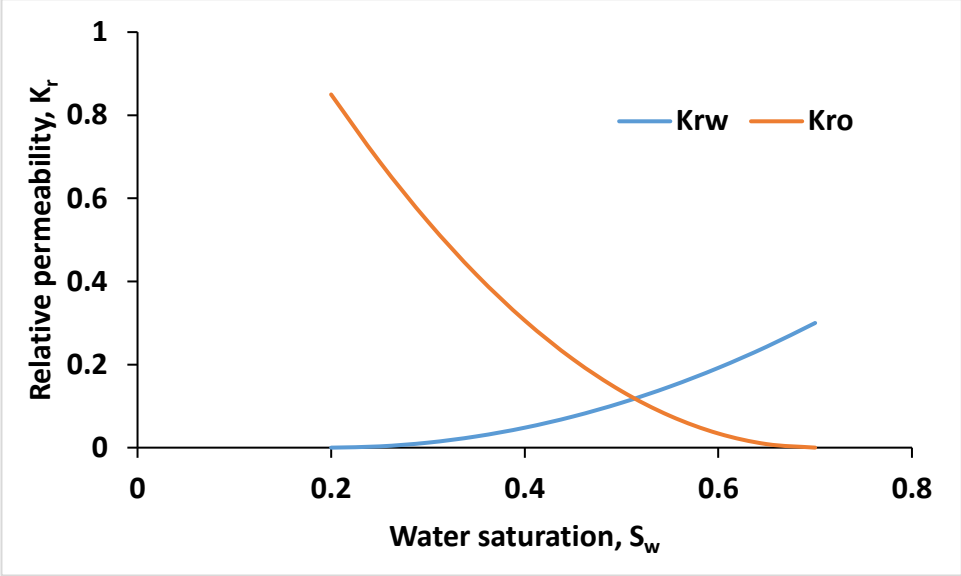

Figure 3.2 Relative permeability of the SGS model

3.3 Prediction of Production Response

Reservoir quantities such as pressure, saturation and flows are predicted by solving, numerically, the multiphase flow equations of the reservoir using a black oil reservoir simulator, ECLIPSE100. Some of the flow simulation results are also needed in predicting the synthetic seismic response.

3.4 Prediction of Seismic Response

The concept for predicting seismic response, or generating synthetic 4D seismic data, either for comparison with the observed seismic or to be used as the ‘’truth case “ in synthetic data history matching, is based on a combination of rock physics, often called a Petro-Elastic Model (PEM). During production, changes in a reservoir’s fluid saturation, pressure, porosity and temperature result in changes in velocity and density that lead to changes in seismic response. The Petro-elastic model is part of any 4D seismic modelling workflow for Seismic History Matching because it provides the link between the static and dynamic properties of a reservoir and the elastic properties of the reservoir rock; mathematical equations that link rock properties such as porosity (Ø), fluid saturation (water saturation S_w, oil saturation S_o, and gas saturation S_g), effective pressure and shale volume to elastic properties of the rock such as the AI.

3.4.1 Rock Physics

Equations 2.1 to 2.12 under the section on time lapse prediction theory contain the basic wave equations for predicting seismic properties from rock properties. As part of the forward modelling of the seismic history matching loop, we want to predict seismic

impedances from flow simulation results. The reservoir flow simulation gives fluid saturations and pressures for each simulation cell which can be transformed using the petro-elastic model (PEM) to predicted impedance. Fluid saturation and pressure changes in the simulation cell are modelled using Gassmann's equation and empirical pressure-effect model respectively.

Pressure changes can result in a change in the fluid modulus and the density, an increase in gas saturation if pressure declines below the bubble point, or changes in the porosity and the dry bulk moduli. The pressure-effect model is obtained by fitting an appropriate mathematical model to measurements on dry core sample, and is used to calculate the dry bulk modulus using (MacBeth, 2004):

$$K_{dry}^{r} = \frac{K_{inf}^{r}}{1 + E_{k}^{r} \exp(-P_{eff}/P_{k}^{r})} \tag{3.1}$$

And the shear modulus μ:

$$\mu_{dry}^{r} = \frac{\mu_{inf}^{r}}{1 + E_{\mu}^{r} \exp(-P_{eff}/P_{\mu}^{r})} \tag{3.2}$$

Where K_{dry}, and K_{inf} are the dry bulk modulus at the temperature and pressure of the simulation cell and dry bulk modulus at standard temperature and pressure respectively. E_k and P_k (and E_μ and P_μ) are the excess compliance present in the rock as a result of geological or mechanical processes, and the stress sensitivity respectively. The subscript r identifies rock type (sand or shale). The effective pressure P_{eff} governs the pressure dependence of velocity and is assumed to be equal to the differential pressure which is difference between the overburden pressure P_c and the reservoir fluid pressure P_f.

$$P_{eff} = P_c - P_f \tag{3.3}$$

Having obtained the pressure-dependent dry bulk and shear moduli, Gassmann's equation (1951) is used to calculate the saturated bulk modulus for shale and sand within a cell at a given reservoir condition and fluid type

The value of the modulus, M is calculated for each simulation cell as follows:

P-Wave Modulus:

$$M = \rho V_p^2 \tag{3.4}$$

S-wave Modulus:

$$\mu = \rho V_s^2 \tag{3.5}$$

Then for each rock type (sand or shale) in the simulation cell, the modulus becomes:

$$M^r = K_{sat}^r + \frac{4\mu^r}{3} \tag{3.6}$$

where r = sand or shale

The shear modulus is unaffected by saturation

If we assume the shale consists of dry frame only then typical laboratory values for K and μ of shale can be used to compute the modulus M^{shale}

The value of the modulus for each simulation cell, M^{cell}, is then obtained from the harmonic average of its values for the rock types weighted by their fractional volumes

$$\frac{1}{M^{cell}} = \frac{NTG}{M^{sand}} + \frac{(1 - NTG)}{M^{shale}} \tag{3.7}$$

where NTG is the net-to-gross of the simulation cell.

3.4.2 Vertical Upscaling for the Impedance Map

For vertical propagation in a layered medium (Backus, 1962), the M^{cell} calculated for each simulation cell in a column can be averaged, using Backus averaging (assuming the column is vertical), for the impedance of a column of cells in the simulation model:

$$I = \sqrt{\langle \rho^{sat} \rangle \langle 1/M^{cell} \rangle^{-1}} \tag{3.8}$$

where ρ is the bulk density of the simulation cell obtained by averaging the densities of the dry rock (or rock frame) and the fluid densities. The brackets, "< >", indicate a vertical volume weighted average of the properties over the reservoir interval; in this case column of cells.

Using Equation 3.8, P-impedance values are calculated for every column of the reservoir simulation grid so that a map of predicted impedance is obtained at the areal resolution of the simulation grid. Similarly, the observed impedance data for a real field study is

calculated by integrating the attributes over the reservoir interval to generate the observed impedance map at the areal resolution of the seismic grid. The Backus averaging approach is valid for reservoir beds that are less than one tenth of the seismic wavelength thick and reservoirs of around one quarter seismic wavelength thick (MacBeth, 1995).

3.4.3 Horizontal Downscaling of the Predicted Impedance

In the part of this study where we use synthetic data, the observed seismic data was synthesised by using the impedances calculated from a coarse grid flow simulation model. Thus, during history matching, the predicted impedances and the observed impedances are at the same scale, and there is no need for horizontal downscaling. In the real field case, however, the predicted impedance is obtained at a coarser scale compared to the scale of the observed seismic data. For instance, if we run simulations on a coarse scale grid measuring 100 × 100 × 6 m, the predicted p-wave impedance is on a scale of the reservoir simulation model while the observed seismic is typically acquired in 12.5m x 12.5m x 25m bins. There is therefore the need to implement a horizontal downscaling so that impedance predictions represent the same volumes as the observed seismic data to enable comparison. We must make a choice between either upscaling the observed data or downscaling the predicted impedances, while considering the following possibilities (Johnston, 2013):

- To construct the simulation model in the seismic scale and compare observed impedance and synthetic impedance on this same scale. This option to the best of our knowledge is not adopted in practice for obvious reasons: it is not common to see seismic-scale geo-models (fine scale models built by geologists on the scale of the seismic grid), and flow simulation at such seismic scale geo-model would require high computation time.

- To run the flow simulation on the geo-model scale and map the synthetic seismic from the geo-model scale to seismic scale for seismic misfit evaluation. This again is not a good option as the flow simulation will be very slow and the mapping of the synthetic seismic to seismic scale is prone to high degree of uncertainty.
- To run the flow simulation on coarse reservoir simulation scale, and upscale the observed impedance data by sampling into the simulation grid using an averaging method (e.g arithmetic average).

- To run the flow simulation on the coarse reservoir simulation scale and downscale the chosen results of the simulation (saturation and pressure, impedance) to seismic impedance scale. For instance, one may choose to downscale saturation and pressure to the seismic impedance scale or interpolate the saturation and pressure to generate maps from simulation scale to seismic impedance scale. One may also choose to downscale the synthetic impedance data to the scale of the observed seismic data. Stephen (2007) opted to keep the observed seismic data as intact as possible, and therefore the option of interpolating the predicted seismic as indicated in Figure 3.3: thick red lines indicate the coarse reservoir simulation cells while large circles show the location at which the impedances are predicted. In Figure 3.3, the simulation grid and seismic grid are shown for the cases where the grids lines are aligned but there may be cases that have offset angle(s). Equation 3.9 is used to interpolate the impedances to obtain values at the small black dots, where the observed seismic would normally be measured. Solid thick arrows indicate the principal directions of the coarse (simulation) and fine (seismic) grids: the gridding system for the observed impedance data is obtained as a set of points defined by the seismic acquisition inline and crossline coordinates and the simulation grid is parallel to the seismic inline discretized to simulation cells with a dimension of 75m x 75m whereas for seismic bins the dimension is 12.5m x 12.5m.

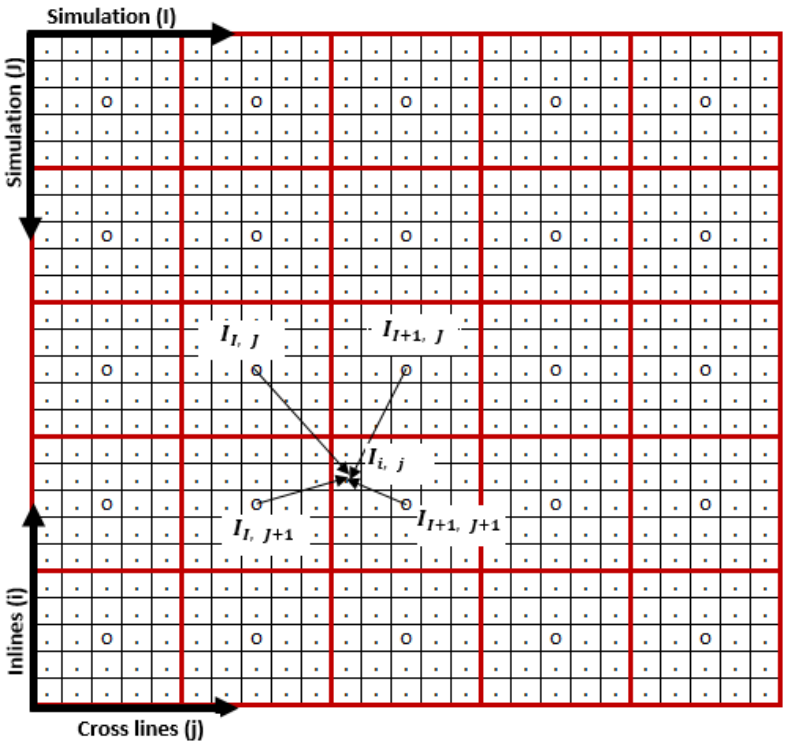

Figure 3.3 Comparison of the coarse and fine grids (Stephen, 2007).

The predicted impedance upscaled at the coarse simulation grid scale (from Equation 4.18), I_{IJ}^{coarse}, and the position vectors of the simulation grid centres and seismic grid centre, r, are used to interpolate and obtain the downscaled impedance at the fine seismic scale, I_{ij}^{fine}, as follows:

$$I_{IJ}^{fine} = \frac{\sum_{IJ} w_{ijIJ} I_{IJ}^{coarse}}{\sum_{IJ} w_{ijIJ}} \tag{3.9}$$

$$w_{ijIJ} = \exp(-\beta(|\vec{r}_{IJ} - \vec{r}_{ij}|) \tag{3.10}$$

The indices I and J identifies the cells on the coarse simulation grid while i and j are the equivalents for the fine seismic bins. $\vec{r}$ is the position vector of the centre of the cells. β is a contant of dimension L^{-1}. Stephen *et al*. (2006) found that $\beta = 0.05\ m^{-1}$gives the best results, minimising the representivity error.

In the part of this thesis where the Norne Field seimic data was used for history matching, we chose to sample the observed seismic (impedance) data into the simulation grid by upscaling using simple averaging.

3.4.4 Normalisation of Seismic Attributes

As per the discussions above, the workflow for seismic to reservoir model comparison begins with the prediction of impedances via a petro-elastic model; the predicted and observed seismic attribute are then mapped in a common grid. The workflow does not end there as the predicted and observed seismic attributes are often in different seismic domains, and so, normalisation is required prior to comparison (Figure 3.4) (Stephen *et al.*, 2006). The observed time-lapse seismic data used in seismic history matching often consists of relative measures of change, for instance; relative impedance. Impedance domain is often considered as the best for comparing predicted and observed data because of balance between time and accuracy (Stephen *et al*., 2006). It is faster to compute impedances than it is to consider full time traces, and impedances can be estimated from observed data by the well-developed full inversion technique or approximations such as CI (Lancaster and Whitcombe 2000). Whereas the forward modelling in our automated seismic history-matching loop predicts seismic in the form of impedance attribute, we may have the observed attribute in the form of reflectivity for which we may not know

the actual units or scale of measurement due to the relative nature of the seismic processing and inversion techniques.

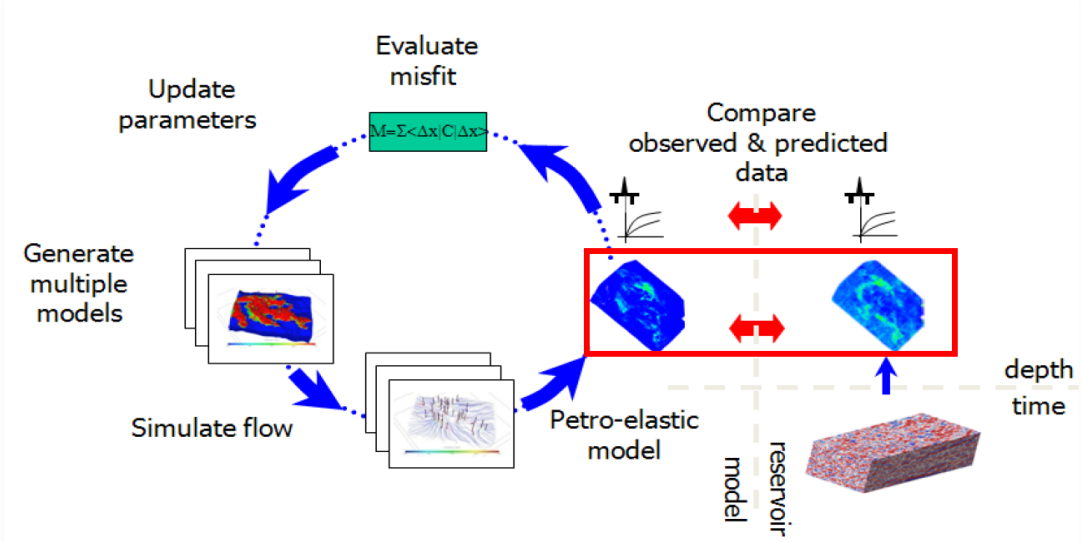

Figure 3.4 Normalization of as impedance maps (seismic data) identified by the red box in the Seismic history matching workflow. (Kazemi et al., 2011).

Kazemi *et al.* (2011) investigated some seismic normalization approaches and assessed their effect on history matching. One of the approaches is well-based and involves using the predictions of 4D signature from selected cells with completions on vertical wells for which the observed water cut has been matched, and derive a normalisation function from a crossplot of the observed versus predicted seismic. History-matched water cut is an indication of good prediction of saturation near the wells. A second approach uses the crossplots of a full-field seismic prediction (using the 4D signatures of all or part of the simulation cells) against the corresponding seismic observation. In both approaches, it is assumed that relationship between synthetic and observed 4D data is approximately linear and least-squares regression suffices as in Figure 3.5.

The steps in the normalization of seismic data begins with a qualitative study of the seismic behaviour of the reservoir so as to establish the link between production activity and 4D seismic signal in the reservoir, especially as it concerns the reservoir's depletion mechanisms and the dominance of either pressure or saturation in the seismic response. For instance, in a saturation dominated time-lapse seismic, one approach is to identify the regions on the observed seismic map where all production and injection wells are located because those are the regions of the high change of attribute (stronger seismic activity) in the observed seismic data resulting from saturation change. In the same vein, the predicted impedance map is studied qualitatively, identifying the similarities and differences with the observed seismic map. For the rest of the reservoir, strong 4D signal is not expected,

and if some seismic signals are identified suggesting some production activities on any region on the observed seismic map without evidence of production, then that signature may be considered to be noise, particularly outside of the region identified as the reservoir. The identified real seismic signals in the observed seismic map and the corresponding signals in the predicted seismic map may not be on the same scale of measurement, but the relationship between them can be utilised in normalising the observed seismic data.

Arwini and Stephen (2011) presented another approach to normalization which was based on the assumption that the effect of changing pressure and saturation induces an equivalent relative change in the reflectivity and impedance throughout the reservoir in both observed and predicted data. In this case, the normalised observed seismic data $I^t_{n,o}$ (for example; relative impedance) at monitor time, t , is obtained by subtracting the areal mean of the baseline data, $\mu^b_{I,o}$, from the raw observed seismic data, I^t_o , at time, t, and dividing by the areal standard deviation of the baseline data, $\sigma^b_{I,o}$, as follows:

$$I^t_{n,o}(t,x,y,z) = \frac{I^t_o(t,x,y,z) - \mu^b_{I,o}}{\sigma^b_{I,o}} \tag{3.11}$$

Predicted seismic attributes are also normalised in the same way to obtain, $I^t_{n,p}$.

$$I^t_{n,p}(t,x,y,z) = \frac{I^t_p(t,x,y,z) - \mu^b_{I,p}}{\sigma^b_{I,p}} \tag{3.12}$$

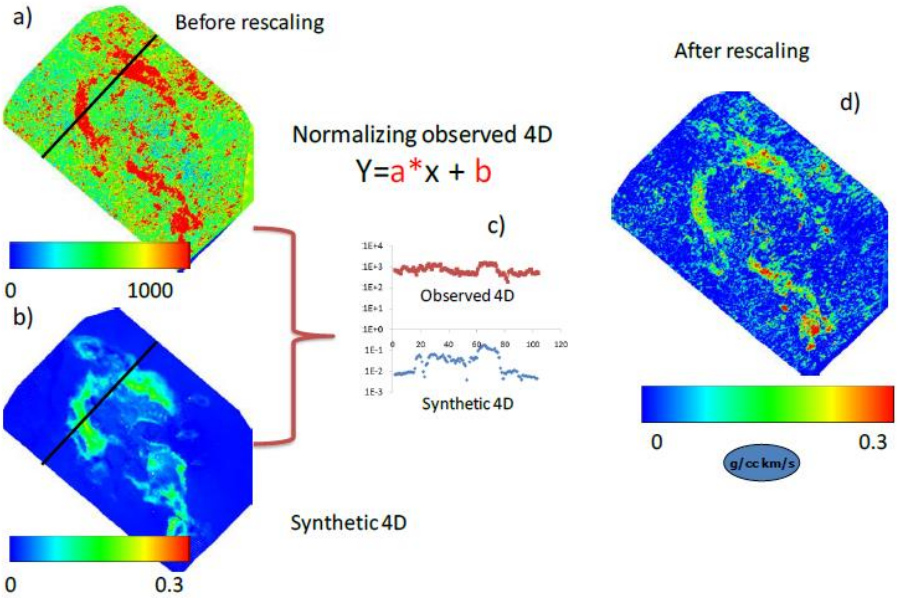

Figure 3.5 Normalization of Observed Seismic. a) Observed time-lapse impedance map before normalization, b) synthetic time-lapse impedance map, c) comparison of observed versus synthetic for the black-colour cross line shows in the maps and d) observed time-lapse impedance map after normalization (Kazemi et al., 2011)

One other major advantage of using the seismic normalisation techniques is that normalised observed and predicted seismic attributes, such as relative impedance or reflectivity, can be compared without the need for full inversion.

In our real field data using the Norne Field seismic, we adopt the full inversion technique using a well-developed inversion tool: HRS-9 Geoview (Hampson-Russell). The inversion process is calibrated by the impedance model (from sonic and density logs) to give absolute AI. The normalisation process described in Kazemi *et al.* (2011) is therefore not needed for our real data but was used for a quality check.

3.5 Observation Data

The fitness function in this study is formulated from a Bayesian viewpoint (section 3.6) such that we can infer the probability distribution of the model parameters conditioned to the *observed data*. In seismic history matching, the models are conditioned to different types of observations categorised into two: *production data* and *time-lapse seismic data*.

Production data refers to the measurements of flow rate (oil production rate, water production rate, gas production rate), pressure (flowing bottom hole pressure), or ratios of flow rates (gas oil ratios, water cut) made in producing or injecting wells. Such measurements at well locations provide valuable information, but are spatially sparse due to the limited number of wells obtainable in a field. On the other hand, the measurements at the well locations are repeated frequently, sometimes as often as every few seconds, so large temporal data are obtained for a field.

Time-lapse seismic data is field-scale (spatially-dense) reservoir surveillance data based on the difference between the seismic attributes (for example; AI, relative impedance, reflectivity) derived from a monitor survey and a baseline survey. The real gain in using the time-lapse data as a history matching constraint ensues from its ability to provide information on saturation and pressure not only at the well locations but also throughout the field. However, unlike production data, time-lapse seismic data has a temporal limitation as just a few seismic surveys are carried out between some time intervals in years (four years interval, for example).

In creating a base model, the reservoir may be characterised using reservoir properties estimates obtained from measurements from boreholes including coring, rock cuttings, well logs, PVT, and pressure tests. These data are often regarded as hard (except for random noise and interpretation error) but unfortunately, they only sample a very smnall

fraction of the total reservoir volume (for example: log, core and PVT data give measurements of a reservoir property in a near-wellbore region that is typically much smaller than the normal size of a reservoir simulation grid block).

In the part of this study where synthetic observation data was used, we generated the history data by running reservoir simulation with the base case model, and assuming the base case to be the 'truth case'. The predicted production responses become the synthetic production history data and the predicted seismic response, using petro-elastic transform, becomes the synthetic seismic history data. We can also introduce noise in the synthetic history data to represent the data error for a more realistic study. We then perturb the model and try to match the synthetic history data.

In the real field study, production history data used were those measured in the Norne Field and the seismic data were the real Norne Field seismic data.

3.5.1 Inaccuracies in Data Measurements

The reason for quantifying the scale of data errors in history matching is that it is meaningless to force our simulation model to match observed data to greater accuracy than required by the measurement accuracy. We may wish to match observed data such as the Producer /Injector Well Bottom Hole Flowing Pressure (WBHP), Field or Well Water Production Rates (WPR), Field or Well Oil Production Rates (OPR) etc. all of which are obtained with measurements devices that have some degree of uncertainty. In the formulation of history matching problems, it is often assumed that the data error is normally distributed and the quantification of the error variance is required.

Pressure error measurements are sometimes estimated as one percent (1%) of the data value (Oliver *et al*. 2008). We can therefore convert the fractional error to standard deviation which we input as weighting factor for the observed pressure variables while setting up the production misfit in our automatic seismic history matching loop. The weighting factor is inputted to be equal to $\left({}^{1}/_{\sigma_d}\right)^2$ where σ_d is the standard deviation of the data error. For example, a pressure data of 1000psi gives 10psi standard error (1% of 1000psi), which translates to a weight of 0.01 [that is: $(1/10)^2$]. Production rates error measurements are sometimes estimated as one percent (1%) of the monthly volume value for field data and ten percent (10%) for individual wells: the larger error value for individual wells is to account for errors in the allocation rates (Oliver *et al*. 2008). We

can therefore convert the fractional error to standard deviation similar to the approach in pressure data error quantification.

All production misfits, defined to compare the different observed production variables and their predicted counterparts, are multiplied by the weighting factor when added to the total misfit. The weighting factor can then be used to arbitrarily scale one misfit against the others, and we may choose to set the weighting factor for a variable to zero so that its misfit is calculated and stored but not used to calculate the total misfit.

Error quantification in time-lapse seismic measurements presents a difficult challenge. Seismic data exists for every grid block and are spatially correlated, giving rise to large amount of data for which data covariance matrix needs to be computed. Besides, seismic processing is non-repeatable and its complicated nature introduces different levels of non-Gaussian noise that are difficult to quantify.

3.6 Calculating the Misfit

Comparative assessment of the different reservoir models generated during history matching is necessary because it guides the optimisation algorithm in selecting a new set of models in generational model selection. For objectivity, model assessment and selection is done quantitatively through a function called *Objective Function, O, or Misfit Function, M.* Following the procedure outlined in Oliver *et al.* (2008) and Tarantola (2005), we can define a global misfit function which calculates the mismatch between the model predictions from the reservoir simulator and the corresponding true value measured in the field. Modelling and measurement errors are both assumed to be independent and Gaussian and are therefore represented by covariance matrix with components that are independent Gaussian variables. Stephen *et al*. (2006) found that errors in seismic history matching could be Gaussian and uncorrelated. With further assumption that the means of each of the components is equal and the variance is, σ_d^2, the covariance reduces to a diagonal matrix of entry, $\sigma_{d,i}^2$ for the ith component of an N_d-dimensional error vector. The misfit function then reduces to the weighted least-squares defined as follows:

$$M = O(m_{sim}) = \sum_{k=1}^{N_d} \frac{\left(d_{obs,k}(m_{true}) - g_k(m_{sim})\right)^2}{\sigma_{d,k}^2} \qquad (3.13)$$

where $d_{obs,k}(m_{true})$ represents kth value of the measured data in the N_d-dimensional vector of the data. m_{sim} is the simulation model, $g(m_{sim})$ is the predictions using the model ion, and d_{obs} stands for the measured or observed data. Using the squares of the residuals as the misfit function in Equation 3.13 is very convenient for this present work because it provides the values which can be used in Bayesian statistics for the calculation of the probability or likelihood of the models.

Equation 3.13 is the global objective function which in seismic history matching can be made to take the shape below:

$$M = \propto * M_p + (1-\propto) * M_s \qquad (3.14)$$

Where M_p is a measure of the total misfit between the observed production data (such as water cut, well pressures, oil rate, water rate etc.) and the corresponding predicted quantities. Similarly, M_s is the misfit between the observed seismic data (in form of AI etc.) and the corresponding predicted quantities. This form of objective function in Equation 3.14 allows us to provide weighting factors $\propto$, to scale or normalise the different forms of observed data. The decision on what a suitable $\propto$ should be can be a challenge in history matching. The weighting factor should be chosen to reflect differences in unit, magnitude and accuracy of production and seismic data; the more accurate data should have higher factor.

Noise in observed data as well as modelling errors affect the comparison of model predictions and observations, distorting the 'objectiveness' of the objective function. In a seismic history matching study by Stephen *et al.* (2007), scale and process dependent model errors were associated with the approximation errors caused by upscaling, and were estimated as the difference between the predictions of the fine scale models and those of the coarse scale modelling errors. Is it possible to calculate or characterise completely the noise in data and modelling errors? If so then the weights assigned to the production and seismic terms could be used to balance the misfit function. Unfortunately, estimation of noise statistics and modelling errors is difficult. For instance, seismic data contains error of different origins from different stages of data acquisition, processing and interpretation, and modelling errors are not often easily calibrated.

One of the approaches adopted in this work in circumventing the problem of choice of weighting factors, is to treat the seismic misfit and production misfit differently and then

combine them to form a multi-objective problem which is then solved by using a multi-objective optimization algorithm. With this approach, systematic errors should be accounted for and random errors can be ignored.

3.7 The Optimisation Tools

In this work, we will generally design the simulation runs to generate an ensemble of models and their corresponding misfits using any of either Neighbourhood Algorithm (NA), Genetic Algorithm (GA), or Particle Swarm Optimisation (PSO). The description of the versions of the algorithms used follow:

3.7.1 The Neighbourhood Algorithm

Originally developed for solving a seismic waveform inversion problem in earthquake seismology by Sambridge (1999a), Neighbourhood Algorithm (NA) is a stochastic optimization which systematically sample the regions of parameter space that contain models of higher data fit. The algorithm has been adapted to the problem of generating multiple history matching models in reservoir characterisation (Christie *et al*., 2002; Subbey *et al*., 2004; Elabed, 2003; Erbas and Christie, 2007; Arwini and Stephen, 2010; Sedighi-Dehkordi and Stephen, 2010; Kazemi and Stephen, 2011 etc.)

The performance of the NA is controlled by four parameters defined as follows:

n_i : sample size for initialisation of the algorithm

it : number of iterations per run

n_s : number of models generated at each iteration, and

n_r : number of best models resampled by the algorithm

The NA workflow starts with a first iteration where an initial set of n_i models are generated randomly in the parameter space. A voronoi cell (V-cell: multidimensional geometrical structures shown in Figure 3.6) is constructed for each of the models to define its neighbourhood. Then for each combination of the randomly generated model parameters, the response in the form of misfit is calculated by solving the forward problem. The calculated misfit values are ranked and the n_r models with the lowest misfit values are selected. It is believed that that the n_r models with the lowest misfit values represents the good points, and there could be more good points or even better points within their respective neighbourhoods defined by the V-Cell s. As a result, n_s new models are generated during the second iteration by performing a uniform random walk in the V-

Cell of each of the n_r chosen models such that the number of samples chosen from each cell is equal to n_s/n_r. The uniform random walk is done using a Gibbs sampler. The misfit values of the n_s samples are calculated and added to the initial ensemble and the voronoi diagram is updated to include all models chosen so far. In a repeat of the workflow, n_r number of models with lowest misfit values are selected again and the search continues in their V-Cell s. The process is repeated until the search reaches a pre-defined convergence.

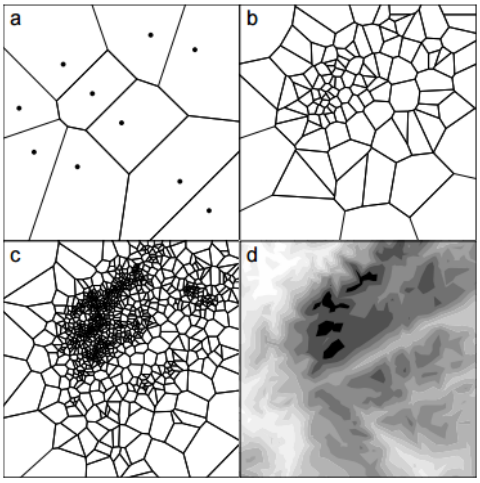

Figure 3.6 (a) The V-Cell s of 10 initial uniform random points in the model space, (b) The V-Cell s of 100 samples generated by a Gibbs sampler using NA. (c) Similar to b) for 1000 samples. (d) contours of the misfit function. (Sambridge 1999a)

The Voronoi diagram is a simple geometrical construction for dividing the N_m-dimensional model space into regions. If we consider a model (or a point) in the model space *S*, designated as m_p having a unique combination of model parameters, the V-Cell about the m_p is a closest neighbour polyhedron containing all the models in S that are closer to m_p than to any other models $m_q \in S$, $q \neq p$. A closest neighbour polyhedron is constructed for each of all the models in *S* to produce the unique regions in the voronoi diagram. If one model has just one closest neighbour, it will simply be inside the V-Cell of the neighbour. If one model has two neighbours (because it is equidistant from the two neighbours), it will be located on the edge between the respective voronoi polyhedran of the two neighbours. Models which are equidistant from three neighbours will be at the vertices of the polyhedron.

The NA workflow is summarised in Figure 3.7

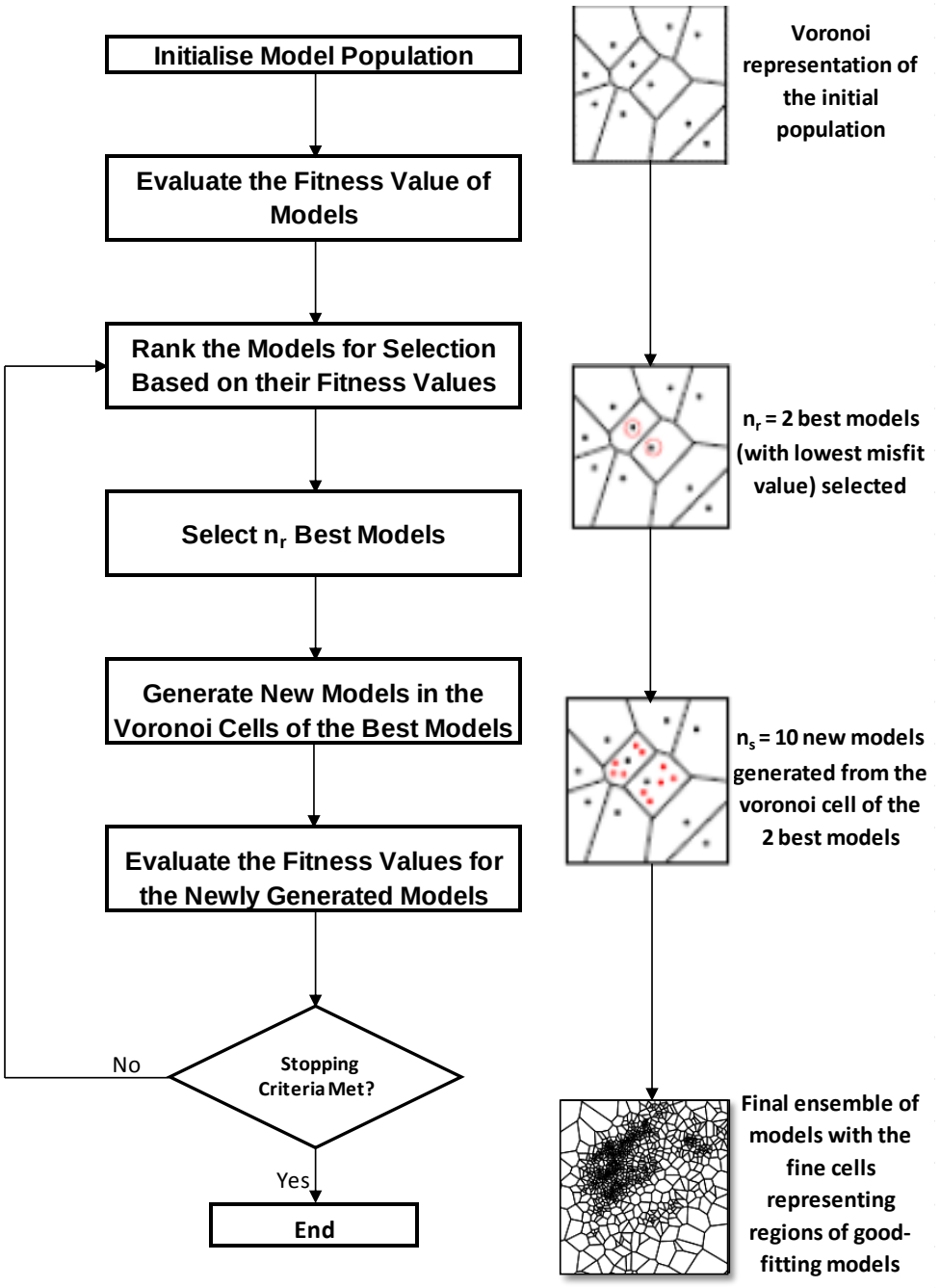

Figure 3.7 Neighbourhood Algorithm workflow and a representation of the model space (Erbas and Christie, 2007).

The NA uses the Gibbs sampler to perform random walks in the V-Cell s to generate new models. As an illustration, consider the 2-dimensional problem with two parameters x and y in Figure 3.8. The aim is to generate three models (i.e n_s/n_r= 3) inside the V-Cell at the centre of the Voronoi diagram. The random walk is started at one of the original n_r models of the lowest misfit for which the V-Cell was constructed: the model defined by parameters (x_o, y_o). An imaginary line [a, b] passing through the point [x_o, y_o] in the random search direction intersects the cell boundaries at *a* and *b*. The search direction is in x-direction, and so, x_1 is randomly chosen as one of the new parameters for the first

new model. A second parameter y_1 is chosen in a similar manner as the search is redirected to y-direction, to produce a new model defined by the parameters (x_1, y_1). The search continues in a similar manner to produce models (x_2, y_2) and (x_3, y_3) which complete the required 3 new model parameter combinations in the V-Cell . This technique can be extended to higher-dimensional parameter space because any imaginary line in a search direction produces intersection points with the cell boundaries which can be calculated following the method of Sambridge (1999a).

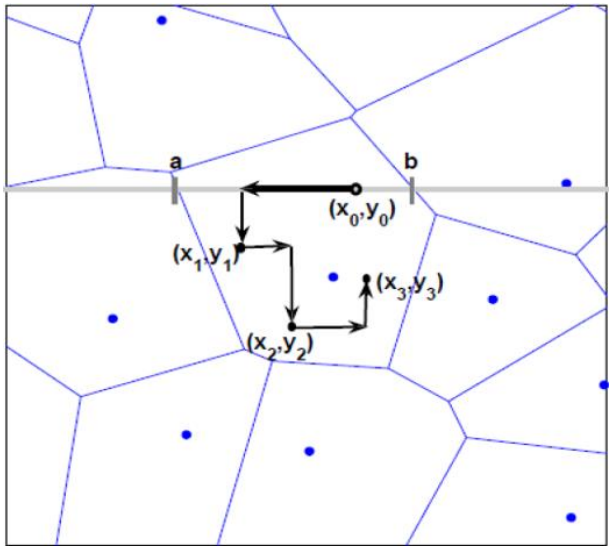

Figure 3.8 A 2-D illustration of uniform random walk in NA-Gibbs Sampler. Here, a walk within one V-Cell has generated three new models (x_1, y_1), (x_2, y_2) and (x_3,y_3) (Subbey et al., 2004)

Just like other direct search methods, the challenges that affect the accuracy of the sampling in NA include the high number of unknown parameters, the existence of multiple minima in the solution space, and the high computational cost of reservoir simulation.'n_s' and 'n_r' are called the tuning parameters because they determine the explorative and exploitative behaviours of the NA algorithm and hence its convergence performance. The ratio n_s:n_r decreases as we increase the number of models resampled relative to the number of models generated at each iteration, thereby increasing the explorative power of the algorithm for greater chance of finding the global minimum, at the expense of convergence speed. On the other hand, exploitative power of the algorithm is increased as n_s:n_r ratio increases (due to high number of models generated at each iteration relative to the number of best models resampled) and could result in higher convergence rate, but higher risk of trapping in a local minimum. Convergence is likely to get trapped in local minima if the best models selected at the early stage of exploration are all located in the same region of the parameter space as the algorithm will disregard other regions for exploration (Elabed, 2003).

In addition to the above, consideration is also given to the dimension or size of the initial sample for NA initialisation ni. It is has been shown that the choice of the size of the initial sample could lead the algorithm to converge to distinct solutions especially for cases where multiple minima exist and for high dimensional problems which requires the updating of a wide range of uncertain parameters (Erbas and Christie, 2007). It is recommended that the initial sample size for NA initialisation should be equal to or greater than 2^{Nm}, where N_m is the number of parameters (Sambridge, 2001). With that, the parameter space will be saturated enough to avoid under-sampled space but care must be taken not to make the initial sample too large as this leads to an oversampled space and slows down convergence.

To sum up, NA like other stochastic methods requires a large number of iterations to find the global minimum and its convergence rate is slow when compared to the deterministic methods. Additional drawbacks in using the NA is the large number of initial samples required for the initial ensemble which increases as the number of model parameters increases. More so, if the n_s/n_r chosen is not appropriate the search could be trapped in the local minima.

There has been efforts by reserachers to modify the NA. For example, Suzuki and Caers (2006) showed that the distance between any two models is correlated to the difference in their production response. They called this 'the similarity distance' and used it to assist the search for history matched models in neighborhood algorithm.

3.7.2 The Genetic Algorithm

Genetic algorithm (GA) was invented by John Holland in the 1960s as a genetics-inspired technique based on "natural selection" for moving from one population of "chromosomes", represented as strings of ones and zeros, to a new population using operators: crossover, mutation, and inversion operators. Since then the algorithm has been adapted to solve either single objective or multi-objective optimisation problems, taking several forms different in their frame work and in their operators. Some details comparing the different Genetic Algorithms can be found in Deb (2001) and Coello (2007). The different forms notwithstanding, the general principle of GA is that: a model space of dimension N_m is searched iteratively starting with an initial population of strings of model parameters, called chromosomes, which are then evolved towards better solutions through a mechanism based on evolution. At any evolutionary stage, the fitness of each individual model in the population is evaluated, ranked, and multiple models are selected from the population of models based on their fitness. The selected models are then

modified using crossover and mutation operators to form a new population for the next iteration. The algorithm terminates depending on the stopping criteria which could be either when the maximum number of generations has been reached or if the fitness of the current population is adequate. A generalised workflow of a genetic algorithm is shown in Figure 3.9.

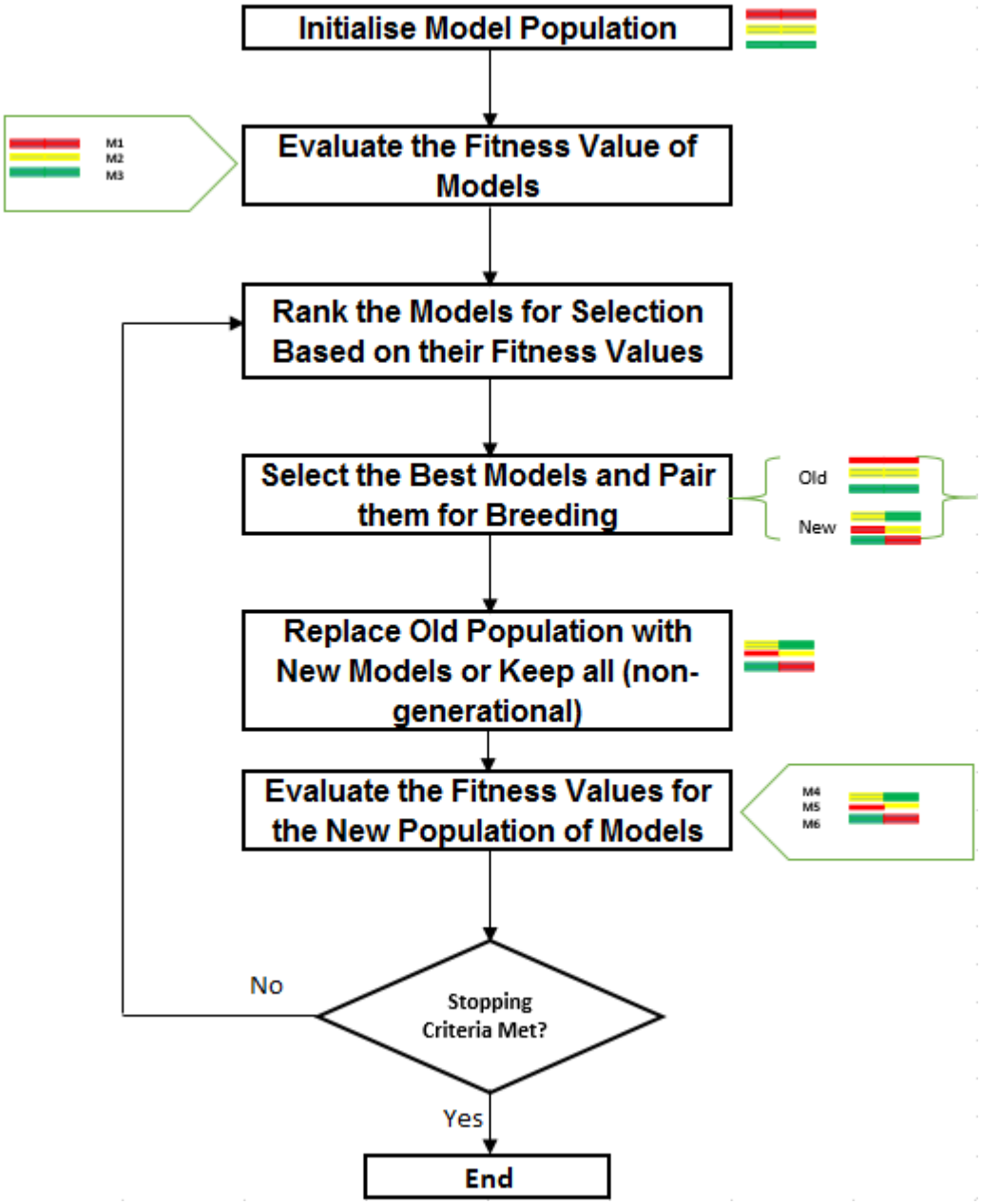

Figure 3.9 Example of a GA flowchart

As stated earlier, there are many genetic algorithm methods but the GA approach adopted in this work is conceptually similar to the NA approach (Figure 3.10).

Like NA, the genetic algorithm used in this work is set using the following four parameters:

n_i : sample size for GA initialisation (initial population)

n_r : number of couples

n_s : number of children per iteration, and

it : maximum number of iterations.

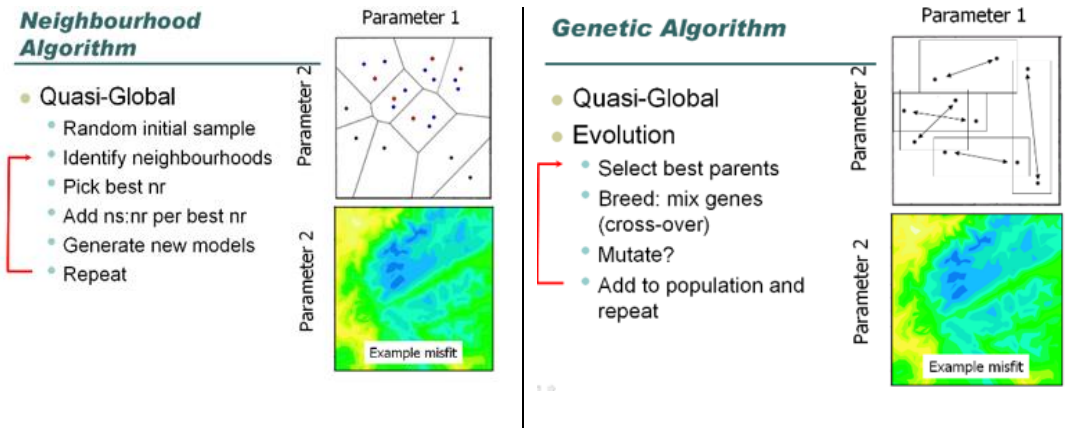

Figure 3.10 Similarities in NA and GA methods (Stephen, 2015)

The GA workflow starts with an initial set of n_i models (initial population) for the first iteration which are generated randomly in the parameter space using the same initialisation strategy used in NA. Then for each combination of the randomly generated model parameters, the response in the form of misfit is calculated by solving the forward problem. The calculated misfit values are ranked and the $2n_r$ (the double of the number of couples defined using n_r in the input) models with the lowest misfit values are selected. These $2n_r$ models (the parents) are believed to be high quality parents (best models) who can reproduce to give high quality offspring, and so they are paired up for breeding/ cross-over. The parents are paired randomly to ensure that the $2n_r$ models are used with uniform likelihood. During the crossover, the parameters of the chosen models are combined in a random manner to generate new models, n_s, of different parameter combinations. To avoid being trapped at the local minima, GA uses a mutation operation on those models. The new models, n_s can then be added to the population and the process is repeated until the search meets a pre-defined convergence criterion.

In GA, the methods of choosing the couples can be important. These may be based on the actual misfit value such that models of lower misfits are more likely to be parents to more children. The $2n_r$ parents are then simply randomly paired up so that n_r unique couples are generated. During cross-over or breeding, the real parameter values in each model can be converted to binary numbers and the bits of specific couples are then mixed. In this work, the parameters are mixed randomly as real numbers.

Real parameters are used because of some issues in binary-coded GAs which includes the necessity of large strings (chromosomes with many genes) to attain desired precision (Deb, 2001). That will result in an increase in the size of the population which will make the GA struggle in its search. Using real parameters requires less storage than binary coded strings and there is no need for decoding the chromosomes before calculation of the misfit in the selection operator. Therefore real parameter GA is faster than binary coded GA. In addition, the mixing of binary digits (during crossover) in the binary-coded GAs may result in offspring models that have no real 'genetic resemblances or correlation' to the parent models. Thus, the binary-coded GAs have weak exploitative ability and convergence problem.

The GA selection operator is not different from the binary GA selector except that we use real parameters to evaluate the misfit values in the selection operator and decoding is not required. In contrast, new crossover and mutation operators need to be defined for the real parameter GA, because the operators used in binary GAs are based on strings and alterations in bits (genes). Because the real parameter crossover operator directly combine two or more parents to create one or more children, it may appear that the crossover and mutation operators have the same concept. But there is still a good reason for using a mutation operator in conjunction with the crossover operator; as offspring is produced from more than one parent in crossover but from one parent in mutation (by perturbation).

Some details on the operators adopted are as follows:

Initialisation: A pseudo-random approach (quasi random number generator, or Saleev-Antonov-Sobol (SAS) (Antonov and Saleev, 1979).) is used to sample from the hypercube defined by the model parameter limits.

Selection operator: The n_r, defined as the number of couples in the input, is used to specify the number of the breeding pairs. This gives $2*n_r$ models to be selected as parents. The n_r and n_s parameters together define the number of children per couple (n_r/n_s). By using a *non-generational* approach, models that have been generated are ranked by misfit,, and the best $2*n_r$ models (with lowest misfit values) are selected as parents. The parents are then randomly paired without weighting.

Cross-over (breeding) Operator: The Blend Crossover (BLX-α) scheme is used to mix parents using a uniform sample based on the difference or separation between the parents (Eshelman and Schaffer, 1993). The interesting property is that the parameters of the offspring models depends on the difference in the parameters of the parent models.

Consider a case of two parents models p and q, if γ_i^p and γ_i^q are the genes (the *ith* parameters in the models) to be crossed, and if we assume that γ_i^p is less than γ_i^q, the Blend Crossover Scheme randomly picks a solution in the range $\{[\gamma_i^p - \alpha(\gamma_i^q - \gamma_i^p)], \gamma_i^q + \alpha(\gamma_i^q - \gamma_i^p)]\}$; where α is a value for the blend crossover. The resulting gene (parameter) in an offspring (Stephen 2009) is:

$$\gamma_i^{child} = \frac{\gamma_i^q + \gamma_i^p}{2} + \propto_i^{child} \left(\gamma_i^q - \gamma_i^P\right) \quad (3.15)$$

Where γ_i is the ith element of the parameter vector, the superscripts *child*, *p* and *q* represent the child that is bred from the parents, *p* and *q* respectively. The value of the blend crossover, α_i^{child} is a random number generated for each child separately and selected on the range *(-r, r)*. Usually *r* =1.0 but Stephen (2009) found that this can lead to false convergence because the separation between parents can decrease to zero faster than convergence to the true misfit.

Thus, if the separations between the parents parameters being paired for breeding are small, the separation or difference between the offspring parameters reproduced and those of the parents is also small. This is a property of the BLX-α search operator that can allow the algorithm to perform an adaptive serach; so, if a random population is initialised over the entire parameter space, the operator can search the entire space at the early stage of the search and concentrate the search more on some regions of the parameter space on the later stages.

Mutation: This randomly perturbs the children by set amounts in order to reduce the chance of false convergence and/or getting trapped in local minima. Mutation can be applied as jump which is a large random perturbations across the prior uncertainty range of the parameter or by creep which is small perturbations within some defined range. Probabilities for jump and creep have to be defined. We may then have to choose which children to keep but we can keep all in a non-generational sense as this maximises the information we have but can lead to trapping.

If we allow jump and creep mutations with probablities P^{jump} and P^{creep} respectively, then for any *ith* parameter of a child model, mutation operation goes this way:

- A random number, *r*, (where $0 < r < 1$) is chosen with uniform probability
- If $0 < r \leq P^{jump}$, the *ith* parameter is randomly changed to any number within the bounds of the prior parameter range. This is jump mutation

- If $P^{jump} < r \leq P^{jump} + P^{creep}$, then creep mutation is applied by perturbing the *ith* parameter within 10% of its current value.

From the foregoing discussion, it is obvious that the GA method provides more choices that can affect the search of parameter than the NA method. The choices available in NA and GA methods are summarised in Figure 3.11. The level of exploitation and exploration of the parameter space by different direct search methods as compared in Sambridge and Mosegaard (2002) shows that NA is more exploitative than the GA in most cases.

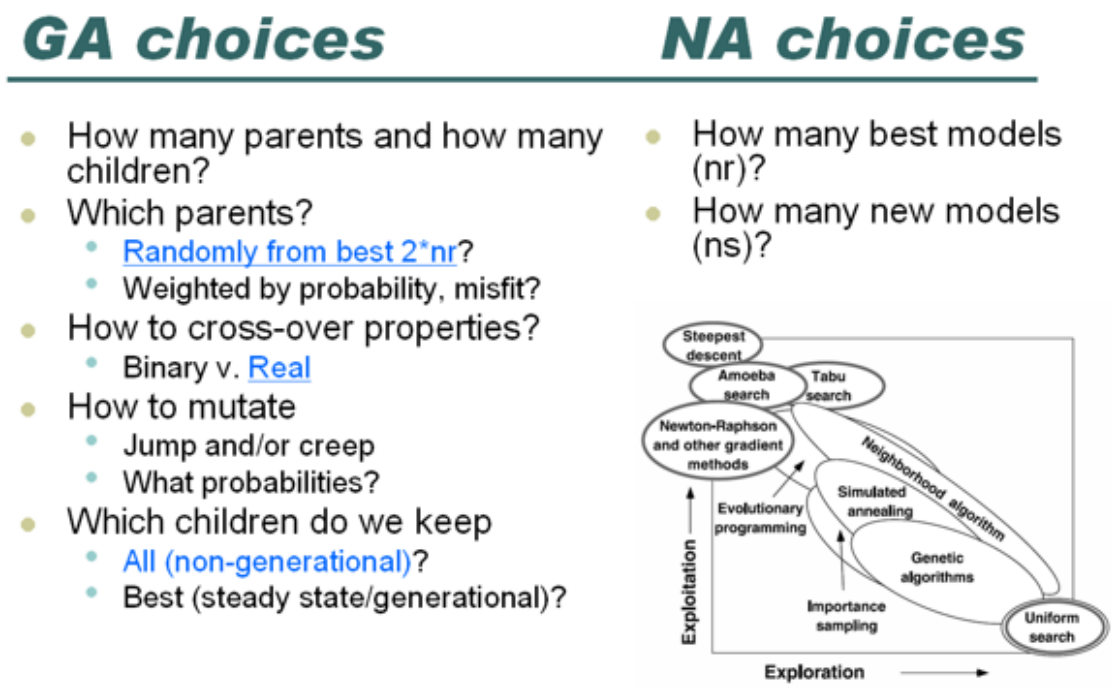

Figure 3.11 Comparison of the choices available in NA and GA methods. Exploitative and explorative powers of the direct search methods (Sambridge and Mosegaard, 2002)

3.7.3 Particle Swarm Optimisation

Another stochastic algorithm utilised in this work is Particle swarm optimization (PSO). The PSO is a population based stochastic optimization technique which simulates the behaviours of bird flocking or fish schooling (Kennedy and Eberhart, 1995). PSO shares many similarities with other evolutionary algorithms such as Genetic Algorithms (GA), but unlike GA, PSO has no crossover and mutation operators. The algorithm has been successfully applied in many history matching cases (Jin *et al.*, 2011; Sagitov and Stephen, 2012, Christie *et al.*, 2013). Previous studies suggest that it is easier to implement than GA and has few parameters to adjust (Sagitov and Stephen, 2012). PSO has also been demonstrated to be more efficient than very fast simulated annealing (VFSA) and neighbourhood algorithm (NA) in optimisation of a problem with complex objective function (Jin *et al.*, 2011).

3.7.3.1 The PSO algorithm

In PSO, each single solution (each model) is like a "bird" in the search space and is called a "particle". The particles (potential solutions) fly through the model space by tracking the current best particles. The algorithm is initialized with ni random particles (models). The fitness of all particles is evaluated and ranked using the misfit function which is to be optimised during history matching. The fitness value of each particle determines its chance of survival, and its velocity determines its direction of flight through the problem space towards the particle with highest fitness value. After the initialisation, the algorithm iteratively searches for the optimal particle. In each iteration, the flight direction of each particle is determined by two other particles: the first is the particles own best fitness so far, or the best from the particles' topological neighbours (the local best), and the other is the particle with the overall best fitness in the entire population (the global best).

The basic elements of a PSO algorithm are summarised as follows:

Step 1: Initialize the swarm from the parameter space
Step 2: Evaluate the fitness of each particle using an objective function
Step 3: Update the local bests and global bests
Step 4: Update the velocity and position of each particle
Step 5: Go to step 2, and repeat until termination criterion is met

In each *ith* iteration, each particle *p* is repositioned to track the positions of the global best (x_{pgb}) and the local best (x_{plb}), by updating its position x_p according to the particle's velocity, v_p:

$$x_p[i] = x_p[i-1] + v_p[i] \tag{3.16}$$

$$v_p[i] = v_p[i-1] + c_1 r_1\left(x_{plb}[i-1] - x_p[i-1]\right) + c_2 r_2\left(x_{pgb}[i-1] - x_p[i-1]\right) \tag{3.17}$$

In Equations 3.16 and 3.17, i is the current iteration, i-1 is the previous iteration, c_1 and c_2 are learning factors which control the attraction to the local best and the global best particles respectively, r_1 and r_2 are numbers drawn from uniform distribution of random numbers in the range 0.0 to 1.0. As the value of c_1 increases the attraction towards the local position increases

and the search with PSO becomes more explorative. On the other hand, increase in the value of c_2 increases the tracking power towards the global best position, facilitating a more exploitative search and faster convergence. Usually $c_1 = c_2 = 2$ is the typical value recommended for the parameters but other values between 0 and 4 have been used in some literatures (Kennedy and Eberhart, 1995; Sagitov and Stephen, 2013). The best values of c1 and c2 may, however, be problem specific. We therefore use a synthetic seismic history matching (a benchmark case) to examine how the balance between the two learning factors (c_1 and c_2) affects the performance of the PSO algorithm.

The calculation of the velocity of the PSO particles using Equation 3.17 has a limitation in that it allows the particle swarm to explode with time as the velocities grow. The velocity is a stochastic variable with an uncontrolled trajectory, and this could lead to a very slow convergence. To prevent this, different techniques for damping the velocities and oscillations have been applied to improve the convergence rate. The velocity equation can be modified by scaling the velocity in the previous iteration with an inertia weight (Shi *et al*., 1998). Alternatively, the swarm movement may be controlled by specifying the maximum velocity, v_{max} $\{if\ v_p[i] > v_{max}, then\ v_p[i] = v_{max}: else\ if\ v_p[i] < -v_{max}, then\ v_p[i] = -v_{max}\}$, or restricting the swarm movement in such a way that no particle flies beyond the model space boundaries $\{if\ x_p[i] > x_{max}, v_p[i] = 0: else\ if\ x_p[i] < -x_{max}, v_p[i] = 0\}$.

3.7.3.2 Tuning the PSO learning factors and inertia weight

Many previous theoretical qualitative have concentrated on mathematical analysis studying the particle trajectories and making suggestions on parameter selections aimed at accelerating convergence rate and avoiding local minima (examples include the works of Clerc and Kennedy, 2002; Van den Bergh, 2006; Campana *et al*, 2006; Poli *et al*., 2007; Trelea, 2003; Jiang *et al*., 2007; Martinez and Gonzalo, 2008).

We will use the synthetic history matching benchmark case described in section 3.2.2 to examine the effects of varying the learning factors and the inertia weight on the stability, hence exploration and exploitation behaviour, of the PSO algorithm, and establish the range of values of the factors that are suitable for seismic history matching. A variant of the PSO velocity equation

proposed in Shi *et al*, 1998 uses the inertia weight, *w*, to scale a previous velocity for more stability. The proposed equation is:

$$v_p[i] = v_p[i-1]w[i] + c_1 r_1\left(x_{plb}[i-1] - x_p[i-1]\right) \qquad (3.18)$$

$$+c_2 r_2\left(x_{pgb}[i-1] - x_p[i-1]\right)$$

Tuning of the PSO parameters means choosing the best values of c_1, c_2 and w to ensure good exploration of the model space and good convergence. In a theoretical analysis, Jiang *et al*. (2007) analysed the convergence of particle swarm theoretically and specified the conditions to ensure convergence through a series of relationships between w and c (where $c = c_1 = c_2$). Given any values of $c_1 = c_2 = c < 4$, the corresponding convergence ranges of w are stipulated in Jiang *et al*. (2007). They proposed that for a stronger exploration and good convergence; $c_1 = c_2 = 1.7$ and $w = 0.715$. On the other hand, Martinez and Gonzalo (2008) proposed some conditions for the stochastic stability of the PSO parameters. They stated that a good choice of inertia weight should be in the range (0.5, 0.8), and the convergence ranges of the learning factors (c_1 and c_2) are obtained through the relationship between the weight and the learning factors. Zhang *et al*. (2015) also propose a guideline for selecting the PSO tuning factors by analysing the dynamic performance of eigenvalues of the particle swarm position, according to control theory. They obtained an expression for the maximum overshoot and angular frequency of damped oscillation and showed how the values of c_1, c_2 and w can be obtained from the overshoot and the frequency. Zhang *et al*, (2015) suggested that the values of the angular frequency, w_d should be in the range$(\pm 2.04, \pm 1.1)$, and the product of the angular frequency and overshoot should always be 1. Other values of c_1, c_2 and w have been suggested in the literatures including: Trelea, 2003 ($c_1 = c_2 = 1.7$, $w = 0.6$), Martinez and Gonzalo, 2008 ($c_1 = c_2 = 1.7$, $w = 0.715$), and Clerc & Kennedy, 2002 ($c_1 = c_2 = 1.494$, $w = 0.729$)

It is obvious from the foregoing that there is no general consensus on what the values of the tuning factors should be. However, most of the researchers agree that $c_1 = c_2 = c > 0$, and $c_1 + c_2 \leq 4$. In the context of the recommended values, we investigate the performance of the algorithm in the synthetic history matching case. The synthetic study is the 6-dimensional history

matching problem in which we update the transmissibility multipliers at some pilot point locations in the reservoir model. We use the PSO to update the multipliers in several number of cases; the values of c_1, c_2 and w are varied systematically so that a distinct set of parameters are set for each case. Table 3.1 shows the values of the PSO parameters used in the various history matching cases. We chose arbitrary values of the angular frequency, w_d, in the range $(1.1, 2.04)$ in accordance with Zhang *et al.* (2015), except in case 15 with w_d value outside the recommended range. The corresponding maximum overshoot, M, and damping ratio, δ, are calculated using:

$$M = {}^{1}/_{w_d} = e^{{}^{-\pi\delta}/_{\sqrt{1-\delta^2}}} \tag{3.19}$$

The inertia constant, w, is calculated using Equation 4.13 (Zhang and Wang, 2009):

$$w = \left(e^{{}^{-\delta w_d}/_{\sqrt{1-\delta^2}}}\right)^2, \tag{3.20}$$

And the learning factors, $c_1 = c_2 = c$, were chosen from the stochastic stability region recommended in Martinez and Gonzalo (2008) ($c_h > c > 0$) where c_h defines the upper sealing of the learning factors, and is calculated using Equation 4.14:

$$c_h = \frac{12(1-w^2)}{7-5w} \tag{3.21}$$

The results of the history matching for the 15 cases presented in Table 3.1 are shown in Figure 3.12. The true value of each of the six reservoir parameter (ie the transmissibility multiplier) is zero, and we expect any good set of PSO tuning parameters to recover those true values at a good convergence rate. In all the cases, the PSO was set to generate a total of 10,500 models after successive iterations following initialisation with 64 random models.

In Figure 3.12, we observed some good convergence rates in Cases 1, 2, 3, 4, 5, 7 and 9. Case 6 showed some signs of convergence, but not as good as the aforementioned cases. In Cases 8, 10, 11, 12, 13, 14 and 15, the models failed to converge or show signs of convergence after generating 10500 models. In general, for the cases that showed good convergence rates, the tuning parameters for the PSO were selected to meet the guidelines proposed in

Martinez and Gonzalo (2008), and the selections were within the angular frequency limits and overshoot proposed in Zhang and Wang (2009) as in Table 3.1. For case 6, the c_1 and c_2 values selected for the PSO were very close to the upper ceiling calculated using Equation 4.14 in accordance to Martinez and Gonzalo (2008). This explains why its convergence rate was lower than the other cases with good convergence.

For the cases where convergence rates were not good, the learning factors were chosen outside the recommended limits, even when the angular frequency, overshoot and inertia weight were within the recommended limits; and in many of the cases $c_1 \neq c_2$.

The foregoing results suggest that the guidelines in Zhang and Wang (2009) combined with the propositions of Martinez and Gonzalo (2008) for selecting the PSO tuning parameters are valid for seismic history matching. Case 2 ($c_1 = c_2 = 1.892$, $w = 0.47$), seems to have the best convergence behaviour. So we will adopt those values in any further history matching with PSO in this work.

Table 3.1. Selection of PSO tuning parameters

	Angular Frequency	Overshoot	Computed Inertia Weight	Martinez and Gonzalo's Proposition	Input c_1	Input c_2
	w_d	M	w	$1 < c < c_h$		
Case 1	2.040	0.490	0.40	0 < c < 2.015	1.971	1.971
Case 2	1.886	0.530	0.47	0 < c < 2.011	1.892	1.892
Case 3	1.729	0.579	0.55	0 < c < 1.971	1.783	1.783
Case 4	1.571	0.636	0.64	0 < c < 1.870	1.640	1.640
Case 5	1.414	0.707	0.73	0 < c < 1.668	1.494	1.494
Case 6	1.257	0.795	0.83	0 < c < 1.297	1.271	1.271
Case 7	1.100	0.909	0.94	0 < c < 0.645	0.996	0.996
Case 8	2.093	0.478	0.551	0 < c < 1.969	2.290	1.710
Case 9	1.637	0.611	0.60	0 < c < 1.922	1.700	1.700
Case 10	1.759	0.673	0.69	0 < c < 1.777	3.790	0.200
Case 11	1.792	0.558	0.74	0 < c < 1.657	2.110	1.890
Case 12	1.697	0.589	0.78	0 < c < 1.516	3.950	0.050
Case 13	1.662	0.602	0.84	0 < c < 1.281	2.000	2.000
Case 14	1.620	0.617	0.90	0 < c < 0.912	1.990	1.990
Case 15	4.678	0.214	0.98	0 < c < 0.226	1.910	1.910

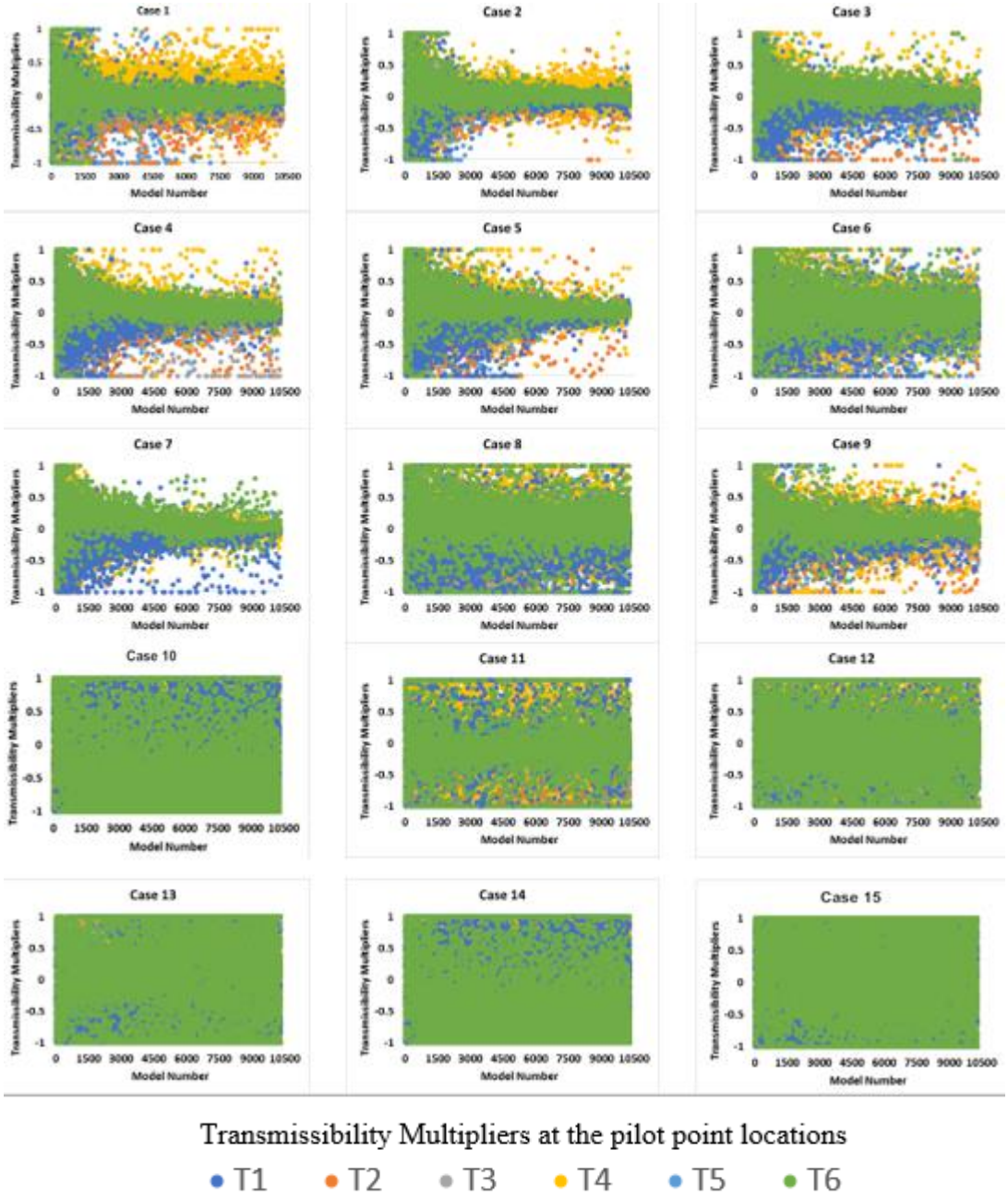

Figure 3.12 The parameter evolution during history matching with PSO for the various cases described in Table 3.1

3.8 Towards Multi-Objective Optimization

A requirement for automatic history matching is that the comparison of the predicted and observed data should be made quantitatively. For each predictable quantity of interest, a misfit value is calculated which is based on the difference in the observed quantity and the predicted quantity at a location in the reservoir and at each time step. The individual misfit values are then summed up to give the value of the global misfit; and that is what most researches do to avoid the complexity in the true multi-objective optimization problem. The multi-objective problem is transformed into a single- objective optimization

with the use of some user defined weights. This approach is reasonably straightforward to apply when using only production data in which case the degrees of accuracy and sample density of the different production variables are comparable and assigning weights to the variables is not an uphill task.

In seismic history matching, on the other hand, we are faced with two major competing objectives. We make use of both seismic and production data which have very different degrees of accuracy and sample density, and are at different scales; so, identifying suitable metric for comparing and assigning weights to their misfits constitute a major difficulty. Hence the subject of this PhD. The observed 4D seismic attribute, such as impedance, is typically derived as a relative property which requires calibration, and there are scale issues requiring a combination of upscaling and downscaling. Therefore, in using the weighted-objectives approach in solving seismic history matching problem; we are faced with a problem of mixing two misfits which are unrelated in any quantitative manner.

The alternative is to modify the optimisation algorithms to handle the objective functions in a muti-objective fashion. The approach has been used in some history matching cases involving different kinds of production variables such as well bottom hole flowing pressures and production rates (Schulze-Riegert *et al*. 2007; Ferraro and Verga 2009, Han *et al*., 2010; Hajizadeh *et al*. 2011; Mohamed *et al*., 2011; Sayyafzadeh *et al*., 2012; Christie *et al*., 2013; Park *et al*., 2013; Stephen, 2013; Olalotiti-Lawal and Datta-Gupta, 2015). Seismic history matching problem was solved as a problem of two objectives in Stephen (2009) using the Multi-objective Optimization Neighbourhood Algorithm (MONA) which is based on dominance.

In dominance-based multi-objective seismic history matching, the goal is to retain all models that satisfy both seismic and production misfits independently. These are called Pareto-optimal models. We will illustrate the principle using the hypothetical diagram in Figure 3.13 where our seismic and production misfits are analogous to the functions f1 and f2. All the points enclosed in boxes in the figure represent feasible solutions of a multi-objective optimisation for the two objective functions, f1 and f2. The points joined by the red line represent the pareto-optimal solutions; which comprises of those models lying on the pareto front for which there are no other models having both the values of f1 and f2 that are lower than theirs. Pareto front is the plot of the objective functions whose non-dominated vectors are in the Pareto optimal set (Deb, 2001). For example, points A and B are Pareto-Optimal solutions because one cannot find any other points on the

feasible region for which either of A and B are dominated (that is, there is no f(X) such that either f1(A) > f1(X) and f2(A) > f2(X) or f1(B) > f1(X) and f2(B) > f2(X) holds: for any point X in the feasible region). Point C, for example, is not on the Pareto front, and therefore not an optimal solution, because it is dominated by both the points A and B.

The multi-objective algorithms used in this research combine the concept of non-domination sorting with the neighbourhood and genetic algorithms. The algorithms are discussed extensively in Chapter 7.

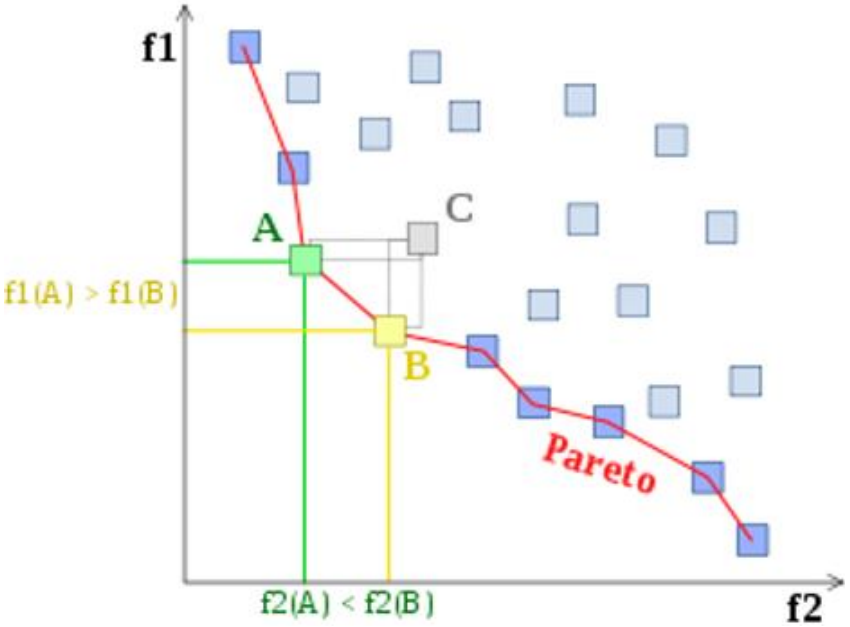

Figure 3.13 Illustration of the pareto frontier (red line) (source: https://en.wikipedia.org/wiki/Multi-objective_optimization)

3.9 Quality of Parameter Estimate

Characterising the uncertainty in the model parameters through *a posteriori* probability density function as a Gaussian distribution around a single minimum will give a wrong estimate of uncertainty if the *a posteriori* probability density function is of more than one mode (Tarantola, 2005; Oliver *et al*., 2008). So, how do we define the quality of parameter estimate? How do we know that our model has converged at the right location? What is the expected value of the misfit function at convergence? What should be the value of the misfit function at the minimum? How do we characterise uncertainty in our parameter estimation?

3.9.1 Misfit Value at Convergence

In deriving Equation 3.13, assumptions have been made regarding the modelling and measurement errors but it is possible that the uncertainties in our models and measurements are underestimated. Too much error in our dataset means that Gaussian distribution is no longer adequate. Tarantola, (2005) suggests that a numerical test (the well-known goodness-of-fit test) could be performed on the value of the objective function at the minimum if the inverse problem is linear. He showed that if the predictions of our model is linear, then the value of twice the misfit function at the minimum has a chi-squared distribution with the mean equal to N_d (number of measurements) and the variance equal to $2N_d$. It is therefore postulated that the expected value of the misfit function at the minimum is:

$$E\left[\mathrm{M}\left(m_{map}\right)\right] = 0.5 * N_d \tag{3.22}$$

where m_{map} is the model that minimises the misfit function, called the maximum *a posteriori* estimate of the model (MAE). Oliver *et al*. (2008) showed through computations with synthetic history-matching that the postulation also applies to non-linear problems. They suggested that the value of the misfit at convergence should satisfy the inequality:

$$N_d - 5\sqrt{2N_d} \leq 2 * \mathrm{M}\left(m_{map}\right) \leq N_d + 5\sqrt{2N_d} \tag{3.23}$$

where N_d is the number of data measurements

Stephen at al. (2007) showed that model error affects model predictions and can be comparable to the data error in size and effect. The model error can be calibrated (Glimm *et al*, 2004; O'Sullivan, 2005; Stephen, 2007) and the mean error used to modify the misfit function, which in turn improves the misfit convergence. However, it may not be worthwhile spending time calibrating the model error if the noise in our data (the data error) is large and dominates the history matching process. The data error can be estimated and its effect removed from the misfit, or used to define the misfit convergence criterion, if we assume that the errors are additive and Gaussian distributed. We consider a case where some uncorrelated Gaussian noise with zero mean and standard deviation σ_d, is added to our data, and modify Equation 3.13 for simplicity, as follows:

$$M = \sum_{k=1}^{N_d} \frac{\left(d_{k,obs} - d_{k,mod}\right)^2}{\sigma_d^2} \tag{3.24}$$

Where $d_{k,obs}$ is our observed data with noise $\epsilon_{k,d}$, and $d_{k,mod}$ is our model prediction with some errors $\epsilon_{k,m}$. We define $d_{k,obs}$ and $d_{k,mod}$ as functions of the 'theoretical' true data without noise(or the 'theoretical' true model prediction) d_k^t, as follows:

$$d_{k,obs} = d_k^t + \epsilon_{k,d} \tag{3.25}$$

$$d_{k,mod} = d_k^t + \epsilon_{k,m} \tag{3.26}$$

and we note that:

$$\sigma_d^2 = f\left(\sum \epsilon_{k,d}^2, \sum \epsilon_{k,m}^2\right) \tag{3.27}$$

We want to define the relationship between the misfit at convergence and the number of data measurements used in history matching. In one case we define this relationship for one case where the data measurements have some errors in form of noise and we ignore the model error, while in the other case we consider both measurement and model errors.

Case I: Misfit due to Noise in the Data

We want to estimate the misfit which is due to the noise in the data, if we can ignore the error in our model. We therefore set the model error, $\epsilon_{k,m} = 0$ so that $\sigma_d^2 = \frac{\sum \epsilon_{k,d}^2}{N_d}$

When we substitute Equations 3.25 and 3.26 (and considering that $\epsilon_{k,m} = 0$ and $\sigma_d^2 = \frac{\sum \epsilon_{k,d}^2}{N_d}$), Equation 3.24 reduces to:

$$M = N_d \tag{3.28}$$

With Equation 3.28, it is postulated that the expected value of the misfit function at the minimum is N_d. Therefore, for a reasonable maximum a posteriori estimate (MAP) of the model, the expected magnitude of the misfit at convergence, if we ignore the model error, equals the number of data measurements.

Case II: Misfit due to Noise in the Data and Model Error

This case follows the same procedure as 'case I', except that in this case $\epsilon_{k,m} \neq 0$, and we assume, as is typically the case, that the noise in the data and model error are not correlated.

With appropriate substitutions into Equation 3.24:

$$M = N_d - 2 * \frac{\sum(\epsilon_{k,d} * \epsilon_{k,m})}{\sigma_d^2} + \frac{\sum \epsilon_{k,m}^2}{\sigma_d^2} \quad (3.29)$$

The term $\frac{\sum(\epsilon_{k,d} * \epsilon_{k,m})}{\sigma_d^2}$ can be neglected because the noise in the data and model error are uncorrelated, giving:

$$M = N_d + \frac{\sum \epsilon_{k,m}^2}{\sigma_d^2} \quad (3.30)$$

The term $\frac{\sum \epsilon_{k,m}^2}{\sigma_d^2}$ represents the misfit due to the model and parameterisation error which should be the misfit at convergence if there is no noise or error in the measurements.

We note here that the results from our analysis of the misfit at convergence does not contradict the findings of Oliver *et al.* (2008) because their definition of objective function makes it take half the value calculated using Equation (3.24).

We investigate the effect of data error in history matching using the SGS synthetic model (see section 3.2.3). We introduce additive noise to the synthetic production data so that the data becomes more representative of real field production data with measurement errors. We then carry out history matching of this data and compare the evolution of the misfit during history matching to the misfit values generated in the case of history matching the synthetic data without noise. In this test cases, four production variables (field water production rates, field oil production rates, producer flowing bottomhole pressure and injector flowing bottomhole pressure) are used to constrain the models generated during history matching. Each synthetic production observable was measured once in a month for a period of 3 years. This gives 36 data measurements for each observable and a total of 144 measurements for the four history variables (N_d =144). Figure 3.14 shows the results for the history matching using the Neighbourhood algorithm (NA), Genetic Algorithm (GA) and Particle Swarm Optimisation (PSO). In the first column (Figure 3.14a for NA, 3.13c for GA and 3.13e for PSO) are the results for the history matching the production data without data error, while the second column (Figure 3.14b for NA, 3.13d for GA and 3.13f for PSO) are the corresponding results for the cases where data error in form of noise was added to the production data.

It is observed that in the cases of the production variables with data error, the production misfit values progressively reduce as history matching continues and eventually settles at some values around the N_d value. The misfits in each case settled at a value of about 170. The net value (170-N_d = 26) not accounted for in each case may be due to model error (parameterisation error). In the cases of production data without noise, the misfit evolution continues even after generating over 5000 models. In real cases, after the misfit settles at N_d, any further history matching will result in fitting the models to data error instead of the true history data.

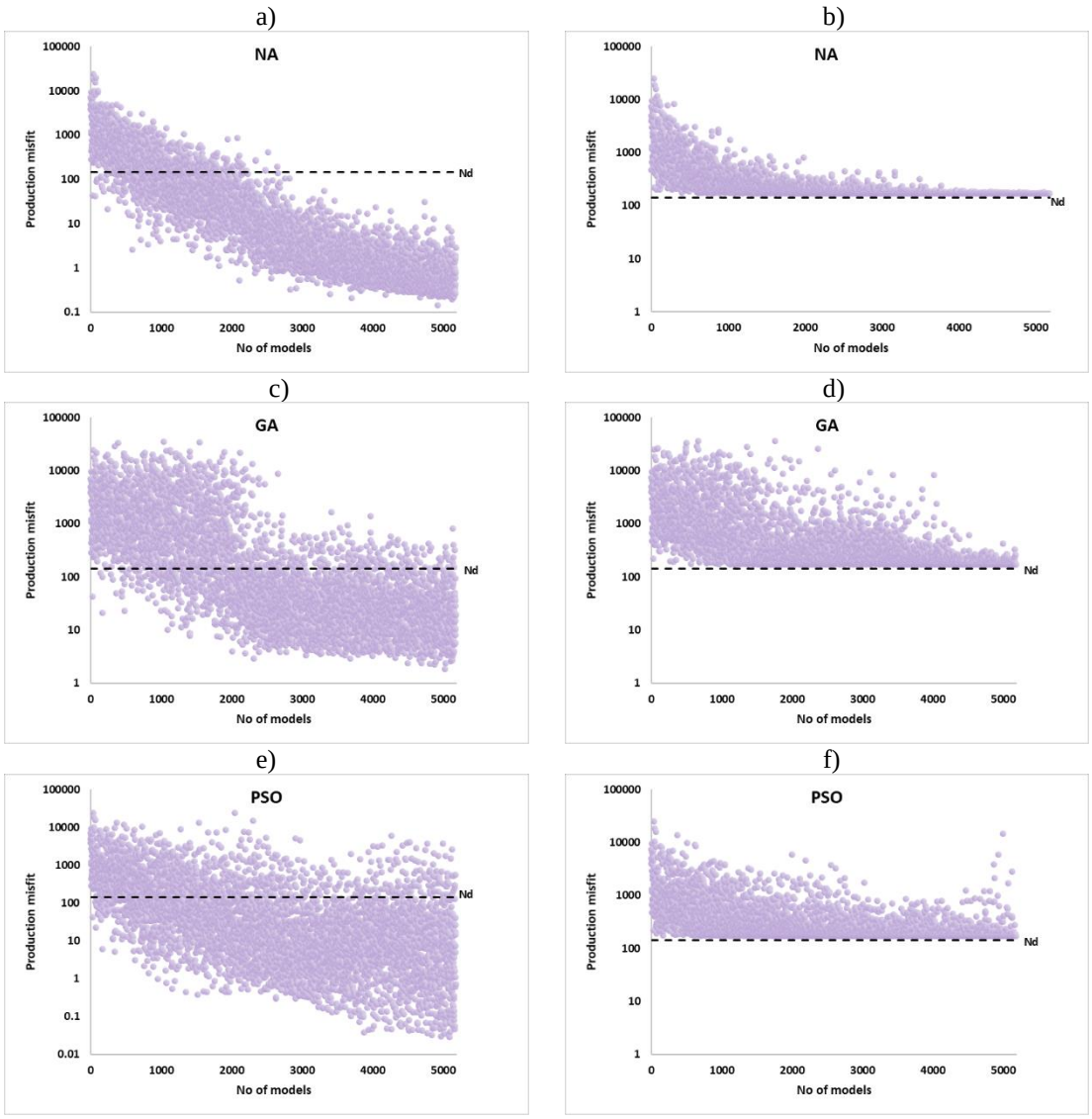

Figure 3.14. The evolution of production misfits in history matching. The production data history matched in the first column has no data error, but the data history matched in the cases on the second column has data error. Three optimisation algorithms were used including: NA (1st row), GA (2nd row) and PSO (3rd row) using GA. The dashed lines are placed at the misfit value of 144 which is equal to the N_d

3.9.2 Uncertainty in Parameter Estimation

A key advantage of stochastic optimisation method lies in identifying multiple realisations of the reservoir model or solutions to the history matching problem and then offer a range of possible outcomes in prediction, as against a single prediction obtainable in manual history matching. Future surveillance data in the form of production and/ or 4D seismic data can then be used to screen out those models with predictions which are not in agreement with measured data, and retain those models which honour the future data. In addition, multiple model solutions allows for the identification of 'good' models as those which honour both the time lapse data and production data. For probabilistic forecasting proxy-models are routinely used as an input to a Monte Carlo sampling process (Fishman 1996). As noted in Greg *et al.* (2006), the likelihood of finding multiple models that honour either the production data or the seismic data is high, but finding those that honour both data simultaneously is very much more challenging. To ensure that good data fitting models are found, it is necessary to generate an ensemble of large number (thousands) of models reflecting as much as possible the different combinations of reservoir model parameters within the specified parameter bound limits

A more robust uncertainty analysis requires that prior information should be integrated with the knowledge provided by the observed data through the framework provided by Bayesian statistics. The full solution of a history matching problem is the *a posteriori* PDF for the model parameters. From the Bayesian perspective, the posterior conditional probability density function PDF(m_{sim}/d_{obs}) for the model m_{sim} given the observed data, d_{obs} is:

$$\mathrm{PDF}(m_{sim}/d_{\mathrm{obs}}) = A_n * \mathrm{L}\left(m_{sim}/d_{\mathrm{obs}}\right) * \mathrm{pdf}\left(m_p\right) \tag{3.31}$$

where $\mathrm{L}\left(m_{sim}/d_{\mathrm{obs}}\right)$ is the likelihood of the model given the data.

Equation 3.31 gives the probability distribution of the models given the measured data. A_n is a constant for normalisation defined in such a way that the integral of the posterior PDF over the model space is equal to one, $\mathrm{pdf}\left(m_p\right)$ denotes the prior probability density function of the parameter model. From the Bayesian point of view, the best combination of parameters in our model, often referred to as the maximum a posteriori (MAP) is that combination which maximizes the $\mathrm{PDF}(m_{sim}/d_{\mathrm{obs}})$. The posterior PDF is however not known and is very difficult to define.

An approximation of the posterior can be resampled using the method of Sambridge (1995) for making statistical inference from any ensemble of models generated during

history matching. After generating an ensemble of models by NA, GA. PSO or any other monte carlo methods, it is useful to qualify the degree of uncertainty of the model parameters by calculating the posterior probability distribution (PPD) because the prior sampling from the optimisation algorithms do not represent the true samples of the posterior PDF. The quality and accuracy of uncertainty qualification will depend on how representative the ensemble distribution of the true PDF is. In this thesis Neighbourhood Bayesian Inference (NABayes) algorithm is used to calculate an approximation of the PPD via a Gibbs sampler (Geman and Geman 1984). In this algorithm (Sambridge 1995), the V-Cell s are constructed to define the neighbourhood for each of the models in the input ensemble. A posterior PDF is defined for each neighbourhood using the Bayesian formulation. Put together, all the neighbourhoods become representative of parameter space and the PPD of unknowns will be interpolated by using the V-Cell s. In the interpolation it is assumed that the known PPD of each model is constant inside each V-Cell . The key merit of NABayes is that during the posterior sampling it does not need to perform any forward modelling during the interpolation procedure thereby saving huge computation time.

NABayes is discussed more extensively and applied in Chapter 5. The appraisal method is also implemented in Chapters 7 and 8.

Chapter 4- Proxy-Assisted History Matching

Overview

Stochastic optimisation techniques require the running of large number of simulations which is expensive and time-consuming. Proxy models in the form of response surfaces can be utilised to speed up the simulation but obtaining some high-quality proxies of reservoir responses has been the challenge. In this chapter, we review the proxy modelling approaches for history matching using different experimental design (ED) techniques in view of reassessing the strengths and weaknesses of the proxy methods. We use proxy models on the SGS synthetic model described in the Chapter 2 to assess the performance of the ED approaches and find out those most suitable for history matching. We also suggest ways of improving the quality of proxy models for history matching.

4.1 Introduction

There has been efforts geared towards tackling the challenge of high CPU time required in stochastic history matching, including efforts to speed up simulation through streamline reservoir simulation (Tang *et al*. 1991; Agarwal and Blunt, 2004: Maschio and Schiozer, 2004; Kretz *et al*., 2004; Moreno *et al*., 2004, Thiele *et al*., 2010; Al-Najem *et al*., 2012; Zhang *et al*., 2014; Tanaka, 2015), and efforts to sort and select a moderately small sample of the equiprobable models to create new ensemble of models and conduct uncertainty analysis through posterior simulation. This chapter will focus on a different approach in which the reservoir response of interest is approximated using response surface methodology (RSM), otherwise called *Proxy Model Approach.*

Using a combination of an automatic history matching and a proxy-modelling workflow, we aim to reduce the high cost of computation which characterises the stochastic approach to history matching problems and reservoir predictions, without sacrificing quality in our solutions.

We will represent the response generated from our simulation runs by proxy functions for the chosen objective functions. In the case of two objective functions, one proxy will be representing the dependency of the production misfit on the model parameters while the other proxy function will consider the dependency of seismic misfit. Our proxy models are generated using a hybrid of genetic programming based symbolic regression method and a deterministic regression algorithm. Pure symbolic regression in genetic programming discovers free-form mathematical models from the ensemble of models and

can easily give several possible solutions. On the other hand, the deterministic regression method lacks the flexibility of the genetic programming based symbolic regression. In our approach, we choose a deterministic mathematical model in the form of a quadratic response surface and then adopt the symbolic regression in our search for the coefficients of all the terms in our chosen model. Some error metrics are used here to determine the quality of the proxies. Also, blind/validation tests, are used in appraising the mathematical models.

With our response surface represented by high quality proxies of the misfit functions, we can afford to:

- Sample a large number of combinations of parameters and analyse the sensitivity of our misfit functions, represented by their respective proxies, to the model parameters.
- Sample a large number of combinations of parameters while minimising our global single misfit function represented by a single proxy, with a single objective optimisation tool such as Genetic Algorithm.
- Sample a large number of combinations of parameters while minimising our multiple misfit functions, represented by the proxies of the chosen misfits, with multi-objective optimisation tool such as the Pareto Based Multi-objective Genetic Algorithm.

4.2 'Proxy' in Oil and Gas Applications: a Literature Review

The worth of a model in effective reservoir management and future field development is not only dependent on its ability to give predictions that match the historical data but also on its ability to accurately predict the future performance of the reservoir. However, history matching is non-unique, and stochastic methods of history matching produce an ensemble of models giving range of probabilities in predictions that give a good match to the historical data. Unfortunately, the different models in the ensemble, despite matching the reservoir past behaviour, will often yield conflicting results when selected for predicting the behaviour of the reservoir in future. Because of this non-uniqueness, it is not uncommon to link the range of the possible models to the uncertainty arising from any chosen reservoir development scenario. It then becomes necessary to develop and adopt the techniques which consider the misfits of the predictions of the models to the historical data, and captures the broadest probable combination of the model variables so

as to evaluate the uncertainty associated with any choice of model made. Considering the complexities and cost of running computer simulations, the task of generating and appraising an ensemble of thousands of models is not an easy one. Fortunately, methods for sampling model parameter and uncertainty analysis runs very much faster when the reservoir simulation response is approximated with a proxy. For history-matching, the misfits carry the information on the observed data, guides the search process and should be a rational target to build a response surface on. Through regression on the available ensemble of models and their corresponding misfits, a response surface function or proxy is obtained to define the mathematical relationship between the variation of the model variables and the misfit function. Sampling the response surface virtually yields an immediate probabilistic distribution of the models and the model response at near-zero cost compared to the time to simulate the same process by running an actual reservoir simulation. The huge time redeemed positions the proxy model as more advantageous when compared to model updating using a reservoir simulator (Amudo *et al*., 2008).

Although the experimental design and response surface modelling applications originated in the field of clinical and agricultural studies, there has been a large body of work applying the concepts in the petroleum industry:

- For screening design: to assess the influence of the various uncertain parameters on the reservoir responses (Damsleth *et al*., 1992; Kjonsvik *et al*., 1994; Jones *et al*., 1997; England and Townsend, 1998; Corre *et al*., 2000; Guerrero *et al*., 2000; Venkataraman, 2000; Manceau *et al*., 2001; White *et al*., 2001; Akshay, 2003; Friedmann *et al*., 2001; Peng and Gupta 2003; Portella *et al*., 2003, White and Royer, 2003; Yeten *et al*., 2005; Amudo *et al*., 2008; Bogatkov and Babadagli, 2009; Jaime *et al*., 2015 etc.) .
- For uncertainty analysis of reservoir simulator responses given different combinations of model parameters (Akshay, 2003; Friedmann *et al*., 2001; Bevillon and Mohagerani, 2015; Jaime and Sadiq, 2015 etc.)
- For history matching (Queipo *et al*., 2000; Kabir and Young, 2001; Manceau *et al*., 2001; White *et al*., 2001; Landa and Güyagüler, 2003; Alessio *et al*., 2005; King *et al*., 2005; Peake *et al*., 2005; Reis, 2006; Castellini *et al*., 2008; Slotte and Smorgrav, 2008; Arwini and Stephen, 2011; He *et al*., 2015 etc.)
- For reservoir management and optimisation of field development programme (Aanonsen *et al*., 1995; Pan and Horne *et al*., 1998; Vincent *et al*., 1998; Guyaguler *et al*., 2000; Kabir *et al*., 2002; Purwar *et al*., 2010; Vincent *et al*.,

2002; Badru and Kabir 2003; Ozdogan *et al*., 2005: Zangl *et al*., 2006; Yeten, 2007; Zerpa *et al*., 2007 etc.)

- For Prediction and Optimisation of Phase behaviour (Ahmadloo *et al*., 2009; Adeyanju *et al*., 2015 etc.)

Table 4.1 gives a summary of some previous studies on the application of experimental design techniques and proxy modelling in oil and gas industry. Whereas the literature adopted in varying degrees the general proxy-modelling workflow, it is pertinent to note that more work needs to be done especially in assessing the quality of the proxy model and its representativeness of the reservoir response. Notably, the major challenge in the application of response surface modelling, which has limited its application in history matching problems, has been: to obtain high quality proxies for the strongly non-linear history matching problems. Zubarev (2009) criticised the use of proxy-modelling methodology for history matching and stressed that its use is not recommended for history matching where the solution space is complex and the number of uncertain parameters is high. Figure 4.1 shows the general workflow commonly adopted in oil and gas applications such as history matching.

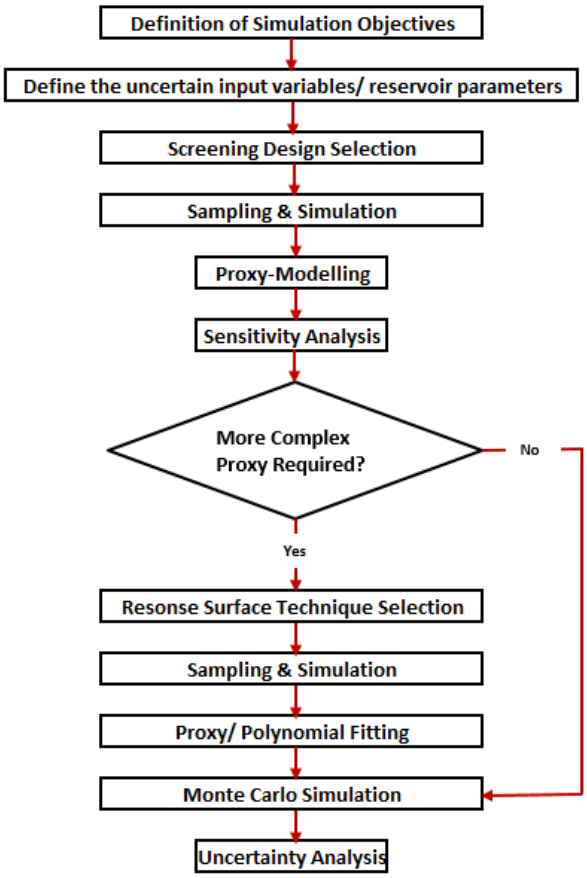

Figure 4.1. General Workflow for Proxy Approach in Reservoir Simulation

Table 4.1 Application of experimental design techniques and proxy modelling in oil and gas studies

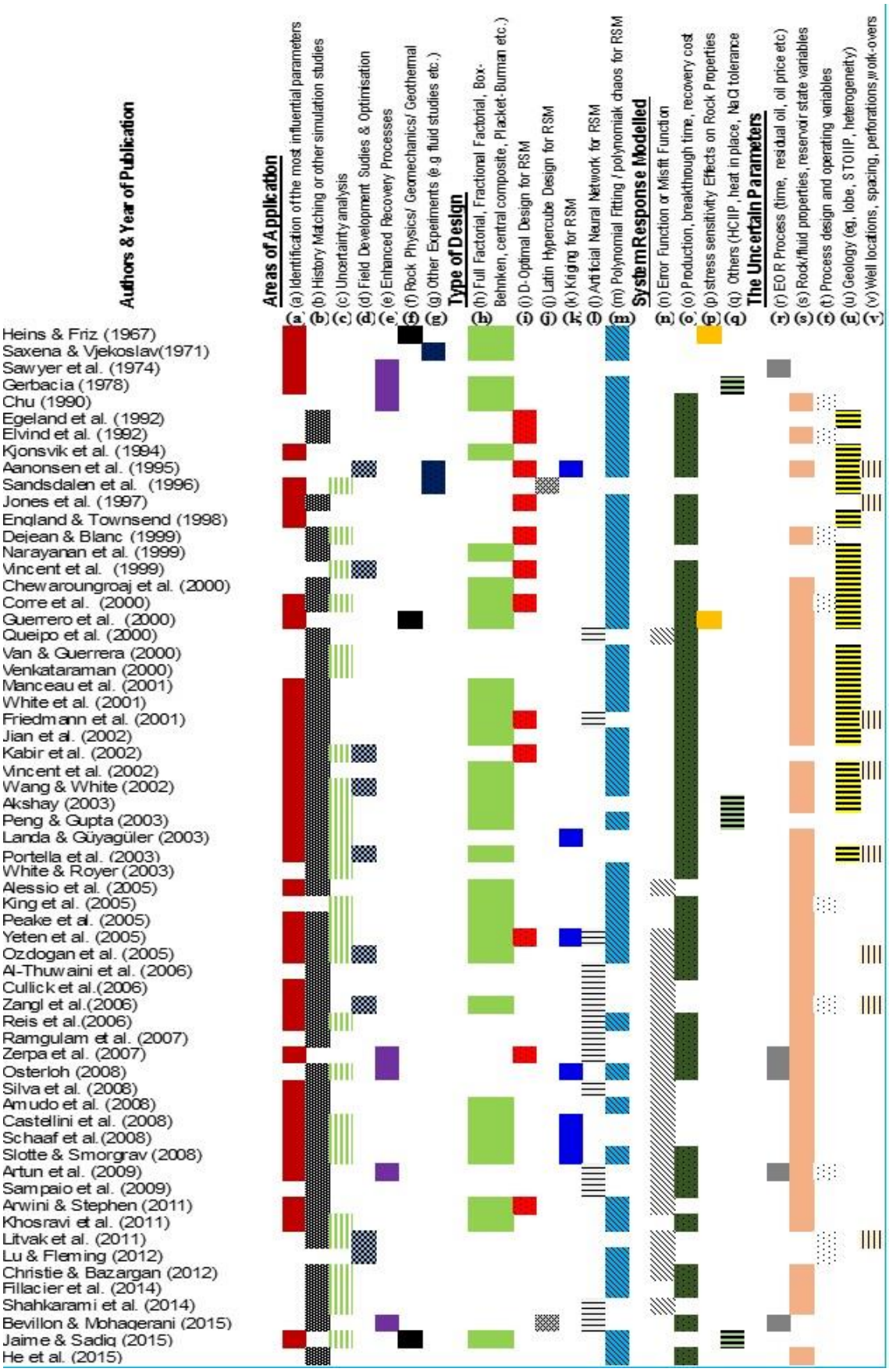

Some applications available for multiple realisation optimation using proxy approaches include MEPO (Schlumberger Software) and CMOST (CMG Software). Features available in MEPO optimizer includes polynomial regression, kriging and neural network. On the other hand, proxy approach to optimisation in CMOST relies on Latin Hypercube Design for generation of initial models, and on either kriging or polynomial regression for building proxy models using training data.

A review of the essential elements of the proxy-modeling workflow for history matching follows.

4.2.1 Proxy Modelling and Simulation Objectives

A proxy model is in general built to act as a surrogate to the actual model and should therefore be a good approximation of it. The design used in selecting the sampling points in the parameter space varies and depends mainly on the objectives of the experiment, simulation and proxy-modelling. Also, a screening design for sensitivity analysis of the variables impact on the response may be chosen, or a response surface modelling (RSM) design which is more robust is chosen for better precision of the approximation to the actual response at any location in the sampling space. The parameter screening designs (mostly factorial and Plackett-Burman designs) are basically linear designs to rank the uncertain variables based on their effect on the response variable(s) of interest. In contrast, the RSM designs are mostly quadratic designs for capturing the quadratic relationship between the uncertain variables and the response variable(s) of interest.

4.2.2 Experimental Design in Proxy-Modelling

In reservoir fluid dynamics, the model parameters typically have different levels of influence on pressure measurements, flow rates and volume measurements and recovery data. The parameter screening stage is often necessary so as to delineate the initial scope for defining the level of uncertainty of the parameters in for instance, history matching. Approximation of the actual model is often done with a second order polynomial. Some of the previous works are listed below in accordance to their experimental design and proxy types:

Methods for Screening: Different designs including full factorial design, factional factorial design, Placket-Burman design (Placket and Burman, 1946) or some subsets and modifications of them, have been adopted by many in oil and gas applications to reduce the number of uncertain parameters to those that significantly impact on the system

response (Saxena and Vjekoslav, 1971; Sawyer *et al*., 1974; Kjonsvik *et al*., 1994; Dejean and Blanc, 1999; Chewaroungroaj *et al*., 2000; Guerrero *et al*., 2000; Corre *et al*., 2000; White *et al*., 2001; Kabir *et al*, 2002; Vincent *et al*., 2002; Zou *et al*., 2002; Akshay, 2003; Friedmann *et al*., 2001; Peng and Gupta, 2003; Portella *et al*., 2003; Jian *et al*., 2004; Esmaiel *et al*., 2005; Zangl *et al*., 2006; Aulia *et al.*, 2017). Two-level designs (such as Plackett-Burman), which set the sampling range to be the maximum and minimum values of the dependent variable is widely applied in screening but lacks the ability to detect any non-linear relationship between the model parameters and the objective function. Oliver *et al*. (2008) discusses some modifications to the fractional factorial designs and Placket-Burman and implies that improvements in unmasking the interaction terms confounded in the main effects is achieved using mirror fold-over designs and Box-Behnken designs (White *et al*., 2001; Friedmann *et al*., 2001; George *et al*, 2005) and Central Composite Designs (Chu, 1990; Dejean and Blanc, 1999; Venkataraman *et al*., 2000; Manceau *et al*., 2001; Wang and White, 2002; Akshay, 2003; Ajibola *et al*., 2013;) but they require making some additional simulation runs or experiments.

Methods for Response Surface Modelling (RSM): The designs for calibrating quadratic use 3 or 5 levels for each model parameter, but not all level combinations as in full factorial design. Some designs previously identified at the screening stage can be modified and adapted for response surface modelling. For example, a central composite design which is commonly used for RSM can be designed by adding some star points to a previously-designed three-level factorial or three-level fractional factorial design so as to add curvature terms to the design. Depending on the size of a history matching problem, Oliver *et al*. (2008) showed that a full factorial design can also be used for RSM if the parameters identified as the most influential using Plackett-Burman screening do not exceed three. But for cases with more than three influential parameters, D-optimal design has been recommended for the maximization of the orthogonality of the set of parameters for limited number of experiments (Myers *et al*., 2009), and has been applied in several oil and gas publications (Elvind *et al*., 1992; Aanonsen 1995; Jones *et al*, 1997; Vincent *et al*., 1998; Corre *et al*., 2000; Kabir *et al*., 2002; Friedmann *et al*., 2001; Esmaiel *et al*., 2005; etc.).

Another design that has been found to be efficient, though has not been widely applied, to RSM is Latin Hypercube Design. Sandsdalen *et al*. (1996) applied the Latin Hypercube technique in a hierarchical model to generate a large number of probable model parameter combinations for uncertainty analysis. Bevillon and Mohagerani (2015) applied Latin-

Hypercube experimental design technique for proxy-modelling and uncertainty analysis of miscible EOR simulation cases based on 19 uncertain parameters. Fedutenko *et al*. (2013) also used Latin-Hypercube Experimental Design in sampling different combinations of operational parameters, that control the predictions of a steam assisted gravity drainage simulation (SAGD), for proxy-modelling to predict the future performance of a SAGD operations. Peng and Gupta, (2004) conducted an in depth comparative study in which Hydrocarbons Initially in Place (HIIP) were predicted through different traditional designs of experiment and through designs based on polynomial fitting, Latin Hypercube Design and Kriging, and found no significant difference in the HIIP evaluated using the different designs. In a similar study, Yeten *et al*., (2005) performed sensitivity analysis, risk analysis and probabilistic forecasting by studying different designs for simulation and proxy-modelling, and reported acceptable results for polynomial-fitting, splines and kriging. On the other hand, the results from Placket-Burman, central composite and D-optimal designs were reported to be unsatisfactory because these types of designs allow sampling only at the domain boundaries.

This work considered the use of some of the sampling methods in building proxy models. The suitability of each method is investigated in proxy-assisted synthetic history matching

4.2.3 Proxy- model Accuracy and Validation

Through validation, proxy-model prediction accuracy is verified by comparing the response values predicted by the model to the results of full numerical simulation for a set of experiments not included in the dataset used for the modelling. The data included in the modelling is called training data while those used for verification are called validation data. The set of data sampled initially from the parameter space may not give proxy-model of reliable quality. The quality of the model should therefore be verified in-between stages of additional simulation runs until high quality model with very good predictability, confirmed with validation data, is obtained. In addition to the check with validation data, the quality of proxy at any time during regression can be measured by various error metrics some of which are described in the following discussions.

Mean Absolute Error (MAE): This metric assumes that noise in the data is double-exponentially distributed. The aim in using this metric is to reduce the mean of the absolute values of the residual error to the barest minimum:

$$MAE = \frac{1}{N_d}\sum_{i=1}^{N_d}|O(m) - O(m)'| \quad (4.1)$$

Where N_d is the number of training dataset

O(m) and *O(m)'* are the actual dataset values and proxy-predicted values respectively

R^2 Goodness of Fit or Coefficient of Determination: The aim in proxy-modelling is to maximise R^2 (for maximum explained variance).

$$R^2 = 1 - \frac{SS_{res}}{SS_{tot}} \quad (4.2)$$

Where $SS_{tot} = \sum_{i=1}^{N_d}\left[O(m) - \overline{O(m)}\right]^2$ is the total sum of squares (proportional to the variance of the data), and

$SS_{res} = \sum_{i=1}^{N_d}[O(m) - O(m)']^2$ is the sum of squares of residuals (proportional to the unexplained variance), also called the residual sum of squares

Aside the more general metrics defined above, other metrics can be used depending on the purpose, for instance: mean square error, logarithm Error, interquartile absolute error, signed difference, maximum error, median error, hybrid correlation, Spearman's rank correlation, log loss error, hinge loss error, slope absolute error etc.

There have been some attempts to integrate one form of the error metric or the other into the history matching workflow. For instance, in an effort to improve on the predictions of kriging proxy-model, Jones *et al.* (1998) included the error of the predictor into the objective function to account for the uncertainty of the proxy-model estimate. In similar approaches, Queipo *et al*. 2000 used the artificial neural network (ANN) as a predictive proxy-model taking the ANN prediction error into account while Slotte *et al.* (2008) included the kriging variance into an objective function in an iterative workflow to improve on the results of history matching using proxy-models.

4.2.4 Suitability of Proxy Approach in History Matching

Various design methodologies have been adopted to obtain maximum amount of information from reservoir simulation response for a minimal number of runs. However, creating high quality proxy-models has been a challenge because reservoir simulation

produces a highly non-linear output. Traditional experimental designs sample at the edge of the parameter space and therefore tend to produce results which may be biased towards the extremes and skewed against the contributions from the parameter locations in the spaces in-between the extremes. Latin Hypercube Designs, in particular, have been demonstrated to be 'space filling' and more efficient. However, considering the non-linear nature of the simulation output, designs that produce a uniformly distributed dataset over the parameter space for simulation runs might not be satisfactory for building of a proxy-model that approximates the reservoir simulation response appropriately.

Zubarev (2009) compared the efficiency of stochastic optimisation using the full simulator to that of proxy-modelling in history matching and concluded that proxy models are not suitable for history matching especially as the solution space and uncertainty increase in complexity. On the other hand some other researchers have demonstrated the usefulness of some proxy approaches in complex history matching problems. Acceptable results have been obtained through the use of polynomial fitting and multi-dimensional kriging for history matching (Junker *et al*., 2006; Osterloh, 2008; Slotte and Smorgrav, 2008). Cullick *et al*. (2006) also found that the results with proxy-model in history matching are good when a nonlinear proxy neural network is used for proxy-model following a small number of numerical simulation runs based on experimental design – highlights of this study can also be found in Denney, 2007. Queipo *et al*., (2000) proposed a methodology for estimating porosity and permeability through the construction of a surrogate of an objective function based on neural net-works, DACE (Design and Analysis of Computer Experiments)/ kriging modelling, and adaptive sampling. Archer *et al*., (2005) demonstrated the suitability of proxy-model in history matching and well-placement by using spline to build response surface of the objective function-based proxy model. Li *et al*. (2005) proposed a modification to the spline-proxy, suitable for outputs characterised as non-linear and non-uniformly distributed, through partitioning of the whole parameter space into sub-domains and performing additional sampling in the most sensitive sub-domains.

We will take a different approach in seeking robust proxy-approximation of the reservoir response and in generating the solution of history matching problem using a Genetic Programming based Symbolic regression. We use proxy-assisted history matching in

- Investigating the performance of the different experimental design techniques and the response surface methodologies in history matching
- Handling conflicting multi-objective functions in seismic history matching.
- Appraising model parameters, analysing uncertainty and making predictions

Key questions to be answered include:

- How reliable are the proxy models derived from the different response surface modeling techniques?
- In what way can the quality of the proxy models be improved?

4.2.5 Proxy-Assisted History Matching: the methodology

We adopt the automated history matching technique shown in Chapter 2 (Figure 2.1) which includes time-lapse seismic data along with production data in conditioning reservoir models. The workflow enables the generation of multiple models using a stochastic approach to inversion in an iterative loop to obtain a good match to production and 4D seismic data. We perform history matching of the SGS model (described in Chapter 3 under section 3.2.3) by updating the six transmissibility multipliers at the pilot point locations. The base case model is fed into the iterative loop where the $\log_{10}$ of the multipliers are perturbed each within the range [-0.3, 0.3] using the pilot point parameterisation scheme. Then multiple models are generated randomly and fed into the forward modelling stage. The forward modelling stage is implemented using a standard reservoir simulation tool (Schlumberger's Eclipse 100) for the prediction of reservoir response variables, and petro-elastic model (PEM) for the prediction of the changes in seismic attributes such as AI. Predictions from the forward modelling stage are compared with the observations. (Stephen *et al*., 2006, Kazemi *et al*., 2011, Arwini and Stephen, 2011).

The evaluation of misfit is done for both the production and seismic data to generate a single global misfit for each model. Using the information available in the form of misfit, the search for the optimal solutions is guided by the optimisation algorithm. This work uses a Genetic Algorithm (GA), the Particle Swarm Optimisation (PSO) and the Neighbourhood Algorithm (NA) all of which are stochastic inversion algorithms with varying degrees of explorative and exploitative capability in search of solution space. Depending on the setting of the optimisation algorithm, certain number of models are generated in the iterative loop together with their respective misfits. This constitutes an ensemble of models which is fed into the next step – proxy-modelling.

The workflow in Figure 4.2 incorporates the proxy-modelling to the automatic history matching workflow. Fewer simulations are run: just enough to represent our reservoir simulator with a response surface model (RSM). The parameter space can then be searched more widely with the RSM. Polynomial fitting using Genetic Programming

Based Symbolic Regression (GP-SR), available in the Nutonian tool – Eureqa, is adopted in proxy-model building. The GP-SR uses a stochastic iterative search technique (the genetic algorithm) to explore the space of all possible symbolic models defined as valid mathematical functions on the given set of input variables, basic functions, and constants. The genetic algorithm searches for a set of mathematical models which minimises a fitness objective, usually defined in form of error metric(s). While the choice of Symbolic regression (SP) enables us to discover free-form mathematical models from an ensemble of models that give high quality response surface models in terms of error metrics, we have chosen to be 'deterministic' in our choice of response surface.

In symbolic regression, mathematical models are approximated by some formula using a few building blocks or basis functions. For example, Taylor series requires just some terminals (such as some variables and constants) and some operators (addition, subtraction, multiplation/ division while Fourier series requires additional trignomatory opertaors such as sines and cosines. We have chosen to represent the relationship between the variation of parameters (such as the transmissibility multiplier at the pilot point locations) and reservoir response (in the form of seismic and/or production misfit or the total misfit) by a quadratic polynomial - which follows from the second order approximation of Taylor series. The GA-based regression returns multiple expressions containing different numbers of basis functions. In our synthetic history matching case which has 6 model parameters (the pilot point multipliers), the full quadratic model requires 28 coefficients (the number of basis functions). The coefficients are generated initially at random or based on some prior information and are then evolved iteratively through the evolutionary process of fitness evaluation, selection and crossover using genetic programming. Proxy models are built on the training data but the identification of the 'best' models at the selection stage is based on the error metric evaluated using the validation data. The quality of proxy at any time during regression can be measured by a number of error metrics, evaluated for comparison and optimisation of proxy models, such as Mean Absolute Error, R^2 Goodness of Fit etc. (see section 4.2.3).

We will review the results of history matching using different sampling methods appropriate for calibrating full quadratic models including the Central Composite Design (CCD) – also known as Box-Wilson design, Box-Behnken Design (BBD), D-optimal Design and compare those to the results generated from designs based on Latin Hypercube Design and the methods based on random number generators.

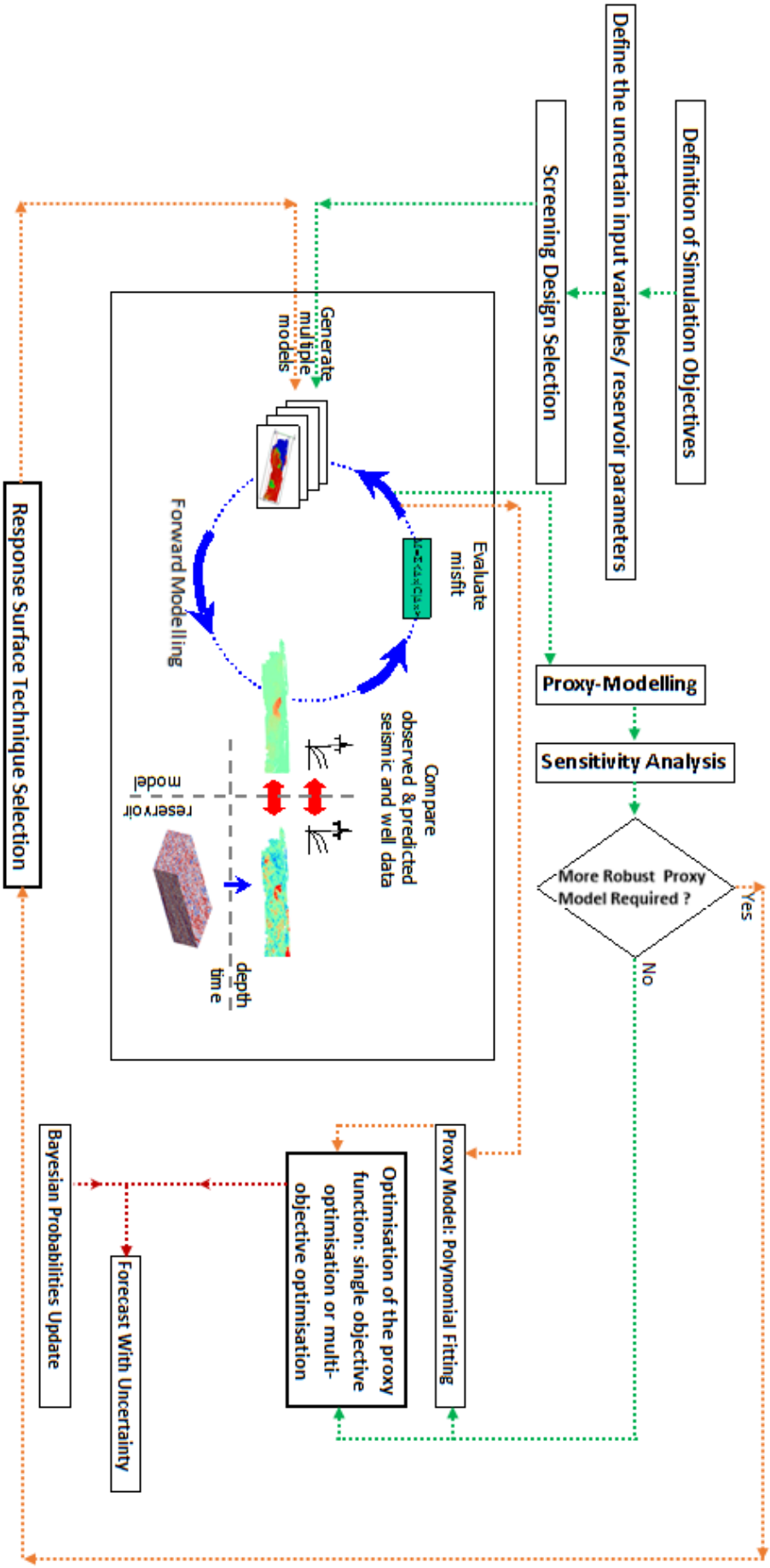

Figure 4.2. Automated History Matching and Response Surface Modeling

We will investigate if the type of optimisation technique (Genetic Algorithm, Particle Swarm Optimisation or Neighbourhood Algorithm) used in generating our ensemble of models matters, given that our proxy-modelling or polynomial fitting will be done through Genetic Programming based Symbolic Regression.

4.2.6 Estimating the Quadratic Coefficients

A quadratic polynomial is often considered sufficient in describing the main effects, the quadratic effects and the second-order parameter interactions (Oliver *et al.*, 2008). We therefore approximate the actual misfit surface using a proxy of the form:

$$M(\underline{T}) = A + \sum_{i=1}^{N_T} B_i T_i + \sum_{i,j=1}^{N_T} C_{(i,j\geq i)} T_i T_j \qquad (4.3)$$

where $M(\underline{T})$ represents the misfit function at any point in the sampled parameter space represented by the vector, $\underline{T}$. N_T is equal to 6 (the number of sensitive model parameters) in our history matching case. The coefficient terms A, B_i and $C(i, j \geq i)$ are regression coefficients which we determine using a GA-based symbolic regression. A is the constant term, $\sum_{i=1}^{N_T} B_i T_i$ is the sum of the main effects, $\sum_{i,j=1}^{N_T} C_{(i,j\geq i)} T_i T_j$ is the sum of interaction effects for $j>i$ and is the sum of quadratic effects for $j=i$. We describe some experimental design techniques and calibrate the quadratic misfit surface using the design points generated by each of the techniques as follows.

The number of coefficients which completely characterises a full quadratic model is $(N_m+2)(N_m+1)/2$ where N_m is the number of uncertain reservoir parameters updated during history matching. In our synthetic history matching method described previously in section 3.2.3 of Chapter 3, $N_m = 6$, and the number of coefficients estimated equals 28. For the various sampling methods described below, the coefficients were estimated for the proxy model for which the total misfit (sum of production and seismic misfits) was considered the response variable (Table 4.2) and for separate production responses (Table 4.3) and seismic responses (Table 4.4) in the form of the misfit between the predicted and the observed data. The parameters in each case are the $\log_{10}$ transmissibility multipliers at the pilot point locations described earlier.

Central Composite Design (CCD) was introduced by Box and Wilson (1951) and is known to be useful in response surface methodology for calibrating full quadratic models. The CCDs are of three types, namely: circumscribed, inscribed, and faced. The different

types are shown in Figure 4.3 for 3 design variables and five levels for each variable. The five levels: low axial, high axial, low factorial, high factorial and the central point, serve to provide enough information to calibrate a second order polynomial, known as quadratic models (Montgomery, 2017). We used the circumscribed CCD to generate design points giving a total of 59 simulation runs.

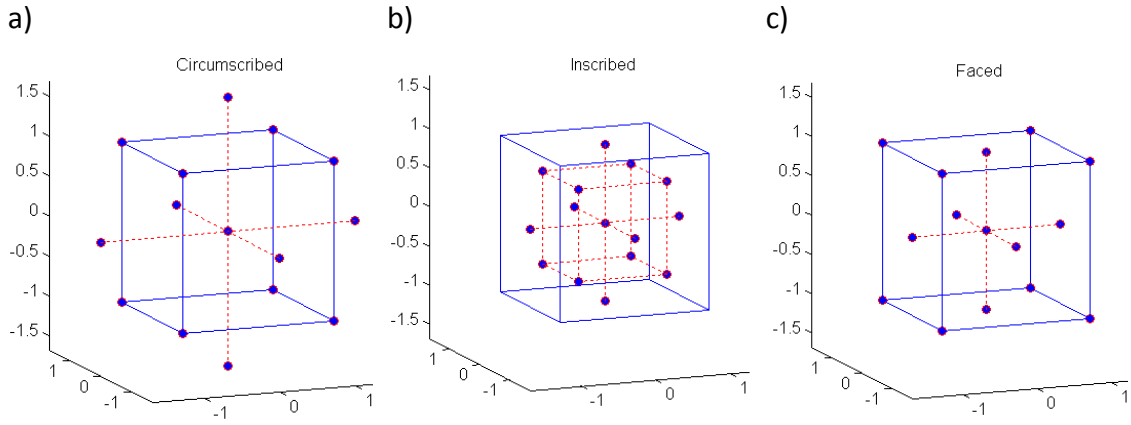

Figure 4.3 Types of central composite design

Box-Behnken Design (Box and Behnken, 1960) is an improvement to the full three-level factorial design aimed at calibrating full quadratic models at reduced number of experimental runs. In this design, corners of the model space are avoided (Figure 4.4), so the design requires fewer experimental runs than the CCDs. The estimates tend to be good over central subset of model space but may be poor in estimating the extreme parameter combinations (Montgomery, 2017). The number of simulation runs generated using the BBD is 54.

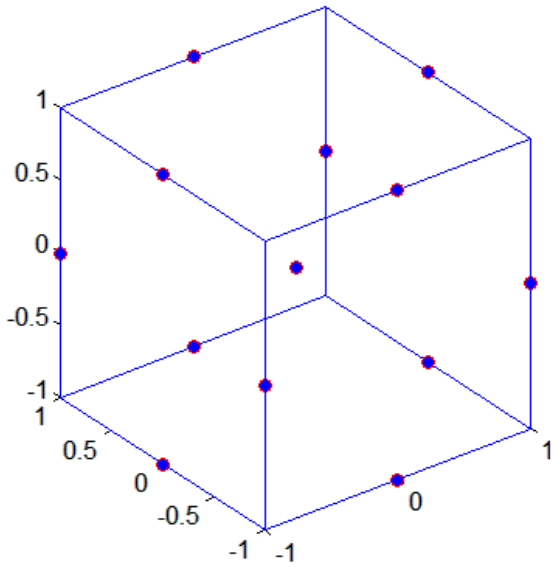

Figure 4.4 Box-Behnken Design (BBD)

D-Optimal Design (DOD) is a model-specific design which uses iterative search algorithm to optimise the design points. The optimality of D-optimal design is model dependent, and the experimenter must specify a candidate set of possible parameter combinations runs before an algorithm can generate the desired or optimal set of experimental runs (Montgomery, 2017)

We chose the entire design space as our candidate set to generate the optimal design consisting of 65 experimental runs.

Latin Hypercube Design (LHD) is a statistical sampling method first introduced by McKay *et al*. (1979), in which samples of parameter values are systematically generated from a multidimensional distribution. LHD (Figure 4.5) ensures that each of the design variables has all parts of its range represented in the samples (Wang, 2003). As in the case of D-Optimal design, we generated 65 design points using the LHD.

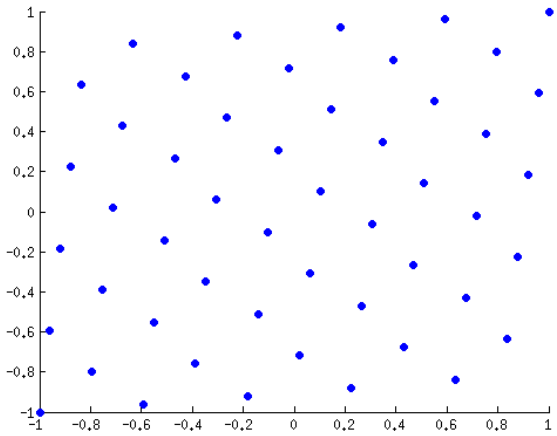

Figure 4.5 Two-Dimensional geometry of Latin Hypercube Samples (Source: http://sumo.intec.ugent.be/node/139)

For comparison, we also calibrated the quadratic model of the reservoir responses using 65 design points generated using random designs. In random designs, the model parameter values for the simulation runs are assigned on the basis of a random process. Two random designs are considered here, namely: ***quasi random number generator*** (QRNG) and ***Saleev-Antonov-Sobol*** (SAS) (Antonov and Saleev, 1979).

We note the difference between the random designs and LHD: in random designs, there may be regions of the design space that are not sampled and other regions that are densely sampled; in LHD, a value is chosen once and only once from each interval of each parameter so that the entire design space is adequately sampled (Wang, 2003). We also note that SAS design points based on sobol sequence (Figure 4.6a) are more evenly

distributed than the QRNG design points (Figure 4.6b) which are sequences of pseudo-random numbers (Morokoff and Russel, 1994).

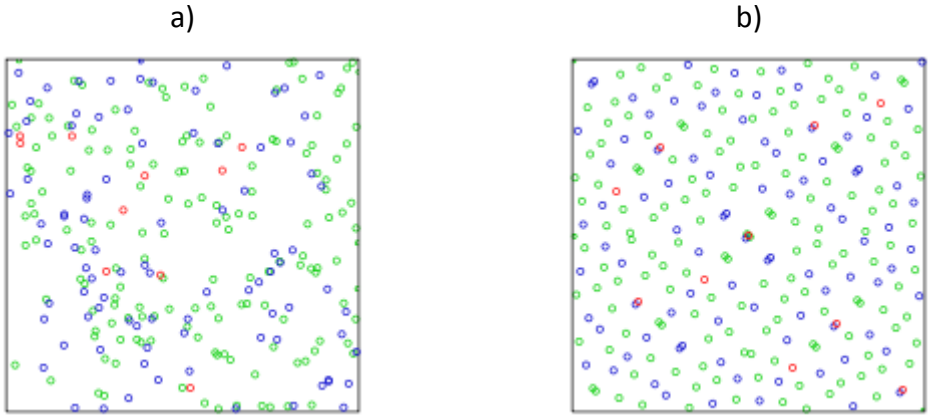

Figure 4.6 Design points from a) quasi-random number, and b) sobol sequence (Source: https://en.wikipedia.org/wiki/Sobol_sequence)

Results

At this point, we test the difference in the quality of proxies derived from the various design methods. It can be seen from Tables 4.2, 4.3 and 4.4 that the various sampling methods resulted in different regression coefficients. The columns to the extreme right of each of the tables (with the headings 'Avg') show the error metrics and regression coefficients for the proxy derived using a combination of the design points (a total of 378 design points) from all the sampling methods. We assess the performance of the deign methods using the error metrics defined previously, especially the R^2 goodness of fit and the mean absolute error (MAE). For more objective assessment of the sampling methods, we derived a matrix of R^2 values from the misfit predictions of each of the proxy models compared to the true misfit data (Table 4.5). The misfit proxies obtained from a sampling method was used to predict the misfits of all the other designs.

Whereas Tables 4.2, 4.3 and 4.4 indicate that the CCD has the highest R^2 goodness of fit for all cases of seismic, production and total misfits, the matrix in Table 4.5 shows that CCD proxy was poor in predicting the actual misfits from the other design points. Except for the DOD, the R^2 values obtained by comparing the predictions of CCD to the actual misfits from the other sampling methods were each below 0.7. Overall, the proxy derived using the LHD gave the most consistent predictions as compared to the actual misfits from the other designs. Except for the SAS, the predictions of the proxies derived from all other sampling methods were poor ($R^2 < 0.7$) when compared to the actual misfits of the LHD points. We conclude that in our synthetic history matchin case the design points from LHD outperformed the conventional methods (CCD, BBD and DOD) for calibrating quadratic models. The SAS also performed well compared with the conventional

methods. It appears that the designs with space-filling properties (especially the LHD) are better in fitting the quadratic models for the highly non-linear reservoir response than the conventional quadratic designs with design points applicable to only rectangular design regions. This observation is consistent with the findings of previous studies on design of experiments, with a general consensus that a good experimental design should fill the design space rather than concentrate on the cubic design boundaries (Simpson *et al*., 1998).

Table 4.2 Calibration coefficients for the full quadratic model of the total misfit

Category of Terms	Regr. Coeff. Term	Total Misfit. Values of Regression Coefficients for the Design Methods						
		CCD	BBD	DOD	LHD	QRNG	SAS	Avg
		R^2 0.95	R^2 0.83	R^2 0.83	R^2 0.90	R^2 0.85	R^2 0.86	R^2 0.87
		MAE 1704	MAE 5519	MAE 4205	MAE 1069	MAE 6560	MAE 2547	MAE 2645
Constant	A	-489	-36	42637	-2199	-12216	1663	1120
Main Effect/ Linear Terms	B_1	32500	29055	24927	13562	15133	12992	22957
	B_2	61000	55786	61092	38544	52059	48583	57470
	B_3	45700	27978	32263	12875	16231	13747	28623
	B_4	37800	39183	39504	29932	41987	24314	35773
	B_5	-12200	-12730	-22443	-9554	-4306	-14688	-16230
	B_6	-12900	-10116	-15596	-5209	-3610	-17424	-12744
Quadratic Terms	$C_{1,1}$	63100	47164	27977	28962	51902	23873	49792
	$C_{2,2}$	27500	51175	22384	57229	57291	44641	36606
	$C_{3,3}$	23200	25404	39212	25653	48716	25174	28959
	$C_{4,4}$	21100	15948	34476	35737	21235	1201	22176
	$C_{5,5}$	3566	8536	5662	7446	1143	34226	6953
	$C_{6,6}$	3600	6046	-24440	-8777	7975	3792	3045
Interaction Terms	$C_{1,2}$	-44900	-34601	-39730	-32535	-24494	-10596	-38252
	$C_{1,3}$	42100	54569	51814	32130	39597	44118	51096
	$C_{1,4}$	-23000	-3925	-23183	-2916	15720	-16894	-17421
	$C_{1,5}$	-5124	-4579	-759	-10956	-20225	-15959	-3530
	$C_{1,6}$	-13300	-12467	-12392	2037	7320	-5711	-9649
	$C_{2,3}$	-9980	15067	-178	6006	-1741	-324	-903
	$C_{2,4}$	38100	57654	42887	61535	58459	72295	48150
	$C_{2,5}$	-10713	-15523	4407	-16076	-14349	-28513	-6677
	$C_{2,6}$	-9151	-5532	4845	-3253	9012	-3442	-5231
	$C_{3,4}$	-56000	-16501	-49739	-20957	-35552	-14470	-44534
	$C_{3,5}$	-3325	-339	-1959	-1605	-2366	-1776	-863
	$C_{3,6}$	-19600	-14249	-15946	3738	-33291	-18325	-17823
	$C_{4,5}$	-11400	-15285	-10082	-16303	-3639	-4768	-7409
	$C_{4,6}$	-1571	3880	1303	-10881	34174	-11350	3067
	$C_{5,6}$	19300	2496	11877	1196	-10128	-13371	14893

Table 4.3 Calibration coefficients for the full quadratic model of the production misfit

Category of Terms	Regr. Coeff. Term	Production Misfit. Values of Regression Coefficients for the Design Methods						
		CCD	BBD	DOD	LHD	QRNG	SAS	Avg
		R^2 0.94	R^2 0.82	R^2 0.83	R^2 0.88	R^2 0.85	R^2 0.86	R^2 0.87
		MAE 1631	MAE 5483	MAE 4501	MAE 1083	MAE 6350	MAE 2522	MAE 2647
Constant	A	-247	98	38828	-3364	-11651	1368	33
Main Effect/ Linear Terms	B_1	31235	29001	25091	13381	15562	12919	22459
	B_2	62036	55350	60739	37640	52373	48845	55031
	B_3	45885	27954	31990	12219	16748	13522	27829
	B_4	37395	38840	39917	30838	41431	24650	35672
	B_5	-11472	-12709	-22207	-9391	-4604	-14373	-16319
	B_6	-13854	-10638	-16466	-4007	-3743	-16715	-11392
Quadratic Terms	$C_{1,1}$	62902	46761	24996	29551	51875	23628	50389
	$C_{2,2}$	27179	51315	28365	55220	54131	44926	37163
	$C_{3,3}$	23085	24828	41147	26755	48452	24484	29540
	$C_{4,4}$	20934	15748	34935	36496	24099	2457	22803
	$C_{5,5}$	3338	7995	1070	8866	225	33514	6398
	$C_{6,6}$	3519	6270	-21825	-7692	6339	3613	2249
Interaction Terms	$C_{1,2}$	-44647	-35199	-39904	-33153	-25719	-10795	-38660
	$C_{1,3}$	42731	54145	51347	32404	38577	44370	47651
	$C_{1,4}$	-22483	-4144	-23145	-5198	14804	-17390	-16600
	$C_{1,5}$	-3914	-4674	-1073	-9968	-19272	-16029	-3636
	$C_{1,6}$	-14170	-12234	-11176	4295	9319	-6017	-11576
	$C_{2,3}$	-10174	14924	-683	3099	-3188	-150	-927
	$C_{2,4}$	36696	58048	42664	63821	58824	72193	50320
	$C_{2,5}$	-10776	-15518	5261	-14008	-16168	-28807	-6552
	$C_{2,6}$	-7339	-5725	-4419	-3173	8528	-4169	-6006
	$C_{3,4}$	56796	-16940	-49309	-21656	-36655	-14891	-42770
	$C_{3,5}$	-4513	-431	-1473	-570	-2910	-2397	-
	$C_{3,6}$	-18439	-14197	-15891	6809	-34370	-18253	-15457
	$C_{4,5}$	-11613	-15138	-10139	-16410	-4968	-5089	-6177
	$C_{4,6}$	-512	3922	1050	-14007	32785	-11443	2953
	$C_{5,6}$	20562	2351	12232	1077	-10522	-13989	12465

Table 4.4 Calibration coefficients for the full quadratic model of the seismic misfit

Category of Terms	Regr. Coeff. Term	Seismic Misfit. Values of Regression Coefficients for the Design Methods						
		CCD	BBD	DOD	LHD	QRNG	SAS	Avg
		R^2 0.92	R^2 0.87	R^2 0.87	R^2 0.92	R^2 0.90	R^2 0.91	R^2 0.80
		MAE = 40	MAE = 70	MAE = 53	MAE = 22	MAE = 167	MAE = 40	MAE 111
Constant	A	-2.04	-0.8	60	-5	29	-2	79.6
Main Effect/ Linear Terms	B_1	157	119	71	72	76	79	88.4
	B_2	181	99	68	81	110	105	91.4
	B_3	187	111	76	64	113	66	89.7
	B_4	148	92	30	32	69	58	59.4
	B_5	57	14	48	-42	12	1	-12.5
	B_6	67	19	3.7	-38	26	54	8.85
Quadratic Terms	$C_{1,1}$	189	149	173	124	154	94	168.8
	$C_{2,2}$	121	149	136	118	124	143	133.5
	$C_{3,3}$	140	245	239	335	291	272	190
	$C_{4,4}$	135	195	272	282	186	233	153.8
	$C_{5,5}$	88	158	23	168	92	214	93
	$C_{6,6}$	93	138	50	121	135	145	100
Interaction Terms	$C_{1,2}$	-13	41	38	93	-20	89	32.4
	$C_{1,3}$	68	189	152	133	204	167	152
	$C_{1,4}$	16	107	115	179	166	109	102
	$C_{1,5}$	27	48	70	95	-15	14	44.4
	$C_{1,6}$	-51	19	38	25	73	64	32.2
	$C_{2,3}$	16	168	161	235	82	186	134
	$C_{2,4}$	75	185	218	287	214	269	196
	$C_{2,5}$	-32	64	128	95	38	48	81.9
	$C_{2,6}$	-38	51	82	140	118	20	53.9
	$C_{3,4}$	-57	140	57	160	153	227	84
	$C_{3,5}$	17	70	110	172	184	124	106
	$C_{3,6}$	-38	22	29	133	19	134	37.4
	$C_{4,5}$	-12	41	123	50	76	90	84
	$C_{4,6}$	39	112	101	134	182	49	105
	$C_{5,6}$	-13	5	62	117	-20	-5	41.5

Table 4.5 Matrix of R^2 for the total misfit predictions of each proxy model versus the data points of the other designs sampling methods.

Proxy Method	Sampling Method					
	BBD	CCD	DOD	LHD	QRNG	SAS
BBD	0.83	0.81	0.78	0.62	0.68	0.61
CCD	0.67	0.95	0.85	0.49	0.63	0.64
DOD	0.75	0.80	0.83	0.41	0.75	0.73
LHD	0.76	0.77	0.75	0.90	0.84	0.85
QRNG	0.68	0.62	0.59	0.55	0.85	0.76
SAS	0.72	0.68	0.70	0.70	0.71	0.86

The regression coefficients are different for the various proxies derived using the different sampling methods. We want to check for the significance of the individual regression coefficients using the t-test statistic which is based on the t distribution. The addition of a significant parameter to a proxy model makes the model more effective, while including an insignificant parameter may worsen the model. For each regression coefficient, the test statistic, t, is calculated as follows:

$$t = \frac{|Regression\ Coefficient|}{\sqrt{MSE * Cov(X)}} \ldots\ldots\ldots\ldots\ldots\ldots\ldots\ldots\ldots\ldots\ldots\ldots (4.4)$$

Where MSE is the mean square error and the Cov(X) is the covariance of the design matrix. We applied the statistic to test the two-sided hypothesis that each of the regression coefficients are not equal to zero. We defined a t-value threshold to correspond to the p-value based on the t distribution within terms of degrees of freedom (dof= n-k+1) and 95% confidence interval, as follows:

$$-T_{\alpha/2,(n-k+1)} < t < T_{\alpha/2,(n-k+1),} \ldots\ldots\ldots\ldots\ldots\ldots\ldots\ldots\ldots\ldots\ldots (4.5)$$

Where α is the confidence interval, n is the total number of design points and k is the number of variables in the model.

The pareto charts in Figures 4.7 to 4.12 ranks the t-values for coefficients of the various seismic and production misfit proxy models. In all cases, the charts show some strong similarity in the ranking but there are some disparities also. For example, the t-values of the BBD production misfit proxy coefficients suggests that the interaction term 'T1*T2' is significant while the seismic proxy suggests that the term is insignificant. Except for the SAS proxies, the observation is the same for all the sampling methods: all the production proxies suggest that the 'T1*T2' is significant and should be included in the models while the seismic proxies suggest that the term is insignificant and should be removed from the regression model. The combined design proxies (Figure 4.13) suggests the same.

The t-test on the production misfit proxy from the combined design (Figure 4.13) suggests that eight regression terms (including T2*T5, $T5^2$, T2*T6, T1*T5, T4*T6, $T6^2$, T2*T3 and T3*T5) should be ignored. All production proxies from the individual designs (Figures 4.7 to 4.12) suggests same except in the QRNG where the 'T4*T6' is accepted and in SAS proxy which accepted 'T5' and 'T2*T5' terms. On the other hand, the terms 'T1*T2', 'T1*T6', 'T5' and 'T6' in the seismic misfit proxy from the combined design

were shown to be insignificant. However, the test on the seismic proxy from the composite design accepted the 'T6' term and the t-statistics on SAS seismic proxy accepted the 'T1*T2' and 'T1*T6' terms.

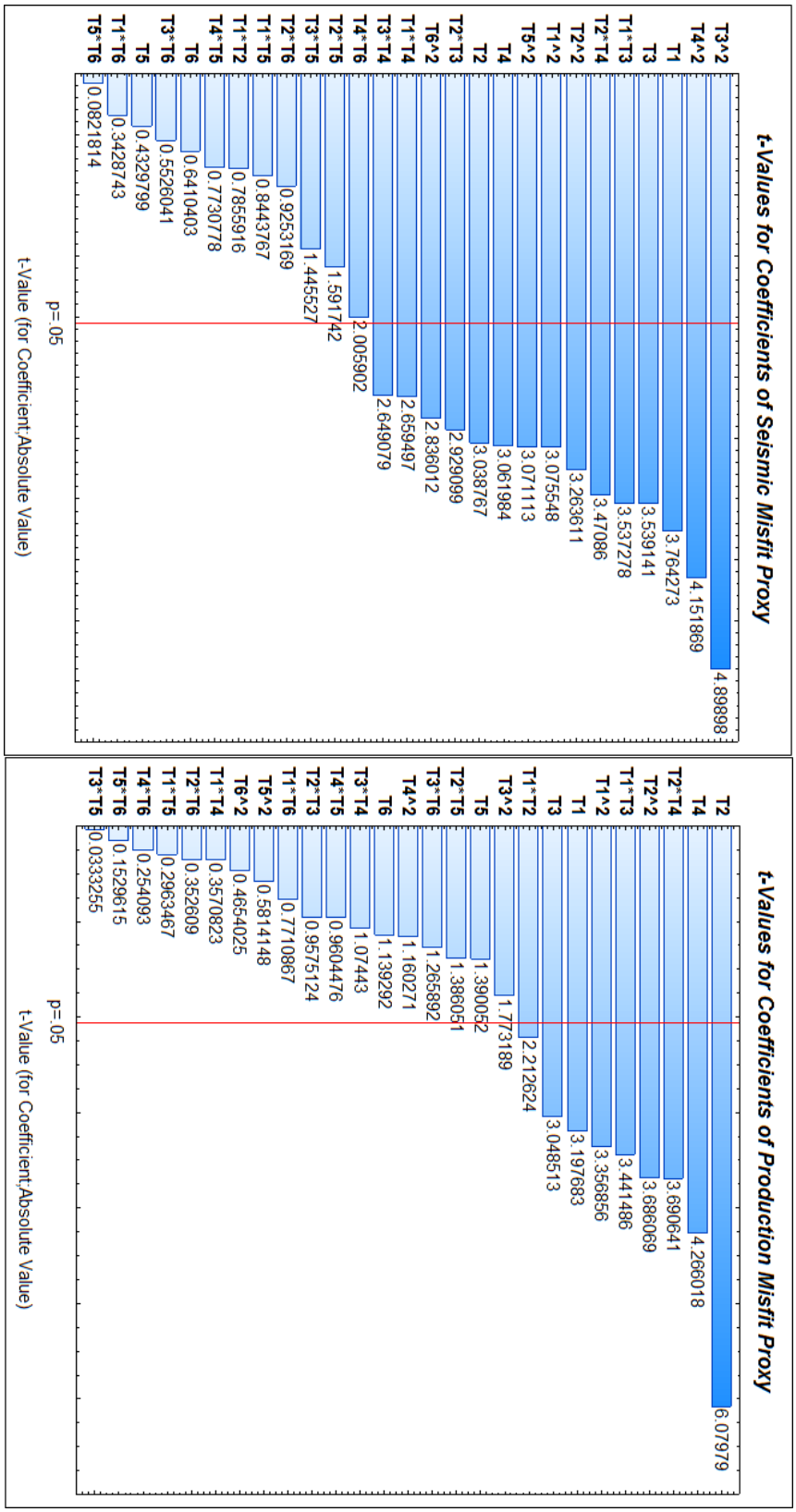

Figure 4.7 Pareto chart of t-values for the coefficients of the seismic (top) and production (bottom) proxies derived using the Box-Behnken Design

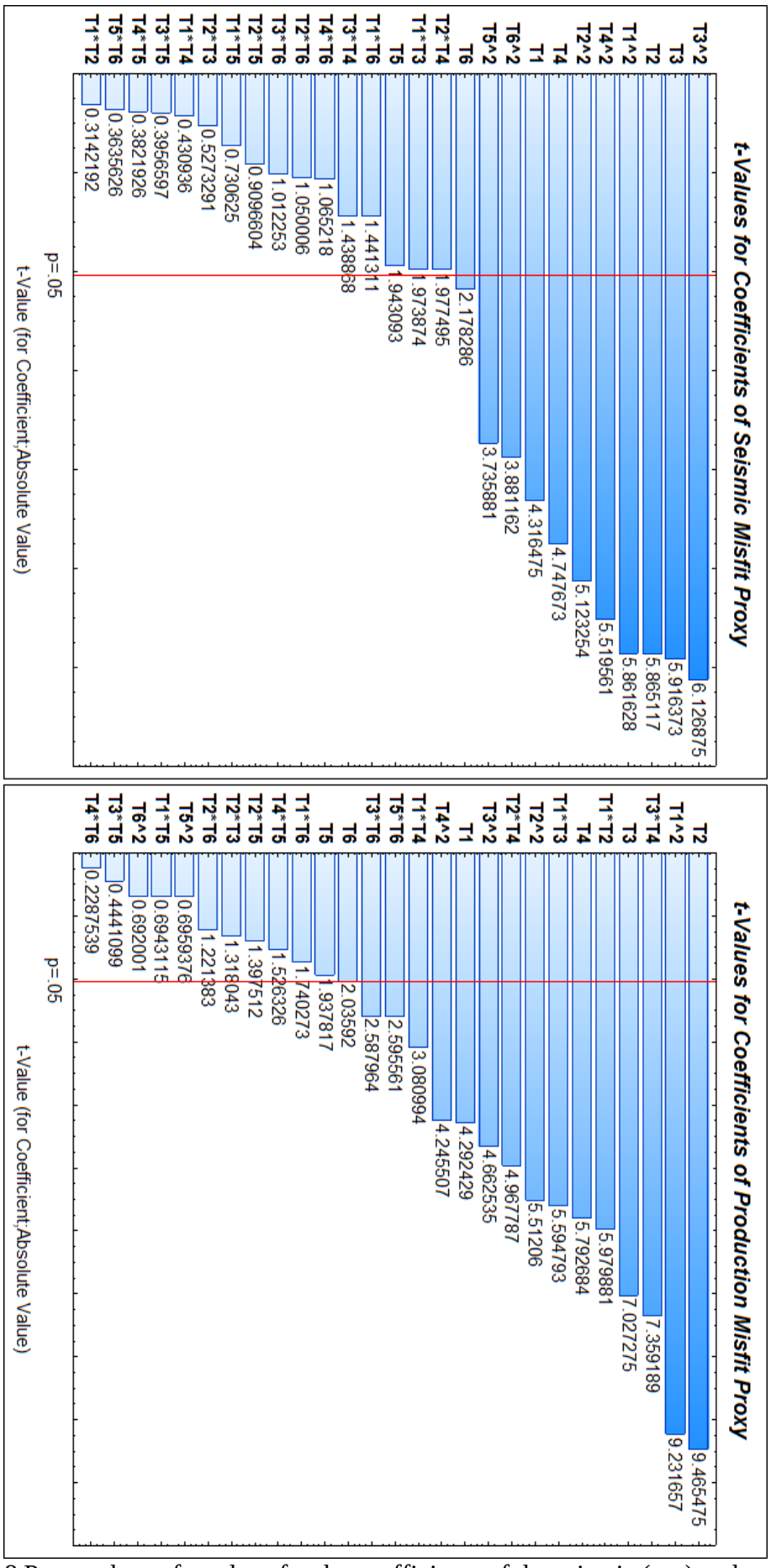

Figure 4.8 Pareto chart of t-values for the coefficients of the seismic (top) and production (bottom) proxies derived using the Central Composite Design

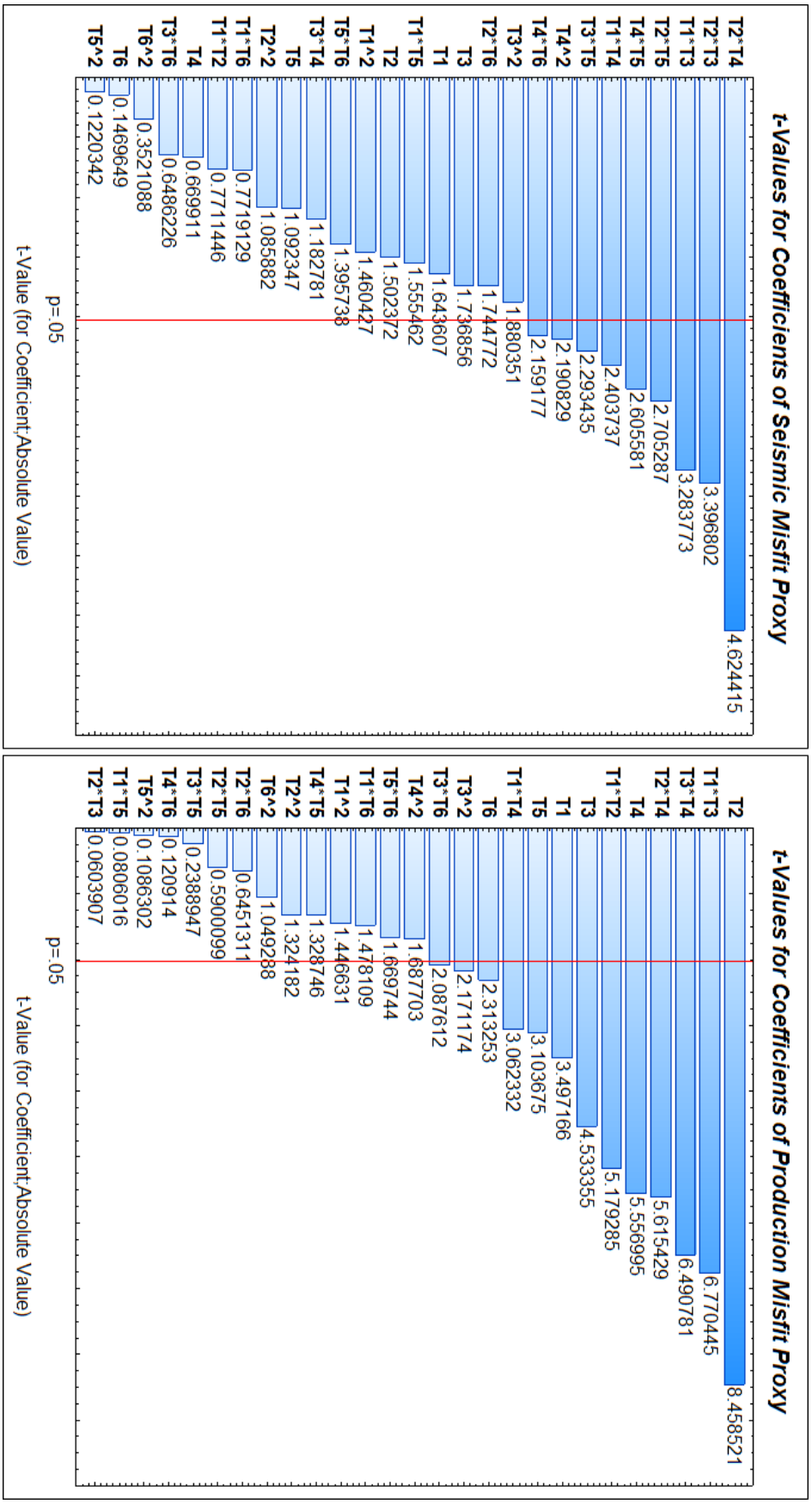

Figure 4.9 Pareto chart of t-values for the coefficients of the seismic (top) and production (bottom) proxies derived using the D-Optimal Design

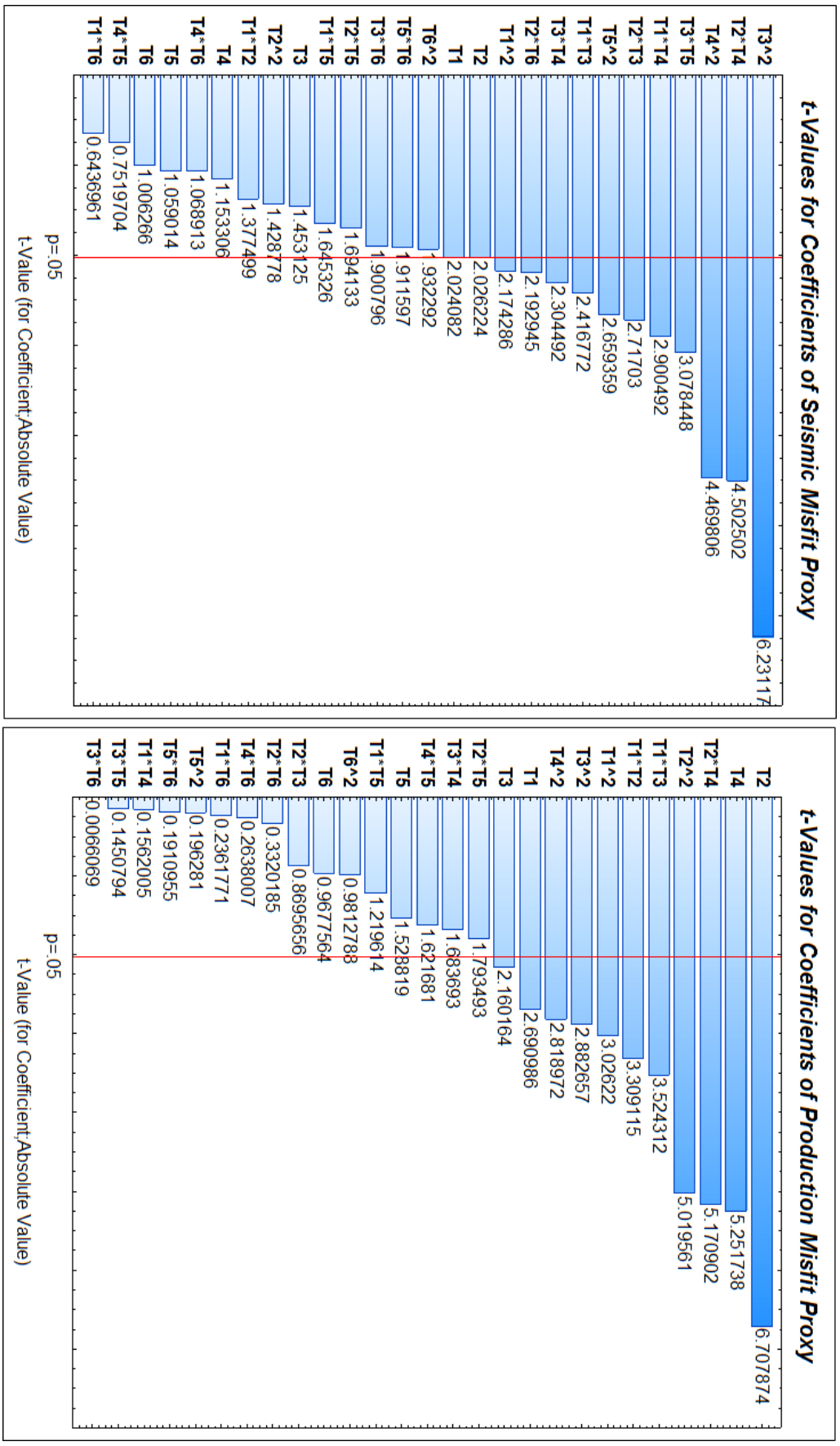

Figure 4.10 Pareto chart of t-values for the coefficients of the seismic (top) and production (bottom) proxies derived using the Latin Hypercube Design

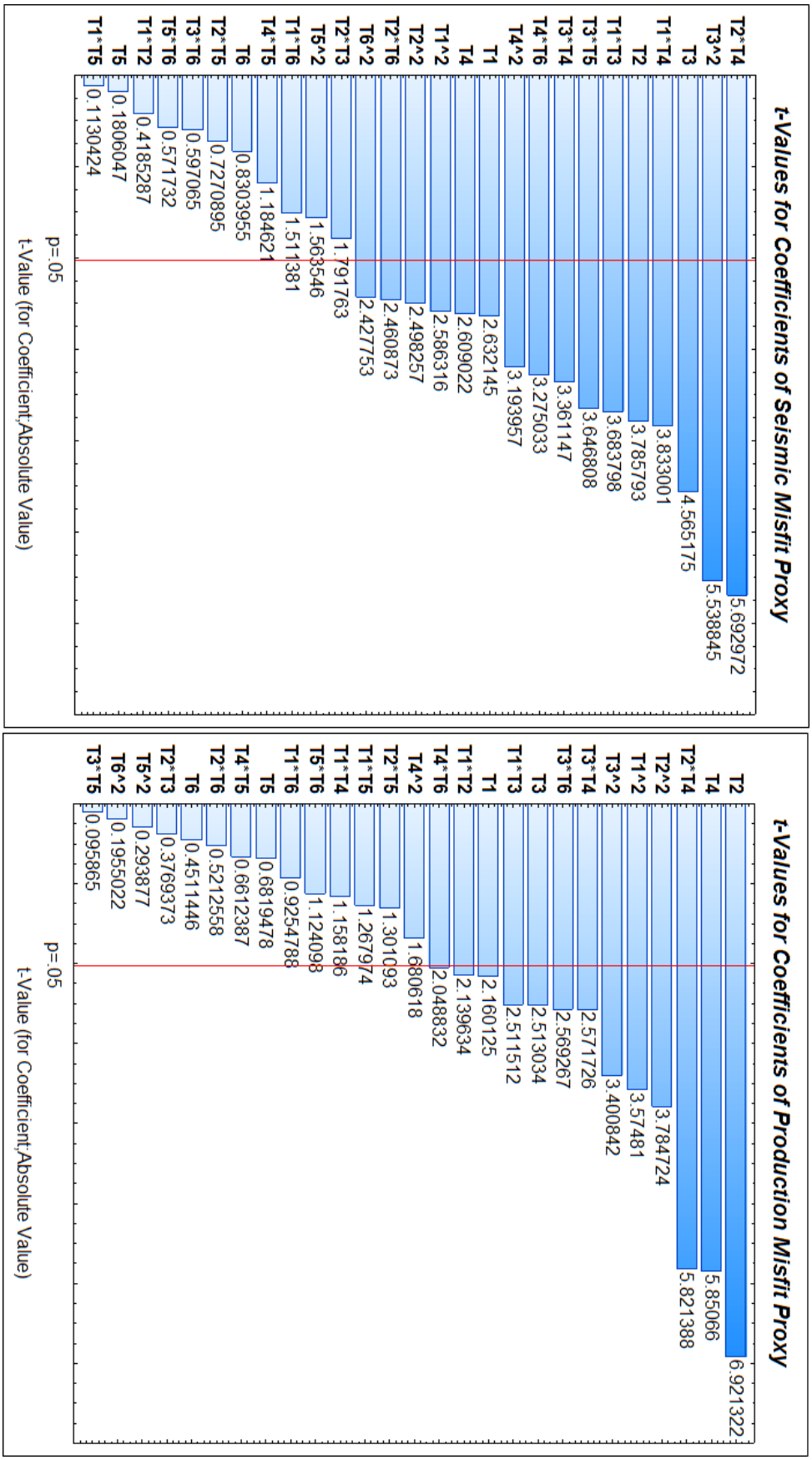

Figure 4.11 Pareto chart of t-values for the coefficients of the seismic (top) and production (bottom) proxies derived using the Quasi Random Number Generator

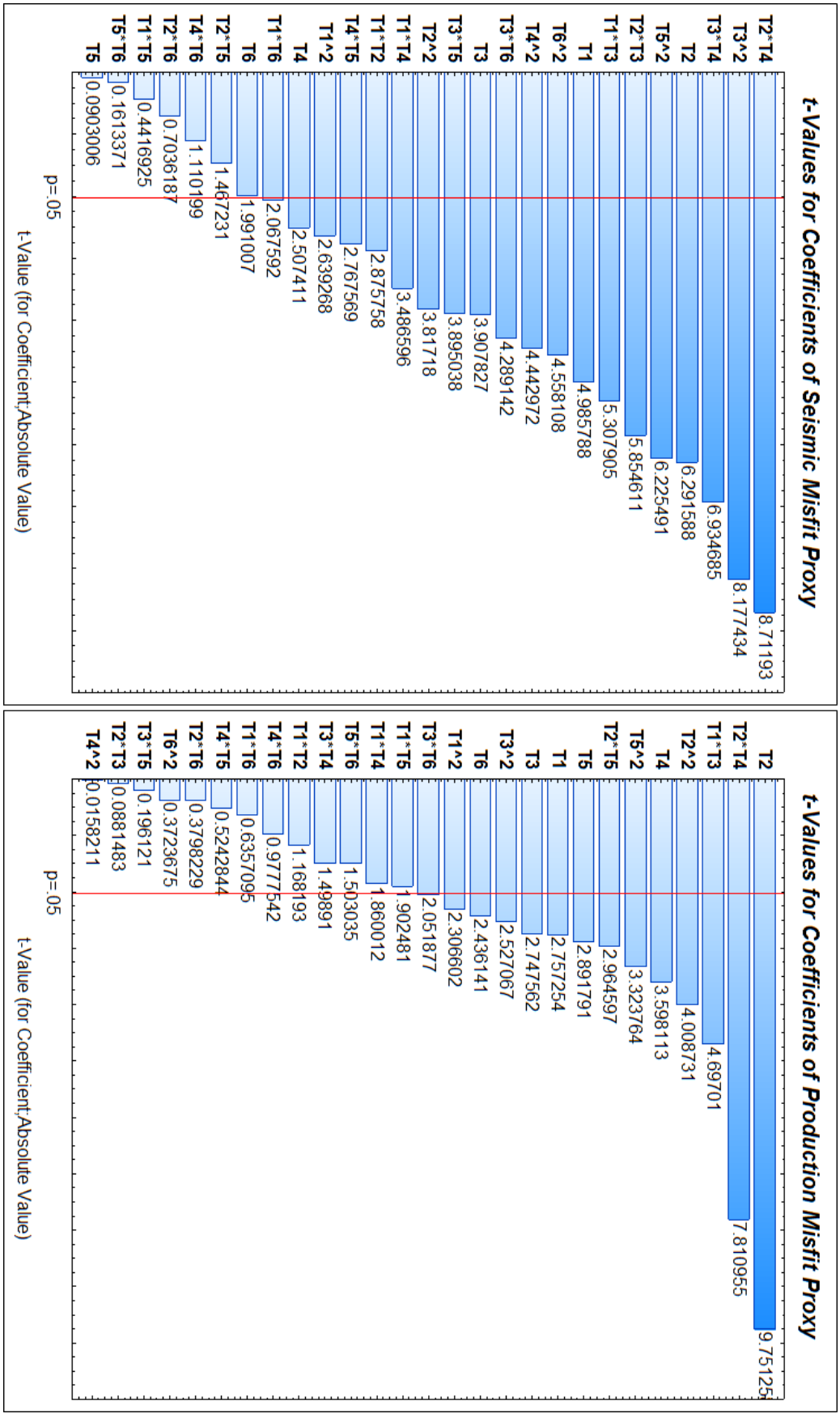

Figure 4.12 Pareto chart of t-values for the coefficients of the seismic (top) and production (bottom) proxies derived using the Saleev-Antonov-Sobol

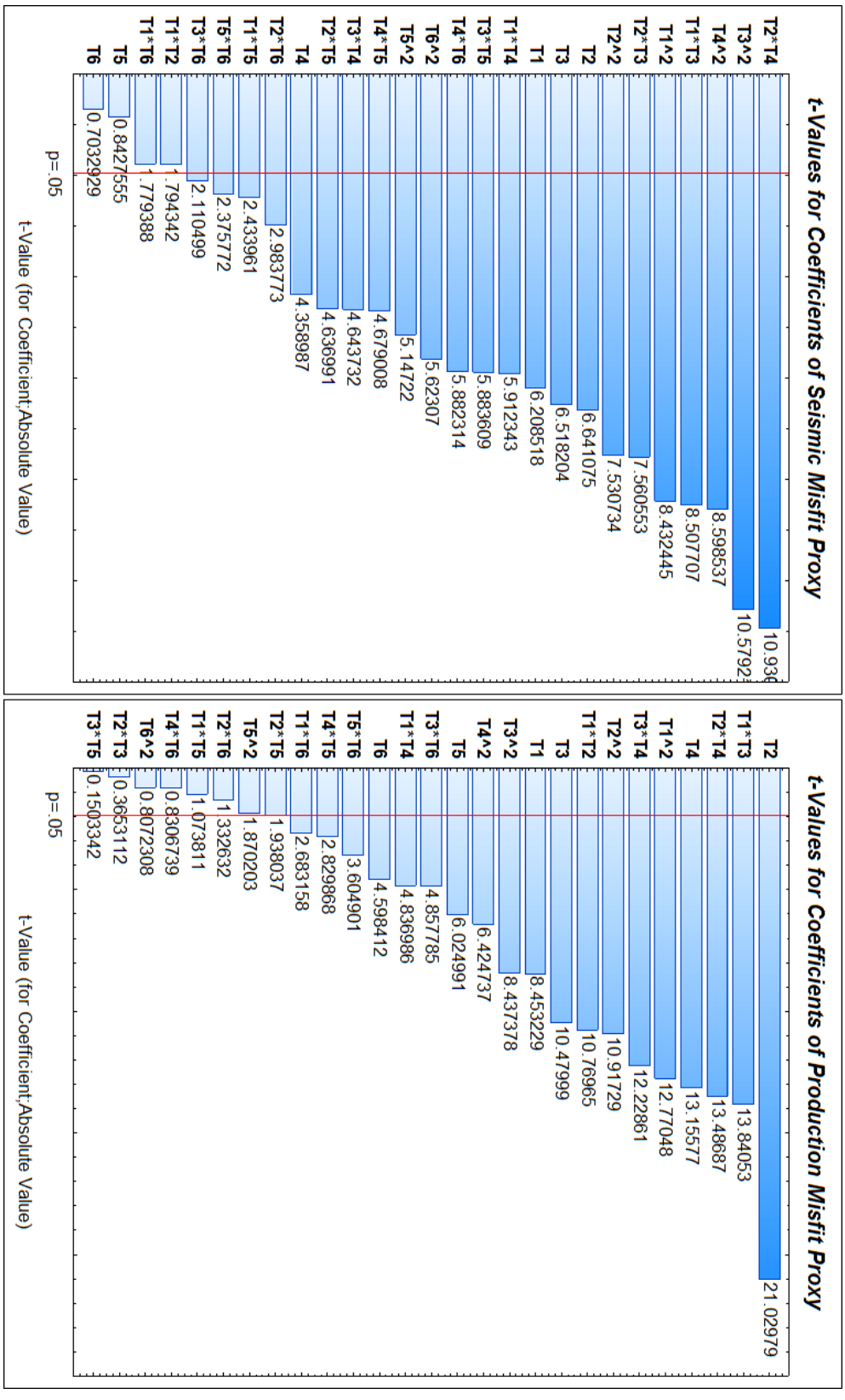

Figure 4.13 Pareto chart of t-values for the coefficients of the seismic (top) and production (bottom) proxies derived using the combined design

If we have a good approximation of the reservoir response in the form of the proxy for the misfit between the predicted and observed then we can treat the history matching problem as a minimisation problem. In this regard, we seek to find some combinations of

the reservoir variables (i.e the pilot point transmissibility multipliers) that will give minimal misfit. We can either minimise the total misfit function by using any optimisation function or we can treat the history matching problem as a multi-objective problem with two objectives: seismic misfit and production misfit. Either way, the minimisation problem is solved at virtually no cost as we do not have to run the time consuming and expensive reservoir simulation to explore the model space adequately and generate as many models as we want. The t-test statistics above indicates that the production and seismic misfits carry different information, and thus we prefer to handle the objectives in a multi-objective fashion by utilising the pareto-based genetic algorithm This method of optimisation was described in the previous chapter. Before we proceed to the optimisation, we want to seek ways to improve the quality of the misfit proxies.

4.2.7 Improving the quality of the proxy

We seek ways to improve the quality of the proxy functions by adding more models to the original models from the experimental design (ED) methods. In other words, we want to derive proxy functions having higher values of R^2 goodness of fit and lower values of the mean absolute error. We increased the number of design points in eight stages to generate up to 2625 design points for each of the DOD, LHD, SAS and QRNG and found that the quality of the proxy produced by these design methods do not improve as the number of the design points used in calibrating the quadratic models increases (Figure 4.14). However, in the case of QRNG the error metrics improve and deteriorate in an irregular manner as the number of design points increase. This is because in sampling the design space with QRNG some regions of the design space are under-sampled while other regions are heavily sampled. In the case of CCD and BBD, there is no flexibility over the choice of the number of design points required to fully calibrate the quadratic models. The number of runs is fixed for any particular number of factors. The number of design points (simulation runs) in CCD and BBD is dimension-dependent (i.e. dependent on the number of design variables) and grows as the number of the variables increase. In initial experiments with these four designs, the design points were chosen to be equal to 65. We arrive at this value using the formula: $D_{p_{min}} = 2^{N_m+1}$, where the number of design points is designated as D_p and the subscript 'min' indicates the minimum design points required to cover the design space 'adequately'; N_m is the number of design variables (which is 6 in the 6D-synthetic study).

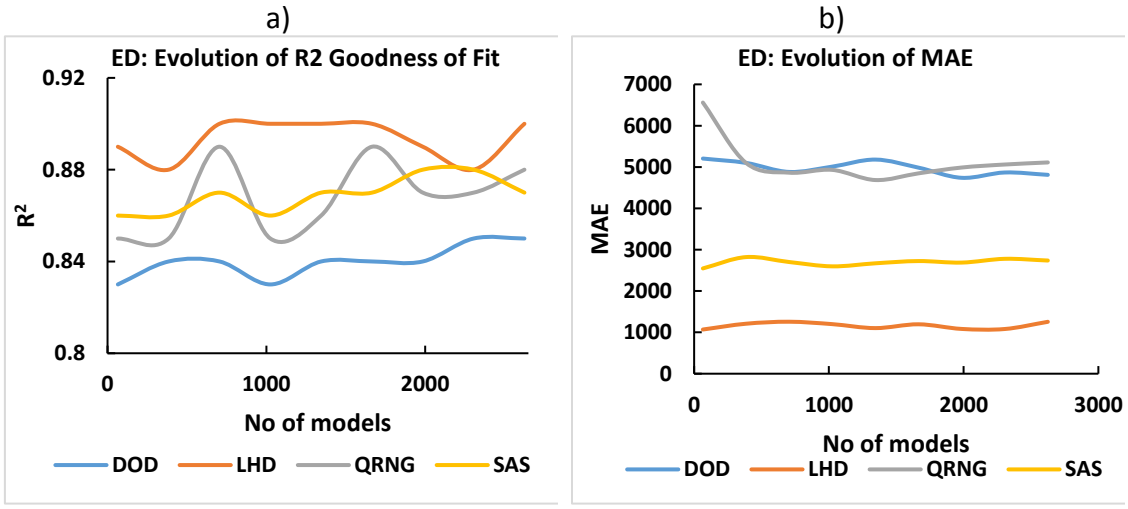

Figure 4.14 The evolution of error metrics in fitting quadratic response surface to the models generated with only the experimental design (ED) techniques (DOD: D-Optimal, LHD: Latin Hypercube, QRNG: Quasi-Randon number, SAS: Saleev-Antonov-Sobol Sampling)

We test a different approach in which the number of models used to calibrate the quadratic proxy is increased by adding models generated during history matching using different optimisation algorithms. We start with initial models generated using any of the experimental design techniques and generate more models to fill up the design space during some optimisation runs. So, models are added sequentially to the initials 65 models from LHD, QRNG, DOD and SAS design techniques. We want to investigate how the additional models generated during optimisation affect the quality of the quadratic response surface obtained from symbolic regression on the ensemble of models. We carry out the investigation for ensembles generated in stages of 5 incremental iterations (Table 4.6) using the neighbourhood algorithm (NA), genetic algorithm (GA) and particle swarm optimisation (PSO).

Table 4.6 Models from optimisation added to the initial Experimental Design (ED) points

Design Technique	No of models
LHD	65
LHD + 5 iterations	385
LHD + 10 iterations	705
LHD + 15 iterations	1025
LHD + 20 iterations	1345
LHD + 25 iterations	1665
LHD + 30 iterations	1985
LHD + 35 iterations	2305
LHD + 40 iterations	2625

The stages are designed in such a way to mimic the eight design stages in the earlier investigation in which the design points were generated through the experimental design techniques only. In each case, we monitored the evolution of the error metrics as the simulation runs progress.

We compare the error metrics for the case where the model parameters are from the design points of the experimental design techniques only (Figure 4.14 above) to those in which the initial design points from the experimental design are combined with the models generated during optimisation (Figure 4.15). The figures show that the additional design points from the various experimental design techniques did not improve the quality of the quadratic proxy of the reservoir response while the addition of models generated during optimisation improves the quality of the proxy. This is reflected in the increases in the R^2 goodness of fit and the decreases in the mean absolute error calculated for the various regression cases using the misfits for the entire 2625 models as the validation data. The increase in R^2 goodness of fit and the decreases in the mean absolute error is observed in all cases of the different optimisation algorithm with different initialisation methods.

The difference between the approach using only the models at the design points of the conventional experimental design techniques (ED) and the approach in which models are added as history matching progresses is in the converging models. Unlike in the case of model parameters generated using only any of the ED, models generated during history matching are converging models which do not just go in to fill spaces but fills the spaces where the true parameter values are more likely to lie. The converging models seem to calibrate the quadratic models much better. The reason is that as optimisation proceeds, the search window reduces so that the response in the form of misfit becomes better approximated by a quadratic function and the quality of the proxy continues to improve until further iteration does not improve the proxy any longer. The quadratic approximation of the reservoir response is a 2nd order Taylor's expansion neglecting higher order terms and beyond a certain window range of model parameters may not be adequate for calibration with the reservoir response.

Furthermore, we want to investigate how the regression coefficients of the quadratic proxy converge as optimisation progresses by monitoring the evolution of the coefficients of the linear terms, interaction terms, quadratic terms and the constants in the proxy model between successive simulation runs. We find that each of the coefficients tend to converge to some values as more models generated during optimisation are added in the ensemble for calibration of the quadratic models.

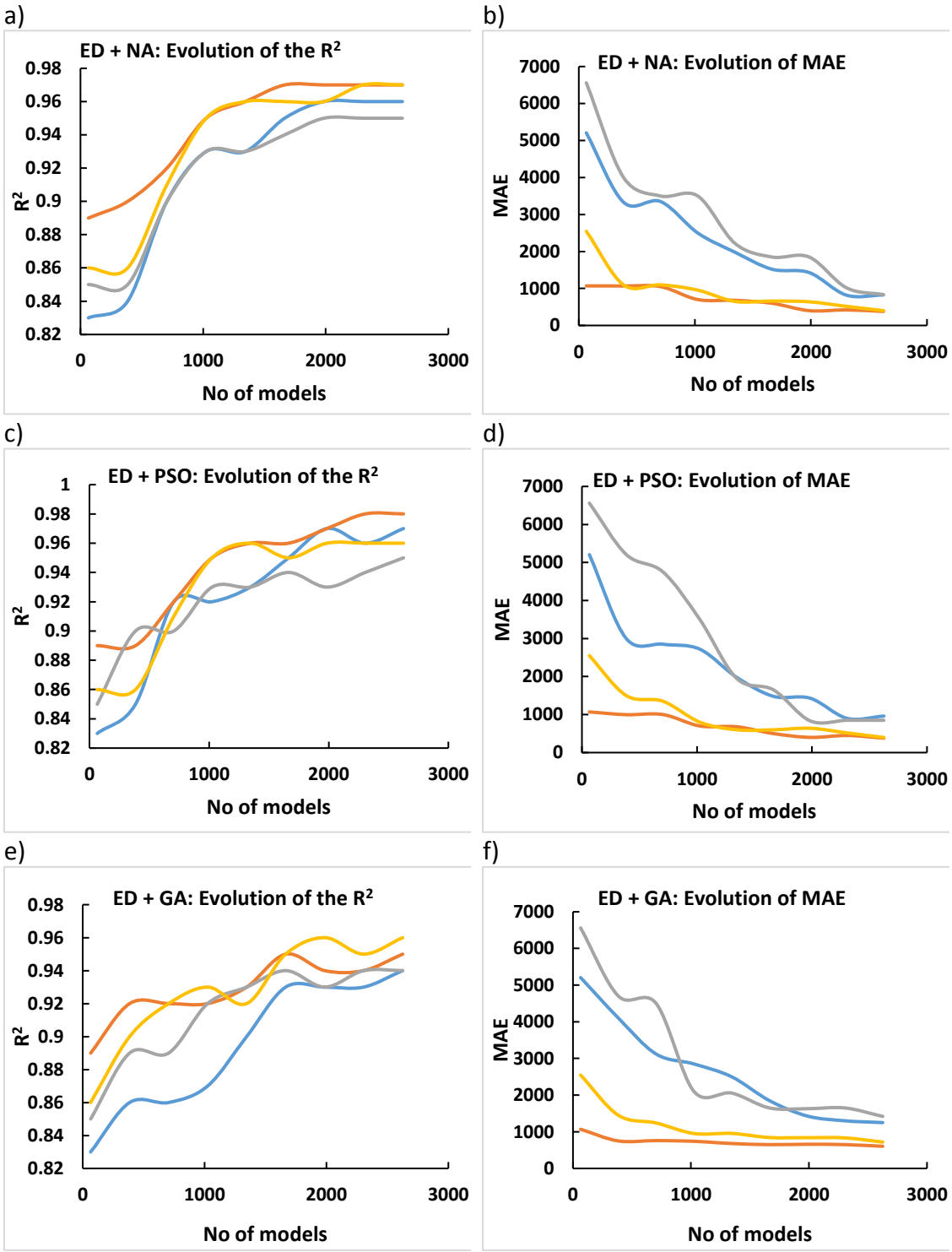

Figure 4.15 The evolution of the goodness of fit (R^2) and the mean absolute error (MAE) for quadratic response surface fitted to the reservoir models. Each of the optimisation was initialised with model parameter points generated using experimental design techniques, including: D-optimal design (blue curves), Latin Hypercube sampling (orange curves), Quasi-Randon number (grey curves), Saleev-Antonov-Sobol sampling (yellow curves)

Figures 4.16, 4.17, 4.18 and 4.19 show the trend of the various coefficients (constants, linear terms, interaction terms and quadratic terms respectively) as the number of iterations increases in the optimisations using the NA, PSO and GA

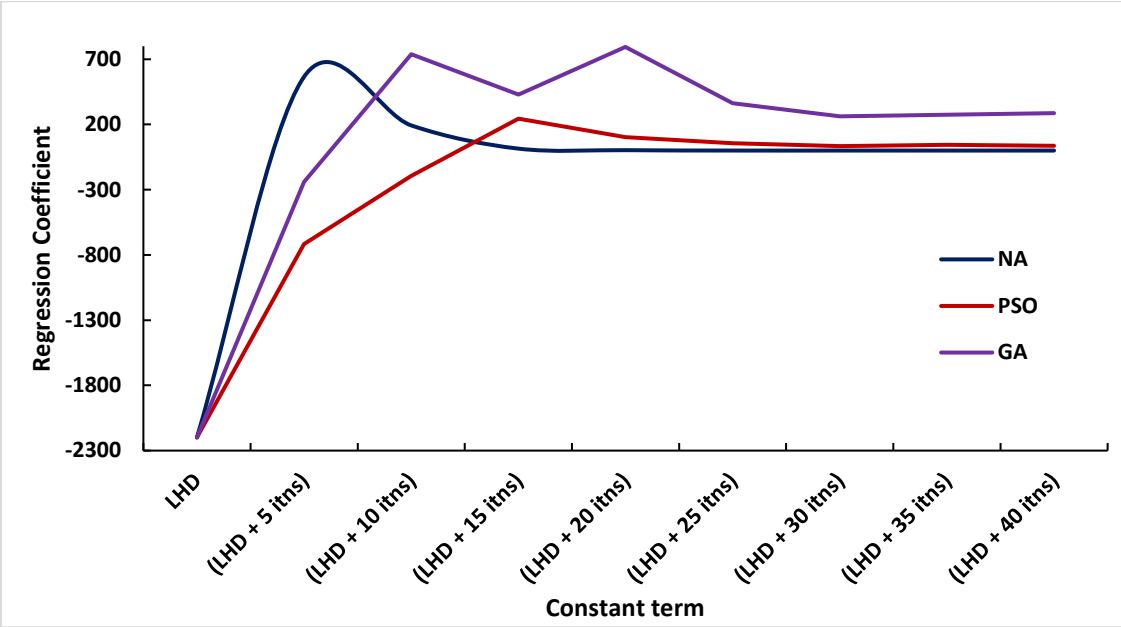

Figure 4.16 Evolution of the constant terms with converging models

a)

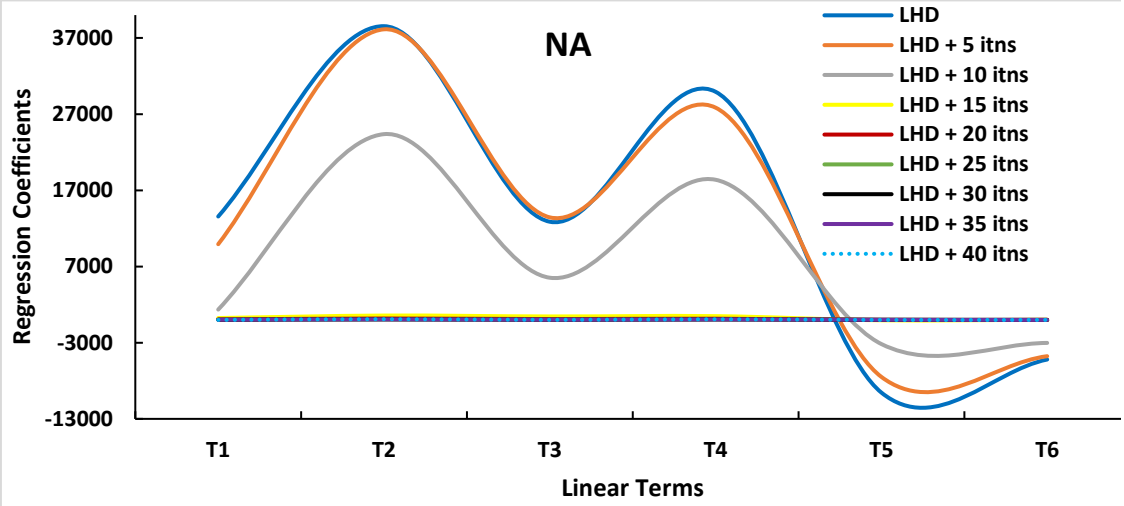

b)

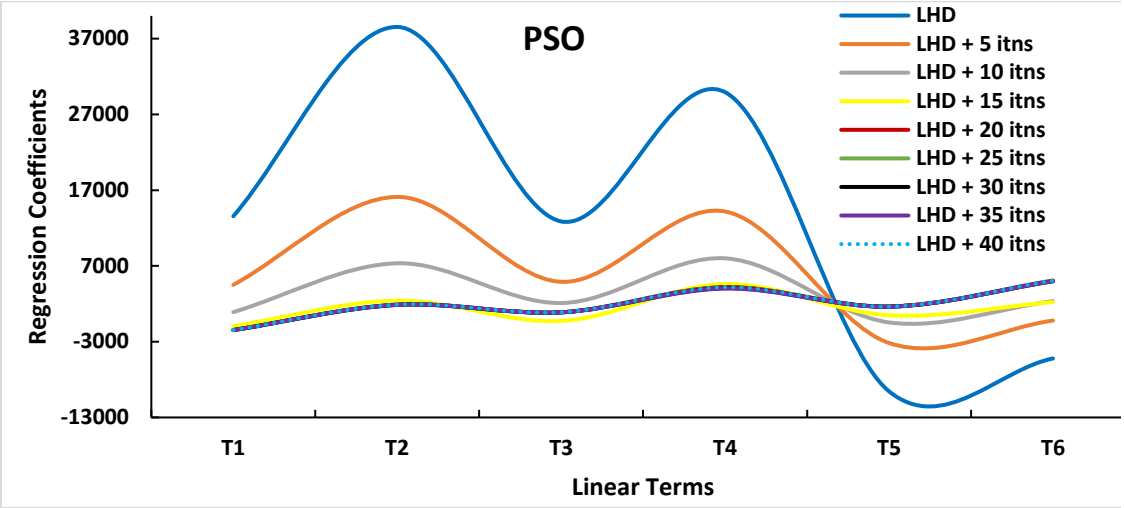

c)

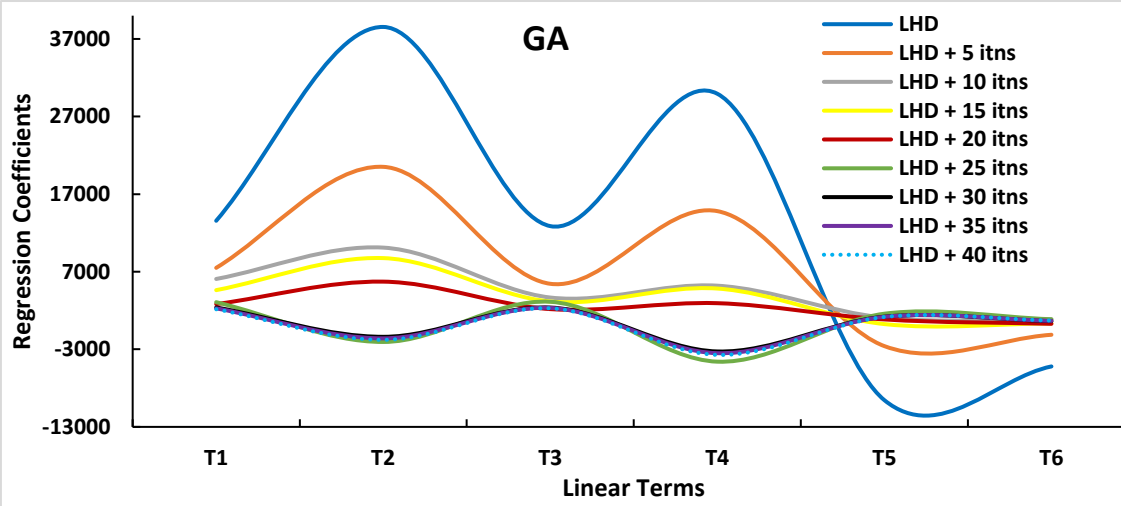

Figure 4.17 Evolution of the coefficients of the linear terms for converging models from optimisation using a) NA, b) PSO, and c) GA

a)

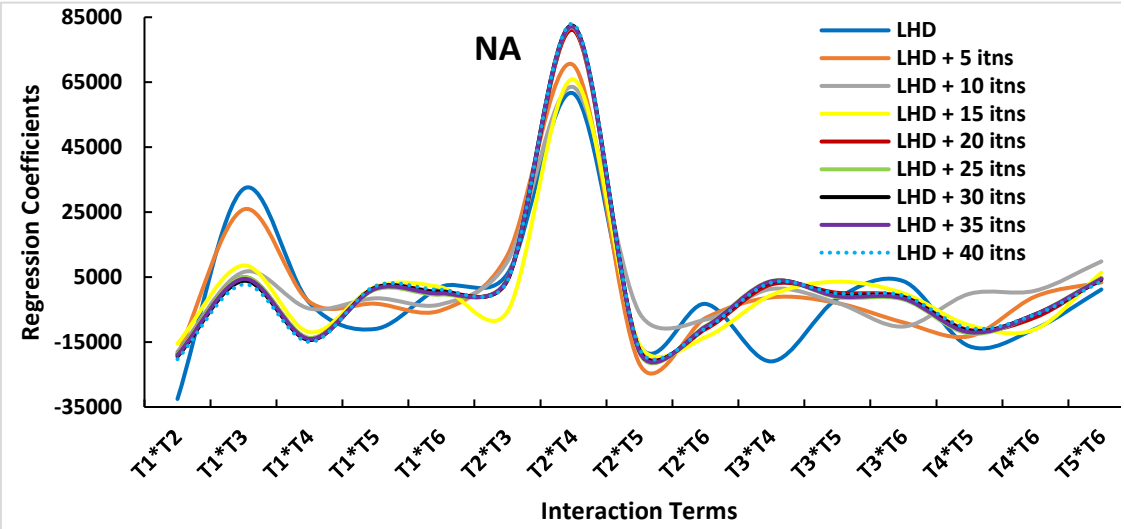

b)

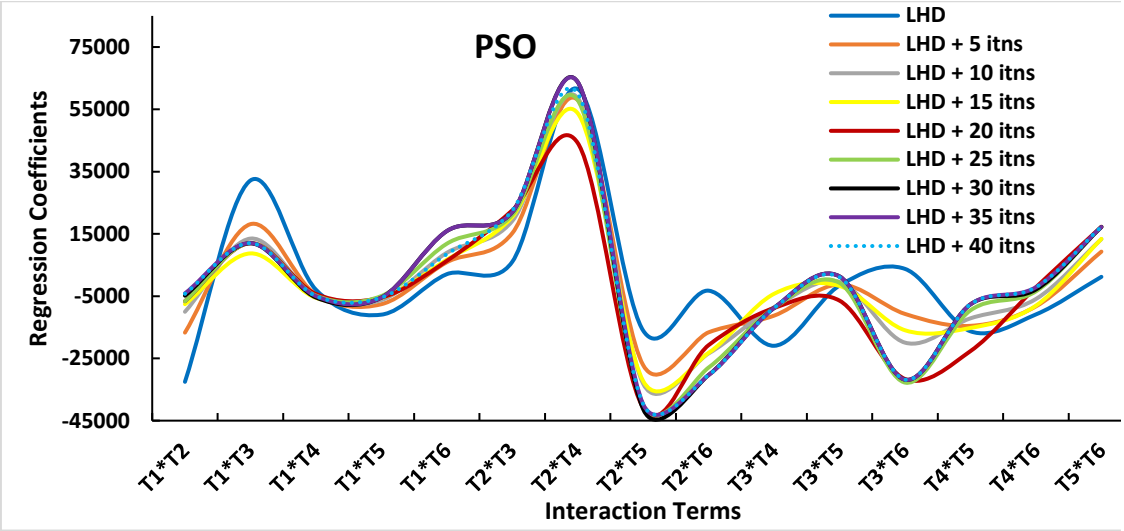

c)

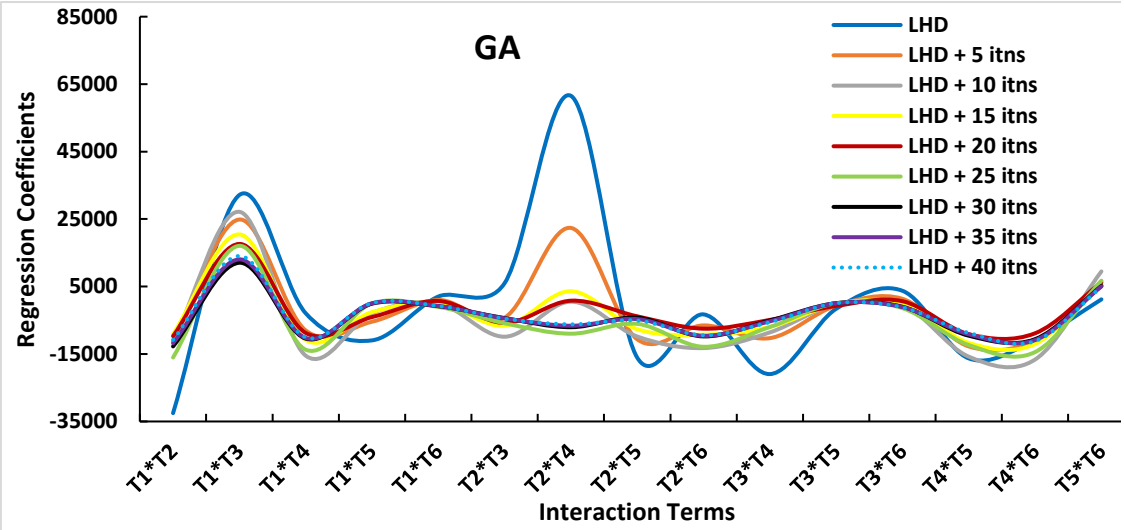

Figure 4.18 Evolution of the coefficients of the interaction terms for converging models from optimisation using a) NA, b) PSO, and c) GA

a)

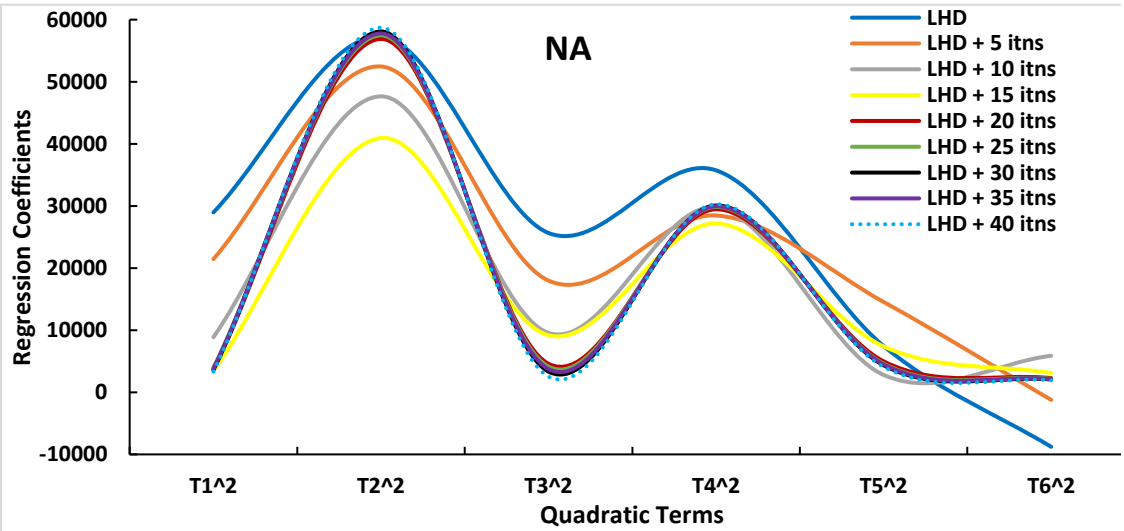

b)

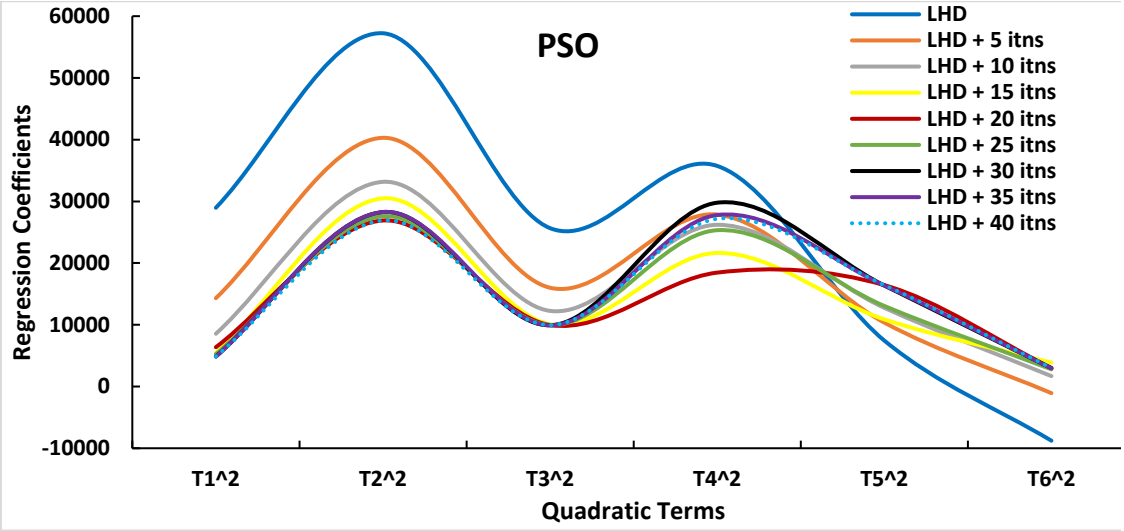

c)

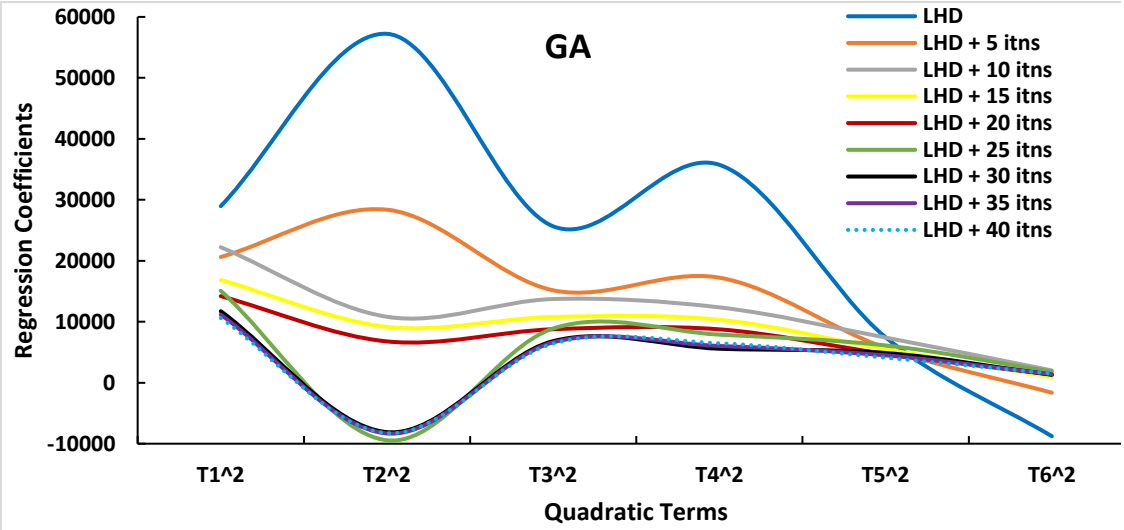

Figure 4.19 Evolution of the coefficients of the quadratic terms for converging models from optimisation using a) NA, b) PSO, and c) GA

4.2.8 Pareto-Based multi-objective optimisation of seismic and production misfits

We have calibrated the quadratic response surface using several experimental techniques to derive some proxies representing the reservoir response in the form of the misfit between the predicted and observed data. We have also shown that the quality of the proxies can be improved by adding some converging models to the ED models. Next, we want to set up some optimisation problems to generate the combination of reservoir parameters that minimise the improved quadratic misfit surfaces (or the proxies). In the synthetic field for which the proxy models were derived, we knew the true solution of the history matching problem. We want to make predictions with the model solutions recovered in the optimisation of the proxy models and compare the predictions with the known history data. We generated an ensemble of 10,000 models uniformly distributed

in the model space. For each combination of parameters, the misfit values are easily calculated using the proxy functions. We then apply a non-dominated sorting algorithm (Srinivas and Kalyanmoy, 1994; Kalyanmoy *et al*., 2002) to the multi-objective problems where the objective functions to be optimised are the polynomial approximation of the various seismic misfit and production misfit. This is like the non-domination sorting which is an integral part of the pareto-based multi-objective optimisation described in section 3.8.

However, unlike the optimisation algorithms in which child models are generated from the initial population based on tournament selection, crossover and mutation, the non-domination sorting algorithm used here merely sorts the 10,000 models and rank them based on the non-domination sorting of the seismic and production misfit proxies. The proxies used here are those derived from the combination of the 65 LHD design points and the GA models from 10 iterations The proxies were subjected to the t-test described in section 4.2.6, and then, the insignificant regression coefficients were set to zero for improved proxy functions. No further expensive computer simulations were run as the misfit values were calculated from the proxies. According to the pareto principle, the models on the Pareto Front are the optimal solutions to the history matching problem. It is seen that the concept has generated models with diversity at the pareto front (Figure 4.20).

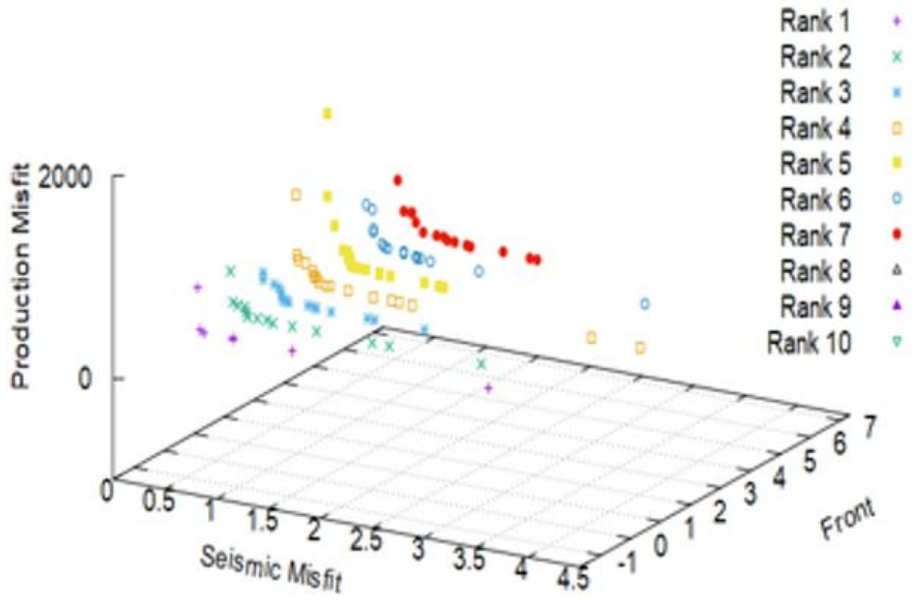

Figure 4.20 Production misfit versus seismic misfit in non-domination sorting of the. misfit functions derived by calibrating quadratic models with design points generated using Latin Hypercube Design plus 705 GA models.

In Figure 4.20, only the first 10 fronts based on ranking are displayed. In this study, there was no additional information that will lead to any subjective preference, so we consider

the pareto optimal solutions to be equally good in the presence of trade-offs between the two conflicting objectives (i.e seismic misfit and production misfit). We are interested in comparing the reservoir quantities simulated using the pareto models with the known synthetic history. First, we present the well water production rates simulated for each of the prior ensemble of models generated using the different ED methods in Figure 4.21.

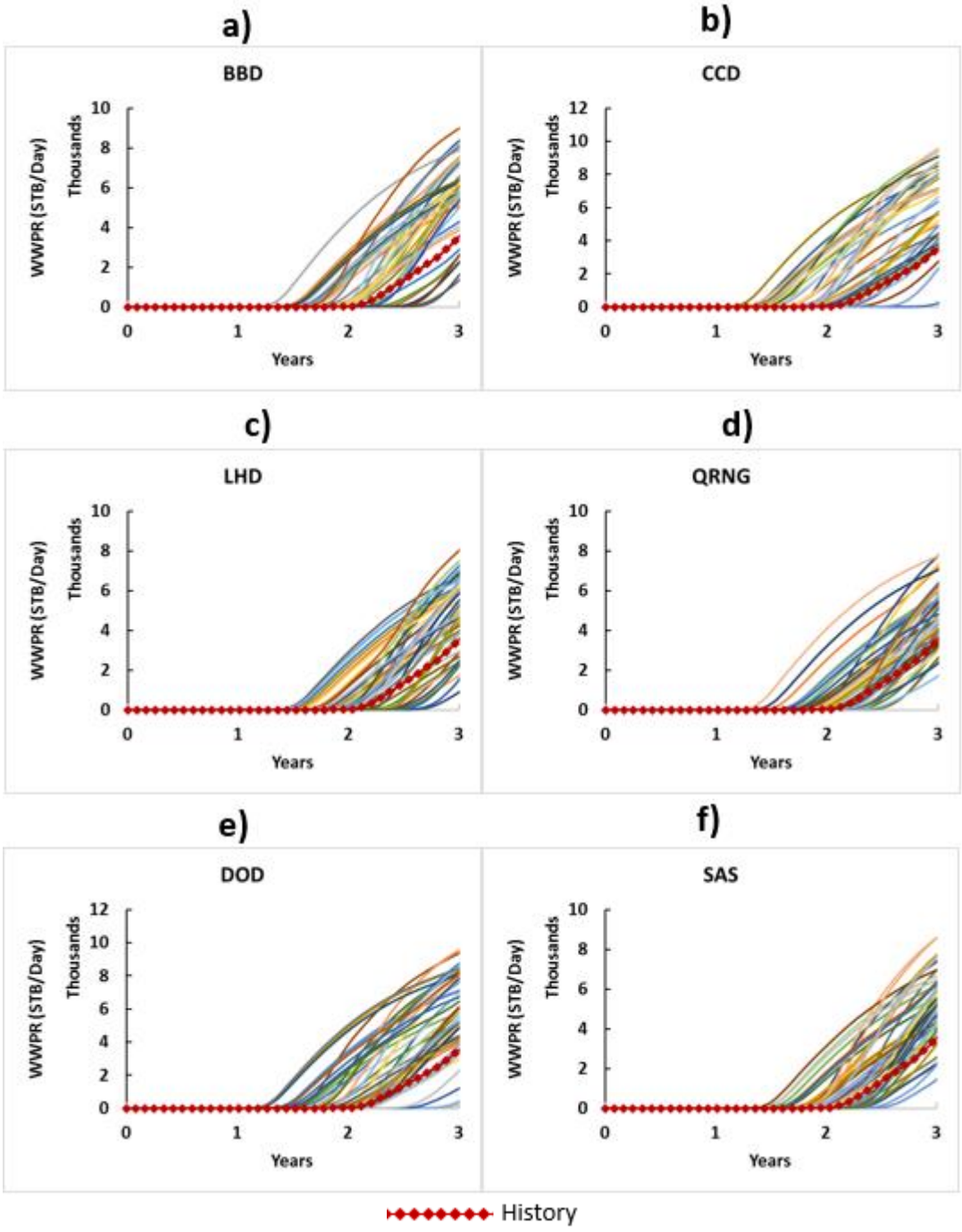

Figure 4.21 Predictions of well water production rates using the prior models generated using a) BBD, b) CCD, c) LHD, d)QRNG, e) DOD, and f) SAS

We made predictions of reservoir quantities using the 22 models in the first two ranks (Rank 1 and Rank 2) of the pareto models in Figure 4.20. The predictions are compared

with those made with the 65 LHD prior models (Figure 4.22). Predictions with the pareto models have reduced the level of uncertainties observed in the prior cases for the reservoir quantities including: producer well bottom hole pressure (Producer WBHP), injector well bottom hole pressure (Injector WBHP), cumulative oil production and field oil production rate (FOPR)

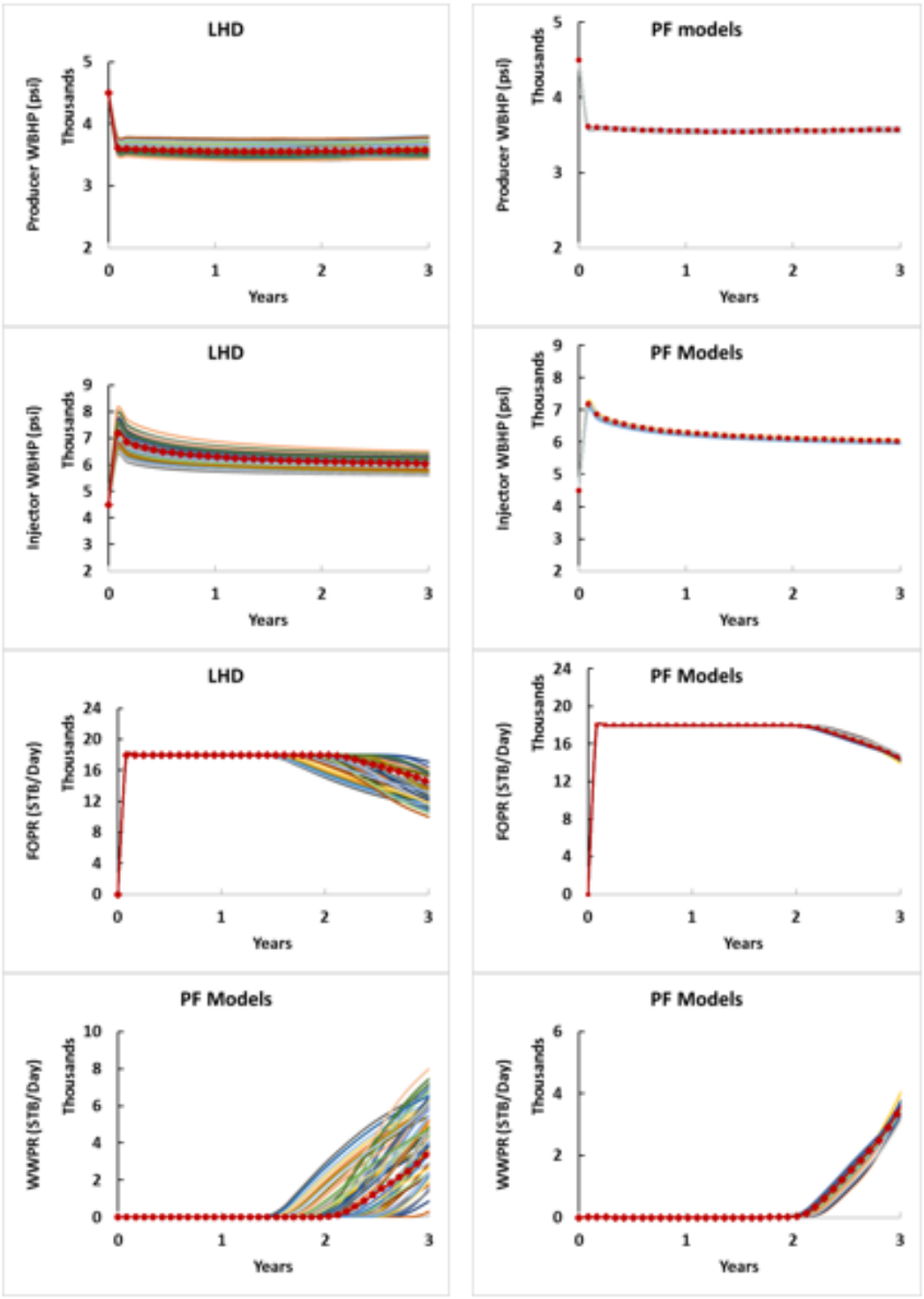

Figure 4.22 Comparing the LHD prior models predictions (left column) to (LHD + GA proxy) PF models predictions (right column)

4.3 Summary and Conclusion

In general, we observe from this synthetic history matching study that the addition of models generated during actual history matching using any optimisation algorithm helps to improve the quality of the quadratic proxy and leads to better representation of the reservoir response with surrogate model. Through the t-test (statistical test of significance), proxy models could be improved through the elimination of insignificant regression coeffiecients We also note that the regression coefficients in the quadratic proxy function are related to the convergence of models, and can therefore be a measure of convergence during history matching.

It is then noted that high quality proxy-models promises to be a good representation of the reservoir simulator in generating solutions to the history matching problems, and in making predictions for the future. We can generate proxy representation of the production misfit and seismic misfit and subject them to Pareto-Based multi-objective optimisation to generate a set of diverse history-matched models for performance predictions and uncertainty analysis. The history-matched models are the optimal solutions representing some trade-offs in the minimisation of conflicting objectives.

In an alternative approach, single-objective based genetic algorithm commonly used in oil & gas applications can be adopted in optimising a proxy approximation of global misfit (sum of seismic and production misfit) to generate a single optimal solution, or several solutions may be generated by using variable weights of individual seismic and production misfits in the single-based genetic algorithm. The use of the proxy models speeds up the optimisation process tremendously.

Chapter 5- Proxy-Assisted Ensemble Appraisal and Probabilistic Forecasting

Overview

The result of history matching is an ensemble of reservoir model parameters and the misfit between each predicted observable and the corresponding history data. In this chapter, we present an approach for making posterior statistical inferences from the ensemble based on proxy modelling; which to our knowledge is a fast multi-realisation probabilistic method for determining the uncertainty in reservoir performance following solution of the history matching problem. It relies on high quality proxy models of the reservoir response developed through a genetic programming based symbolic regression. As a result, the expense of solving the forward problem is avoided at this appraisal stage. However, the probability distribution of parameters is initially unknown so the model space is resampled systematically according to an estimate of the posterior probability density function. This results in the calculation of the Bayesian statistical measures of model plausibility and the correlations of the model parameters. The effectiveness of the approach is demonstrated here on model realisations generated using three different stochastic search methods – the Neighbourhood Algorithm (NA), the Genetic Algorithm (GA) and Particle Swarm Optimisation (PSO), but it is equally applicable to models generated through any other stochastic search methods or any method that generates multiple realisation of models. The results suggest that the new approach may well be a valid and fast alternative to the existing methodologies for ensemble apparaisal and stochastic reservoir performance forecast. MCMC resampling with the proxy model takes minutes instead of hours.

5.1 Introduction

In general, the history matching workflow for predicting flow in oil and gas reservoirs is highly non-linear and so the direct stochastic forecast of the reservoir performance is very difficult, if not impossible. We are therefore restricted to make estimates of stochastic distributions of the reservoir observables from a large number of realisations drawn from the distribution of the reservoir models reflecting the uncertainty in the reservoir parameters. This requires that we use an appropriate method which samples the correct probability distribution of the possible reservoir models.

There are several documented applications on the use of various Monte Carlo direct search methods for the generation of independent multiple realisations of the reservoir model during history matching. Few are documented on the difficult subject of stochastic sampling of the multivariate distributions. In a two-stage process consisting of a search stage and an appraisal stage, Sambridge (1999a, 1999b) presented a method of performing geophysical inversion by searching the multidimensional model space to find the best data-fitting models using the Neighbourhood Algorithm (NA). Then the appraisal of the ensemble was demonstrated using the Neighbourhood Algorithm Bayesian inference algorithm (NABayes). This approach approximates the posterior distributions by using the properties of V-Cell s and model misfit values.

Christie *et al*. (2002) and Subbey *et al*. (2004) adopted the approach of Sambridge (1999a, 1999b) to constrain reservoir model realisations using production data. Rotondi *et al*. (2006) took a similar approach to forecast hydrocarbon production in an offshore gas field. Stephen and MacBeth (2006) also used NA and NABayes to generate reservoir models and update the model probabilities within a Bayesian framework. They investigated the reduction of uncertainty of the reservoir parameters where time-lapse seismic data was included in the history matching workflow. Mohamed *et al*. (2010) compared the efficiency of three direct search methods – NA, Particle Swarm Optimisation (PSO) and Hamiltonian Monte Carlo (HMC) - in history matching and uncertainty quantification. They found that the results of the uncertainty in production forecast were similar for all the algorithms, but only HMC, a variant of Markov Chain Monte Carlo (MCMC), has the capability to sample the posterior directly. Bonet-Cunha (1996) and Hamid *et al*. (2015) used MCMC to sample the posterior probability density from an ensemble generated through a stochastic Gaussian Process driven by Simulated Annealing (SA) and Differential Evolution (DE) algorithm respectively.

Other notable works geared towards making inferences from the reservoir model statistics and calculating the uncertainty in predictions include Randomised Maximum Likelihood (RML) and Ensemble Kalman Filter (EnKF) within a Bayesian framework (Gao *et al*. 2005), a comparison of MCMC and NABayes (Okano 2013) among others.

In this paper, our approach to solving the problem of using history matching as a basis for forecasting is in two stages: (1) searching the multidimensional model space to generate an ensemble of models and their corresponding misfits to the history data, and (2) making statistical inferences from the ensemble and quantifying the uncertainty in model

predictions. Stage (2) is similar in principle to NABayes but is much faster and does not require specialised skills.

5.2 The History Matching and Appraisal Workflow

We adopt an Automated Seismic History Matching (ASHM) workflow technique described in Stephen *et al*. 2006, Stephen and MacBeth 2006 and Stephen 2007 (Figure 5.1) and appraise the models in a proxy-assisted bayesian framework

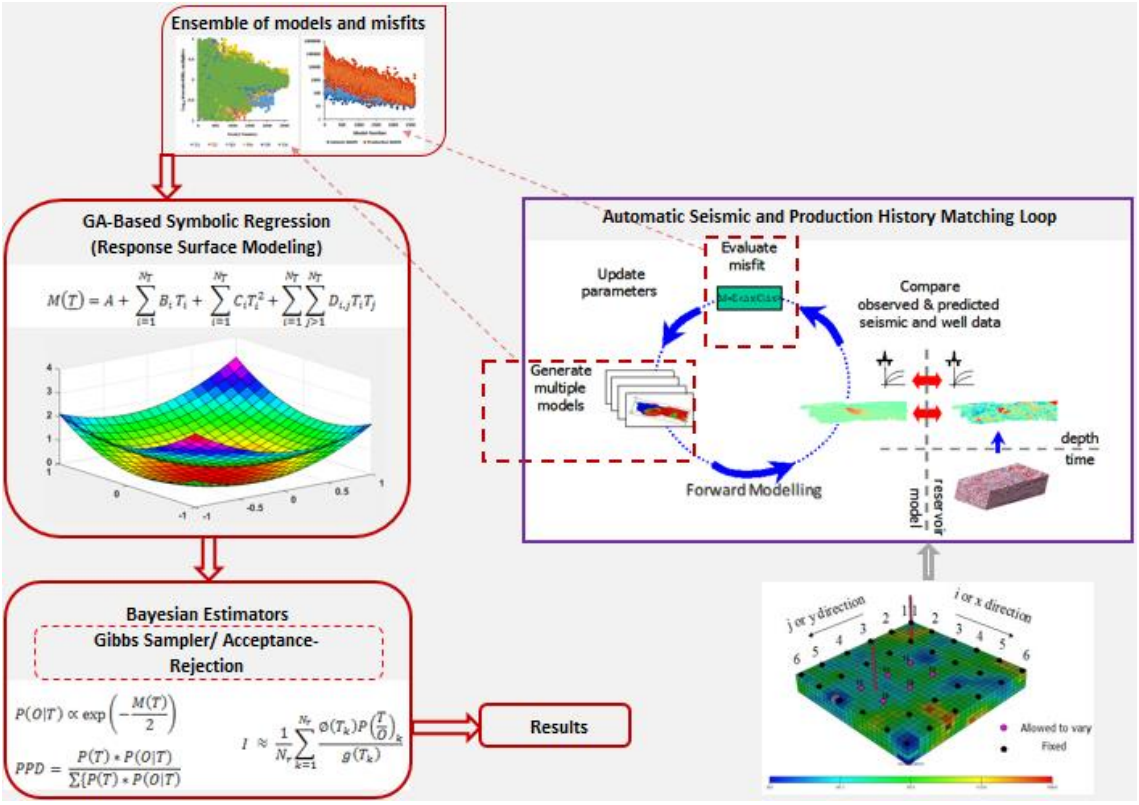

Figure 5.1. Seismic history matching workflow and appraisal workflow.

The workflow allows the inclusion of time-lapse seismic data along with production data to condition reservoir models. The approach enables the generation of multiple models using a stochastic approach in an iterative history matching loop to obtain good production and seismic data fitting models. The approach we use is equally valid with or without time-lapse seismic data. The ensemble of models and the misfits are used to calibrate a quadratic proxy using the symbolic regression. The posterior models are then generated by sampling the proxy model.

The Simulation Model

A Black Oil simulator (Eclipse 100 manual) is used to solve the forward problem and generate predicted data for each model. The reservoir model is the SGS model (Figure

5.2), described in Chapter 3 under section 3.2.3. In Figure 5.2, the six pink symbols indicate the pilot points at which the transmissibility modifiers are updated during history matching. Changes to transmmisibility values at the pilot points (identified with the parameters: T1, T2, T3, T4, T5 and T6) are propagated to cells in between using kriging. Black symbols in Figure 5.2 indicate pilot points where no changes are made.

We populate the initial ensemble of models by randomly sampling the six-dimensional parameter space with the multipliers at the pilot points allowed to vary from 0.1 to 10 (which implies that the $\log_{10}$ of the multipliers vary from -1 to 1).

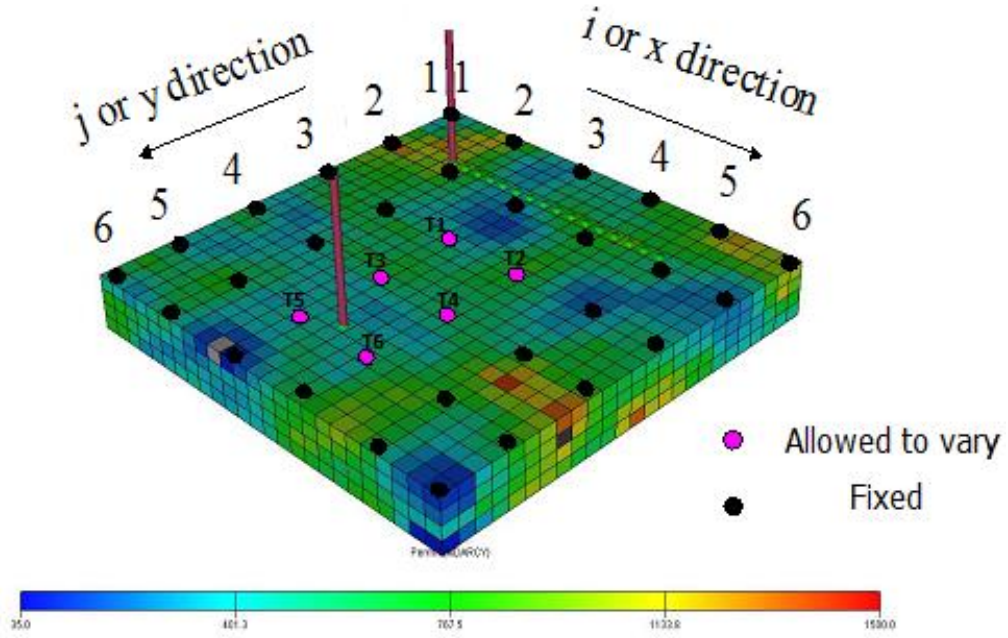

Figure 5.2 Using Pilot Point Scheme (Stephen 2007). The values of the Log_{10} transmissibility multipliers at the pilot point location (3,3), (4,3), (3,4), (4,4), (3,5) and (4,5), on the lattice, are designated as T_1, T_2, T_3, T_4, T_5 and T_6 respectively. The cells are coloured with permeability on a logarithmic scale

5.3 Evaluating the Fitness Function

For each of the models generated while searching the parameter space, a misfit function is evaluated to compare the observed and predicted seismic and production data. We compare the observations and the predictions for each of the chosen observables using the following weighted least-squares metric:

$$M = \sum_j \sum_i \left(\frac{d_{o\,i,j} - d_{s\,i,j}}{\sigma_d} \right)^2 , \ldots\ldots\ldots\ldots\ldots\ldots\ldots\ldots\ldots\ldots (5.1)$$

where M is the misfit value for each observable, $d_{o\ i,j}$ is the value of history data j at the i^{th} timestep, $d_{s\ i,j}$ is the corresponding data predicted by our simulator for each model, and σ_d is the standard error in the history data and represents the observation uncertainty.
The weighted least-squares metric is used as we assume that the data/model errors are independent and Gaussian (Oliver *et al.*, 2008).

We match the synthetically generated seismic and production history data simultaneously. For the time lapse seismic data, the observed (history) data are: change in AI in the first year, second year and over both years of production. On the other hand, production data such as Producer Bottom Hole Pressure and Injector Bottom Hole Pressure, the Producer Water Production Rate and the Field Oil Production are chosen to constrain the models within a 3-year production history with each data point measured on a monthly basis. The producer is controlled by the liquid rate and minimum bottomhole pressure. The well initially produces at the designated liquid rate of 18,000 STB/DAY and will switch to Bottom Hole Pressure (BHP) control if the BHP is below the minimum limit assigned as 2500 psi. The minimum pressure limit was neither reached in the 3 years of history matching nor in the 6 years of forecast. The injector on the other hand is controlled by the reservoir rate and upper limit of pressure. It is constrained to inject water at a rate that is just enough to replace the reservoir voidage created by oil and water production and will switch to pressure control if the injector pressure reaches its upper limit though this was never reached.

5.4 Searching the Model Space

Within the iterative loop of the ASHM, the choice of new transmissibility multipliers may be controlled using any direct search Monte Carlo method.

Initialising the Search: The Neighbourhood Algorithm (NA), Genetic Algorithm (GA) and Particle Swarm Optimisation (PSO) methods are used here to generate different study cases and are conceptually similar. Each of the sampling algorithms require an initial ensemble of ni models chosen stochastically. A Sobol-Antonov-Saleev (SAS) approach is adopted in sampling from a sample cube (a hypercube) to avoid random clusters. We can also use a Quasi-Random Number Generator (QRNG).

Searching the best Data Fitting Regions:

(a) Neighbourhood Algorithm: we generated an ensemble of 2625 models using the Neighbourhood Algorithm (NA, Sambridge, 1999a) described under section 3.7.1 in Chapter 3.

(b) Genetic Algorithm: Like NA, we generated an ensemble of 2625 models using the real number version of the Genetic Algorithm described under section 3.7.2 in Chapter 3. It is important to note that the routine for selecting parents in GA matters. One type of GA involves the calibration of the misfit/fitness values to probability such that better fitting models are more likely paired as couples to produce children. In our own case, we chose to pair the nr couples randomly. The original approach to cross-over will be to convert the real parameter values to bytes (strings of bits) followed by mixing the bits to produce the offspring. The downside of this approach is that convergence becomes more difficult with the GA as mixing of bits is almost arbitrary while the real number approach enables a gradual alteration of numbers.

(b) Particle Swarm Optimisation:

For this work, the PSO tuning parameters were set to $c_1 = c_2 = 1.892$, $w = 0.47$. This choice of PSO tuning parameters ensures that the algorithm's stability and convergence criteria are met (see section 3.7.3 in Chapter 3). The optimisation was set such that the particles internal velocities, and hence position, are updated.

Figure 5.3 shows the evolution of parameters during history matching when using the NA, GA and PSO methods. In all cases, the total number of iterations, $N_{it} = 40$, the initial number of models, $n_i = 65$, the number of models per iteration is $n_s = 64$. For NA, the number of best models selected, $n_r = 32$. This is the same as the number of couples chosen for the GA. In each of the three cases, 2625 models were generated.

Figures. 5.3a, 5.3c and 5.3e show the evolution of the parameters for NA, GA and PSO respectively run starting from the SAS initialisation. The SAS random number generator picks the middle values of all parameters as its first model. In the synthetic case, this is the answer we are looking for. While it would be unrealistic to find the solution right away in practice, we include this example to examine the sampling under what we would consider to be ideal conditions. Thus, we measure the apparent convergence rate. Similarly, the evolution of parameters is depicted for the cases in which NA, GA and PSO are initialised using QRNG method (Figures. 5.3b, 5.3d and 5.3f respectively). In this case the answer is

not known and we may find that we get stuck in local minima if they exist. Misfit values for each of the ensembles are plotted against the model index numbers to reveal the misfit evolution during the sampling stage (Figures. 5.4a, 5.4c and 5.4e for SAS-initialised runs, and Figures. 5.4b, 5.4d and 5.4f for runs initialised using the quasi-random number generator). We observed a different trend throughout the cases but the misfit is reduced as the iteration continues. Also in all cases, both the seismic and production misfits are respectively reduced in the process (e.g., Figure 5.5).

The trends in Figure 5.3 show that different solutions are found for the history matching problem depending on which algorithm is used and the type of initialisation. The NA optimization in Figure 3a finds the truth case with the smallest number of iterations. The success here is partly because the SAS-initialised models find the answer right away from the way we have set up the search space and there is no noise in the system. The case in Figure 5.3a. merely measures the ideal rate of convergence and how the algorithm performs the sampling. In real cases, however, NA optimisation may get trapped in a local minimum particularly if the NA tuning parameters are not set properly. GA and PSO, on the other hand, seem to explore the model space better but converge more slowly towards the true solution which is known from the start in Figures 5.3c and e. We find that the behaviour of the optimisation algorithms are dependent on the tuning parameters used as well. To find a global minimum at efficient convergence rate requires a proper selection of the optimiser tuning parameters: for example in the case of GA, creep and jump; or in the case of PSO, the Inertia constant, best global constant and best local constant.

For the purpose of this study, we will go ahead and appraise the results as we have them. The selection of tuning parameters and their effects on several optimisation algorithms are discussed in Yasin (2011). Moreover, to avoid the bias resulting from SAS initialisation models, we prefer to continue the appraisal on only the results for optimisation cases initialised using the QRNG (Figures. 5.3b, 5.3d, 5.3f, 5.4b, 5.4d, and 5.4f). Here, we found that it was no longer easy for NA to find the true solution since, unlike the SAS method, the QRNG initialisation method does not pick the middle values of all parameter bounds as the first model. This allows us to make a fair comparison of the results derived from the NA, GA and PSO. The evolution of seismic and production misfits are shown in Figure 5. We further note though, that NA by its nature does not preserve diversity as much as GA and PSO, because the NA optimisation system is designed to reduce the search space which is often done efficiently depending on its shape.

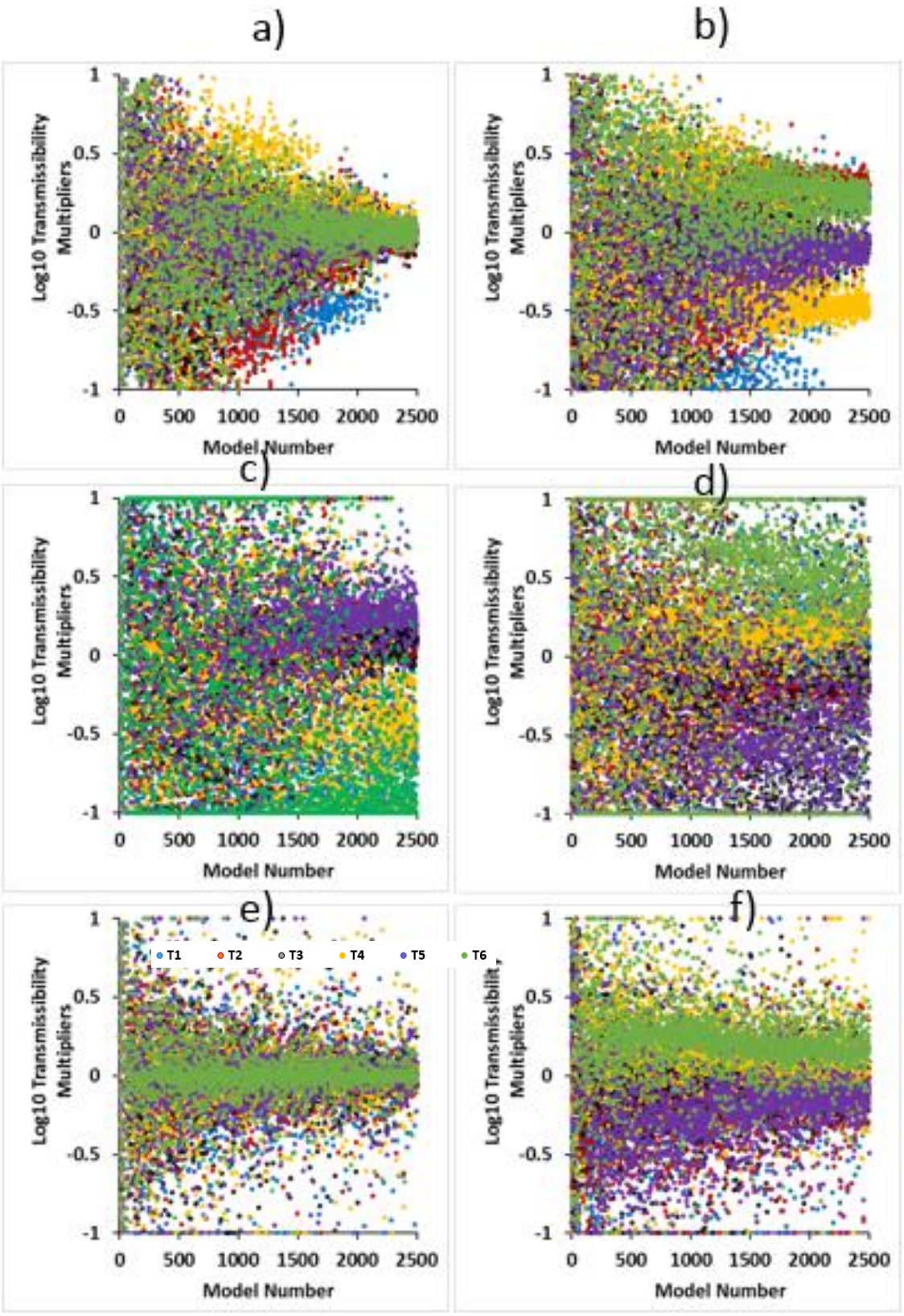

Figure 5.3 The evolution of reservoir parameter during optimisation with (a) NA initialised with Sobol-Antonov-Saleev (SAS), (b) NA initialised with quai-random number generator (QRNG), (c) GA initialised with SAS, (d) GA initialised with QRNG, (d) PSO initialised with SAS, (e) PSO initialised with QRNG. The $\log_{10}$ transmissibility multipliers at pilot point locations 1 to 6 are designated as T1, T2, T3, T4, T5 and T6 respectively.

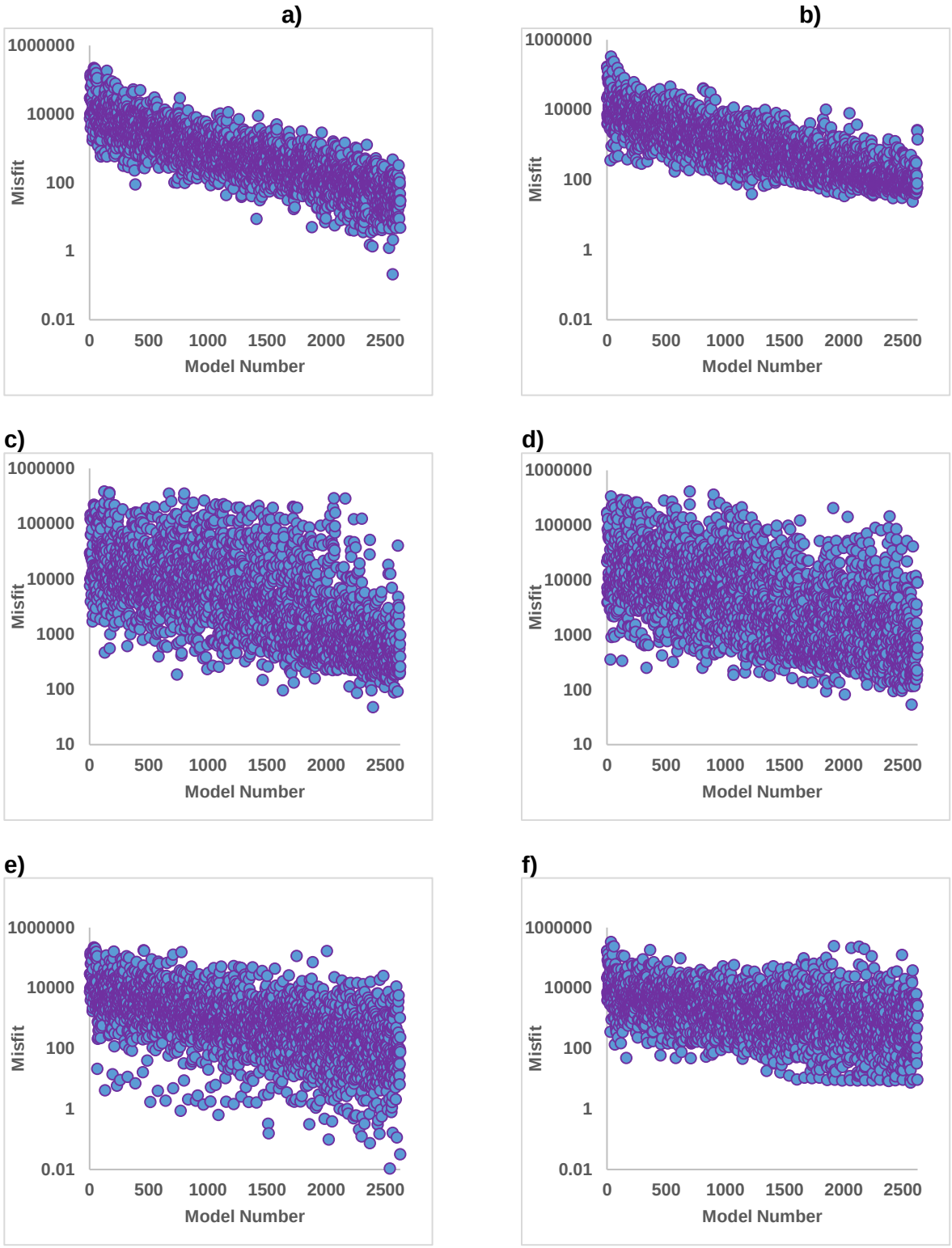

Figure 5.4 The evolution of total misfit corresponding to the cases in Figure 5.3a, 5.3b, 5.3c, 5.3d, 5.3e, and 5.3f respectively

Figure 5.5 below shows the evolution of seismic and production misfit for the various optimisations initialised with the QRNG.

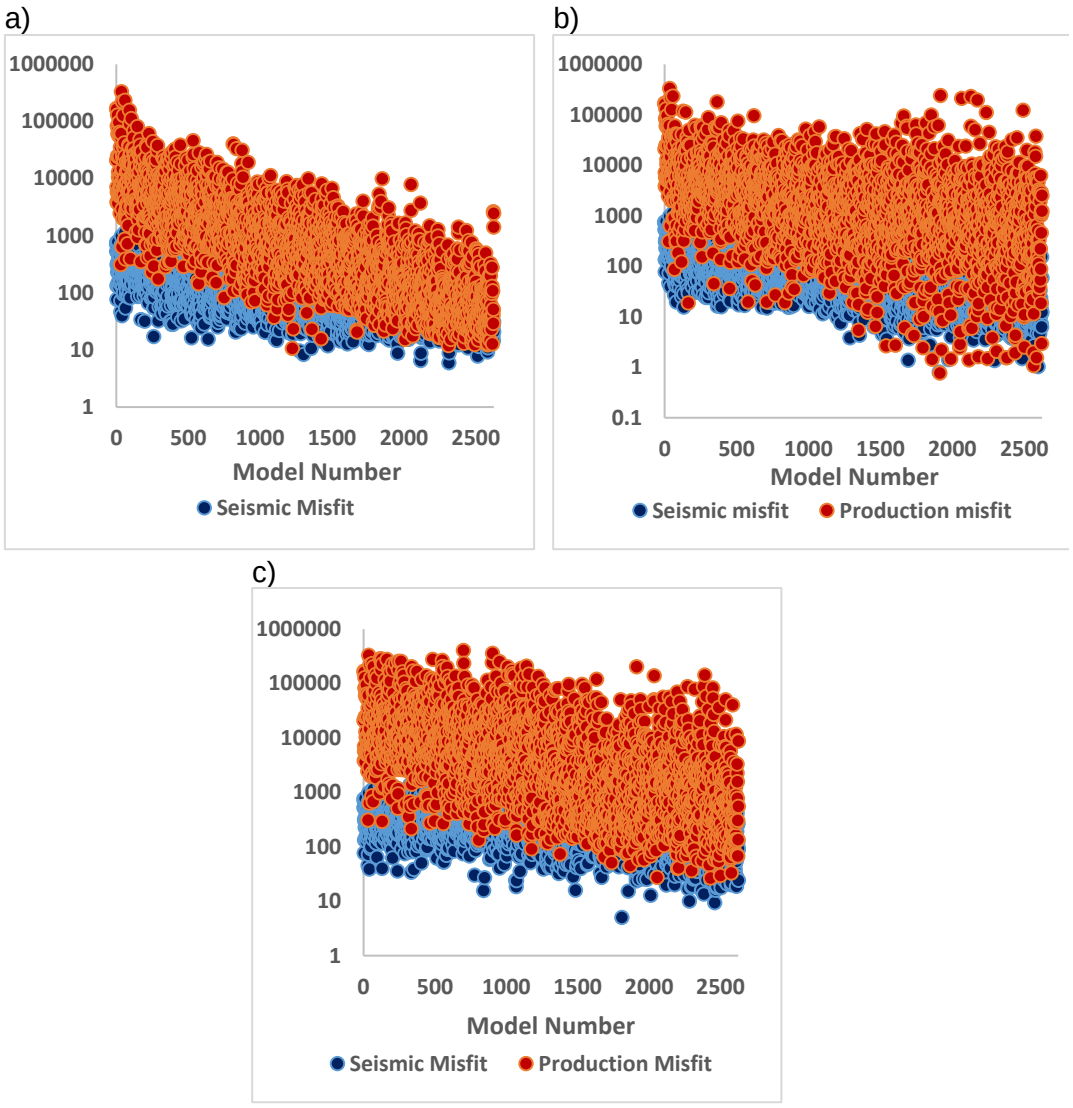

Figure 5.5 The evolution of misfit of seismic and production data for (a) NA, (b) PSO, and (c) GA initialised with quasi-random numbers

5.5 Making Inferences from the Ensemble

After history matching, we consider that we have sampled the parameter space sufficiently and intend to make use of the entire ensemble of model parameters together with their misfit values to make statistical inferences within the Bayesian framework. From the viewpoint of Bayesian probability, a complete solution of an inverse problem, including history matching, can only be represented by the posterior probability density function (PPD) for the model parameters (Mosegaard & Tarantola 1995; Oliver *et al.* 2008; Tarantola 2005).

For any combination of model parameters T_i (i = 1, …, N_T) in N_T-dimensional model space, the posterior probability distribution (PPD) is defined as the conditional probability distribution of the models given the history data, and is obtained from:

$$P(T|O) = \frac{P(T) * P(O|T)}{\sum\{P(T) * P(O|T)} \quad , \ldots\ldots\ldots\ldots\ldots\ldots\ldots\ldots (5.3)$$

Where:

$P(T)$ is the prior probability distribution of the models, $P(O|T)$ is the conditional probability distribution for observed data given the model *T* and is equal to the likelihood function, $L(T|O)$.

$\sum\{P(T) * P(O|T)$ is the normalisation constant defined in such a way as to make the integral of the posterior probability distribution over the permissible model parameter range equal to 1.

We consider a definition of $P(O|T)$ as a measure of the relative fitness of the models to the observations through its relationship with the misfit values (M) in the equation below (Tarantola 2005):

$$P(O|T) \propto \exp\left(-\frac{M}{2}\right), \ldots\ldots\ldots\ldots\ldots\ldots\ldots\ldots\ldots\ldots\ldots\ldots\ldots\ldots (5.4)$$

It will be seen later that the evaluation of the Bayesian indicators of a model's plausibility requires multivariate integration as the $P(O|T)$, and hence the PPD is a multivariate function. To make the integration faster and simpler we approximate the PPD using a proxy function. Considering Eq. 3, it is implied that the posterior probability density function is known only at the locations in the model space for which the optimisation algorithm generated the model parameters. In other words, the PPD is known only for those points defined by the parameter values of the 2625 models sampled during the search stage. To fill the gaps, a proxy model can be generated. A quadratic polynomial is often considered sufficient in describing the main effects, the quadratic effects and the second-order parameter interactions (Oliver *et al*. 2008). We therefore approximate the actual misfit surface using a proxy of the form:

$$M(\underline{T}) = A + \sum_{i=1}^{N_T} B_i T_i + \sum_{i,j=1}^{N_T} C_{(i,j\geq i)} T_i T_j \, , \ldots\ldots\ldots\ldots\ldots\ldots\ldots\ldots\ldots\ldots\ldots\ldots\ldots (5.5)$$

where $M(\underline{T})$ represents the misfit function at any point in the sampled parameter space represented by the vector, $\underline{T}$. N_T is equal to 6 in our history matching case. The coefficient terms A, B_i and $C(i, j \geq i)$ are regression coefficients which were determined using a GA-based symbolic regression. We apply the symbolic regression to those results of our history matching problem for which the optimisation is initialised using the quasi random number generator, to obtain the misfit as proxy function (Eq. 4). The resulting regression coefficients are shown in Table 5.1.

Table 5.1 Values of regression coefficients for the misfit proxy from symbolic regression

Category of Terms	Regression Coefficient Term	Regression Coefficient		
		NA R^2= 0.940	GA R^2= 0.910	PSO R^2= 0.935
Constant	A	11.68	31.25	11.43
Main Effect/ Linear Terms	B_1	968	583.75	709.91
	B_2	-280	-60.14	-115.83
	B_3	599.6	405.39	664.39
	B_4	-372.9	-199.13	-366.76
	B_5	229.4	149.28	150.4
	B_6	-165	69.53	-54.25
Quadratic Terms	$C_{1,1}$	1090	3207.02	1782.32
	$C_{2,2}$	3620	3157.37	2470.36
	$C_{3,3}$	6462	4027.02	3032.79
	$C_{4,4}$	2488	1726.43	2601.35
	$C_{5,5}$	4093	2103.23	2031.94
	$C_{6,6}$	3438	2047.77	1845.23
Interaction Terms	$C_{1,2}$	-12100	-7193.03	-8727.25
	$C_{1,3}$	9232	5462.38	1589.73
	$C_{1,4}$	-7623	-32.92	-1124.36
	$C_{1,5}$	-63.52	-3.67	-264.1
	$C_{1,6}$	-369	127.97	-224.51
	$C_{2,3}$	4.362	-63.69	-50.84
	$C_{2,4}$	810	348.04	-374.58
	$C_{2,5}$	-3502	-1336.86	-1807.78
	$C_{2,6}$	-952	-126.47	-503.62
	$C_{3,4}$	692.8	360.69	48.36
	$C_{3,5}$	-330.15	-572.18	-117.8
	$C_{3,6}$	-5981	-6681.9	-2663.21
	$C_{4,5}$	-4485	-1312.36	-1021.03
	$C_{4,6}$	8183	812.46	179.27
	$C_{5,6}$	416.6	3417.32	2111.01

For any combination of parameter sets T, the un-normalised PPD is then calculated using:

$$P(T|O) = \exp[-0.5 * M(T)] \ldots\ldots\ldots\ldots\ldots\ldots\ldots\ldots\ldots\ldots\ldots\ldots (5.6)$$

Probability distributions over the model space are central to the appraisal of model parameters. However, in making statistical inference in high dimensional spaces, it is often difficult to use distributions as measures of central tendency. For example, the mean, the mode or the median, and the measures of dispersion such as standard deviations and

covariance tend to lose their statistical value especially in cases of multimodal distributions. We estimate those as the properties of the PPD regardless of whether or not they are multimodal, and consider that they still characterise the complete solution to the history matching problem.

To add more meaning to their statistical values, we perform analysis of the resolution of the models generated during history matching. The misfit function in this history matching case is a function of six variables and representation of the distribution function is non-trivial. We have chosen to sample the probability density as described in the following section. This will estimate the desired properties of the PPD expressed in the form of Bayesian Integrals using multidimensional Monte Carlo (MC) integration over the model space (Tarantola, 2005).

5.6 Sampling the Posterior Probability Density

Tarantola (2005) identified two issues that occur when using Monte Carlo methods for sampling the probability distribution in multi-dimensional space: there is a problem finding the regions of high probability and it is difficult to sample the regions with the right density.

We adopt a sampling method which relies on a combination of proxy modelling and Markov Chain Monte Carlo, and we use the Gibbs sampler (Geman & Geman 1984) to importance sample the proxy approximation of the posterior probability distribution.

5.6.1 The Gibbs Sampler

The Gibbs Sampler can generate models from the parameter space such that the samples will follow a distribution which asymptotically assumes the shape of a given distribution: in this case the posterior probability distribution (PPD) approximated by a proxy function. We will illustrate how the sampler works in the case of our N_m-dimension problem (N_m = 6 in this study). We want to obtain N_r samples of $\underline{T} = \{T_1, \ldots, T_{N_m}\}$ from the posterior probability distribution approximated by the multidimensional PPD proxy function, $P_{pr}(T_1, \ldots, T_{N_m})$. The Gibbs algorithm starts its journey from an initial arbitrary point in the space to generate the jth sample, $\underline{T}^j = \{T_1^j, \ldots, T_{N_m}^j\}$. From this point it makes a transition to the next sample point $\underline{T}^{j+1}$ by taking a stepwise walk along each of the six axes of the parameters in turn. For each step along an axis a random deviate is drawn from the conditional probability density defined by $P_{pr}\left(T_i^{(j+1)} | T_1^{(j+1)}, \ldots, T_{(i-1)}^{(j+1)}, T_{i+1}^{j}, \ldots, T_{N_m}^{j}\right)$.

This means that to sample a parameter $T_i^{(j+1)}$ component of a sample model $T^{((j+1)}$along a parameter axis, i, the Gibbs Sampler draws a randon deviate from the distribution of this parameter conditioned on all other parameters sampled so far. One new model vector is thus generated when the sampler completes its walks, once per axis, in one iteration. The process is repeated N_r times. The Gibbs Sampler further simplifies the multidimensional integration problem such that the marginal distribution of any model parameter or any subset of the parameters is simply the samples for that parameter or subset of parameters, and the expected value of any parameter becomes a simple average over all the samples. The use of a proxy model to approximate the actual posterior probability distribution makes the sampling easy, reduces the computation time considerably such that one need not worry about the computational cost of the Gibbs Sampler. However, one may wish to reduce the computation time even further and improve the sampling of the parameter space by using several independent random walks each starting at a different initial point in model space.

5.6.2 Acceptance-Rejection Method

The Gibbs sampler draws random deviates from the conditionals but the samples we want to keep are those with high probablity indicated by the region under the curve of the posterior density function defined in the multidimensional space. The procedure for generating the random deviate, accepting or rejecting samples on each parameter axis to ultimately create the 1-D conditionals is highlighted as follows:

i. The axis is divided into N_{disc} discrete intervals to define the sample points $T_i^1, \dots, T_i^{N_{(disc+1)}}$, along the axis in the Gibbs Sampler.

ii. The conditional posterior probability density along the axis is calculated at the boundaries/edges of the discrete intervals and defined as a step function. The maximum value of the conditional probability along the axis, P_{pr}^{max}, is found, which is then used to define the height of a uniform comparison function over all intervals on the axis

iii. A step is proposed by generating a uniform random variable, T_i^p, between the upper and lower bounds of an axis, and its conditional ppd, $P_{pr}(T_i^p)$, is computed

iv. Another uniform random number, *U*, is generated in the interval (0,1) to be used in accepting or rejecting the proposed variable

v. The proposal in 'iii' is accepted if the inequality, $\frac{P_{pr}(T_i^p)}{P_{pr}^{max}} \geq U$, holds. In order to avoid the problem of numerical underflow, the inequality is redefined as:

$$\log U \leq log\left[P_{pr}(T_i^p)\right] - \log[P_{pr}^{max}]$$

If the proposal is not accepted, the steps are repeated until an accepted step is produced, and the process goes on accordingly to generate a density distribution for the accepted proposal which has been proven to be the required 1-dimensional conditional probability density function (Press *et al.* 1992).

5.7 The Bayesian Estimators

We have seen that for any sample model, T, in the multidimensional model manifold, M, the Posterior Probability Density is multidimensional. We approximate the PPD using a proxy model (Equations 4 and 5) which is a function of the model parameters. The parameter space is then sampled according to the PPD in the manner described in the previous section.

We are interested in some properties of the multidimensional PPD (see Tarantola, 2005 and Sambridge, 1999b for more details) enumerated below:

i. The Maximum of the Posterior PDF

The model corresponding to the maximum PPD is of interest and conveys different meanings depending on whether prior information on the models is available or not. If we ignore the prior information, then the model is called the Maximum Likelihood Estimate (MLE) and corresponds to model with the best fit to the data.

$$MLE = \underset{m}{argmin}\ P(T|O) \quad \ldots\ldots\ldots\ldots\ldots\ldots\ldots\ldots\ldots\ldots\ldots\ldots\ldots\ldots\ldots\ldots (5.7)$$

If we consider prior information on the model then from the Bayesian viewpoint, the best estimate of m is the model which maximises the a posteriori PDF and is called the Maximum a Posteriori (MAP) estimate

ii. **The posterior Mean Model**

The posterior mean is calculated for each of the parameters of the model. If we consider a parameter T_i (herein T = 1, 2, 3 …6) then the mean is given by the Bayesian integral:

$$\widehat{T_i} = \int_M T_i\ P(T|O)dT \quad \ldots\ldots\ldots\ldots\ldots\ldots\ldots\ldots\ldots\ldots\ldots\ldots\ldots\ldots\ldots\ldots\ldots (5.8)$$

iii. **The posterior Model Covariance Matrix**

This contains information on the correlation between model parameters and we can infer the variances and hence the standard deviations of model parameters from the diagonal elements. The covariance between any two parameters, T_i and T_j is calculated using the Bayesian integral:

$$Cov(T_iT_j) = \int_M T_iT_j \; P(T|O)dT - \widehat{T_i}\;\widehat{T_j} \quad \ldots\ldots\ldots\ldots\ldots\ldots\ldots\ldots\ldots\ldots\ldots (5.9)$$

iv. **The posterior Model Correlation Matrix**

The off-diagonal elements of this matrix carry the same information as the covariance matrix but becomes more relevant when the model parameters differ in dimension and scale. The correlation between any two parameters, T_i and T_j is calculated using:

$$Corr(T_iT_j) = \frac{Cov(T_iT_j)}{\sqrt{Cov(T_iT_i) * Cov(T_jT_j)}} \quad \ldots\ldots\ldots\ldots\ldots\ldots\ldots\ldots\ldots\ldots\ldots\ldots\ldots (5.10)$$

v. **The Model Resolution**

The elements of the resolution matrix give information on the extent to which the real reservoir has been resolved by the model parameters. The concept of resolution operator is especially true in linear problems but is approximately valid for nonlinear problems. If we define the prior model covariance between two parameters as $Cov(T_iT_j)_{prior}$ which is determined from the prior model, then for the parameters, T_i and T_j, Tarantola (2005) shows that the resolution operator can be approximated using:

$$R = I - Cov(T_iT_j)^{-1}_{prior} * Cov(T_iT_j) \quad \ldots\ldots\ldots\ldots\ldots\ldots\ldots\ldots\ldots\ldots\ldots\ldots\ldots\ldots (5.11)$$

Where I is the identity matrix

A simple interpretation of Equation (5.11) is as resolution operator R tends to the identity, the posterior covariance tends to zero, which implies that our parameters have been well resolved.

We can also define the non-dimensional resolution matrix for the case where the model parameters differ in dimension and scale by normalising the elements of the matrix by any appropriate ratio of the parameters scale length; using, for instance, the ratio of the standard deviation determined using the prior covariance matrix.

vi. **The Marginal Posterior Probability Density**

The one-dimensional marginal PPD for a model parameter, T_i, is evaluated by integrating the PPD over the remaining $N_m - 1$ parameters (where N_m is the model dimension):

$$f_M(T_i) = \int \dots \int P(T|O) \prod_{\substack{r=1 \\ r \neq i}}^{N_m} dT_r \quad \dots\dots\dots\dots\dots\dots\dots\dots\dots\dots\dots\dots\dots\dots (5.12)$$

Two-dimensional marginal PPD can be defined in a similar way for any combination of two model parameters. The marginal are very useful in that they indicate the level of information provided on a parameter or combination of parameters when all possible variations of the other parameters are considered.

Evaluating the Integrals

The simplest method of evaluating the Bayesian integrals for a finite multidimensional space is by defining a regular grid of points in the model space and computing the integrands at each point of the grid and then approximate the Bayesian integral by a discrete sum. Unfortunately, the method becomes impracticable as the model dimensions increases, say $N_m \geq 4$ (Tarantola, 2005). The values of the various Bayesian integrals discussed in the foregoing text are therefore estimated using monte carlo numerical integration method in the multidimensional manifold by replacing the regular grid of points with a Sobol quasi-random sequence (Sobol, 1967) generated using the Numerical Recipes (William *et al*, 1992). Following the methods of Tarantola (Tarantola, 2005), we see that all the Bayesian integrals in Equations 5.7, to 5.12 follow the shape:

$$I = \int_M \dot{\emptyset}(T) P\left(\frac{T}{O}\right) dT \quad \dots\dots\dots\dots\dots\dots\dots\dots\dots\dots\dots\dots (5.13)$$

Where $\emptyset(T)$ is the integrand defined over the multidimensional space. With Monte Carlo numerical integration, Equation (5.13) becomes:

$$I \approx \frac{1}{N_r} \sum_{k=1}^{N_r} \frac{\emptyset(T_k) P\left(\frac{T}{O}\right)_k}{g(T_k)} \quad \dots\dots\dots\dots\dots\dots\dots\dots\dots\dots\dots\dots\dots\dots (5.14)$$

Where $T_1 \dots T_{N_r}$ is a suite of T_k collectively independent resampled points randomly distributed over the model space with a sampling density $g(T_k)$, which is a normalized probability density over the model space, ($\int_M g(T)\, dT = 1$).

Equation 5.14 is simply a weighted average of, $\emptyset(T_k)$ over the resampled ensemble; and the weights $\frac{P(T/O)_k}{g(T_k)}$ is dependent on the sampling method adopted. For importance sampling technique such as the Gibbs sampler, the integrand is importance sampled so that the sampling density asymptotically tends towards the shape of the posterior

distribution, $g(T_k) \approx P(T/O)_k$ (see Carlin, 1994 for details of proof of convergence), and the weights become unity so that the integration task reduces to trivial evaluation of simple averages over the resampled ensemble.

$$I \approx \frac{1}{N_r}\sum_{k=1}^{N_r} \emptyset(T_k) \quad \ldots\ldots\ldots\ldots\ldots\ldots\ldots\ldots\ldots\ldots\ldots\ldots\ldots\ldots (5.15)$$

This is not the case in uniform Monte Carlo sampling where the weights must be applied to the samples during integration.

5.8 Unbiased Approach to Probabilistic Forecasting

As with all nonlinear inverse problems, the full solution to a history matching problem is the posterior probability density function. However, as noted in Oliver *et al* (2008), the complete construction of the posterior PDF is generally impractical as there is an infinite number of plausible solutions. We have resampled the posterior probability distribution to obtain N_r (in this study N_r = 10,000) samples of models which are distributed according to the posterior probability density, and hence represent the solution to the history matching problem.

We can now make predictions using these models and define an uncertainty envelope in predictions. Normally, making predictions requires solution of the forward problem (running computer simulation) and this could become burdensome for large values of N_r. We need to make predictions with fewer representative models (say N_{rr} = 100 models) but we must ensure that this selection from the N_r 'posterior' models is unbiased. Therefore, we adopt a sampling method which relies on the inversion method (Tarantola 2005). We assign equal probability values to each of the posterior models and compute the cumulative density function (CDF). This becomes the cumulative density function of the n-dimensional equiprobable models**.** To ensure that the sampling of the posterior is unbiased, the N_{rr} forecasting models are realised by sampling the n-dimensional CDF.

Predictions of production and seismic observables of interest and the definition of their uncertainty envelopes are then made with the N_{rr} models.

5.9 Weighted Probability Approach to Forecasting

In another approach to quantify the uncertainty in our predictions, we apply weights in the form of relative probability of each model. The NABayes Gibbs sampler is used and the posterior probabilities are computed using the voronoi approximation of the PPD. In NABayes, each model m_i, in the original ensemble of size N_T, generated using any of the

stochastic optimisation algorithms (NA, GA, PSO etc) is represented by a V-Cell (Sambridge, 1999b). The relative probability of a model x_i, is calculated by taking counts of the frequency of visits f_i, to the model (or its V-Cell) during NABayes random walks (equation 5.16).

$$x_i = f_i \Big/ \sum_{j=1}^{N_T} f_j \text{ , ……………………………………………..……} (5.16)$$

Such that,

$$\sum_{j=1}^{N_T} x_j = 1$$

The relative probabilities calculated from eq. 5.16, are applied as weights to the predictions of the respective models to define the uncertainty envelopes in the forecasting of the pressure and production profiles.

This approach differs from the forecasting method described previously where prediction uncertainty was estimated with the assumption that the models that meet the acceptance criteria in Gibb's sampling are equally probable.

5.10 Statistical Inferences from the posterior probabilities

Uncertainty quantification requires predictions from several hundreds to thousands of model realizations. As noted previously, making predictions with this large number of realisations is computationally prohibitive. Our method of forecasting involves resampling to generate fewer representative models from the larger population of models. We make statistical propositions through a number of calculations to estimate the credible interval so that we can simply represent the uncertainty envelope by the mean, P10 and P90 only. First we determine the arithmetic means of the predictions $\mu(t)$, from eq. 5.17, and the standard deviations of the predicted quantities $\sigma(t)$, as follows:

$$\mu(t) = \sum_{j=1}^{N_T} x_j \, Q_j(t), \text{………………………………………………} (5.17)$$

$$\sigma(t) = \left(\sum_{j=1}^{N_T} x_j \, {Q_j}^2(t) - \langle \mu(t) \rangle^2 \right)^{0.5}, \ldots\ldots\ldots\ldots\ldots\ldots\ldots\ldots\ldots\ldots\ldots\ldots\ldots\ldots (5.18)$$

where x_j is the weight of the models determined using Equation 5.16, and is equal for all models in the case of equally probable models. $Q_j(t)$ is the profile of the predicted quantity (example: pressure and production profiles) for a model m_j. The pressure and production profiles are temporally varying property with the independent variable, *t*, designating the time steps.

If we assume that the predicted quantities follow a known probability distribution (such as normal or log-normal distribution) then we can estimate the P10 and P90 profiles for the quantities by transforming the mean and the standard deviation of the respective quantities calculated using Equations 5.17 and 5.18. In the case of normally distributed quantities, we can simply estimate the P10 and P90 using Gaussian statistics (Equations 5.18 and 5.20).

$$P10 = \mu(t) - 1.28\sigma(t), \ldots\ldots\ldots\ldots\ldots\ldots\ldots\ldots\ldots\ldots\ldots\ldots\ldots\ldots\ldots\ldots\ldots\ldots\ldots (5.18)$$

$$P90 = \mu(t) + 1.28\sigma(t), \ldots\ldots\ldots\ldots\ldots\ldots\ldots\ldots\ldots\ldots\ldots\ldots\ldots\ldots\ldots\ldots\ldots\ldots\ldots (5.19)$$

If we assume a log-normal distribution, then we note that the natural logarithm of the predicted quantities, $\ln\left(Q_j(t)\right)$, follow normal distribution. So, we start by transforming the mean and standard deviation computed from Equations 5.17 and 5.18 to the mean and standard deviation of a normal deviation.

$$\mu(t) = \exp\left(\mu_n(t) + \frac{\sigma_n(t)}{2}\right), \ldots\ldots\ldots\ldots\ldots\ldots\ldots\ldots\ldots\ldots\ldots\ldots\ldots\ldots\ldots\ldots\ldots (5.20)$$

$$\sigma^2(t) = \mu(t)\left[\exp\left(\sigma_n(t)\right) - 1\right]^{\frac{1}{2}}, \ldots\ldots\ldots\ldots\ldots\ldots\ldots\ldots\ldots\ldots\ldots\ldots\ldots\ldots\ldots\ldots\ldots\ldots (5.21)$$

Where $\mu_n(t)$ and $\sigma_n(t)$ are the mean and standard deviation of the normally distributed quantities (i.e. natural logarithm of predicted quantities). We then use the concept of standard normal distribution or z-scores (Kenney and Keeping, 1962) to relate the mean

and standard deviation of the normal distribution to the natural logarithms of the P10 and P90 of the predicted quantities, as follows:

$$-1.28 = \frac{[lnP10(t) - \mu_n(t)]}{\sigma_n(t)} \text{, … … … … … … … … … … … … … … … … (5.22)}$$

$$1.28 = \frac{[lnP90(t) - \mu_n(t)]}{\sigma_n(t)} \text{, … … … … … … … … … … … … … … … … (5.23)}$$

The $P10(t)$ and the $P90(t)$ are then obtained from Eqiuations 5.22 and 5.23 define the uncertainty envelope in the predicted quantities.

Furthermore, we can perform uncertainy analysis on the posterior models for spatial quantities such as seismic (impedance) maps, water saturation and oil pressure per grid cell. Maps or volumes of arithmetic means is calculated for a spatial variable, *S*, using:

$$\mu(x, y, z, t) = \sum_{j=1}^{N_T} x_j \, S_j(x, y, z, t), \text{ … … … … … … … … … … … … … … … … (5.24)}$$

And we can similarly calculate the standard deviations to estimate the spread of the predicted spatial quantities over the posterior ensemble, as follows:

$$\sigma(x, y, z, t) = \left(\sum_{j=1}^{N_T} x_j \, {S_j}^2(x, y, z, t) - \langle \mu(t) \rangle^2 \right)^{0.5} \text{, … … … … … … … … … … (5.25)}$$

(x,y,z,t) indicates that the quantity *S*, varies spatially and temporally: *(x,y,z)* is the position of the grid cell at which the property is being predicted while and *t* is the time of seismic surveys .

5.11 Appraisal Results and Discussion

Using the Monte Carlo method of numerical integration (Tarantola, 2005), the Bayesian integrals are evaluated for the properties of the PPD to enable us make statistical inferences. The probability distribution of the resampled ensemble of models gives the one dimensional marginal distribution if projected to the respective parameter axes (Figure 5.6)**.** Compared to the uniform prior distribution, the history matching process has produced posterior distributions with narrow peaks resulting from the conditioning of the

models by the history data. All the marginal distributions are unimodal although there are minor bumps on some of them. Generally, it is observed that the marginals are characterised by peaks at which the various parameter values correspond approximately to zeros: the values set for the reference model. The resampling approach has been able to create one-dimensional posterior marginals from which one can infer the values of the reservoir model parameters. This is particularly true for the posterior derived from the NA ensemble. In this synthetic case, NA algorithm converges faster than the GA and the PSO giving a high density regions that approximates the true solution.

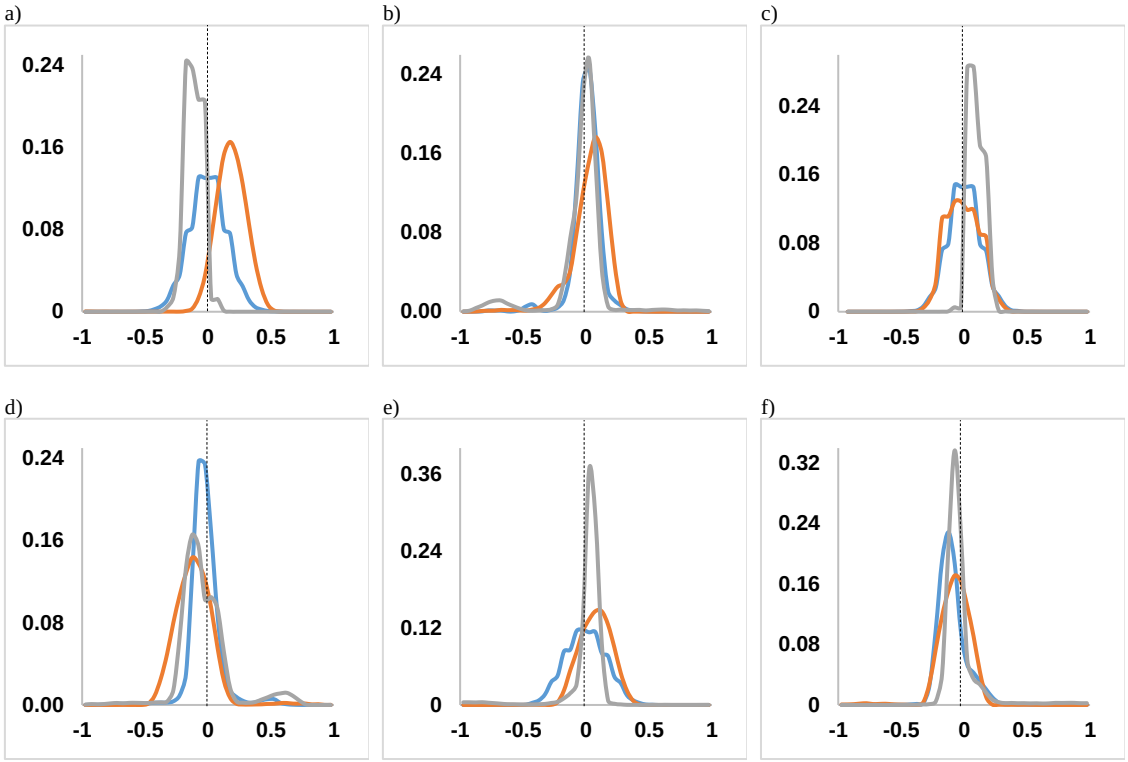

Figure 5.6 The one-dimensional marginal posterior distribution functions for (a) T1, (b) T2, (c) T3, (d) T4, (e) T5, and (f) T6 based on resampling using the proxy misfit. Curve Colour: NA –Blue. GA – Orange, PSO – Grey. All marginal distributions are unimodal with peaks lying approximately at the true parameter values (dashed black lines). The respective proxy misfits used are response surface approximation of the data in Figures. 5.3b, 5.4b for NA, Figures 5 3d, 5.4d for GA and Figures. 5.3f, 5.4f for PSO.

In the case of GA and PSO, most of the peaks do not lie at the true values and the curves differ considerably between the different methods of generating the input ensemble. The same history data were used to provide information to constrain the models during the search stage and the difference in the properties of the PPD reflects the differences in the type of ensembles generated by the different search methods. Because this is a synthetic case for which we know the truth, we may deduce that the input ensemble distribution from NA is superior to both the GA and the PSO such that the parameter space has been

better searched. However, the ensemble from GA and PSO is dependent on the choice of tuning parameters in the optimisation algorithm, and the tuning parameters chosen in this case may not have been the best for this synthetic case. We can adjust the GA tuning parameters (creep and jump mutation operators) and the PSO tuning parameters (such as the multipliers for Inertia, the local best model and the global best models) to produce some different ensemble distribution for each of the search algorithm. The tuning parameters may affect the quality of sampling and determines the information that may be contained in the input ensemble.

Figure 5.7 also compares the one-dimensional marginals of the various input ensembles to their corresponding posteriors marginals obtained using the proxy representation of the misfit. Shown in the figure are the one-dimensional marginals where posterior probabilities were computed from the proxy approximation of the PPD and posteriors computed using the voronoi approximation of the PPD as in NABayes. We also compare against the "raw" estimates of the PPD dervied from the history matching results without resampling. Both posterior marginals (proxy and NABayes) differ in shape and skewness from the raw marginal distributions of the parameters; indicating that the original distribution of the parameters from the input ensemble are not distributed according to the posterior probability density. Overall, the resampled one-dimensional posterior marginals have widths and peaks which differ greatly from those of the original distribution of the input ensemble; indicating that some valuable information from the data has further constrained the models. At this point, one may wish to note that sampling from the raw marginals for probabilistic forecasting, as the frequentist statisticians would like to do, is not appropriate from the Bayesian viewpoint. The distribution of the raw marginals is dependent on which ever technique was used in the search stage of the inverse problem.

In all cases the marginals derived from the proxy approximation of the PPD do not equal to those derived using the voronoi approximation . This is expected given the inherent flaws in approximating the non-linear reservoir response using a polynomial function. On the other hand, the voronoi approximation of NABayes is itself imprecise. At this point, we need to point out that the major difference between the two approaches is in the mode of approximation of the PPD. In our approach, we have approximated the PPD via the likelihood function by using polynomials derived from the ensemble of models and their corresponding misfit values, using Genetic-Based Symbolic Regression.

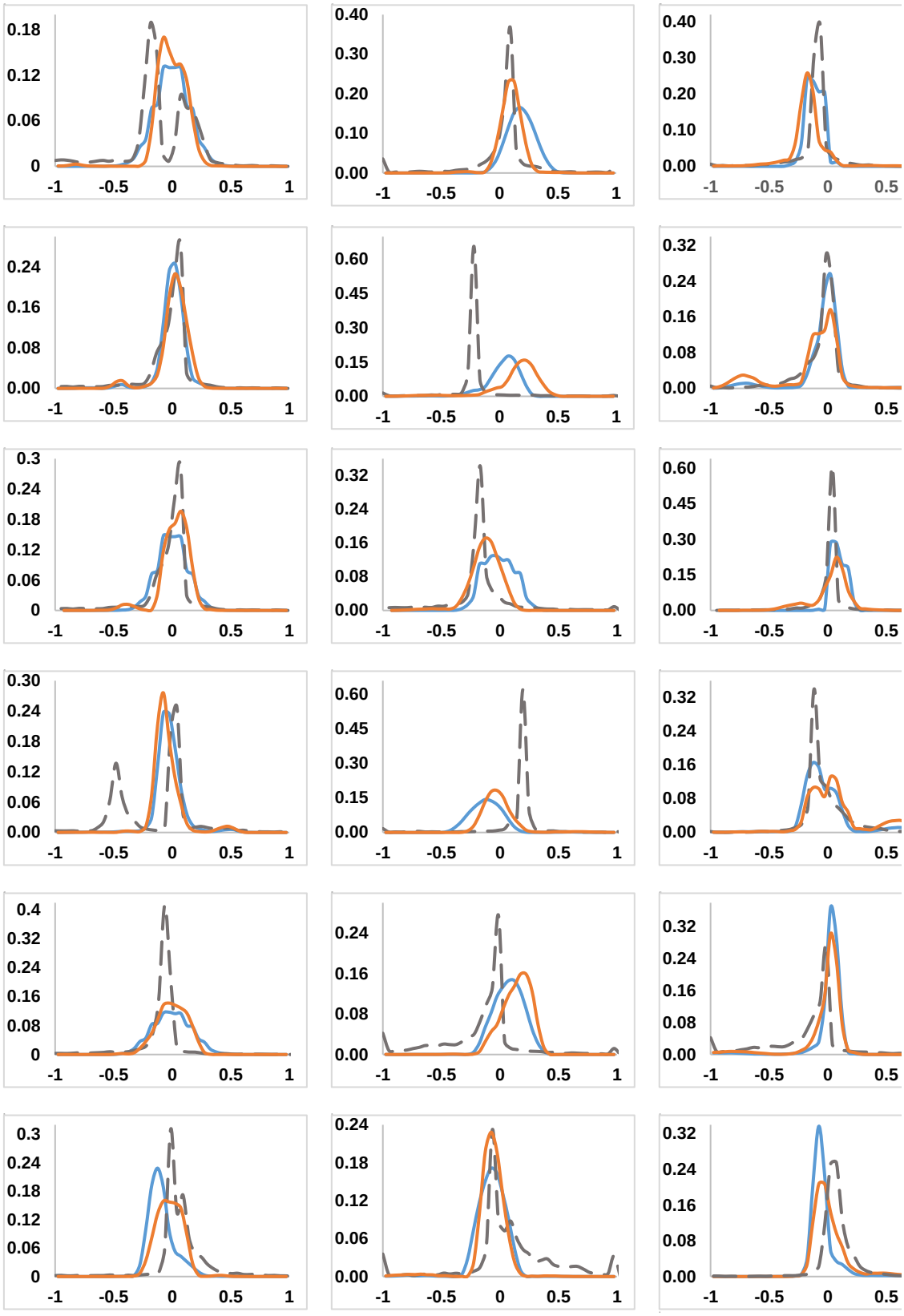

Figure 5.7 Overlay of one-dimensional raw marginal distribution (dash grey curves), the posterior marginals from proxy (blue curves) and the posterior marginals from NABayes (orange curves) for NA ensemble (1st column), GA ensemble (2nd column), and PSO ensemble (3rd column): initialisation of each optimisation was done using the QRNG. The distributions for T1, T2, T3, T4, T5 and T6 are in 1st row, 2nd row, 3rd row, 4th row, 5th row and 6th row respectively

In contrast, NABayes approximates the PPD everywhere in parameter space using the Neighbourhood approximation of the PPD from the input ensemble; in which case V-Cell s are used to identify the neighbourhoods around models (Sambridge 1999b). It is also a proxy method. Although in the case of the polynomial approximation, the error metrics in the symbolic regression indicates high quality proxy approximation of reservoir responses using the training data, the effect of the variances between the validation data and the true responses explains the disparity in the PPD. Specifically, the training of different ensembles results in different error metrics, for example: R-squared goodness of fit values were 94% (for NA), 91% (GA), 93.5% (PSO).

However, the proxy-aided appraisal speeds up the process tremendously and allows a greater volume of posterior samples to be generated within a short time without any need for parallel computation. For instance, resampling of 100,000 posterior models (from 1000 random walks and 100 steps per walk) which takes NABayes about 3 hours, takes the proxy-driven process just about 1 minute to complete. We consider that the results of the proxy-driven approach are satisfactory enough (from comparison to NABayes results) and will complete the appraisal and forecasting process using its posterior results. A summary model statistics containing the mean and standard deviation of the posterior models derived from the polynomial proxy approximation of the PPD is shown in Table 5.2

Table 5.2 Expectation values of the posterior distribution from the polynomial-proxy method.

Log_{10}Transmissibility Multipliers	Posterior Mean			Standard Deviation		
	NA	GA	PSO	NA	GA	PSO
T1	-0.033	0.183	-0.169	0.114	0.121	0.139
T2	0.004	0.067	-0.038	0.116	0.163	0.212
T3	-0.006	-0.148	0.092	0.102	0.124	0.138
T4	-0.024	-0.111	-0.034	0.127	0.152	0.206
T5	0.125	0.077	0.010	0.111	0.124	0.157
T6	-0.093	-0.073	-0.031	0.113	0.129	0.154

Next, we make inferences from the two-dimensional posterior marginal distribution for various pairs of parameters. Two-dimensional marginals provide information on the distribution of any pair of parameters, as the possible variations of other parameters are considered: it is a bivariate probability density function evaluated for any pair of parameters in a perspective of the distributions of the other parameters. For an insight on how the 2-D marginal distributions reveal the level of information provided by the history matching data, we plot a contour profile for selected pair of parameters (Figures. 5.8, 5.9, and 5.10).

It is obvious from the contour profiles that there is a strong link between the respective peaks of the model parameters and their true values, showing that our approach to resampling has trained the posterior probability distribution well. However, a closer look at some pairs of parameters show some traces of secondary peaks (e.g., Figure 5.8b) which should not be neglected even as we place more importance on the primary peaks. Overall, the primary peaks of the 2-D posterior marginals are near to the true values of the parameters. As in the case of one-dimensional marginal distributions, Figures. 5.8, 5.9 and 5.10 reveal some marked differences in the shape of the 2-D marginal distributions for the different ensembles, reflecting the varying degree of conditioning provided by the history matching data to the model parameters.

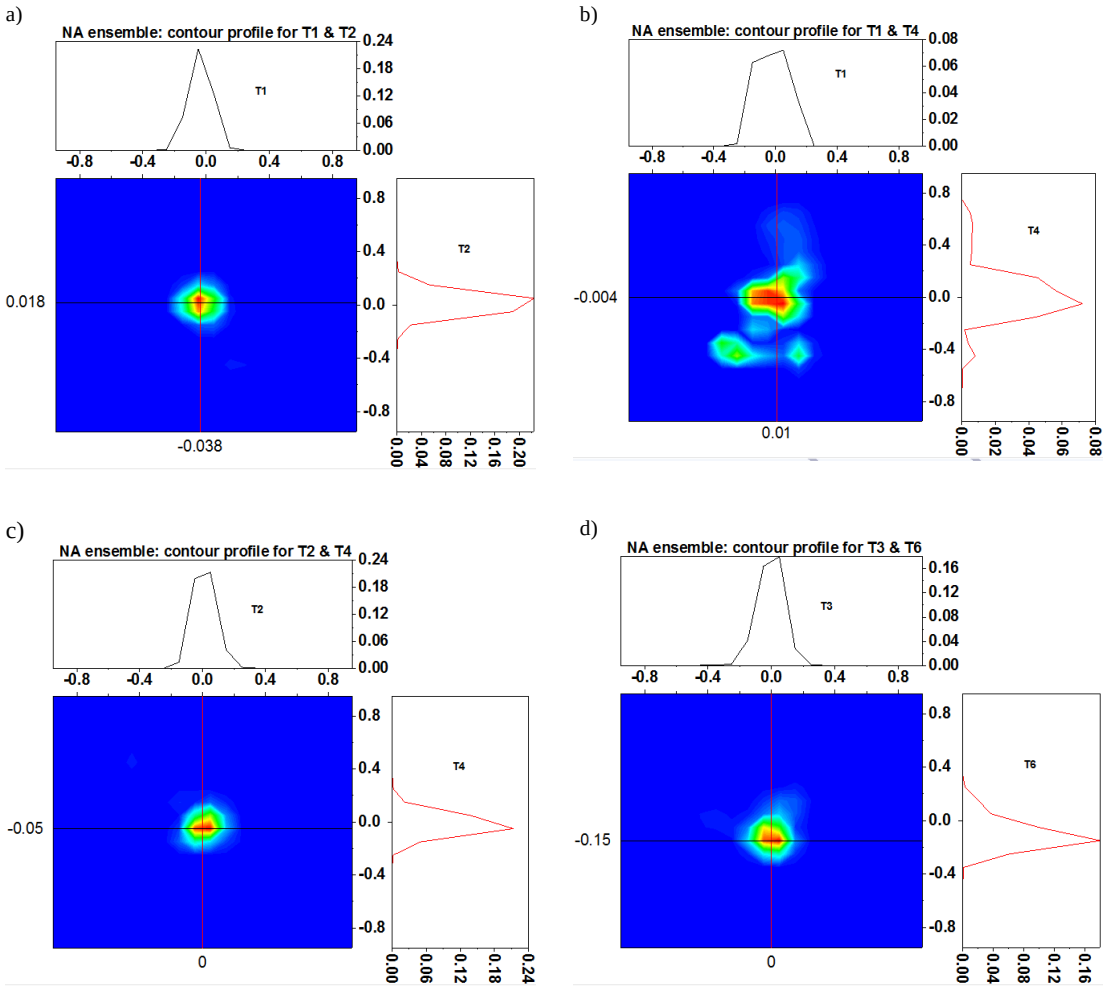

Figure 5.8 The contour profiles of the NA ensemble two-dimensional marginal posterior distribution functions for the parameter pairs a) T1 and T2, b) T1 and T4, c) T2 and T4, and d) T3 and T6. Overall the primary peaks are close to the intersection of the sections through the true values of the parameters, [0, 0].

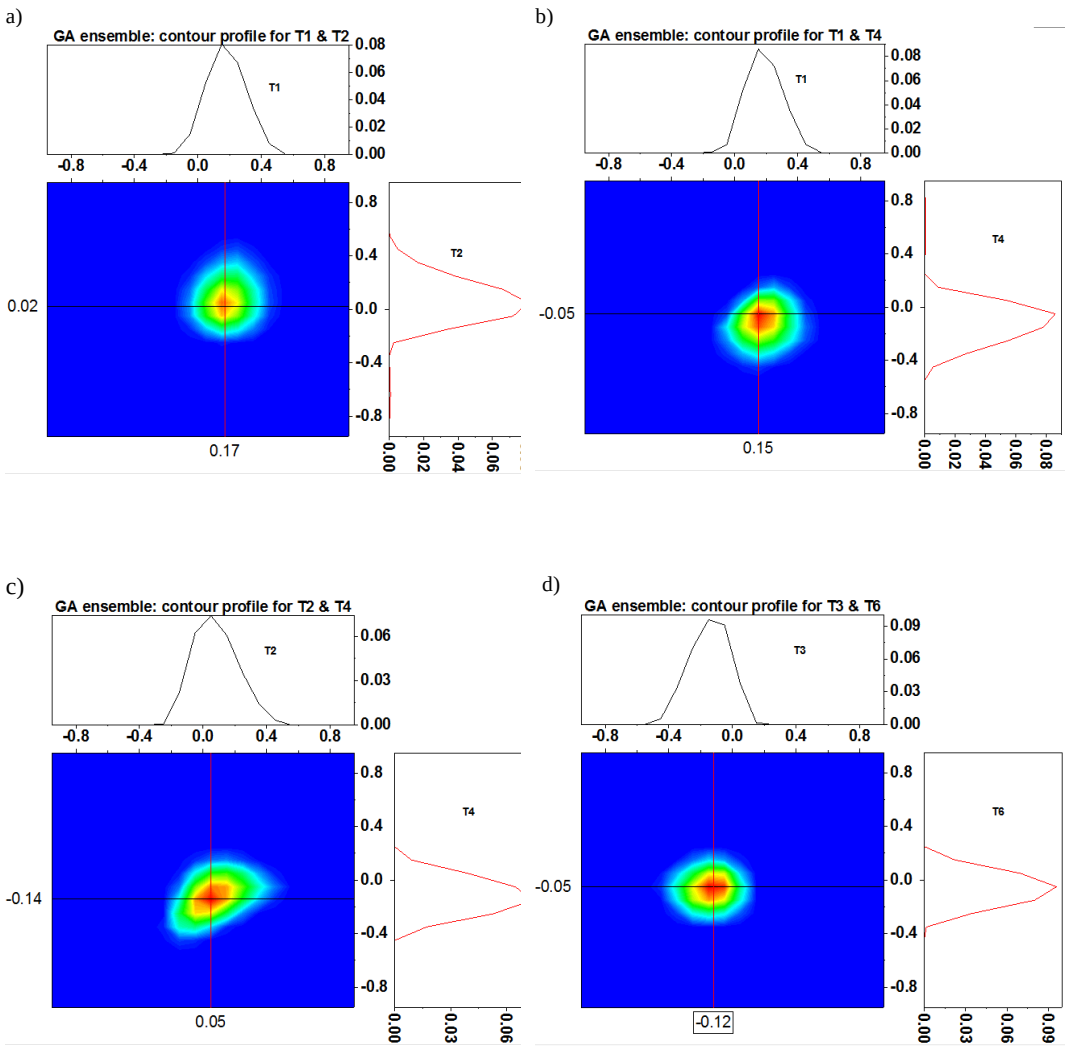

Figure 5.9 The contour profiles of the GA ensemble two-dimensional marginal posterior distribution functions for the parameter pairs(a) T1 and T2, (b) T1 and T4, (c) T2 and T4, and (d) T3 and T6. Overall the primary peaks are close to the intersection of the sections through the true values of the parameters, [0, 0].

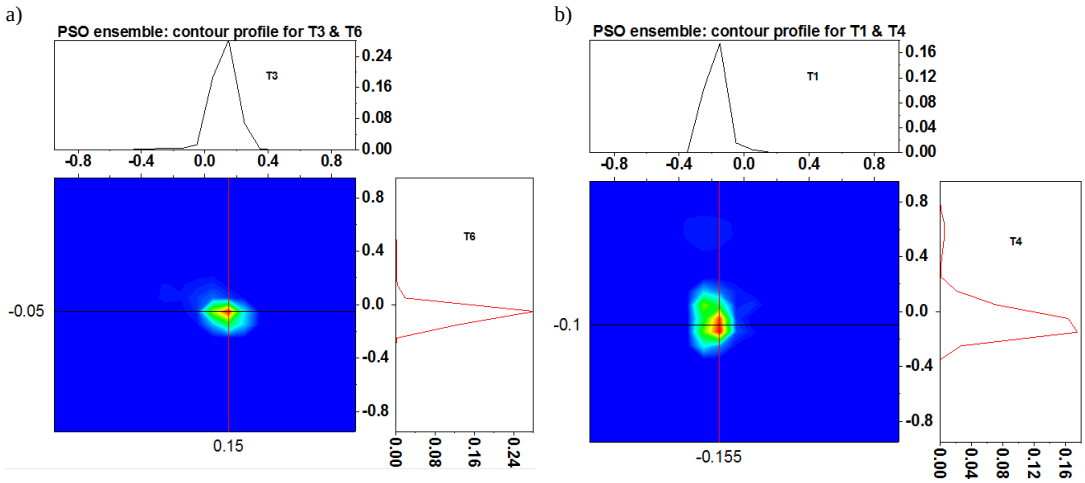

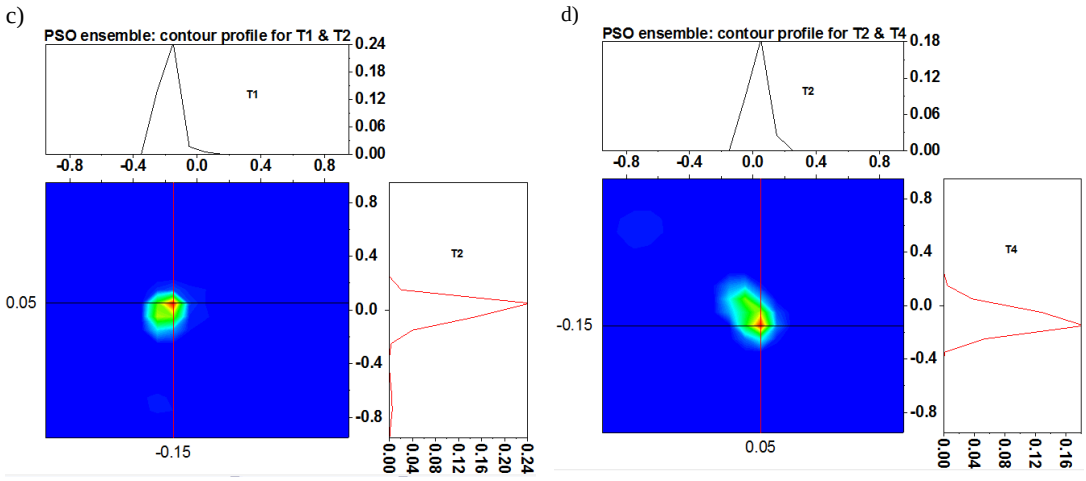

Figure 5.10 The contour profiles of the PSO ensemble two-dimensional marginal posterior distribution functions for the parameter pairs a) T1 and T2, b) T1 and T4, c) T2 and T4, and d) T3 and T6. Overall the primary peaks are close to the intersection of the sections through the true values of the parameters, [0, 0].

The next properties of the PPD worthy of study are the posterior covariance matrix and the posterior correlation matrix. We will examine only the posterior covariance matrix as the model parameters are of the same type and dimension, and both kinds of matrix reveal the same information about the resampled ensemble. Figure 5.11 reveals the pattern in the posterior covariance matrix evaluated for the 6 model parameters.

The diagonal elements of the covariance matrix are the variance of the parameters: the square root of each of the variance gives the standard deviation for the respective parameter. The pattern of the off-diagonal elements reflects the level of correlations between the model parameters. The matrix shows negative correlations between some parameters and positive correlations between some others but the patterns are very subtle and hardly noticeable. We observe in all cases that the amplitude of the correlations between the parameters are relatively low which suggest that the parameters are independently resolved and may have been well constrained by the history data.

In the case of PSO, correlations between the parameters show bright amplitude for T2/T4 pair which is consistent with the negative correlation observed for the same pair in NA posterior covariance matrix.

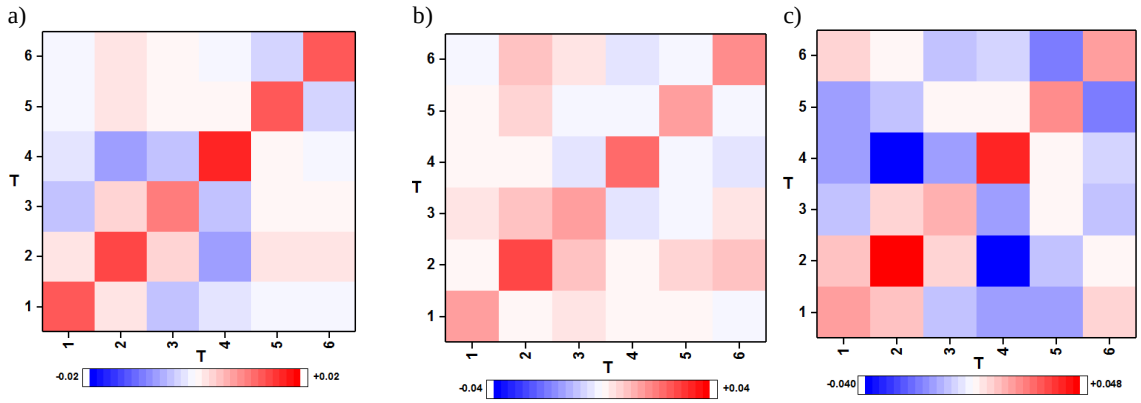

Figure 5.11 The posterior covariance matrix derived for a) NA ensemble, b) GA ensemble, and c) PSO ensemble. The patterns established by the off-diagonal elements show that the correlations between the model parameters are generally strong.

Finally, we examine the resolution operator as a property of the PPD for information on the extent to which model parameters have been resolved with respect to the true reservoir model parameters. Figure 5.12 shows a very strong diagonal element approximately equal to unity for each of the model parameter and unnoticeable patterns in the off-diagonal resolution operators. Overall, the resolution matrix gives an impression that each of the six parameters are well independently resolved for the NA and GA but slightly less so for PSO because of the strong negative correlation between T2 and T4. This is expected and is very much consistent with the information revealed by other Bayesian pointers such as the posterior marginal probability posterior covariance/correlation matrices.

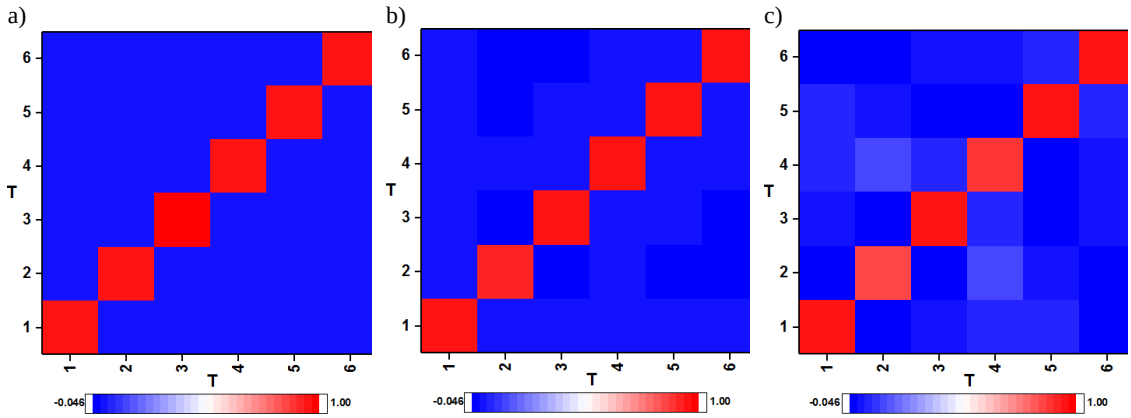

Figure 5.12 The posterior resolution matrix derived for a) NA ensemble, b) GA ensemble, and c) PSO ensemble

5.12 Results of Forecasting and Discussion

We demonstrate our approach to forecasting using the results of optimisation with the Neighbourhood Algorithm (NA), Genetic Algorithm (GA) and Particle Swarm Optimisation (PSO), each initialised with quasi-random number generator. The results of

posterior analysis and the predictions of the posterior models, from the posterior sampling of the ensembles generated during optimisation with the three optimisation algorithms, are shown in Figures 5.13 to 5.19.
Seismic and production data measured in the first 3 years of production were used to constrain the models during the optimisation (history matching). In the forecast period (Year 3 to Year 8), the predictions of the posterior models are also compared to those of the true model.

The predicted quantities include cumulative oil production (Figure 5.13), field oil recovery efficiency (Figure 5.14), flowing bottom hole pressure of the producer (Figure 5.15), bottom hole pressure of the injector (Figure 5.16), field oil production rates (Figure 5.17) and field water production rates (Figure 5.18). The behaviour of the field within an eight-year period is represented in the uncertainty envelope of the predicted quantities using statistics such as the mean, P10 and P90.

The statistical inferences are made in three scenarios, described below. The scenerios distinguish the different we have resampled models from the posterior distribution and how those models were used for forecasting. In each scenario, the Gibbs sampler generated 1,000,000 posterior models from 100 random walks of 10,000 steps each.

Scenario I: posterior models are generated from the polynomial-proxy approximation of the PPD. Using the stratified sampling approach (for unbiased sampling), 100 out of the 1,000,000 posterior models are selected to predict the quantities of interest. The 100 models, as well as their respective predictions, are assumed to be equally probable, and so, equal weights are assigned to the predictions to determine the prediction statistics (mean, P10 and P90). The P10 and P90 profiles are the dashed blue lines and solid blue lines in Figures 5.13 to 5.18.

Scenario II: posterior models are generated from the voronoi approximation of the PPD in an approach described in Sambridge (1999b). Quantities of interest are predicted by running simulation using only 100 models from unbiased sampling of the posterior models. The models are assumed to be equally probable and the predicted quantities are assigned equal weights/probabilities to determine the prediction statistics. The P10 and P90 profiles are the dashed red lines and solid red lines in Figures 5.13 to 5.18

Scenario III: the posterior sampling is done in the manner of Scenario II**.** However, predictions of quantities are not made with the resampled models rather the frequency of

visits to the models originally in the NA, GA, or PSO ensemble are monitored during the posterior sampling. The probability of each model is then calculated based on the frequency of visits and weights are assigned to the predicted quantities to determine the prediction statistics. Out of the 2625 models in each of the ensemble, only 167 models were visited at least once in the case of NA, 108 models were visited in the PSO ensemble while only 77 models were visited in the GA ensemble. For each of the ensemble, the relative probability of 39 most visited models are shown in Figure 5.19. The relative probability is assigned as weights to the predictions of the models to determine the statistics of the predicted quantities.

We found that the various posterior models honoured the history data at different levels of fitness, defining the uncertainty range. Compared to the spread of the predictions of the initialisation models, the uncertainty range in all cases has been significantly reduced in the predictions using the posterior models. The production profiles of the initial models represent a much wider range of uncertainty. On the other hand, the posterior models have been constrained by the information from the history data. In all cases, the posterior models show very good predictability even after 8 years of production.

The results also show that despite the differences noted earlier in the performance of the different optimisation algorithms (NA, GA and PSO), the posterior models derived from their respective ensembles show similar behaviour in matching the history data as well as in forecasting. This behaviour is reflected in the three approaches to forecasting described in this paper. It is also observed that even when the uncertainty range differs slightly depending on the approach, the mean of the predicted quantities tends to be the same for all the approaches and for all the optimisation algorithms but with small difference in uncertainty. Considering the cumulative oil production (FOPT), for example, the uncertainty ranges of 6.0%, 4.5% and 7.4 % are identified respectively for the posteriors of NA, GA and PSO derived from the posterior sampling of the polynomial-proxy PPD. The 6% uncertainty range in the FOPT predicted with NA posterior, for instance, is 3.3 % above the true data and 2.7% below the truth. So, with the NA posterior, 90% of the cumulative oil production estimates exceed 31.91 million stock-tank barrel while just 10% of the estimates exceed 33.87 million stock-tank barrel.

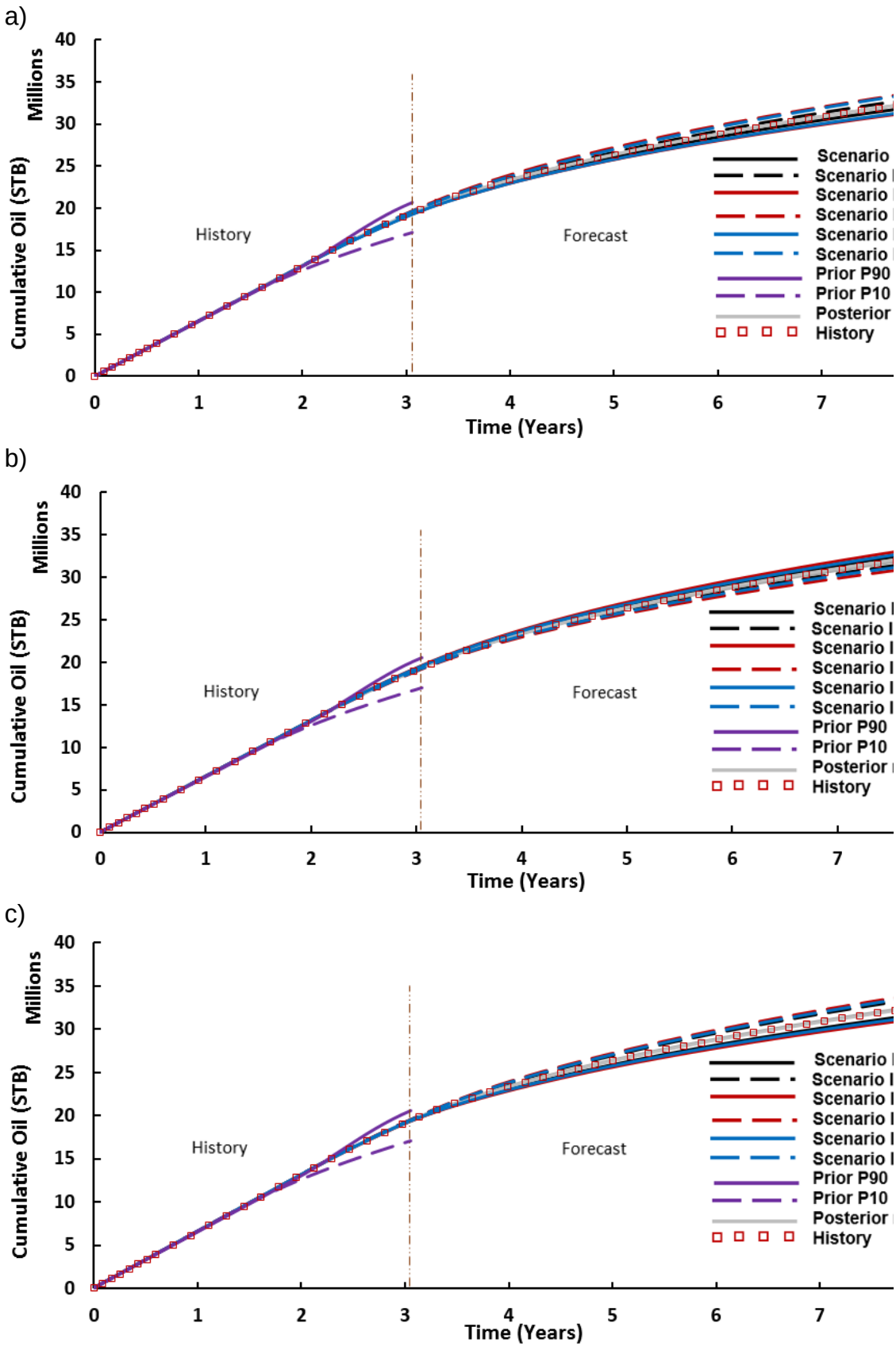

Figure 5.13 The uncertainty envelope in cumulative oil production from the predictions using models from posterior sampling of a) NA models, b) GA models, and c) PSO models.

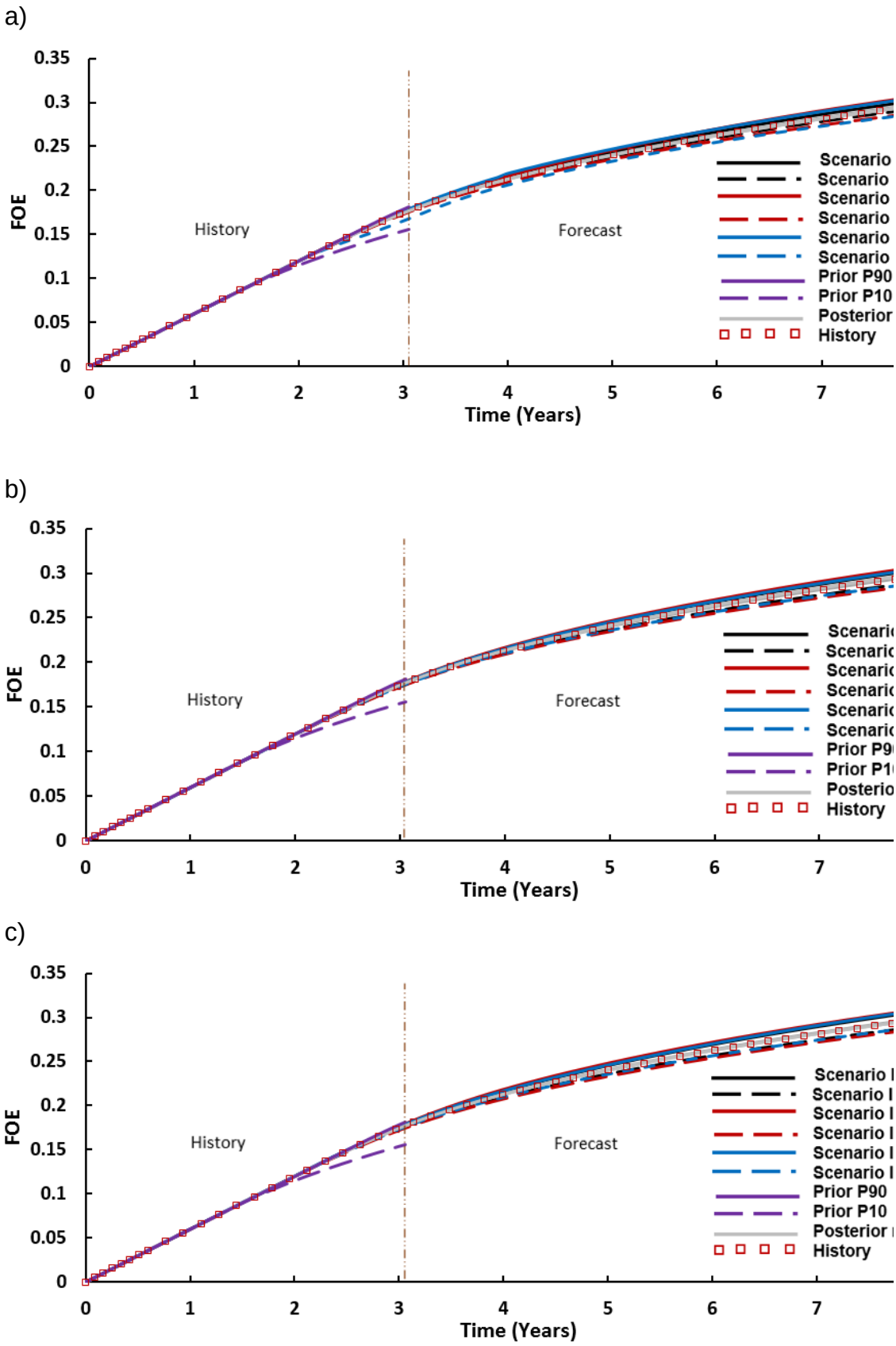

Figure 5.14—The uncertainty envelope in field oil recovery efficiency (FOE) from the predictions using models from posterior sampling of a) NA models, b) GA models, and c) PSO models.

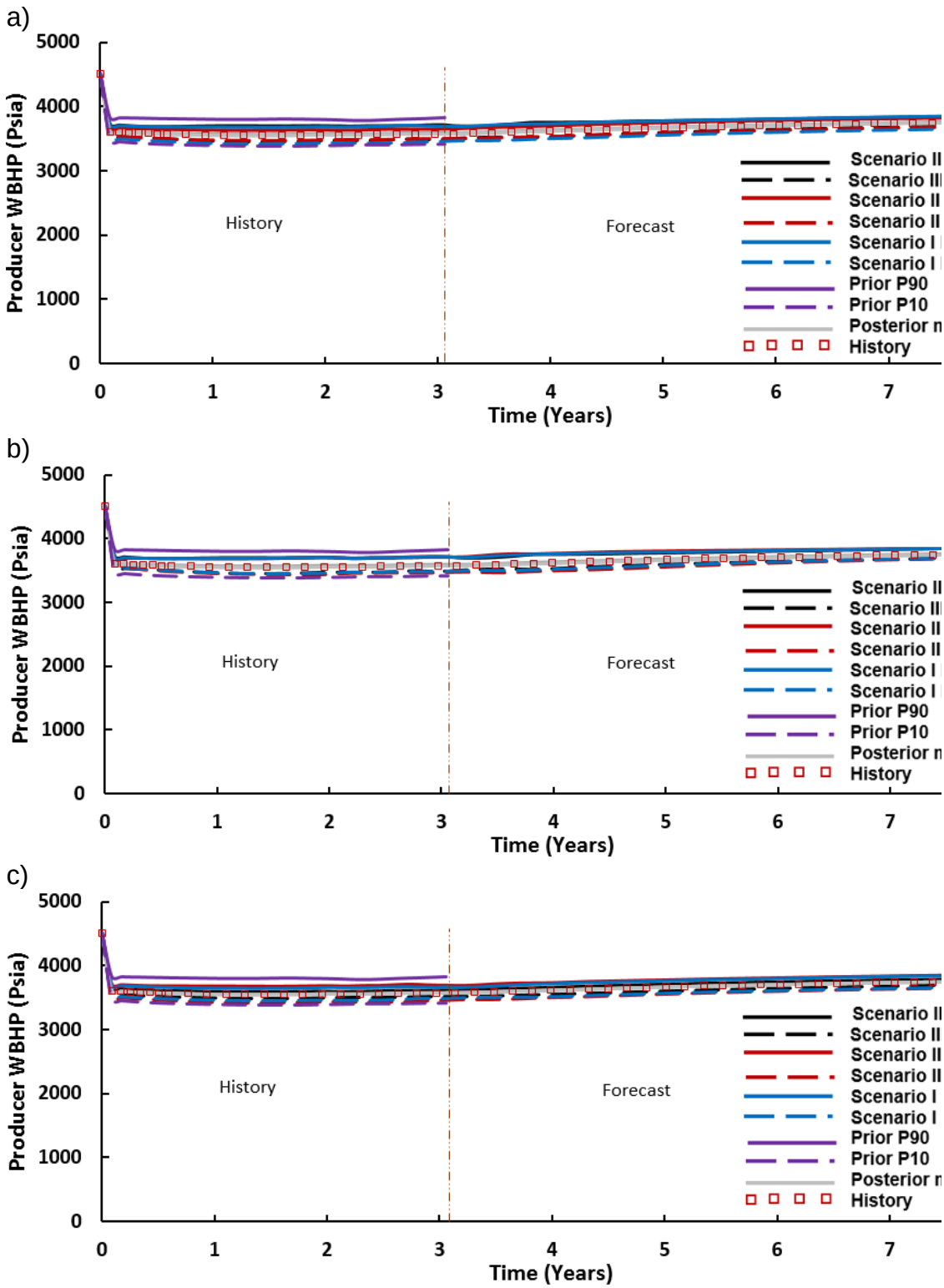

Figure 5.15 The uncertainty envelope in the flowing well bottom hole pressure (WBHP) from the predictions using models from posterior sampling of a) NA models, b) GA models, and c) PSO models.

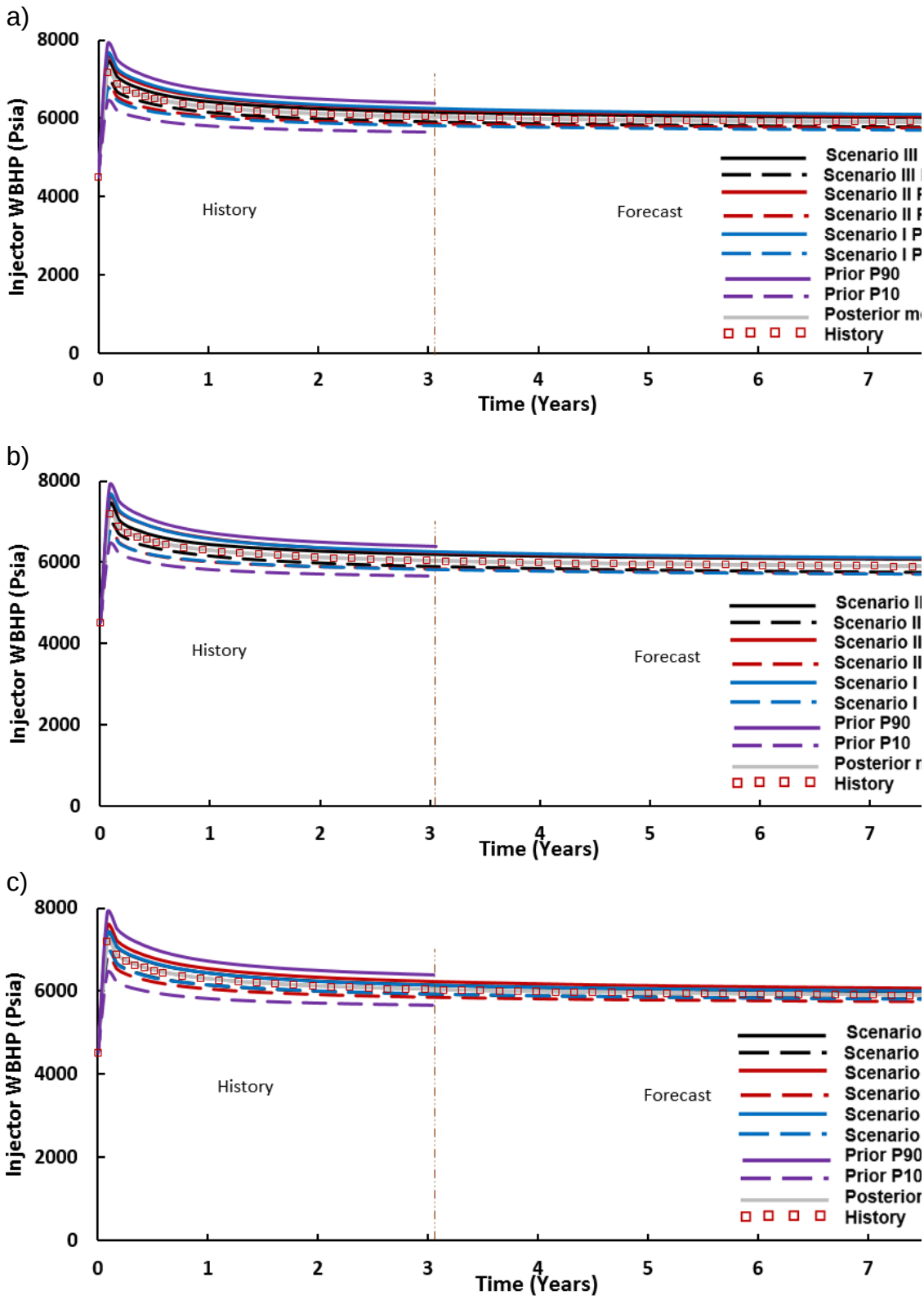

Figure 5.16 The uncertainty envelope in the injector well bottom hole pressure (WBHP) from the predictions using models from posterior sampling of a) NA models, b) GA models, and c) PSO models.

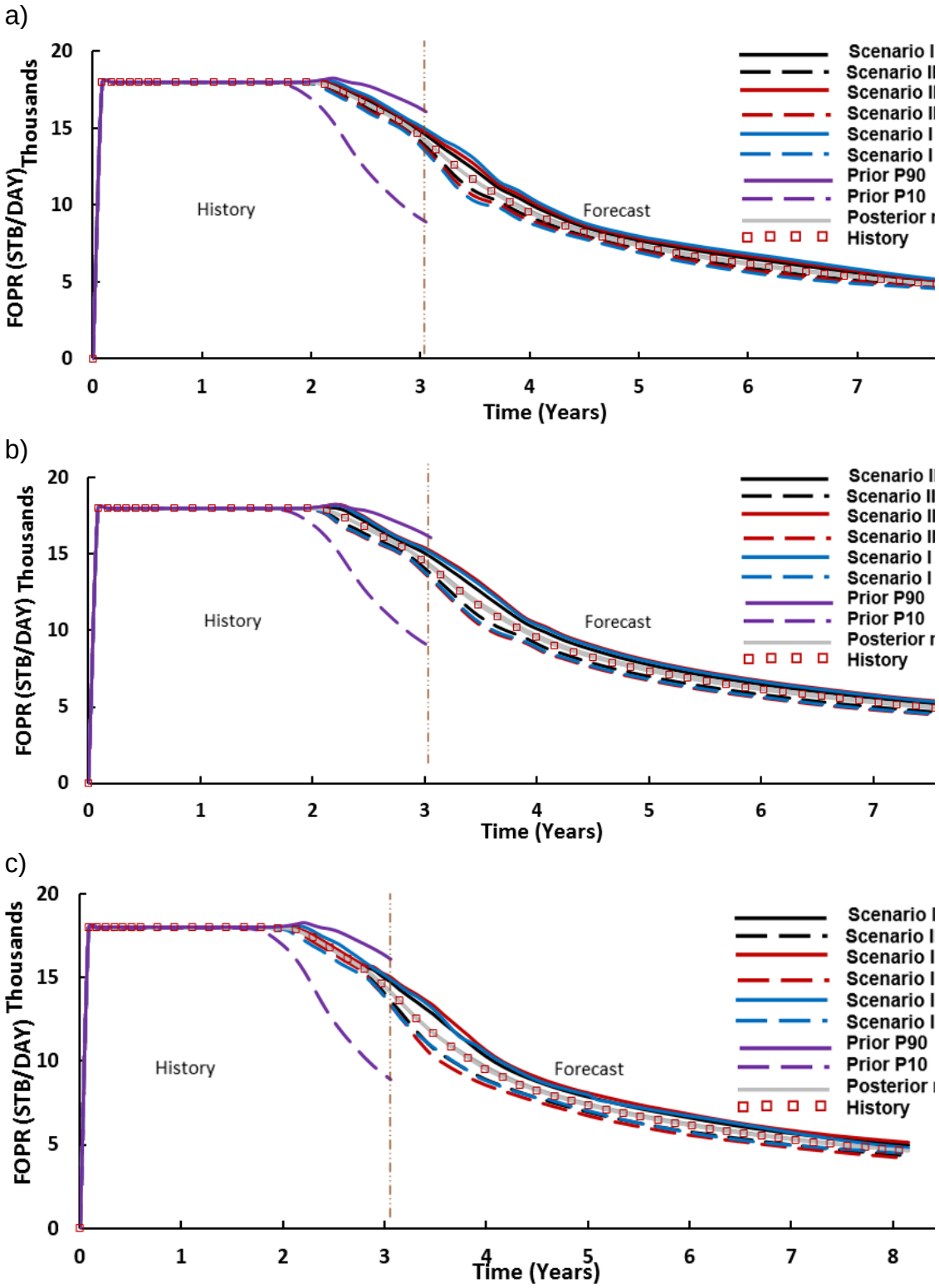

Figure 5.17 The uncertainty envelope in field oil production rate (FOPR) from the predictions using models from posterior sampling of a) NA models, b) GA models, and c) PSO models.

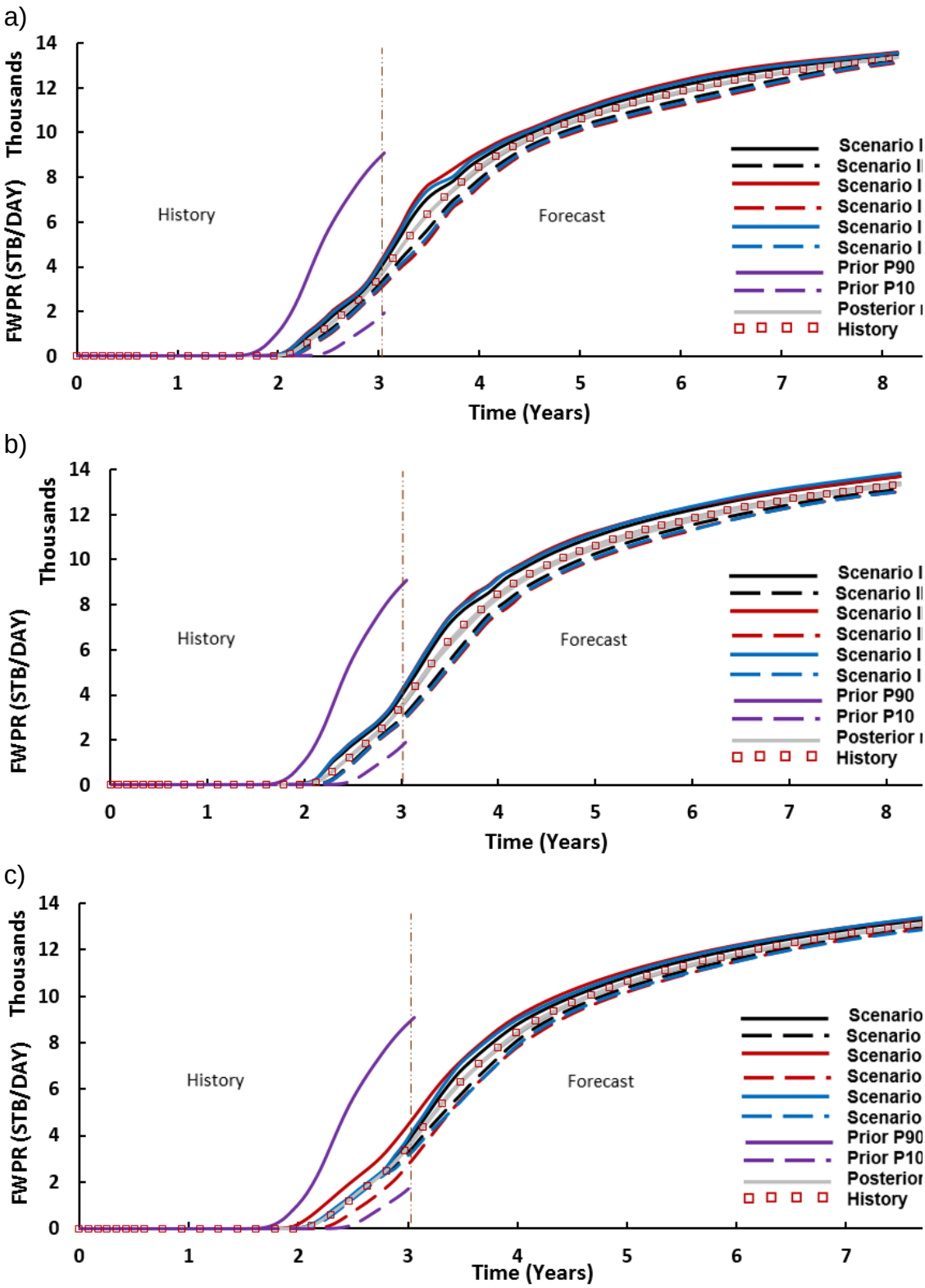

Figure 5.18 The uncertainty envelope in field water production rate (FWPR) from the predictions using models from posterior sampling of a) NA models, b) GA models, and c) PSO models.

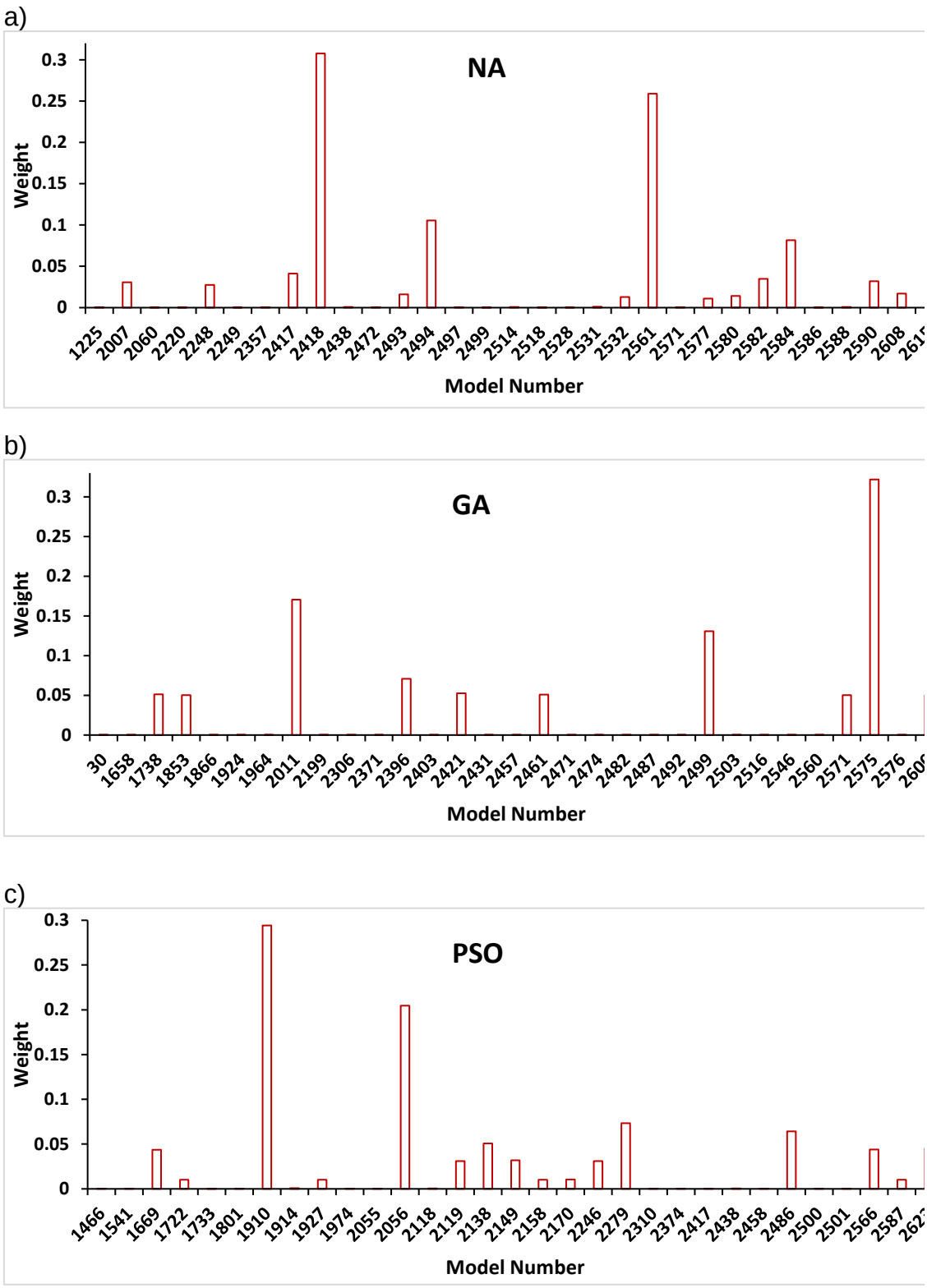

Figure 5.19 The weights of the posterior models determined from the frequency of visits to respective V-Cell s of the a) NA models, b) GA models, and c) PSO models

We also compare the seismic predictions of the posterior models to the true seismic data, and represent the uncertainty in the predictions. We apply the method described for spatially and temporally varying quantity to quantify the uncertainty in the predictions of

three impedance differences. Figure 5.20 is the mean seismic predictions of the posterior models generated using the proxy-approximation of the PPD while Figure 5.21 shows the standard deviations in the predicted quantity.

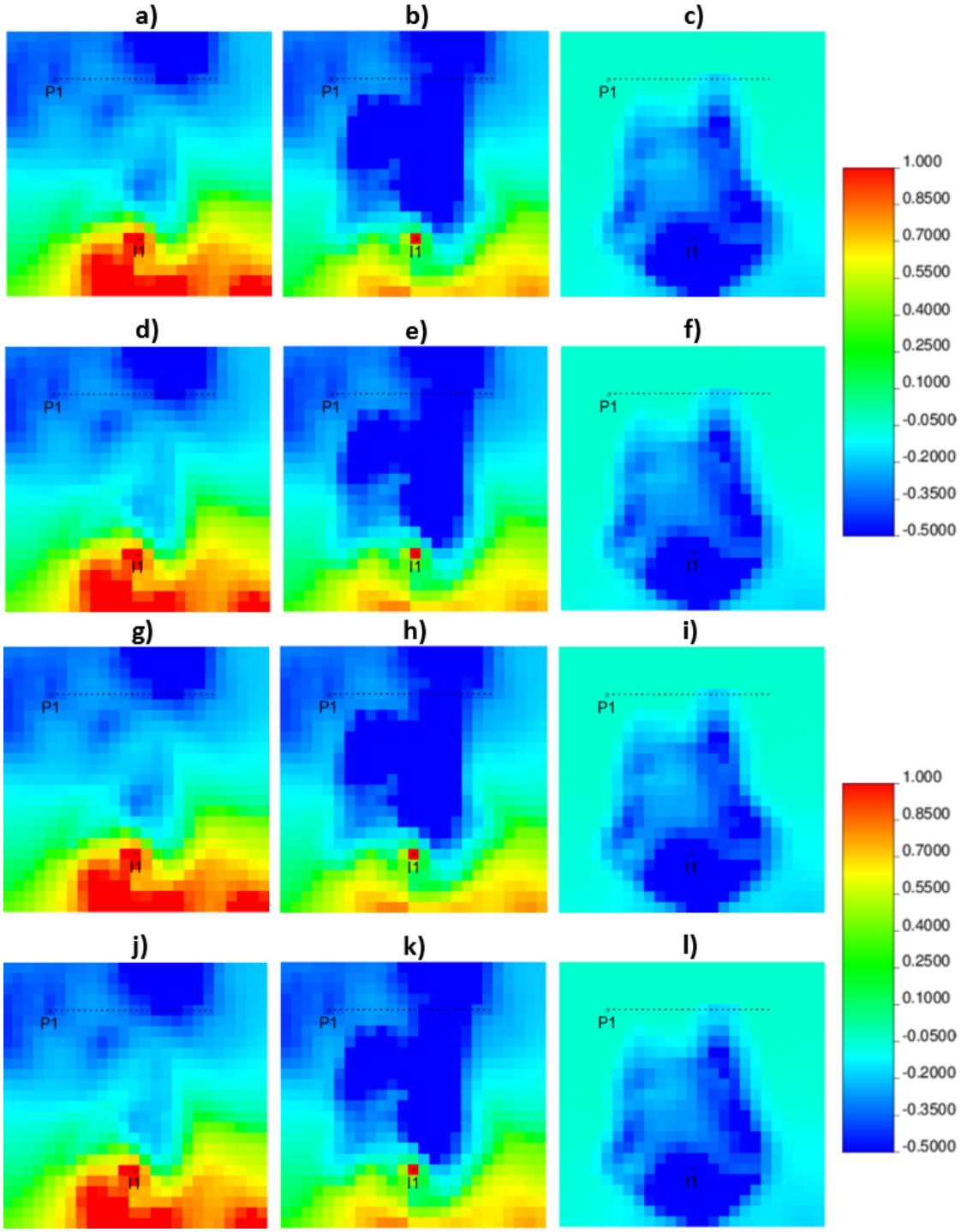

Figure 5.20 Normalised mean time lapse seismic predictions of the posterior models. The predictions from posterior sampling of NA ensemble (1st row), PSO ensemble (second row), and GA ensemble (third row) are compared to the true seismic data (fourth row). The first column shows the time lapse impedance between Pre-production and Year 1, column two shows the difference between Year 1 and Year 3 impedance, while the third column shows the difference in Year 2 and Year 3 impedance.

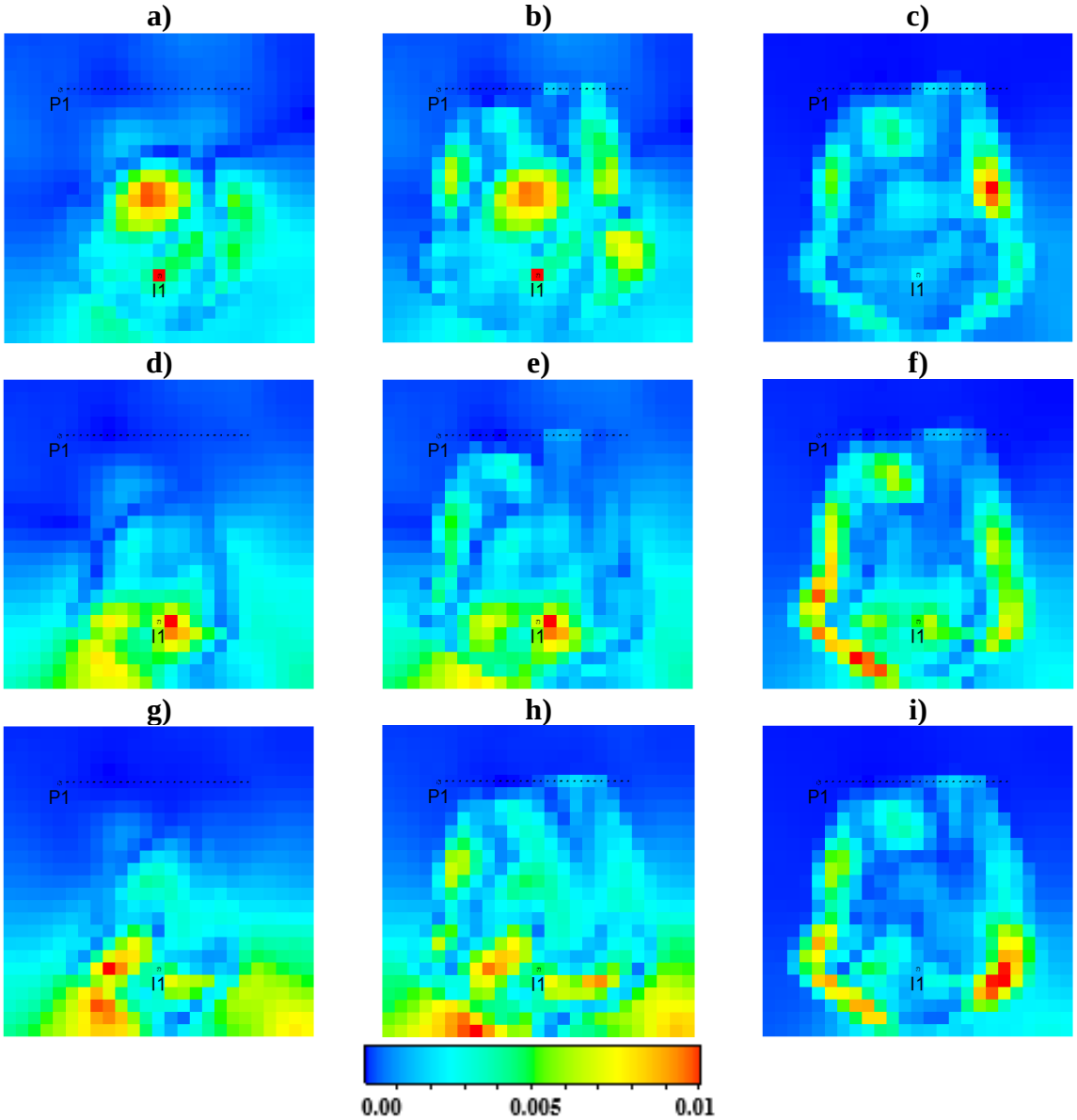

Figure 5.21 The uncertainty in the time lapse seismic predictions of the posterior models. The maps show the standard deviations in the predicted time lapse impedance corresponding to the maps in Fig. 5.20 for the posterior predictions derived from the NA ensemble (1st row), PSO ensemble (second row), and GA ensemble (third row). The first column shows the uncertainty in the time lapse impedance between Pre-production and Year 1, column two shows the uncertainty in the time lapse difference between Year 1 and Year 3 impedance, while the third column shows the uncertainty in the difference of Year 2 and Year 3 impedance.

Pre-production data represents the baseline survey while Year 1, Year 2 and Year 3 are the monitor surveys. The differences in the impedance maps (e.g., Year 2 - Year 3) reflects the time-lapse change due to the production activity within the one year interval. We have chosen the nomenclature to subtract new survey from older survey. Old survey minus new gives a red impedance colour in the plots for pressure up and gas out of solution, blue for water saturation increase and pressure draw down. It is observed that the pressure effect was dominant around the injector area during the first year of production while in the

subsequent years, saturation effect dominates. It is observed that the mean seismic predictions of the posterior models match the true seismic data reasonably well. This lends more credence to the model and demonstrates another benefit of incorporating seismic data in history matching.

It is interesting to note that the parameters of the different models selected for probabilistic forecasting differ from one another but some of them gave a close match to the true data. This is due to non-uniqueness of history matching, and justifies the effort put in appraising the models to ascertain the level of confidence that should be placed on them, as well as the effort in quantification of uncertainty in the predictions.

5.13 Summary and Conclusion.

In this thesis, we have been able to show that valuable information can be extracted from an input ensemble of models generated during the history matching process using an approach that is simple, fast and accurate. We have compared the results of three approaches to forecasting reservoir quantities from posterior models generated using different optimisation algorithms.

The approaches presented in this thesis have been applied to some ensembles generated in an automatic seismic history matching workflow using a synthetic reservoir model for which the true model parameters are known. Although the application here was to a simple reservoir model, with an ensemble generated using a Neighbourhood Algorithm, Genetic Algorithm and Particle Swarm Optimisation, it can equally be applied to any ensemble generated through any form of stochastic history matching; as no assumption was made regarding the distribution of the parameters of the input ensemble. We also note that in adopting the appraisal approach presented in this paper, there was no notion or preconceived idea of what should be the ‘good’ or ‘bad’ models. All the combinations of the model parameters generated during the history matching together with their misfit values are used for the appraisal within Bayesian framework. We, therefore, draw conclusions as follows:

i. The use of proxy models made it possible to have a fast and relatively accurate alternative to the existing approaches for ensemble appraisal within Bayesian framework. The results here are comparable to the results obtained using NABayes but the use of Proxy models makes the process much faster allowing us to generate larger volumes of posterior samples which also ensures convergence of the sampler.

ii. Although the method has its limitations, it includes all models in the ensemble in obtaining the Bayesian indicators of model resolution and trade-off in the various model parameters A combination (concatenation) of all models from different search methods such as NA, GA and PSO may be considered as one ensemble which when subjected to appraisal will maximise the value of information obtained from history matching
iii. The reservoir quantity prediction using the posterior models gave similar results irrespective of the optimisation algorithm used to generate the input ensemble: the results of the uncertainty in production and seismic prediction were similar for all the algorithms
iv. The approach presented here enables the assessment of the level of confidence that should be placed on the models for more realistic and accurate predictions
v. The approach to appraisal coupled with the unbiased sampling method presented here is novel and gives a systematic probabilistic forecasting that can be relied on for reservoir development strategies and planning.
vi. The approach is applicable to ensembles of models generated through any stochastic search methods, which include Differential Evolution, Genetic Algorithm, Particle Swarm Optimisation , Hamiltonian Monte Carlo, Neighbourhood Algorithm, Simulated Annealing etc.
vii. The procedure presented is simple and does not require specialised skills.

Chapter 6- Norne Field Review and Development Studies

6.1 Field Overview

Discovered in December 1991, Norne oil field issituated in the blocks 6608/10 and 6508/1 in the southern part of the Nordland II area the Norwegian Sea, for which the water depth is approximately 380 m (refer to Figure 6.1 for the field's location relative to the neighbouring field). The Heidrun field which is located about 80km south of Norne Field. It is regarded as Norne Field's analogue field for fault analysis as no faults has been cored from Norne for intra-reservoir fault permeability measurement (Statoil 2005)..

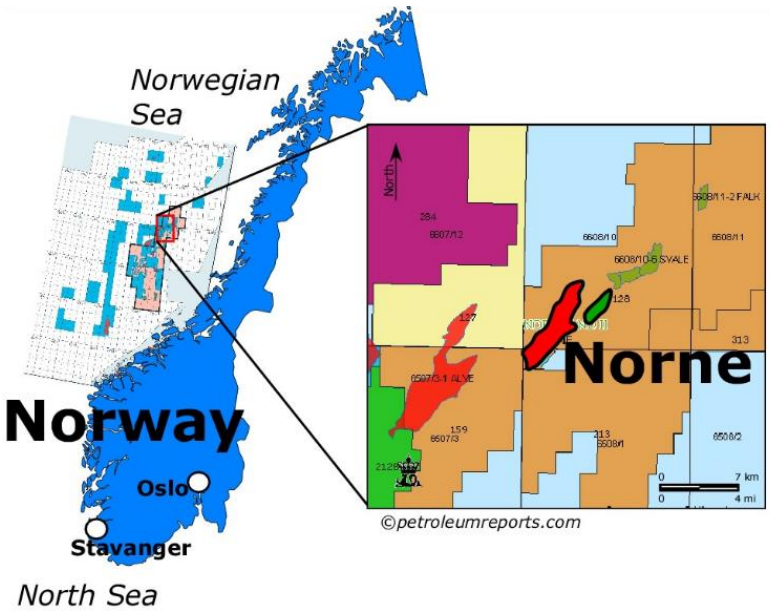

Figure 6.1 Norne Field and nearby fields (petroleumreports.com)

Norne Field is approximately 9 km x 3 km and consists of four segments; Norne Field C-, D-, E- and G-segment (Figure 6.2). The Norne Field C-, D and E-segment lie in the Norne Field Main structure and houses about 97% of the OOIP (oil initially in place), while the Norne Field G-segment is the North-East Segment of the field. The main segment was discovered with well 6608/10-2 and appraised with well 6608/10-3 while well 6608/10-4 discovered oil in the North-East (G-) segment. The field is being developed with 5 templates at the sea bottom tied to an FPSO (Floating Production, Storage and Offloading) and is jointly operated by Statoil and its partners (SDFI/Petoro, Norsk Hydro, Eni Norge AS and Shell Enterprise). Based on the discovery well 6608/10-2, the oil leg is 110 m thick while the overlying gas column is 25 m. Overall, the Oil in place (STOIIP) is 164.2 $MMSm^3$ and Gas in place is 29.9 GSm^3. Oil production commenced in November 1997. The cumulative oil production as at the end of year 2007

stood at 77 MMSm^3 which is 86% of the recoverable reserves (Steffensen and Karstad, 1996; Statoil, 2001).

a) b)

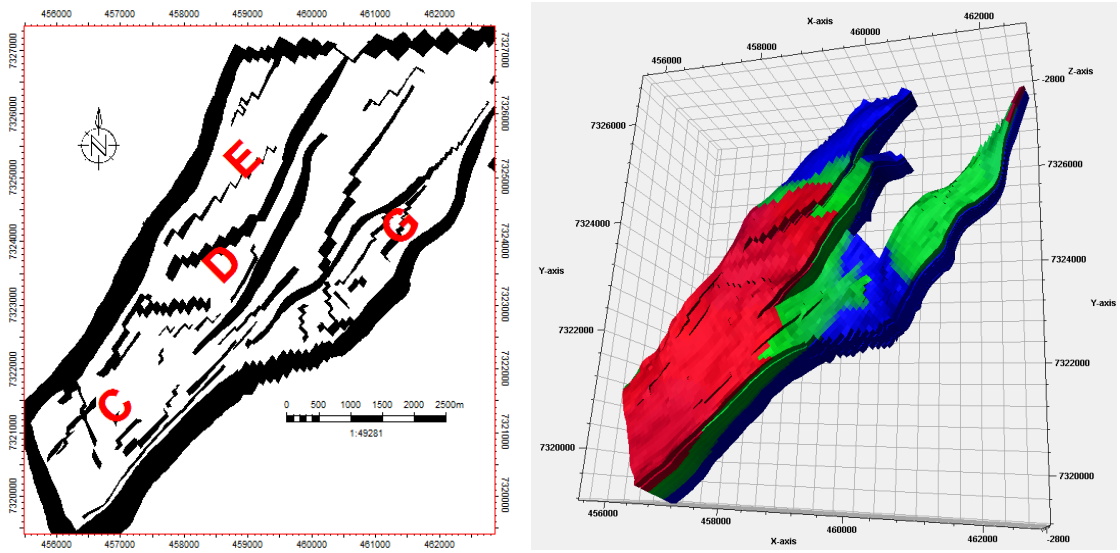

Figure 6.2 Norne Field Maps showing a) the Compartments and Segments b) The initial Fluid Saturations (Red is gas, Green is Oil, Blue is water)

6.2 Geology and Reservoir Characteristics

6.2.1 Reservoir Zonation (Statoil 2001)

The Norne Field hydrocarbons are contained in Lower- to Middle Jurassic reservoir sandstones buried at 2500-2700m. The reservoir sandstones are predominantly fine-grained sub-arkosic arenites with sorting ranging from well to very well sorted, porosity range of 0.20-0.30 and permeability in the range of 20-2500 mD . The reservoir unit is made up of five formations (from base to top): Tilje, Tofte, Ile, Not and Garn Fms. The Garn Fm is generally filled with gas in the Norne Field Main structure with gas oil contact (GOC) being very close to the top of the Not Fm. However, the northern flank of the Norne Field structure dips towards the north-northwest with an oil leg in the Garn Fm and no gas cap (Figure 6.2 and Table 6.1). The Ile and Tofte Fms contain most of the oil (approximately 80%) with pressure support from the aquifer located in the Tilje Fm and below the Tilje Fm. The Not Fm is considered a sealing shale barrier resulting in nil communication between the Garn Fm and Ile Fm. (Statoil, 2001, 2004; Eirik, 2010).

The positions of the contacts (GOC and WOC) in the different segments and formations are summarised in Table 6.1 (Statoil, 2004) below:

Table 6.1 Norne Field reservoir Fluid Contact Positions: depth in metres (Statoil, 2004)

Fm	C-Segment		D-Segment		E-Segment		G-Segment	
	OWC	GOC	OWC	GOC	OWC	GOC	OWC	GOC
Garn	2692	2582	2692	2582	2618	2582	2585	No gas cap
Ile	2693	2585	2693	2585	2693	2585	Water	Water
Tofte	2693	2585	2693	2585	2693	2585	Water	Water
Tilje	2693	2585	2693	2585	2693	2585	Water	Water

The present reservoir zonation, used in ECLIPSE reservoir simulation, consists of 22 reservoir layers (Table 6.2) and slightly differs from the original geological zonation shown in Figure 6.3 and 6.4. In the present zonation, the Ile and Tofte zones have been further subdivided and Tilje zones have been simplified. The boundaries between the layers are picked at the SB (Sequence Boundaries) and MFS (Maximum Flooding Surfaces), such that they correspond to the actual change in layers' lithology in the reservoir (Statoil, 2001).

Table 6.2 Norne Field reservoir Zonation (Based on Reservoir Model)

Formation	Zone/ Layer #	Zone/ Layer	Formation	Zone/ Layer #	Zone/ Layer
Garn	1	Garn 3	Tofte	12	Tofte 2.2
Garn	2	Garn 2	Tofte	13	Tofte 2.1.3
Garn	3	Garn 1	Tofte	14	Tofte 2.1.2
Not	4	Not	Tofte	15	Tofte 2.1.1
Ile	5	Ile 2.2	Tofte	16	Tofte 1.2.2
Ile	6	Ile 2.1.3	Tofte	17	Tofte 1.2.1
Ile	7	Ile 2.1.2	Tofte	18	Tofte 1.1
Ile	8	Ile 2.1.1	Tilje	19	Tilje 4
Ile	9	Ile 1.3	Tilje	20	Tilje 3
Ile	10	Ile 1.2	Tilje	21	Tilje 2
Ile	11	Ile 1.1	Tilje	22	Tilje 1

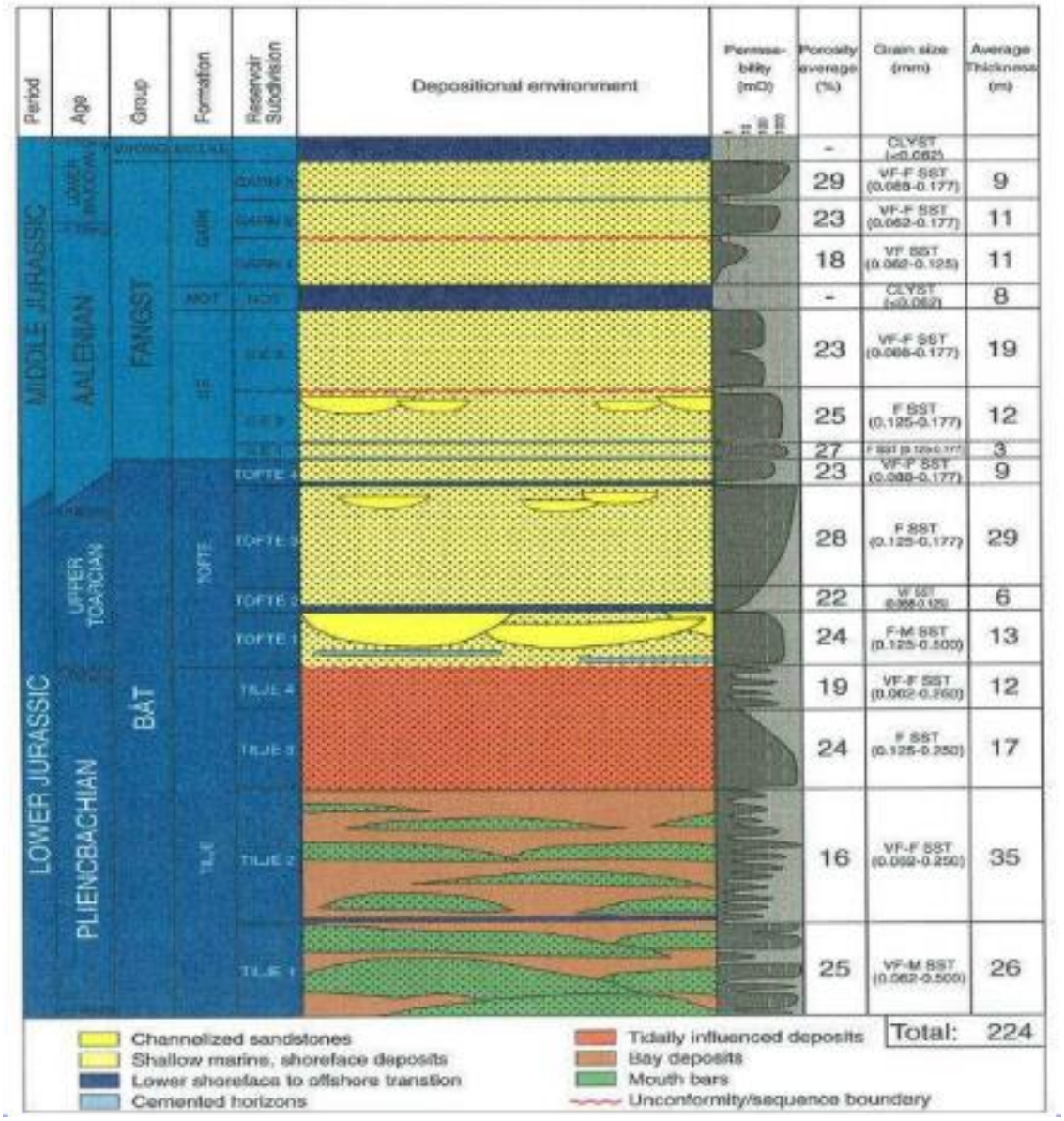

Figure 6.3 Stratigraphic Layers in Norne Field reservoir (Statoil, 2001)

The source rocks are believed to be from the Early Jurassic coal bedded Are Fm and Late Jurassic Spekk Fm while the Melke Fm is the cap rock. The total reservoir thickness, from Top Åre/ Base Tilje to Top Garn, varies over the field – from approximately 260m in the southern parts to about 120m in the northern parts. The decrease in thickness is more pronounced in the Ile and Tilje Fms because of increased erosion to the north (Figure 6.4)

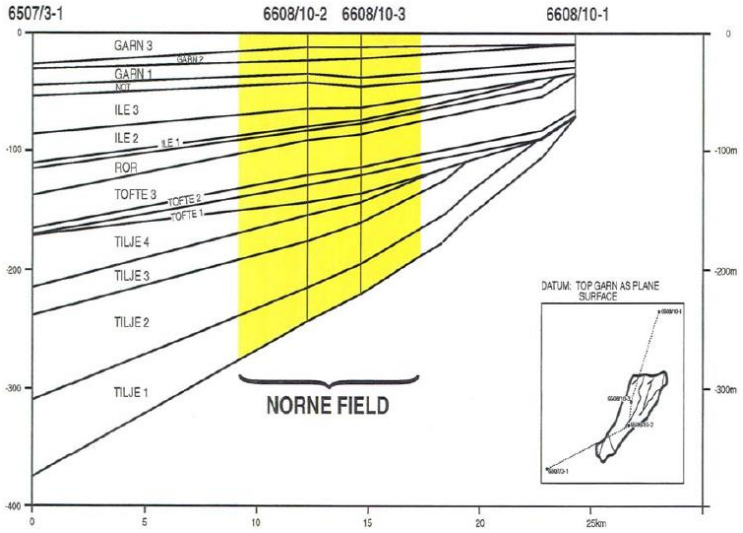

Figure 6.4 Cross-section Through Norne Field reservoir Layers Isochores [Statoil, 2005]

The stratigaphy and depositional sequence in Figure 6.5 shows the important stratigraphic units in Norne Field.

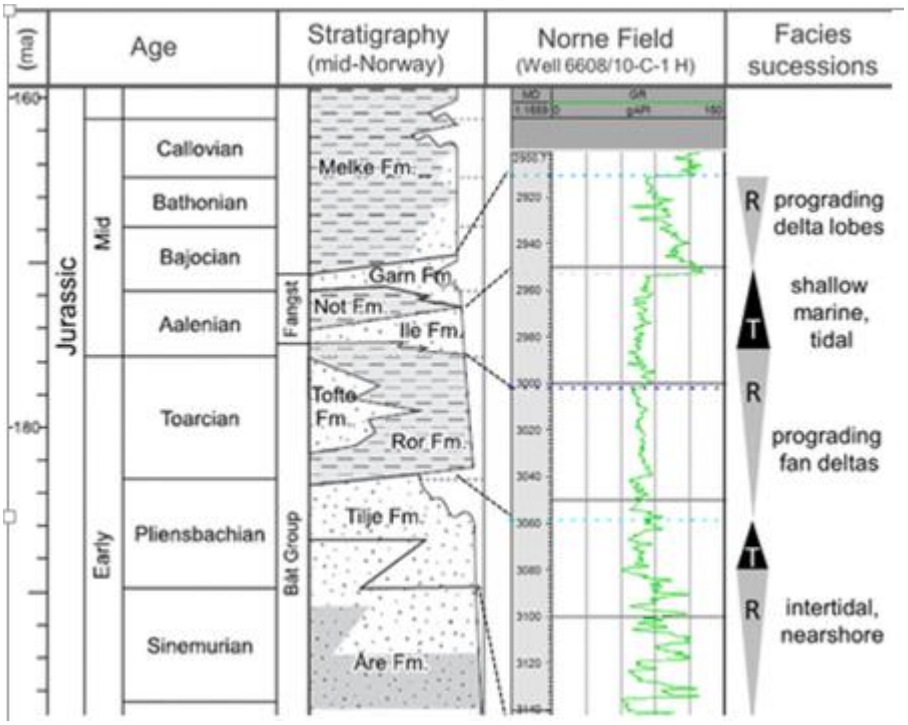

Figure 6.5 Norne Field Stratigaphy and Depositional Sequence at Well 6608/10-C-1 H (Gil and Denis, 2016)

Brief description of the important stratigraphic units, from Åre to Garn Fm, follows:

The Åre Fm is the deepest Fm in Norne Field and is mainly comprised of 2-10 m thick channel sandstones interbedded with mudstones, shales and coals. The total thickness of the Fm varies; it was found to be more than 800 m thick in well 6608/10-2. The depositional environment for this Fm is reported to be probably alluvial to delta plain setting, transported from a source area to the east.

The Tilje Fm is mainly comprised of sand with some clay and conglomerates deposited in a marginal marine, tidally affected environment. The zone is characterised by fluctuating depositional environment and consists of highly bioturbated shale, sandstones of varying thicknesses, conglomerate beds and laminated shales.

The Tofte Fm was deposited on top of the unconformity on the top of Tilje Fm. The depositional environment was marine from foreshore to offshore and the mean thickness of the Fm across the Norne Field is 50 m..

The Ror Fm is a very 8.5 m thick fine shaly unit deposited in a lower shoreface environment with low sediment supply, and is assumed to have good reservoir quality. A calcareous cemented unit on top of the Fm may be a stratigraphic barrier to vertical fluid flow.

The Ile Fm is a 32-40 m thick good quality reservoir sandstone deposited in the shoreface environment. The reservoir quality in the regressive depositions of the Ile Fm is very good but decreases toward the top of the Fm.

The Not Fm is a 7.5 m thick, dark grey to black claystone with siltstone lamina was also deposited in a quiet marine environment. It has a coarsening upward sequence which continues into the overlying Garn Fm (indicating deposition during regression).

The Garn Fm is a 35 m thick sandstone deposited in near shore environment with some tidal influence.

The Melke Fm is the reservoir cap rock dominated by claystones deposited in offshore transitional to lower shoreface environment and of thicknesses varying from 212 m to 160 m in the wells 6608/10-2 and 6608/10-3. The Melke Fm is not well developd to provide the requisite reservoir qualities and therefore acts as a seal in the Norne Field.

6.2.2 Reservoir Communications and Barriers (Statoil, 2001).

In the Norne Field, there are several faults and stratigraphic barriers which affect lateral and vertical flow, and are the key reservoir uncertainties in the Norne Field. Studies

carried out on seismic data helped in identification of the faults especially the major faults. These faults are incorporated in the reservoir simulation model as fault planes divided into sections according to the reservoir zonation, and assigned transmissibility multipliers, depending on the width of the fault zone, the permeability of the fault rock and matrix as well as grid block dimensions in the simulation model. Unfortunately, no faults or shear fractures were encountered in Norne Field's core samples for fault permeability measurements and an analogue field's measurement (the Heidrun Field) has been chosen as an analogue for the Norne Field. Three main fault category recognised in Heidrun's core study (cataclasite, phyllosilicate and clay smear) were modelled by assigning average permeability values to each category.

On the other hand, the stratigraphic barriers present in the Norne Field were assessed using cores and logs for determination of their lateral extent and thickness variation. Selection of core plugs were done using Norne Field core photography and Kv (average vertical permeability) measurements were made for each barrier. Pressure development in the field and Formation Multi Tester (FMT) data clearly indicate the level of influence which the stratigraphic barriers have on the reservoir flow processes. The most influential barriers to flow are the claystone formation between Tilje 3 and Tilje 2 Fms, the calcareous cemented layers at top Tofte Fm between Ile 1 and Tofte 4 Fms, and the shaly Not Fm. These barriers have all been interpreted to be continuous over the entire field. The thick shaly Not Fm (7-10 m thick across Norne Field) have been verified to be sealing through FMT data. Other continuous intervals which limit vertical fluid flow in the field are the carbonate cemented layer at top Garn 2 Fm between Garn 3 and Garn 2 Fms, the carbonate cementations and clay content at base Ile 3 between Ile 3 and Ile 2, the carbonate cemented layers at base Ile 2 between Ile 2 and Ile 1, and the significant grain size contrast between Tofte 2 and Tofte 1.

6.3 Well Plans: Drainage and Injection strategy (Verlo and Hetland, 2008)

Norne Field has a unique drainage strategy because of its complex geology. In consideration of the general Norne Field structure, especially the location of the faults, and the fluid contacts (GOC and OWC), the initial wellbore locations were strategically chosen so as to place:

- The Water injectors at the flanks of the reservoir
- The Gas injectors at the structural highs of the reservoir

- The oil producers between gas and water injectors to delay gas and water breakthrough
- The oil producers at some distance away from the major faults to avoid gas inflow.

Subsequent reservoir simulation studies helped in optimizing the initial well locations with regard to gas and water breakthrough times.

Some of the initial set of development wells in Norne Field were drilled as vertical wells but the wells have been side-tracked to target specific zones in view of optimising field recovery. The current drainage strategy favours field development with only horizontal wells. Norne Field has six subsea wellhead templates: 4 templates for the producers (named B, D, E, K) and 2 templates for water/gas injectors (named C and F). To maximize drainage and increase recovery, more than 50 wells have been drilled including pilot wells, multilateral wells draining from multiple targets and sidetrack wells from main boreholes. The number of active wells in the field as at the end of 2006 was 17 which comprises of 11 oil producers, 3 gas injectors and 3 water injectors. All the wells in Norne Field were completed in line with the field's drainage strategy depicted in Figure 6.6

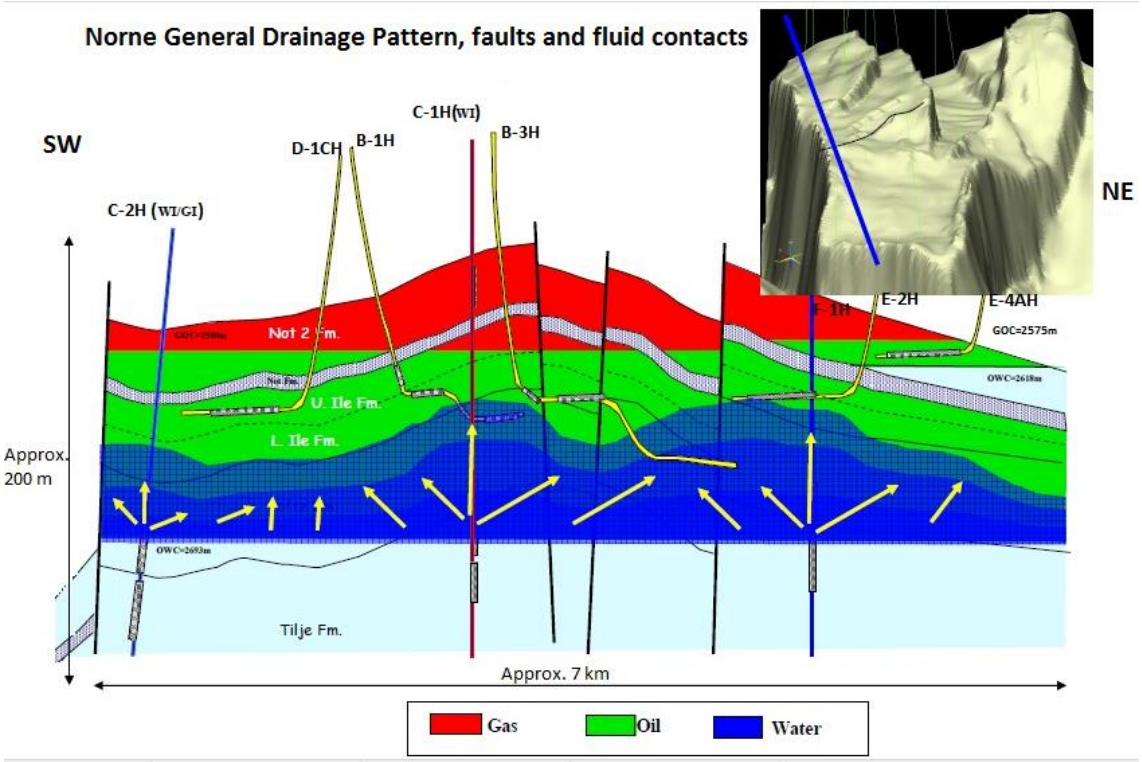

Figure 6.6 NE-SW Norne Field Cross section showing the drainage pattern with faults and fluid contacts locations (Adapted from http://www.ntnu.no). The Ile and Tofte Fms contribute to most fluid produced and the production mechanism has been driven with bottom and side injection.

The drainage strategy at start was to re-inject produced gas into the gas cap and inject water into the water zone. However, it turns out that the shaly Not Fm is sealing over the Norne Field Main Structure and the pressure in the gas cap became high as the pressure support from the injected gas is not communicated across seal. As a result, the gas injection strategy was successfully changed to deep gas injection; for injection into the water zone and the deeper part of the oil zone. On the other hand, the prediction of gas dynamics in the reservoir became more complex and uncertain. In addition, the field started producing at higher GOR than expected which forced the operators to restrict production volume in order not to exceed the field's gas handling capacity. More so, export of gas from the field was started in order to reduce the volume of gas injected, obtain a balanced injection strategy and control the GOR. Pressure support have been achieved through both water and gas injection into the reservoir. The deep gas injection was, however, stopped in 2005. In 2006 the field management was partially reverted to the initial strategy by injecting gas into the gas cap through the C-wells in order to prevent pressure depletion (Figure 6.7).

With over 50 wells to date and 86.42 million Sm^3 of oil produced(out of 90.7 million Sm^3 expected ultimate oil recovery), it is a challenging to plan and mature new targets that meet the economic requirements. Accordingly, the current field development plan is such to allows small targets to be developed economically, and requires the identification of meagre bypassed areas in the Norne Field complex drainage patterns (Huang *et al.*, 2013).

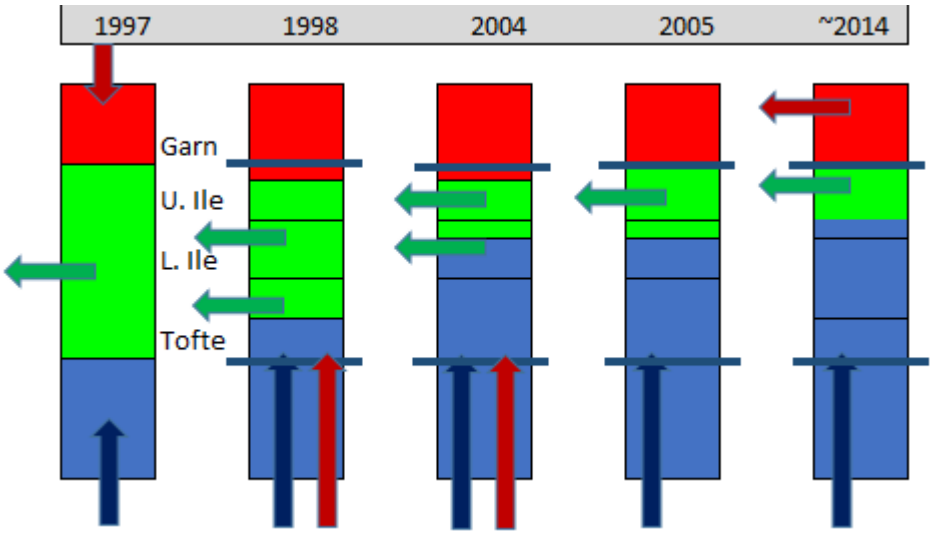

Figure 6.7 Norne Field Drainage Strategy from pre-start to 2014 (Adapted from http://www.ntnu.no/)

A more extensive description of the development of Norne Field from discovery to production can be found in Steffensen and Karstad (1996). Further discussions on Norne

Field horizontal wells development and the techniques to control gas lift are made in Selle *et al*. (2008) and Al-Kasim (2002).

6.4 Norne Field Seismic Data: Quality Control and Post processing

A typical time lapse seismic project allows both visual inspection of 4D seismic data and some quantitative techniques for improving the reservoir simulation model, so that knowledge acquired from the 4D seismic study can be applied for effective reservoir management. Depending on the quality of the acquired seismic and the level of processing, the project workflow entails processes such as feasibility study, time lapse analysis of actual surveys, mapping the calibrated 3D surveys and interpreting their differences to determine the areas that have production-induced changes, seismic inversion, seismic attribute extraction, comparison of the time lapse seismic differences to the synthetic traces to determine the type of production activity, validating the time lapse results through reconciliation with produced volumes and seismic history matching

In the coming sections, we will review and quality check the Norne Field seismic datasets noting what has been done in respect to the aforementioned items, and may subject the datasets to further processing where it is deemed necessary.

6.4.1 Acquisition and Processing

A total of 6 seismic surveys have been conducted on the Norne Field, starting with the first conventional base survey in 1992 (named ST9203) and followed by the high quality five Q-marine surveys acquired during the producing life of the field, with good repeatability, for time-lapsed purposes, in July 2001, August 2003, August 2004, July/August 2006 and June 2008. The first 2001 3D survey, named ST0103, was acquired in the Norne Field area for reservoir characterization. This was followed by the acquisition of another 3D survey covering 40 km^2, named ST0113, over the Norne Field itself for the purpose of identifying time-lapse changes in the Norne Field reservoir; monitoring the oil water contact and drainage of the field. In June 2003, a 2nd Q-marine survey named ST0305, covering some 85 km^2, was acquired as identically as possible to ST0113. The 3rd Q-marine survey over Norne Field, named ST0409, was acquired as identically as possible to ST0113 and ST0305 July 2004 but covered a larger area, approximately 146 km^2. This enabled comparisons of time-lapse changes in the reservoir to be made amongst the 2001, 2003 and 2004 surveys. In July/August 2006, another Q-marine survey, named ST0603, was acquired over Norne Field as identically as possible to ST0409, to allow the identification and assessment of time-lapse changes in Norne

Field reservoir as against production over the period 2001 – 2006 (Rwechungura *et al*., 2010)

In the case of all the Q-acquisitions (time-lapse surveys), single source and six steerable streamers separated by 50 m were used and the geometry were all consistent with the base Q-Survey (2001 survey). In addition, although the acquisitions were made with steerable streamers, steering was avoided entirely in all cases and all lines were acquired as close as possible to zero feather for better repeatability. In all Q-Survey cases, repeatability is good and the survey data is of high quality except in the area around and under the Norne Field FPSO. As a result, coverage under the production vessel was obtained through undershoot performed in the monitor surveys and processed to generate a fairly acceptable repeatability (Osdal, 2004). The configuration was different in the case of 1992 seismic survey which was conducted using a dual source and three streamers separated by 100 m, and was a big 3D exploration survey; not designed as a 4D baseline survey. The average Normalised root-mean-square (NRMS) values for the 1992 base versus Q-marine and Q-marine versus Q-marine are approximately 40% and 20% respectively (Eirik, 2010). Therefore the 2001 Q-marine seismic survey is considered as the base seismic survey for time lapse analysis.

A peak according to the Statoil (2006) processing report indicates a transition from a lower AI to a higher AI and a trough indicates a transition from a higher AI to a lower AI which is the SEG normal polarity. The dominant frequency and wavelength of the seismic surveys are at 30 Hz and 80m respectively.

6.4.2 Calibration and Analysis of Norne Field Time Lapse Data

Before using any time-lapse seismic surveys recorded at different times in a field's production history it is recommended that the survey volumes be calibrated to remove any spurious differences arising from acquisition and processing as well as the changes due to the near surface seismic effects. As part of this study, we have subjected the various Norne Field time-lapse seismic volumes to some 4D seismic quality control (QC) to ensure that the effects in the volumes of interest being compared are the production-related 4D differences. The 4D seismic QC includes the analysis of the differences in the data sets in terms of seismic amplitudes, phase, time, normalised root-mean-square amplitude.

6.4.3 Comparing the Time-Lapse Seismic Attributes

We aim to analyse the various Norne Field time lapse surveys with reference with the base time lapse survey by comparing the seismic attributes following the two Norne Field horizons which define the Norne Field reservoir – Top Garn/Not and Top Aare. These horizons respectively define the top and base of the Norne Field reservoir in time domain and are used in our analysis to window the seismic data in vertical direction and to guide the analysis in horizontal direction.

We begin our comparison through preliminary inspection of the differences in the seismic signatures between the various time-lapse monitor vintages - 2003, 2004, 2006 and the base vintage -2001 (Figure 6.8). Blue indicates that the seismic amplitudes of the monitor volumes are higher than that of the base at that time and bin location, green indicates higher seismic amplitudes in the base volume and white indicates that the amplitudes of the base and monitor volumes are approximately equal. We expect that if there were no production-induced effects, the display should be white throughout except for spurious differences related to acquisition and processing. We observe a lot of bright amplitude in the window bounded by the two marker horizons in the areas around the producer and injector wells: the blue colours in the reservoir zone delineated by the top and base reservoirs (Top Garn/Not and Top Aare) in Figure 6.8 are likely due to production-induced effects. However, there are also some observable differences (indicated by non-white colours) in zones that are not reservoirs (and would not have had production-induced effects) - these are likely caused by other factors rather than production. Therefore, there is the need to quality check the 4D vintage data matching by cross-correlation of the various monitor seismic volumes with the base volume. The result of the QC step guides us in making decision on whether there is any need to calibrate the monitor volumes to remove spurious differences in the monitor volumes and leave only the production-induced differences.

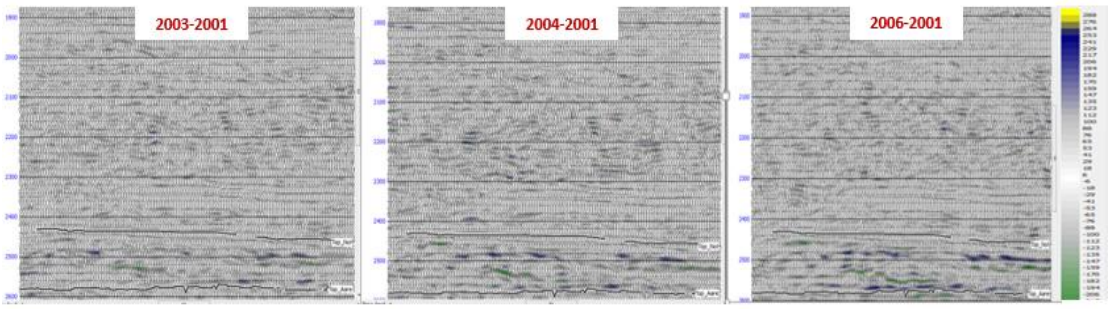

Figure 6.8 Differences between the base (2001) seismic volume and the monitor volumes (from left to right are 2003, 2004, 2006)

By using the cross-correlation tool provided in HRS-9 Geoview (Hampson-Russell), we estimate the correlation coefficients which defines the common signal between pairs of traces in the base and monitor surveys, and determine the differences in the timing between events in the surveys as well as the differences in the phase and frequency contents. In Figure 6.9, the base and the respective monitor seismic volumes are compared using cross-correlation data determined for the vertical window defining the reservoir zone: the target Event is the top reservoir with 200ms analysis window below target which brackets the top horizon and the reservoir between the Top Not and Top Aare.

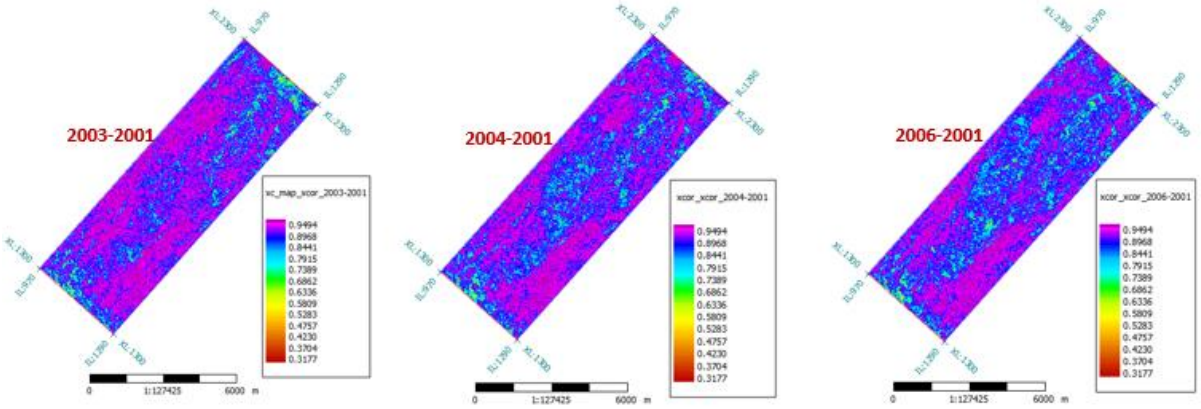

Figure 6.9 Map of correlation coefficients for the cross-correlation between the base (2001) seismic volume and the monitor volumes (from left to right are 2003, 2004, 2006). The maps represent the data from top reservoir to 200ms window below top reservoir

The correlation maps indicate that with no further processing of the seismic datasets, the average correlation coefficients of the monitor surveys referenced to the base 2001 dataset are 91.2%, 90.5% and 90% for the 2003, 2004, 2006 respectively. The band of blue and patches of green indicating lower correlation, below 80%) mostly coincide with the areas of well locations in which production-induced effects are expected in the various monitor survey data. The blue bands/ green patches in the 2003 – 2001 map becomes more noticeable in 2004-2001 correlation map and even more noticeable in 2006 affirming that the observed lower correlation reflects production effect. Should there be any need for further processing of the monitor surveys for 4D data matching, these areas need to be left out of the processing window so that these production-induced effects will not be tampered with in the final differencing.

The seismic time differences were determined and the map of the time shift between the base and monitor vintages are shown in Figure 6.10

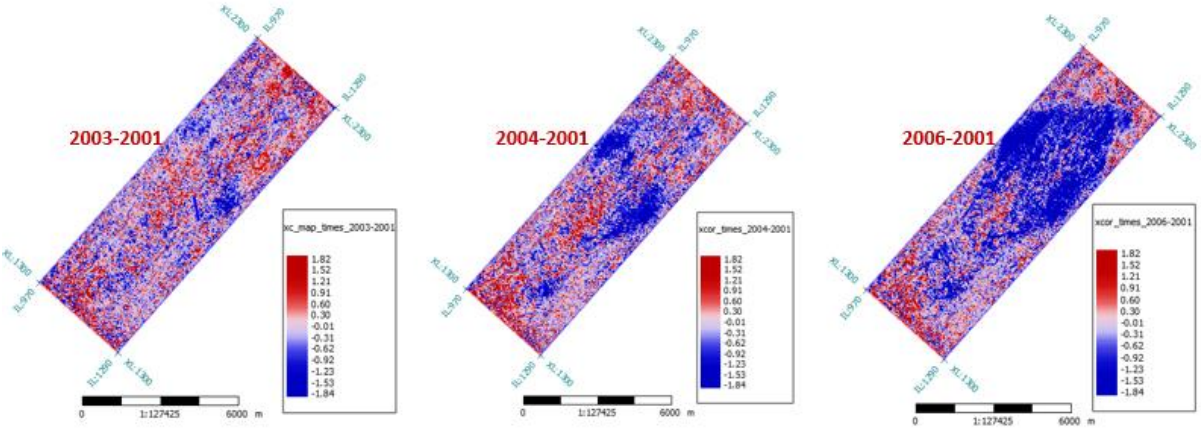

Figure 6.10 The correlation time difference map between the base (2001) seismic volume and the monitor volumes (from left to right are 2003, 2004, 2006). The maps represent the data from top reservoir to 200ms window below top reservoir.

The correlation time shift map shows that there are average bulk shift of -0.008ms, -0.14ms and -0.5ms between the 2003, 2004, 2006 time lapse data respectively and the base 2001 dataset. So the time shift averages (ms) between the base and the various monitor surveys are negligible.

As a further check on how closely the trends of each monitor seismic volume follow the trend of the base volume, the predictability between volumes are determined (Figure 6.11). Where predictability at any time, t, is the square of the cross-correlation of the traces of the base and monitor volumes summed up over the sample window, divided by the product of the autocorrelation of each of the base and monitor volume also summed up over the sample window.

The predictability, $Pred$, is defined as:

$$Pred = \frac{\sum(r_{mb}(t))^2}{\sum r_{bb}(t) * r_{mm}(t)} \tag{6.1}$$

Where r_{mb} is the cross-correlation between the base (b) and monitor (m) volumes, r_{bb} and r_{mm} are the autocorrelation of the base volume and monitor volume respectively.

The predictability (Figure 6.11) is approximately equal to 100%, except in some areas (mostly around the well locations where there are production-induced effects). The average value of predictability is about 92.3%, 91.6% and 91% respectively for 2003, 2004 and 2006 time lapse data: so the trends of the respective datasets with reference to base 2001 dataset are very close to each other. The bands of yellowish green indicating relatively lower predictability values (about 82%) are observed mostly in the areas affected by production.

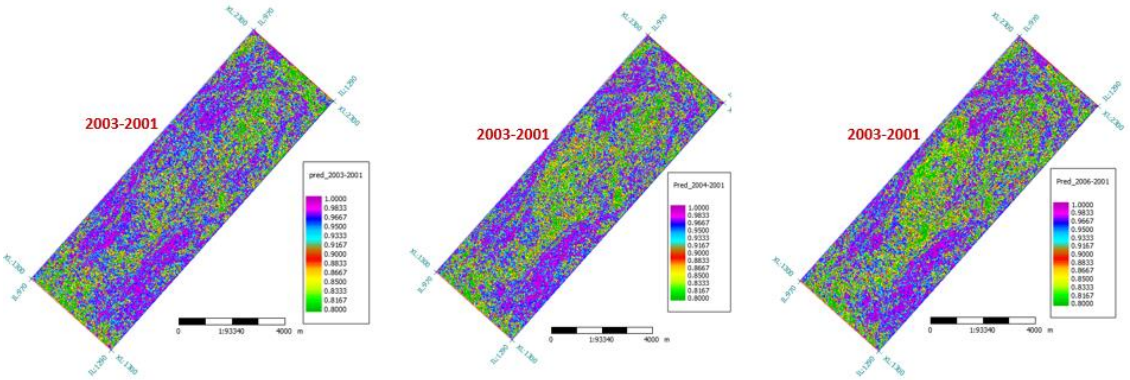

Figure 6.11 The predictability map between the base (2001) seismic volume and the monitor volumes (from left to right are 2003, 2004, 2006). The maps represent the data from the top reservoir and 200ms window below the top reservoir.

From the above, it is inferred that the datasets are of very good predictability and high correlation in areas where production effects are not expected, indicating a good 4D match. The time difference in the seismic events of the different datasets are also negligible. Therefore, there is no need for further calibration of the time and phase shifts; and no need to apply phase and time shifts. Besides, the amplitude spectrum matches indicating that between the various two datasets the wavelets have been matched (Figure 6.12).

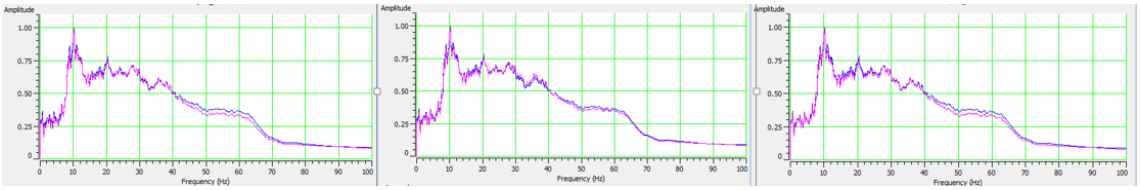

Figure 6.12 Comparison of the Amplitude Spectrum the base (2001) seismic (the blue curves) and those of the monitor seismic (the pink curves; from left to right are 2003, 2004, 2006).

Having seen that the wavelets of the various monitor and base datasets match, a further quality check on a correlation window above the reservoir zone (a window that brackets the Top Garn Fm and ends in the shallow data, about 30ms above the top reservoir) confirms that the near surface effects (trace by trace time delays, caused by shallow statics) have been corrected. We observe that the cross-correlation is smooth and very high (about 98%) in the shallow regions corresponding to the areal location of the Norne Field reservoir and the time shifts are very small (about 0.03ms). Unlike in the results of the previous correlations within the reservoir window, the shallow statics do not indicate any trend in the well locations. The statics are already optimized and reflects the quality of the 4D match at the near surface where no production-induced differences are expected (Figure 6.13). Therefore, no time variant statics need be applied to the shallow data.

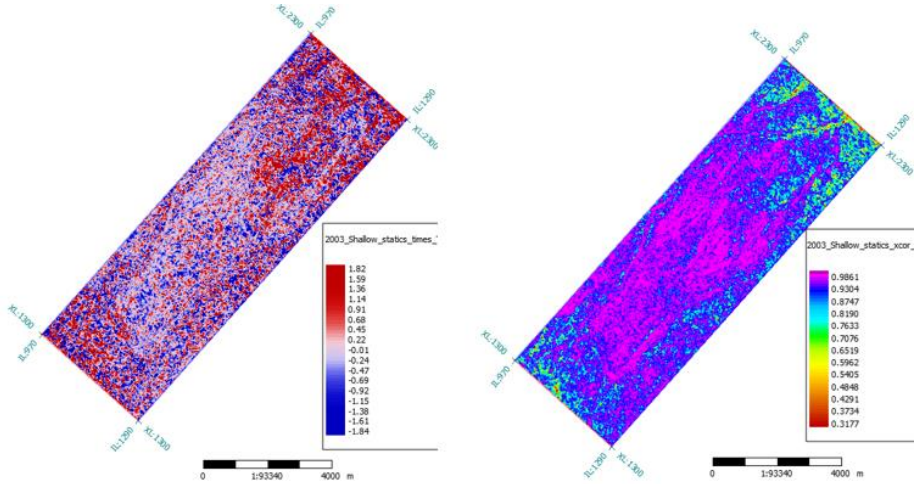

Figure 6.13 The map of time difference (Left) and cross-correlation (Right) between the base (2001) seismic volume and the 2003 monitor volume. The correlation window was chosen above the reservoir zone to check for near surface effects. The purple region indicates very high cross-correlation and occur at the shallow region corresponding to the reservoir areal section. The time difference at this region is negligible.

The 4D QC confirms that the acquired seismic data is of good repeatability and of high quality: there were no problems of significance observed in QC and the pair of traces between any two vintages match in acquisition geometry. A time lapse QC function, the RMS factors, were estimated for all monitor vintages with the 2001 vintage as reference, and is approximately equal to 1 in all the cases (example: the RMS factors in Figure 6.14 estimated for the 2006 seismic volume). The factors measure the values of the Root Mean Square velocity within a monitor volume compared to the RMS velocity within the reference volume. Since our values in all cases approximate unity it means that the repeatability of all the monitor volumes with respect to the 2001 reference volume is very high, and there is no need to apply any RMS factor to the monitor volumes.

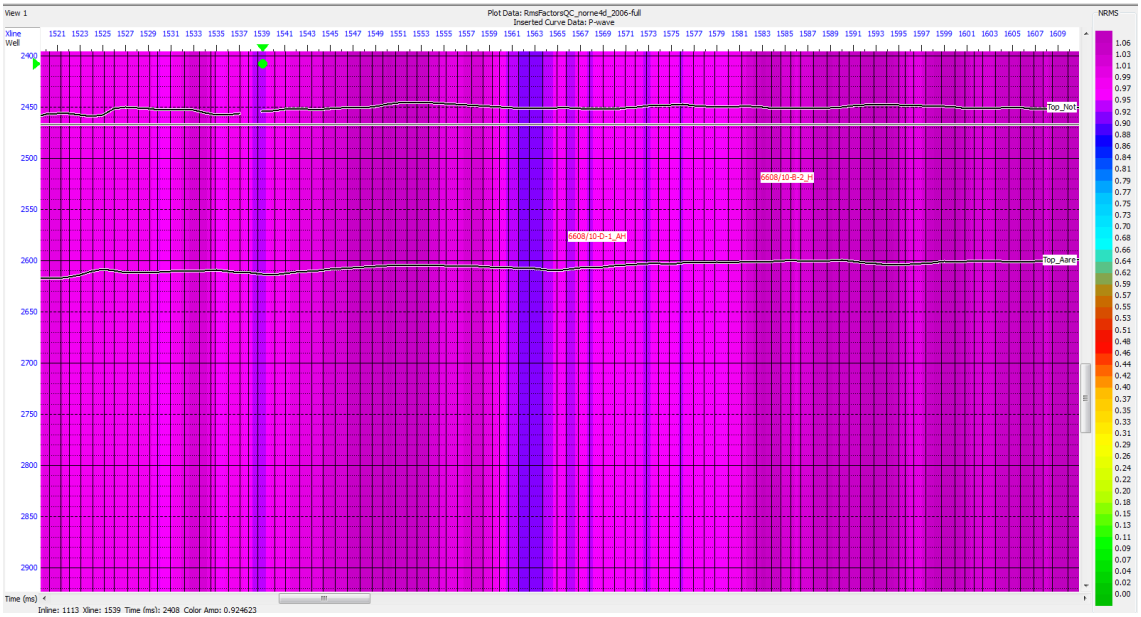

Figure 6.14 Slice of RMS factors for 2006 and 2001 vintages: estimates of the RMS factors required to balance the amplitudes of the surveys. The factors are approximately equal to 1 indicating that the amplitudes of the surveys are balanced, and the repeatability is very good.

To further analyse and confirm the repeatability of the datasets, we create some normalised difference of the Root Mean Square of the seismic amplitudes (NRMS) maps in the non-reservoir regions where there are no production-induced changes. The NRMS measures the relative difference between traces in base and the respective monitor volumes and is dependent on time, phase and amplitude differences. Within a given time window, NRMS of the monitor and base seismic traces is defined as follows (Kragh and Christie, 2002):

$$NRMS = \frac{2 * RMS(mm - bb)}{RMS(mm) + RMS(bb)} \qquad 6.2$$

Where, $RMS(mm)$ is the RMS map of the monitor, $RMS(bb)$ is the RMS map of the base, and $RMS(mm - bb)$ is the RMS of the differences between the monitor and the base on a sample by sample basis. NRMS takes values in the range, $0 \leq NRMS \leq 2$, where the upper bound is obtainable for traces (monitor and base) which are purely anti-correlated; such as the case of the traces having a phase shift of 180 degree, or a case where one of the volumes is of zero seismic value. The lower extreme, 0, is an ideal case (a utopia) representing an exact match between the base and monitor, and can only be obtainable in practice if a seismic volume is being compared to itself. For the case of one seismic trace having half the amplitude of the other, NRMS value equals 0.67. We generated some NRMS difference maps for non-reservoir regions of the Norne Field 4D

seismic with all data within a 300ms window above the top reservoir (Figures 6.17 a, b, c), and for non-reservoir regions with all data within a 300ms window below the base of Norne Field reservoir (Figures 6.17 d, e, f). We also generated similar maps with all data within the window bounded by the top and base horizons (Figure 6.15 g, h, i).

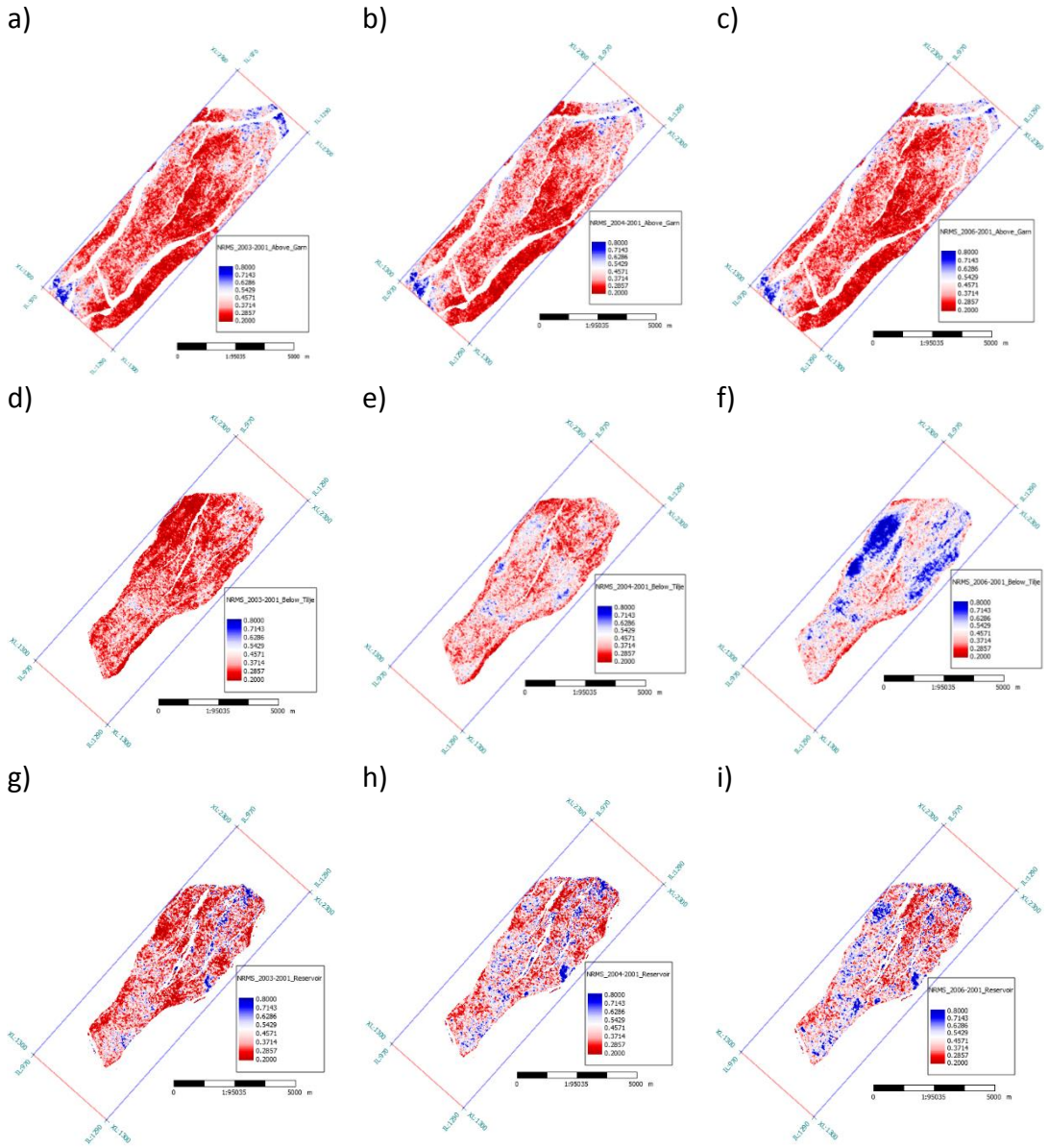

Figure 6.15 1 The NRMS difference maps generated for all values within: 300ms window above the Top Garn for a) 2003 – 2001, b) 2004 – 2001, c) 2006 – 2001; 300ms window below the base Tilje for d) 2003 – 2001, e) 2004 – 2001, f) 2006 – 2001; and within the reservoir bounded by the Top Garn and Base Tilje for g) 2003 – 2001, h) 2004 – 2001, i) 2006 – 2001.

Within the specified window of interest above the reservoir zone the mean values of the NRMS values is about 0.35. The mean NRMS values in the reservoir increases from 0.37 for the 2003-2001 difference map to 0.43 for the 2004-2001, and increased further to 0.46 for the 2006-2001 reflecting an increasing effect due to production-induced changes from 2001 time lapse to 2006 time lapse. The maps generated for values within the reservoir

zone shows that the NRMS values are very much higher in the areas where production or injection activity has more influence (the bright blue colours). The large changes in NRMS in the reservoir zone reveals the changes in reflectivity due to production during the time period between any two surveys. As for the non-reservoir regions beneath the base Tilje, the pattern reflects the velocity changes in the reservoir which affects the seismic events beneath. Time-variant filter has already been applied to compensate for the changes in velocity (Statoil (2006) and we will not make any further calibration to correct the time variant shift so as to avoid removing important differences in reflectivity within the reservoir zone between any two surveys – of course, there are limits to the repeatability that can be achieved without damage to the desirable reservoir differences (Waggoner, 2003). On the other hand, a volume corrected for only non-variant-time is useful for time delay interpretation

In general, the values of NRMS for the non-reservoir zones is low for both the regions below and above the reservoir suggesting to us that the repeatability is very good. High NRMS can indicate poor repeatability but, in the case of Figure 6.15 (g,h,i), the relatively higher values observed in the reservoir zone (which are even higher at the well locations) is indicative of production signal.

Finally, the aerial extent of the production-affected zones can be defined through creating amplitude slices from the monitor – base difference volume. The final normalized difference amplitude map shows that data matching has reduced the differences to about 30% of the original signal level in areas that were not affected by production. However, in the areas near the wells, the difference in amplitude is often greater than 50% of the original signal level. This large change in reflectivity is due to changes caused by production during the period between the two surveys.

6.4.3 Norne Field Seismic Inversion Results

6.4.3.1 General inversion workflow

The workflow presented in Figure 6.16 was applied to the four available seismic vintages (2001, 2003, 2004, and 2006) for inversion of the post-stack volumes to AI volumes. The workflow ensures that the seismic volumes are calibrated as described in section 6.4.2, before the inversion methods described in Chapter 2 (section 2.6.3). The inversion workflow applies to several 4D inversion methods including model-based inversion, bandlimited inversion, CI, linear programming spike inversion and maximum likelihood

spike inversion. The inversion methods were described in some details in section 2.6.3 of Chapter 2.

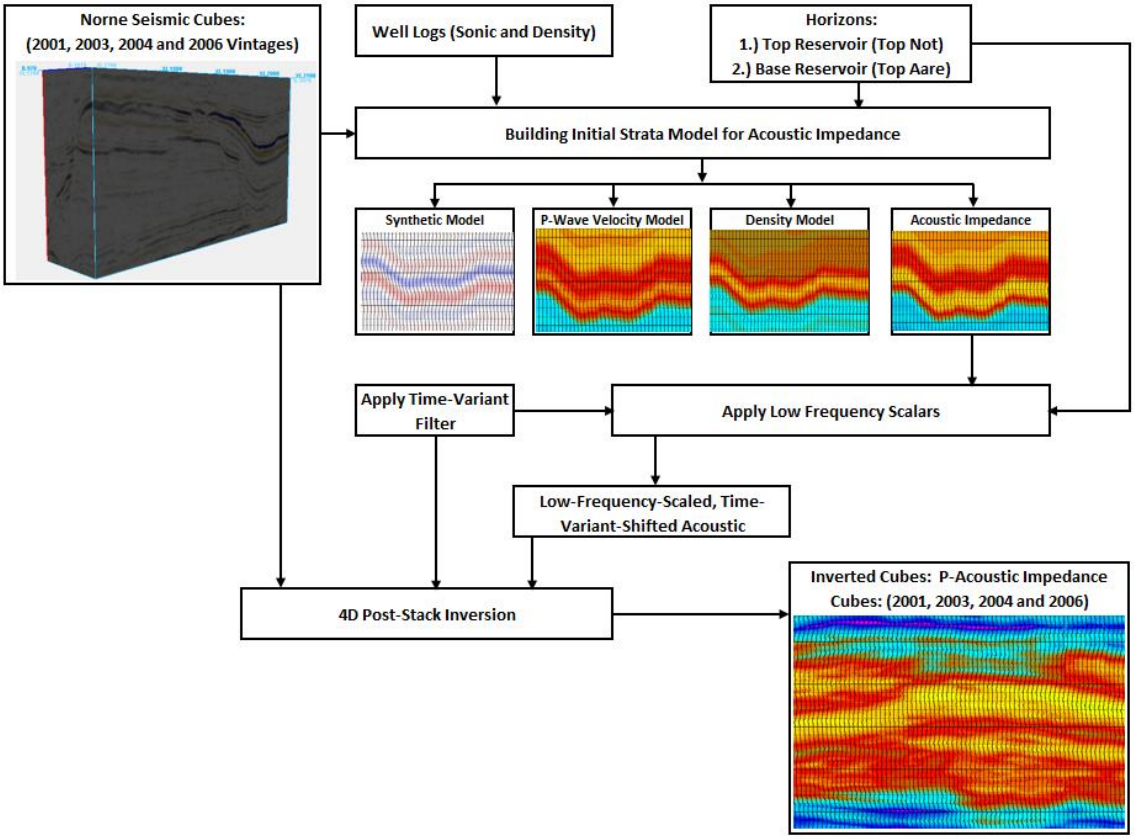

Figure 6.16 2 Model-Based Inversion Workflow Applied to 2001, 2003, 2004 and 2006 Seismic Volumes

6.4.3.1 Genetic inversion workflow

The GI workflow (Figure 6.17) differs slightly from the general workflow presented in the previous section. Unlike other 4D inversion techniques for which the general workflow applies, most of which are based on strong and constraining prior information that are difficult to acquire, the required inputs in the case of GI are only the seismic amplitude, and the well logs. In GI, AI logs (well logs) are used as training data and initial property modelling is not needed. The GI method was also described in some details in section 2.6.3 of Chapter 2.

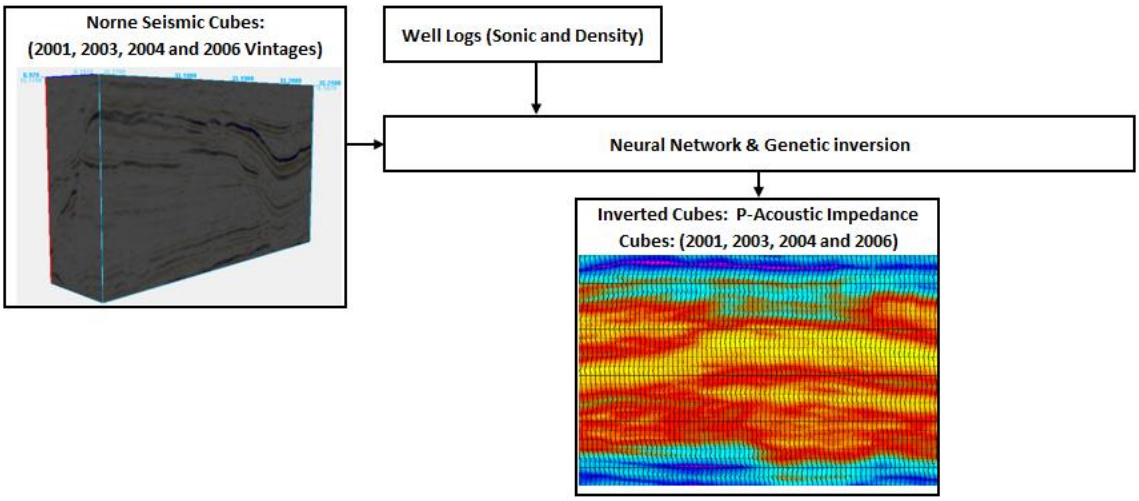

Figure 6.173 GI Workflow Applied to 2001, 2003, 2004 and 2006 Seismic Volumes

6.4.3.2 From Seismic Grid to Simulation Grid

The AI volumes generated from the above workflows are in the fine seismic grid covering the entire area targeted during seismic survey. For incorporating the impedance data in the quantitative history matching workflow, we are interested in the impedance values in the reservoir zones. These impedance values are the observed values which are going to be compared to the values predicted by the simulation models generated during optimisation (history matching). The observed values are in the time domain while values predicted using the simulation models are in the depth-domain. Proper comparison can only be done in the same domain; and for obvious reason, we have chosen the depth domain. Therefore we need to carry out time-to-depth conversion of the acoustic impedance (AI) volumes. After the domain conversion, we sample the impedance values from the seismic grid to the simulation grid using an appropriate averaging technique. The procedure for the Norne Field impedance volumes in *Schlumberger Petrel* (2017) is as follows:

i. Import the AI volumes in SEG-Y format

   These are the impedance volumes generated as the result of the inversion from either the workflows in Figure 6.16 or 19 or both.

ii. Import the average velocity data

   The velocity data provided as file data named "time-depth-conversion/St0103_Norne_2003_depthconversion.avf.gz'' can be found in

   http://www.ipt.ntnu.no/~norne/Full-Norne/time-depth-conversion_tdq/Velocity%20Model_zipped%20in%20unix/

   This data contain several thousand points. Each point is characterised by its position in the x-direction, position in the y-direction, the position in the z-direction, and the average velocity. The data is input as petrel points with attributes (in ASCII format) with attribute setting set to elevation time

iii. Make a 3D grid for interpolation of the velocity data

This is done by first creating a rectangular boundary polygon that covers the entire seismic area. With the boundary polygon and any of the seismic horizon data (Top Not or Top Aare), top and bottom surfaces of a 3D grid is created at the depths of 0ms and -4000ms respectively. A simple 3D grid of 100m x 100m of about 400 layers is then made using the top and bottom surfaces and corner point gridding method.

iv. Sample the point velocity data into the 3D grid

The point velocity data from 'ii' is sampled into the 3D grid in 'iii' and moving average is used to interpolate velocity values to ensure that every grid cell has a velocity value.

v. Build a velocity model

A velocity model (Figure 6.18) for time-to-depth domain conversion is made in the *Geophysiscs* tab of *Petrel* using the top and bottom surfaces and the 3D interpolated average velocity

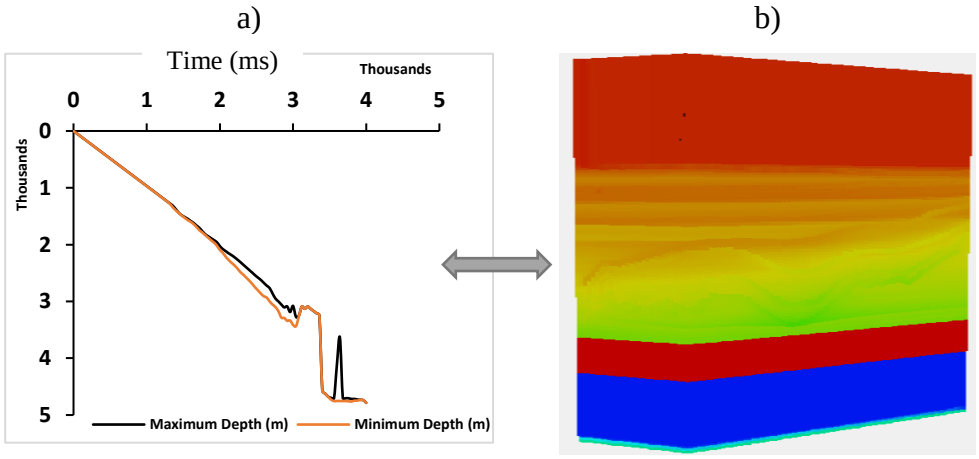

Figure 6.18 Building a velocity model: a) Time vs Depth, b) velocity model cube

vi. Time to Depth Conversion

The AI volumes resulting from the workflows in Figure 6.16 and 6.19 are converted from time to depth domain using the velocity model in Figure 6.18b. The converted domain is then cropped in depth to generate only the volumes large enough to contain the reservoir volume. The region housed by subsea depths -2250 to 3150 mSS is adequate in this regard.

vii. Seismic Sampling

Using the arithmetic averaging method, the AI values in the cropped volumes are sampled into the Norne Field reservoir simulation grid through the geometrical

modelling process in *Petrel*. The process creates a model of the impedance of each of the vintages (2001, 2003, 2004 and 2006) so that each grid cell of the reservoir simulation model has an impedance value that can be compared to any predicted AI.

6.4.3.3 Mapping of Acoustic Impedance

The reservoir models of the AI created under "6.4.3.2vii" above can be used in the history matching workflow such that grid cell by grid cell comparison of the observed and predicted impedance be made. However, for the Norne Field reservoir simulation model which consists of 113344 cells, of which 44927 cells are active, the computation time for such cell by cell comparison is very high. Besides, we want to compare the observed and the predicted data for those areas of the reservoir where confidence in the accuracy of the seismic data is high. We also note that the presence of gas in certain areas of the reservoir affects the seismic modelling process and we want to avoid such areas to minimise the 'difficult to quantify' data errors that might be introduced into the history matching process. Therefore, we do not want to include the topmost four layers (Garn Fm) in the Norne Field reservoir zonation. The topmost three layers (Garn 3, Garn 2, Garn 1 Fms) are filled mostly by gas, especially in the Norne Field Main structure where the gas oil contact (GOC) is very close to the top of the Not Fm. On the other hand, the fourth layer is the Not Fm: a completely sealing shale barrier between the Garn Fm and Ile Fms, which will have no significance in the dynamics of the reservoir seismic data.

We then want to compare the impedance values in layers 5 to 22. In order to minimise the reservoir simulation time, we want both our predicted impedance and observed impedance in the form of depth averaged maps before comparison. With the depth-averaged maps, we have just 5152 cells instead of 113344 cells for predicted-observed impedance comparison.

Figure 6.19 shows some of the impedance volumes generated for the different vintages, using model-based seismic inversion techniques. Figure 6.20 shows examples of the time-lapse impedance maps at some layers, generated as the difference between the several vintages and the base survey. The 2001 survey is taken as the base. We have chosen the nomenclature to subtract new survey from an older survey. Old survey minus new gives a red impedance colour in the plots for pressure up and gas out of solution (softening effect), blue for water saturation increase and pressure draw down (hardening effect). For comparison, impedance volumes were similarly generated using other inversion techniques and mapped into the reservoir simulation grid. Figure 6.21 compares the

inversion results obtained using three different inversion techniques (model-based inversion, CI and GI) using the 2001-2006 impedance maps at some layers.

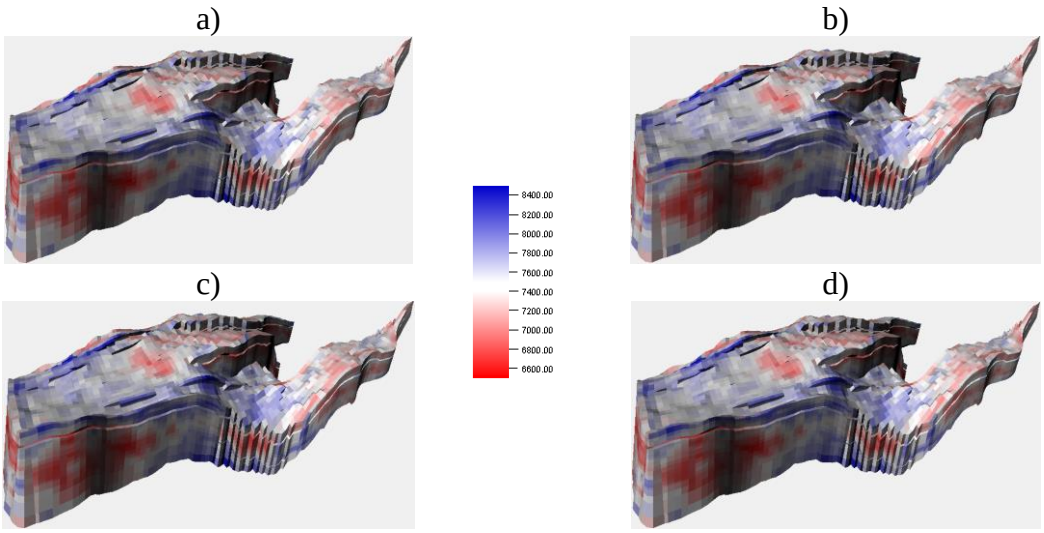

Figure 6.19 Model-Based inversion and mapping results: a) to d) are the impedance volumes for 2001, 2003, 2004 and 2006 data

6.5 Norne Field 4D Studes and Applications– Case Studies

Different applications of the Norne Field 4D seismic and value that the time lapse data have provided on the reservoir management on the Norne Field have been discussed by different authors including: Osdal and Alsos (2002), Osdal et.al (2004, 2006 and 2008), Cheng and Osdal (2008), Osdal and Alsos (2010) and Huang et. al, (2013). The application has historically been focused on monitoring of the OWC movement over the different dates of surveys, mapping the drainage pattern, locating new drilling targets, and qualitative history matching. The Norne Field has a huge underlying water filled Tilje Fm. The sealing capacity of carbonate cemented barriers and faults are regarded as the key uncertainties controlling the flooding pattern and rise of OWC across the field.

Production-induced time lapse effects are not seen on the Norne Field top reservoir reflector because the water front moves upwards inside the horst block of the Norne Field flat horst structure (Osdal *et al.*, 2006). For this reason, the interpretation of Norne Field 4D seismic has been mostly, or wholly, based on the differences between data from any chosen set(s) of two different surveys. In some cases, the difference data on the other is not very easy to interpret especially in areas with complicated production-induced effect, such as mix of gas and water injection, strong pressure increase at some injector locations and areas in which reservoir pressure has gone below bubble point.

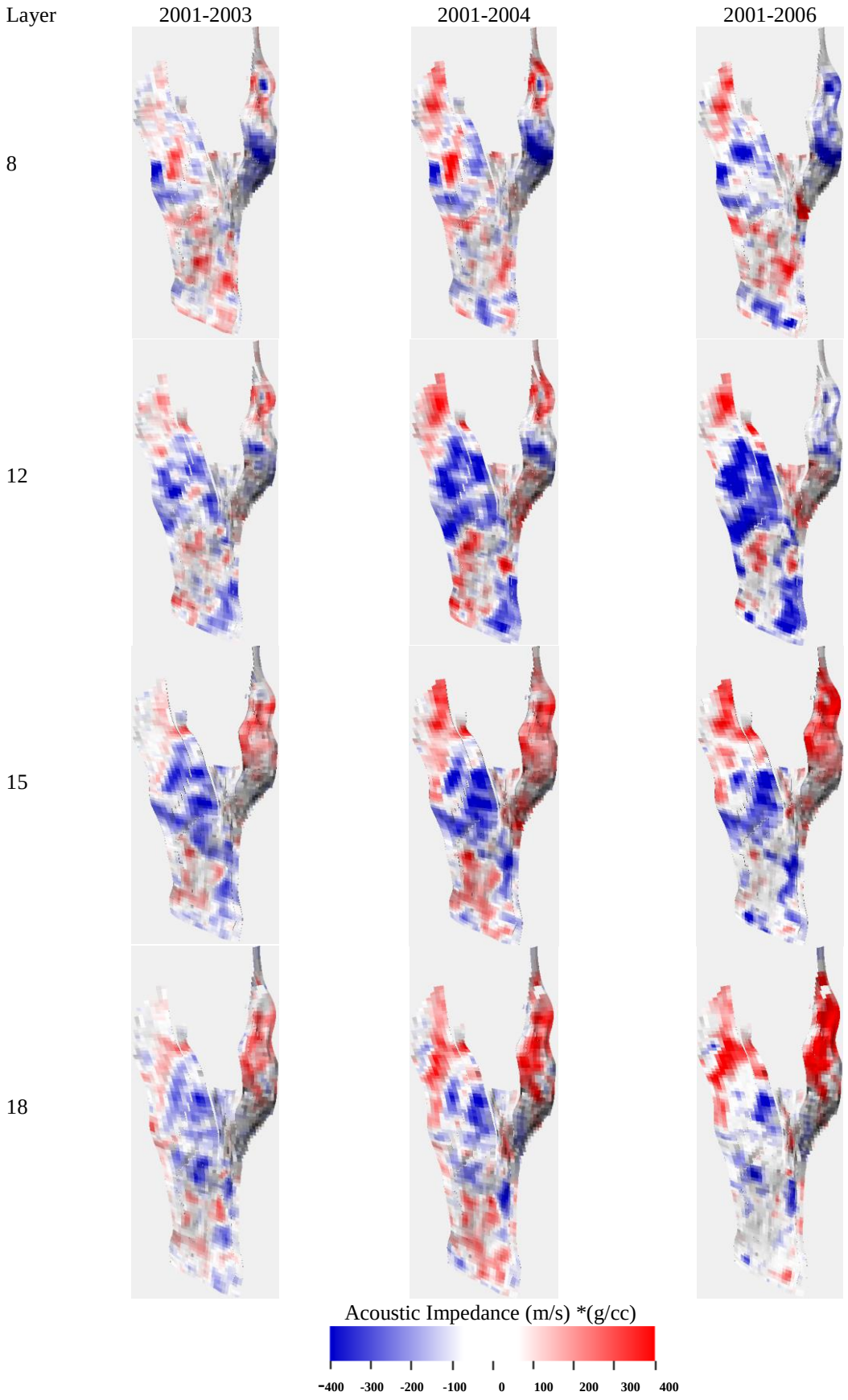

Figure 6.20 Maps of time-lapse AI derived from model-based inversion

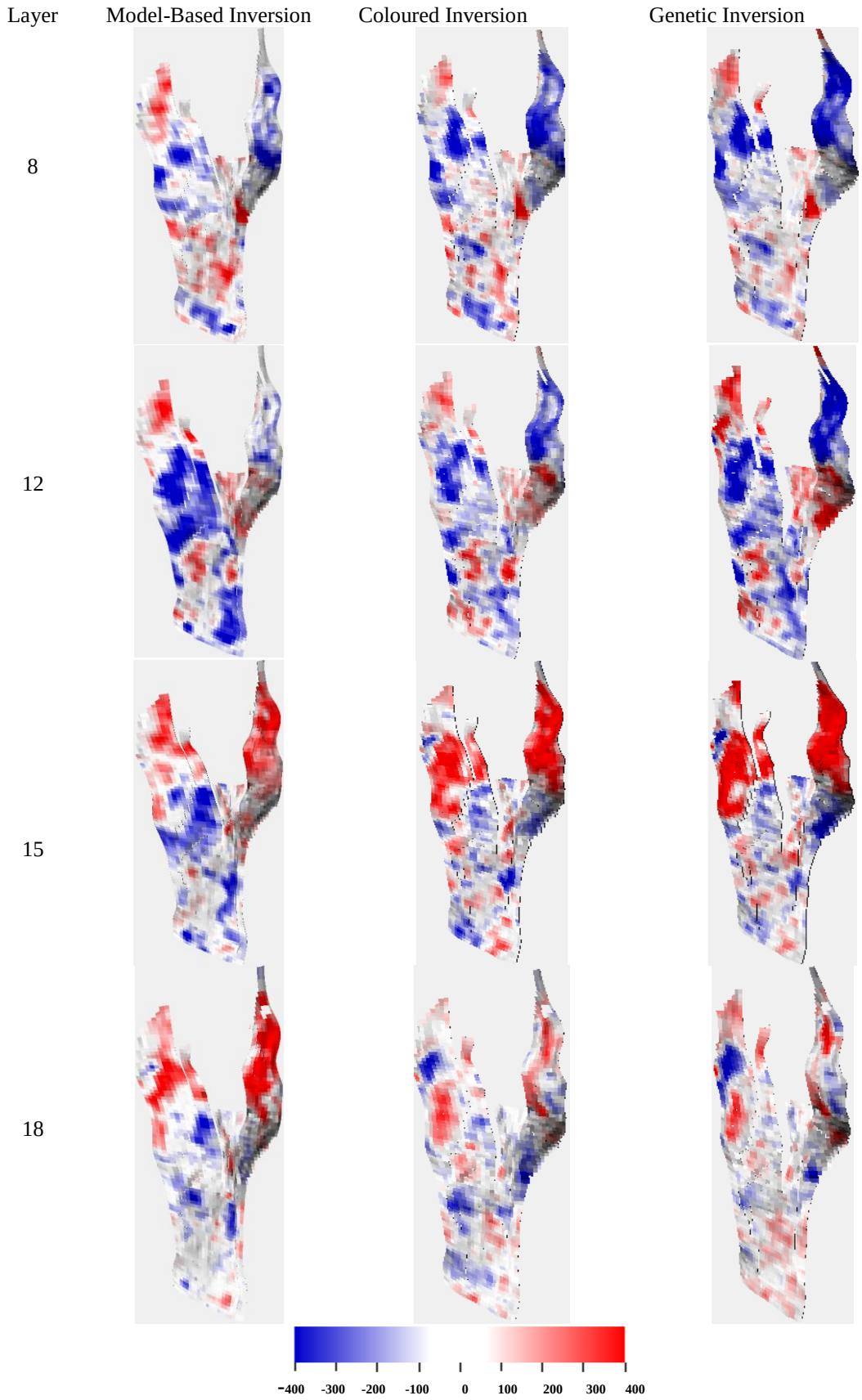

Figure 6.21 Comparing the maps of 2001-2006 time-lapse AI derived from model-based inversion (1st column)

6.5.1 Acoustic Response to Reservoir Changes

Explicit interpretation of the 4D signals in Norne Field is considered to be challenging because of a combination of complex pressure evolution, gas dissolution and liberation, inter- and intra-segment connectivity and the consequent complex drainage patterns. The result is that it is difficult to resolve ambiguity in the 4D effects driven by change in saturation and those driven by change in pressure. In order to determine the areas where 4D signals might be mostly dominated by water saturation change, Huang *et al*., (2013) determined a threshold pressure (Figure 6.22) below which the P-wave velocity, and hence the amplitude signal, at Norne Field is independent of pressure by calibrating the time lapse signals to the pressure data from wells. From this, it was shown that below a threshold pressure of 310 bar, pressure changes result in no seismic velocity changes. Reservoir pressure in each segment and intra-segment can be estimated using wellhead pressures and RFT data so that analysis with the pressure dependence model can help resolve the ambiguity in differentiating the saturation-induced effects from pressure-induced effects. In addition, Huang *et al*., 2013 also demonstrated that the identification and understanding of flood pattern in the field could be facilitated by using inverted AI derived by the stochastic inversion method. The 4D seismic interpretation could be further complicated by issues arising from failing well integrity. For instance, the gas/water injector well C-1H injector was drilled in 1998 and perforated near the base Tofte Fm and the upper part of the Tilje Fm. However, an amplitude difference map (Figure 6.23) reveals a hardening effect in the unperforated Ile Fm which is suspected to be likely due to effect of water saturation increase in the Ile Fm due to leakage from eroded casing (Huang *et al*., 2013).

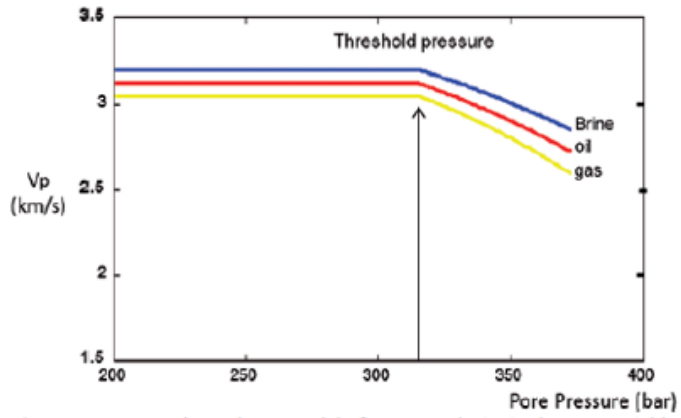

Figure 6.22 The dependency of Norne Field sonic velocity (V_p) on reservoir pressure (Huang et al., 2013)

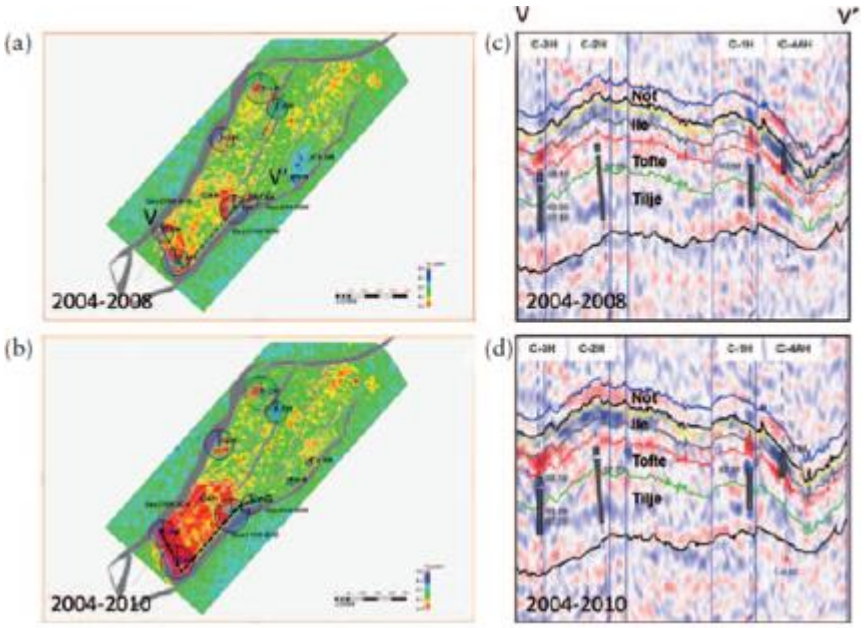

Figure 6.23 Time shift from a window 100m above and below top Tilje Fm for a) 2004-2008 and b)2004-2010. Amplitude differences for c)2004-2008 and b) 2004-2010 on section V-V' through injector C-1H and three other neighbouring injectors (Huang et al., 2013)

Time lapse seismic modelling study has also been carried out to study the percentage changes in amplitude at the top reservoir level for all the possible scenarios, including flooding in the Not Fm, pressure increase in the Ile Fm, and their combined amplitude response. Huang *et al*., (2013) reviewed the 4D amplitude response to a series of water saturation levels and showed that when the maximum water saturation (70–80%) is reached, 25% amplitude change should be expected at the top Not level. In contrast, when the reservoir pressure increases to the maximum possible pressure change in the Ile Fm (~400–440 bar), it yields less than 10% amplitude change, so a 10% amplitude threshold was applied to the seismic difference data. The flooding in the Not Fm has been confirmed by the results from reservoir saturation tool (RST) acquired in 2010.

Osdal *et al*. (2006) studied the effects of varying rise of OWC from 0–70 m through seismic modelling (Figure 6.24).

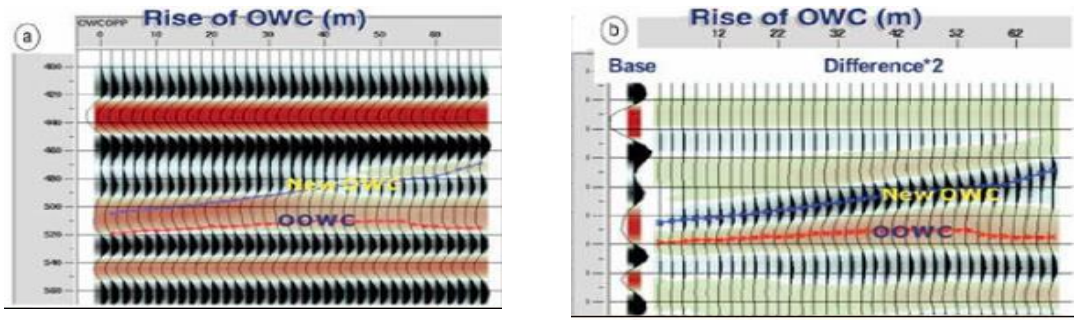

Figure 6.24 Results of the seismic modelling study for varying rise of OWC from 0–70 m (a) on one seismic vintage, and the (b) differences for varying rise of OWC and the first base trace. (Osdal and Alsos 2002)

The study showed that it is very difficult to recognise a new OWC on an individual survey (Figure 6.24a) but the new OWC could be easily interpreted on the difference between two seismic data. (Figure 6.24b).

The difference in interpretability between the individual surveys and the difference surveys is further illustrated by NE-SW section through the 2001 and 2004 seismic data. It is observed that the OWC is not noticeable on the individual vintages (Figure 6.25a and b) but the new OWC is easily noticed on the difference between the seismic data (Figure 6.25c). The OWC has risen over time between the 2001 survey and 2004 survey as reflected by the event in red colour (hardening event). The red event is interpreted as the position of the 2004 OWC. The black event just below the red event is a result of the accompanying softening and is interpreted as the 2001 OWC.

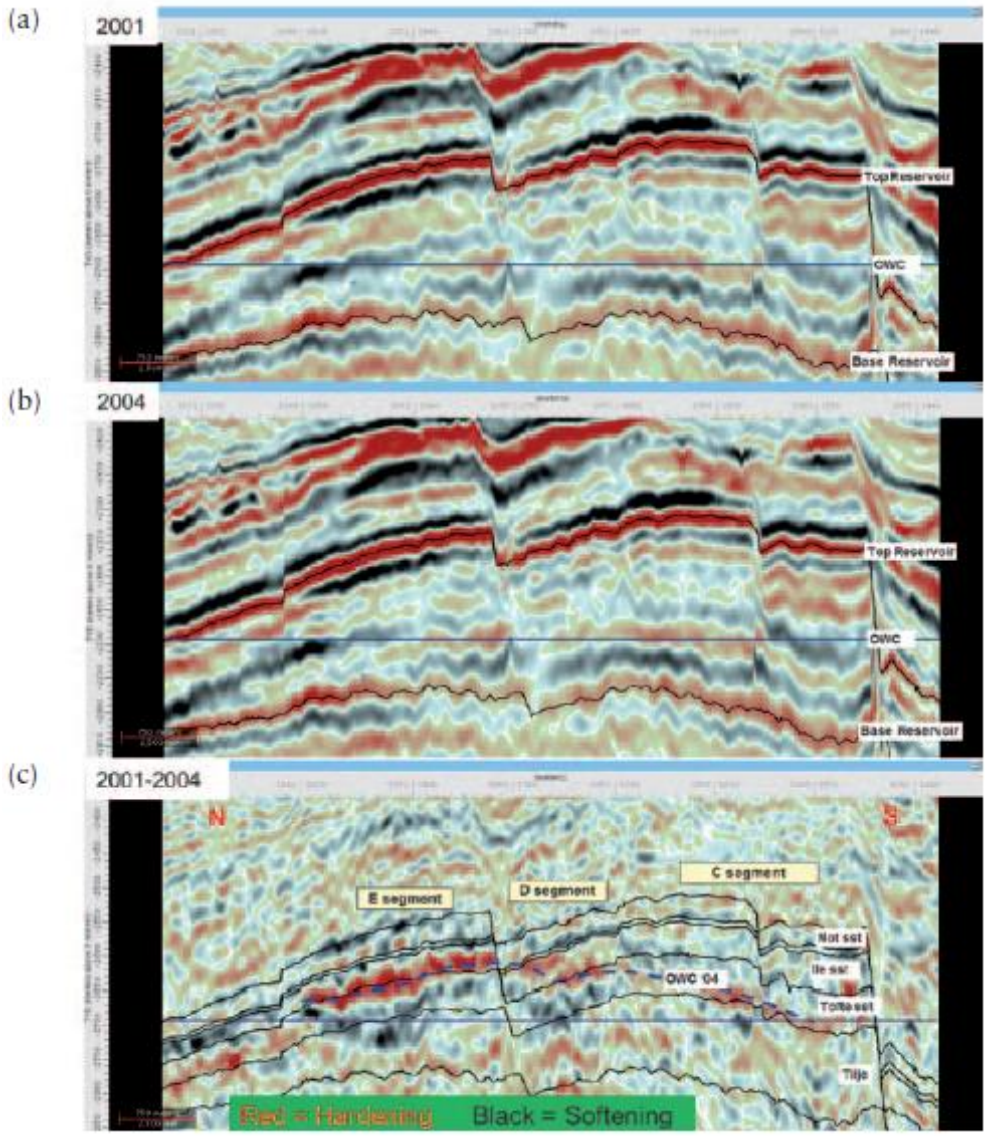

Figure 6.25 A NE–SW section through (a) the 2001 survey, (b) the 2004 survey, and (c) the 2001–2004 difference data. (Osdal and Alsos, 2010 in Huang et al., 2013).

Moreover, Osdal *et al*., 2006 showed that it is much easier to detect a change in OWC if the difference data is in the form of AI data (Figure 6.26a) instead of seismic reflectivity amplitude (Figure 6.26b). The red colour in Figure 6.26b indicates increase in AI associated with water flooding as OWC rises.

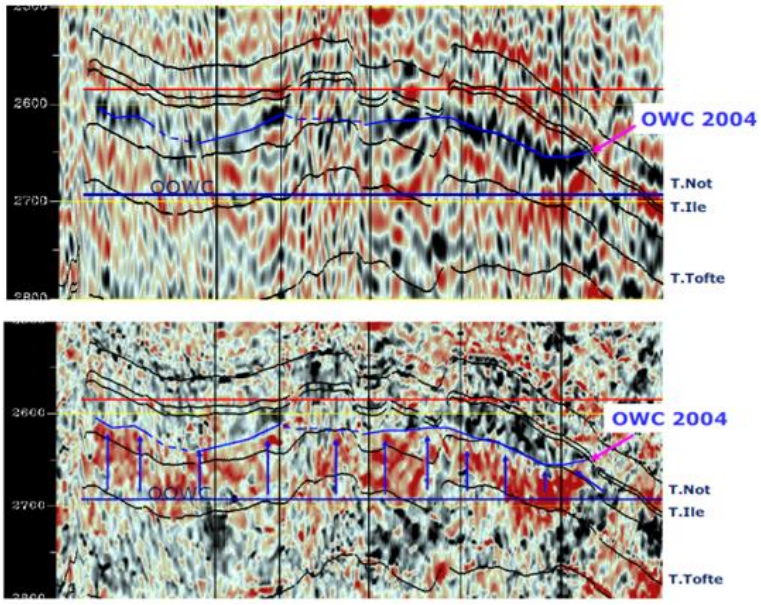

Figure 6.26 (Top) 4D difference in seismic amplitude, and (bottom) 4D difference in AI: the red colour indicates increase in the AI associated with water flooding (Osdal B, 2006)

6.5.2 Qualitative Use of Norne Field Time Lapse Seismic Data

As noted in Johnston (2013), the comparison between the predictions from reservoir simulation and the seismic data can occur in one of several domains (Figure 6.27). In the Norne Field case, one challenge is related to what one should compare. In principle, seismic/synthetic seismic, inverted impedance/modelled impedance and inverted saturation and pressure/modelled saturation and pressure can be compared.

Comparison in amplitude domain requires some difficult and time-consuming convolution process to convert acoustic properties and wavelet to the required time traces. As Stephen *et al.* (2006) observed, it is also difficult and time consuming to perform inversion of seismic data to saturation and pressure through the deconvolution of the wavelet with observed amplitudes (as proposed by Landrø *et al.*, 2001). We therefore choose the acouctic impedance as the domain for comparison of predicted and observed seismic data in this work.

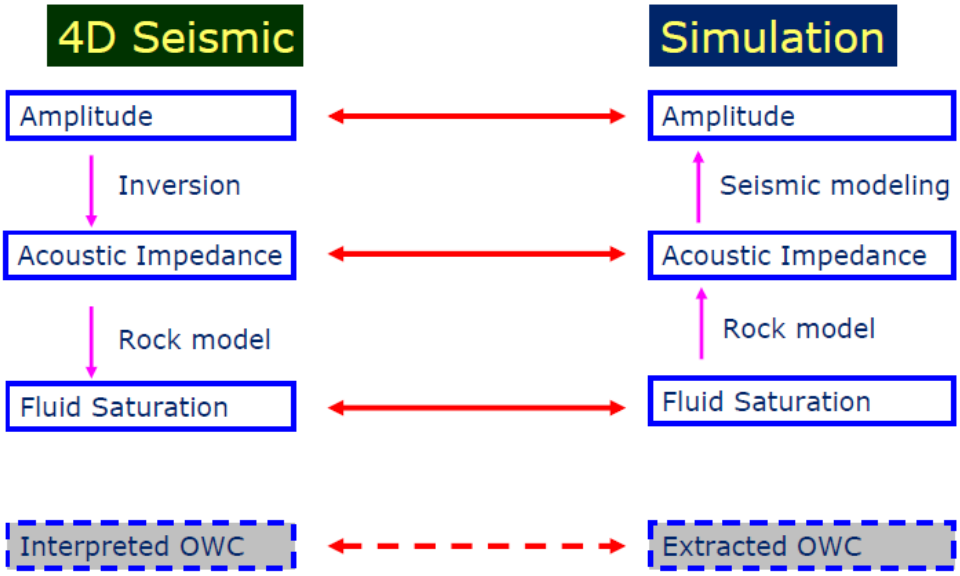

Figure 6.27 Different domains for comparing time lapse

In Norne Field, time-lapse seismic has proven to be very useful in mapping reservoir compartmentalisation, in determining the sealing, or otherwise, capacity of a fault. Several authors have concluded that the interpretation of the oil water contact (OWC) at Norne Field is best done by using the difference data obtained from the different vintages after appropriate processing (Osdal 2006; Cheng and Osdal, 2008; Eirik, 2010; Huang *et al*., 2013). The Q-marine acquisitions inverted on board Q-marine vessel for AI and poisson's ratio have been used for time lapse analysis, especially in tracking the oil-water contact positions and movements. The time lapse data in the form of reflectivity amplitude and AI have been used to adjust the simulation model making predictions of saturation changes which the simulation model did not predict.

Cheng and Osdal (2008) presented a methodology for updating the model using 4D seismic data: by interpretation of fluid flow pattern and saturation changes in the reservoir, and comparison of model-predicted water saturation and saturation from time-lapse seismic to update the simulation model thereafter for better match. For instance, in Cheng and Osdal (2008), the simulation model predicted that water in the Garn Fm was moving in the northwest and south of one of the Norne Field wells whereas the time lapse seismic data clearly showed that the movement of water was to the east.

Mapping of the OWC in the field has been essential in well planning to target the oil resource areas and avoid swept zones. Typical example is the planning of the producer well D-1CH for which the 2003 OWC, interpreted shortly after acquisition, enabled a change to the original well plan to avoid the zone around well C-2H and avoid early water breakthrough (Huang *et al*., 2013).

4D seismic data has also been useful in revealing the location of major flow barriers and baffles, which were crucial for the positioning of some wells or preliminary calibration of the simulation model. Several examples are discussed in Osdal *et al*., (2006). An example discussed in Osdal and Alsos (2010) also shows how some drilling targets were identified in the Norne Field by applying time lapse seismic interpretation.

Time lapse studies on G-segment is considered very challenging because the signals in this area represent the resultant effect of complex drainage patterns, and some concurrent reservoir dynamics including: pressure evolution, gas dissolution and gas ex-solution. Huang *et al*. (2013) discussed this complexity in view of information gathered from mapping several 4D differences. Intra-segment barriers affect pressure communication between the intra-segments of the G-segment resulting in dynamic and complex pressure evolution in the segment. Further complications due to pressure dependency model of the Norne Field seismic velocity was discussed in Huang *et al*. (2013).

Time lapse interpretation has also been useful in planning well intervention in Norne Field, especially in the aging injection wells that may be suffering from well integrity problems. Some examples of such well intervention plans guided by 4D interpretation are discussed in Huang *et al*., (2013). 4D seismic signals are particularly beneficial in this regard by helping in detection of leakages of injected fluids through eroded casings into unperforated intervals (examples are C-1H and C-3H).

6.5.3 Quantitative Use of 4D Seismic

There have been studies which incorporated the time lapse seismic as dynamic data in history matching of Norne Field reservoir simulation model. EI Ouair *et al*. (2005) demonstrated the usefulness of quantitative 4D seismic data in understanding the Norne Field reservoir flow dynamics and guiding the identification of infill drilling targets. They deployed a gradient-based optimisation in computer-assisted history matching to reduce the mismatch between the simulated and observed values of 4D seismic (in the form of relative changes in AI) and RFT pressure, by updating fault transmissibility and vertical transmissibility multipliers across the E-segment of the field. Examination of the misfit of both RFT (Figure 6.28) and 4D seismic data (Figure 6.29) predicted by the simulation models shows that for the predictions with the updated reservoir simulation model there are significant improvements in the RFT pressure data match, and the match between the observed and predicted changes in AI and water saturation improved greatly.

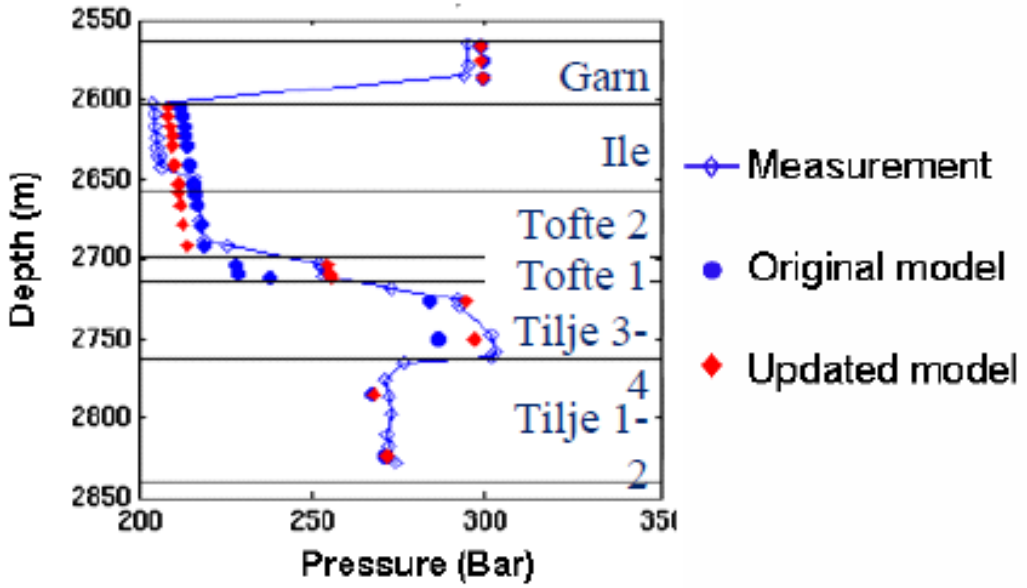

Figure 6.28 RFT Pressure Data for one of Norne Field's E-segment well (EI Ouair et al., 2005)

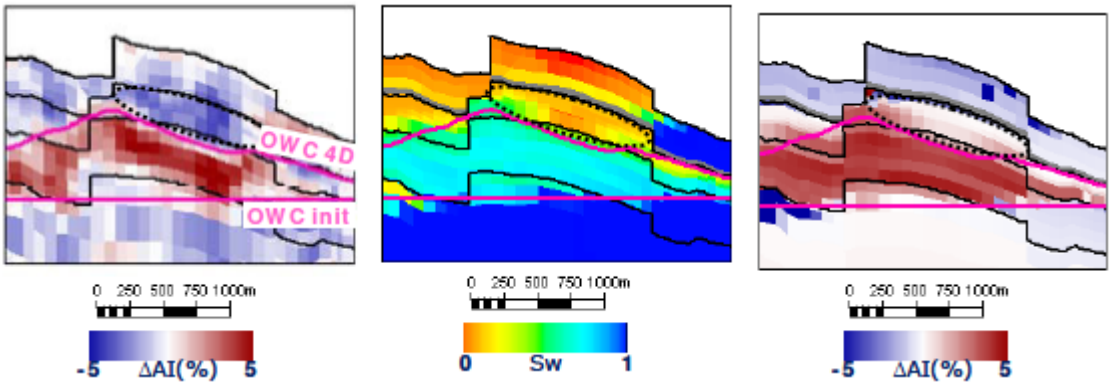

Figure 6.29 2003-2001 time lapse difference in a) observed AI, b) simulated water saturation using updated model, and c) predicted AI with updated model. (EI Ouair et al., 2005)

Amit (2013) carried out history matching of production and time-lapse seismic data using particle swarm optimisation to update a range of sensitive reservoir variables to match the 1997 to 2004 observed oil, gas, water rates and bottom hole pressure in the Norne Field E-segment wells and 2001 to 2004 normalised impedance change in the segment reservoir. One of the problems in the inverted seismic used as observed data is noise. Amit (2013) applied 3% noise filter to the absolute change in the impedance to remove noise and retain just the significant changes.

Santos *et al*. (2016) presented a semi-quantitative approach to updating the Norne Field reservoir model involving qualitative comparison of predictions from simulation to seismic model and the real seismic data; highlighting the inconsistencies in the predicted responses and the observed data, distinguishing the seismic effects resulting from

pressure and saturation, and relying on the knowledge gained from the qualitative analysis to understand the limitations of the 4D seismic data available, and assess the degree of confidence that should be placed on the time lapse data in quantitative model updating.

Other efforts to incorporate time lapse quantitatively for Norne Field simulation model updates include: Dadashpour *et al*. (2007), Lygren *et al*. (2005) etc.

6.6 Norne Field Simulation Model

6.6.1 Description of the Base Model

The original geological model for Norne Field was built based on the interpretation of the first conventional base 3D seismic survey acquired in 1992(ST9203) but has over time been modified and refined to reflect changes in geology and reservoir dynamics as additional surveys are acquired and/or interpretations and re-interpretations made. From 1994 to 2006, the field had been simulated using the following four different Eclipse black-oil simulation models:

- The 40x70x16 model, based on a1994 interpretation of the survey ST9203.
- The 56x124x24 model, based on a 1998 interpretation of the survey ST9203.
- The 46x112x22 model, based on a 2004 interpretation of the Time lapse surveys ST0103, ST0305, ST0409.
- The 55x136x32 model based on a 2006 interpretation of the Time lapse surveys ST0103, ST0305, ST0409 and ST0603.

For the purpose of this thesis, the model with grid dimensions 46x112x22 will be used as the base case model for simulation. The grid consists of 113344 cells, of which 44927 cells are active, with average grid block size of 100m x 95m x 10m. The grid aligns at an angle of 52.9 degrees. As indicated on the model's UTM coordinates (Table 6.3), the maximum and minimum depth points of the grid are -2439m and -3090m respectively. The grid differs from the earlier ones as it was based on new structural and isochore maps produced in 2004, as well as fault polygons updated in the same year. It was generated and populated with petrophysical properties using RMS.The geological model comprises of 20 structural maps, while the reservoir simulation consists of 22 layers. The CPU time for simulation is about 4 hours for the history period – for production history matching from 1997 to 2006 (Eirik, 2010; Statoil, 2005).

Table 6.3 UTM coordinates and depth of the Norne Field simulation model

Axis	Min	Max	Delta
X	455465.75	462761	7295.27
Y	7319112.25	7327079	7966.75
Depth	-3090.13	-2439.11	651.02

Porosity, permeability and net-to-gross, shown in Figure 6.30a-c respectively, are imported from the geological model. Permeability in the vertical direction is represented as the ratio of vertical permeability to horizontal permeability, while MULTZ-maps generated from well and pressure data, and imported from the geological model, are used to model the vertical barriers to flow. The transmissibility values of the MULTZ-maps are potential candidates for updating during history matching. Figure 6.30d shows the initial oil saturation of the simulation model.

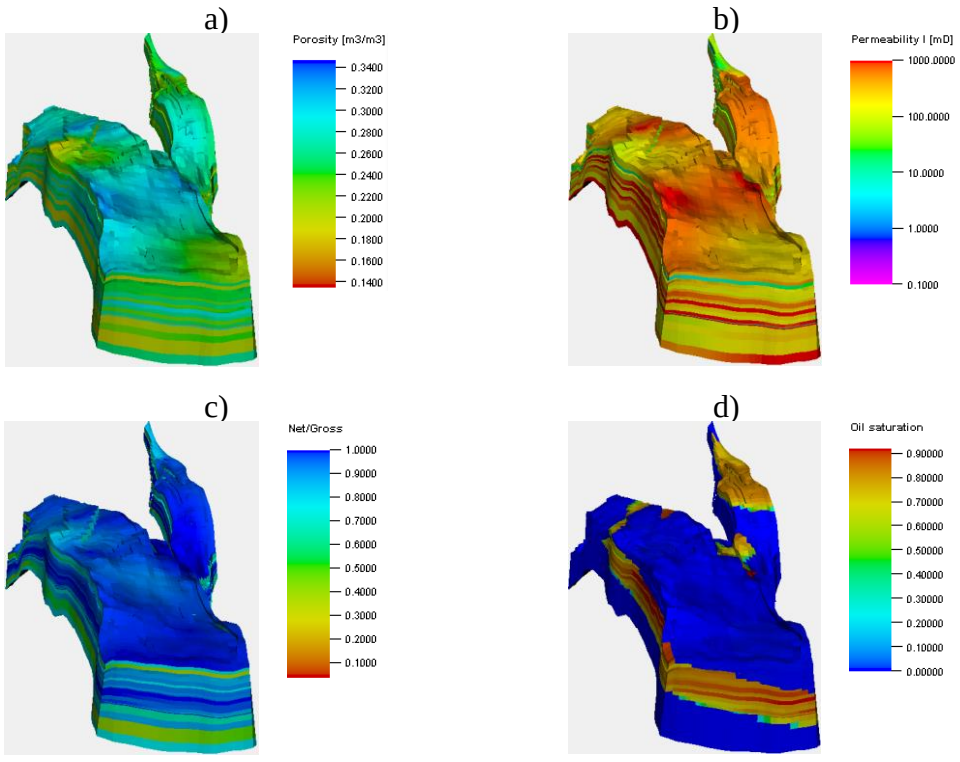

Figure 6.30 Norne Field simulation model showing a) Porosity, b) Permeability, c) NTG and d) Initial oil saturation

The Norne Field is highly compartmentalised with several 'minor' faults with transmissibility modelled using the Eclipse keyword MULTFLT. Some flow regions are also defined based on the main compartments of the field defined by the major faults. The

transmissibility across those defined flow regions are modelled with the keyword MULTREGT and can be adjusted during history matching. All faults cutting the Garn Fm and the reservoir formations below are considered to have transmissibility equal to zero (sealing faults) based on information gathered from pressure measurements. However, faults within the Ile, Tofte and Tilje Fms are assigned transmissibility values of 0.1 and can respectively be updated during history matching.

For the initialisation of the Eclipse model, two different Corey type relative permeability curves are assigned for the oil-wet system, one for the Tofte Fm, and the other for the other formations. Likewise, two different relative permeability curves are assigned for the gas-oil system, one for all absolute permeability values less than 250 mD, and the other for all absolute permeability values greater than 250 mD. Because some injectors are for water and gas injection and need be modelled as WAG injectors, the keyword for Eclipse WAG-hysteresis is used. No Saturation and relative permeability end-points scaling is used in the model. Rather, eleven permeability intervals are defined in the model based on well data, and a bound water saturation/ connate water saturation value (SWL) is assigned to each interval. Scaled relative permeability and capillary pressure curves are then assigned to each of the intervals. The endpoint values (SWL) may be used as tuning parameters..

6.6.2 Identifying Key Uncertainties

Experimental design methods can be used to identify and select parameters of importance based on the sensitivity. In Amit (2013), Principal Component Analysis (PCA) is used to investigate variables such as porosity and permeability model, relative permeability curves, pore compressibility, rock physics models for elastic properties of the rocks and spatial scales of saturation distribution in reservoir sensitivity study, and identified sensitive parameters which were updated in the history matching of oil, gas, water rates and bottom hole pressure and seismic data in the Norne Field E-segment. Amit (2013) ranked the parameters and inferred that rock physics model (presence or absence of cement in the rock) is the most important parameter for time-lapse seismic modeling of the Norne Field while relative permeability curves are the most important parameter for modeling the flow response of the field.

However, from the operator's point of view, flow and pressure communication between formations or regions across faults and stratigraphic barriers are the most important factor in history matching the Norne Field simulation model. Flooding coming from the

water/gas injectors are controlled through fault zonation and fault transmissibility while the oil-water contact rise over time is controlled by adjusting the vertical transmissibility in the stratigraphic barriers (Statoil, 2005). This thesis will aim at adjusting the transmissibility of the carbonate cement barriers at the stratigraphic surfaces to generate models that better match the field water production and the flow response of the model in general

6.6.3 Review of Norne Field Previous History Matching

In this section we discuss, previous history matching studies in Norne Field by the operator, Statoil. Special attention was paid to matching the field pressure, field water cut development, and matching oil and gas production by using data such as pressures from formation tester logs, field measured GOR and water cut, and OWC interpreted from the time lapse data (Statoil, 2005)

In order to get at the correct basis for matching pressures, the reservoir simulation has been done under reservoir volume control. The main parameters updated in the previous history matching cases has been the transmissibilities of the faults and vertical barriers. Adjustments of the relative permeability curves have also been made. In adjusting the history matching parameters, it has been observed that widely different set of parameters can give responses acceptable fitness to the measured production volumes and pressures. In order to reduce this non-uniqueness, and reduce the uncertainty of the model predictions, the time lapse data is expected to provide additional data and dimension.

The vertical barriers to flow are identified as the parameters affecting the pressure, and so for obtaining pressure match the MULTZ parameters are updated. The MULTZ-maps are the vertical barrier maps obtained from observations from wells which are assigned some transmissibility values updated during history matching. Using this approach, Statoil, 2005 showed that the overall pressure match was good except in some well locations where pressure seems to be sensitive to the model geometry – examples are the pressure match in wells F-2H and C-4H both of which are located at the outer edge of the Norne Field main reservoir.

Attempts were also made by Statoil to qualitatively interpret the time-lapse data and match the oil water contact rise in the model with those observed on the seismic data. Synthetic seismic created from the simulation model was compared visually with the measured 4D seismic data or impedance data. Special attention was paid to visual

comparison between the OWC surface interpreted from the time lapse seismic data with the saturation changes simulated using the model. While making the comparison, the vertical barriers that have been updated earlier during the pressure match are further modified to get a better match of the rise in the OWC. As Statoil (2005) pointed out, the rise in the simulated OWC using the 'pressure-matched' model, as compared to the rise observed on the seismic data, shows that OWC development in the model was being prevented by vertical barriers which were too tight. It was therefore assumed that there may be some faults that were not resolved at the seismic scales which may be important for vertical water movement. For instance, to get a more even rise in OWC throughout the C-segment while allowing for local coning around some wells (example, C-2H and B-1H), holes have been created/enlarged in some vertical barriers (Ile1-Ile2 barrier in the middle and southern part of C-segment, Tilje-Tofte barrier near well C-2H and Tofte1-Tofte2 barrier near wells C-2H and B-1H), while some barriers have been made tighter (Tofte1-Tofte2 barrier in the C-segment, Tilje-Tofte barrier in the D-segment).

Visual comparison of saturation and attributes maps generated using the simulation model to the observed time lapse impedance maps also indicated areas for adjustment of fault transmissibility values so as to match the observed time lapse data. Observations from the seismic data has led to extension of C_10 fault north of E-3H while the faults along the SW-NE (main fault direction) in the C-segment have been made tighter.

The observed time-lapse data indicate an undrained area south of the injector well C-1 H and a higher rise in the OWC west of the injector. This observation was confirmed from tracer data which indicate that water from the injector C-1H reaches the wells B-1H and D-3AH in the north of the C-segment before getting to the well B-2H in the south of the segment. To improve the match south of C-1H, the injection water had to be directed from C-1H westwards as against southwards as in the previous model. Consequently, while the faults C_12, C_08 and C_01 around the injector C-1H are kept relatively open in the Tilje and Lower Tofte Fm, they have been made tighter in Ile and upper Tofte Fm. For the same reason, two additional faults which are respectively perpendicular to C_01 and C_08 were introduced south of C-1H. However, huge uncertainty remains over the areal extent of the pronounced rise in OWC predicted by the simulation model around well B-1H since the time lapse data in the west of the well is of very poor quality. On the other hand, the area around the injector C-3H was very uncertain because the large amount of free gas makes the 4D data difficult to interpret (Statoil, 2005)

With the results from the pressure and time lapse matches, further local adjustments were been made in the transmissibility values of some faults and vertical barriers so as to match the water cut and the GOR of the individual producer wells. Relative permeability curves were given slight adjustments to match the profiles of field GOR and water cut. Rapid increase in field water cut observed in the 2002 field measurements and onwards means that the model had to be adjusted so as to have more mobile water. The adjustments notwithstanding, the model field GOR was observed to be too low in 2004 due to low GOR in wells D-1 CH and D-2H in that period (Statoil, 2005).

There were suggestions to implement saturation end-point scaling in the model and investigate the impact of the end-point values on reservoir response. With end-point values bearing uncertainty, they were suggested as candidate tuning parameters in history matching. The saturation end point values that could be implemented include the end-point values for drainage and the end-point values for imbibition (Statoil, 2005).

Seismic history matching of the Norne Field has also been implemented in computer-assisted (automated) history matching workflow. For instance, Lygren *et al*. (2005) implemented a gradient-based optimisation on a global objective function comprising of 4D seismic (AI) data and RFT pressure measurements. Fault transmissibility and vertical transmissibility (MULTZ: selected using layers with RFT discontinuities) multipliers were updated iteratively to obtain a reasonable match of both 4D seismic data and RFT. In addition, new insight was gained about the possible reservoir flow patterns, and where the model matches the 4D seismic it is used with confidence for well planning.

Dadashpour *et al*. (2007) used nonlinear Gauss-Newton optimization technique in automatic history matching workflow to estimate and update reservoir porosity and permeability by integrating both production history (in the form of well pressures and flow rates) and 4D seismic data in the form of zero offset amplitudes and amplitude versus offset (AVO) gradients. They tested the approach on a two-dimensional semi-synthetic data based on field data from Norne Field, and observed that using only 4D seismic data is more accurate for permeability and porosity estimation than using only production profile; and integration of both data reduces the non-uniqueness of the reservoir parameter models.

On the other hand, Eirik (2010) presented a study on the sensitivity of production response given Norne Field fault transmissibility and horizontal permeability and noted some high level of uncertainties in the C-segment's fault properties which could not be resolved

through automatic history matching using only production data. He suggested that incorporation of time-lapse seismic data in the history matching workflow could enhance the understanding of flow and saturation patterns and general flow, and help in resolving the uncertainties.

6.6.4 Seismic Signatures at the Injector Locations

One major challenge in interpreting the time lapse signatures of Norne Field is that the OWC moves up unevenly inside the flat horst structure making it difficult for the time lapse effects to be seen on the top reservoir reflector (Osdal et.al, 2006). This challenge is further complicated due to pressure changes arising from production below bubble point, strong pressure increase around the injector areas (Alsos et.al, 2009), as well as the mixed effect of gas and water from Water Alternating Gas Injection (WAG) at some injector locations.

Before using the inverted seismic data maps (impedance data from section 6.4.3) for history matching, we quality check them by noting the reservoir changes arising from pressure changes, gas distribution and water front movement to be sure that they are consistent with what is known in the theory, summarised in Table 2.2 in Chapter 2 of this thesis.

We apply our qualitative check to the impedance data derived from seismic inversion by assessing the 4D difference signatures in the time-lapse vintages (2003-2001, 2004-2001 and 2006-2001) based on the injection history. All active injectors (as at 2006) are used in this study and include: C-1H, C-2H, C-3H, C-4H, C-4AH, F-1H, F-2H, F-3H and F-4H (Figure 6.31).

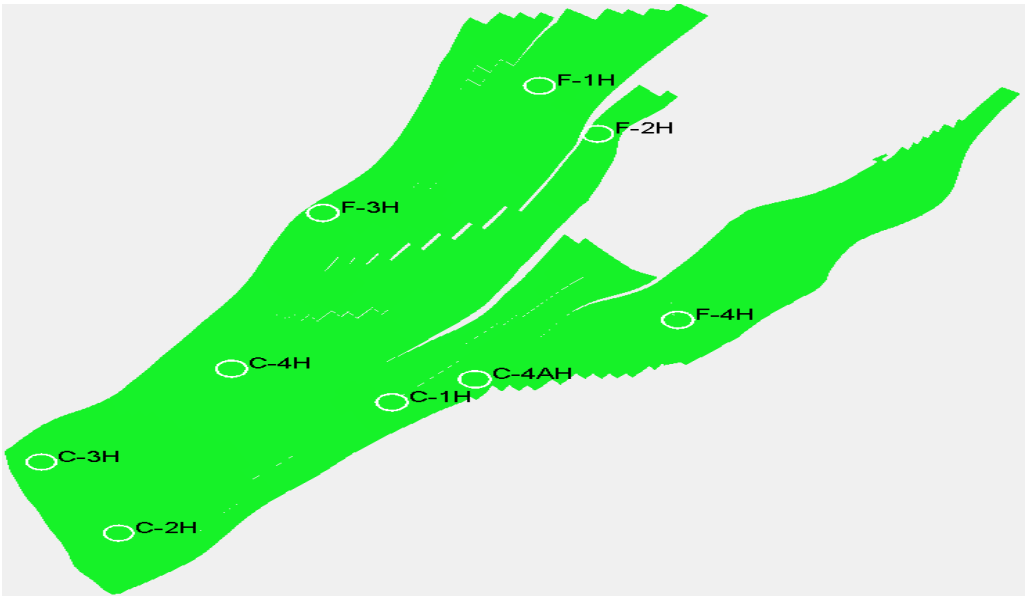

Figure 6.31 Map showing the injector well locations

C-1H was designed for WAG. The perforation interval was between Top Tofte 1.2.2 and Base Tilje 3 to allow injection of water or gas into the water leg. Water injection in well C-1H started on 21st July 1998. There was switch to gas injection on November 10 1999, and gas injection through the well continued till June 19 2001. This was about the time the 2001 4D seismic was shot, and the region around the injector perforation should be expected to have low impedance due to softening effect of gas. However, the well was then switched to water injection, and it continued to inject water until August 14 2002 when it switched again to inject gas for a short period (approximately 2 weeks). The well was switched to inject water again from September 2 2002 to January 2 2003 followed by another short period (9 days) of gas injection, short period of water injection (9 days), and another short period of gas injection (3 weeks). Within the period from February 14 2003 to July 10 2003, the well injected water continuously. The 2003 4D seismic was shot at about this time. Therefore, for the time lapse effect due to the injection activity at C-1H between the first 4D survey in 2001 and second survey in 2003 is complicated by the mixed effect of gas and water. An inverted AI section through the well shows hardening effect (blue colour) at the region in the vicinity of C-1H perforation (Figure 6.32a). This is a reflection of long period of water injection as compared to the much shorter period of gas injection within the 2001-2003 time lapse period. The period between the second survey in 2003 and the third survey in 2004 followed a similar WAG injection pattern resulting in slightly more noticeable hardening effect in the 2001-2004 impedance section (Figure 6.32c). From the time of 2004 survey to the time of fourth survey in 2006, only water was injected through well C-1H, and further increase in impedance is easily noticeable (Figure 6.32d). Note that we have chosen the nomenclature to subtract new survey from older survey. Old survey minus new gives a red impedance colour in the plots for pressure up or gas out of solution, blue for water saturation increase or pressure draw down.

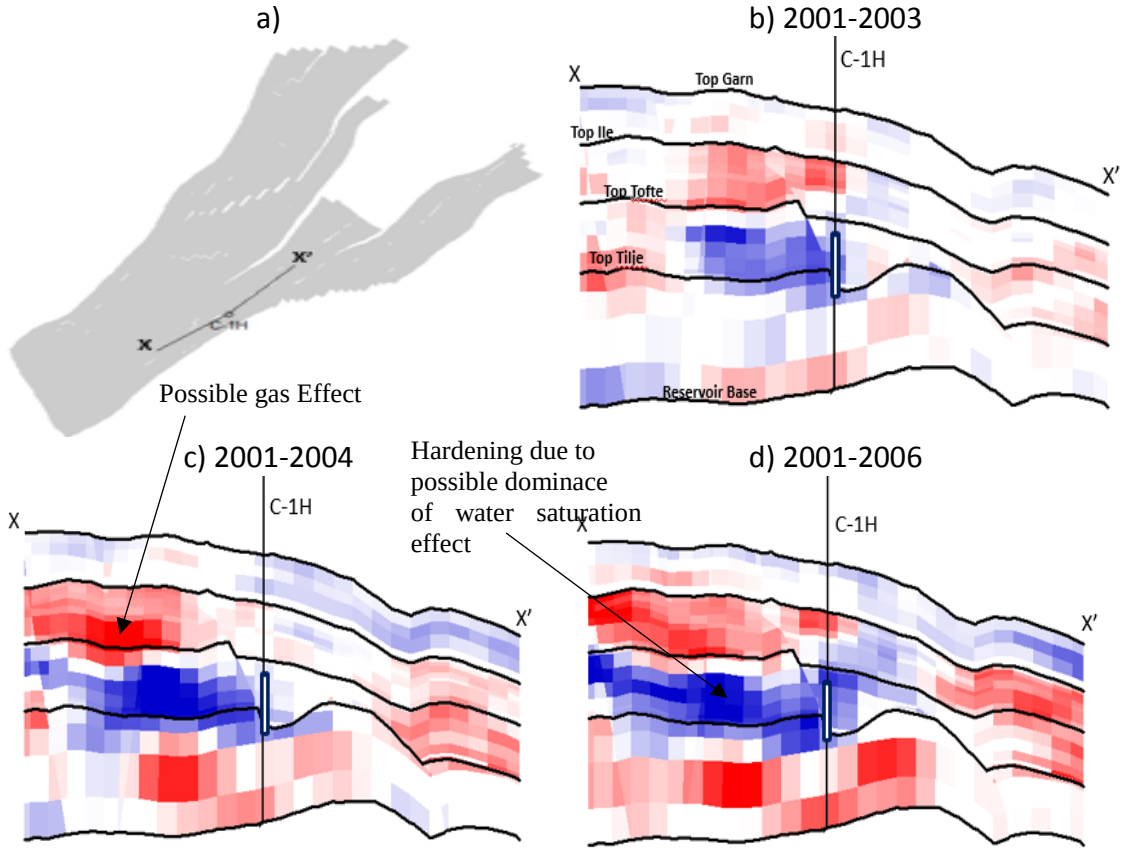

Figure 6.32 a) A section X-X' through the injector C-1H well path. The AI on section X-X' for the: b) 2001-2003 difference survey, c) 2001-2004 difference survey, and d) 2001-2006 difference survey.

C-2H was also designed for WAG. The perforation interval was originally between Top Tilje 4 and Base Tilje 3 to allow injection of water or gas into the water leg. Injection of water through the perforation started on 21st January 1999. The well was not switched for gas injection within the period under review (July 2001 – July 2006) but from July 15 1999 injection of water into the well was through re-completed interval between Top Tofte 2.1.2 and Base Tilje 3. It does appear that the effect of increased pressure around the perforated interval of the injector dominated the seismic response as gradual decrease in impedance (red colour) is noted especially for the period between 2001 and 2004 and the period between 2001 and 2006 (Figures 6.35b and 6.35c). However, in the area above the completion and going northwards, a saturation effect dominates evident in the rising water contacts between the survey times. The green and purple dotted lines in Figure 6.33d are the 4D interpretations of the 2006 OWC and 2001 OWC respectively by Statoil (this can be found here: http://www.ipt.ntnu.no/~norne/Full-Norne/horisons/). The increase in impedance due to rising water contacts is reflected in the hardening events (blue colours). Below the 2001 OWC line, pressure-driven effect is easily recognised (the red signal is a softening effect)

In the Norne Field, the rise of the OWC is easier to interpret in some parts (for example around the water injector C-2H). On the other hand, the effect of gas injection around the OWC and in the water zone masks the effect of the OWC rise (Oddvar *et al*. 2006) in other areas (Oddvar *et al*. 2006).

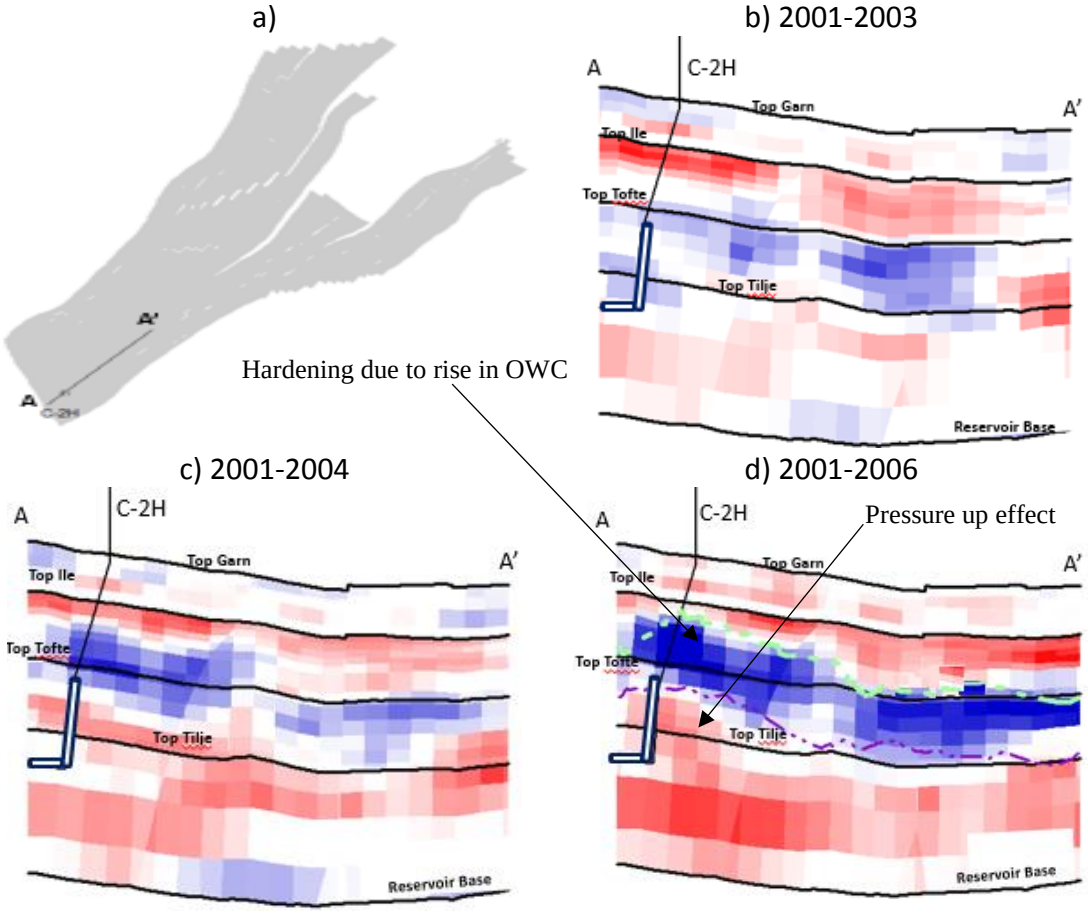

Figure 6.33 a) A section A-A' through the injector C-2H well path. The AI on section A-A' for the: b) 2001-2003 difference survey, c) 2001-2004 difference survey, and d) 2001-2006 difference survey: the green dotted line is the 2006 OWC and the purple dotted line is the 2001 OWC. The signature here correlates nicely with the oil water contacts.

Well C-3H is another water injector in the Norne Field which can easily be converted to inject gas. Similar to C-2H, it is located in the southern part of the field and injects water into the water leg through the perforation interval which is between Top Tofte 2.1.2 and Base Tile 4. Injection started on 21st May 1999. Looking at the period under study, C-3H was switched from water injection to gas injection on August 16 2001. It was switched to inject water on September 10 2001 and again to gas injector on December 29 2001. After a long period of gas injection, the well was switched to inject water on October 14 2002 and back to gas on January 2 2003. Gas injection continued until July 10 2003. So, for time lapse between 2001 and 2003, C-3H had much more period of gas injection than water injection. The interpretation of OWC is difficult here and the OWC map provided

by Statoil does not cover the area around this injector. Although the well is in the southern part of the field, the effect of gas injection around the OWC interferes with the effect of the OWC rise. The reservoir pressure in the vicinity of C-3H is below the Norne Field seismic threshold pressure (see section 6.5.1), and so pressure changes result in no significant seismic velocity change. Saturation effects therefore dominate the changes in impedance. The softening effect of gas in the vicinity of the injector is observed in the difference between the 2001 and 2003 AI (Figure 6.34b). The water alternating gas injection continued to the time of the third 4D survey (July 2004), but for the period from 19 January 2004 to 25 July 2004 and from September 20 2004 to the time of fourth 4D survey (August 2006), the well injected only water. The overall effect is increased hardening around the injector location (Figures 6.36b and 6.36d). The bounding fault of the main field which is located north of the well may be the reason for the hardening effect noticed mostly south of the well.

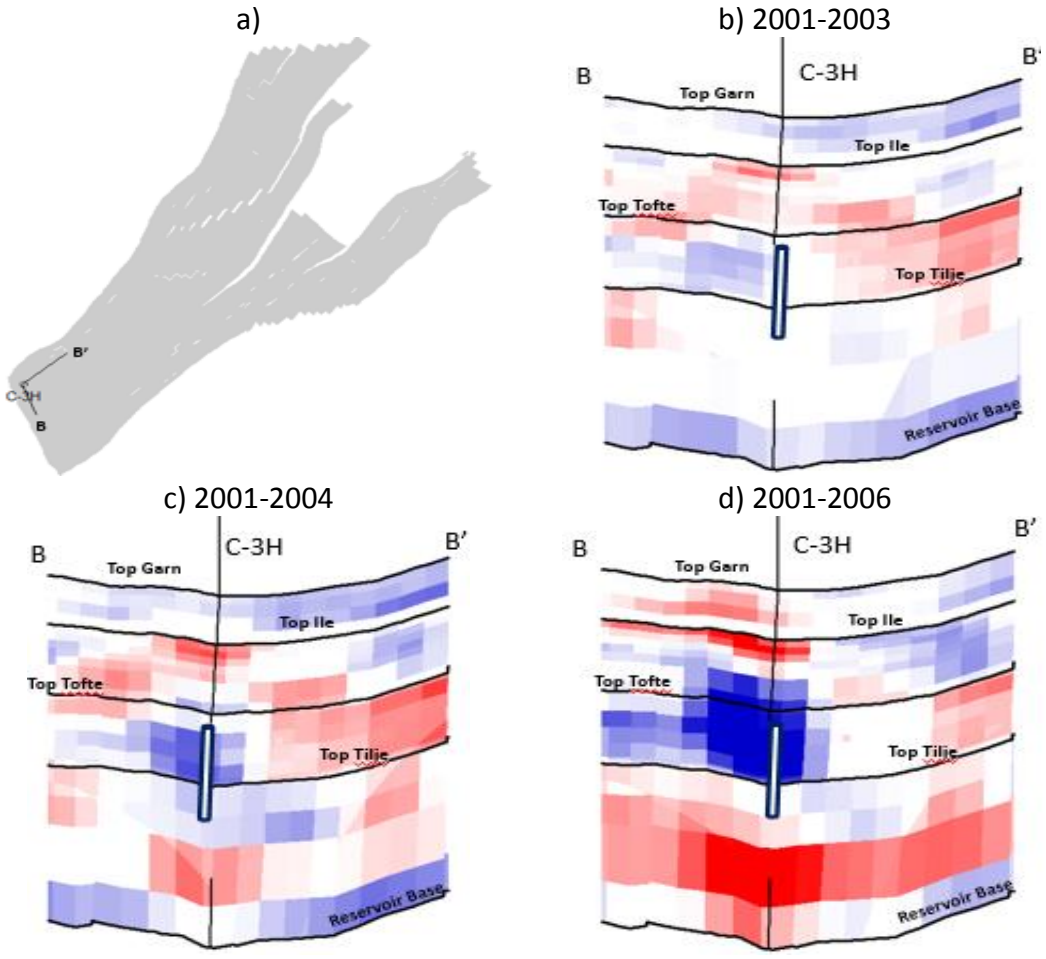

Figure 6.34 a) A section B-B' through the injector C-3H well path. The AI on section B-B' for the: b) 2001-2003 difference survey, c) 2001-2004 difference survey, and d) 2001-2006 difference survey. Overall, the area around the injector C-3H is very uncertain because the large amount of free gas makes the 4D data difficult to interpret (Statoil, 2005)

Pressure Testing (Repeat formation Testers, RFT) in well C-3H showed that the communications between the Ile, Tofte and Tilje Fms were poor which explained why the injections from C-1H and C-2H increased the pressure only in the Tilje Fm (softening effect in Tilje Fm) and not in the Tofte Fm (Statoil, 1999).

Next, we look at the signal around well C-4H which was a vertical gas injector. The well injected only gas into the water leg through perforations between Top Tofte 1.2.2 and Base Tilje 3. Injection started on November 22 1997 but the well was shut on November 8 2003, and then plugged because it was contributing to high gas production in the neighbouring producer wells. As expected, the difference in impedance between 2001 and 2003, as well as 2001 and 2004, shows strong softening (red colour) in the vicinity of the well (Figure 6.35b and 6.37c).

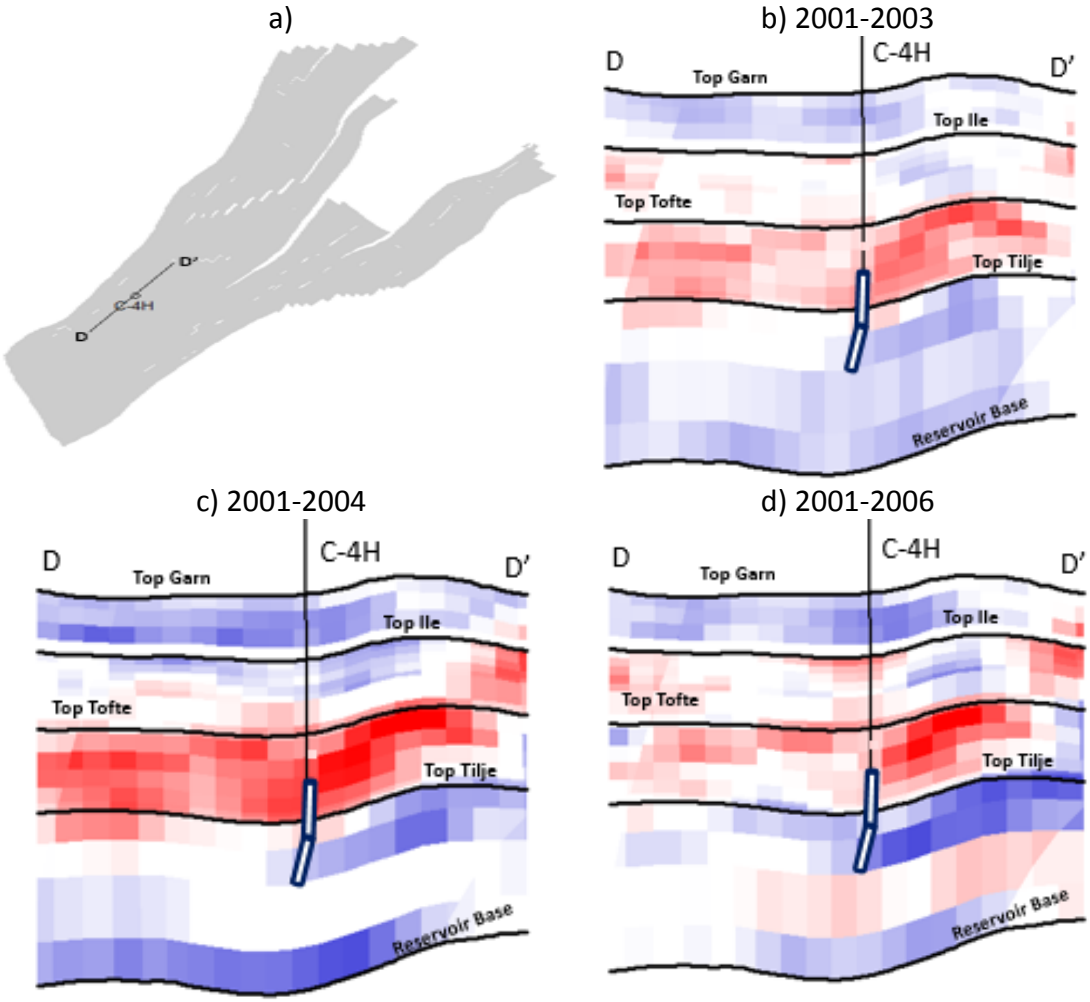

Figure 6.35 a) A section D-D' through the injector C-4H well path. The AI on section D-D' for the: b) 2001-2003 difference survey, c) 2001-2004 difference survey, and d) 2001-2006 difference survey. The red signal (softening) around the injector perforation interval is interpreted as gas-driven effect

After well C-4H was plugged. It was side-tracked to well C-AH which was perforated for injection into Ile Fm (between Top Ile 2.2 and Base Ile 1.2). Injection of water through

well C-AH started on January 20 2004. As expected, the difference in impedance between 2001 and 2003 shows no strong signal indicating a period of no injection activity (Figure 6.36). As illustrated in the figures, 2001-2004 and 2001-2006 AI difference sections through the well path of C-4AH show some strong softening signal in the vicinity of the perforations in Ile Fm. As it turned out, C-4AH was placed in a confined fault block between the C-segment and G-segment. The softening signal indicates decrease in AI resulting from pressure build up in the confined area.

Surprisingly, some strong hardening events are seen near C-4AH well path in the Garn Fm indicating increase in impedance. The increase in impedance is unexpected because the well was not perforated in the Garn Fm, and upward communication across the sealing Not shale would normally be impossible. The hardening was therefore originally interpreted to be the side lobe effect of the strong softening signal at the perforated Ile Fm (Huang *et al*., 2013). Flooding of the Garn Fm was not ruled out and the results of 2010 Reservoir Saturation Tool (RST) recordings in the well confirmed that the Garn Fm was flooded. It is still unclear what caused the movement to the Not Fm but a temperature log acquired in 2010 suggested that no injected water entered the Garn Fm from the Ile Fm (Huang *et al*., 2013). So, the possibility of water moving into Garn Fm from Ile Fm through fractures from excessive injection pressure is ruled out. A possible explanation will be water encroachment from the aquifer through the down flank of the area located between the C and G-segment.

a)

b) 2001-2003

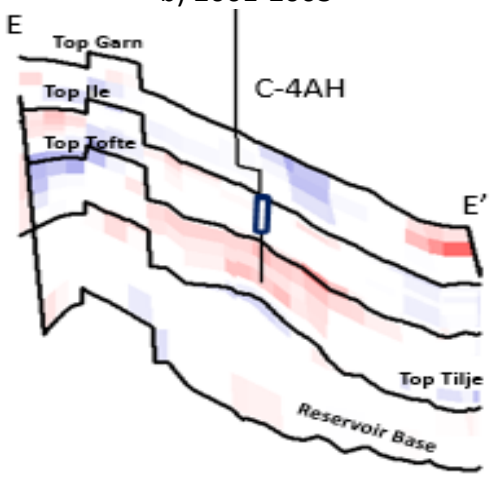

c) 2001-2004

d) 2001-2006

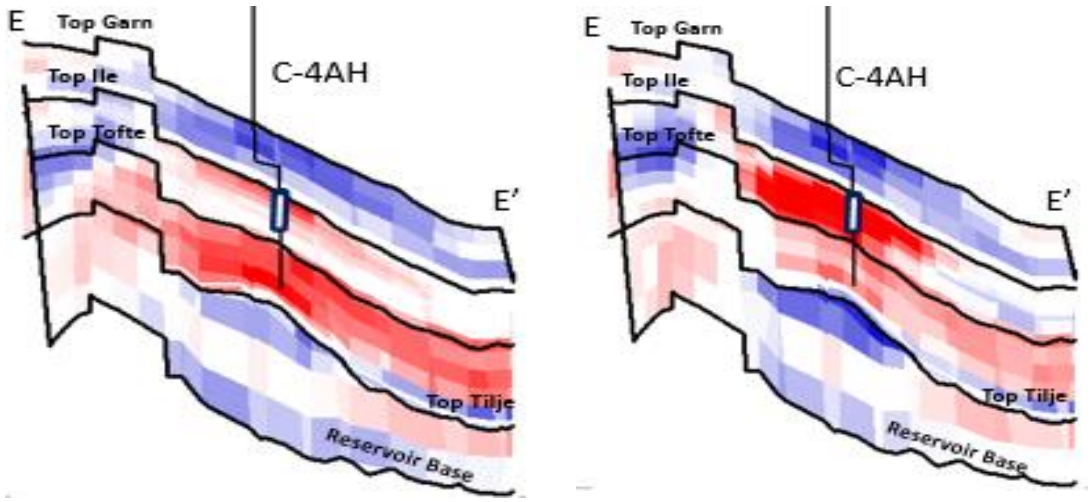

Figure 6.36 a) A section E-E' through the injector C-4AH well path. The AI on section E-E' for the: b) 2001-2003 difference survey, c) 2001-2004 difference survey, and d) 2001-2006 difference survey. The red signal (softening) around the injector perforation interval is interpreted as pressure-driven effect

So far, we have looked at the injectors at the C-segment of Norne Field. Next we study the information carried by the difference data in the AIs of the 4D vintages based on the injection history for the injectors in the E-Segment (F-1H and F-3H), D-Segment (F-2H) and G-Segment (F-4H).

Well F-1H is a water injector located in the North of the E-Segment, designed to inject water in the water leg through perforations between the Top Ile 2.2 Fm and Base Tofte 2.1.1. Injection from the well commenced in September 1999, and for the period under review only water was injected. The softening signal in the vicinity of well F-1H (Figure 6.37b, 6.39c and 6.39d) indicates the effect of pressure. Interpretation of pressure-driven time lapse in the Norne Field is difficult because of the pressure dependency of Norne Field P-wave velocity (discussed under section 6.5.1). The pressure at the vicinity of F-1H exceeds the threshold pressure of 310 bar, exemplified in the pressure map of Tofte Fm comparing the simulated pressures in 2003 (Figure 6.38b), 2004 (Figure 6.38c) and 2006 (Figure 6.38d) to the initial pressure (Figure 6.38a).

Above the threshold pressure, as mentioned previously, pressure changes result in significant P-wave velocity changes in Norne Field. The softening signals are therefore strong as pressure effect dominates saturation effects. Besides, pressure testing from the well confirmed good communications between the Ile and Tofte Fms (Statoil, 1999).

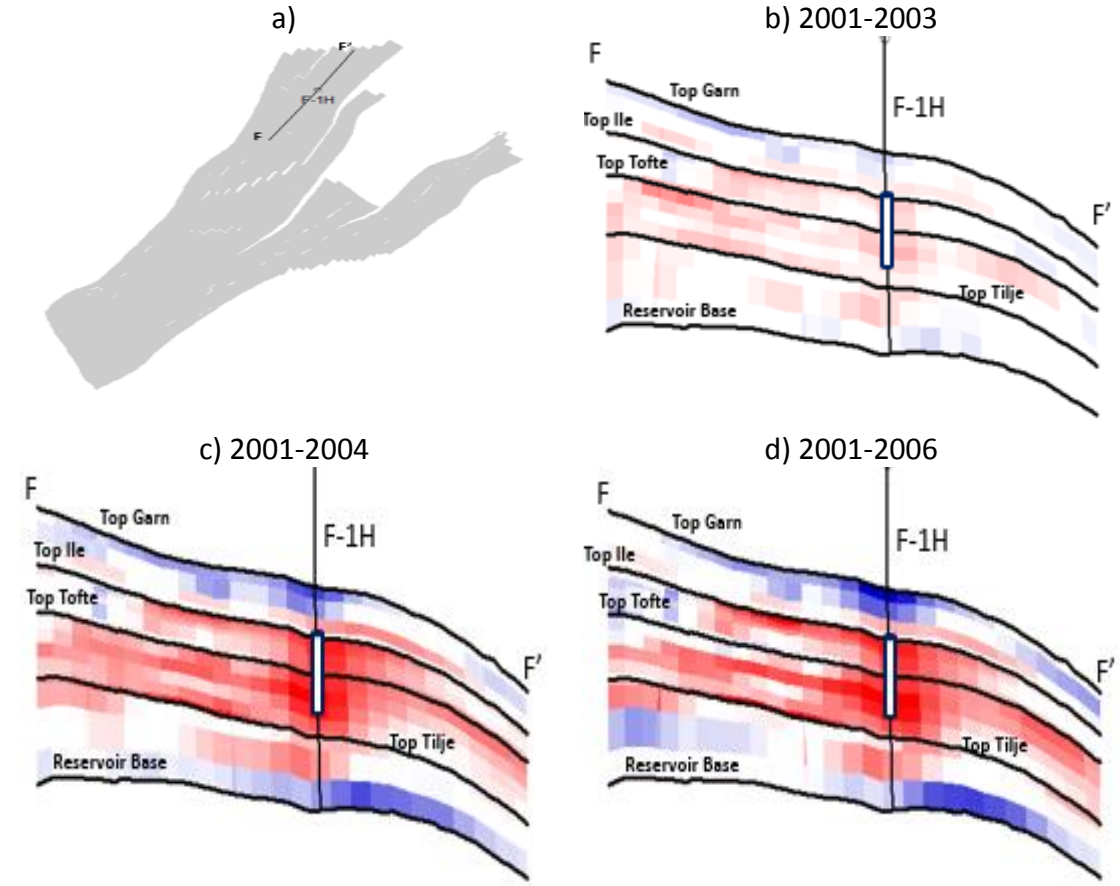

Figure 6.37 a) A section F-F' through the injector F-1H well path. The AI on section F-F' for the: b) 2001-2003 difference survey, c) 2001-2004 difference survey, and d) 2001-2006 difference survey. The red signal (softening) around the injector perforation interval is interpreted as pressure-driven effect

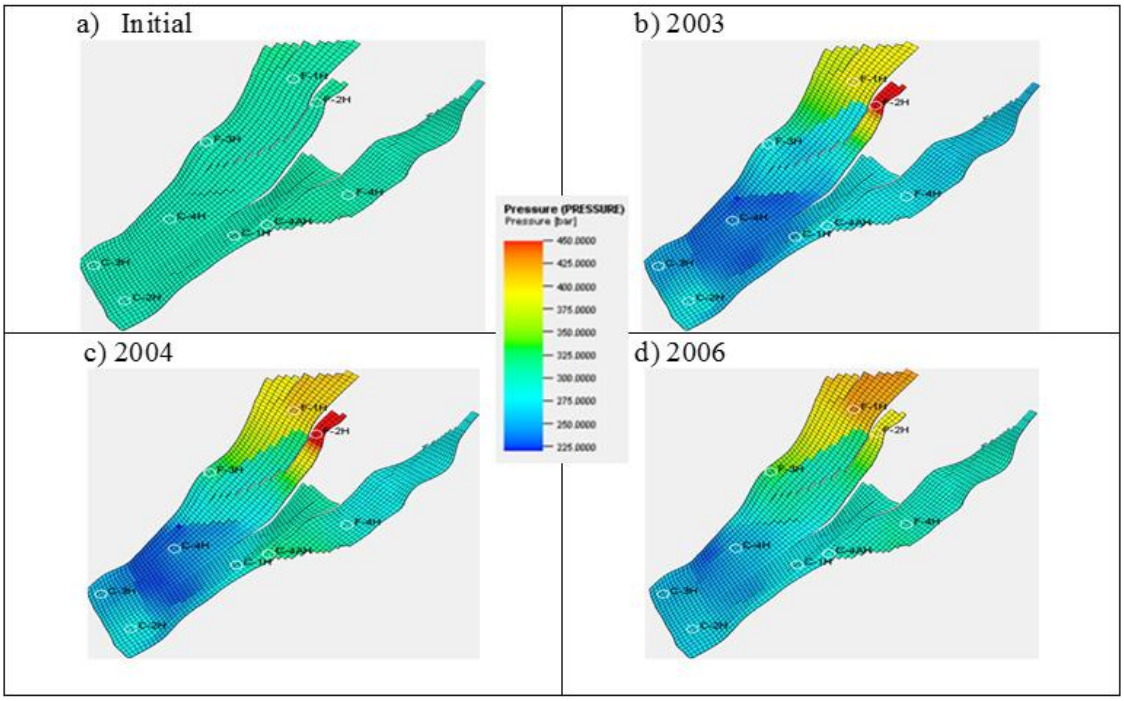

Figure 6.38 Comparing the reservoir simulation pressures at a) initial conditions to pressures in year b) 2003 difference survey, c) 2004, and d) 2006 mapped for Tofte Fm. The high pressures at injector F-1H and F-2H is evident in the maps during injections.

Well F-2H is a water injector located in the north of the D-Segment perforated within the interval of Top Ile 2.2 Fm and Base Tofte 2.1.1. Fluid injection through this well started on October 13 1999, and only water was injected within the period under review. Similar to F-1H, the reservoir pressure around F-2H is high (above the previously mentioned threshold) and pressure testing in this well also confirmed that the communication between the Ile and Tofte Fms is good (Statoil, 1999). Pressure-driven effects (softening due to pressure increase around the injector area) dominate the seismic signal in the vicinity of the well completion interval (Figure 6.39).

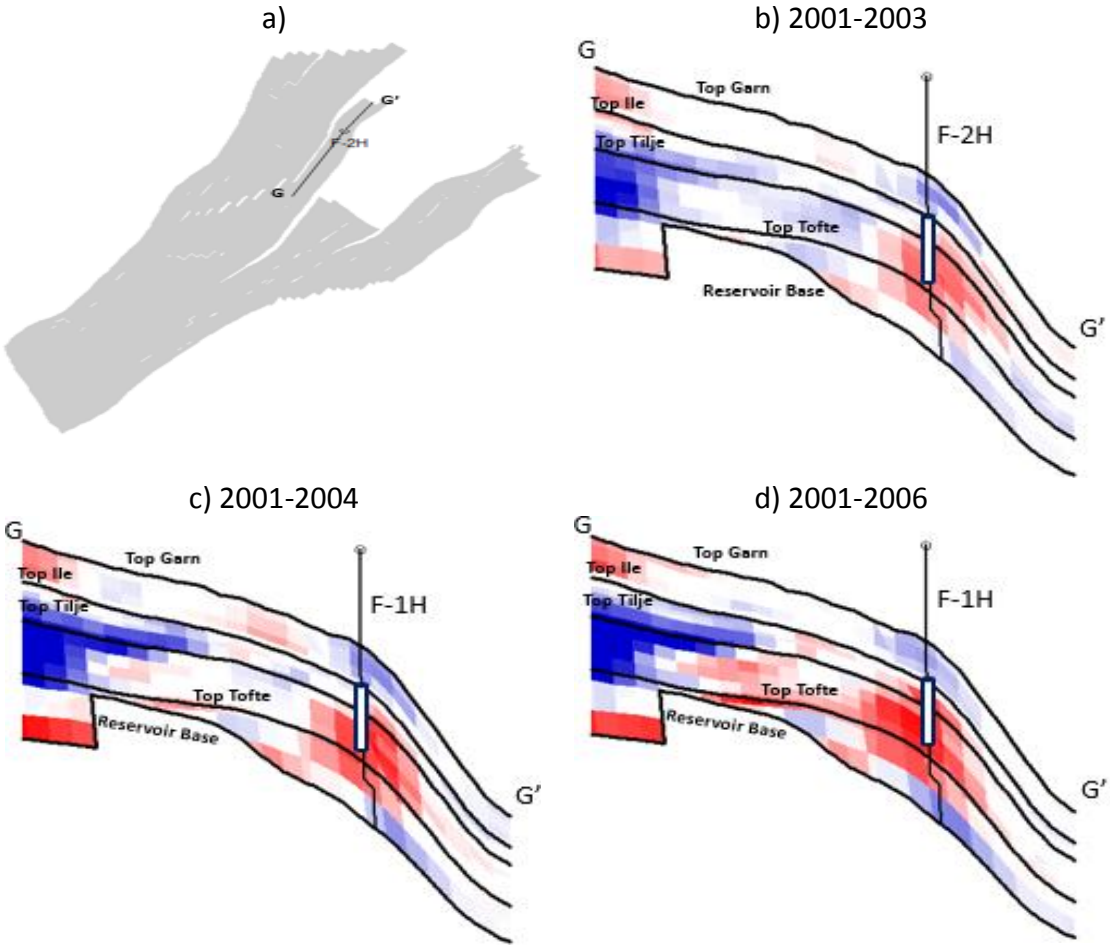

Figure 6.39 a) A section G-G' through the injector F-2H well path in the D-Segment. The AI on section G-G' for the: b) 2001-2003 difference survey, c) 2001-2004 difference survey, and d) 2001-2006 difference survey. The red signal (softening) around the injector perforation interval is interpreted as pressure-driven effect

Next, we interpret the observed impedance signal near the water injector F-3H located in the south-western part of the E-segment. The perforation interval for this well is within the interval between Top Tofte 2.1.3 and Base Tilje 3. Injection of water through the well started on September 22 2000, and only water was injected during the time lapse periods under review. Again, softening effect (red colour) is observed due to the pressure increase

in the vicinity of well perforation while hardening event (blue colour) is observed due to the rising oil water contact in the Tofte Fm (Figure 6.40).

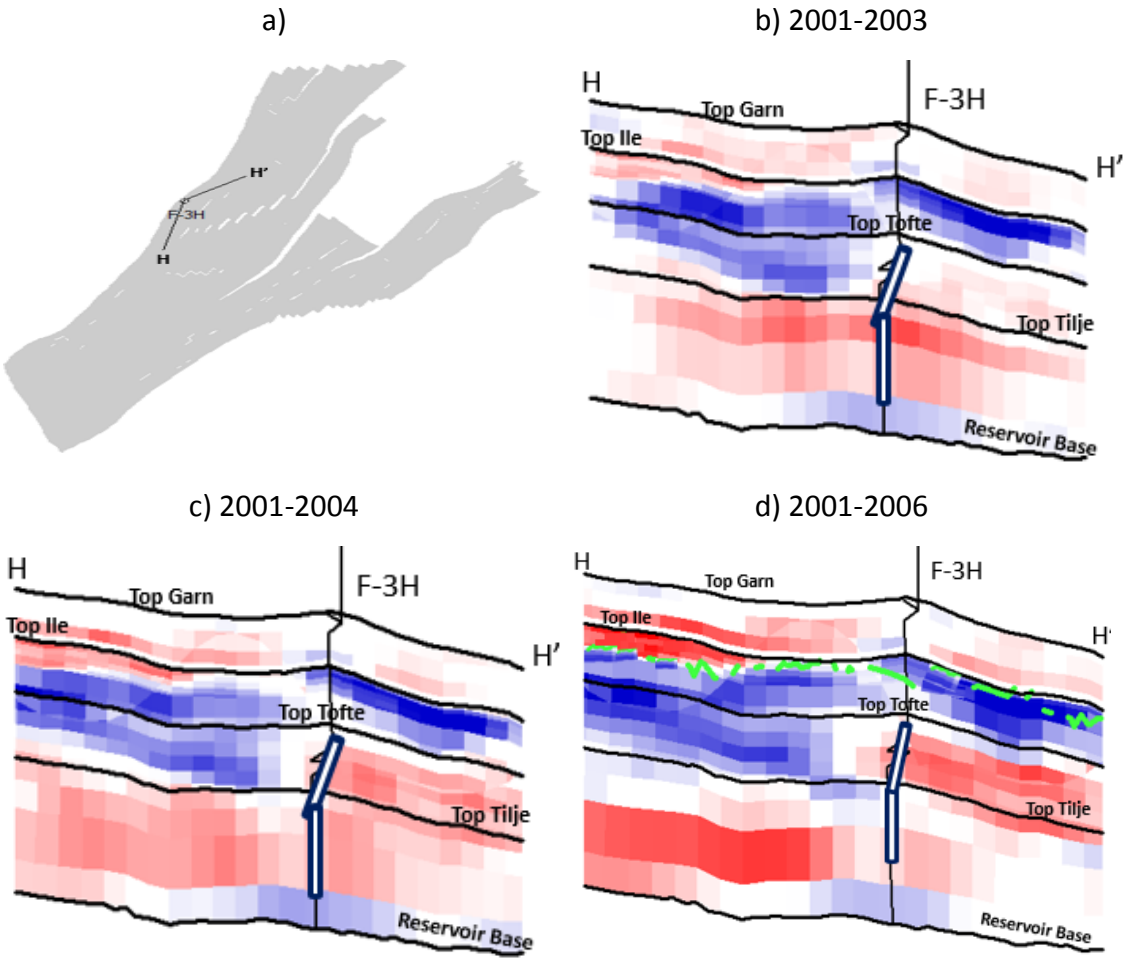

Figure 6.40 a) A section H-H' through the injector F-3H well path in the E-Segment. The AI on section H-H' for the: b) 2001-2003 difference survey, c) 2001-2004 difference survey, and d) 2001-2006 difference survey. The red signal (softening) around the injector perforation interval is interpreted as pressure-driven effect. Water rise from is responsible for the hardening event (blue colour) and the 2006 OWC (the green dotted line) is interpretable here.

Lastly, we look at the seismic behaviour around the injector F-4H which was completed in the Garn Fm downflank of G-Segment. Injection through F-4H started on September 10 2001 to provide pressure support for the oil producer E-4AH. The producer (E-4AH) began production in July 2000. The G-segment is an oil accumulation in the Garn Fm with no initial gas cap but at the time of first time lapse survey in 2001, pressure in the G-segment had depleted below the bubble point resulting in gas ex-solution: the pressure was approximately 200 bar in July 2001 (Statoil, 1999). The difference between the gas accumulation in 2001 and 1997 is shown Figure 6.41a. There was no pressure barrier between the E-4AH and the rest of the G-Segment; so, the entire oil accumulation in the segment experienced the pressure drop and gas ex-solution. This resulted in low

impedance across the Garn Fm of the G-segment. Injection from F-4H then resulted in a pressure increase in the segment. As expected there is softening in impedance around the injector (Figure 6.41b) but away from the well in a northward direction, hardening events are seen and are attributed to gas dissolution in oil due to pressure increase.

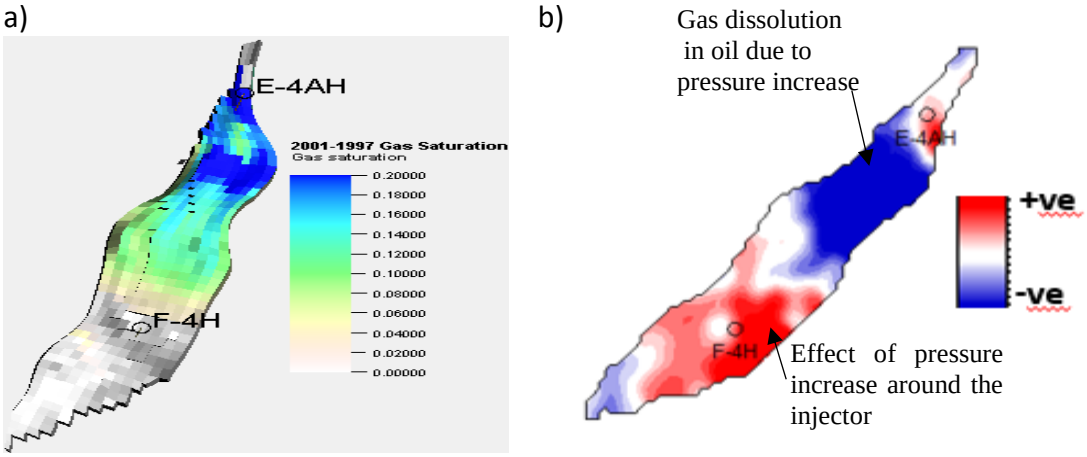

Figure 6.41 Map of the Top Garn in G-segment showing a) Difference in Gas saturation from the Norne Field simulation model between 2001 and 1997, and b) Change in AI 2001-2003: the 2003 impedance data was subtracted from the reference 2001 impedance data so that positive values (red colour) indicates softening event while negative values (blue colour) indicates hardening.

6.6.5 Seismic Signatures at the Producer Locations

In the previous section, it has been demonstrated that 4D signals in the Norne Field is difficult to interpret in some parts of the field due to the pressure dependency of the P-wave velocity. This is further complicated by a combination of gas ex-solution, gas dissolution, WAG injection scheme and complex drainage patterns. G-segment is a typical example of where dynamic pressure evolution caused gas dissolution and ex-solution making it challenging to carry out unambiguous interpretation of the 4D signatures. However, in some other parts of the field the 4D signal is dominated by saturation effect, making it easier to interpret the upward movement of water front or rise in OWC. It is possible to identify the saturation-dominated areas by looking at some sections through the simulation model populated with the observed impedance data.

We look at the interpretation sections through some producing wells in the D- and E-segment to see how the changes in impedance at this section correlate with the known oil-water-contacts. Parts of the reservoir with wells producing water within the time intervals of the 4D seismic are preferred. However, any part of the reservoir for which seismic signal is dominated by saturation (water movement) effect is suitable for the analysis as well. In this regard, the producers chosen for the interpretation sections are: i) oil wells producing water (E-1H, E-2H, E-3CH, D-3AH and D-4AH, and ii) oil well

producing at nil watercut (D-3H). Other criteria for choosing the wells include: the reservoir pressures at well vicinity should be above the oil bubble point, and the pressures are below the threshold level so that pressure changes result in no significant velocity changes. For the selected wells, therefore, the change in impedance observed in the section through the well is due to hardening effect of rising water front. The quantitative information gathered from these sections will be analysed with the information from the predicted impedance and may be useful in further calibration of our observed seismic data.

The oil producer E-1H is a good candidate for the study because it produces some water. Water breakthrough on this well started on May 1 2002 and covers the time lapse period under review. Well E-2H is also an oil producer producing with some water-cut, and is expected to be saturated with water in the vicinity of the wellbore. The oil well produced water from February 2002 to July 2005 which is within the time lapse period under review. E-3CH produced water for 17 months starting from July 2005 while D-3AH produced water from July 2002 to June 2005. Water production from well D-4AH started in January 2004 and lasted for about 2 years. The 2001-2006 impedance change was calculated on the respective sections passing through each of the wells (shown in Figures 6.44b, 6.45b, 6.46b, 6.47b, 6.48b, and 6.49b, where the green dotted line is the 2006 OWC interpreted by Statoil). This is compared to the water saturation obtained on the sections from the reservoir simulation model, shown in Figures 6.44c, 6.45c, 6.46c, 6.47c, 6.48c, and 6.48c. In all cases, the 2001-2006 impedance change correlates well with the 2006 oil-water-contact. Also, the simulated water saturation on the same respective sections across the wells show some patterns similar to the change in impedance. Some cells that are saturated with water in both the observed impedance and the simulation model will be selected, and the predicted and observed impedance in those cells will be used to derive a relationship for calibrating the observed seismic. The differences in the pattern of the water saturation interpreted from the observed impedance data and the pattern of the water saturation from the simulation represent the misfit which is intended to be reduced through history matching.

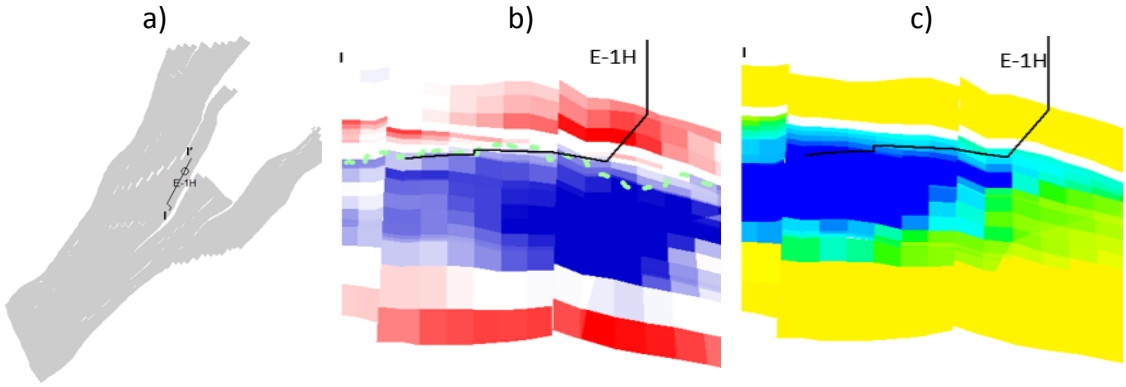

Figure 6.42 a) A section I-I' through the producer E-1H well path in the E-Segment, b) The AI section I-I' for the 2001-2006 difference survey: upward water movement is responsible for the hardening event (blue colour) and the 2006 OWC (the green dotted line) is interpretable here, and c) The 2006-2001 difference in simulated water saturation on section I-I'.

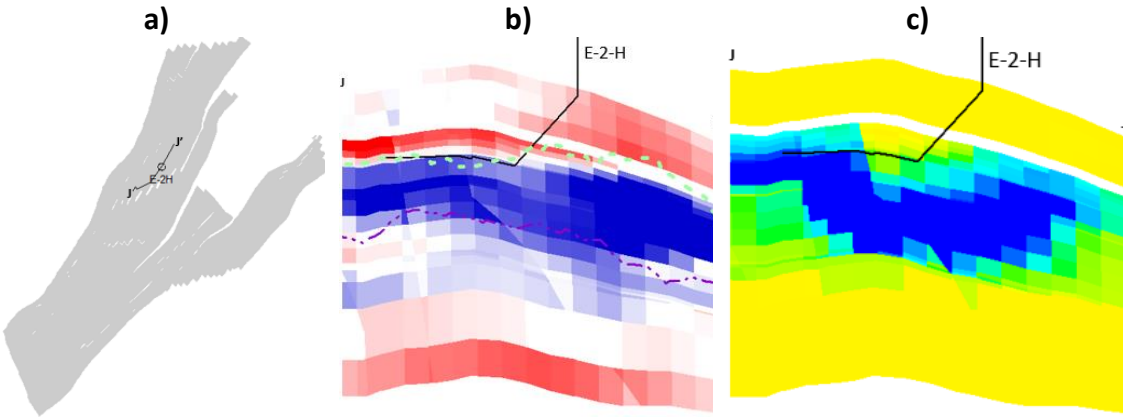

Figure 6.43 a) A section J-J' through the producer E-2H well path in the E-Segment, b) The AI section J-J' for the 2001-2006 difference survey: upward water movement is responsible for the hardening event (blue colour) and the 2006 OWC (the green dotted line) is interpretable here, and c) The 2006-2001 difference in simulated water saturation on section J-J'.

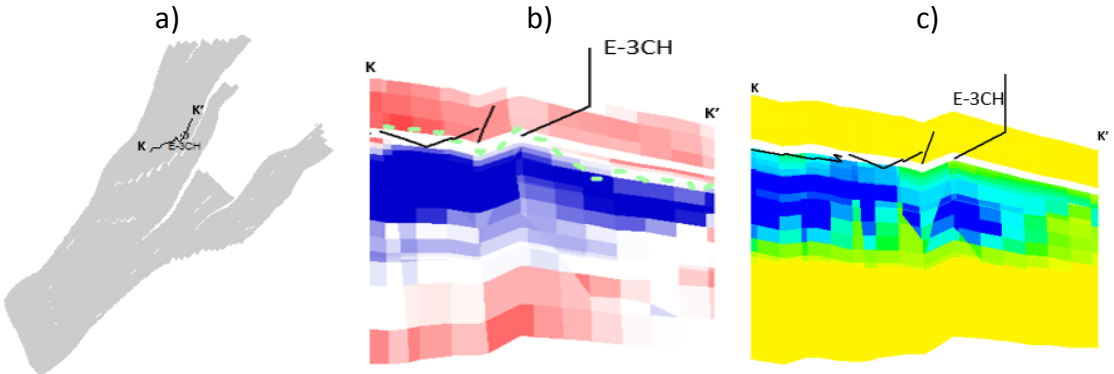

Figure 6.44 a) A section K-K' through the producer E-3CH well path in the E-Segment, b) The AI section K-K' for the 2001-2006 difference survey: upward water movement is responsible for the hardening event (blue colour) and the 2006 OWC (the green dotted line) is interpretable here, and c) The 2006-2001 difference in simulated water saturation on section K-K'.

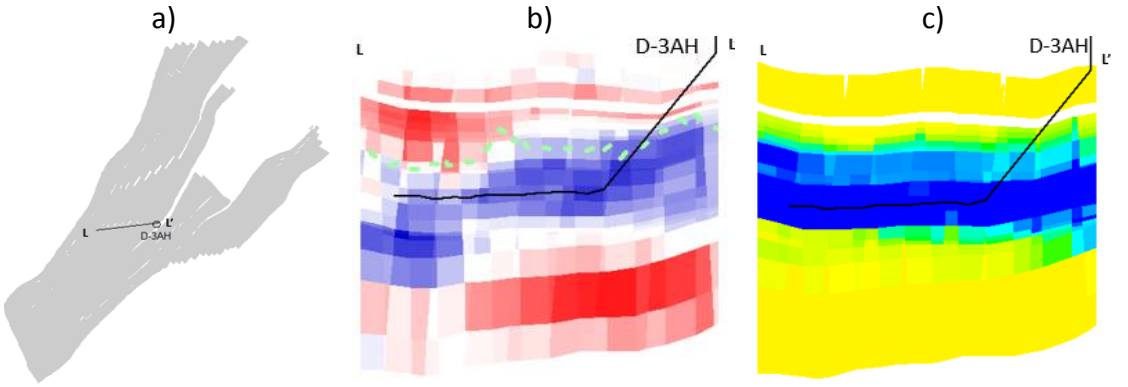

Figure 6.45 a) A section L-L' through the producer D-3AH well path, b) The AI section L-L' for the 2001-2006 difference survey: upward water movement is responsible for the hardening event (blue colour) and the 2006 OWC (the green dotted line) is interpretable here, and c) The 2006-2001 difference in simulated water saturation on section L-L'.

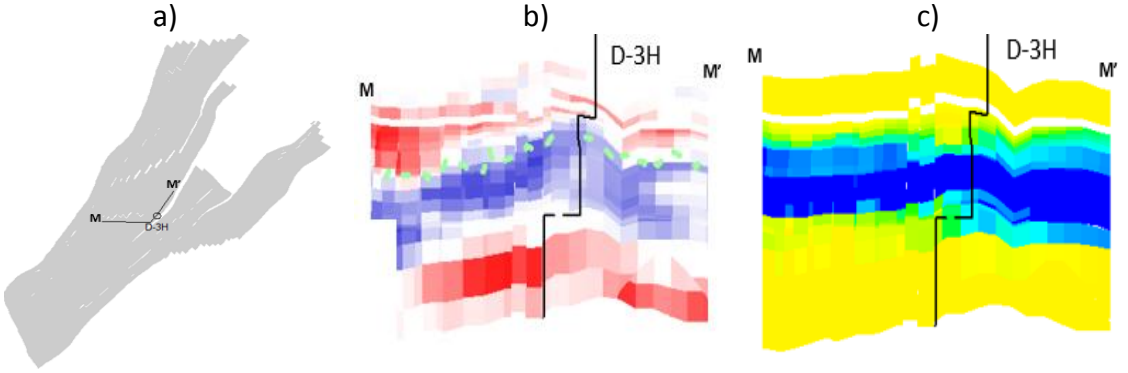

Figure 6.46 a) A section M-M' through the producer D-3H well path, b) The AI section M-M' for the 2001-2006 difference survey: upward water movement is responsible for the hardening event (blue colour) and the 2006 OWC (the green dotted line) is interpretable here, and c) The 2006-2001 difference in simulated water saturation on section M-M'.

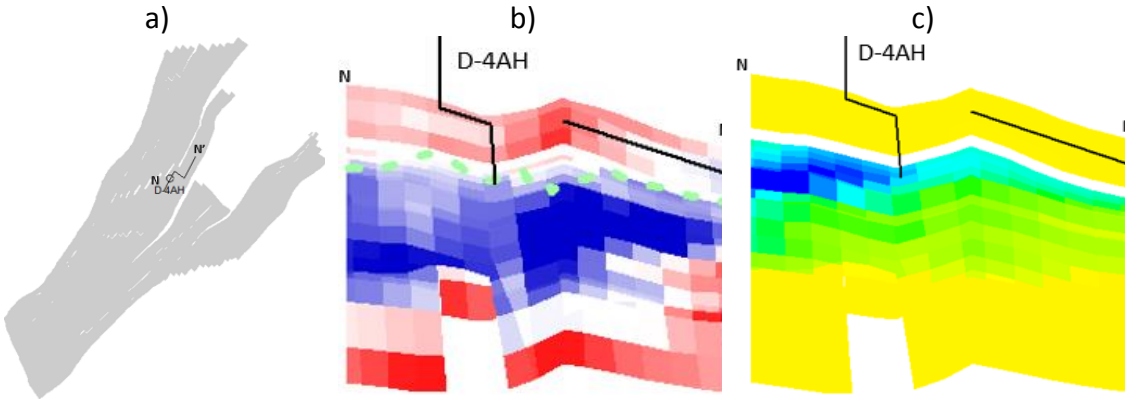

Figure 6.47 a) A section N-N' through the producer D-4AH well path, b) The AI section N-N' for the 2001-2006 difference survey: upward water movement is responsible for the hardening event (blue colour) and the 2006 OWC (the green dotted line) is interpretable here, and c) The 2006-2001 difference in simulated water saturation on section N-N'.

The observed impedance can be correlated with the predicted impedance for the cells or regions where change in impedance indicate water movement and a scalar function can be derived for the normalisation of the observed impedance. We can derive the normalisation equation, or scalar function, by selecting a number of cells from those regions in the Norne Field model for which we have high confidence that the observed 4D signal is a result of saturation effects.

Figure 6.48 shows an arbitrary section cutting across several regions of the reservoir where water saturation effects dominate the observed time lapse signals. The 2001-2006 time lapse impedance data in Figure 6.48b shows that the hardening effect is due to upward movement of water, and the impedance section correlates well with the 2001 and 2006 OWCs interpreted by Statoil. Figure 6.48c shows the reservoir model simulated water saturation on the same arbitrary section. A cut-off value was applied to both the observed water saturation (> 0.46) and the observed impedance difference (< -100) to identify the cells where very strong time lapse signals correspond to high water saturation. The result of the filtering is shown in Figure 6.48d where the cells coloured in blue are the cells selected for deriving the relationship between the observed impedance and the predicted impedance. The relationship in the form of scalar function will then be used to normalise the observed 4D AI data before integrating the data into the Seismic History Matching scheme.

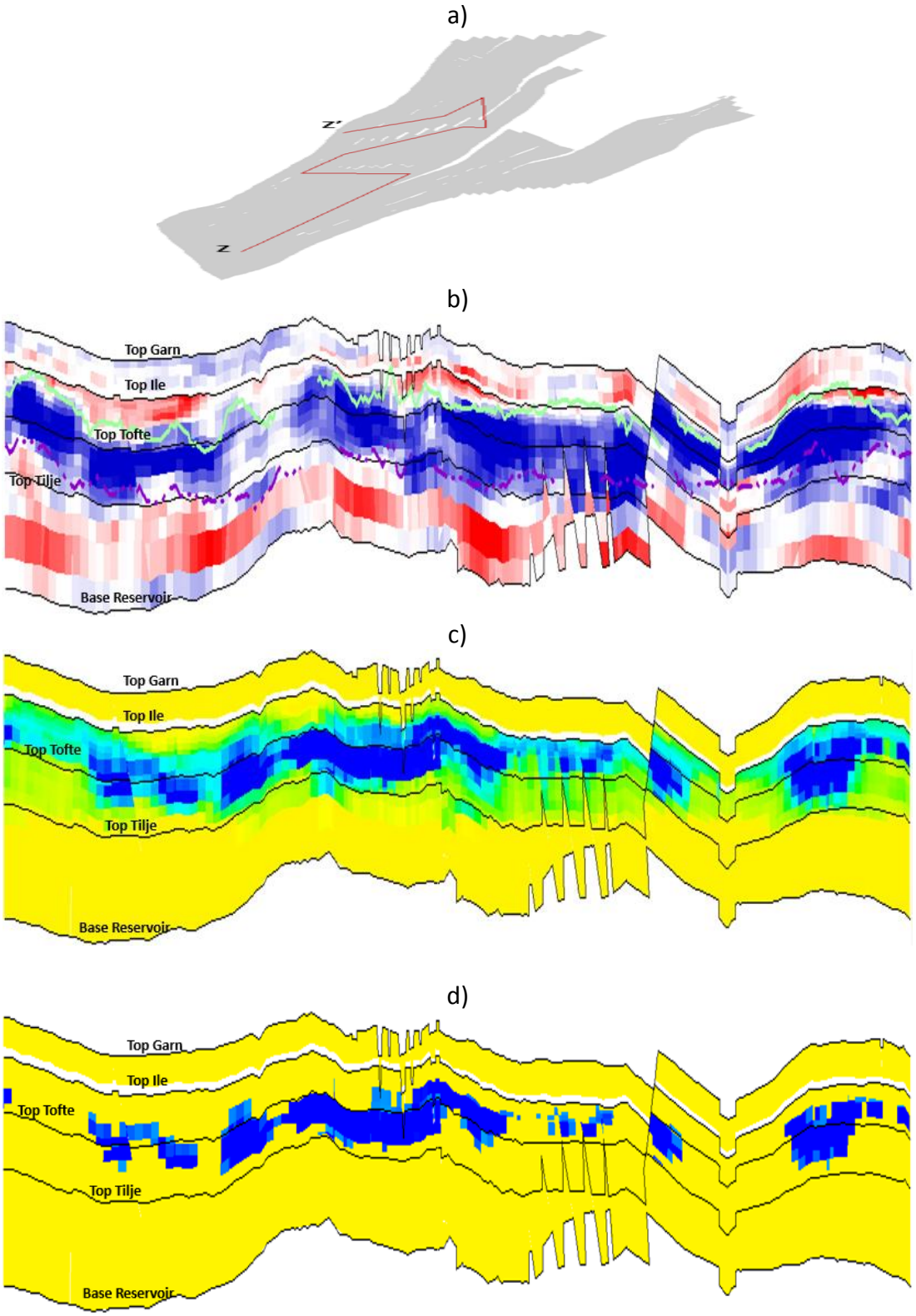

Figure 6.48 a) An arbitrary section Z-Z' in the Norne Field showing: b) 2001-2006 difference in AI, c) 2006-2001 difference in simulated water saturation: upward water movement is responsible for the hardening event (blue colour) and the oil water contacts (green line for 2006 OWC and purple line for 2001 OWC) are interpretable here, and d) areas at which water saturation and AI met the imposed cut off values

6.6.6 Identifying the Norne Field Flooding Pattern and OWC movement

It is observed that the inverted AI correlates well with the interpreted oil water contacts. This is especially the case in those regions of the field where saturation effects dominate, hardening effect indicates the oil-water contact rise and the pattern of water flooding in the Norne Field. Before integrating the time lapse seismic data into the automatic history matching workflow, the 2001, 2003, 2004 and 2006 4D seismic data in the form of maps and sections, together with the base simulation model are used here to track and monitor the movement of the oil-water contacts and to establish the flooding pattern in the Norne Field. By calibrating the Norne Field water saturation with the normalised AI using logs at some pilot wells, Cheng and Osdal (2008) derived a relationship for estimating change in water saturation (Figure 6.49).

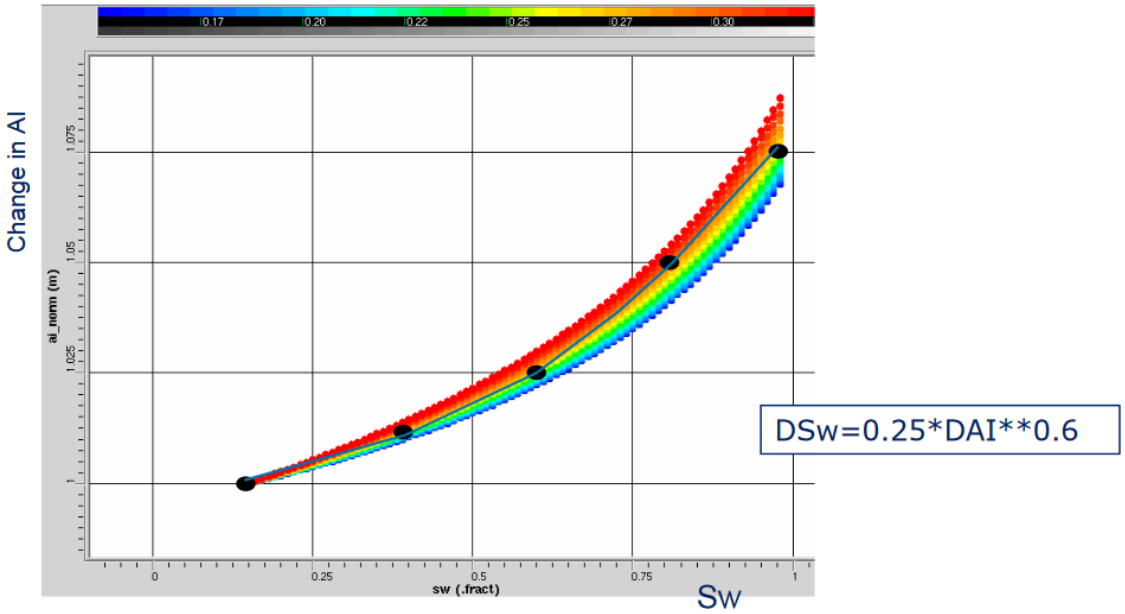

Figure 6.49 Estimation of water saturation from the AI (Cheng and Osdal, 2008)

Maps of the observed AI, the simulated water saturation and the corresponding estimated water saturation at some selected layers are shown in Figure 6.50.

Comparison of the water saturation estimated using the observed AI and the water saturation from the simulation model shows some close similarity between the two at several areas but also there are some noticeable discrepancies in some areas. The reservoir model properties within or around those non-matching areas are likely candidates for updating during history matching. For example, vertical transmissibility may be varied depending on the discrepancy in the flooding pattern established with the estimated water saturation and the simulated water saturation. The local barriers in the carbonate cemented layers such as the Ile 2.1.1/Ile 1.3, Ile 1.2/Ile 1.1, Ile 1.1/Tofte 2.2, Tofte 2.1.1/Tofte 1.2.2

are also candidates for updating the vertical transmissibility in the reserve model as they control the rise of water-oil contacts (see the next section for sensitivity studies).

For illustration, the maps of 2001-2006 AI showing only the areas where hardening occurs are compared to the corresponding maps of change in water saturation from the simulation model in Figure 6.50. By making this comparison, the cells, regions, or faults that need updating may be identified. That is, the juxtaposition of the observed hardening (increased impedance) and the simulated water saturation may help in identifying the cells around which the updating of vertical transmissibility and/or fault transmissibility may result in better matching models.

6.7 Sensitivity to Stratigraphic Barriers

In the Norne Field simulation model, the direction of flow of injected fluid (water/gas) is guided by adjusting the fault zonation and fault transmissibility, and upward movement of water is controlled by adjusting the vertical transmissibility. Fault transmissibility is modelled and adjusted using the Eclipse keyword MULTFLT while transmissibility between regions is modelled and controlled using the keyword MULTREGT. Vertical transmissibility is modelled by implementing vertical barriers as MULTZ-maps. The transmissibility values of the MULTZ-maps are adjusted during history matching. We intend to predict the historical flow behaviour of the Norne Field more accurately by matching the water and oil production rates at the well location. As a result, the values of the transmissibility of the stratigraphic barriers which control the movement of water in the vertical direction are the parameters of interest in model updating. However, before proceeding with large scale automatic history matching, it is necessary to investigate the sensitivity of seismic and production to the proposed history matching parameters.

The sensitivity of the seismic and production observables to the transmissibility values of Norne Field MULTZ-maps are investigated to identify the maps and local areas on maps that may significantly affect the response in history matching observables such as water rates, oil rates and AI. Different realisations of MULTZ-maps are generated by using the structural framework of the Norne Field reservoir built by Statoil based on interpreted horizon and faults. Local stratigraphic barriers are simulated as discrete variables to represent the multi-location uncertainties on the MULTZ-maps using sequential indicator simulation. There are 22 layers of the Norne Field reservoir model which implies 23 stratigraphic boundaries. Of interest are the stratigraphic surfaces/maps representing the top or/and base of those layers which affect the fluid flow most.

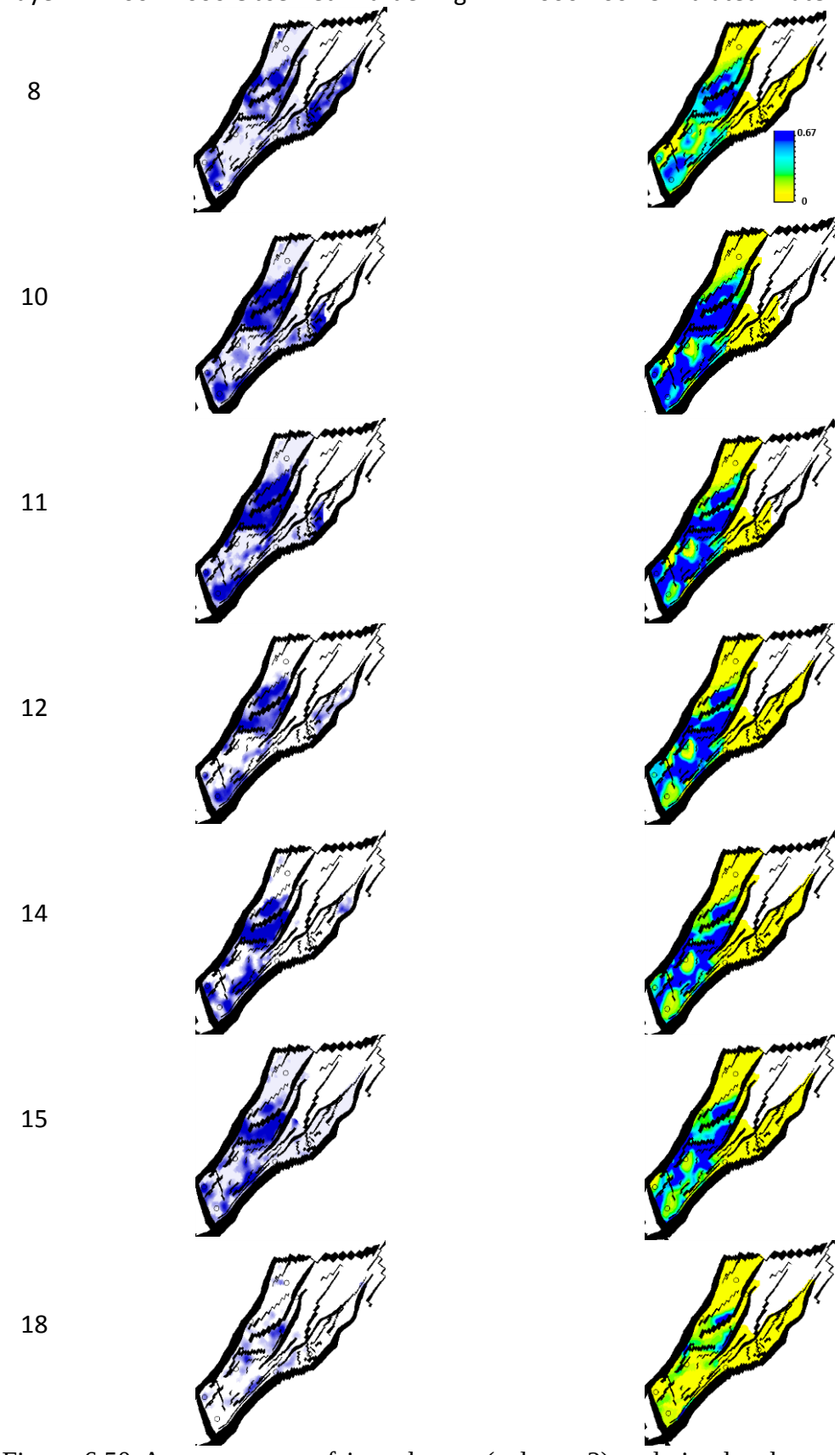

Figure 6.50 Average maps of impedances (column 2) and simulated water saturation (column 3) comparing the areas of the reservoir where hardening (blue in impedance maps) occurred to the areas with increasing simulated water saturation.

Ten (10) realisations of MULTZ-maps are generated for each layer-to-layer boundary of interest using spherical variogram with vertical anisotropic range equal to 200 and 0.0001 nugget. The azimuth and dip of the major direction are zero and the anisotropy range assigned to both the major direction and minor direction is 400. The MULTZ-map realisations are included in turn into the reservoir simulation model to make predictions of water and oil flow rates and also to predict the seismic response in the form of AI. Figure 6.51 shows some of the MULTZ-maps realisations where SIS_i (i= 1,…10) indicates a realisation using sequential indicator simulation. Layers with no significant effects were ignored.

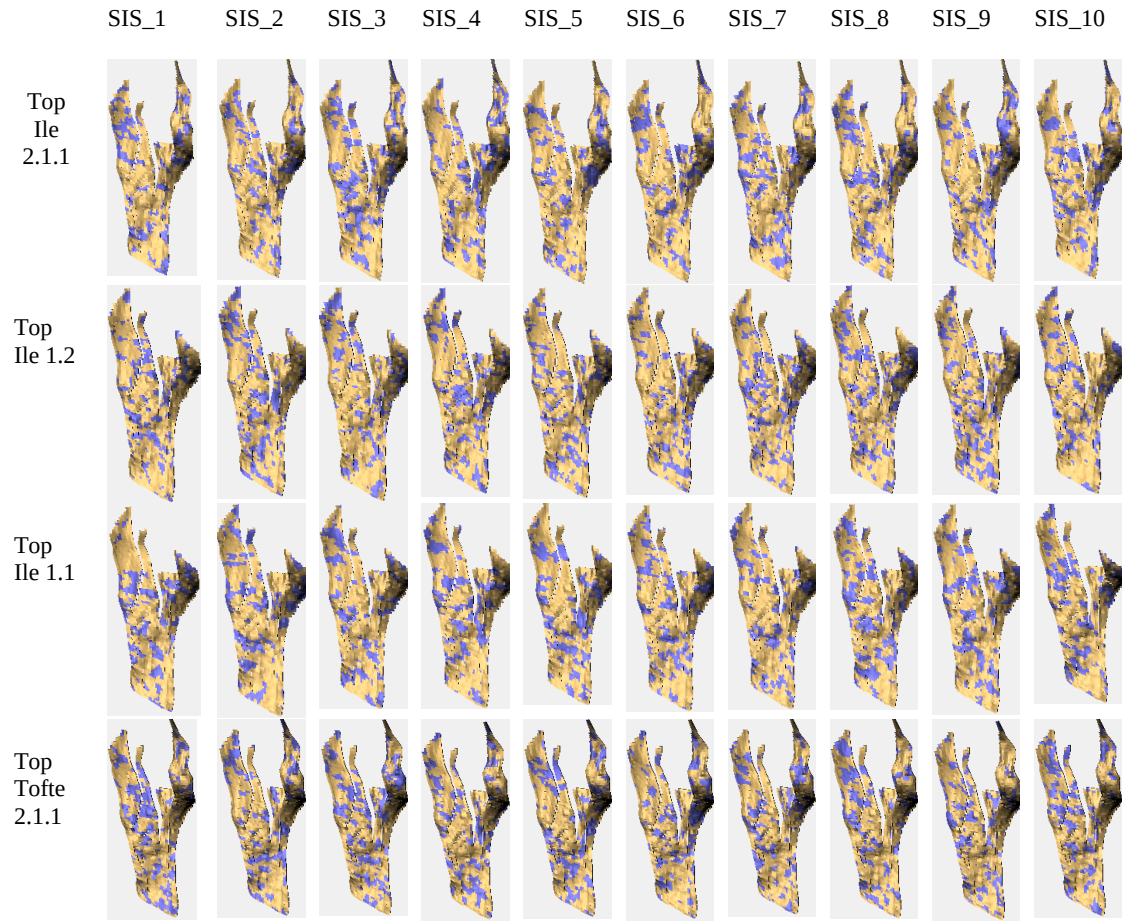

Figure 6.51 Realisations of MULTZ-maps for investigating the sensitivity of reservoir response to vertical transmissibility (see Table 6.2 for cell layers)

The ten realisations of MULTZ-maps for each of Top Ile2.1.1, Top Ile1.2, Top, Top Ile 1.1 and Top Tofte 2.1.1 only shown as examples. On each map, 25% of the variogram-generated map area are the modelled local barriers to vertical flow with transmissibility of zero (pink colours), while the other 75% are modelled (in yellow colours) are modelled to have transmissibility of one. The values of transmissibility assumed by these maps act as multipliers on the transmissibilities calculated by the reservoir simulator for the same vertical face at each grid block.

The misfit between the predictions (well water production rates and well water production rates) of the base case model and the observed production data water are evaluated. Wells are selected for the sensitivity study based on their ranking of the misfits calculated as the root mean square (RMS) of the the predictions of the base model and the history data. Table 6.4 shows the RMS values obtained for the misfits in well water production rates (WWPR) and well oil production rates (WOPR). The wells with higher RMS values (especially in WWPR RMS) are selected and include: B-3H, E-1H, D-1CH, E-2H, B-2H, D-3AH, E-2AH, E-3CH, D-1H, B-1BH, D-2H, E-3AH, B-4BH, B-1H, E-3H, K-3H, B-2H, E-1H, E-2H, D-4H, B-4H, B-4DH and E-4AH.

Table 6.4 Root mean square of production of Norne Field producing wells over the production history.

Well	RMS Water Product-ion	Well	RMS Water Product-ion	Well	RMS Oil Product-ion	Well	RMS Oil Product-ion
B-3H	1152.24	E-3AH	424.57	K-3H	1625.87	D-2H	894.34
E-1H	1150.89	B-4BH	396.79	E-3CH	1501.86	B-4H	772.40
D-1CH	1120.88	B-1H	350.96	D-1H	1366.91	B-4DH	743.73
E-2H	1089.73	E-3H	319.93	B-2H	1185.40	E-4AH	617.15
B-2H	1027.75	D-4H	202.27	B-1H	1179.94	B-1BH	548.40
D-3AH	766.68	E-4AH	189.87	E-1H	1115.62	E-3H	536.55
E-2AH	701.33	B-4DH	171.42	E-2H	1033.12	E-2AH	524.18
E-3CH	682.18	D-3BH	128.83	B-3H	999.84	B-4BH	490.55
D-1H	650.81	D-4AH	80.61	D-4H	984.34	E-3AH	476.42
B-1BH	614.24	K-3H	75.06	D-3AH	963.55	D-3BH	444.23
D-2H	462.04	B-4H	1.74	D-1CH	958.11	D-4AH	234.81

For each well, the mean value of the misfits in WWPR and WOPR are calculated for the responses of the ten MULTZ-maps realisations at each stratigraphic top. The misfits are normalised about the mean to obtain the relative misfit:

$$Relative\ RMS\ (\%) = \ 100\ \times \frac{(RMS - mean\ RMS)}{mean\ RMS}$$

The relative RMS is then used as a measure of sensitivity. The sensitivity is considered insignificant if a scenario satisfies the inequality: -10% < relative misfit < 10%. The

higher the absolute value of the relative misfit, the more sensitive the reservoir response is to the transmissibility of the MULTZ-map. The results are plotted for some stratigraphic tops in Figure 6.52 for well water production rates and Figure 6.53 for well oil production rates. It is seen from the figures that the predicted water and oil production from the producing wells are sensitive to changes in the vertical transmissibility of Top Ile 2.1.1, Top Ile 1.2, Top Ile 1.1, Top Tofte 2.1.1 making them the good candidates for history matching. On the other hand, production response is much less sensitive to changes in the transmissibility of Top Garn 2 and Top Tilje 2, so history matching with these parameters will not make any significant improvement to the predictions of the reservoir model.

Looking at the relative misfit values for the production wells for any variation of the MULTZ-maps, the information on what vertical transmissibility affects each well production is also revealed. The information from Figure 6.52 and 6.55 can be useful in guiding the selection of the right location on the MULTZ-maps to implement the vertical transmissibility update during history matching. For instance, well E-3CH in the E-segment is the most affected by the changes in the vertical transmissibility values at the top of Ile 2.1.1 Fm. Well E-3CH was drilled as an infill production well based on the information provided by the 2003 time lapse data but produced at high water-cuts starting in July 2005. There have been efforts to history match production in this well using the qualitative information gathered from 4D data (example is Lygren *et al.*, 2005). Figure 6.54 shows the location of the well on two different realisations of the Top Ile 2.1.1 MULTZ-map. The difference in the two realisations is the distribution of the carbonate cements representing zero vertical transmissibility around the completed zone of the well. The map in Figure 6.54a has the least carbonate cement in the vicinity of the perforation and gives the highest positive value for relative misfit while the map in Figure 6.54b has the most carbonate cement and gives the highest negative value. To obtain a better match of the history data in well E-3CH may require automatic history matching of the well production data by varying the vertical transmissibility around the area outlined in red in Figure 6.54b.

For each realisation of the MULTZ-maps, predictions of the seismic behaviour of the model at time intervals corresponding to the time of Norne Field 4D seismic acquisitions are also made. Figure 6.55 - 6.62 show the 2001-2006 AI difference predictions made with some of the realisations. The AI maps were generated through backus averaging for the reservoir layers 5 to 22. The top layers 1 to 3 were not included in the averaging because the gas cap in these layers will further complicate the interpretation of the seismic

signals. Thus, changes made to the MULTZ-maps at the top Garn 2 will have no effect on the averaged seismic signals. Layers 10 and 15 are known to have significant impact on Norne Field production and are therefore used as examples here to show the effect of varying MULTZ values on seismic. Layer 4 is the sealing shale layer (Not Fm) and is inactive in the reservoir model.

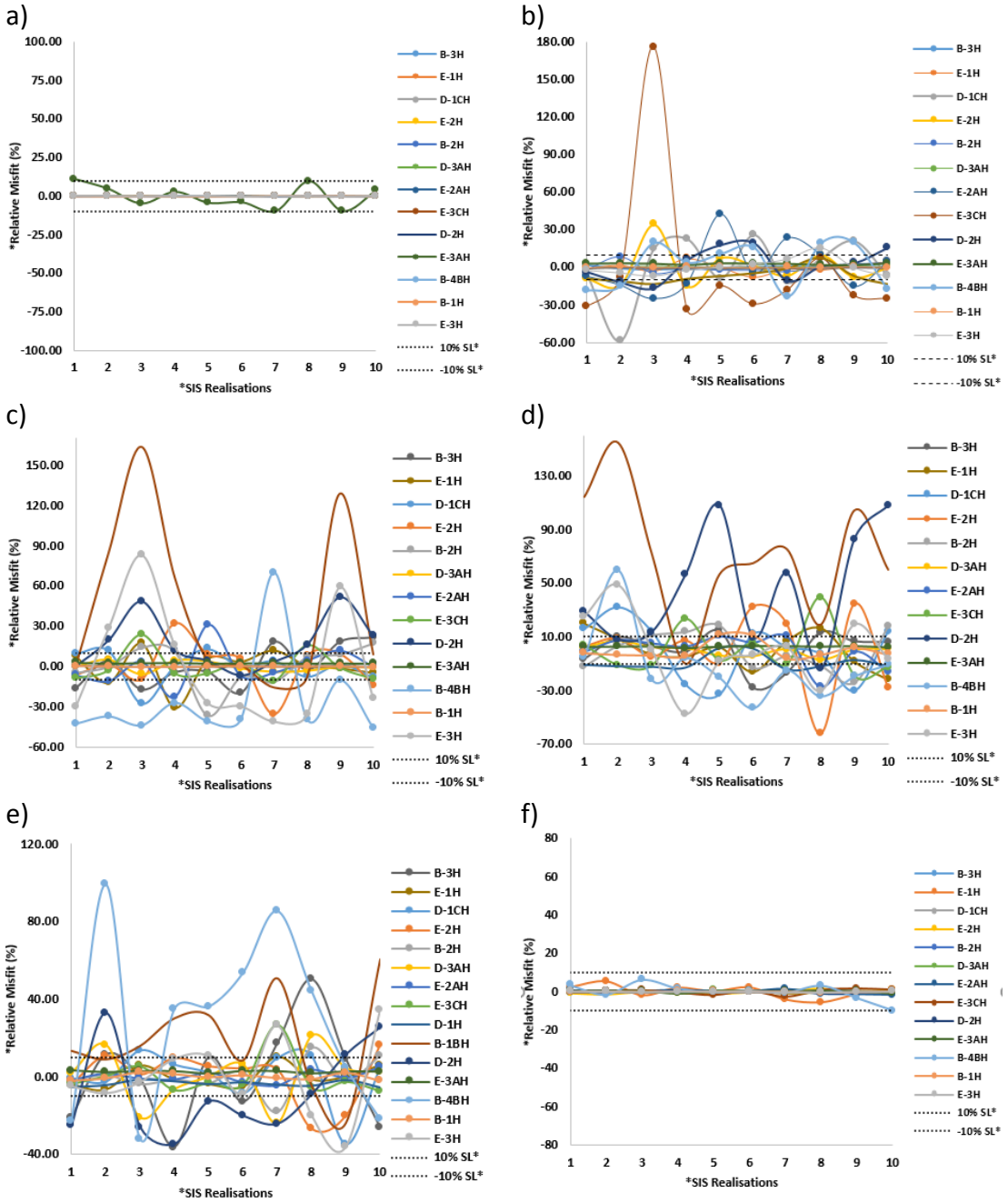

*SIS Realisations – Ten realisations of the MULTZ-maps
SL* - Sensitivity cut-off Line

Figure 6.52 Sensitivity of well water production rates (WWPR) to the MULTZ-maps at a) Top Garn 2, b) Top Ile 2.1.1, c) Top Ile 1.2, d) Top Ile 1.1, e) Top Tofte 2.1.1, and f) Top Tilje 2

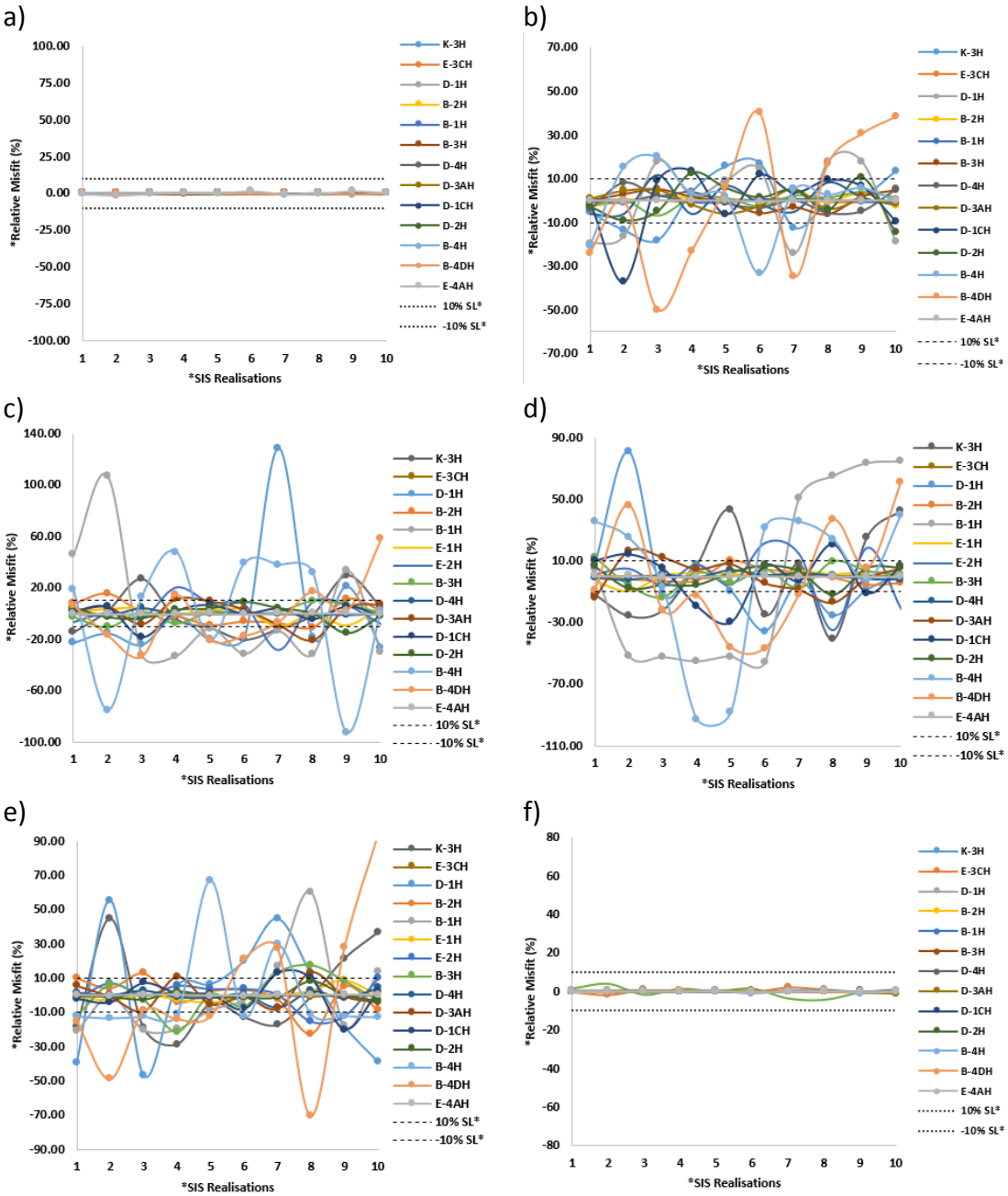

*SIS Realisations – Ten realisations of the MULTZ-maps
SL* - Sensitivity cut-off Line

Figure 6.53 Sensitivity of well oil production rates (WOPR) to the MULTZ-maps at a) Top Garn 2, b) Top Ile 2.1.1, c) Top Ile 1.2, d) Top Ile 1.1, e) Top Tofte 2.1.1, and f) Top Tilje 2

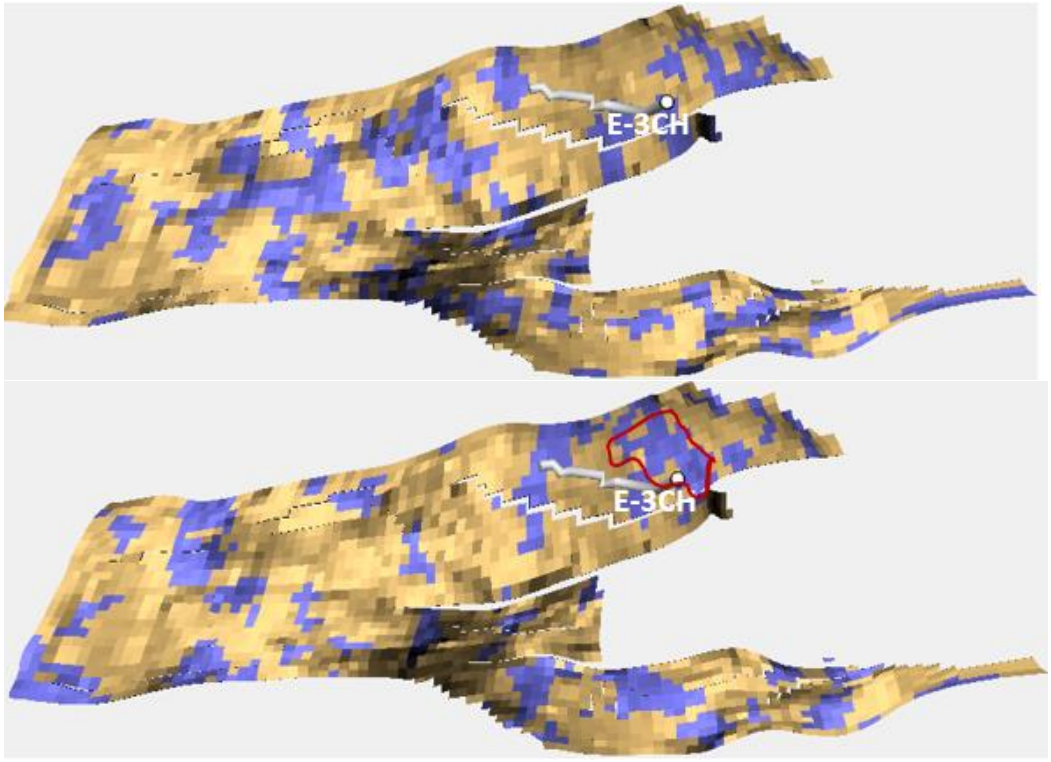

Figure 6.54 Two different realisation of MULTZ-maps at Top Ile 2.1.1. The red outline is an area of marked difference between the two maps in the E-Segment and may be responsible for the difference in predictions.

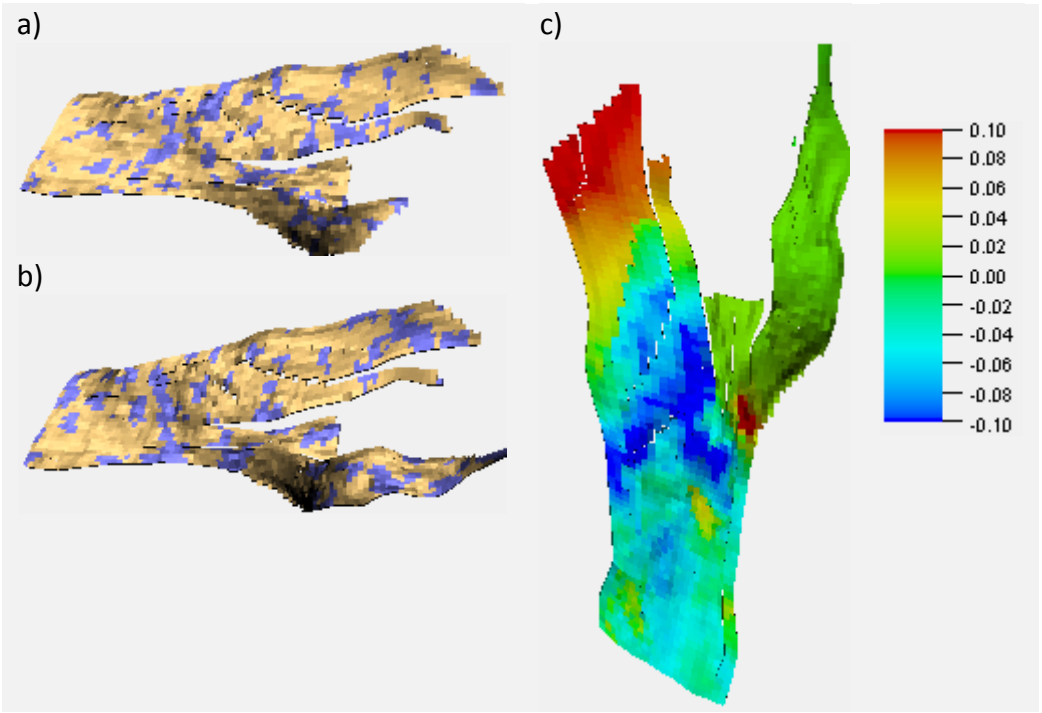

Figure 6.55 Sensitivity of seismic response to MULTZ-map. a) SIS realisation 1 at k=10, b) SIS realisation 2 at k=15, c) Normalised 2001-2006 depth-average impedance map

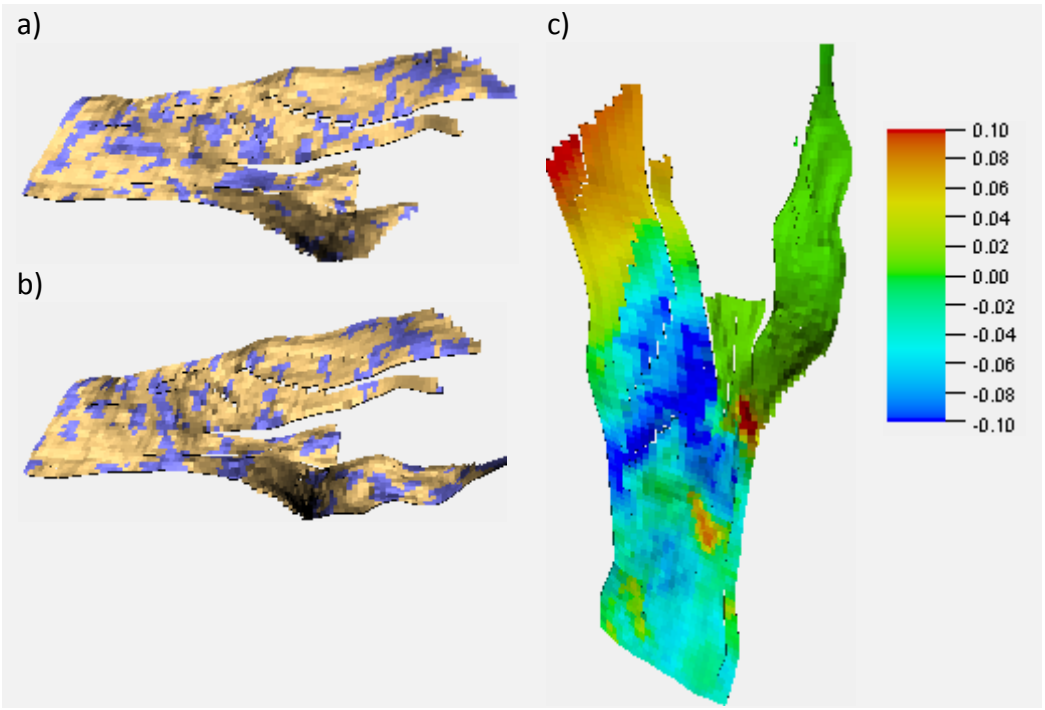

Figure 6.56 Sensitivity of seismic response to MULTZ-map. a) SIS realisation 2 at k=10, b) SIS realisation 7 at k=15, c) Normalised 2001-2006 depth-average impedance map

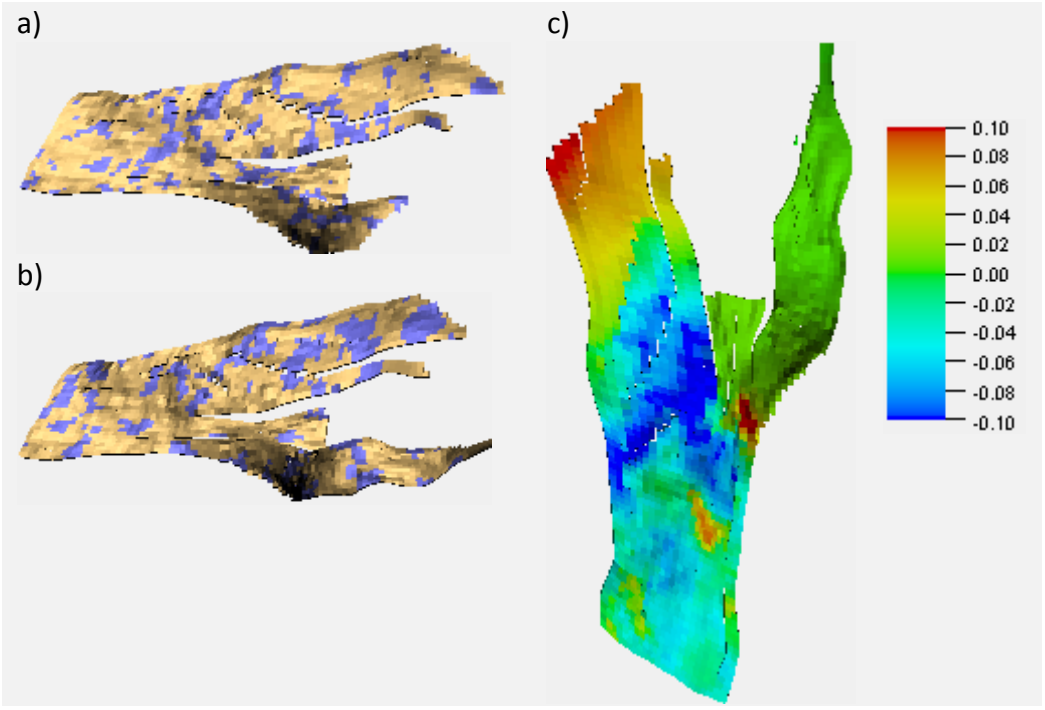

Figure 6.57 Sensitivity of seismic response to MULTZ-map. a) SIS realisation 1 at k=10, b) SIS realisation 8 at k=15, c) Normalised 2001-2006 depth-average impedance map

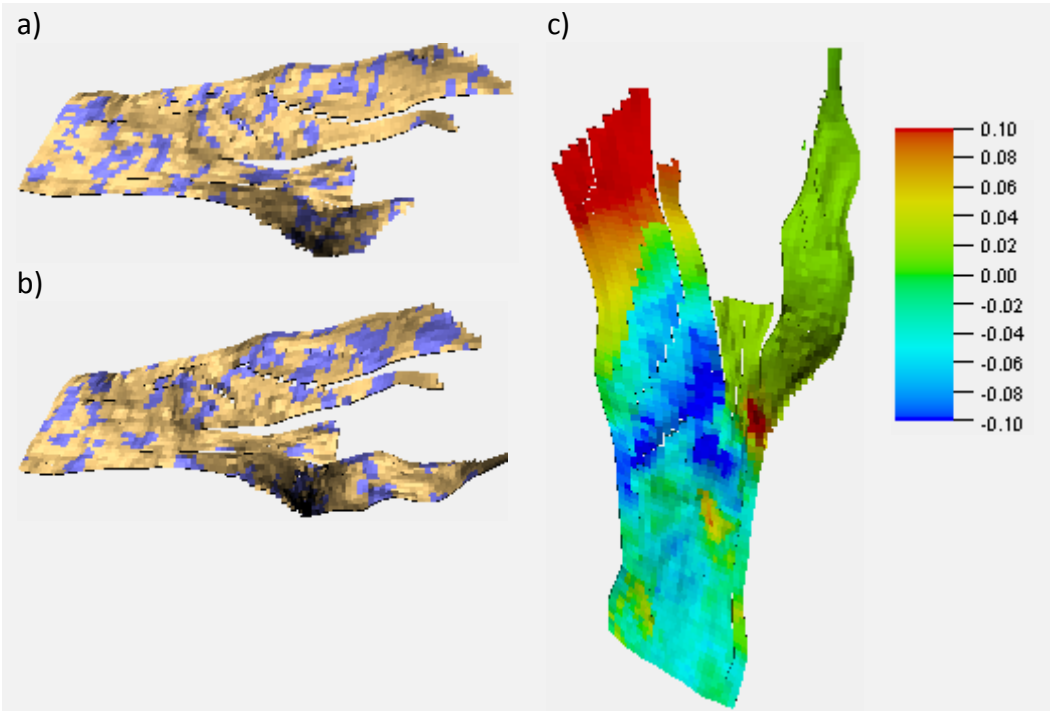

Figure 6.58 Sensitivity of seismic response to MULTZ-map. a) SIS realisation 5 at k=10, b) SIS realisation 8 at k=15, c) Normalised 2001-2006 depth-average impedance map

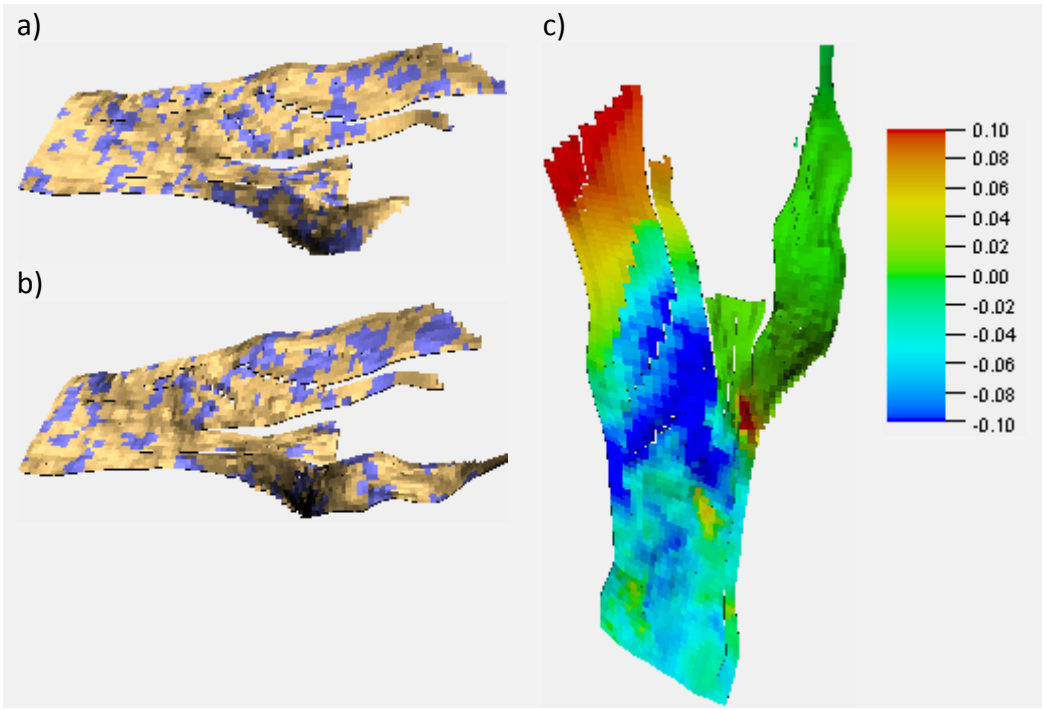

Figure 6.59 Sensitivity of seismic response to MULTZ-map. a) SIS realisation 8 at k=10, b) SIS realisation 8 at k=15, c) Normalised 2001-2006 depth-average impedance map

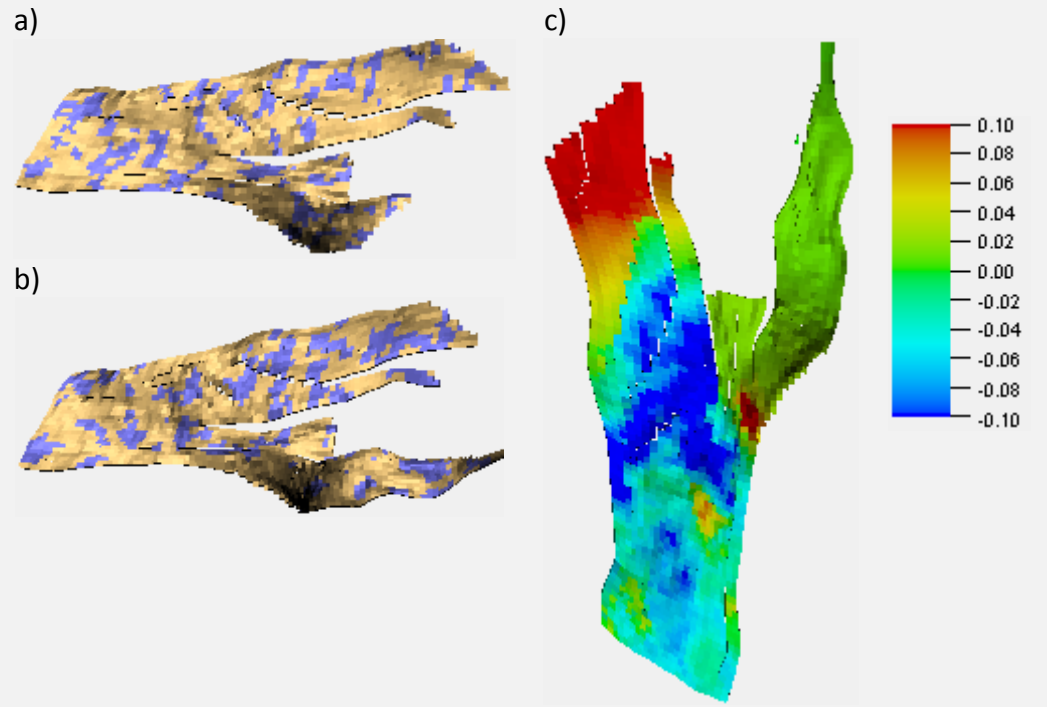

Figure 6.60 Sensitivity of seismic response to MULTZ-map. a) SIS realisation 5 at k=10, b) SIS realisation 10 at k=15, c) Normalised 2001-2006 depth-average impedance map

Chapter 7– Dynamic Screening of Fronts in Multi-Objective History Matching

Overview

History matching of reservoir models involves data assimilation from many well measurements, and in some cases, time lapse seismic. The information provided by the various data are often conflicting. Higher match quality in one sometimes lead to deteriorating match in another. Proper formulation of the objectives is necessary to avoid bias in data assimilation and increase the chance of finding an acceptable overall match. A suite of new algorithms is proposed to handle history matching problems with many conflicting objectives.

The suite of algorithms called Dynamic Screening of Front in Multi-Objective Optimisation (DSFMO) allows the formulation of history matching problems in multi-objective fashion, as against the conventional single objective approach. In the algorithm, new concepts for dynamic selection of models at the Pareto fronts, called under-sampling and oversampling are introduced, and are combined with the conventional non-domination sorting algorithm [Deb et al. (2002)] to maximise the exploration of the objective space, and strike a balance between ensuring diversity in the optimal solutions and convergence of the algorithm. Two variants of the algorithm are presented in this paper: DSFMO with the neighbourhood algorithm (DSFMONA), and DSFMO with genetic algorithm (DSFMOGA). The algorithms have been discussed and tested in some synthetic benchmark cases with many competing objectives, and in Chapter 8, their implementations are demonstrated seismic and production history matching of the highly compartmentalised real 3D field application – the Norwegian field.

The results of many objectives problems solved with DSFMO are compared to the results of the traditional single objective, as well as to the results of dual objective containing only seismic and production match criteria. The results show that DSFMOGA and DSFMONA find better sets of solutions that match all the sets of observed datasets. In some cases, DSFMO is also shown to improve the convergence rates. The DSFMO models represent the spread in the posterior models more accurately than the traditional single objective optimisation, and improves the predictability of posterior models. It is also shown that DSFMO yields models at the Pareto front that give better estimate of uncertainty in predictions than the well-known NABayes (Neighbourhood Algorithm for Bayesian Inference) method. Results of posterior analysis, using Bayesian indicators, show that in solving large-objective history matching problems with DSFMO gives better

data assimilation than both the sum-objective single objective method and dual-objective optimisation.

To the best of my knowledge DSFMO is a novel approach to optimisation for any history matching problem formulated with many objectives. The algorithm handles large-objective problem. It has been demonstrated to be unaffected by the curse of dimensionality even in history matching problems with more than 10-dimensional objective space. In view of the applications presented in this thesis, DSFMO has proven to be a breakthrough in resolving problems with many conflicting objectives. The algorithm is robust and can be relied on as a useful tool for predictions and uncertainty analyses in reservoirs of complex geology.

7.1 Introduction

Stochastic optimisation algorithms have been given more attention in recent years as the standard technique for updating models in automatic history matching workflows and for assessing the uncertainty in model predictions. The growing interest in the application of population-based algorithms has been attributed to its ability to find global solutions and to the improvement in the performance of the computing facilities. Most importantly though is the important change in the mind set of reservoir engineers leading to increase in the importance placed on including multiple realizations of reservoir models in predictions to account for uncertainties (Walker and Pettigrew, 2006).

Historically, most stochastic history matching studies adopted algorithms with a global single-objective approach in the formulation of the match metric. However, history matching is fundamentally a multi-objective problem, as there are multiple wells, and match criteria in well and field levels; and in some cases, 4D seismic data. These criteria are conflicting in many cases, for example: improvement in the match of historical oil production rate in a well might lead to more mismatch to the GOR in another well and vice versa. The common practice among reservoir engineers is to use a simple weighted sum-objective as a single objective function which is then minimized during history matching to obtain best possible matches for different observables at well and field scales. Transforming an N-dimensional objective problem (where N>1 is the number of objectives) into a one-dimensional problem simplifies the history matching problem but often results in an incomplete exploration of the solution space (Deb *et al*. 2000).

Among the history matching studies in which the single objective algorithms are adopted are: genetic algorithm (Mohamed *et al*., 2010), Particle Swarm Optimisation (Christie *et al*., 2013), Ant Colony Optimisation algorithm (Hajizadeh, 2010), Estimation of

Distribution Algorithms (Abdollahzadeh *et al.*, 2013), Neighbourhood Algorithm (Sedighi-Dehkordi and Stephen, 2009), ensemble Kalman filter (Naevdal, 2005). A common feature of all the algorithms is that they explore the model space to find some combinations of model parameters in the optimal solution domain corresponding to the global minimum. The problem though is the dependency of single-objective history matching on the magnitude of the individual objectives. The objective-sum (weighted sum of squares for the objective function) referred to as a global misfit is often composed of individual misfits each of which is either a function of the predictions at a well location or predictions of seismic behaviour. There is the tendency that the single-objective approach will bias the search of the model space to favour those solutions in the direction of reducing some individual objectives with large order of magnitudes than others. A common approach to tackling the issue of magnitude is to assign different weights (positive scalars) to the individual objectives and aggregating them but this adds some subjectivity towards the assessment of models among the competing objectives. The problem of dependency on magnitudes is highlighted in the works of Kabir *et al.*, (2003), Aanonsen (2003) etc.

There have been suggestions that the use of varying weights single objective during optimisation could help resolve the scale-dependency problem (Evan, 2005) but there is no guarantee that the entire ensemble of solutions resulting from this approach satisfies all the individual objectives. In addition, the use of the repeated (varying) weight single objectives impairs the parallel computation ability of the stochastic history matching workflow (Min *et al*. 2014).

The use of many objectives, instead of one global objective, in history matching helps to eliminate the subjectivity inherent in the mathematical formulation with weight factors (Nicklow *et al*., 2010). The goal of multi-objective history matching is to obtain a set of Pareto-optimal solutions (red curve in Figure 7.1) in posterior space or optimal domain called the Pareto-optimal front (PF) (Deb *et al*., 2000). The optimal solutions represent some multiple trade-off reservoir models which can be used in probabilistic forecasting. Pareto-optimality is the state of the optimal allocation of resources.

In this chapter, we focus on the use of many objectives in history matching of reservoir models. There have been several history matching studies with different forms of multi-objective optimisation algorithms including the use of : Strength Pareto Evolutionary Algorithm (SPEA) to history matching a synthetic reservoir model derived from a real North Sea reservoir model (Schulze-Riegert *et al*., 2007) and in Ferraro (2009) in a synthetic project comparing single-objective and multi-objective history matching.;

differential evolution for multiobjective optimisation using Pareto ranking (DEMOPR) for history matching and uncertainty quantification of the PUNQ-S3 reservoir (Hajizadeh *et al*., 2011); genetic algorithm based multi-objective matching history matching in a waterflooding project with irregular shut-in (Han *et al*., 2010); Non-dominated Sorting Genetic Algorithm (NSGA-II) (Deb *et al*. 2000) combined with streamline simulation for reducing the cost of running reservoir simulation during history matching, applied in history matching of multiple synthetic examples and the benchmark reservoir, the Brugge field, including the matching of production and seismic data with uncertainty and conflicting information (Park *et al*., 2013); multi-objective genetic algorithm in comparing the performance of the multi-objective history matching to single-objective with different covariance matrices in a synthetic field study (Sayyafzadeh *et al*., 2012); multiobjective particle swarm optimisation technique applied in history matching of a challenging synthetic reservoir and the uncertainty quantification (Mohamed *et al*., 2011); comparison of single objective and multi objective versions of Particle Swarm Optimisation in history matching of Zagadka field in western Siberia (Christie *et al*., 2013); optimal objective-grouping-selection technique applied to two case studies of history matching (Zagadka Field and PUNQ-S3) based on multi-objective particle swarm (Hutahaean *et al*., 2017), seismic history matching with saturation indicators using multi-objective neighbourhood algorithm (Stephen, 2013), and a recent study by Hutahaean *et al*. (2015) using multiobjective approach on standard industry benchmark case to demonstrate that model realisations from multiobjective history matching are more robust and reliable for probabilistic reservoir performance forecasting than model-solutions realised from history matching using weighted-sum objective.

These previous studies, however, focused on applications with no more than two or three competing objectives. More robust multi-objective algorithm is needed for applications requiring the inclusion of more than three individual objectives. Ideally, each history matching observable at the well location, for instance, should be assigned a match criterion. The number of match criteria or objectives then grows as the number history matching wells increases. The inclusion of 4D seismic further increases the objectives. As the number of objectives increases, the more difficult it becomes to approximate the Pareto-optimal front because its structure becomes complicated with increasing dimension. For instance, if the history matching problem is formulated with N number of competing objectives, then the problem of obtaining the Pareto-optimal front becomes an N-1 dimensional problem in objective space. If it is desired that each dimension of the Pareto-optimal front has P models spread across the front, then a total of P^{N-1} models

would be needed to describe the N-1 dimensional optimal front (Deb and Saxena, 2005). Among the difficulties in resolving the many-objective optimisation problems include the high computational cost, inefficiency of selection operators, poor scalability, and difficulty in visualization of the objective space (Saxena e tal.,2013). The difficulties are referred to as the "curse of dimensionality" (Bellman, 1957). As P^{N-1} increases, the population size needs to be increased accordingly; otherwise the solutions will be biased towards some certain parts of the Pareto optimal front. This complexity also leads to the deterioration of convergence towards the optimal front. Having a large number of objectives also deteriorate the convergence speed by increasing the probability that most of the solutions are non-dominated to each other in the non-optimal solution domain. As a result, it has become a common practice to compromise on some of the objectives by grouping them into just two or three objectives so that N does not go beyond three. (Ishibuchi *et al*., 2008, Hutahaean *et al*., 2015). Notable among such grouping method is the ε-constraints method proposed by Chankong and Haimes (2008). The ε-constraints method was proposed to reduce the number of objectives, and still achieve efficient points in a non-convex Pareto curve, by selecting only one objective out of the many objectives to be minimized and placing some constraints on the other objectives such that they are always less than or equal to a given target value (ε-value). However, the method becomes inefficient as the number of objectives increases, and the need to select appropriate bounds for the (ε-values) to obtain a complete Pareto optimal front makes the method either unfeasible or cumbersome (Park *et al*., 2013)

In all cases of Pareto-based multi-objective optimisation, the principle of non-domination ranking is applied. In any population of models $M\ \{m_1, m_2, \ldots..m_{Nm}\}$ *where* N_m is the total number of models in the population, a solution m_1 is regarded as better than solution m_2 if two conditions are satisfied simultaneously: i) the fitness $Oi(m_1)$ is not worse than $Oi(m_2)$ for all $i \in \{1, 2, \ldots, N_f\}$; where *Oi* is the *ith* fitness function and N_f is the number of objective/fitness functions, ii). The model m_1 has better fitness than m_2 in at least one objective, i.e. $Oi(m_1)$ is better than $Oi(m_2)$ for at least one $I \in \{1, 2, \ldots, N_f\}$. By this definition of the non-domination, it is possible to identify a model solution as a high-quality solution when it has superior fitness only for a few objectives but its overall fitness is relatively poor. This may result in a divergence problem where model solutions generated during optimisation grow away from the optimal front.

In this chapter we present a novel form of Pareto-based multi-objective algorithm, called Dynamic Screening of Fronts in Many-Objective Optimisation (DSFMO). The algorithm is aimed at identifying and selecting good solutions on the fronts, eliminating bad and

redundant solutions from the population so that multiple solutions are generated in the neighbourhood of the good solutions, maintaining the diversity of multi-objective on the Pareto Front while preventing divergence, and handling multi-objective problems where the objectives are more than three. Many case studies are presented. We demonstrate the robustness of the algorithm with multiple synthetic and real examples and compare it with the traditional single objective approach. We start by testing the algorithm using benchmark synthetic equations for which the solutions are known ab initio, then on two benchmark synthetic reservoir simulation model, followed by validation using a more complex real field model – the Statoil Norne Field (in Chapter 8).

7.2 Formulation of multi-objective history matching

We give a brief review of two approaches to multi-objective optimisation: the Pareto-based method and the varying weight sum-objective.

7.2.1 Pareto-Based Approach

The mathematical formulation of many objective optimization problem can be stated as follows:

$$min\ O(m) = \left(O_1(m)\ , O_2(m)\ , \dots , O_{N_f}\right), \dots\dots\dots\dots\dots\dots\dots\dots\dots\dots\dots\dots\dots\dots\dots\dots\dots\dots (7.1)$$

Subject to:

$$m = \left(m_1\ , m_2\ , \dots , m_{N_p}\right) \in M$$

$$O(m) = \left(O_1(m)\ , O_2(m)\ , \dots , O_{N_f}\right) \in O$$

Where $O(m)$ is a vector of objective functions and N_f is the number of objectives in the objective function space O. M is the model space which defines the set of constraints on the N_p model parameters. In the case of history matching problems, $O(m)$ is a vector of misfit functions often defined in the general L2 norm as the difference between the values of the quantities predicted using the models, $g(m)$ and the quantities measured in the field, d.

$$\mathrm{O}(m) = \langle d|C^{-1}|g(m)\rangle\ , \dots\dots\dots\dots\dots\dots\dots\dots\dots\dots (7.2)$$

with covariance matrix, C, which is the combined model and data error matrices

The mapping of the model space (M) into the objective function space (O) is illustrated in Figure 7.1 for the case of 2 objectives (i.e N_f =2). The mapping functions $O_1(m)$ and $O_2(m)$ maps the two models m_1 and m_2 into the objective space. In this illustration m_1 dominates m_2 (i.e. $m_1 \succ m_2$) because it meets the two conditions for non-domination formulated as follows (Deb *et al*. 2000):

$\forall\ i \in \{1, 2, \dots, N_f\}: O_i(m_1) \leq O_i(m_2)\ \Lambda\ \exists j \in \{1, 2, \dots, N_f\}: O_j(m_1) < O_j(m_2), \dots\dots\dots\dots\dots\dots\dots$(7.3)

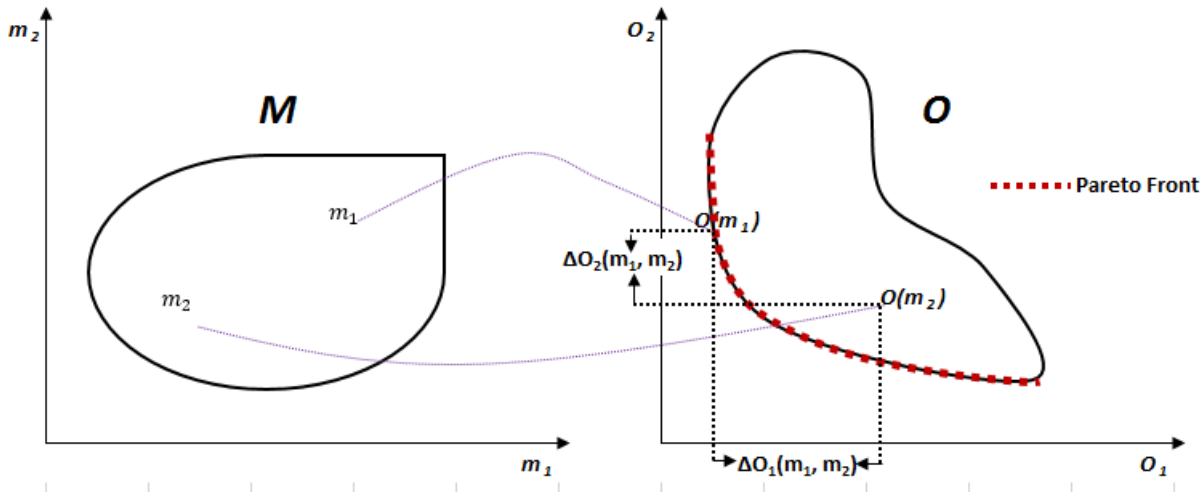

Figure 7.1 Mapping from model space into objective function space

In Figure 1, m_1 is not dominated by any other model. Thus, m_1 lies on the Pareto Front indicated by the red dashed line. Like m_1, there may be other models that are non-dominated within the entire model space. At the end of optimisation, the set of all non-dominated models are called the Pareto optimal solutions and when the set is mapped into the objective space, they constitute Pareto-optimal front (red dotted line in Figure 7.1) (Zitzler and Thiele 1999). The level of competition between the objectives determine the shape that the Pareto Front assumes. In the case of conflicting objectives, the shape carries information on the correlation and the trade-off between different objectives in the optimal solution domain. This information can be quantified by measuring the slope of the front. Generally, given any solution set, the nature of correlation (negative or positive) between any two objectives can be determined as a trade-off ratio (Kitayama and Koetsu, 2012). For the case illustrated in Figure 7.1, the trade-off ratio (TR) is defined as follows:

$$TR_{ij}(m_1, m_2) = \frac{O_i(m_1) - O_i(m_2)}{O_j(m_1) - O_j(m_2)} = \frac{\Delta O_1(m_1, m_2)}{\Delta O_2(m_1, m_2)}, \ldots\ldots\ldots\ldots\ldots\ldots\ldots\ldots\ldots\ldots\ldots\ldots (7.4)$$

The real benefit of the multi-objective function occurs when the minima of the objective functions occur at different parameter sets. If all the objectives have the same global minimum solution (which is often not the case) then we expect that the multi-objective optimisation will revert to a single sum-objective optimisation in behaviour without loss of generality. On the other hand, if the solution space for each of the objectives is characterised by a distinct solution then an effective multi-objective approach will be expected to sample from a range of equally likely solutions that lie between those of the separate objectives functions.

7.2.2 Varying weight-sum objective

The mathematical formulation given as equation 1 can be simplified by scaling each of the objectives with a dynamic weight and summing up the objectives in an approach similar to the aggregated single objective. The difference between the two is that while the weights in the aggregated single objectives are predetermined and static, the weights in the varying weight-sum objectives are varied systematically to cover some defined range during optimisation. We can reformulate the multi-objective problem for the varying weight approach as follows:

$$min\, O(m) = \sum_{i=1}^{N_f} \omega_i O_i(m)\,, \ldots\ldots\ldots\ldots\ldots\ldots\ldots\ldots\ldots\ldots\ldots\ldots\ldots\ldots\ldots\ldots\ldots\ldots (7.5)$$

Subject to:

$$0 \leq \omega_i \leq 1$$

$$\sum_{i=1}^{N_f} \omega_i = 1$$

$$m = \left(m_1\,, m_2\,, \ldots, m_{N_p}\right) \in M$$

Where ω_i is the weight assigned to the *ith* objective

The idea of varying weights in the multi-objective optimisation has gained some attention because in using the sum-objective single objective optimisation the determination of the weights assigned to the objectives is a major challenge. What has been proven is that the quality of solution sets generated during optimisation is dependent on the consistency between the distribution of the assigned weights and the shape of the Pareto Front (Liu *et al*., 2016; Cheng *et al*., 2015; Zhang *et al*., 2017; Wang *et al*., 2017; Cai *et al*., (2017); Asafuddoula *et al*., 2017; Wang *et al*., 2013; Tian *et al*., 2017; Xiang *et al*., 2017). A set of weight vectors assigned to the objectives may result to a good distribution of solutions on a particular front shape but fail on another shape. Since the shape of Pareto Front is not known beforehand for any problem, it becomes difficult to pre-determine what the set of appropriate weights should be (Hajizadeh *et al*. 2011). The varying weight-sum objective has been proposed to adapt the weights during the optimisation process so that some good distribution of weights are assigned iteratively as the optimisation progresses. However, as noted in Park (2013), the Dynamic Weight-sum Objective approach will likely be computationally prohibitive and its computation cannot be easily parallelised. In addition, it is difficult to develop heuristic algorithm that will be initialised by certain weights vectors and iteratively modify the weight vectors to attain the desired uniform distribution of models on the Pareto Front.

7.3 Dynamic Screening of Fronts in Many-Objective Optimisation (DSFMO)

This study proposes a robust Pareto-based technique that can handle optimisation problems with more than three objectives so that history matching problems with many well response based match criteria can be handled more effectively. The basic idea of this algorithm is to regroup the entire population of models into fronts based on non-domination sorting and then screening the model solutions in the fronts using some dynamic steps presented here.

A suite of processes for progressive screening of the Pareto Fronts are integrated into the conventional non-domination multi-objective algorithm to give a new optimiser, called DSFMO, which aims at:

i. Finding a set of non-dominated solutions at the Pareto Front which optimally balances the trade-offs among the objectives.
ii. Ensuring that solutions at the fronts are as uniformly distributed as possible
iii. Maximising the diversity and spread of the non-dominated solutions to capture the front as much as possible
iv. Maximising the number of quality models at the Pareto Front while discarding the bad models
v. Solving multi-objective problems with more than 3 objectives

Two versions of the new optimiser are presented here: i) Dynamic Screening of Fronts in Many-objective Genetic Algorithm(DSFMOGA), ii) Dynamic Screening of Fronts in Many-objective Neighbourhood Algorithm (DSFMONA). The distinguishing feature of these algorithms is that diversity and elitism are both ensured using the concepts of oversampling and under-sampling so that best models solutions are selected from the *ith* iteration step, and if necessary from preceding iteration step(s), and feed into the *(i+1)th* iteration step. The mechanism for selecting the best models ensures that the bad models are discarded while maintaining diversity among trade off solutions at the fronts. This helps to avoid divergence problems and speed up convergence towards the Pareto optimal front.

7.3.1 Dynamic Screening of Fronts in Multi-Objective Genetic Algorithm

The new algorithm, Dynamic Screening of Fronts in Multi-Objective Genetic Algorithm (DSFMOGA), depicted in Figure 7.2 is described for minimisation problems as follows: After an initialisation step where an N_p population of models is generated by random sampling from the parameter space, the entire initial population is sorted into fronts of

different ranks using the non-domination sorting technique (described in Srinivas and Deb, 1994). The non-dominated solutions are then put in the first ranked front. The solution set in the second ranked front is determined by neglecting the set in the first rank and subjecting the rest of the population to non-domination sorting. The third ranked front is found in the same manner by neglecting the first and the second. The sorting process continues that way until no more dominated elements are found in the population. In assigning ranks to the elements in the population, the rank of an element, e is $R_e = N_e + 1$, where N_e is the total number of fronts occupied by all elements dominating e. Since the number of elements dominating the solutions at the first ranked front is zero ($N_e = 0$), the rank of these elements in the Pareto Front is one ($R_e = 1$).

Then the second phase of ranking is performed based on the global fitness values of the solutions in the ranks. Global fitness is measured by the magnitude of the objective-sum (sum of all the objectives for any element). Then, ranking re-allocation is done to convert the non-domination rank into fitness-based rank using the 'undersampling' and 'oversampling' technique.

The algorithm allows the user to specify the number of models that should be selected in any given generation. This number can be referred to as the number of children per iteration, n_s $(=2n_r)$, where n_r is the number of couples. In the case where ***'normal sampling'*** occurs, the algorithm chooses the $2n_r$ models (2 times the number of couples) as 'parents' from the models at the first ranked front to be paired up for breeding, i.e. 'cross-over'. This situation rarely occurs because it requires that the number of models on the first ranked front is exactly equal to $2n_r$.

There may be cases in which the number of elements of the Pareto Front are less than $2n_r$. More models are needed to have a complete set of couples. This situation is called ***undersampling***. The algorithm has the capability to handle this situation through a number of options: (i) select only the models at the first ranked front, n_f and set $2n_r = n_f$, (ii) Sample ($2n_r - n_f$) models randomly from higher ranked Pareto Fronts and add to the n_f models from the first rank to become the couples, or (iii) Select ($2n_r - n_f$) models with the best global fitness from higher ranked Pareto Fronts and add to the n_f models to become the couples.

In some other cases there may be more models on the Pareto Front than are needed for the new generation, and the situation is called ***oversampling.*** DSFMOGA handles this in three ways: (i) Sample the needed $2n_r$ models randomly over the first ranked Pareto Front, (ii) Select the needed $2n_r$ parent models with the best global fitness from the first ranked Pareto Fronts, or (iii) Select the needed $2n_r$ parent models from the best models on the

first ranked Pareto Front based on crowding-distance sorting. The crowding-distance is a measure of population density evaluated as follows over a front between two models of the same rank, (Deb *et al*., 2002):

$$D_c^j = \sum_{i=1}^{N_f} \frac{D_i^j}{O_i^{max} - O_i^{min}} \quad \forall j = 1, \ldots., N_p, \ldots\ldots\ldots\ldots\ldots\ldots\ldots\ldots\ldots\ldots\ldots\ldots\ldots\ldots\ldots\ldots (7.6)$$

Where the Pareto front is composed of N_p models, D_c^j is the crowding-distance for the *jth* model, D_i^j is the distance between the two closest neighbours to the *jth* model, the parameters O_i^{max} and O_i^{min} are the maximum and minimum values for the *ith* objective and N_f is the number of objectives. Selection of models which are sparsely-distributed (and hence, larger crowding-distances) is preferred to densely-distributed models (with smaller crowding-distances) to favour diversity.

Couples are combined randomly so that all $2n_r$ models selected from any of the afore-mentioned options are used with uniform likelihood. Parametric elements of the $2n_r$ models are randomly combined during the crossover process to generate new models. In real-coded genetic operator, this implies that a new model is randomly picked from a hypercube surrounding the parameter space volume between the models and in a small volume either side. There is also the option to perturb these models through jump and/or creep process (i.e. mutation) so that the optimisation process is not trapped by the local minima. Then the new n_s models are added to the pre-existing population and the iterative process that began with non-domination sorting is repeated.

Since the user has control over the choice of the input value n_r, proper selection of this value can help ensure elitism and diversity since solutions of the current population can be merged with some good-fitting models from the previous population. The best value of the input nr value will be within a certain bound which is problem-specific, and the onus is on the user to make an appropriate choice to avoid a catch-22 situation between diversity and convergence.

7.3.2 Dynamic Screening of Fronts in Multi-objective Neighbourhood Algorithm (DSFMONA)

The ***DSFMONA*** and ***DSFMOGA*** approaches are conceptually similar (see Figure 7.2 and Figure 7.3). The conventional Neighbourhood Algorithm (NA) (Sambridge, 1999) is modified in DSFMONA to use ranking of models through the processes of non-domination sorting, under-sampling, and oversampling to select the best models in multi-objective optimisation instead of just the global misfit values. As in DSFMOGA, the

process begins with an initialisation step where an N_p population of models is generated as random samples bounded by the parameter space. The entire initial population is sorted into fronts and ranked as before, followed by the selection of n_r parent models through the process of normal sampling, undersampling, or oversampling (whichever applies). The neighbourhood of each model in the selected n_r models is identified in the multi-dimensional model space as V-Cell s. For each of the models, the V-Cell identifies the volume of the polyhedron housing the model and its nearest neighbourhood. These neighbourhoods are then re-sampled through some uniform random walks to generate n_s new models. In each of the V-Cell n_s/n_r models are generated.

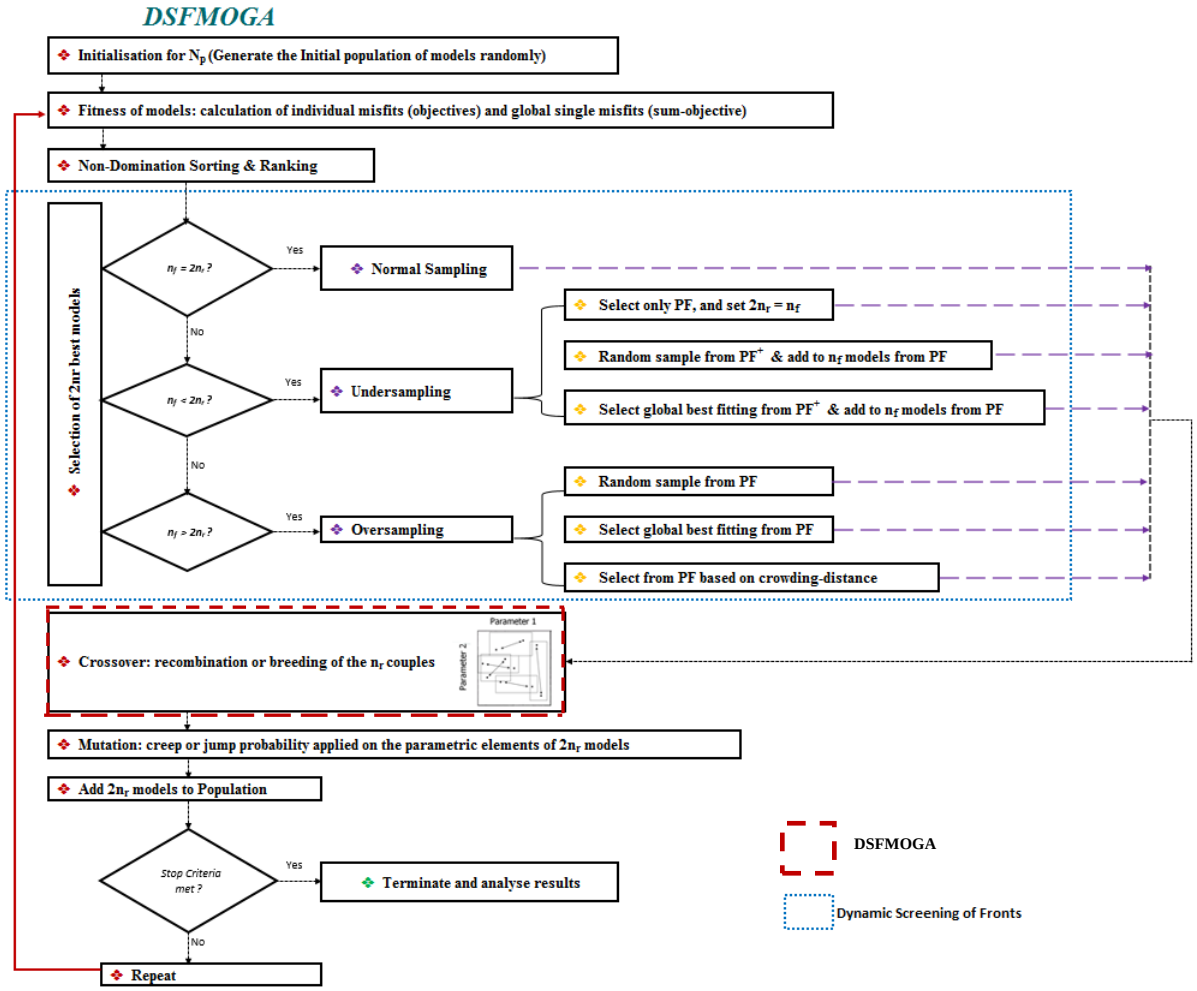

Figure 7.2 Flowchart of Dynamic Screening of Fronts in Multi-objective Genetic Algorithm (DSFMOGA)

The exploration and exploitation abilities of ***DSFMONA*** over the models in the Pareto Front rely on those two tuning parameters, n_r and n_s, and the user has control over the input values specified. The larger the n_r value the more the exploration but the large the n_s:n_r ratio the more the exploitation. Exploration encourages diversity while exploitation boosts convergence. The new n_s models are added to the pre-existing population and the iterative process that began with non-domination sorting is repeated.

We will compare the techniques described in the preceding sections in synthetic and real field history matching cases, but first we set up some test functions with conflicting objectives to verify the working of the DSFMO.

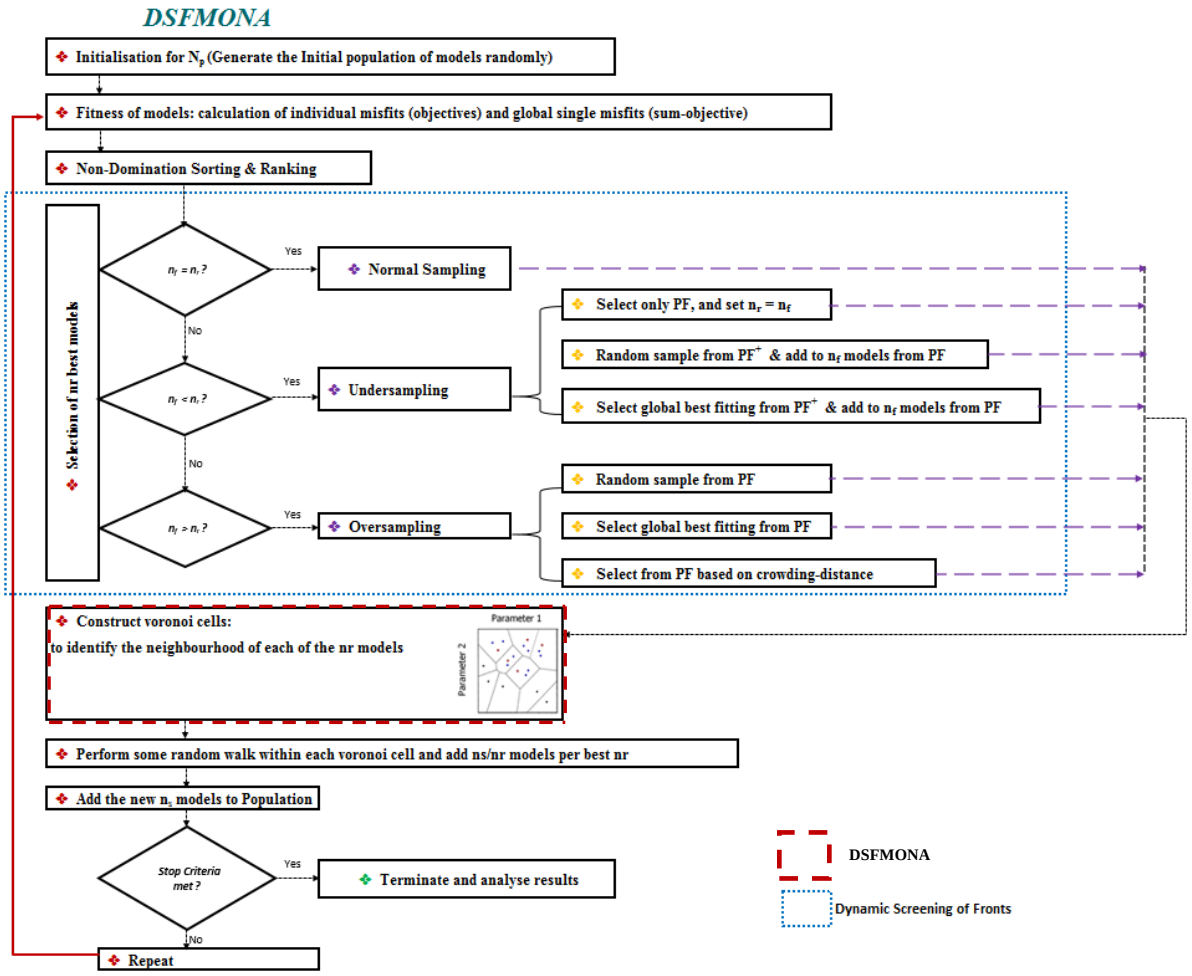

Figure 7.3 Flowchart of Dynamic Screening of Fronts in Multi-objective Genetic Algorithm (DSFMONA)

7.4 Test function with many conflicting objectives

We examine the working of DSFMO under conditions of conflicting objectives using some synthetic polynomials with known solutions. We define different cases of polynomial for examination of several scenarios as follows:

7.4.1 General Case

The polynomials are all of the form defined in equation 7.7 below. The different cases defined thereafter differ in the values of the real constants, α and β:

Minimise:

$$O(m) = \sum_{j=1,i=1}^{N_p} \alpha_j \, (m_i - \beta_k)^{\gamma}, \dots \dots \dots \dots \dots \dots \dots \dots \dots \dots \dots \dots \dots \dots \dots \dots \dots \dots \dots .. (7.7)$$

Subject to:

$$m = \left(m_1, m_2, \ldots, m_{N_p}\right) \in M$$

$$O(m) = \left(O_1(m), O_2(m), \ldots, O_{N_f}\right) \in O$$

In order to understand the nature of the problem let us consider a case of *three objectives and two parametric elements (α = 1, β_1 = -0.25, β_2 = 0.25, β_3 = 0.5, γ=2),* so we state the problem explicitly as follows:

Minimise:

$$O_1(m) = \sum_{i=1}^{2} (m_i - 0.25)^2, \ldots\ldots\ldots\ldots\ldots\ldots\ldots\ldots\ldots\ldots\ldots\ldots\ldots\ldots\ldots\ldots\ldots\ldots\ldots\ldots (7.8)$$

$$O_2(m) = \sum_{i=1}^{2} (m_i + 0.25)^2, \ldots\ldots\ldots\ldots\ldots\ldots\ldots\ldots\ldots\ldots\ldots\ldots\ldots\ldots\ldots\ldots\ldots\ldots\ldots\ldots (7.9)$$

$$O_3(m) = \sum_{i=1}^{2} (m_i + 0.5)^2, \ldots\ldots\ldots\ldots\ldots\ldots\ldots\ldots\ldots\ldots\ldots\ldots\ldots\ldots\ldots\ldots\ldots\ldots\ldots\ldots (7.10)$$

Subject to

$$-1 \leq m_i \leq 1$$

Figure 7.4 shows the different pairs of the individual objective functions for the first two parameters, where it can be seen that they all have different minimum or optimum value. Finding a global minimum that will satisfy all the objectives at the same is not a trivial task as they all compete with one another.

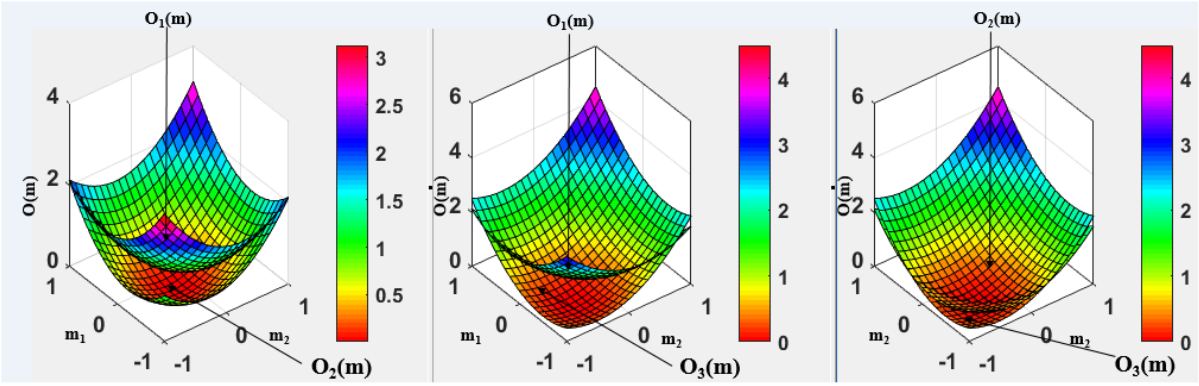

Figure 7.4 3D view of pairs of the objectives

The weighted sum-approach formulation for the same problem is:

Minimise:

$$O_1(m) = \omega_1 \times O_1(m) + \omega_2 \times O_2(m) + \omega_3 \times O_3(m), \ldots\ldots\ldots\ldots\ldots\ldots\ldots\ldots\ldots\ldots (7.11)$$

Subject to

$$-1 \leq m_i \leq 1$$

Figure 7.5 shows three cases of equation 7.11 plotted for the first two parametric elements for cases of : (i) Equal weighting factors ($\omega_1 = \omega_2 = \omega_3 = 1$), (ii) $\omega_1 = 10$, $\omega_2 = 1$ $\omega_3 = 1$ and (iii) $\omega_1 = 1$, $\omega_2 = 1$ $\omega_3 = 10$. As observed, changing the weighting factors obviously changed the global minimum and will affect the nature of the solution.

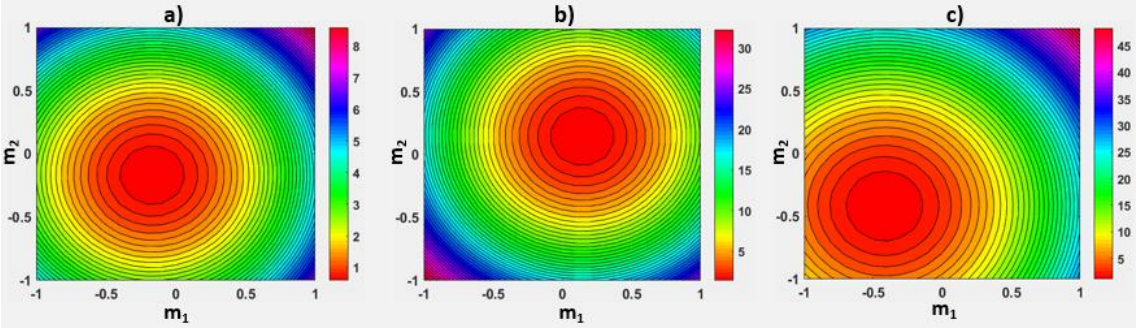

Figure 7.5 2D view for the aggregated weighted-objectives: a) Equal weighting factors ($\omega_1 = \omega_2 = \omega_3 = 1$), b) $\omega_1 = 10$, $\omega_2 = 1$ $\omega_3 = 1$ and c) $\omega_1 = 1$, $\omega_2 = 1$ $\omega_3 = 10$

The true value of the parameters occur at $m_1 = m_2 = m_3 = 0.25$ if we consider the first objective ($O_1(m)$) alone, at $m_1 = m_2 = m_3 = -0.25$ if we consider only the second objective ($O_2(m)$), and at $m_1 = m_2 = m_3 = 0.5$ if only the third objective ($O_3(m)$) is considered. The trade-off solution corresponding to the global minimum should be somewhere between these values.

7.4.2 Screening the fronts for best models

The goal in pareto-based multi-objective optimisation is to obtain the optimal Pareto front (PF). The real optimal PF is unknown but we want the returned PF to be as close as possible. It is also desired that the returned front should have a large set of diverse solutions on it. The selection of models for the next iteration in Pareto-based multi-objective optimisation is based on the concept of dominance.

The concept of dominance in multi-objective optimisation allows us to use the models on the pareto front as the "best" models in the NA and GA algorithms instead of using the total misfit However, this concept alone does not always give the best possible final PF. In DSFMO, the concept is combined with a number of different options for selection of models. A set of two parameters, defined earlier as "undersampled" and "oversampled", makes one option. At the end of each iterations, this set of two parameters determine how the models at the fronts are screened for the set of new model parameters fed into the next iteration. We want to investigate the effects that these options may have in the results of multi-objective optimisation problem. First, we designate the options as follows:

U1_O1: New models are taken from the PF only in the case of 'undersampled', and

New models are sampled randomly over the Pareto front in the case of 'oversampled'

U1_O2: New models are taken from the PF only in the case of 'undersampled', and Selection of new models is biased towards the lowest sum of misfits in 'oversampled'

U2_O1: New models are taken from both the PF and the ranks in 'undersampled', and New models are sampled randomly over the Pareto front in the case of ` 'oversampled'

U2_O2: New models are taken from both the PF and the ranks in 'undersampled', and Selection of new models is biased towards the lowest sum of misfits in ` 'oversampled'

We will study the performance of DSFMO in a series of experiments using the different options. We want to compare the performance of the respective options as the number of objectives in multi-objective problems increase. For this purpose, we set up some bench synthetic multi-objective problems each with 10 model parameters (10P). We will test the algorithm for problems with 3 objectives *(3O-10P),* 5 objectives *(5O-10P),* 7 objectives *(7O-10P),* 10 objectives *(10O-10P), and* 14 objectives *(14O-10P).* The multi-objective problems are of the form defined in Equation 7.7

For the experiments, DSFMO is set up to minimise the objectives in multi-objective fashion using GA, initialised with 64 models, and produces 32 models per iteration. The total number of iterations is 40 giving a total of 1344 models

Experiment 1: 3O-10P, and (α = 2, β_1 = -0.25, β_2 = 0.25, β_3 = 0.5, γ=2)

For comparison, we juxtapose the trend of the individual objectives and total objectives resulting from optimisation using the different options (Figure 7.6). We observe a similar trend in all options and note the slight differences. The trends indicate that the 'undersampled' cases in which new models are taken from the PF only (U1_O1 and U1_O2) start off at higher convergence rates than the undersampled in which new models are selected from both the PF and the ranks (U2_O1 and U2_O2). The option U1_O2 resulted in convergence to the least values of objectives O_2(m), O_3(m) but gave the worst performance in minimising O_1(m). It does appear as if optimisation using option U1_O2 is skewed against O_1(m). All the options gave similar convergence trend for the sum of the objectives [T(m)]. Overall, U2_O1 resulted in the least bias in minimising the objectives and gave the best performance in the convergence of the sum of the objectives.

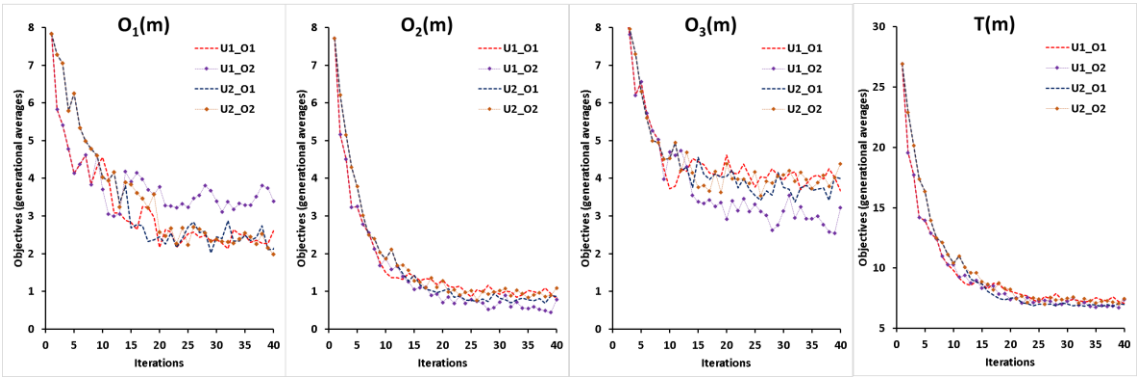

Figure 7.6 Evolution of the individual objectives and sum misfit in 3O-10P optimisation

In Figure 7.7 the each of the 10 parametric elements are shown for each of the 4 optimisation options. In all cases, the elements converged to values which represent the trade-off between the various objectives. Although there are slight differences in the trends observed in the parameters for the different options, the convergence of the parameters looked good in all options.

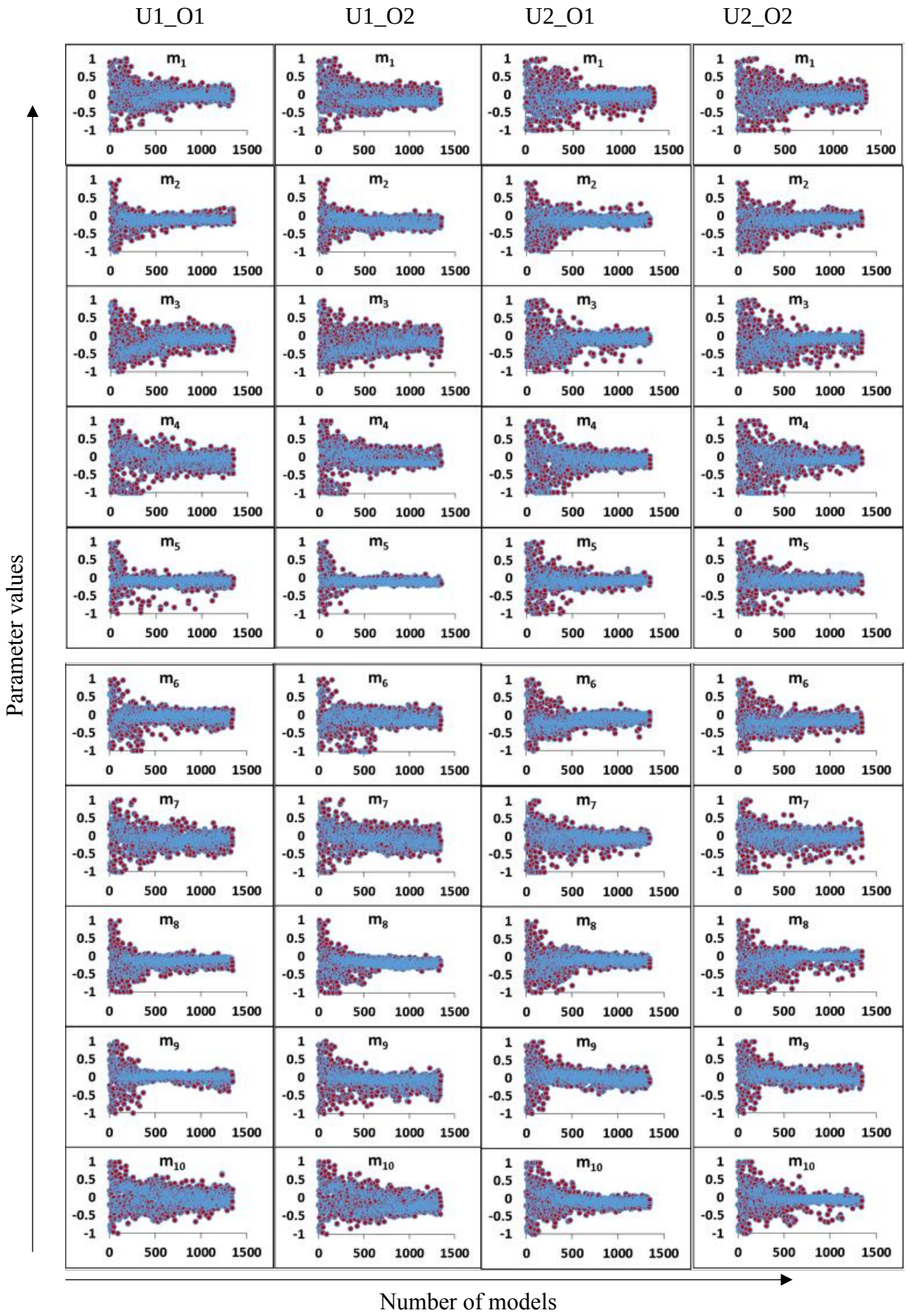

Figure 7.7 Evolution of parametric elements during the 3O-10P optimisation

Experiment 2: 5O-10P, and (α = 2, β_1 = -0.25, β_2 = 0.25, β_3 = 0.5, β_4 = -0.3, β_5 = 0.3, γ=2)

The trend of the individual objectives and total objectives during the optimisation using the different options are in Figure 7.8. The results show a similar pattern to Experiment 1, with U1_O1 and U1_O2 starting off at higher convergence rates than the U2_O1 and U2_O2. The slight bias observed in option U1_O2 in Experiment 1, is observed in both options U1_O1 and U1_O2. The objectives O_1(m) and O_4(m) appear to be favoured by options U1_O1 and U1_O2 at the expense of the other objectives, especially O_3(m). On the other hand, option U2_O2 returned models optimised in favour of O_3(m) and O_5(m), and strongly skewed against O_1(m), and O_4(m). Similar to the observations in Experiment 1, all the options gave similar convergence trend for the sum of the objectives [T(m)] with U1_O1 showing the trend with least values. However, U2_O1 again showed the least bias in minimising the objectives.

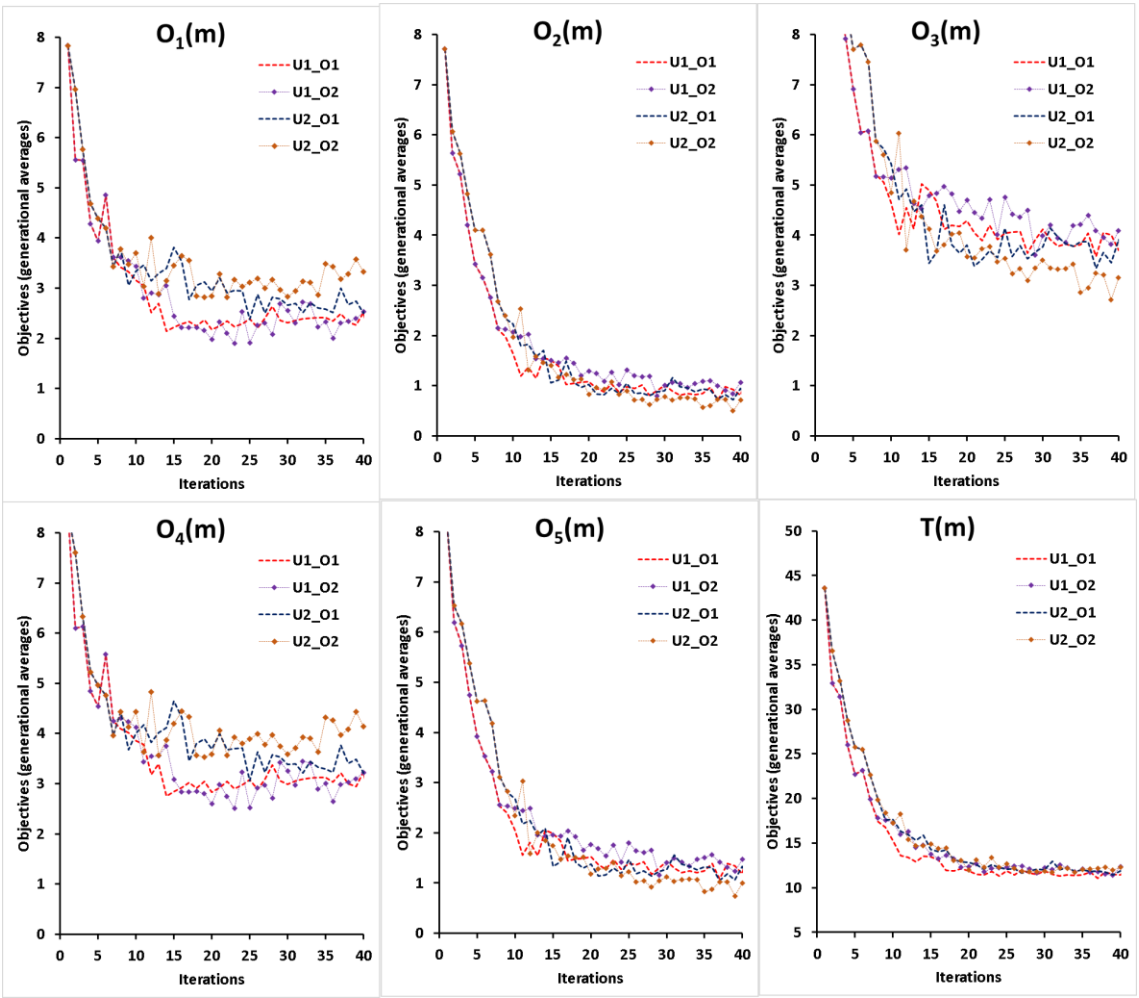

Figure 7.8 Evolution of the individual objectives and sum misfit in 5O-10P optimisation

The plot of the values of the parametric elements as the optimisation progresses (Figure 7.9) shows good convergence of all elements for all the options considered.

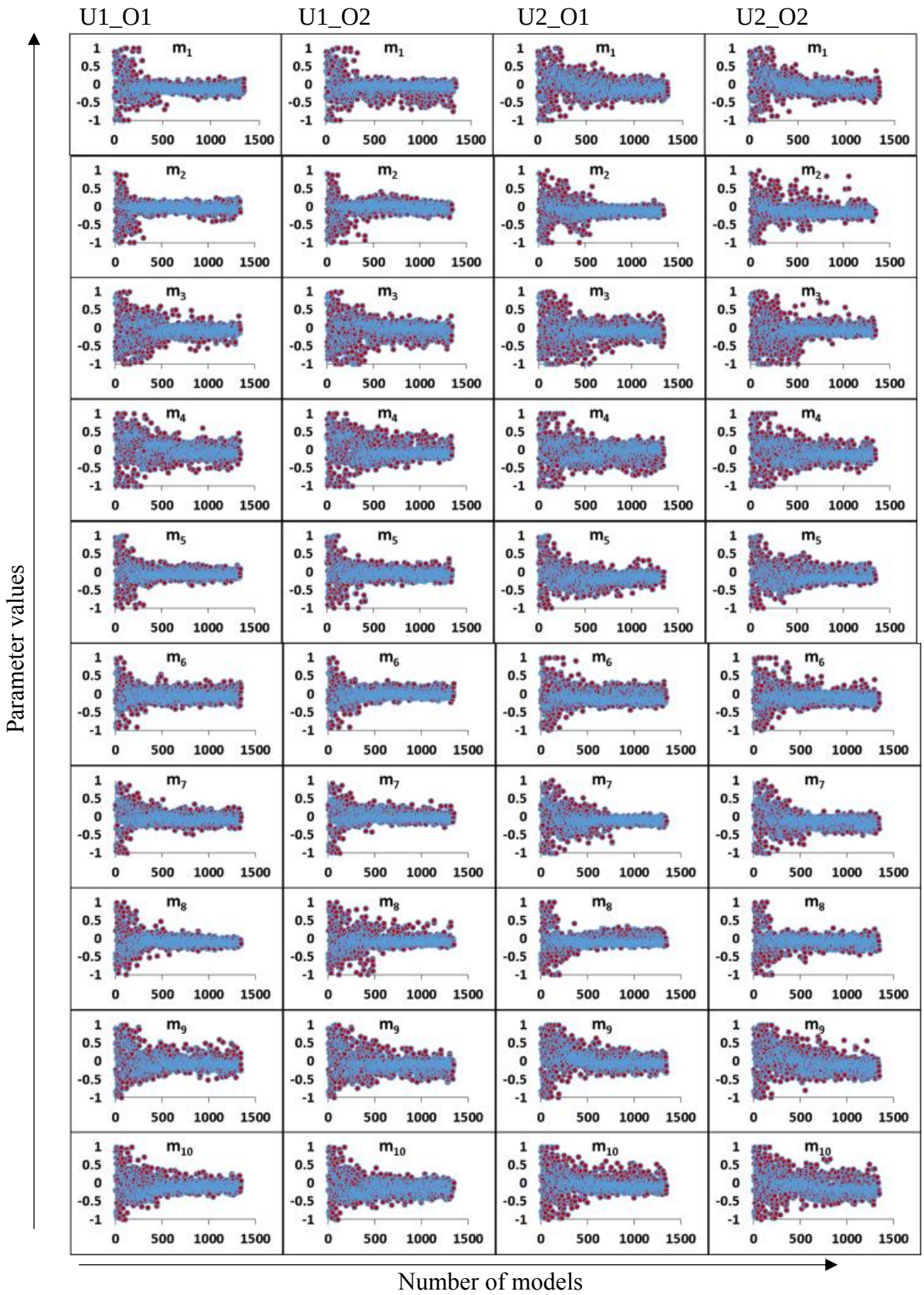

Figure 7.9 Evolution of parametric elements during the 5O-10P optimisation

Experiment 3: 7O-10P, and ($\alpha = 2$, $\beta_1 = -0.25$, $\beta_2 = 0.25$, $\beta_3 = 0.5$, $\beta_4 = -0.3$, $\beta_5 = 0.3$, $\beta_6 = 0.4$, $\beta_7 = -0.15$, $\gamma=2$)

As in the previous experiments, we look at the trends of the individual misfits and the sum misfit (Figure 7.10). Here, a problem of 7 conflicting objectives was optimised using

the different options available in DSFMO algorithm. Except, for slight difference, the start-off convergence rates were much closer for all options compared to the previous experiments. The slight bias observed in option U1_O2 in Experiment 1, is observed in both options U1_O1 and U1_O2. The optimisation using either option U1_O1 or U1_O2 favours the objectives O_1(m), O_4(m) and O_7(m)appear and is particularly skewed against the minimisation of O_3(m). Similar to the behaviour in Experiment 2, option U2_O2 returned models optimised in favour of O_3(m), O_5(m) and O_6(m), and strongly skewed against O_1(m), O_4(m) and O_7(m). All the options gave similar convergence trend for the sum of the objectives [T(m)] with U1_O1 showing the trend with least values. However, as in the previous cases, the results of U2_O1 indicates the least bias in minimising the objectives.

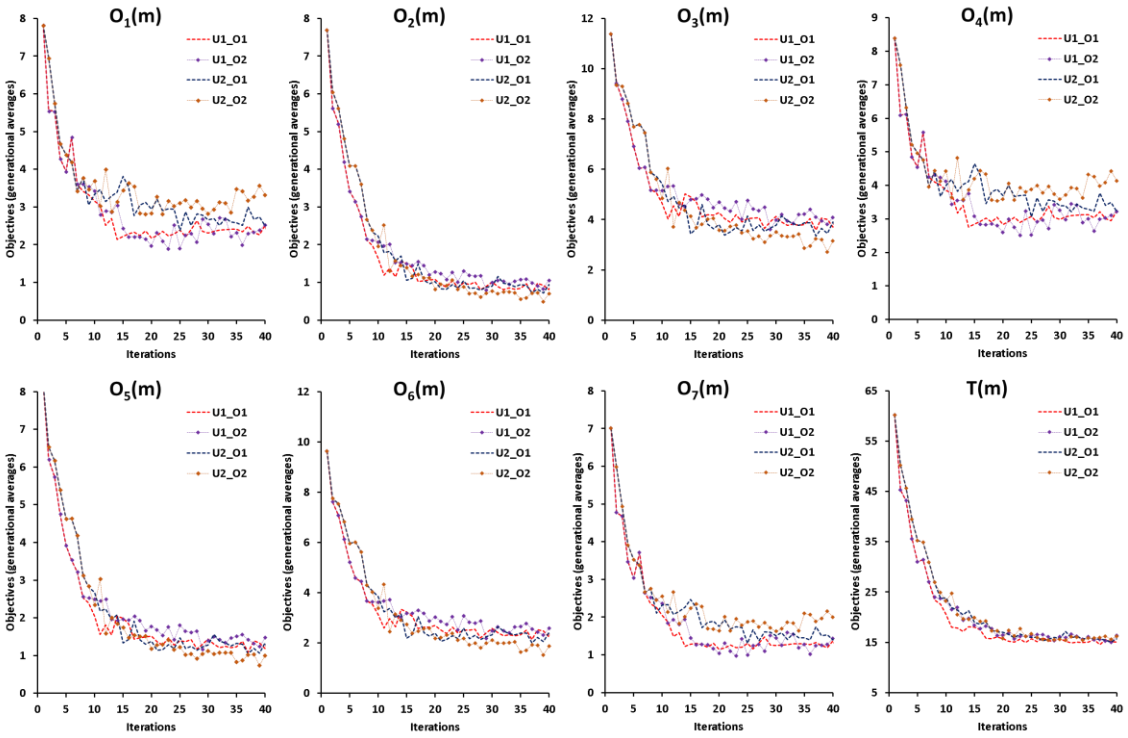

Figure 7.10 Evolution of the individual objectives and sum misfit in 7O-10P optimisation

As in the previous experiments, the parameters of the models converged to values corresponding to the trade-off in the objectives in all options (Figure 7.11). All the options have done well in optimising the problem of 7 conflicting objectives.

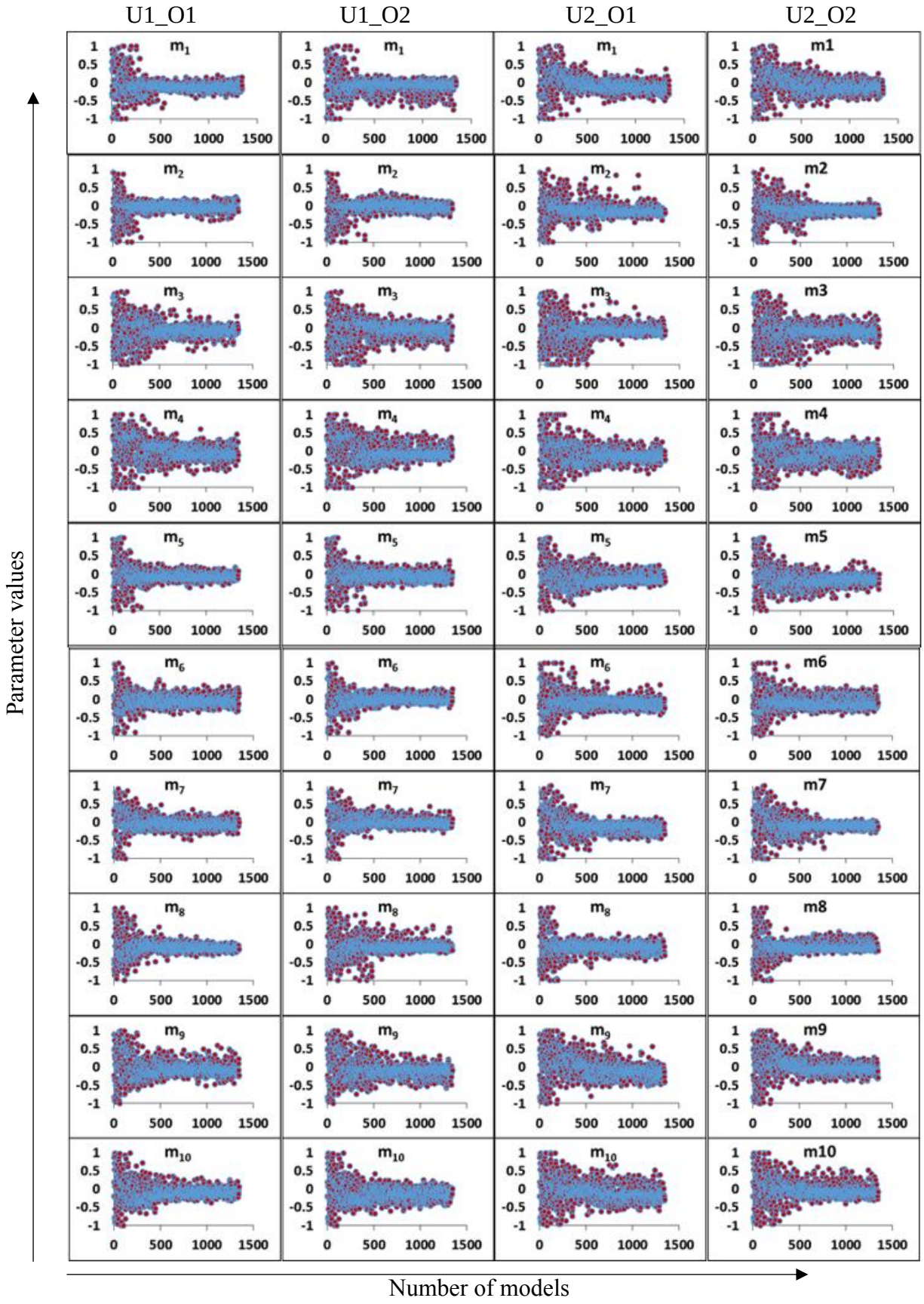

Figure 7.11 Evolution of parametric elements during the 7O-10P optimisation

Experiment 4: 10O-10P, and (α = 2, β_1 = -0.25, β_2 = 0.25, β_3 = 0.5, β_4 = -0.5, β_5 = 0.3,β_6 = -0.3, β_7 = -0.15, β_8 = 0.15, β_9 = -0.7, β_{10} = 0.7, γ=2)

For this problem of 10 conflicting objectives, the trends of the individual misfits and the sum misfit (in Figure 7.12) indicate clearly that option U2_O1 outperforms the other options in minimising the objectives. Other options show different degrees of bias in minimising the individual objectives. Option U1_O2 is biased towards the objectives $O_2(m)$, $O_3(m)$, $O_5(m)$ and $O_{10}(m)$, against the objectives $O_1(m)$, $O_4(m)$, $O_6(m)$ and $O_9(m)$. The results of options U1_O1 and U2_O1 do not indicate clear bias but their trends indicate poor convergence compared to U2_O1.

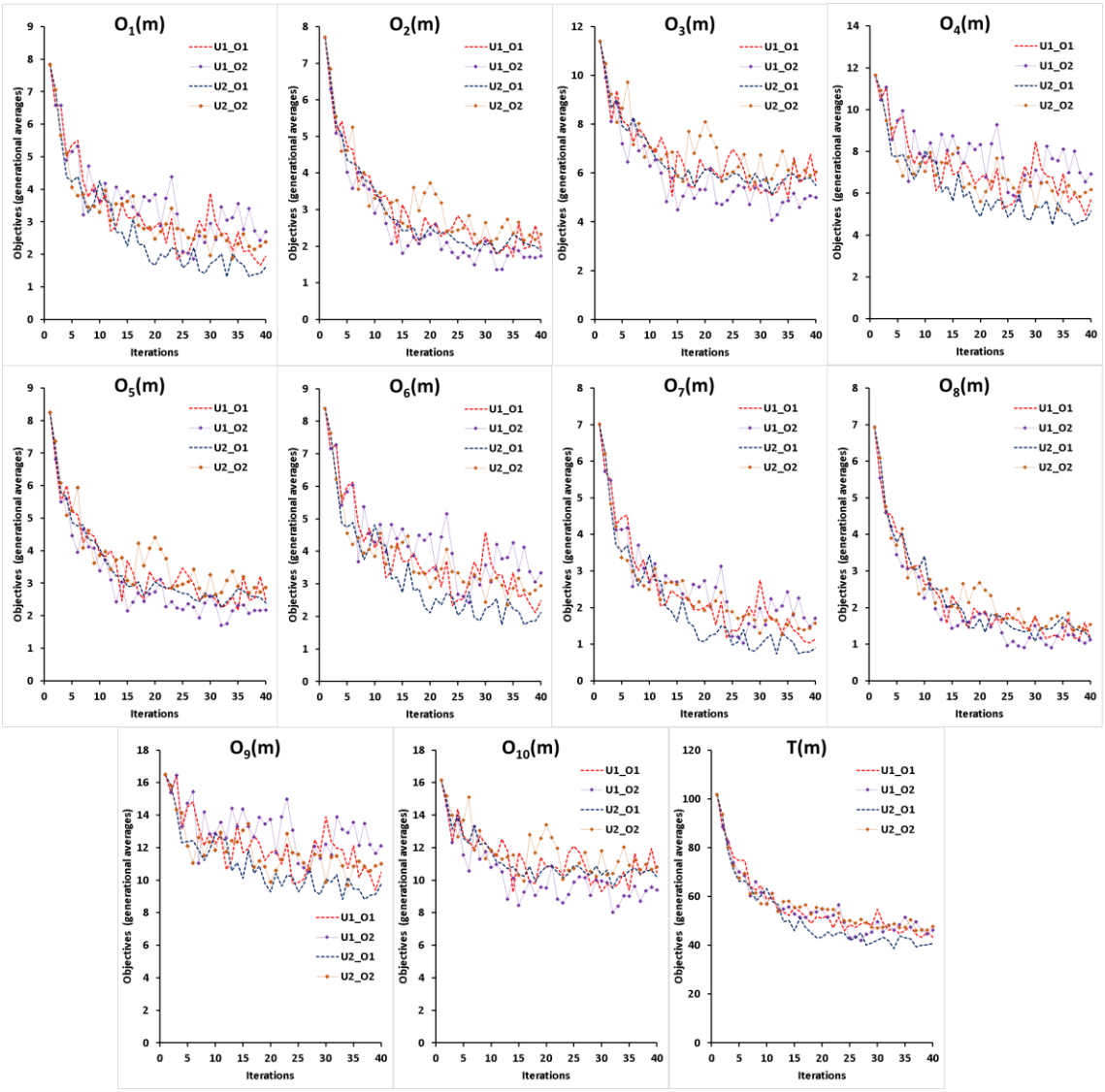

Figure 7.12 Evolution of the individual objectives and sum misfit in 10O-10P optimisation

The plots in Figure 7.13 also indicates the superiority of U2_O1. The convergence of the parametric elements is clearly better for this option.

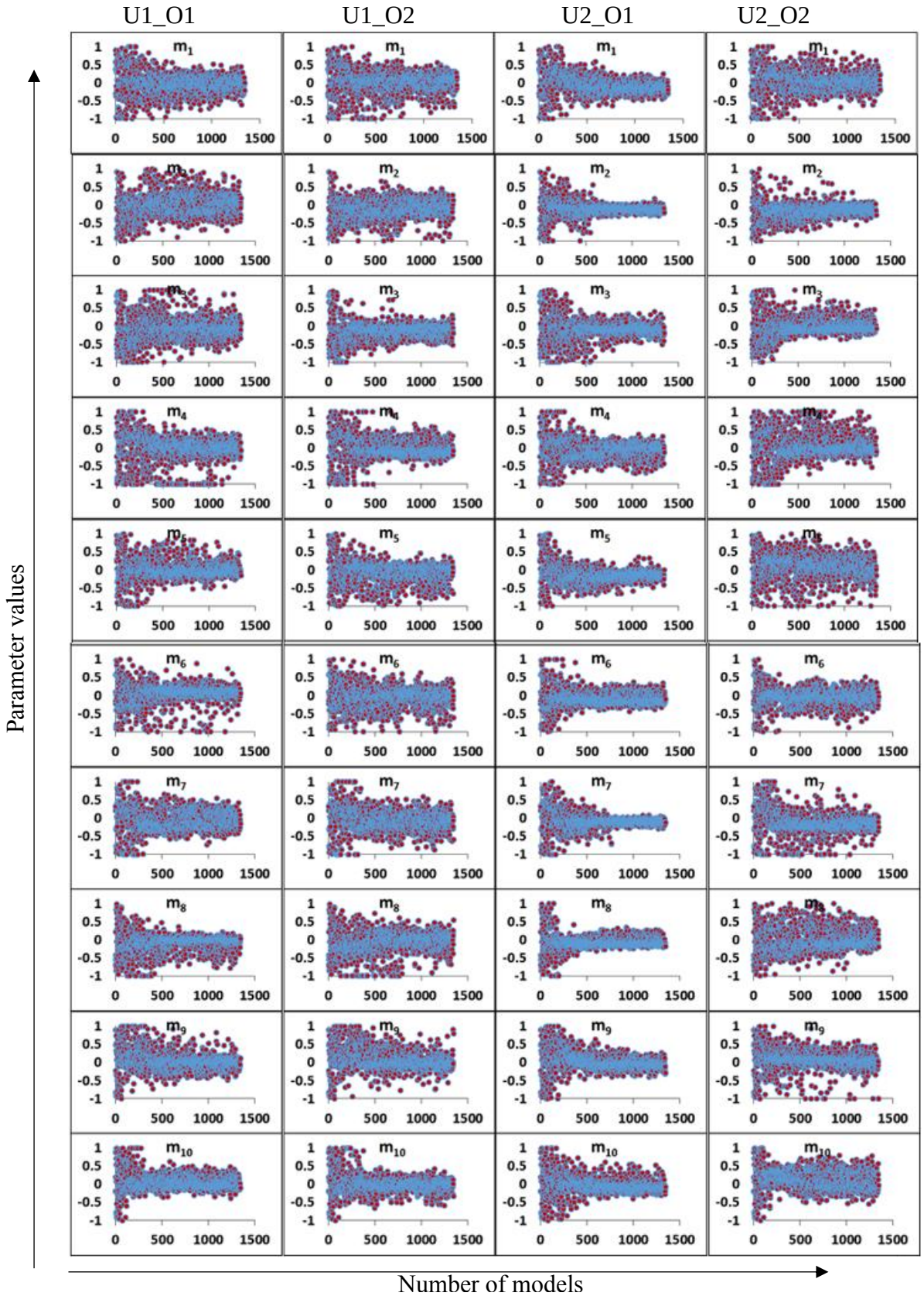

Figure 7.13 Evolution of parametric elements during the 10O-10P optimisation

Experiment 5: 14O-10P, and ($\alpha = 2$, $\beta_1 = -0.25$, $\beta_2 = 0.25$, $\beta_3 = 0.5$, $\beta_4 = -0.5$, $\beta_5 = 0.3$, $\beta_6 = -0.3$, $\beta_7 = -0.15$, $\beta_8 = 0.15$, $\beta_9 = -0.7$, $\beta_{10} = 0.7$, $\beta_{11} = -0.6$, $\beta_{12} = 0.6$, $\beta_{13} = -0.4$, $\beta_{14} = 0.4$, $\gamma=2$)

We further test the DSFMO algorithm in a problem of even larger dimension of objectives ; a problem of 14 conflicting objectives. The trends of the individual misfits and the sum misfit (Figure 7.14) confirms the superiority of option U2_O1, especially in a problem with large conflicting objectives. The behaviours of the other options are also consistent with the observations in Experiment 4. The trends indicate clearly that optimisation using options other than U2_O1 are skewed against some objectives, in favour of some others. Returns of option U1_O1 are biased towards $O_1(m)$, $O_4(m)$, $O_6(m)$ while those of option U2_O2 are in favour of $O_1(m)$, $O_4(m)$, $O_6(m)$, $O_7(m)$, $O_9(m)$, $O_{11}(m)$ and $O_{13}(m)$. On the other hand, U1_O2 is biased towards minimising $O_2(m)$, $O_3(m)$, $O_5(m)$, $O_8(m)$, $O_{10}(m)$, $O_{12}(m)$ and $O_{14}(m)$. the trend of the sum misfit also clearly shows that option U2_O1 return superior results in problems of large objectives.

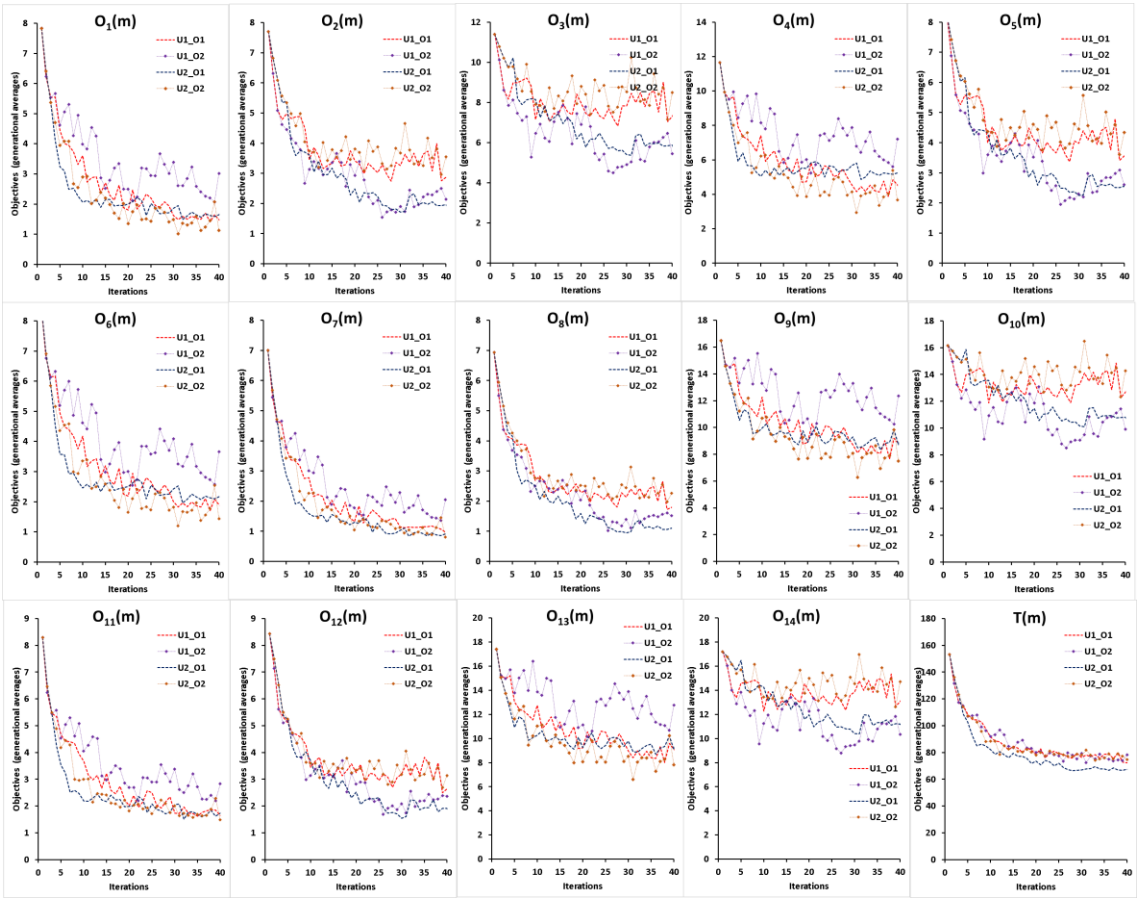

Figure 7.14 Evolution of the individual objectives and sum misfit in 14O-10P optimisation

Like in Experiment 4, the plots in Figure 7.15 clearly indicate that option U2_O1 returned the best converging models.

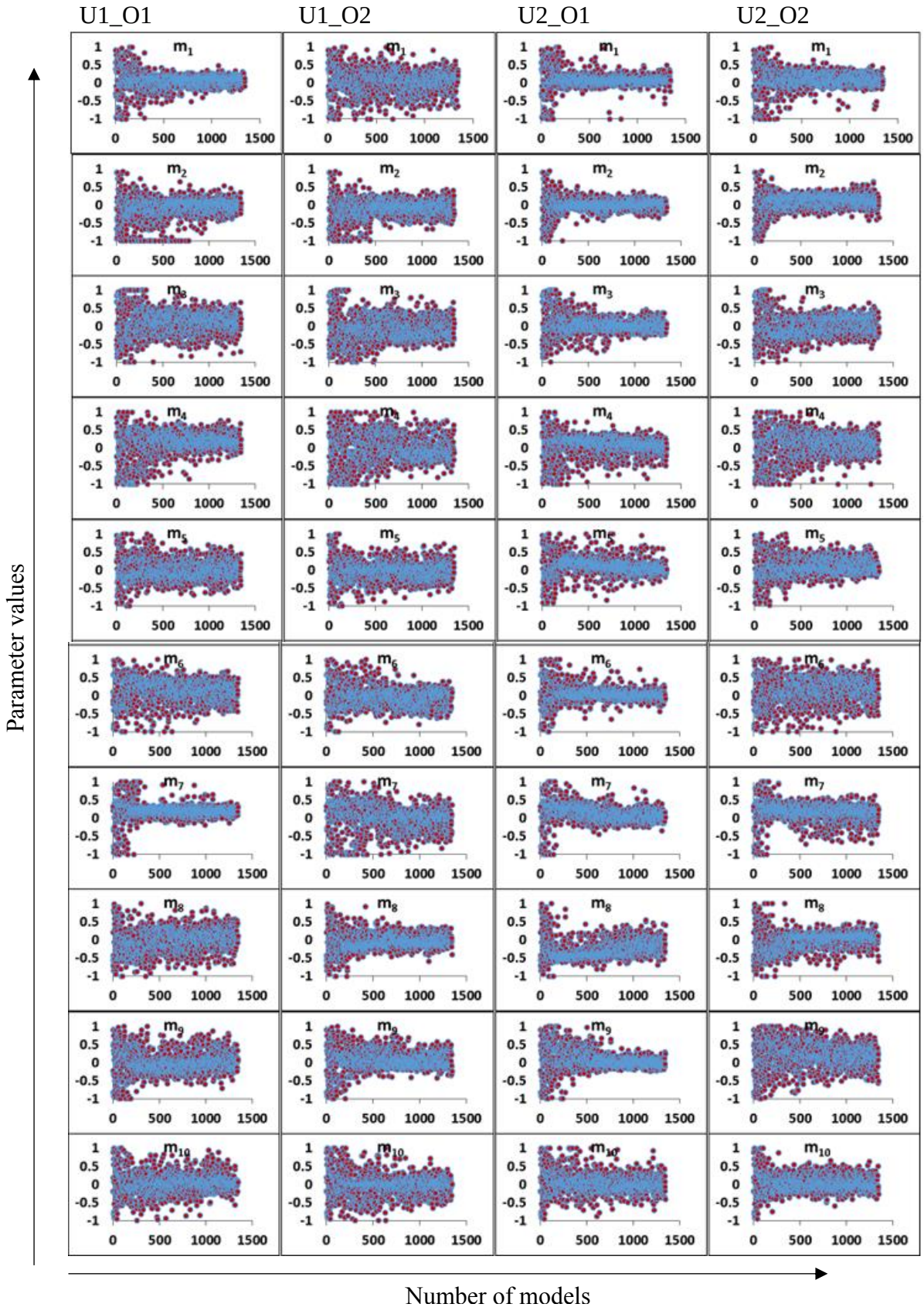

Figure 7.15 Evolution of parametric elements during the 14O-10P optimisation

The above experiments demonstrated the strengths and weaknesses of the different options for screening the fronts available in the DSFMO codes. We observed the differences in the returns of the different options, and conclude that the U2_O1 showed

signs of superiority over the others especially as the number of the conflicting objectives increases.

Next we set up other cases to compare the performance of DSFMO (using option U2_O1) to the performance of single objective optimisation, and other multi-objective problems with reduced dimensionality.

7.4.3 Comparing to cases with reduced dimensionality

We will attempt to solve the problem stated in equation 7.7 for several cases of 3 objectives and 10 parameters problems (3O-10P), 3 objectives and 27 parameters problems (3O-27P), and the more complex cases of 7 objectives and 10 parameters problems (7O-10P) and 7 objectives and 27 parameters problems (7O-27P) using DSFMO. We will compare the results of optimisation with DSFMO to the results obtained through cases in which objectives are aggregated to reduce the dimensions in objective space (especially, the aggregated sum-objective approach). As done previously, DSFMO is set up to minimise the objectives in multi-objective fashion using GA, initialised with 64 models, and produces 32 models per iteration. The total number of iterations is 40 giving a total of 1344 models

Case 1: 3O-10P, and (α = 2, β_1 = -0.25, β_2 = 0.25, β_3 = 0.5, γ=2)

In Figure 7.16 pairs of the objectives are plotted to review the pareto ranking resulting from DSFMOGA. For clarity, only the first 10 ranks are plotted. As expected, the nature and shape of the fronts established by the objective pair, *O_1(m) and O_2(m)*, in Figure 7.16a and the objective pair, *O_1(m) and O_3(m)*, in Figure 7.16b indicate that the objective pairs, are in competition; the objectives are in negative correlation (anti-correlation). On the other hand the objective pair *O_2(m) and O_3(m)*, are mostly positively correlated.

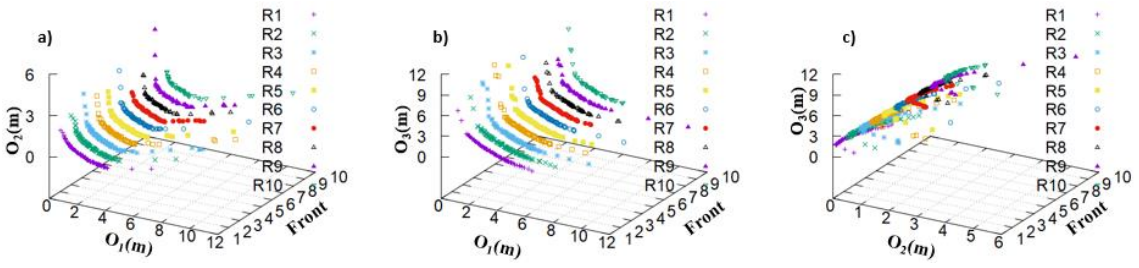

Figure 7.16 Ranking in optimisation using DSFMOGA for the objective pairs: a) O_1(m) and O_2(m), b) O_1(m) and O_3(m), c) O_2(m) and O_3(m)

We compare the parameter evolution for case 1 during the optimisation with DSFMOGA to the corresponding parameter evolution for the case where objectives are aggregated and optimised as a single-objective (Figure 7.17).

Calculation of the value of each of the parametric elements in the expected trade-off solution for this synthetic polynomial example is simple. In the case of a sum-objective approach, it is equal to the weighted average of all the true solutions derived from the objectives when each of the objectives are optimised/minimised in isolation, as expressed in equation 7.12:

$$\forall i = 1, \ldots., N_p: \qquad m_i^t = \frac{1}{N_f} \sum_{j=1}^{N_f} arg \min_{m \in M} O_i(m), \ldots\ldots\ldots\ldots\ldots\ldots\ldots\ldots\ldots (7.12)$$

Where m_i^t is the expected value of any parametric element in the trade-off solution.

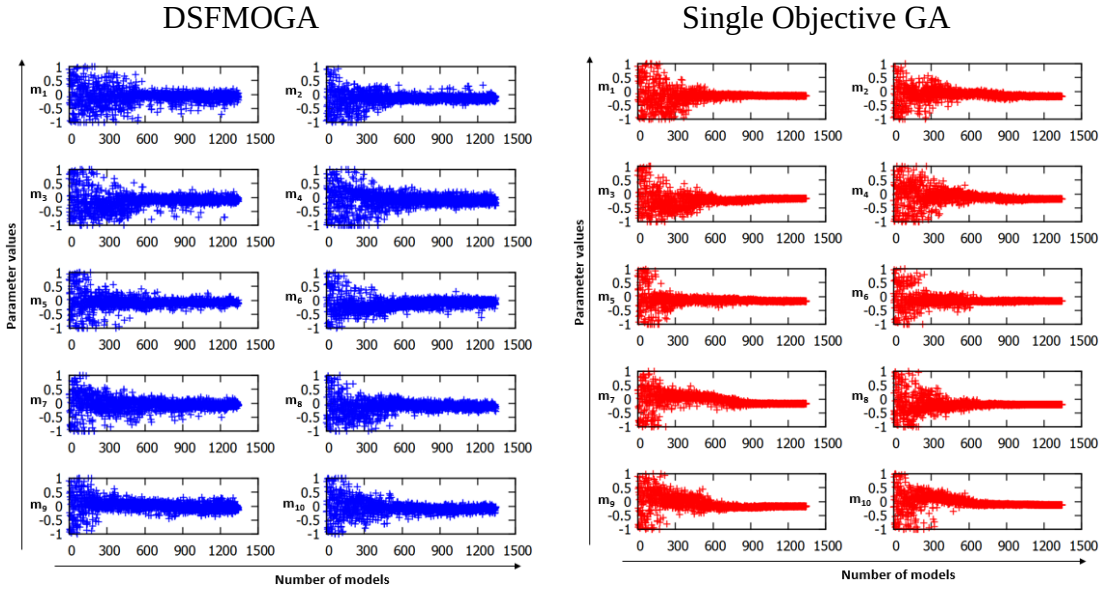

Figure 7.17 Evolution of parametric elements during optimisation with DSFMOGA vs Single Objective GA for 3O-10P

Comparing the results presented in Figure 7.17, we see that in the case of DSFMOGA all the parameters, m_i (i = 1, 2, …, 10) converged towards some trade off values. In single-objective GA, the parameters converged to the average value which is approximately equal to 0.17; the objectives are assigned equal weights, so each parametric element converged to the average value of the true parameter values in the individual objectives. In Figure 7.18, we show the evolution of the individual components of the global misfit for the DSFMOGA and the single objective GA. The DSFMOGA gives much better exploration of the model space in search of the trade-off solutions. This indicates that DSFMOGA is less liable to be trapped at the local minima than single objective GA. The outcome of Figure 7.18b is a distribution of solutions that minimise the different objectives,

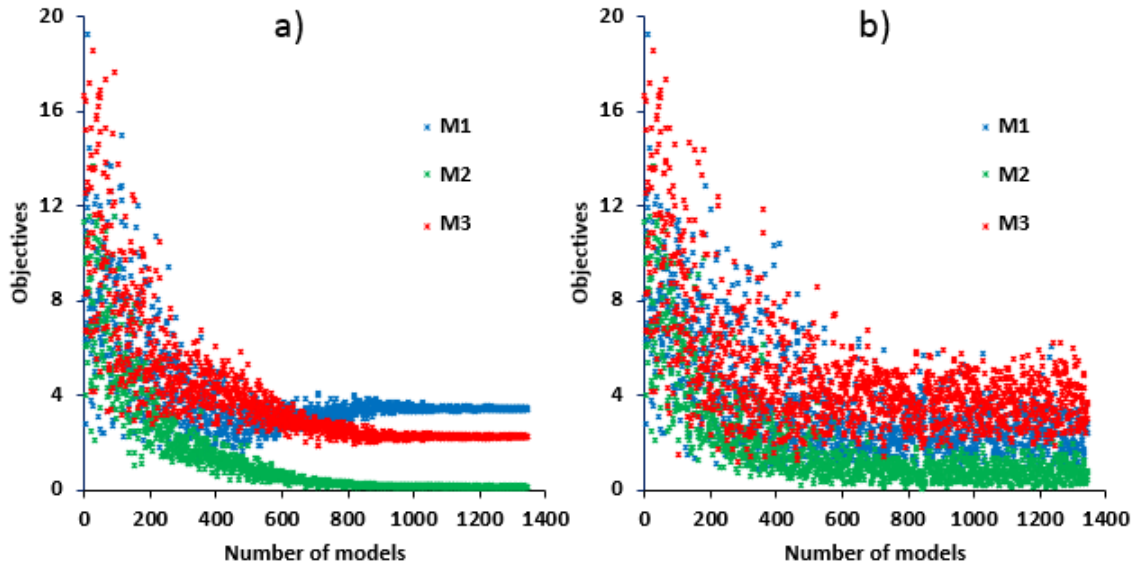

Figure 7.18 Evolution of the three objectives in optimisation using a) single objective GA, b) DSFMOGA

Case 2: 7O-10P, and (α = 2, β_1 = -0.25, β_2 = 0.25, β_3 = 0.5, β_4 = -0.3, β_5 = 0.3, β_6 = 0.4, β_6 = -0.15, γ=2)

This case has 7 conflicting objectives and 10 parameters, and the objectives are assigned equal weights. The results of Case 2 are presented in Figures 7.19 and 7.20

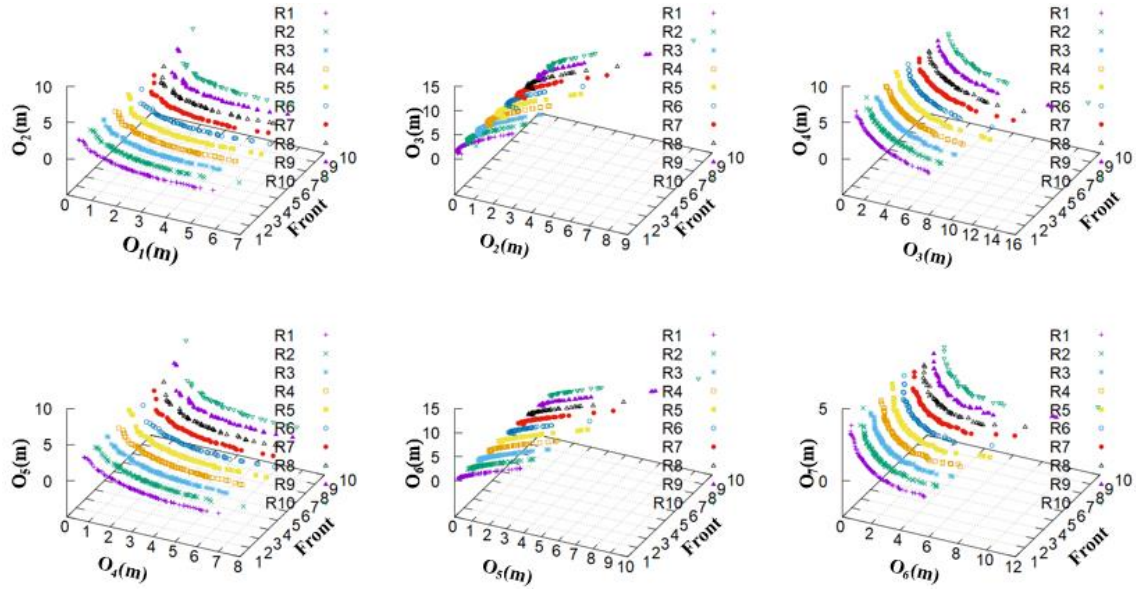

Figure 7.19 Pareto plot of the objective pairs in Case 2: 7O-10P

The observations in the results presented in Figures 7.19 and 7.20, are consistent with the observations made in Case 1. We see that while both the single objective GA and the DSFMOGA search for the optimal solutions, the search space explored by the single objective technique is narrower for all parameter plots presented in Figure 7.20. Trade-

off solutions were find by DSFMOGA even for larger number of conflicting objectives and model parameters.

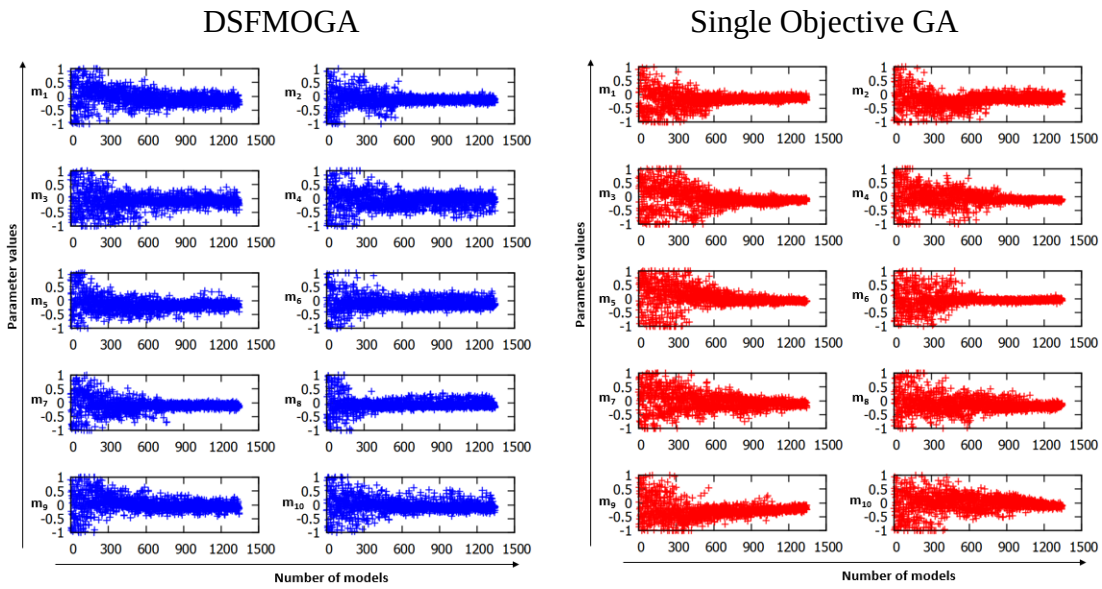

Figure 7.20 Paremeter evolution for Case 2: 7O-10P

Case 3: 7O-10P, and ($\alpha_1 = \alpha_4 = \alpha_7 = 1$ and $\alpha_2 = \alpha_3 = \alpha_5 = \alpha_6 = 3$, $\beta_1 = -0.25$, $\beta_2 = 0.25$, $\beta_3 = 0.5$, $\beta_4 = -0.3$, $\beta_5 = 0.3$, $\beta_6 = 0.4$, $\beta_7 = -0.15$, $\gamma=2$)

Like in Case 2, this case has 7 conflicting objectives and 10 parameters but with differing weight factors. The results of Case 3 are presented in Figures 7.21, 7.22 and 7.23

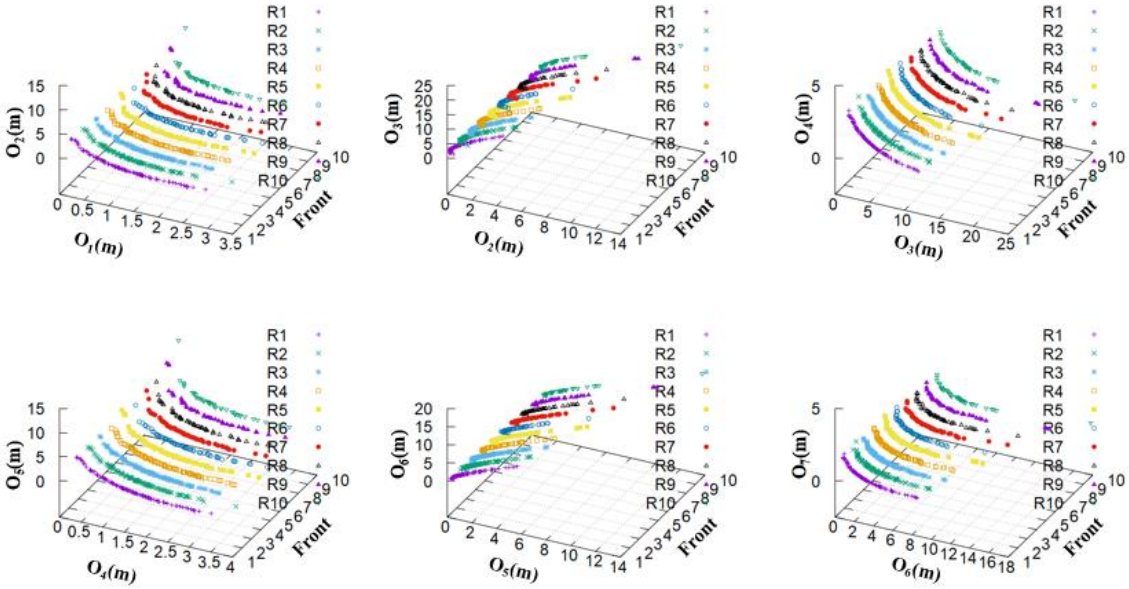

Figure 7.21 The evolution of fronts in the objective pairs for Case 3: 7O-10P

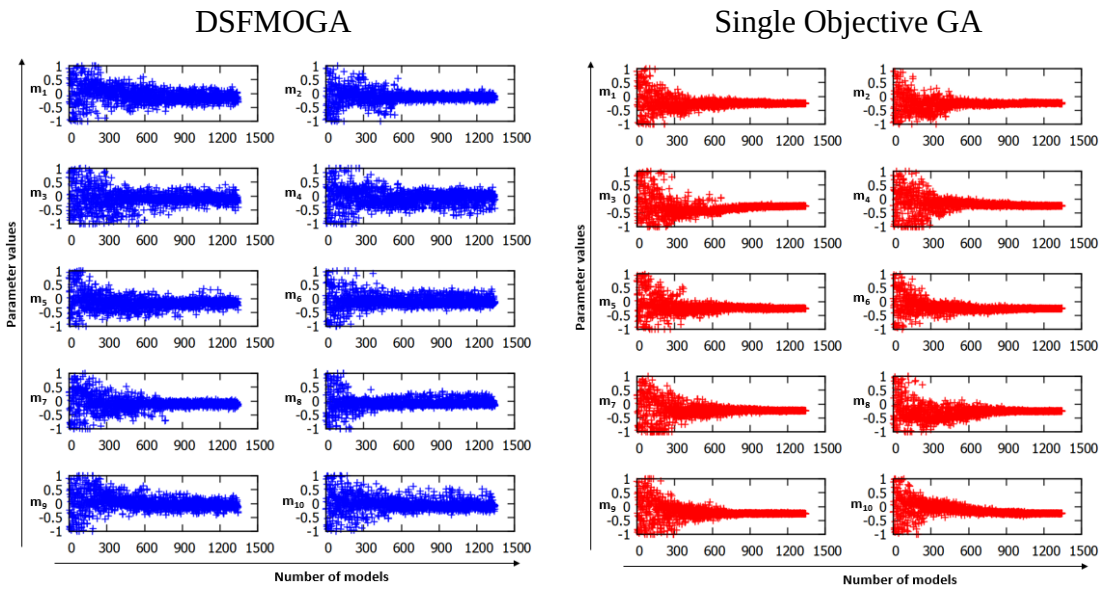

Figure 7.22 The parameter evolution for Case 3: 7O-10P

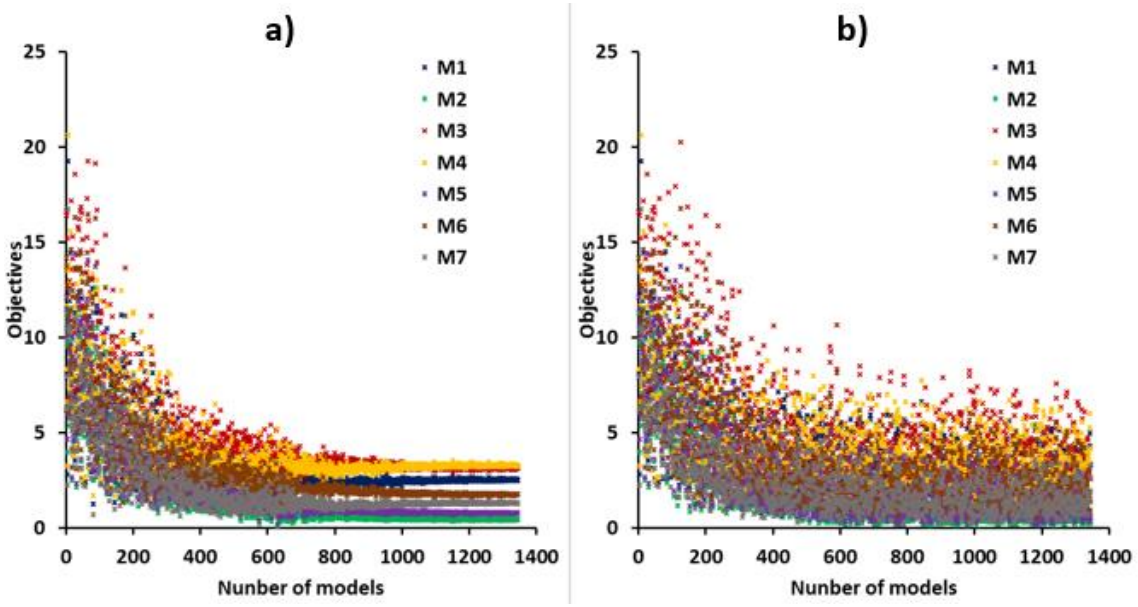

Figure 7.23 Evolution of individual objectives in Case 3 for a) Single objective GA, b) DSFMOGA

We notice the difference in the results between Case 2: 7O-10P (Figures 7.19 and 7.20) and Case 3: 7O-10P (Figures 7.21, 7.22, 7.23). Case 2 and Case 3 are defined in such a way to represent the same problem which ideally should have the same solution. The difference between the two cases is in the magnitude of the scalars assigned to the objective functions. In case 2, all the objectives were assigned equal weight ($\alpha = 2$) while in Case 3 the objectives $O_2(m)$, $O_3(m)$, $O_5(m)$, $O_6(m)$, are assigned weights which are three times the weights of the objectives $O_1(m)$, $O_4(m)$, $O_7(m)$.

We see that there are no differences in the results of optimisation using DSFMOGA as we compare Case 2 and Case 3, while huge differences are easily noticeable in the results

of the single-objective GA. This is another area where the strength of DSFMO lies. It shows that in using the DSFMO, we need not worry over what the arbitrary weights assigned to the different objectives should be. DSFMO is able to find solutions in the pareto feasible region irrespective of what the weights are. In single-objective GA, the search for solution is biased towards the objectives with higher weights.

Case 4: 7O-27P, and (α = 2, β_1 = -0.25, β_2 = 0.25, β_3 = 0.5, β_4 = -0.3, β_5 = 0.3, β_6 = 0.4, β_7 = -0.15, γ=2)

In Case 4, we want to test the capability of DSFMO in resolving more complex problems. The number of parameters here is 27 and the number of objectives is 7. The results are presented in Figures 7.24 and 7.25.

Through the plots of the objective pairs in Figure 7.24, DSFMO is demonstrated to be effective in resolving the many-parameter problem: the pareto fronts evolved towards lower solutions and each of the 27 parameters converged towards the trade-off solutions. On the other hand, single objective GA narrowed the search towards a global optimum and some of the parameters seem to converge towards some local minima.

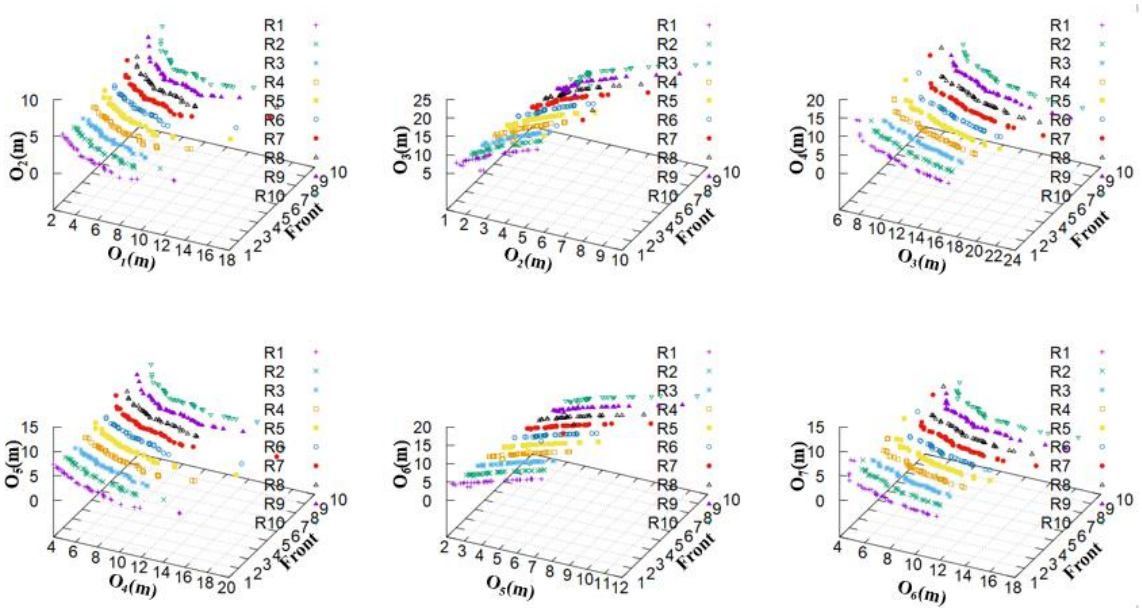

Figure 7.24 The evolution of the pareto fronts for the objective pairs in Case 4: 7O-27P

Consistent with the observations in the previous cases, the shape of the fronts in Figure 7.24 reflects the nature of correlation, conflict or trade off expected of each pair of objectives. If the objectives were to be treated on a single basis, we would have expected *$O_1(m)$, $O_4(m)$, $O_7(m)$* to converge to positive parameter values and *$O_2(m)$, $O_3(m)$, $O_5(m)$ $O_6(m)$,* to negative values. This is so if we consider the definition of the problem in Case 4 (i.e. considering the *βi* values). For example, the objective pair *$O_1(m)$ and $O_2(m)$,*

$O_4(m)$ and $O_3(m)$, $O_4(m)$ and $O_5(m)$, $O_6(m)$ and $O_7(m)$ are expected to have negative correlation because in each pair, one objective has a true individual solution that is negative while the other is positive.

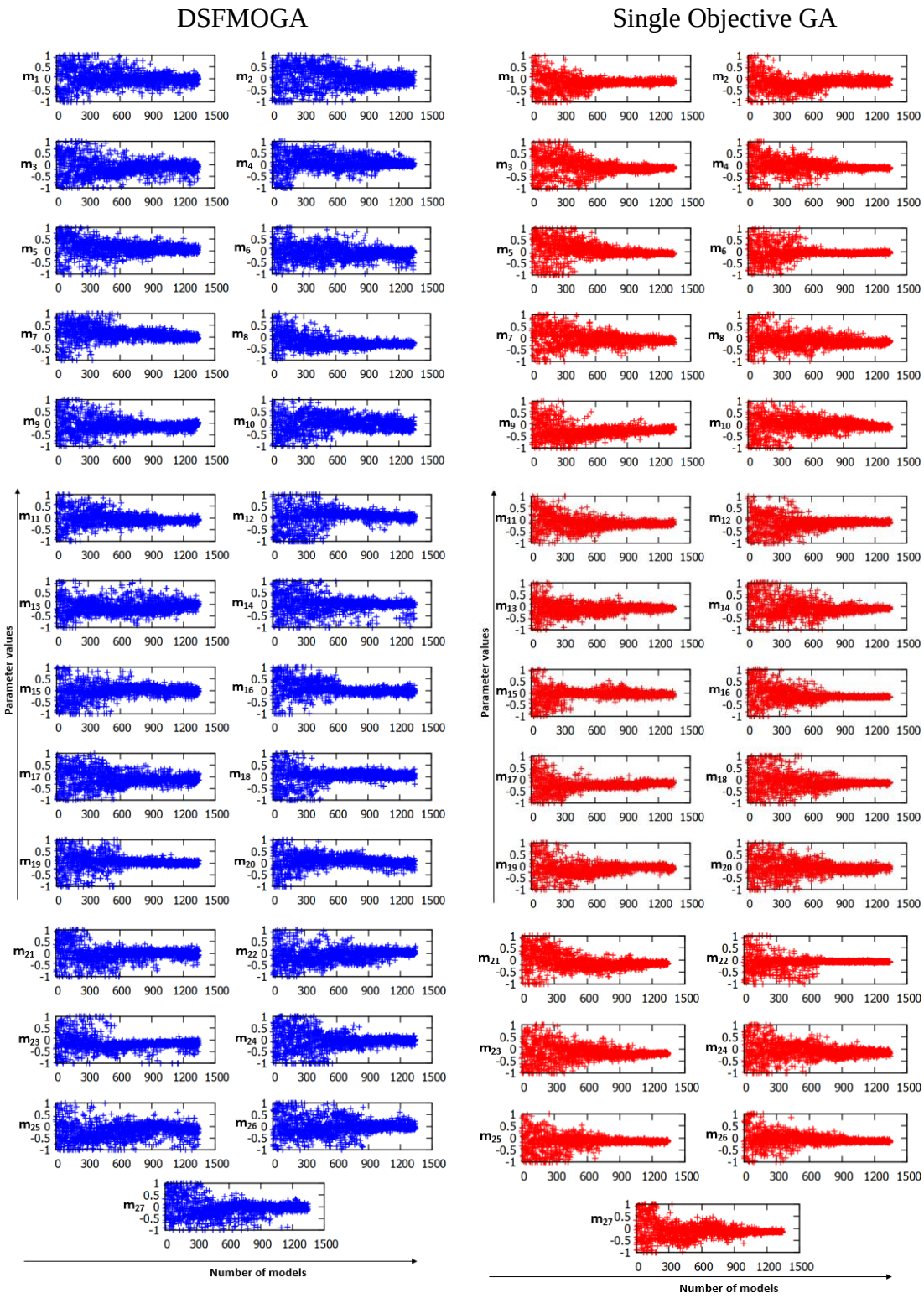

Figure 7.25 The evolution of parameters in Case 4: 7O-27P

The shape of the front in the plot shows this – the front mostly trends downwards from left to right. On the other hand, the objectives pairs *$O_2(m)$ and $O_3(m)$, $O_5(m)$ and $O_6(m)$*

are expected to be positively correlated as the independent solution of the objectives in a pair is either both positive or both negative. The shape of their fronts trend upwards from left to right as expected.

Case 5: 7O-27P, and ($\alpha_1 = \alpha_4 = \alpha_7 = 1$ and $\alpha_2 = \alpha_3 = \alpha_5 = \alpha_6 = 3$, $\beta_1 = -0.25$, $\beta_2 = 0.25$, $\beta_3 = 0.5$, $\beta_4 = -0.3$, $\beta_5 = 0.3$, $\beta_6 = 0.4$, $\beta_7 = -0.15$, $\gamma=2$)

As a final test to demonstrate the capability of DSFMO, we create a problem that is similar to Case 4 with 7 objectives and 27 parameters, but in this case we assign different weights to the objectives. The essence of this test is to validate the observations made in Case 3 in a problem of many parameters.

As in Case 3, the objectives $O_2(m)$, $O_3(m)$, $O_5(m)$, $O_6(m)$, are assigned weights which are three times the weights of the objectives $O_1(m)$, $O_4(m)$, $O_7(m)$. The results of optimisation of this problem are presented in Figures 7.26 and 7.27. The observations from the results are consistent with the observations in the previous cases. For instance, there is no difference in the results of optimisation using DSFMOGA in Cases 4 and 5 which is a confirmation that DSFMO is not affected by arbitrary weights. The results of single objective GA in Cases 4 and 5, on the other hand, differ very significantly since the capability of the single objective optimizer in searching the model space is influenced by the weights assigned to the individual objectives.

We therefore conclude that DSFMO is very robust in resolving problems of conflicting objectives in many objectives problems.

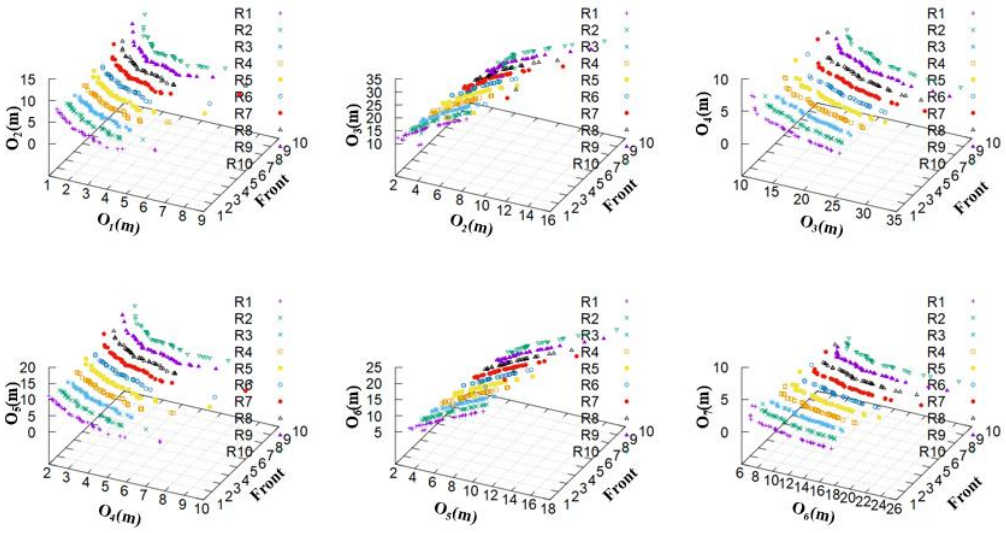

Figure 7.26 The evolution of the pareto fronts for the objective pairs in Case 5: 7O-27P

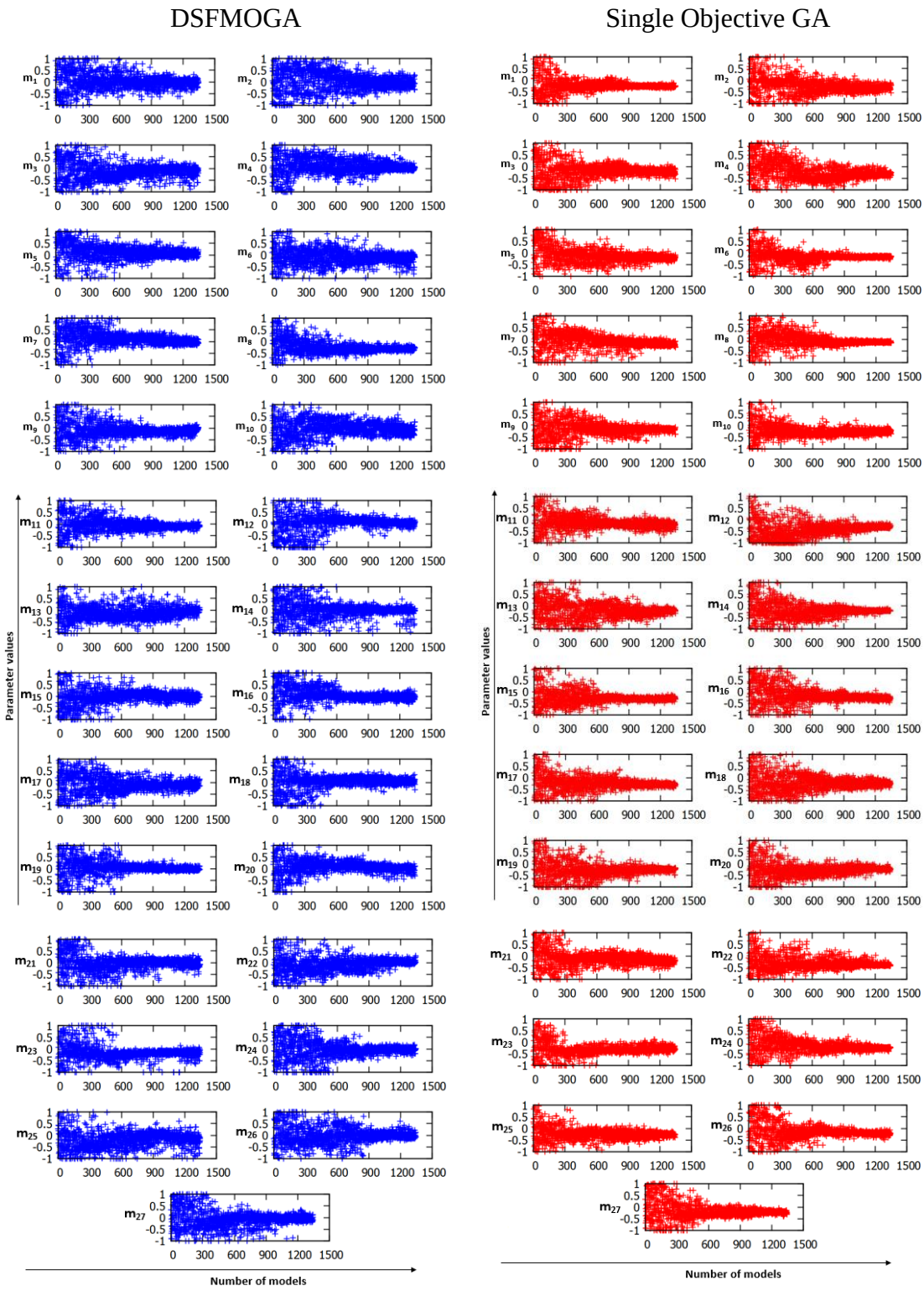

Figure 7.27 The evolution of parameters in Case 5: 7O-27P

Next, we will apply the algorithm in reservoir simulation cases starting with history matching of synthetic reservoir models for which we assume that the solutions are not known.

7.5 Synthetic Benchmark Case - SGSIM4 Model

Our second step in validating the capability of the DSFMO is through a synthetic 3D reservoir simulation model. We call this model SGSIM4. The model represents a medium size oil field produced through water flooding with two producers and two injectors (Figure 7.28). The uncertain parameters are the permeabilities in the grid cells.

a) b)

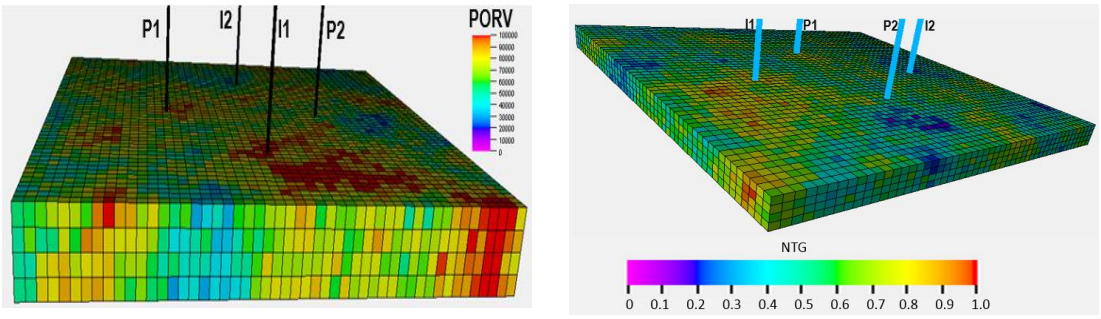

Figure 7.28 SGSIM4 Simulation model, a) Pore volume (PORV) b) Net-to-Gross (NTG)

The simulation grid has 50 x 50 x 4 cells populated with Net:Gros and permeability values using Sequential Gaussian Simulation. The model was built on a cartesian grid and the dimension of each cell is 100m x 100m x 7.2m. The permeability is log normally distributed and had an average permeability of 975mD. There are 10,000 permeability values (each per one grid cell) distributed in the grid cells. It is not practicable to perform history matching by considering the permeabilities in each cell as the decision variables. We used pilot point parameterization scheme (De Marsily *et al.*, 1984) to reduce the number of unknown parameters. On top of the 50 x 50 x 4 simulation grids, we create a grid that is 5 x 5 x 1 cells and the pilot points are located at the corners. The pilot points are located around the well regions where sensitivity to changes in reservoir properties are high.

The wells are all vertical, located at different (I, J) locations: (15, 25) for P1, (35, 25) for P2, (26, 38) for I1 and (26, 12) for I2, and are completed across all layers. The producers, P1 and P2, operate at a liquid rate of 18,000 STB/day. The injector is on pressure control and the field remains above bubble point. With 10-cells separation distance in the x-y direction, the six pilot points are placed at the corners and indexed accordingly using (i,j) lattice co-ordinates at (21, 21), (31, 21), (21, 31), (31, 31), (21, 41), (31, 41), and we designate the reservoir properties to be modified at these locations as m_1, m_2, m_3, m_4, m_5 and m_6 respectively (Figure 7.29). For this study we chose to update the horizontal permeability at the pilot locations through permeability multipliers. We sampled $\log_{10}$ of the multipliers in the range (-1, 1) for all parameters (at the locations identified by the six

pink symbols in Figure 7.29), so that the actual multipliers at the pilot points are allowed to vary from 0.1 to 10. Changes to the permeability multipliers at the pilot points are propagated to cells in between using a geostatistical method (Kriging). Black symbols in the figure indicate fixed pilot points where no changes are made.

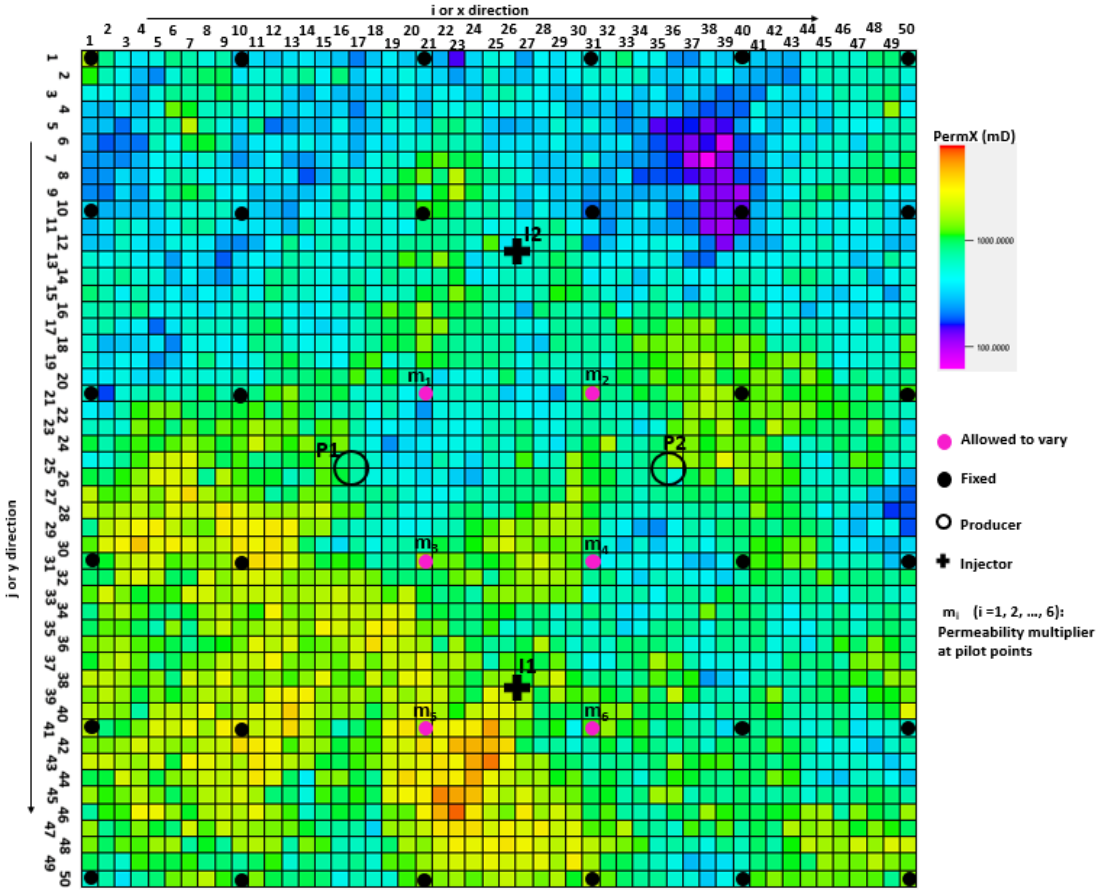

Figure 7.29 Pilot point locations on SGSIM4 Simulation model

In the base case simulation model, which is also the true model, the value of each of the multipliers is 1 which corresponds to the log10 of the multipliers being 0. We chose to sample the parameters on $\log_{10}$ scale when changing pilot points to avoid bias in sampling the parameter space by the optimisation algorithm.

7.5.1 Synthetic Benchmark Case 1

Permeability is treated as the only unknown variable, and we perturbed the model by varying the horizontal permeability. Both seismic and production history data are obtained from the predictions of a single realisation (the base case simulation model) for which all the permeability multipliers are equal to 1. The seismic history is the impedance attributes predicted with the approach presented by Stephen *et al*. (2006). Three seismic surveys are predicted using a petro-elastic model and fluid saturations and pressures from the base case simulations. For production history, well water production rates and

injection rates were predicted from the base case model taken from the simulation at monthly intervals.

Stephen (2007) found that at the spatial and temporal resolutions of the seismic and production data, noise is often uncorrelated. We do not add noise to the synthetic data therefore as the noise can be subtracted from the misfit values as a constant term. Instead, we assume that the estimates of the data errors are known. We incorporate the errors as standard deviations in the objective function, so that they become the weightings in the objective terms. The weighting is equal to the reciprocal of the square of standard deviation of data error. For the production observations (well water production and injection rates), we assume a reasonable accuracy of 100 BBL/day which gives a weighting of 0.0001 for each of the production observable. The impedance error is also reasonably assumed to be 0.015 g/cc km/s for each time lapse difference map. Each of the producers operated at a liquid rate of 18,000 STB/day and the injectors were run at pressure control such that the bottom hole injection pressures do not exceed 10,000 psi.

7.5.1.1 Automatic History Matching

In a broad sense, two optimisation algorithms (Neighbourhood Algorithm, NA and Genetic Algorithm, GA) are adopted in this work. For each of the algorithms, we test and compare the results for six different optimisation techniques, namely:

i) single objective optimisation using seismic data only (SOS),
ii) single objective optimisation using production data only (SOP),
iii) Single sum-objective optimisation using production and seismic data (SOPS),
iv) Pareto-based multi-objective optimisation with dual objectives: seismic data and sum-objective for production (DOPS),
v) Dynamic screening of pareto fronts using production data only (MOP), and
vi) Dynamic screening of pareto fronts using production data and seismic data (MOPS).

History matching was carried out by applying multipliers to change permeability in all the pilot point locations and spreading the changes across the model through kriging. In all cases, 128 models are generated initially and then 32 new models are made per iteration. After 40 iterations in each case, 1408 models are generated (Figures 7.30, 7.31, 7.32 and 7.33). For reservoir simulation, Eclipse is used in this study. To speed up the simulation runs the parallel capability of the simulator was linked with the parallel optimization through MPI implementations. This enabled multiple concurrent simulations runs to be made synchronously and asynchronously on multiple cores. The

maximum CPU load was maintained throughout the history matching run thereby saving enormous time.

Figure 7.30 show the parameters in all cases evolving towards the true solutions. The difference though is in the way the parameter space is explored. The exploration is increased in MOP and MOPS than in SOPS but this did not stop the parameters from evolving rapidly towards the true solution.

We also observe in Figure 7.31 (plotted for the case of DSFMOGA) that the misfit values evolve to lower values. The misfit values are scaled to their logarithm to base 10 values. The magnitude of the misfit values is dependent on the scale of the seismic and the production misfit. The magnitude of the seismic misfits is higher than the magnitude of the production misfits. This explains why SOP and MOP converged to lower misfit values and SOS to higher misfit values. The misfit values at the convergence of SOPS, DOPS and MOPS are somewhat in-between the values at the convergence of the SOP/MOP and SOS which reflects the history matching of both seismic and production data. We make distinction, however, in the convergence behaviour of the SOPS and DOPS/MOPS. The convergence of SOPS followed a narrow path to reach the solution. This kind of behaviour can easily lead to false convergence to a local minimum in a problem that has multiple minima. DOPS and MOPS are spread across the objective space as the DSFMOGA continues to search for those solutions representing the trade-off in seismic and production fitness, while maintaining the path to convergence. This increases the chance that the algorithm will not be trapped in any local minimum.

On the other hand, the trend of the misfit values for DSFMONA tend to suggest that it diminishes the exploratory power of the DSFMO. The difference in exploration between the different optimisation cases presented in Figure 7.32 under DSFMONA is not easily discernible. This does not mean that DSFMONA does not have exploration power but it is a reflection of the type of history matching problem under study. DSFMONA is built around the principles behind the development of the NA. It therefore tends to sample the model space more in the immediate neighbourhood surrounding the good data fitting models. In this synthetic example where the conflicts between the objectives are not strong, the DSFMONA behaves more like NA. The difference in results are therefore not easily noticed.

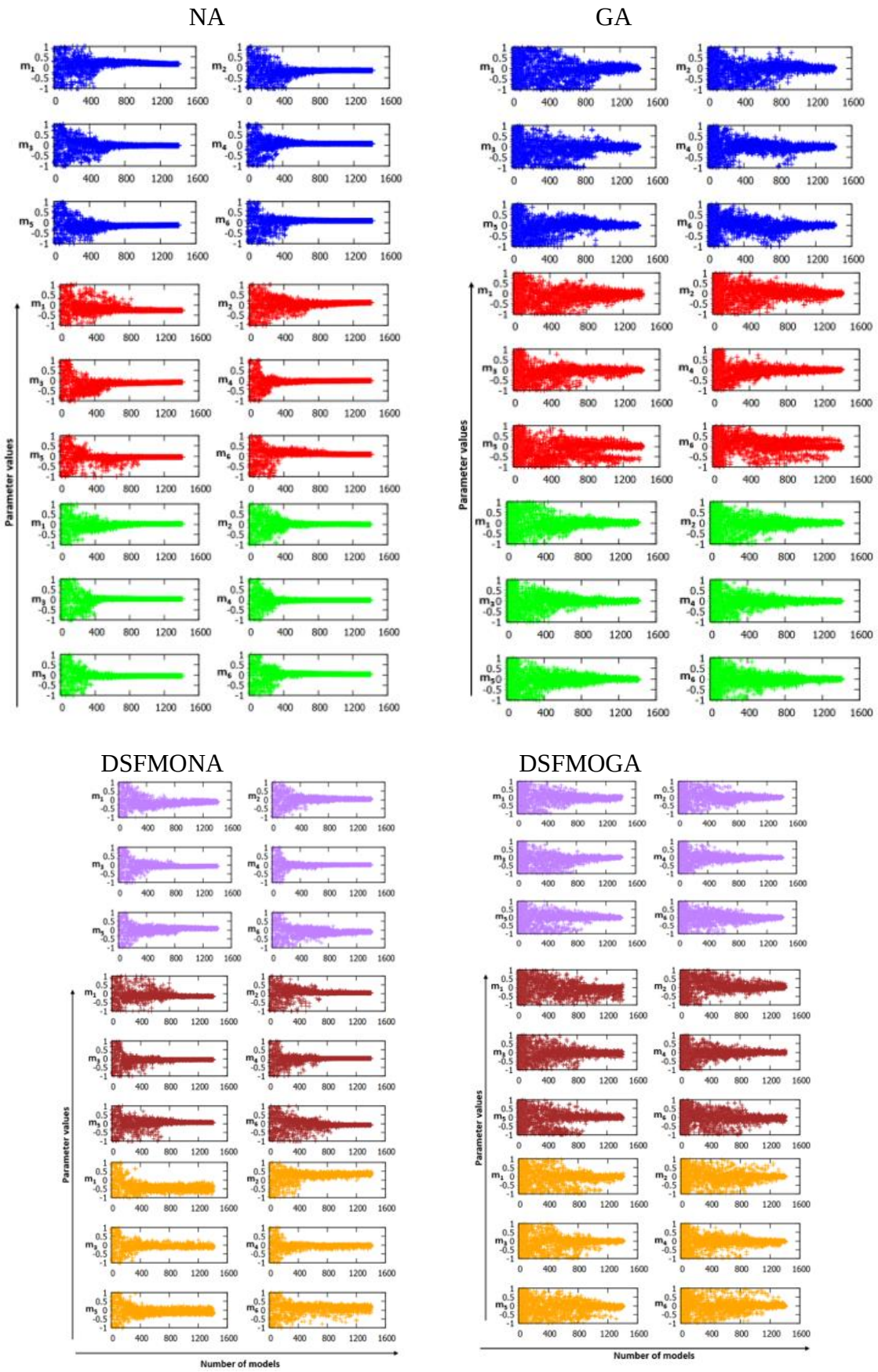

Figure 7.30 Parameter evolution during history matching using SOS (blue), SOP (red), SOPS (green), DOPS (purple), MOP (brown), and MOPS (orange)

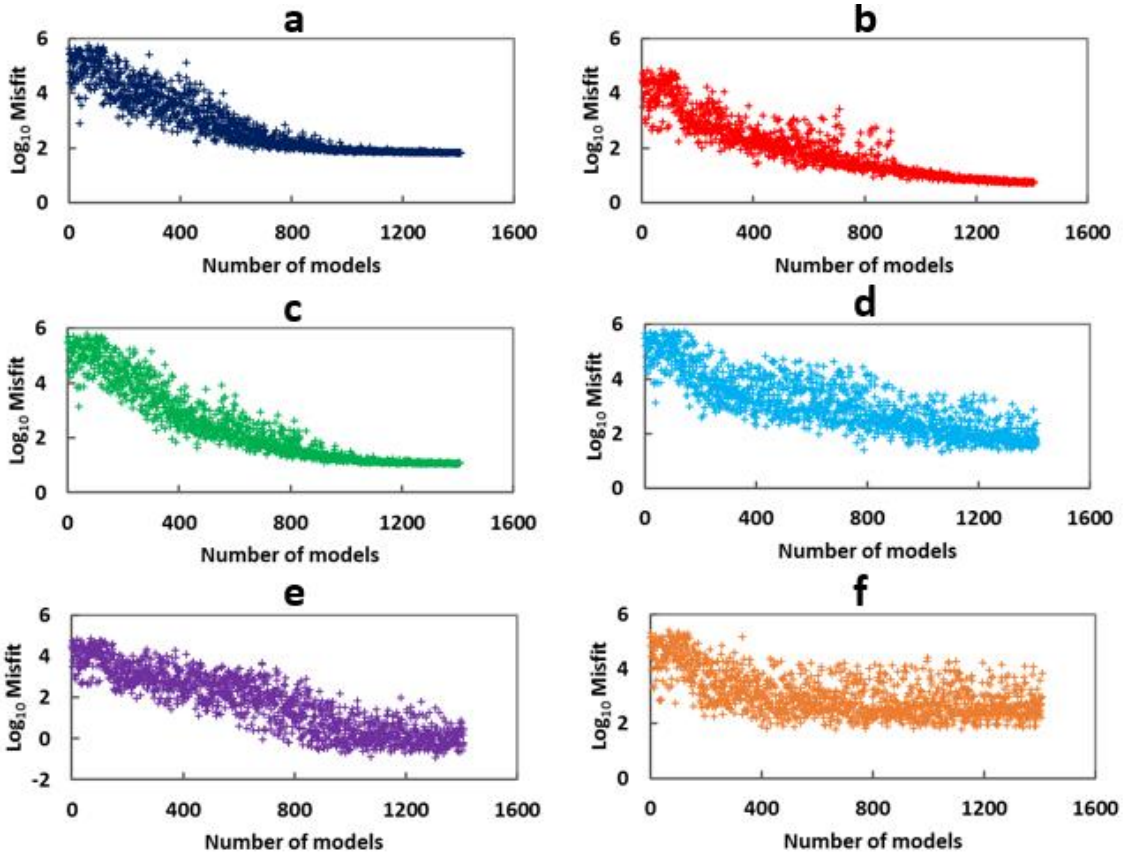

Figure 7.31 Evolution of misfits in GA optimisation using a) SOS b) SOP, c) SOPS d) DOPS, e) MOP f) MOPS. The misfit values are the $\log_{10}$ values

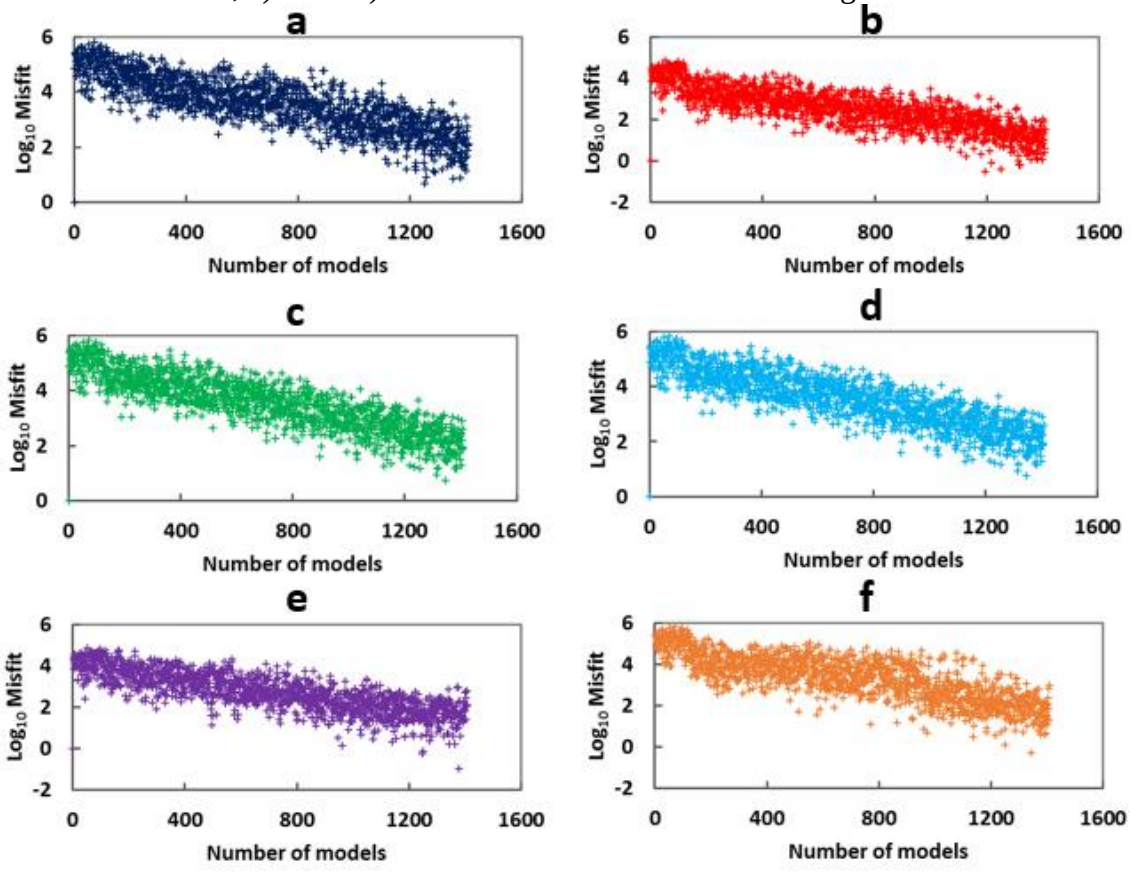

Figure 7.32 Evolution of misfits in NA optimisation using a) SOS b) SOP, c) SOPS d) DOPS, e) MOP f) MOPS. The misfit values are the log10 values

It does appear as if DSFMO speeds up the convergence rates at the early iteration stages if we compare the evolution of the average misfit per iteration (Figure 7.33). However, the later generational averages suggest no significant differences in the performance of MOPS, SOPS and DOPS in terms of convergence rates for most of the misfit components, such as the: time lapse difference between year 1 and year 2 (S1), time lapse difference between year 1 and year 3 (S2), time lapse difference between year 2 and year 3 (S3), water production rates of the wells (P1 and P2). In the same vein, MOP is observed to have no significant difference in convergence rates compared to the sum-objective analogue, SOP.

In the misfit convergence rates of the water injection rates (I1 and I2), the observations are different. DOPS and SOPS show slight superiority in the convergence rates over the trends observed in MOPS. The convergence rates observed in SOP were also slightly higher than the rate in MOP. It does appear as the sum-objective methods biased their respective search of the objective space towards water injection rates. This is very possible if we consider the scales of the misfits in production and injection rates. The magnitude of the misfit components of the water injection rates are about the double of the misfit values of the water production rates.

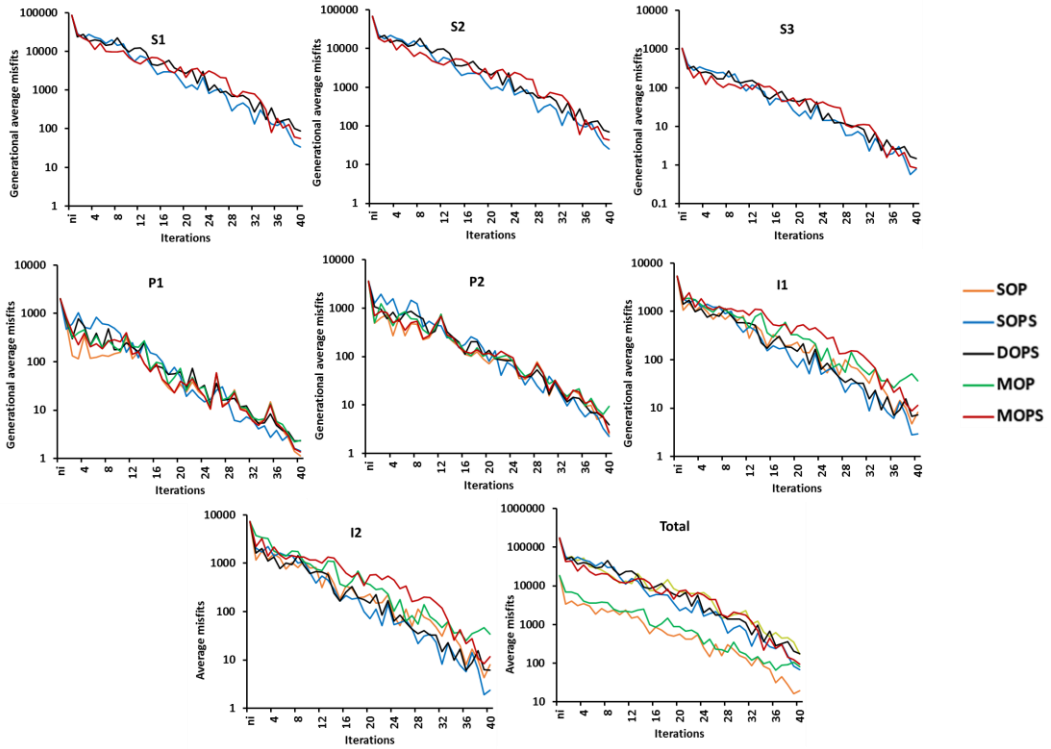

Figure 7.33 The trend in the evolution of the average misfit per iteration in optimisation with NA. The component misfits including time lapse differences: a) S1, b) S2, c) S3, well observables: d) P1, e) P2, f) I1, g) I2, and (h) the total misfit

In the plots of the pareto fronts (Figure 7.34 for DOPS using DSFMOGA, Figure 7.35 for MOPS using DSFMOGA, Figure 7.36 for MOP using DSFMOGA, Figure 7.37 for DOPS using DSFMONA, Figure 7.38 for MOP using DSFMONA, Fig 7.39 for MOPS using DSFMOGA), the misfit components are plotted in pairs to reveal the evolution of the fronts in the pareto-based optimisation techniques. The time lapse misfit components are summed up and represented as one component called seismic misfit. All the misfit component values are normalised on the scale of 0 to 1 as we are only interested in the trends rather than the magnitude of the misfit values. In all cases the pareto fronts in the objective space evolve towards lower solutions. This demonstrates that both the DSFMOGA and DSFMONA are effective in multi-objective optimisation even when the components of the objectives to be optimised are more than 2.

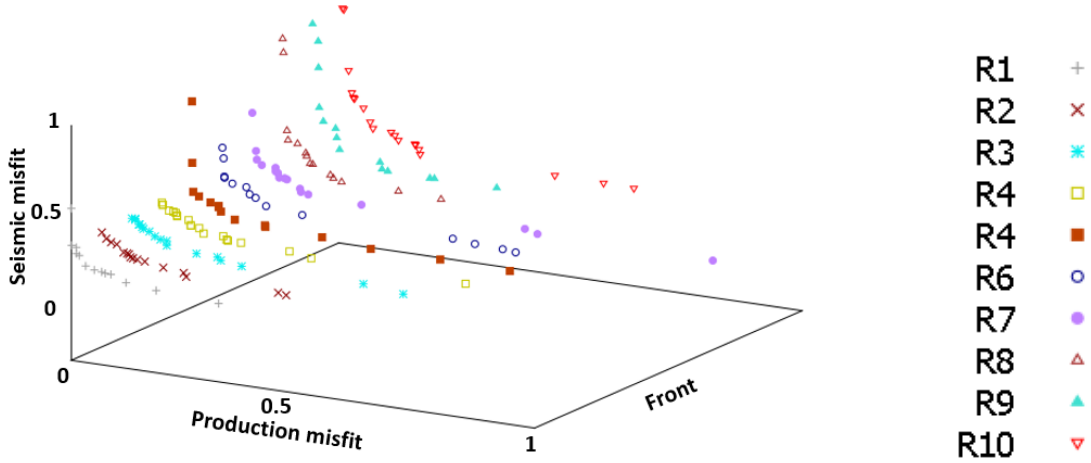

Figure 7.34 The evolution of the fronts in DOPS using DSFMOGA.

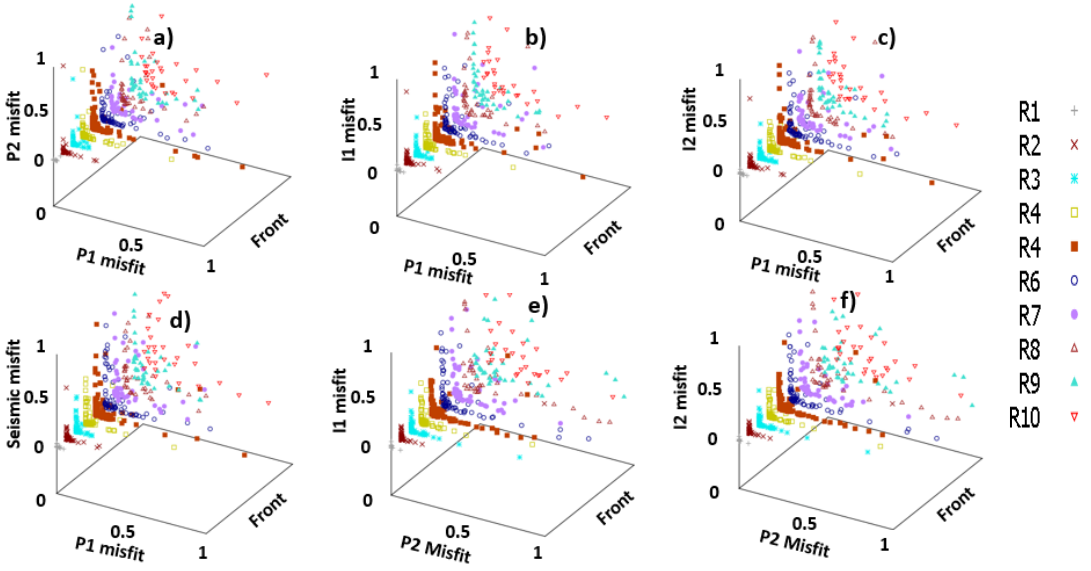

Figure 7.35 The evolution of the fronts in MOP using DSFMOGA.

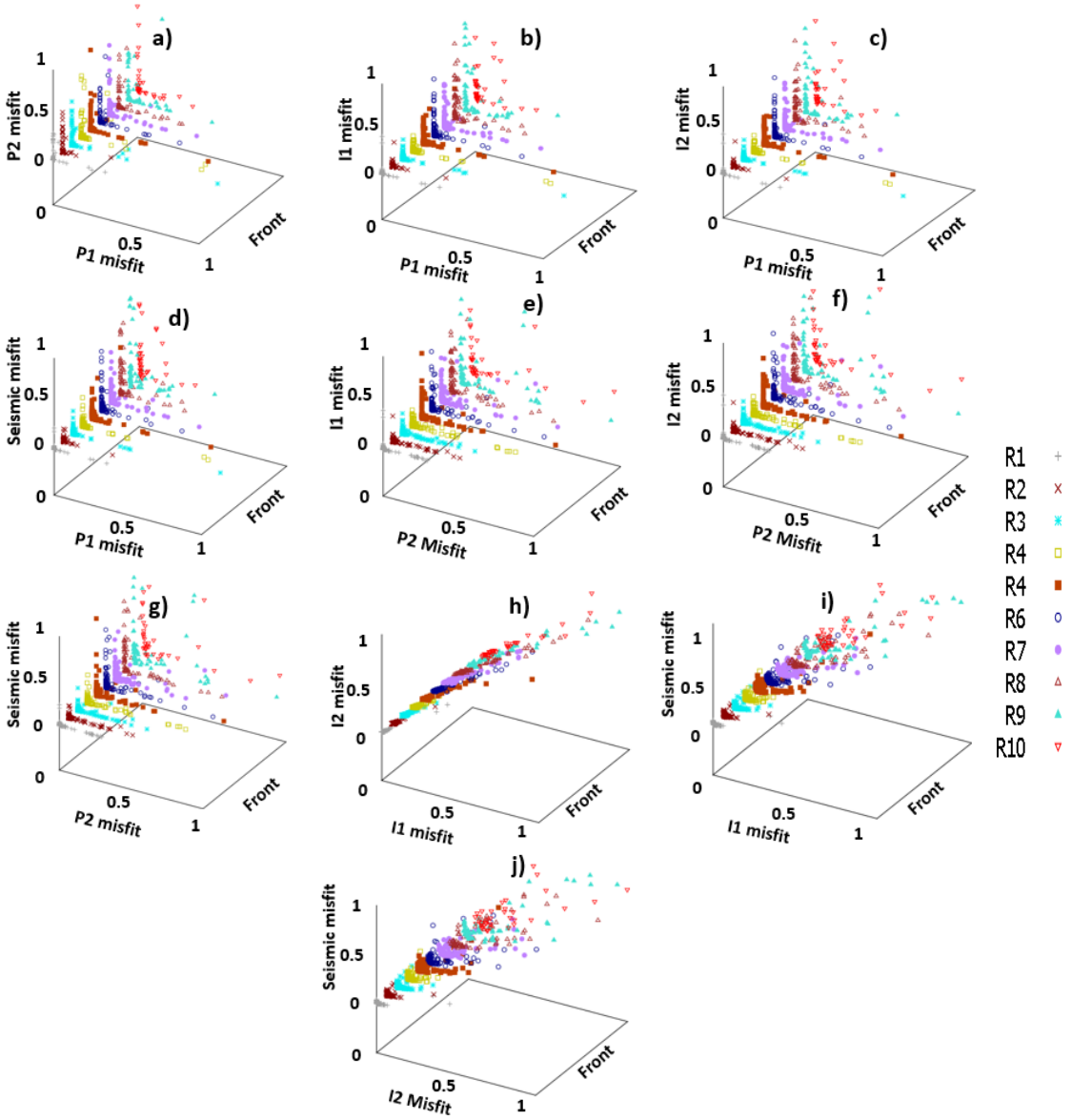

Figure 7.36 The evolution of the fronts in MOPS using DSFMOGA.

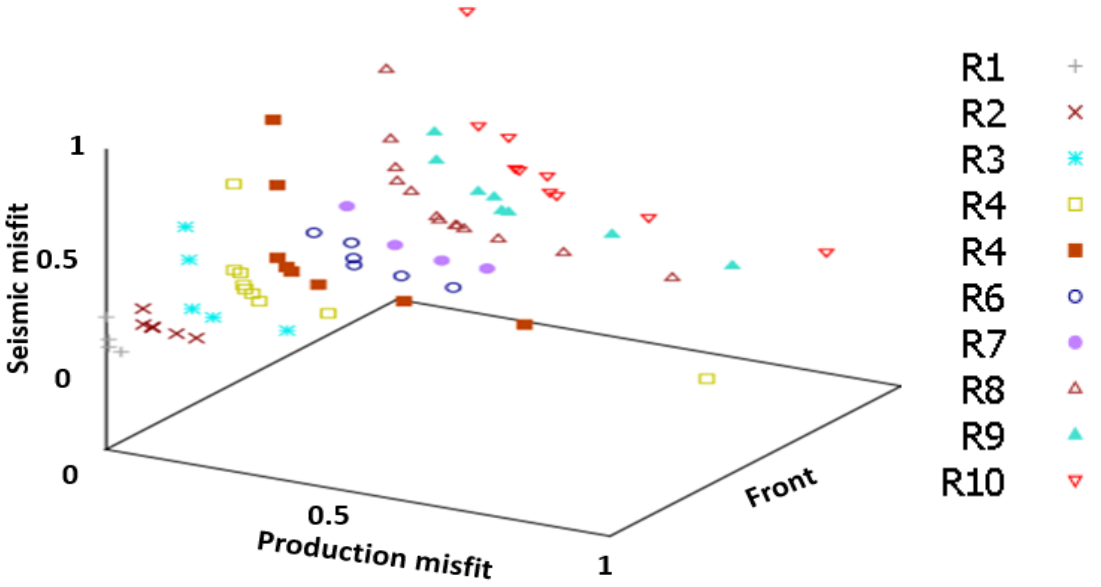

Figure 7.37 The evolution of the fronts in DOPS using DSFMONA.

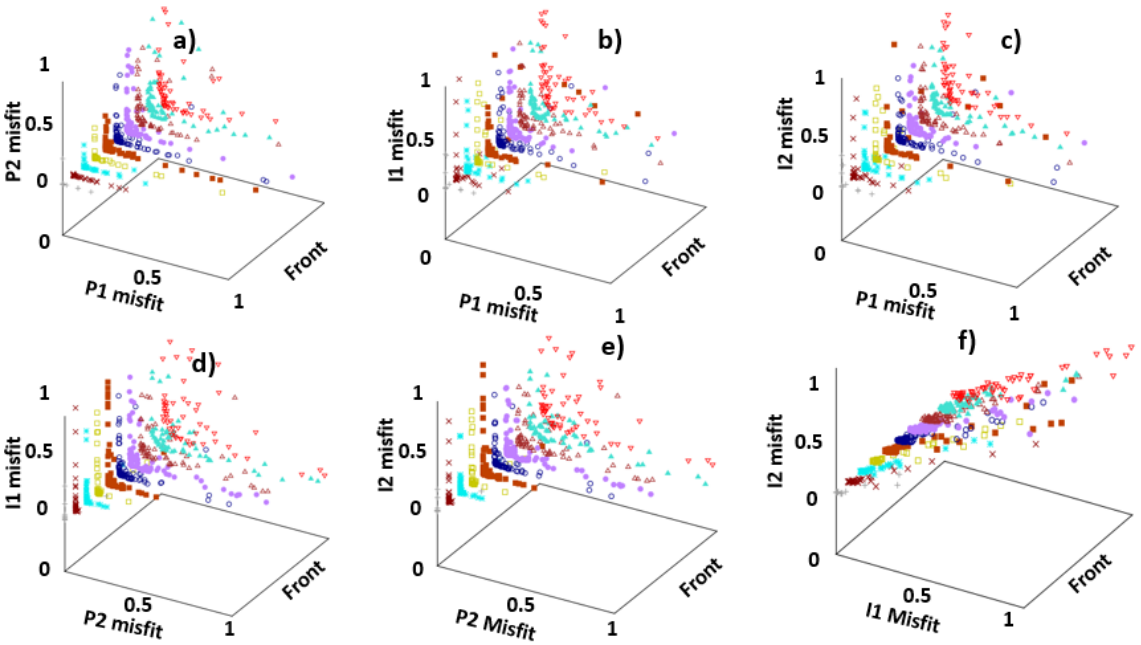

Figure 7.38 The evolution of the fronts in MOP using DSFMONA.

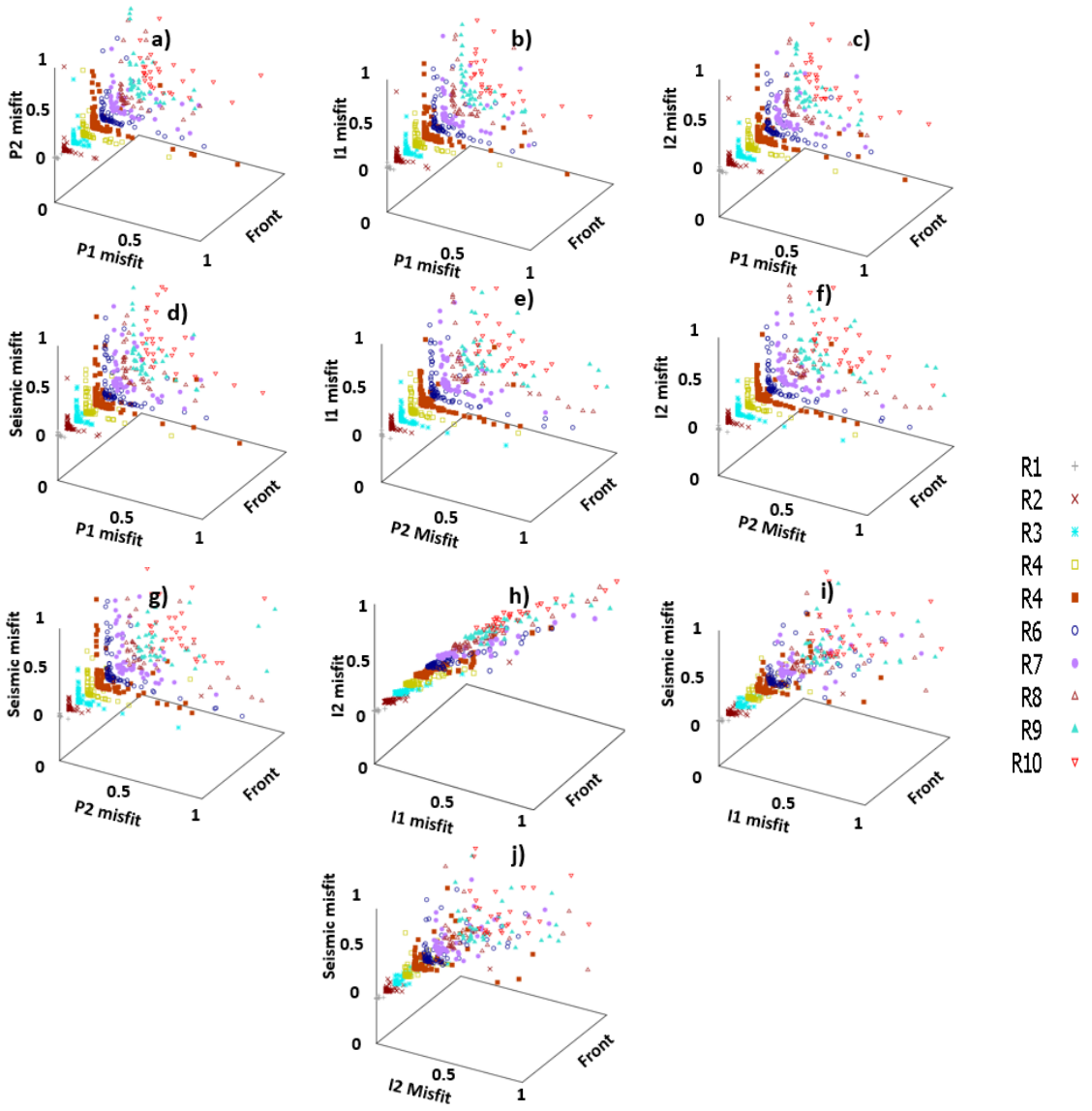

Figure 7.39 The evolution of the fronts in MOPS using DSFMONA.

As a final note in this history matching case, each of the optimisation techniques performed very well in finding the true solution of the history matching problem. Although some slight differences are observed in their performances, the benefits of using DSFMO are not readily obvious. The obvious explanation is that our history data are not truly representative of data of different sources. All the history data (time-lapse data, well injection and production rates) were derived as synthetic data using the same model. The time lapse data were derived from the same simulated saturation and pressure values which simulate the production profiles. The synthetic history derived here does not carry as much bias as may arise in practice due to measurement errors, inversion errors, domain and scale issues etc which is common in seismic and production history matching. Both the seismic and production history in this synthetic example represent the same physical properties that are modelled. The conflict between the various misfit components are not very strong, and as a result, data assimilation in the optimisation loop was easy for all the techniques presented.

7.5.1.2 Trade-off ratio

As a measure of the conflict between the various objectives, we calculate the trade-off ratios on every front of each pair of the misfit components. For each pair, all the ratios from the various fronts are then combined, binned and represented in Figures 7.40 (for MOPS using DSFMOGA) and 7.41 (for MOPS using DSFMONA). 'S' represents the sum of the seismic components of the misfit.

The trade-off ratios are measures of the correlation between the objective pairs and can be positive or negative. In all the cases the correlation between points on the fronts are concentrated at the near-zero neighbourhoods. Away from the zero trade-off ratios, the density reduces drastically in both the negative and positive direction. These represent very low trade-off ratios which reflects the week conflict amongst the objectives. The DSFMO is expected to outperform the conventional NA and GA as the conflict between the various data used to constrain the model in the history matching becomes stronger.

In the next synthetic study using the same simulation model, we will introduce bias in the history data to increase the conflict in information carried by the history data. We will see how this affects the trade-off ratio and study it's relative impact using DSFMO in seismic and production history matching.

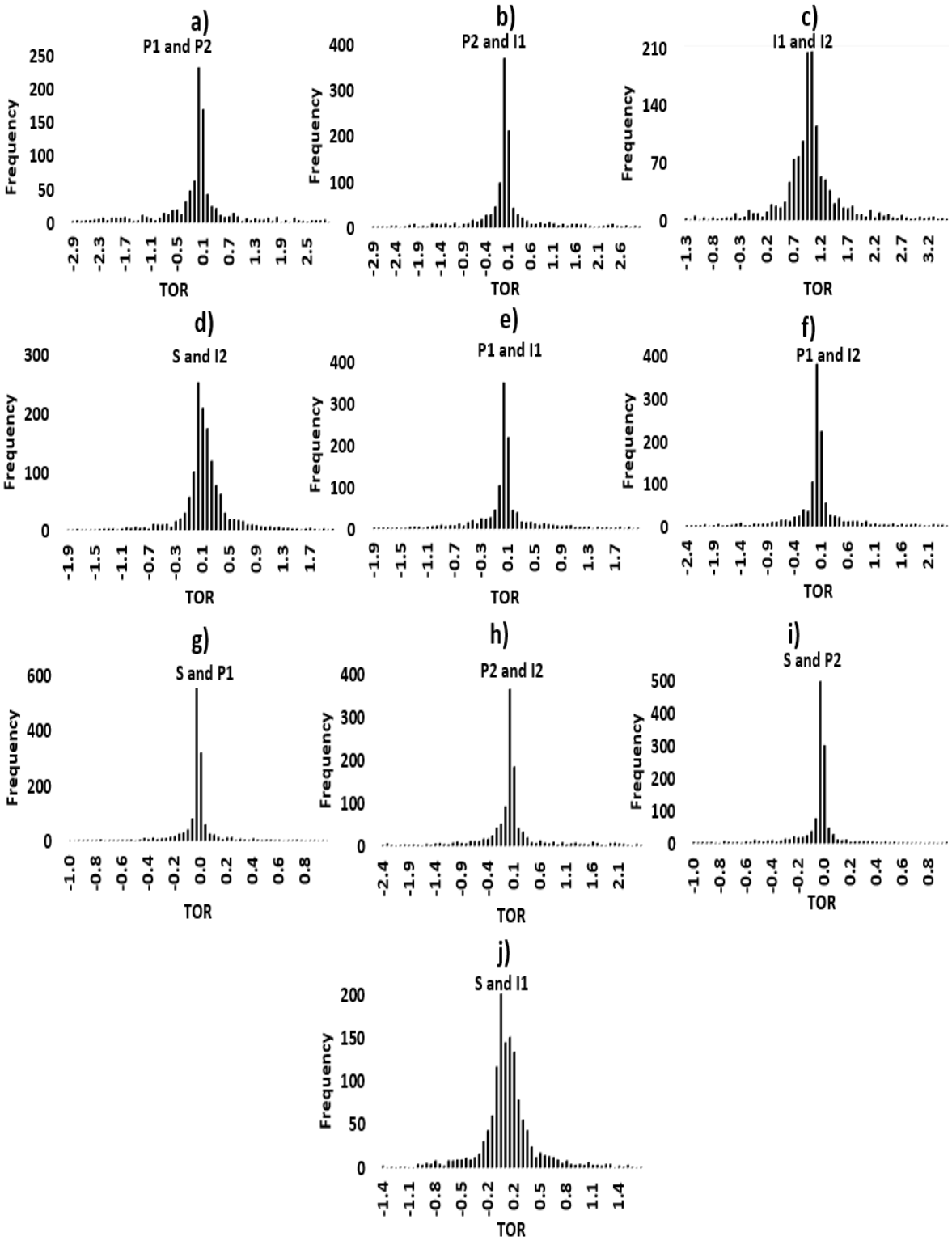

Figure 7.40 Trade-off Ratios for MOPS using DSFMOGA

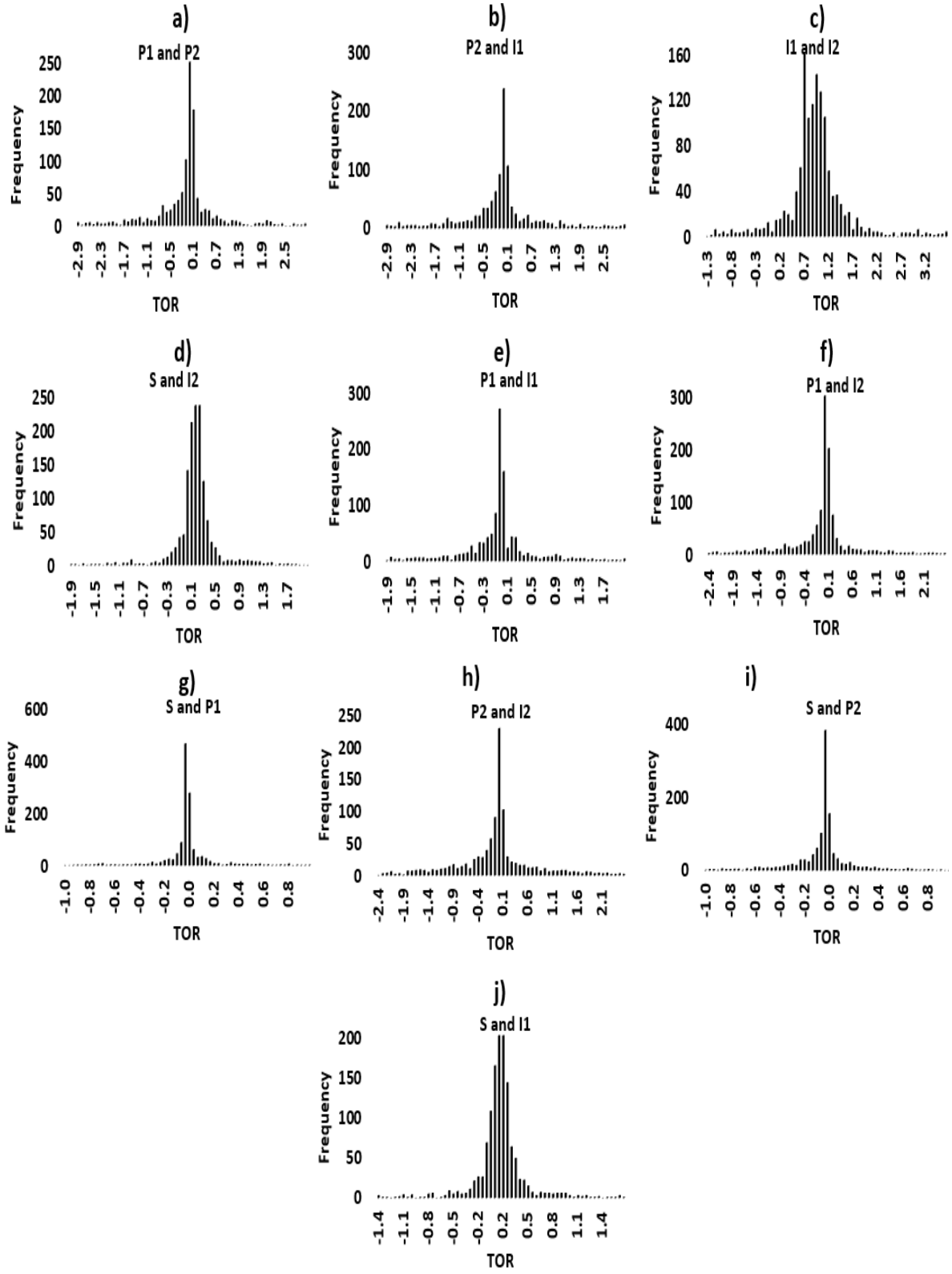

Figure 7.41 Trade-off Ratios for MOPS using DSFMONA

7.5.2 Synthetic Benchmark Case 2

We create another case with more conflicting information between seismic and production data. In practice, we often find that the time lapse seismic data tends to suggest alternative optimum parameters compared to production data from the wells. The

inconsistency may be due to issues with either inversion, calibration, scaling, seismic modelling and noise. Due to measurements errors, the constraining data may also suggest different model properties such as NTG, porosity, permeability and rock physics properties. The real benefit in using the multi-objective function over single objective function manifests when the minimum of the production and seismic misfits occur at different sets of parameter combinations. In this study, we mimic this inconsistency by introducing bias in the synthetic histories (Figure 7.42).

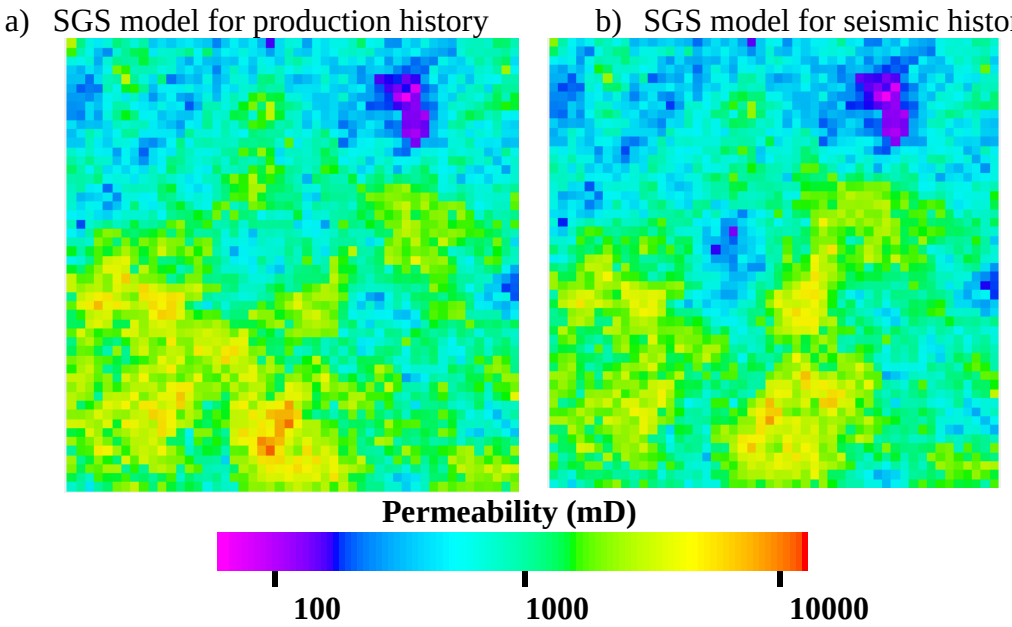

Figure 7.42 Permeability field of the two realisations used in generating the synthetic data for a) production history matching, and b) seismic history matching

Following the steps in case 1, we synthesize the seismic and production history data from the predictions of two known but different realisations of the same reservoir simulation model. The production history data in this case is the same as the history in Case 1 but the seismic history was generated as a synthetic data from a model having different permeability field. Every other information in benchmark case 1, including the model properties and the production and injection constraints, remain the same. The task is to find the ensemble of trade-off models on pareto front in an optimisation loop containing the conflicting seismic and production history.

As in the previous benchmark study, history matching of this model is done in six different ways (SOS, SOP, SOPS, DOPS, MOP and MOPS) using DSFMOGA, starting with 128 initial models. Then 32 new models are generated per iteration to generate a total of 1408 models after 40 iterations.

To compare the nature and magnitude of the conflict amongst the objectives in this case to the previous case, we show the trade-off ratios (Figure 7.41) calculated on the fronts defined by the relationship between the various objective pairs, as done previously. We see a distribution of large trade-off ratios away from zero values especially in the pair of objectives between seismic misfits and the misfits in any of the well observables (Figures. 7.43d, 7.43g, 7.43i, and 7.43j). The trade-offs in the objective space are relatively large because of the conflicting information.

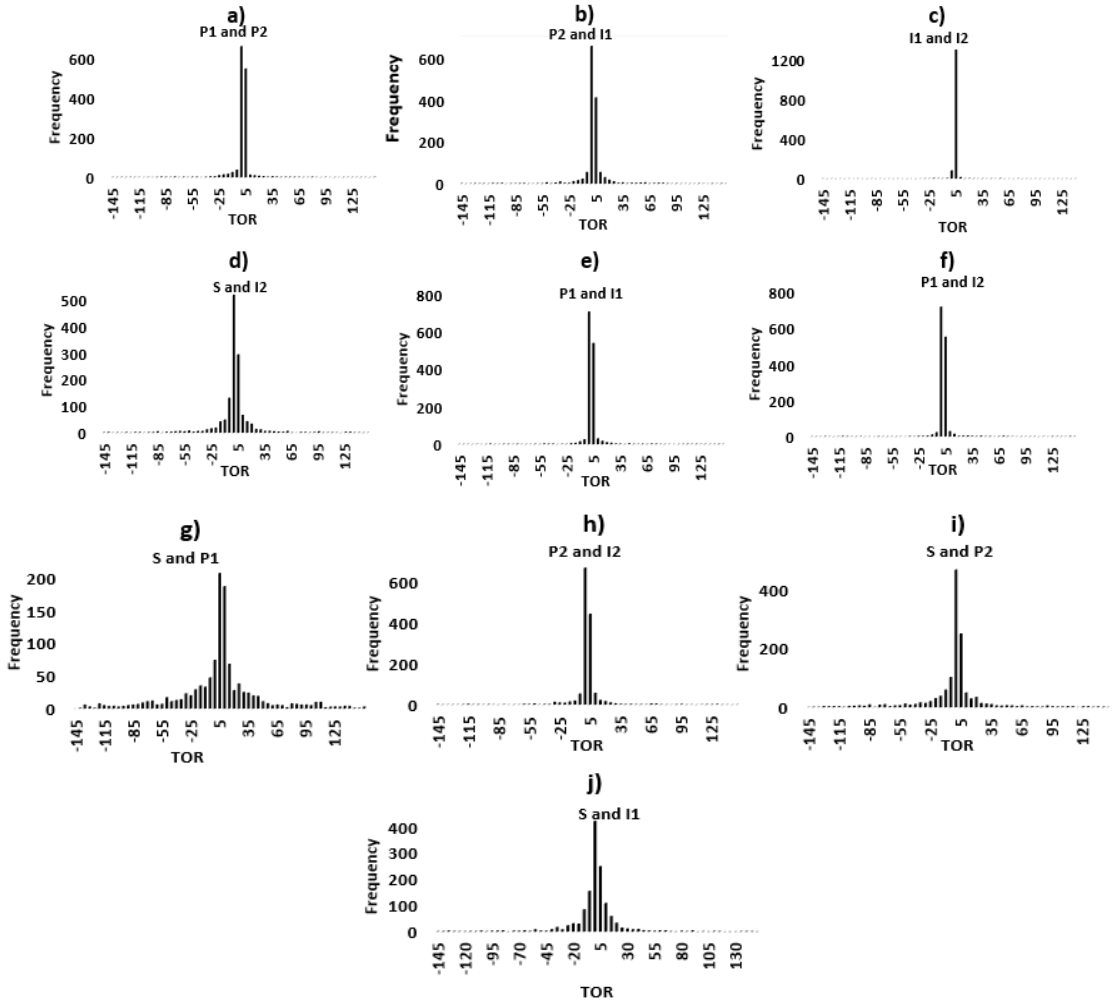

Figure 7.43 Trade-off ratios for MOPS using DSFMOGA in benchmark case 2

The large magnitude of the trade-off ratios is indicative of the strong conflict between the seismic and production components of the objectives. In this problem, the data representing the true seismic does not represent the same petrophysical properties in the model as the data representing the well observables. Therefore, finding the true solution of the history matching problem becomes very difficult. Considering the petrophysical properties of the two realisations from which the synthetic history data were derived (Figure 7.42), it is obvious that a 'true solution' does not exist. Reason is that there are several possible solutions depending on the importance placed on each of the synthetic

history. If we ignore the seismic history, then Figure 7.42a becomes the true permeability field but if we ignore the production history, Figure 7.42b becomes the true solution. In practice, one wishes to incorporate both the seismic history and production history to take advantages of the benefits that each offer. Production history offers high temporal resolution at the well locations while seismic history offers high spatial resolution providing information that helps in resolving the inter-well property variability that well observables would not resolve. The best solution to the above problem therefore should be an ensemble of models representing the trade-off between the solutions suggested by the conflicting objectives. In the absence of any information (subjective or objective) regarding the importance that should be placed on the objectives, we want an algorithm that will assimilate the various history data without bias while respecting the conflict or trade-off between them. We will show how DSFMOGA performs in this regard.

The misfit components are plotted in pairs to reveal the evolution of the fronts in the pareto-based optimisation techniques (Figure 7.44 for DOPS and Figure 7.45 for MOPS using DSFMONA).

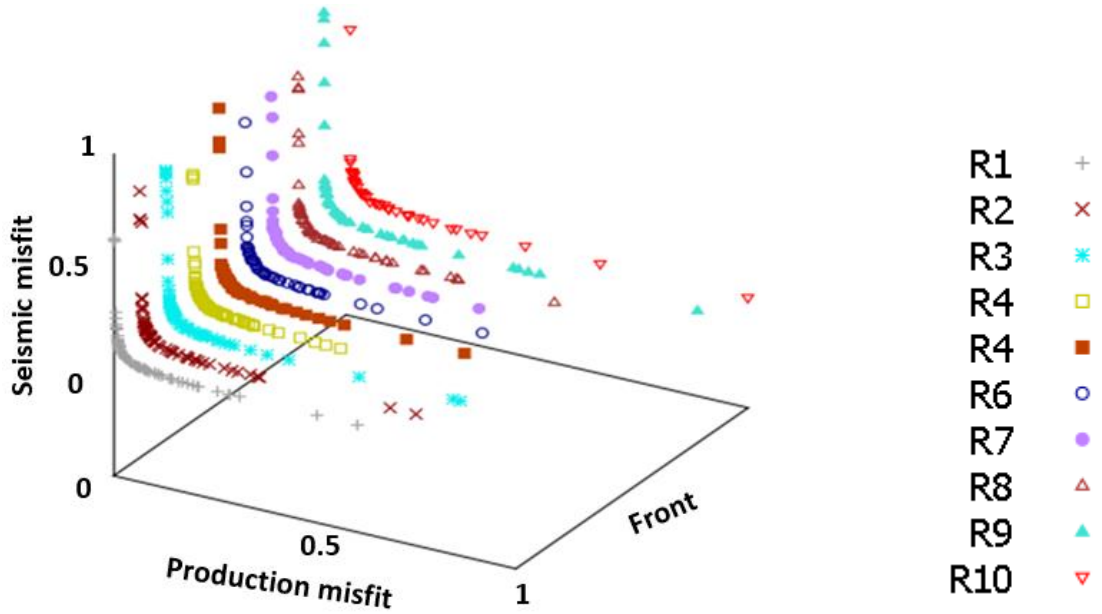

Figure 7.44 The evolution of fronts for DOPS in Benchmark case 2 using DSFMONA

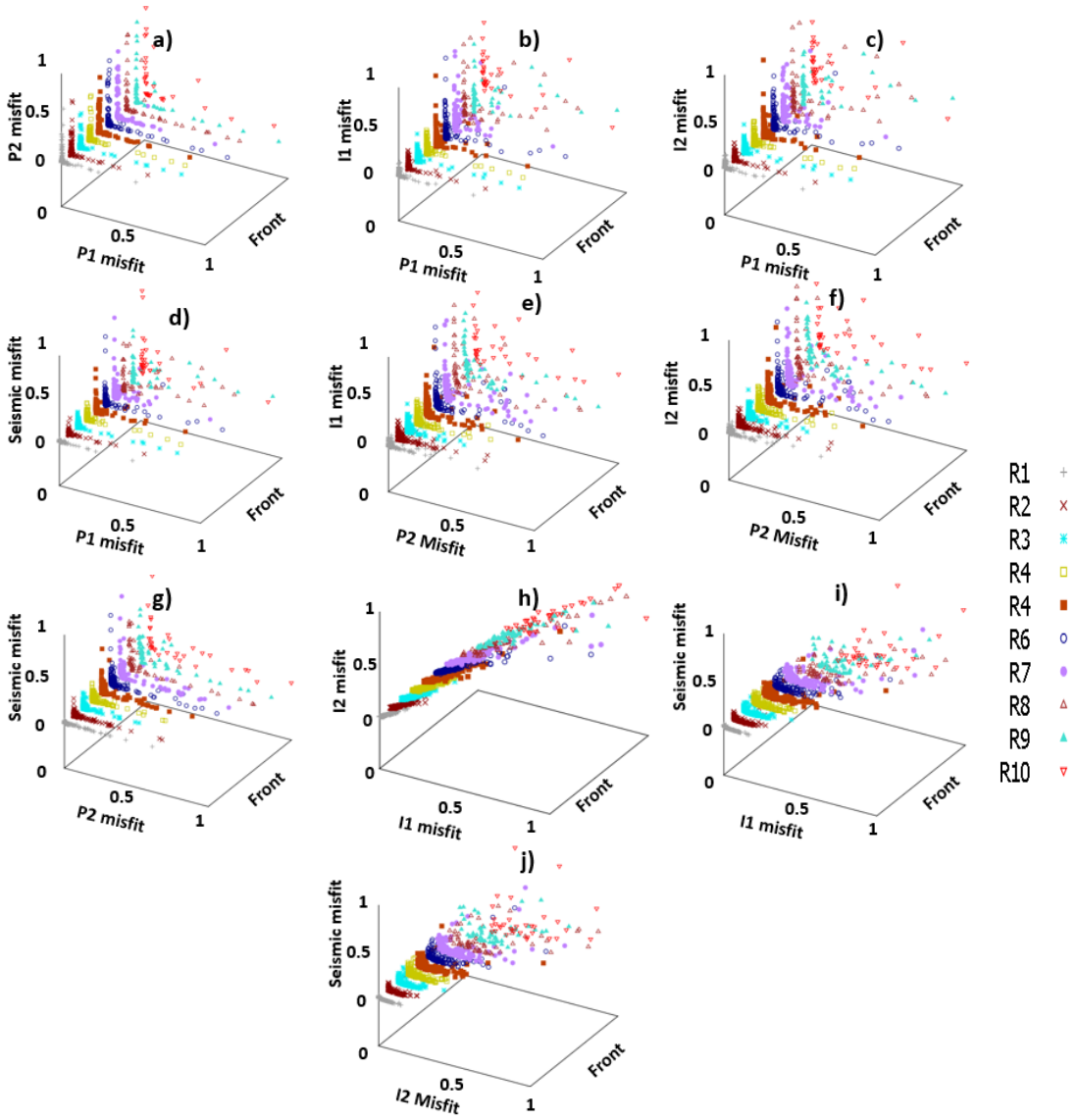

Figure 7.45 The evolution of fronts for MOPS in Benchmark case 2 using DSFMONA

We look at how the different optimisation methods (ie. SOS, SOP, SOPS, DOPS, MOP and MOPS) explore the objective space through the maximum-average-minimum plot of the misfit component values per iteration (Figure 7.46 for seismic misfits, Figure 7.47 for the misfits in P1 water production rates, Figure 7.48 for misfits in P2 water production rates, Figure 7.49 for misfits in I1 water injection rates and Figure 7.50 for misfits in I2 water injection rates). We want to compare particularly, the performance of the sum-objective single objective methods and the pareto-based multi-objective optimisation using DSFMO (i.e SOP vs MOP, SOPS vs MOPS/DOPS).

A rough assessment of the performance can be made by comparing the trend or evolution of the average misfits by iterations. The trend gives a rough idea of misfit convergence and convergence rates. The differences in the maximum and minimum values are indicative of the spread in exploration of the objective space during the search for lower

misfit values. The minimum values may also be a rough measure of the likelihood that some number of good-data fitting models are found during optimisation.

Comparing Figures 7.46b and 7.46d (the misfits in the time lapse seismic), Figures 7.47b and 7.47e (the misfits in the P1 water production), Figures 7.48b and 7.48e (the misfits in the P2 water production), Figures 7.49b and 7.49e (the misfits in the I1 water injection), Figures 7.50b and 7.50e (the misfits in the I2 water injection), we observe that optimisation with DSFMO (i.e the MOPS) outperforms the single sum-objective optimisation (as in SOPS).

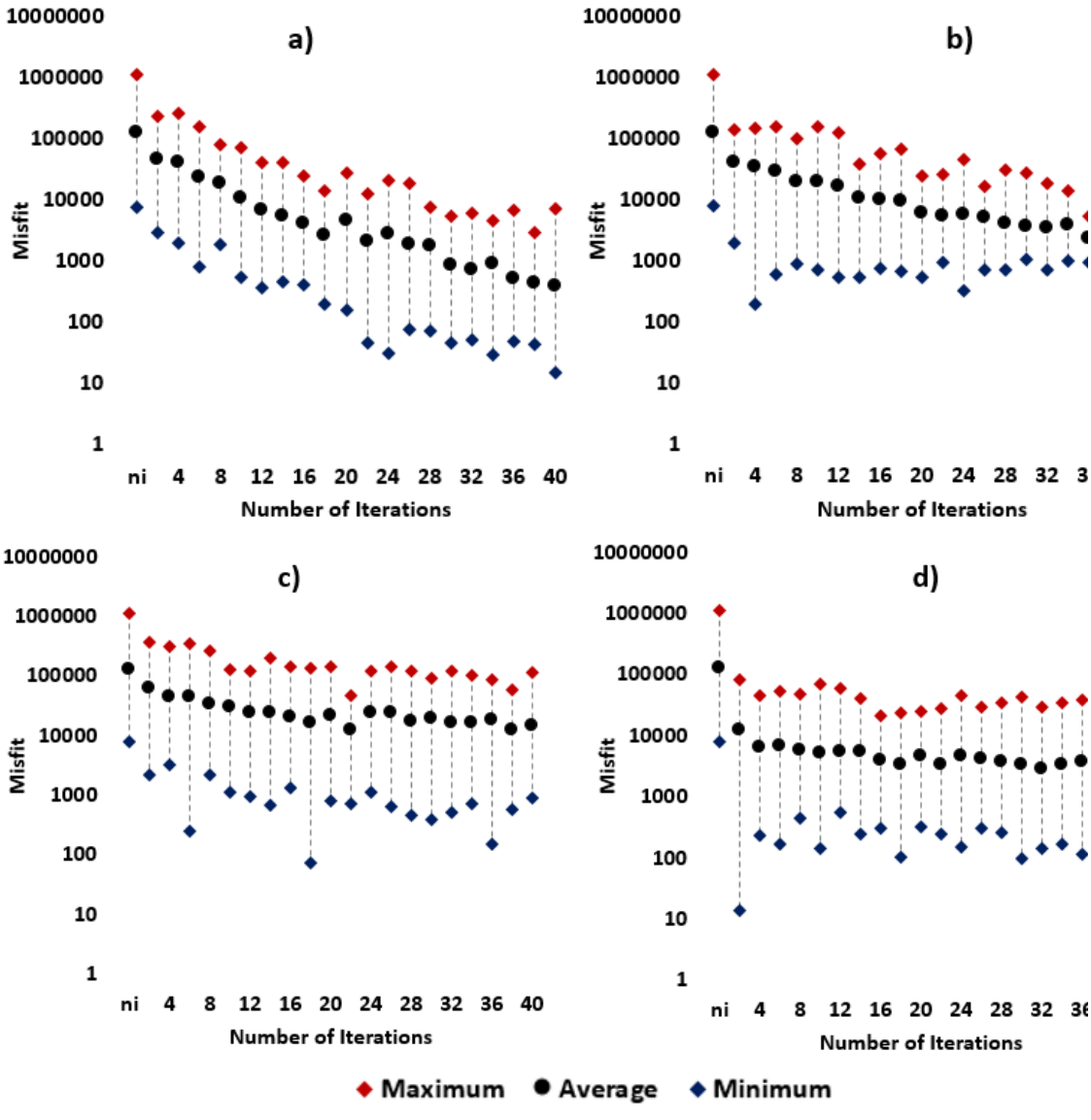

Figure 7.46 Seismic misfits for optimisation using a) SOS, b) SOPS, c) DOPS and d) MOPS

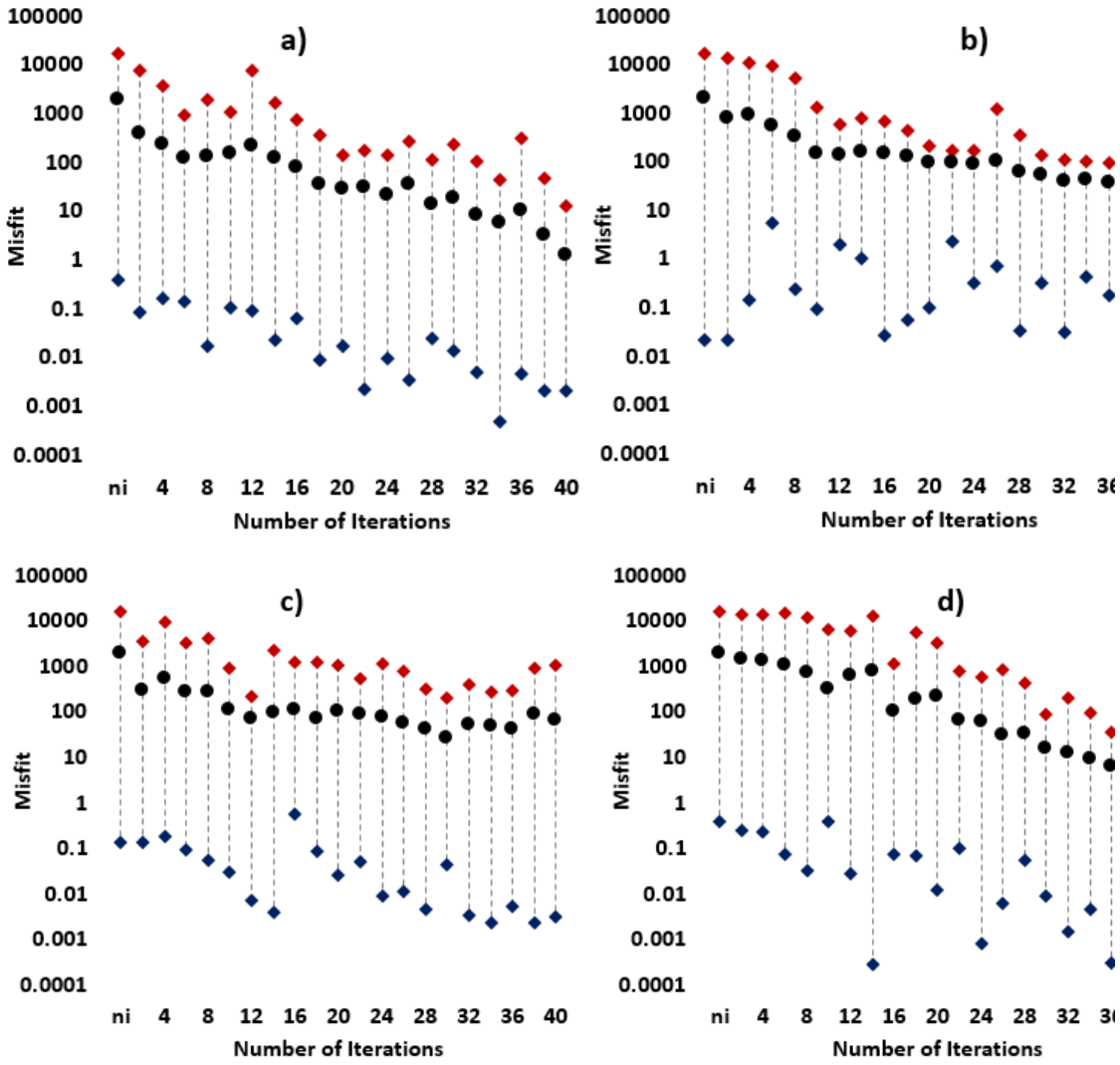

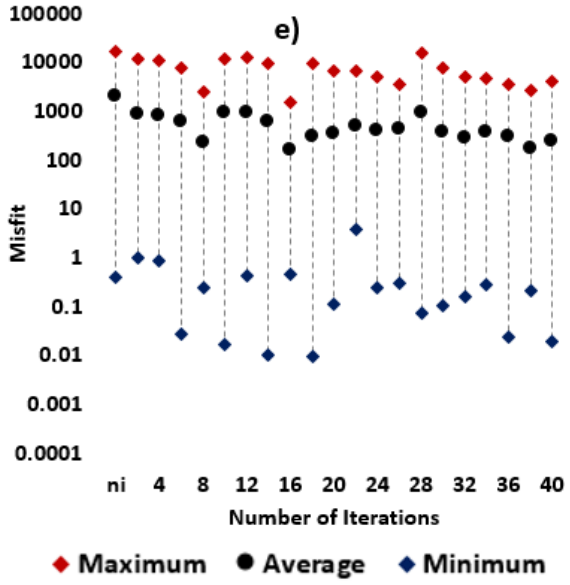

Figure 7.47 Misfit evolution for P1 water rates for optimisation using a) SOP, b) SOPS, c) DOPS, d) MOP, and e) MOPS

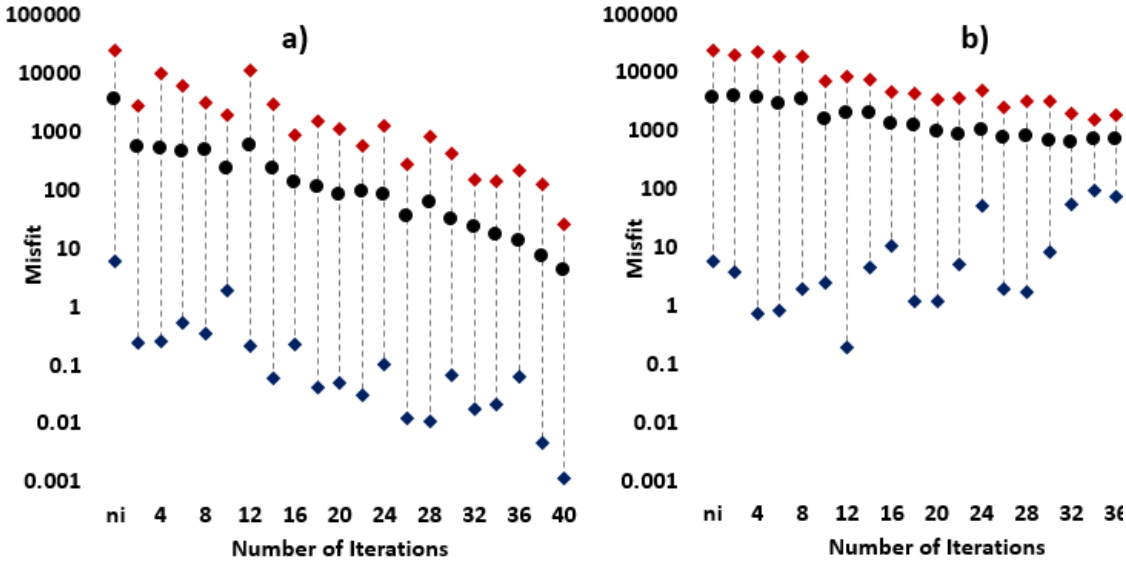

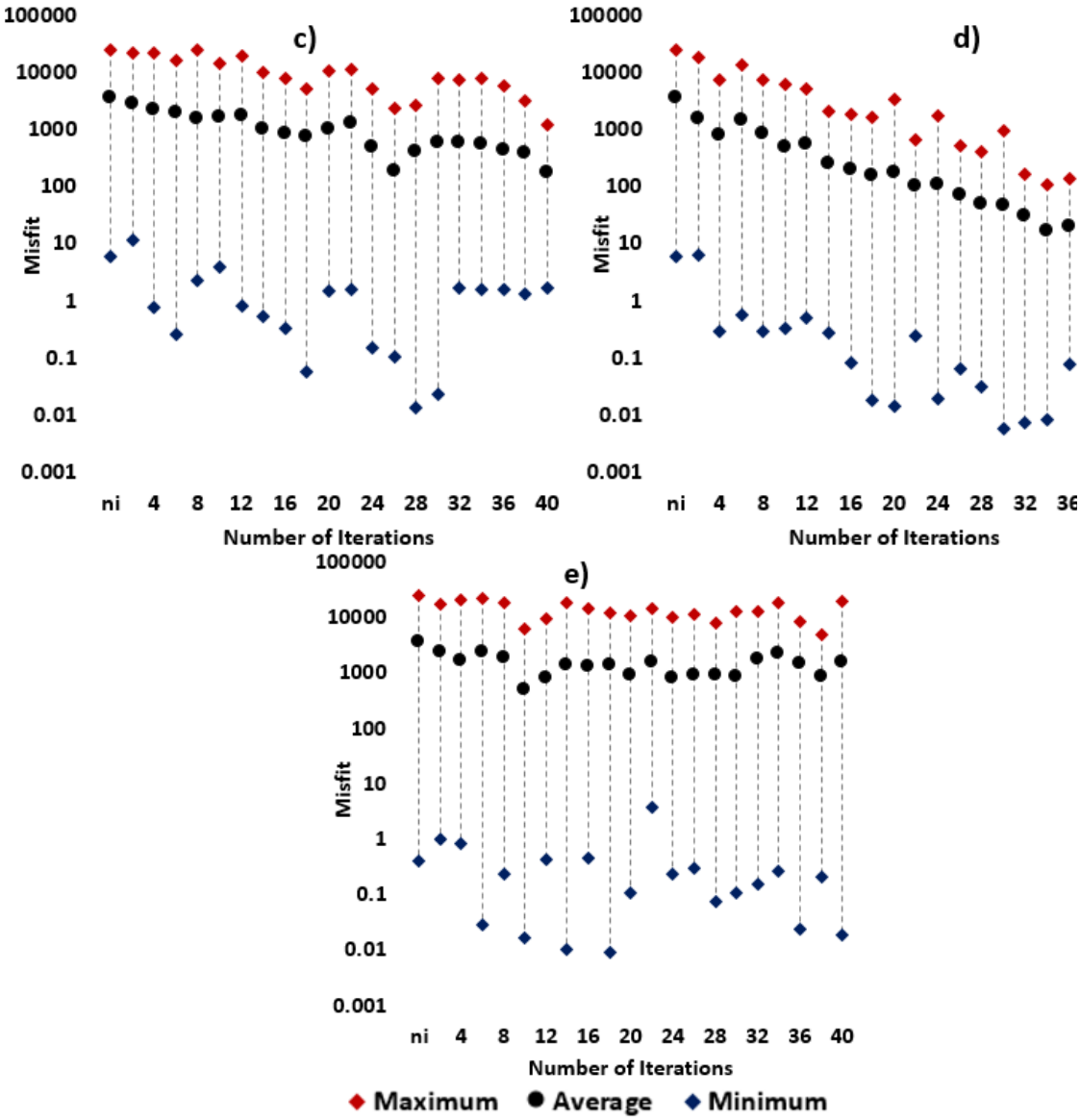

Figure 7.48 Evolution of the P2 water rates misfit for optimisation using a) SOP, b) SOPS, c) DOPS, d) MOP, and e) MOPS

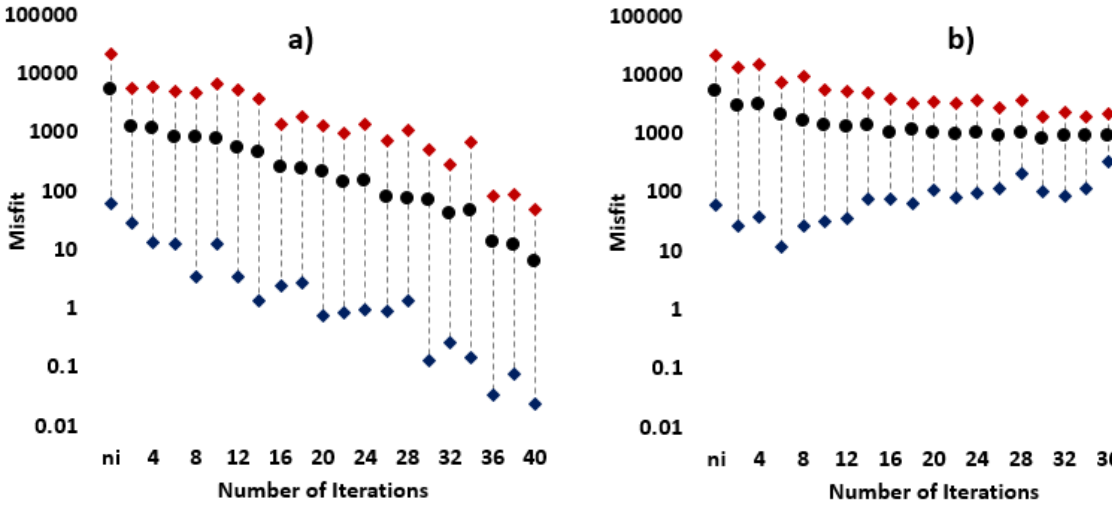

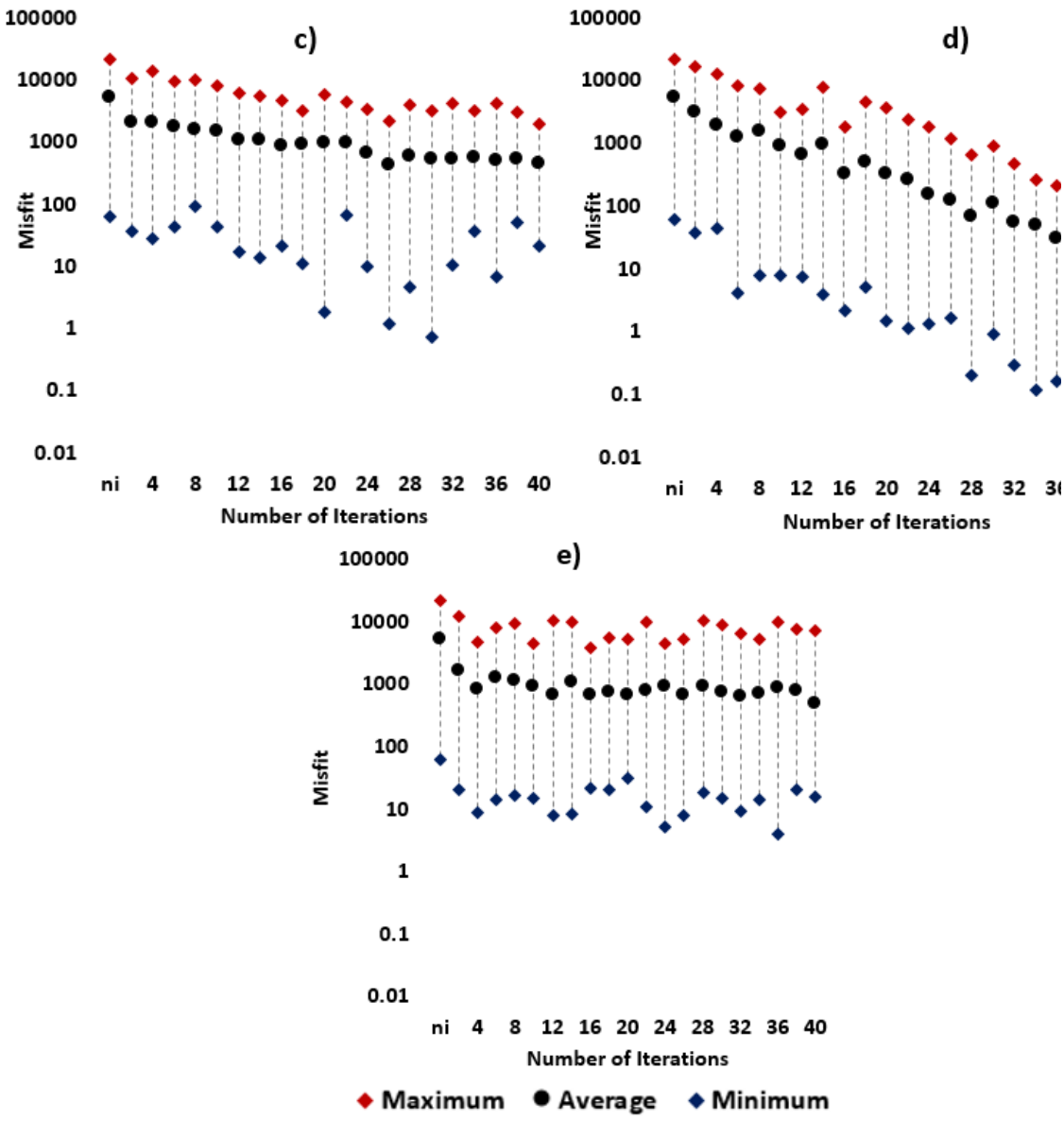

Figure 7.49 Misfits in I1 injections for optimisation using a) SOP, b) SOPS, c) DOPS, d) MOP, and e) MOPS

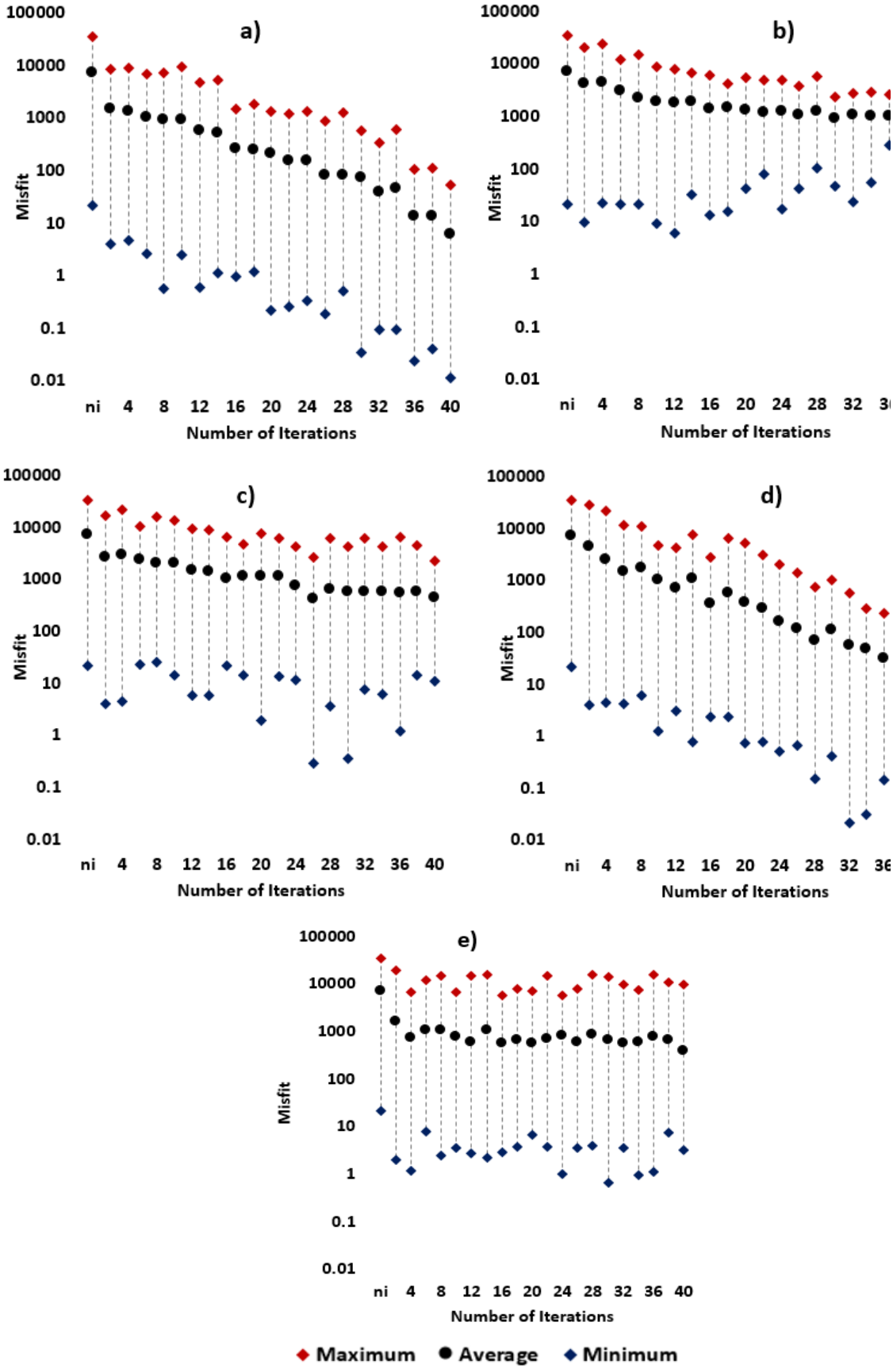

Figure 7.50 Misfits in injection rates of I2 for optimisation using a) SOP, b) SOPS, c) DOPS, d) MOP, and e) MOPS

In the maximum-average-minimum plots, the trends of the misfit in the time lapse seismic show that the MOPS method maintained more diversity than SOPS as the optimisation progressed, as evident in the spread between the maximum and minimum values of misfits at each iteration. The MOPS also produced more lower values of misfit (better data-fitting models). The SOPS struggled to maintain a spread in the objective space as the maximum values continued to trend downwards while minimum values did not go lower as the optimisation progressed. It does appear as if the SOPS converged towards a local minimum. The SOPS was biased in its search towards minimising some individual misfits and was particularly outperformed in reducing the misfits of I1 and I2 injection rates as well as the water rates in well P2. Also, the MOPS performed slightly better than DOPS judging by the magnitude of the minimum values.

The evolution of the misfit values for DOPS follow a similar trend to the MOPS because both methods use DSFMO. Although DOPS allows only two objectives where all components of the production misfits are summed as one, we note that the conflict between the components of the production misfits are not very strong. Both DOPS and MOPS treat all the seismic components as a single aggregated seismic misfit. As we have seen in Figure 7.41, the large trade-off ratios exist only between seismic-production misfit pairs. The behaviour observed of SOS in Figure 7.46a is expected as it considers only seismic misfit. In the absence of conflicting objectives, single aggregate objective optimisation performs better.

We observe similar behaviours in Figures 7.47, 7.48, 7.49 and 7.50, where it is obvious that MOPS outperform SOPS. In all cases, SOP and MOP behaved in very similar manner. Both SOP and MOP use only production data for history matching the reservoir model. Since, the trade-off between the production misfit components are weak, MOP offers no benefit over SOP. MOP is more beneficial in multi-objective problems with conflicting production misfit components. In all cases the behaviour of the DOPS came very close to the behaviour of the MOPS for the reason given earlier.

We make a general distinction in the observations made from the foregoing synthetic study. The SOPS which uses the conventional single-objective approach sums up all the misfit components from different wells and time lapse seismic. In history matching using seismic data, optimisation algorithms are known to be sensitive to changes in fitness values in different parts of the reservoir, and in history matching using production data, the algorithms are sensitive to changes in the match quality across various well observables. In real reservoirs, model parameterisation is often made considering the spatial structure of the reservoir and in compartmentalised reservoirs, it is essential that

parameterisation reflect this structure. Combining conflicting data in one single objective reduces the sensitivity of the algorithms to the fitness quality and the impact of local model perturbations may not be felt in the global model history match. Accounting for the misfit components by wells located in different parts of the reservoir and by seismic allows the optimisation algorithms to trade off multiple models that may fit the data from one well or group of wells but fail to match the other(s). This explains why the DSFMO outperforms the conventional NA and GA in our synthetic study.

7.5.3 Posterior analysis and uncertainty quantification.

We present two approaches to uncertainty analysis of the models generated using the pareto-based multi-objective history matching. We want to quantify the uncertainty in the posterior model predictions.

In the first approach we use a variant of the NABayes (Sambridge, 1999b), the weighted probability approach, described in Chapter five of this thesis. In this approach, we apply weights in the form of relative probability of each from the input ensemble generated from history matching. Just like in NABayes, each of the 1408 models generated using DSFMO is represented by a V-Cell and posterior probabilities are computed using the voronoi approximation of the PPD.

Gibbs sampler is used to perform random walks to resample the posterior. 100 random walks were performed by the Gibbs sampler each from a different starting cell and 100 steps are made in each of the random walk to give a total of 10,000 model visits. The relative probability of each model, is then calculated by taking counts of the frequency of visits, to the model (or its V-Cell).

We take note of the number of models visited at least once: 117 models were visited at least once in SOS, 150 models were visited in SOP, 76 models were visited in SOPS, 78 models were visited in DOPS, 81 models were visited in MOP and 71 models were visited in MOPS. The distribution of the visited models according to the frequency of visits are shown in Figure 7.51. The relative frequencies of visits are then applied as weights to the predictions of the models to determine the mean and standard deviations of the predictions. Then using gaussian statistics, we define the uncertainty envelope in the predicted quantities.

We are interested in the predictions made using the posterior models derived from MOPS using DSFMOGA. As stated earlier, 71 models were visited at least once in MOPS. We select at random, 21 out of the 71 visited models and show their respective updated

permeabilities in Figure 7.52. We see slight differences in the permeability maps. These differences will reflect in the uncertainty of the predictions made with these models, and the contribution of each model to the profile of the predicted quantities and the uncertainties depends on the number of times the model is visited during the NABayes walks.

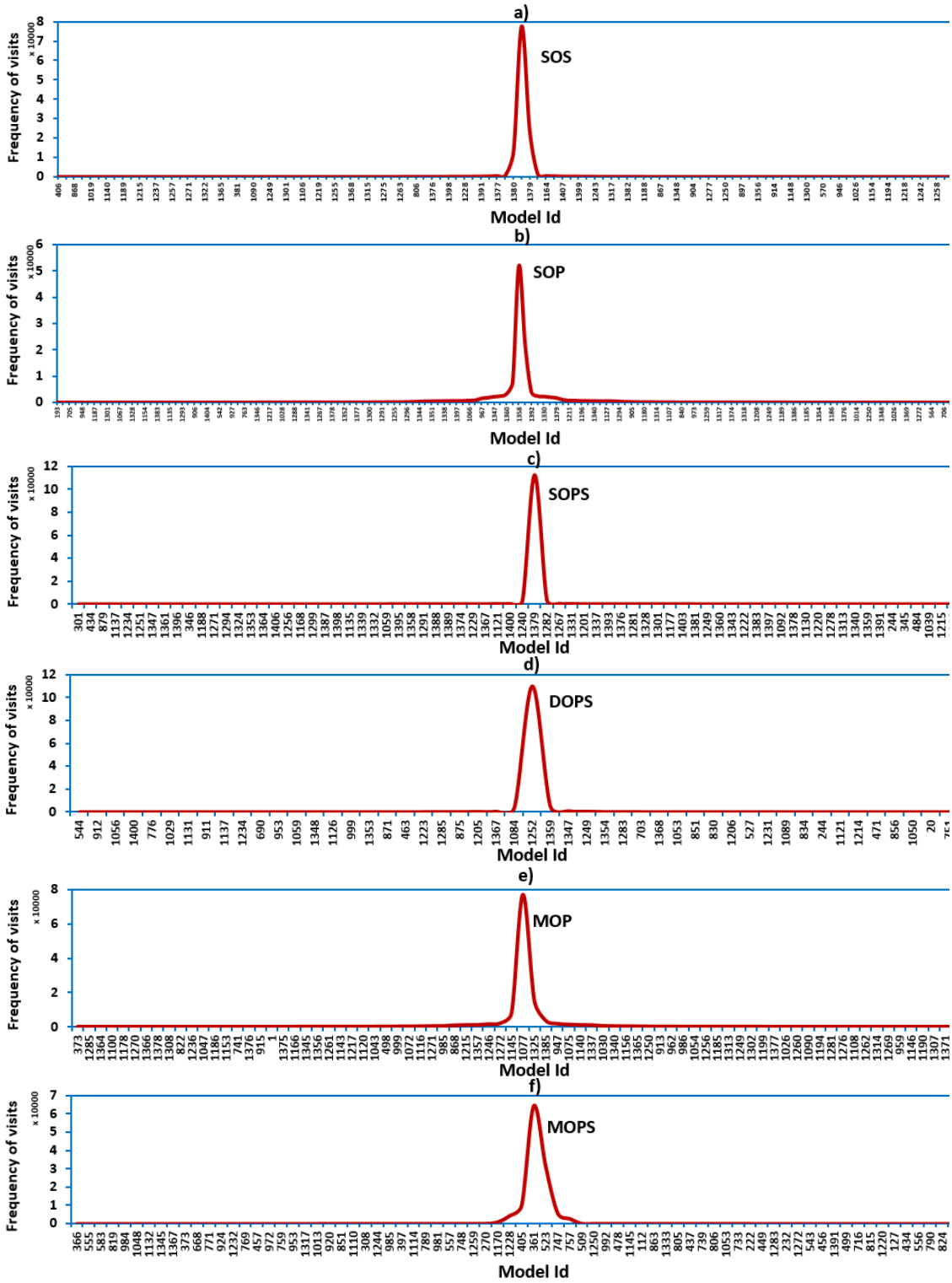

Figure 7.51 Models visited during the posterior walk and the frequency of visits for ensembles generated using a) SOS, b) SOP, c) SOPS, d) DOPS, e) MOP, and f) MOPS

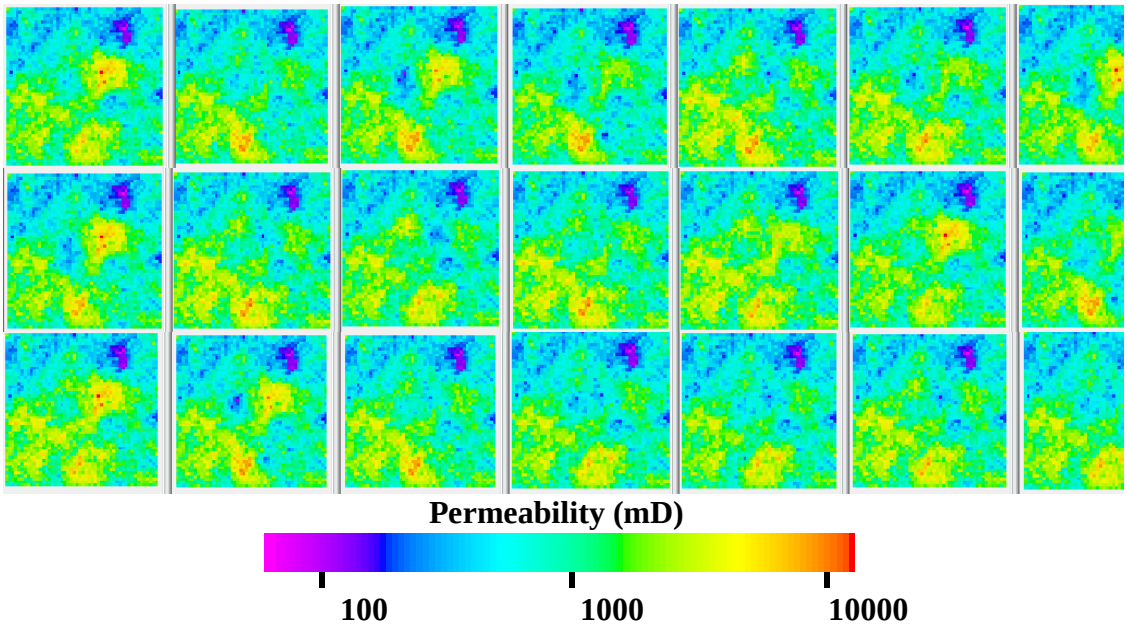

Figure 7.52 Permeability Field of 21 models selected from posterior walks

As an alternative to the weighted probability model approach, a much easier approach is to select the best ranked models in the pareto front. We call this the PF-based approach. If we assume these models to be equally probable, then the bounds formed by the predictions from these models becomes the uncertainty envelope. As we will see from the results, this approach is perhaps a better approach for uncertainty quantification after history matching a reservoir model with multiple conflicting data sources. In the MOPS using DSFMOGA, the ensemble of 1408 are distributed in different fronts depending mostly on the non-domination ranking. We show this distribution in Figure 7.53, where 193 models are on the first front.

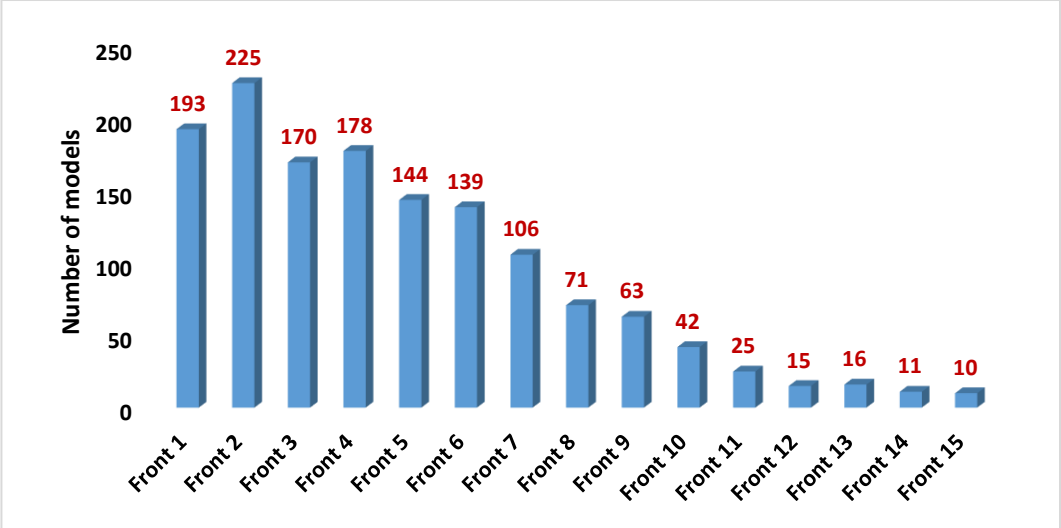

Figure 7.53 Distribution of the MOPS models in the fronts

We are interested in those 193 models for uncertainty quantification. We can further reduce this number by choosing the best ranked out of these models based on crowding distance. For this study, we select 21 best ranked models. The updated permeability for the 21 models are shown in Figure 7.54.

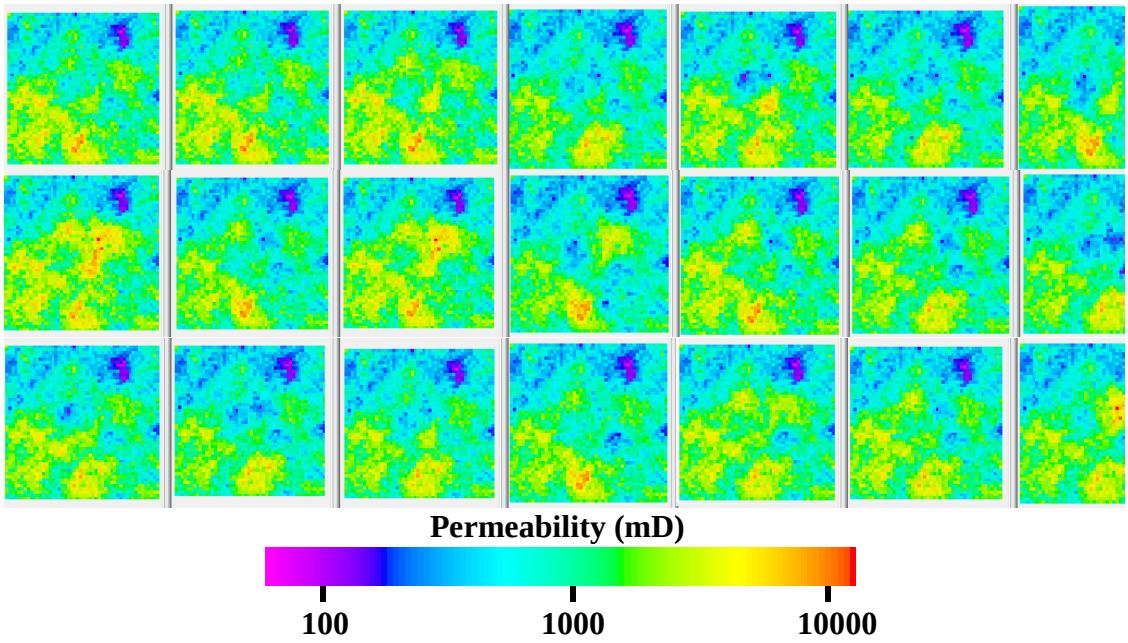

Figure 7.54 Permeability field of 21 models selected from the pareto front

We make predictions with the chosen models for quantities such as the field oil production rates (FOPR) and field water production rates (FWPR) and compare the predicted quantities with the truth (synthetic history). But first, we show the spread in the predictions made with the prior models in Figure 7.55. The predictions made using the 21 models from the weighted probability approach are compared to those made with the 21 models from the pareto front in Figures 7.56 and 7.57. For the weighted probability approach, the mean values of the predicted quantities are shown as dashed purple lines in Figures 7.56b and 7.57b. Then the P10 (the dashed orange lines) and P90 (dashed grey lines) profiles are determined from the mean profiles using gaussian statistics. In all plots of the predicted quantities, we include the predictions made with the true model from which the seismic history was derived (S_truth), and the predictions of the true model from which the production history was derived (P_truth). Through history matching, the large uncertainty envelopes defined by the prior models have been reduced.

We found that for all the predicted quantities, the models from the pareto front give predictions with spread enough to define the uncertainty in both the seismic and production quantities. The ‘true histories’ in this case lie within the uncertainty bounds. On the other hand, we found that in some quantities, either one or two of the ‘true histories’ lie outside the uncertainty envelope bounded by the P10 and P90 quantities

from the weighted probability/NABayes approach. The results of the NABayes-based approach show very narrow range of prediction outcomes suggesting relatively small uncertainty associated with the predictions.

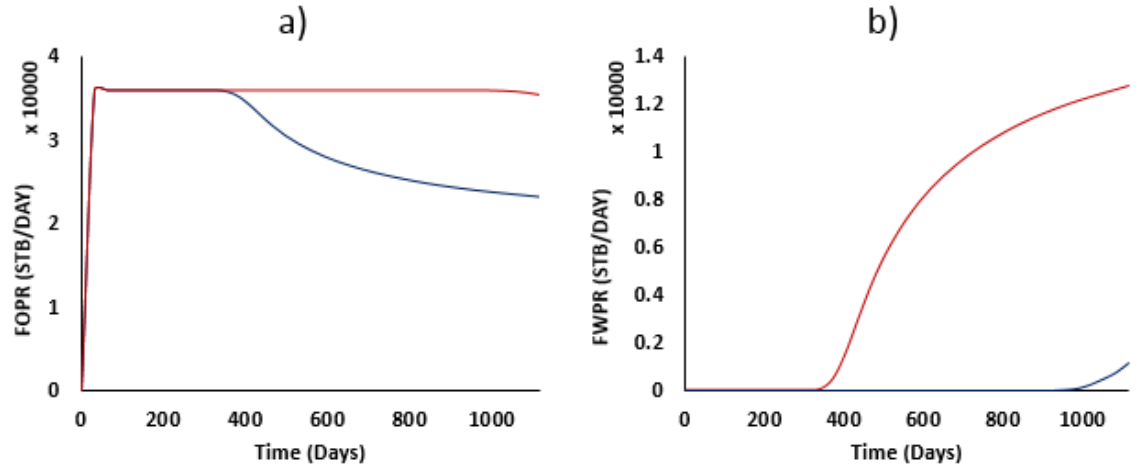

Figure 7.55 The spread in the predictions of the prior models for a) FOPR and b) FWPR

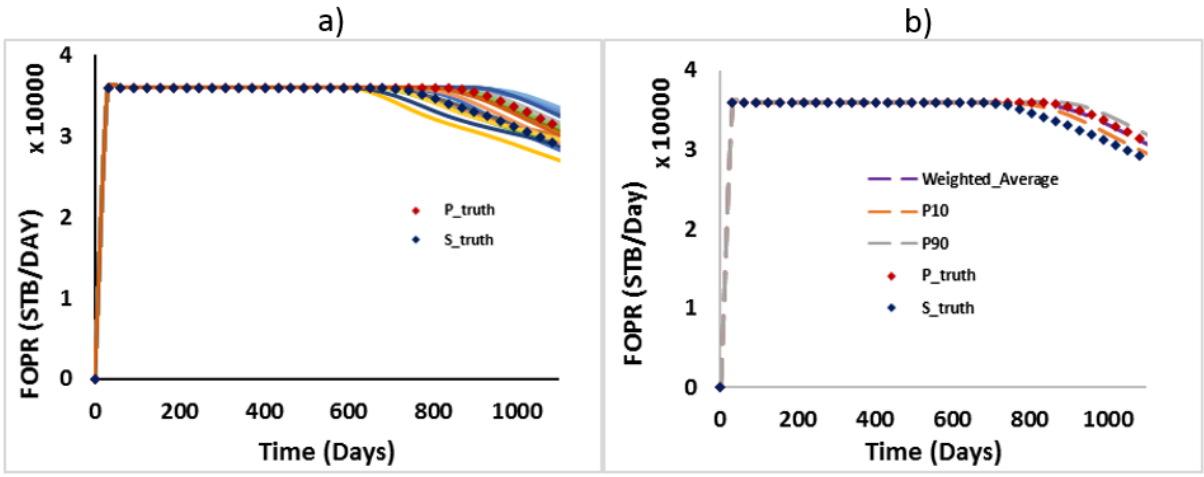

Figure 7.56 FOPR uncertainty envelope defined by a) pareto predictions b) weighted probability

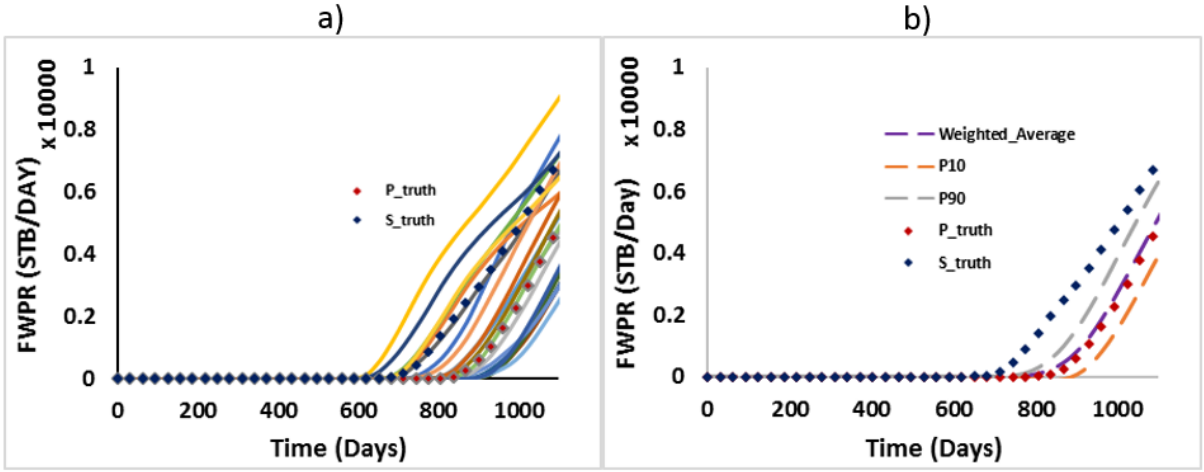

Figure 7.57 FWPR uncertainty envelope defined by a) pareto predictions b) weighted probability

The PF-based approach to uncertainty quantification is proven to be superior to the NABayes approach in this study for which conflicting history data are used to history match the reservoir model. Perhaps, this is expected. NABayes builds the voronoi approximation of the PPD based on a single misfit obtained by summing all individual misfits per model. In a problem of conflicting objectives, each misfit component carries a different information which may be lost partially or in entirety in the sum-objective. Appraisal using NABayes then misses out on some information provided by the various data during history matching. The spread in the predictions using the Pareto models gives a more realistic uncertainty quantification.

We can also make prediction of seismic quantities using the models on the pareto front (PF). We show examples of such predictions in Figure 7.58 for the AI predictions at the end of the third year of production using the 21 PF models. The predictions represent the spread in the predicted quantity and can be compared to the true seismic in Figure 7.59c.

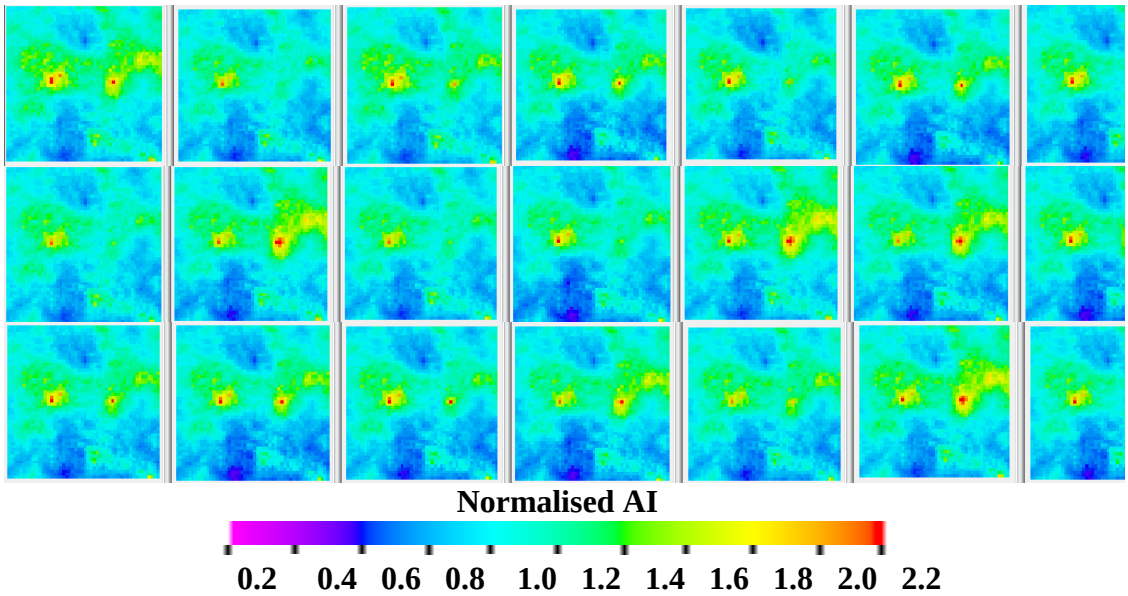

Figure 7.58 Predictions of Acoustic Impedance (AI) at the end of the 3rd production year with the 21 models from the pareto front

We distinguish between the predictions using models selected using either the PF-approach or the weighted probability approach, and 'bad models'. For illustration, we select one model at random out of the 178 models from Front 4 shown previously in Figure 7.53. Shown in Figure 7.59a is the permeability field of the chosen model. This updated permeability obviously did not reproduce some of the features in either of the two reference models (i.e. the true models). We make seismic prediction with this model (Figure 7.59b) and compare with the true seismic prediction (Figure 7.59c). We also predict the production quantities using the bad models and compare with the 'true quantities' in Figure 7.59. It is obvious that this bad model, rejected during the screening

of the fronts in DSFMO gives predictions that are too far away from matching the true quantities.

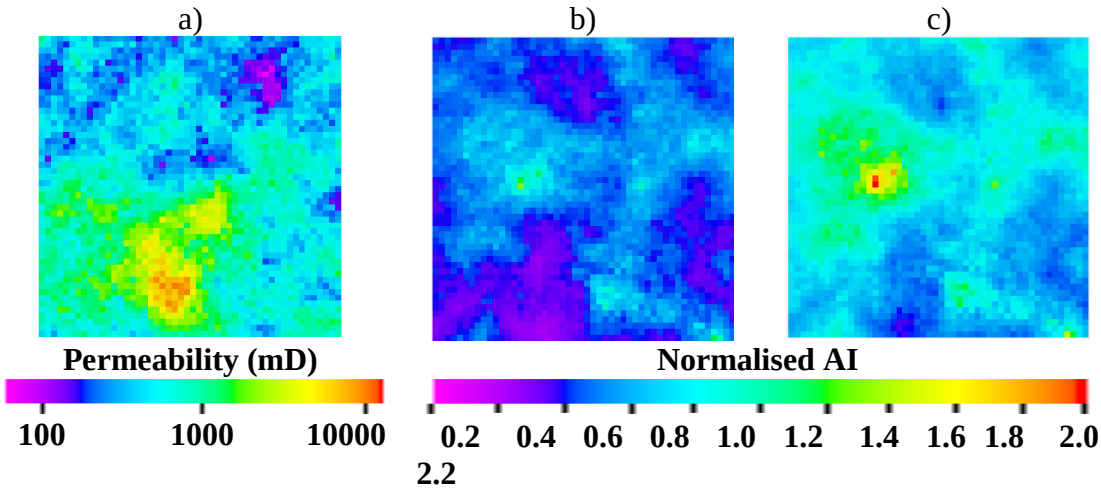

Figure 7.59 Permeability field of one of the bad models (a)), the AI prediction using the bad model (b)), and the AI prediction using the true model (c))

7.6 Summary and Conclusions

This chapter described a suite of algorithms, DSFMO, for performing optimisation in multi-objective fashion. The algorithms incorporate a range of options for screening the fronts in pareto-based approach to handling problems with many conflicting objectives. The options have been tested in various studies using benchmark problems to select the option most suited to problems of large objectives and large model parameters.

The algorithms were tested in synthetic history matching problems and compared in performance to single objective optimisation. The results show that DSFMO approach considers the good fitting models of all the individual objectives to provide a more diverse global ensemble of history matched models converging towards the lower overall misfits. The SOP and SOPS (single objective optimisation) concentrate on finding some models with the lowest misfit values while MOP and MOPS focus on finding all non-dominated solutions in the pareto front that balance among all the conflicting objectives.

The DSFMO provides four main benefits to history matching over single sum-objective optimisation, in the study involving conflicting objectives:

(i) reduces the chance of convergence into a false optimum point,

(ii) improves the chance of finding global best fitting models,

(iii) improves diversity in the history matched models, and

(iv) improves the quality of forecasting and uncertainty quantification.

The key advantage here is the increased diversity in the models found that produce the same and even better data fitting models. Compared to NABayes, the pareto-based approach was shown to provide a range of predicted outcomes and more realistic insight into the uncertainty associated with the predictions of future production.

Chapter 8– History Matching of the Norne Field

Overview

As reviewed in Chapter 6, the Norne Field reservoir is structurally complex. Local and field-wide stratigraphic barriers in the reservoir results in complex drainage and flooding pattern which make history matching very challenging. The reservoir model zonation is made of 22 layers. Hence, there are 21 maps separating the layer interfaces with transmissibility modelled using the Eclipse keyword MULTZ. The transmissibility values of the MULTZ-maps are potential candidates for updating during history matching. Previous studies reviewed in Chapter 6, as well as the sensitivity studies in this work indicate that the Norne Field flooding Pattern and oil water movement is most sensitive to the MULTZ maps at layer 10/11 and layer 15/16. The purpose of this chapter is to generate better data-fitting models by updating the values of the transmissibility of the MULTZ maps at those two interfaces. In this chapter, history matching is carried out in many ways as practical application of the several of the methods already studied and validated in the previous chapters using the synthetic fields. Emphasis is on multi-objective history matching using well water production rates and the AI data derived from full inversion of the Norne Field seismic data.

8.1 Developing a simulation case for the area of Study

Norne Field reservoir simulation model is made up of 113344 grid cells, of which 44927 cells are active (see section 6.6 in Chapter 6 for more details). Running the full Norne Field reservoir simulation model in stochastic history matching is computationally prohibitive. It takes approximately 20 minutes of CPU time to run one full model on 16GB 64-bit OS Intel Core PC. In stochastic history matching, it is not unusual to run tens of thousands of models in maximising the search of the model space for best data fitting models. One way to deal with such a large model is to divide the full model into sectors so that simulation is only performed on any chosen sector. With this, quick simulations are performed on small areas of interest, with smaller memory requirements. For instance, the full model may be divided into three sectors, namely: Sector C, Sector D-E and Sector G (Figure 8.1). Sector C is made up of the C-Segment, Sector D-E is made up of the D- and the E-Segments while Sector G is made of the G-Segment. Flux boundary conditions between the sectors are then created from a full Norne Field run and included in the sector models so that the predictions of the sector models do not vary

significantly from the results of full field simulation (for more technical description see ECLIPSE manual)(Schlumberger,2017).

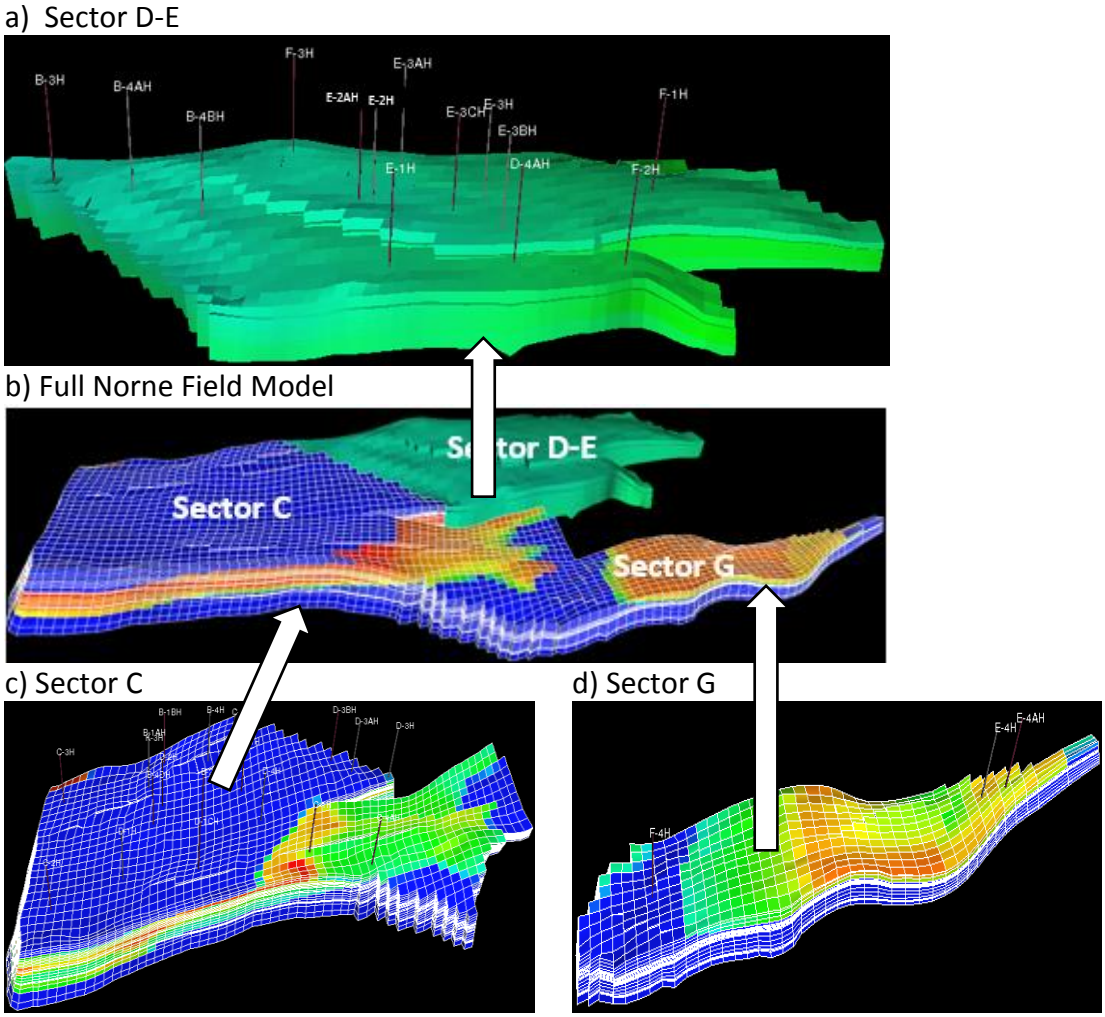

Figure 8.1 Simulation models for a) Sector D-E, b) Full Norne Field, c) Sector C, and d) Sector G. Sector D-E is coloured green for easy identification of the sector boundaries

Each of the sectors in Figure 8.1 can be simulated individually. However, sector models only approximate the full model because it is very difficult to carve out representative models that satisfactorily minimise the flux across the simulation boundaries for all simulation times. They may be satisfactory for some reservoir quantity prediction but will introduce additional modelling error in our history matching. We want to minimise error as much as possible.

We prefer to simulate the entire field as our area of study, and allow the drainage and flooding patterns to form freely. As a result, we adopt parallel computation. Using clusters of PCs, we parallelize the running of flow simulations taking advantage of the enormous volume of distributed memory available in the cluster systems. This substantially reduces the clock time to make the required thousands of flow simulations.

Parallel computations are implemented using the Message Passing Interface (MPI): the OpenMPI on Linux cluster. For example, different realisations of the simuation models are run concurrently on multiple processors at maximum CPU load thereby saving enormous time. OPTI-RES.exe is the executable programme for history matching which enables the use of different optimisation algorithms in the Heriot-Watt University's OptiRes (Optimisation for Reservoir Simulation) codes (Stephen, 2018). In addition, 16 processors were assigned per node for any process run on the cluster system such that the processors will not share computation time and run two or more of the simulations alternately.

The history matching algorithms were set up so that in one iteration models are spread across the available processors in a node for independent but concurrent simulations. After forward simulation, best models need be selected for the next iteration at which point excahange of information among the different models in different processors is necessary. However, some processors may be slower than the others. A method for synchronising the processes after each iteration may be needed. Two options are available to facilitate the information interchange. One option is to allow the different processors to continue with the best models evaluated so far over all processors and communicate same to the processors. With this option, the best models are selected without waiting for the slower processors to complete their iteration. This may lead to reduction of the overall time per iteration but may miss out some 'best models' at each iteration. The second option is to wait for all the processors to finish the computation at each iteration after which the best models are selected over the entire ensemble for the next iteration. We prefer not to miss out any of the 'best models' at each iteration, and therefore, we have adopted the second option in this work.

8.2 Base Case and History Data

The basecase values of the vertical multipliers at the 27 MULTZ regions defined on layer 10 and layer 15 of the basecase model is shown in Table 8.1.

In Figures 8.2 and 8.3, the observed seismic and observed well water production rates are respectively compared to the corresponding quantities predicted using the basecase reservoir model.

Table 8.1 Basecase values of the vertical transmissibility multipliers

MULTZ Region	Basecase Transmissibility Multiplier
R1	0.005
R2	0.03
R3	0.05
R4	0.25
R5	0.25
R6	0.25
R7	0.25
R8	0.5
R9	0.5
R10	0.5
R11	0.5
R12	0.01
R13	0.05
R14	0.005
R15	0.005
R16	0.25
R17	0.000001
R18	0.005
R19	0.0008
R20	0.01
R21	0.0035
R22	0.00003
R23	0.00003
R24	0.00003
R25	0.00003
R26	0.00003
R27	0.00003

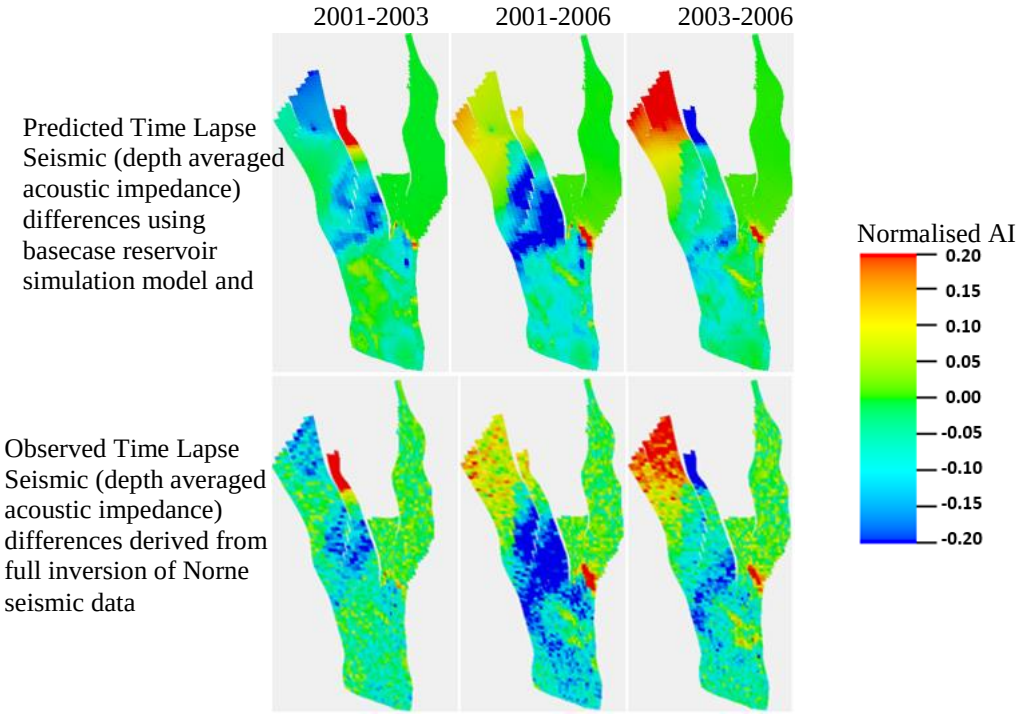

Figure 8.2 Comparing the base case seismic prediction with the observed seismic

Except for some subtle differences, the seismic signatures predicted using the base case model matches the observed seismic closely. This is expected as the basecase model used in this study has been updated in several studies (some of which were highlighted in Chapter 6) using the Norne Field time lapse seismic. There are, however, some high levels of mismatch between the predicted well water production rates (WWPR) and the observed water rates, as shown in Figure 8.3.

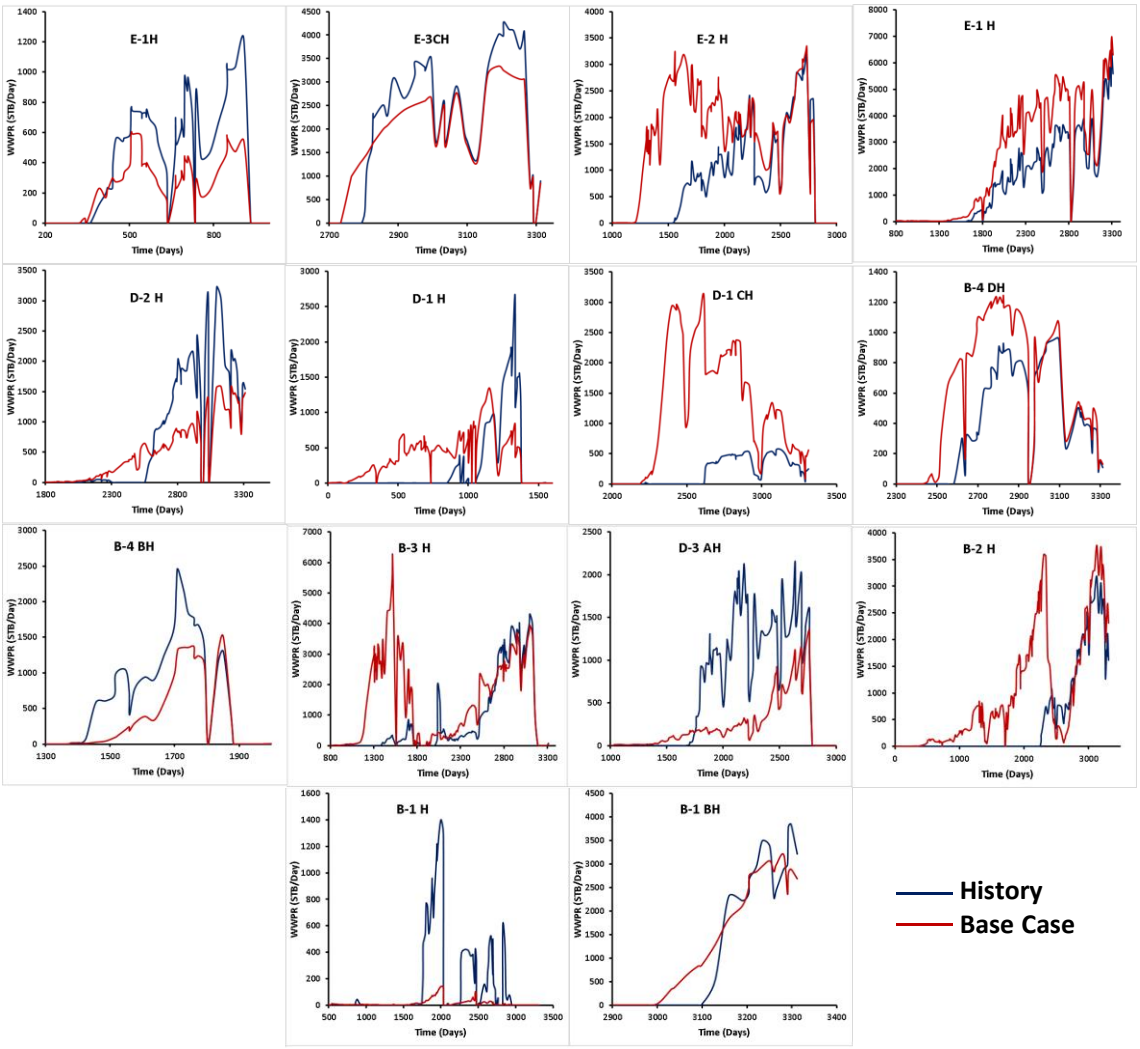

Figure 8.3 Comparison of the well water production profiles established with the base case simulation (red lines) to the history (blue lines)

Our aim is to close the gap between the predicted and historical water rates through multi-objective history matching. We use the misfits between the predicted and measured water rates at the 14 producers listed previously as the match criteria. Although the seismic predictions of the basecase model seems to have a good match to the measured seismic, we will also include the seismic data as a match criterion. The seismic data will serve as

additional constraints to the model as we prefer predictions from models which fit both the seismic and production data reasonably.

8.3 Impact of local MULTZ values on well responses

We were interested in updating the vertical transmissibility values of the local barriers on layer 10 and layer 15 (Figure 8.4 and 8.5) as these have significant influence on the Norne Field flooding pattern. The sensistivity analysis of Norne Field stratigraphic barriers were done in Chapter 6, under section 6.7. We were interested in generating models with good fit to well water production rates and time lapse seismic data. Before proceeding with the history matching, the Norne Field MULTZ maps were divided into some MULTZ sub-regions considering the drainage pattern in the simulation model, the positioning of the wells and fault boundaries. Sensitivity analysis was carried out to determine the regions with vertical transmissibility influencing the individual responses of each of the Norne Field producing wells.

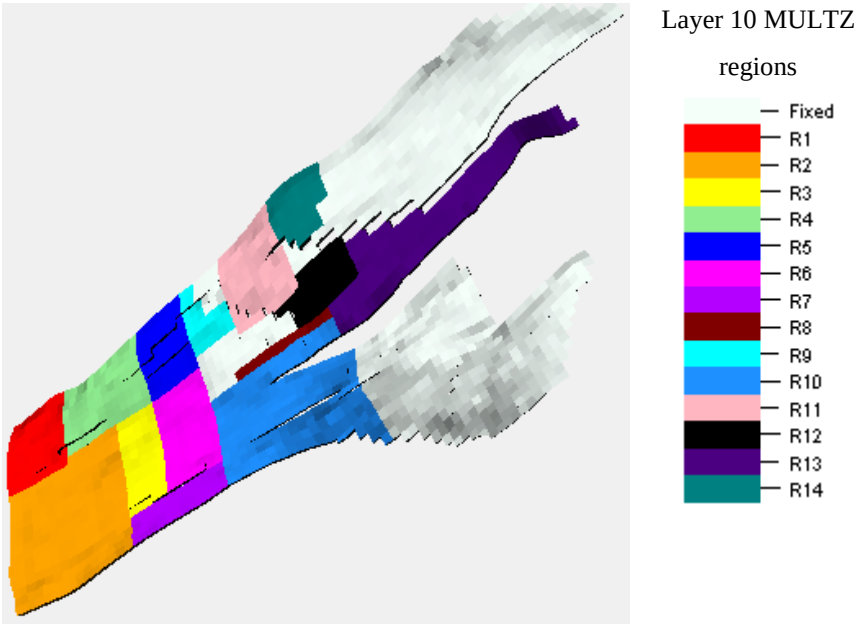

Figure 8.4 Regions of the MULTZ maps on Layer 15 with vertical transmissibility multipliers designated as R15 to R27

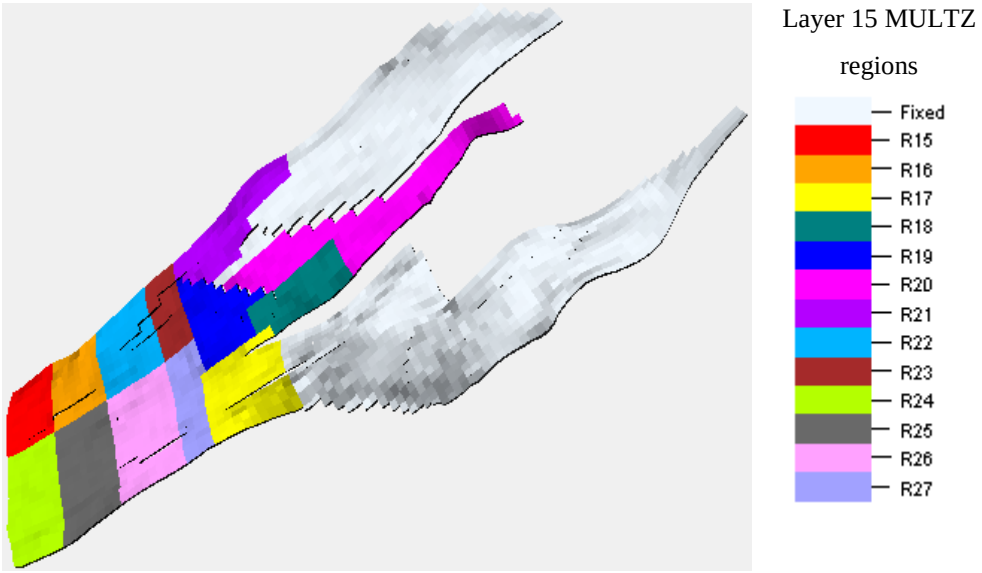

Figure 8.5 Regions of the MULTZ maps on Layer 15 with vertical transmissibility multipliers designated as R15 to R27

We deploy two approaches to sensitivity analysis, namely: 1.) Differential Sensitivity Analysis using proxy models, 2.) Pearson's product moment correlation coefficient

Sensitivity Approach 1:

With proxy-model approximation of reservoir response, it is easy to evaluate the relative impact within this model that a parameter has on the response variable. In using the Differential Sensitivity Analysis (DSA), we assess the sensitivity on MULTZ regional parameters without regard to the combined variability resulting from considering all input MULTZ parameters simultaneously. By using proxy models, defining the relationship between the dependent and independent variables, the DSA becomes easier (Atherton *et al*., 1975). The dependent variables are the water production rates (Q_w) at the wells while the independent variables are the regional MULTZ parameters (R_i). Neglecting higher order partials, second-order Taylor series approximation applied to the Q_w as a function of R_i, gives quadratic proxy models. The quadratic models are then calibrated using the input values from experimental design and the corresponding output values from reservoir simulation. If we assume that there is no correlation between input parameters (Atherton *et al*., 1975; Gardner *et al*., 1981), then the sensitivity, φ_i, for any independent variable can be calculated from the partial derivative of the dependent variable with respect to the independent variable evaluated at all input data point k = 1, …., N (Equation 8.1):

$$S_{pr} = \left(\frac{1}{N} * \sum_{k=1}^{N} \left|\frac{\partial Q_w}{\partial R}\right|_k\right) * \frac{\sigma(R)}{\sigma(Q_w)}, \ldots\ldots\ldots\ldots\ldots\ldots\ldots\ldots\ldots\ldots\ldots\ldots (8.1)$$

where the quotient, $\frac{\sigma(R)}{\sigma(Q_w)}$, is introduced to normalize the sensitivity values and $\sigma(Q_w)$, $\sigma(R)$ are the standard deviation of Q_w and the standard deviation of R in the input data respectively. S_{pr} denotes the sensitivity by proxy approach.

We can also determine the nature of the impact that an independent variable has on the response variable. This is possible through the definition of positive impact and negative impact. Positive impact of an independent variable can be defined as the likelihood that increasing this variable will increase the value of the response variable, while negative impact is the likelihood that increasing the value of the variable decreases the response value.

Expressed in percentage, for example, 85% (positive) means that 85% of the time, increases in the variable lead to increase in response and 15 % of the time, increase in the variable results in either decrease in the response or nil impact. Positive impact is calculated as the percentage of data points where $\frac{\partial Q_w}{\partial R} > 0$, while negative impact is the percent of data points where $\frac{\partial Q_w}{\partial R} < 0$. More so, we can determine the magnitude of the positive impact and negative impact. When Equation 8.1 is evaluated at only the points where $\frac{\partial Q_w}{\partial R} > 0$, we have a measure of the magnitude of the positive impact, and when evaluated at only the points where $\frac{\partial Q_w}{\partial R} < 0$, it is the magnitude of the negative impact.

We show examples of the differential sensitivity analysis applied in the case of local changes in Norne Field MULTZ maps at layers 10 and 15 to see how the changes affect the responses of some selected wells. With the results of the differential sensitivity analysis the pattern shown in Figure 8.6 is established

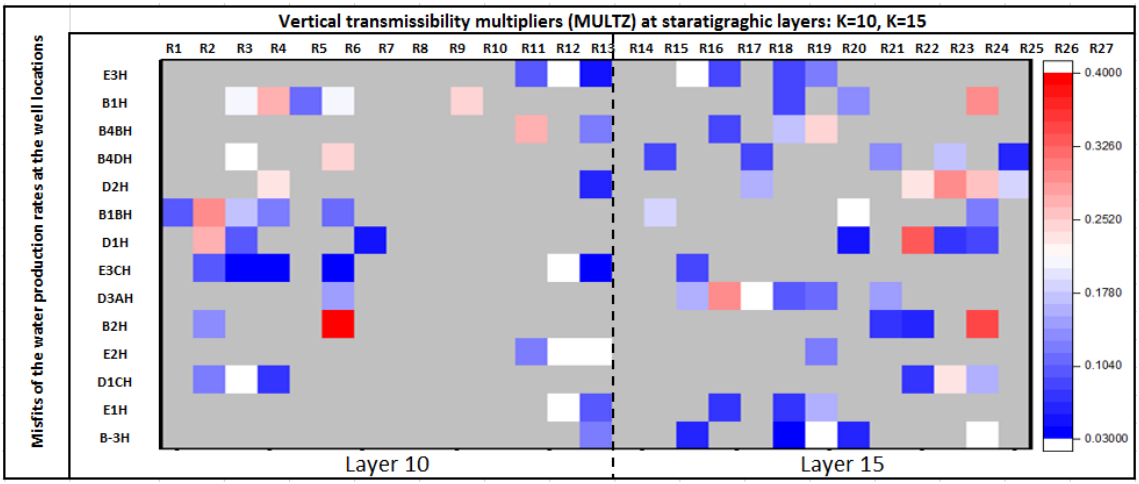

Figure 8.6 Sensitivity of well production rates to changes in vertical transmissibility multipliers (Proxy Differential Sensitivity Analysis). The grey colour indicates zero sensitivity

Sensitivity Approach 2:

The sensitivity done in the previous section assesses the individual MULTZ without regard to the contributions of other regional MULTZ. However, parameter sensitivity does not depend only on the range and distribution of an individual parameter, but also on the range and distribution of other influential parameters to which the model response is sensitive (Iman *et al*., 1981). In order to assess the impact of the individual regional MULTZ parameters while considering the combined variability resulting from all other parameters simultaneously, we use Pearson's product moment correlation coefficient (Gardner *et al*., 1981). An array of 500 combinations of the MULTZ values generated using Latin Hypercube Sampling together with their respective simulator output in the form of well water production rates provide the means for determining the MULTZ linear correlation and sensitivity. We calculate Pearson's product moment correlation coefficient, PPMCC for any regional MULTZ parameters, R_i (I = 1, …, 27) and any well water production rates from reservoir simulation (Q_w) using Equation 8.2.

$$PPMCC = \frac{\sum_{k=1}^{N}(R_k - \bar{R})(Q_{w_k} - \overline{Q_w})}{\sqrt{\sum_{k=1}^{N}(R_k - \bar{R})^2}\sqrt{\sum_{k=1}^{N}(Q_{w_k} - \overline{Q_w})^2}}, \ldots\ldots\ldots\ldots\ldots\ldots\ldots\ldots\ldots\ldots 8.2$$

Where N is the number of data points

With the results of the Pearson's product moment correlation coefficient, the pattern shown in Figure 8.7 is established. The larger the absolute value of the PPMCC the stronger the degree of linear relationship between the MULTZ parameter and the well response. A negative value of PPMCC indicates the well response is inversely related to

the MULTZ region (e.g. the regional MULTZ, R13 and the wells, E1H and E3H). The positions of the wells on the layer 15 MULTZ map are shown in Figure 8.8

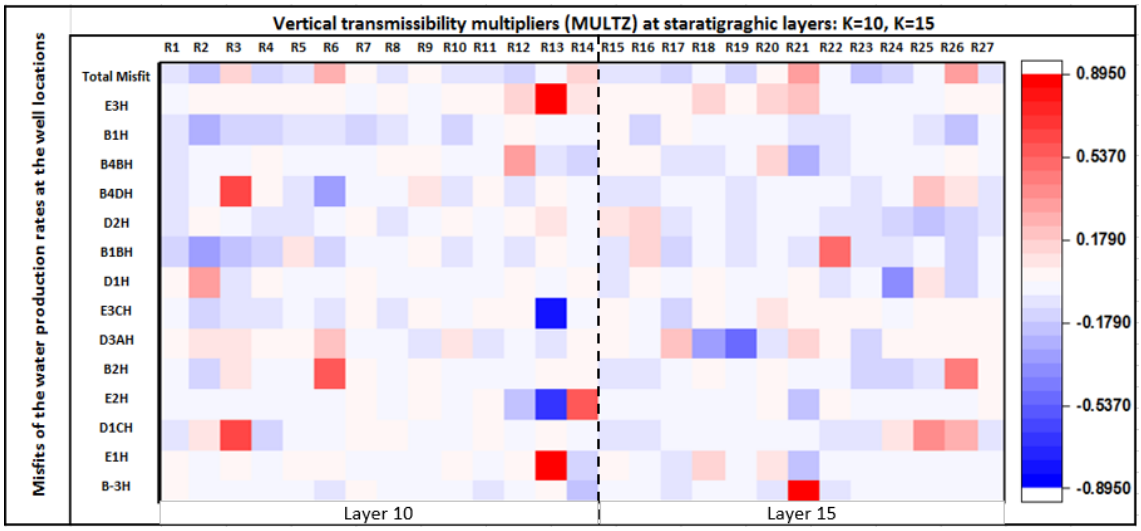

Figure 8.7 Sensitivity of well water production rates to changes in vertical transmissibility multipliers (Pearson's Coefficents)

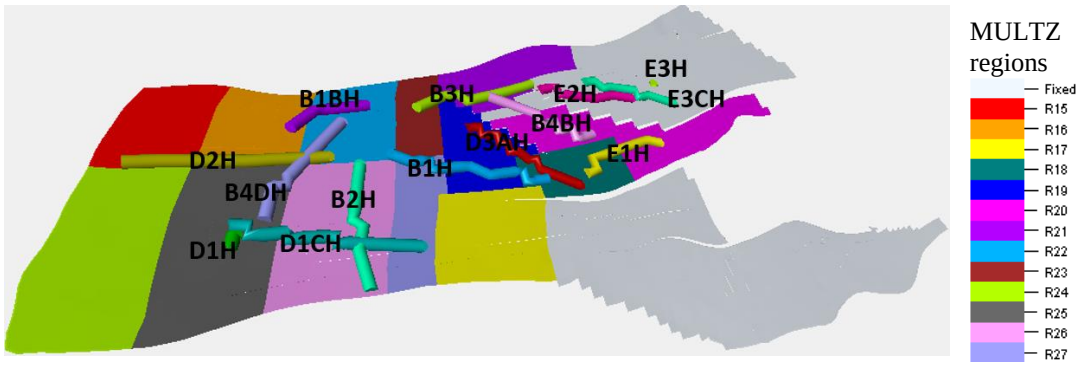

Figure 8.8 Norne Field wells on Layer 15 MULTZ map

Norne Field is highly compartmentalised with complex flooding pattern, so we expect some dependency in well responses. In other words, the response of a given well may be dependent on the response of the other. We assess this dependency between the wells through the linear correlation calculated using Equation 8.2 but between wells instead of between wells and MULTS parameters. As shown in Figure 8.9, some wells are highly dependent on each other (e.g. E1H and E2H, E1H and E3H, E1H and E3CH etc) while some others are non-correlated (e.g D1H and E1H, D1H and D3AH etc).

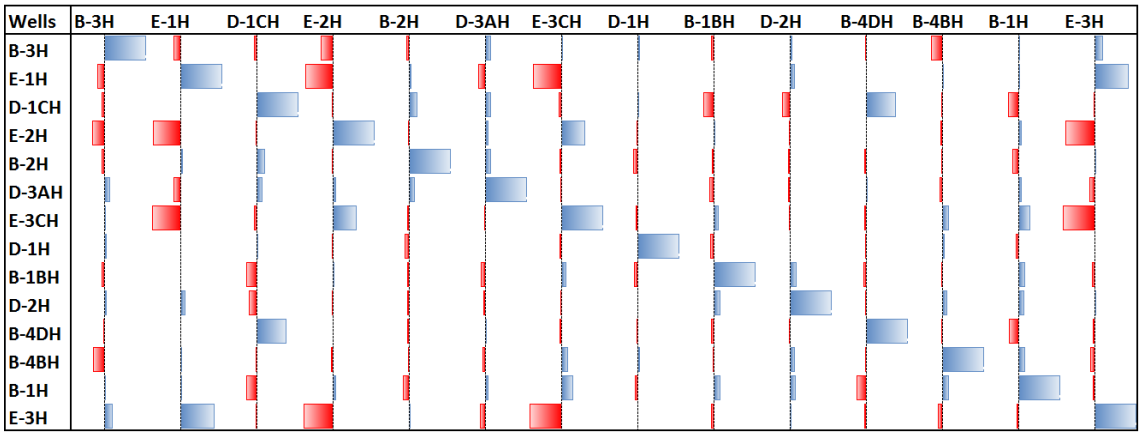

Figure 8.9 Norne Field well correlations assessed through the sensitivity of water production rates to changes in vertical transmissibility multipliers (Pearson's Coefficents). Blue indicates positive correlation while red indicates nehative correlation.

The difficulty posed by the wells' dependency on one another can be exemplified using the case of wells E-1H, E-2H, E-3CHand E-3H which are all sensitive to changes in the R13 regional MULTZ (Figures 8.6 and 8.7). We see from Figure 8.7 that increase in the value of R13 results in decrease in the water production from wells E1H and E3H and increase in the water production from both well E2H and E-3CH. Any attempt to history match the water production in these wells result in conflicting objectives as the match in well E-3CH and E2H deteriorate as we try to adjust R13 to match E1H and E3H.

8.4. Reparameterisation and well grouping

In Chapter 7, the capability of DSFMO in resolving multi-objective problems was demonstrated in several multi-objective problems. The algorithm was shown to be robust in many cases but, as expected, its performance deteriorates with increasing number of objectives. Performance of the algorithms is also affected by parameterisation. In the case of Norne Field, we expect further difficulty due to the high level of well correlations depicted in Figure 8.9.

We want to regroup the 14 wells to minimise the effect of the correlation but first we need to reparameterise the MULTZ regions on layers 10 and 15. The Pearson's coefficients shown previously in Figure 8.7 reveals that some of the R-parameters have little or no significant influence on the responses of the wells (e.g R1, R4, R5, R7 and R8). Some other parameters influence the well responses in the same manner and need be grouped together as one parameter (e.g R18 and R19 both have positive correlation with well D3AH, and both are neighboring regions). In this manner, the 27 parameters are reduced

to 10 parameters (RP1 to RP10) shown in Table 8.2, Figure 8.10 (for layer 10), and Figure 8.11 (for layer 15).

Table 8.2 Reparameterization of the MULTZ regions

Old MULTZ Parameter	New MULTZ Parameter	Remarks on Reservoir Response
R1, R4, R5, R7, R8	Fixed at base value	Negligible influence
R2	RP1	Affects mostly the responses of wells D-1H and B-1BH
R3	RP2	Affects mostly the responses of wells D1CH and B4DH
R6	RP3	Affects mostly the responses of wells B-2H and B4DH
R9, R10, R11, R15, R16	Fixed at base value	Negligible influence
R12	RP4	Affects mostly the responses of wells E-2H and B4BH
R13	RP5	Significant impact on wells E1H, E2H, E3CH and E3H
R14	RP6	Affects B3H and E2H
R17	RP7	Significant impact on well D3AH
R18		
R19		
R20	Fixed at base value	Negligible influence
R21	RP8	Significant impact on well B3H
R22	RP9	Significant impact on well B1BH
R23		
R24	RP10	Affect mostly the response of wells D1H, D1CH, D2H, B4DH, B2H and B1H
R25		
R26		
R27		

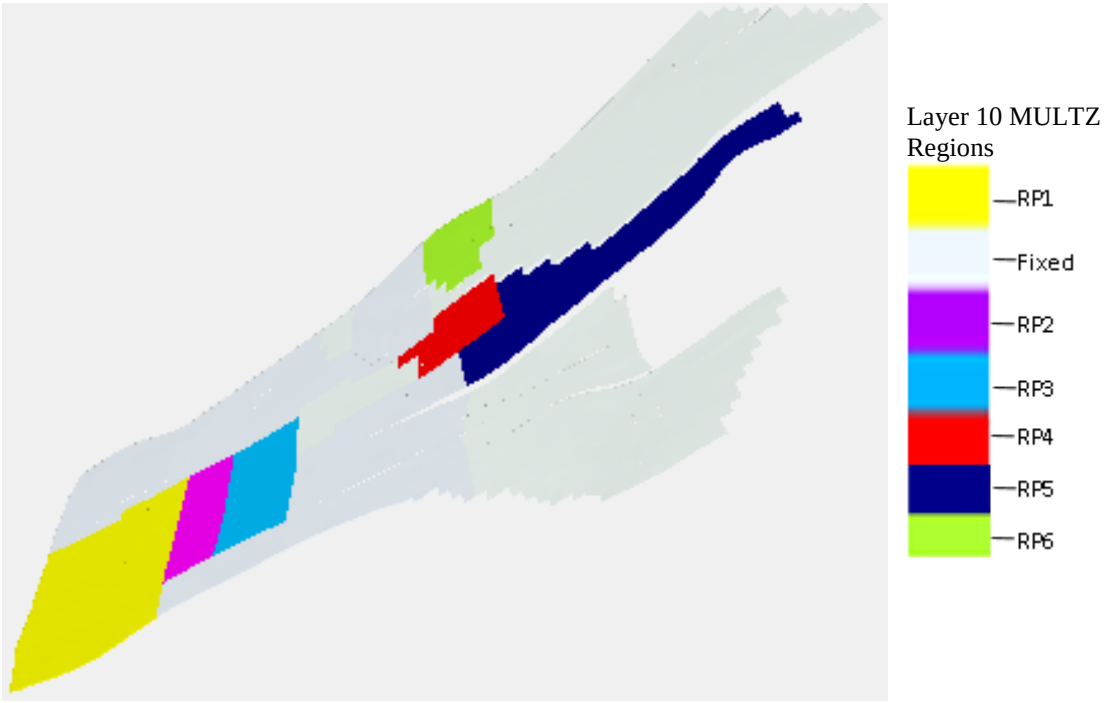

Figure 8.10 Regions of the reparameterised MULTZ maps on Layer 10 with vertical transmissibility multipliers designated as RP15 to RP6

Figure 8.11 Regions of the reparameterised MULTZ maps on Layer 15 with vertical transmissibility multipliers designated as RP7 to RP10

The 27D problem has now reduced to a 10D problem (where D is the inverse problem dimension: number of parametric elements in the model). As done previously in the case of the 27D model, the sensitivity of the well responses to changes in the 10D model wass performed using the Pearson's product moment correlation coefficient. The calculated coefficients are shown in Figure 8.12

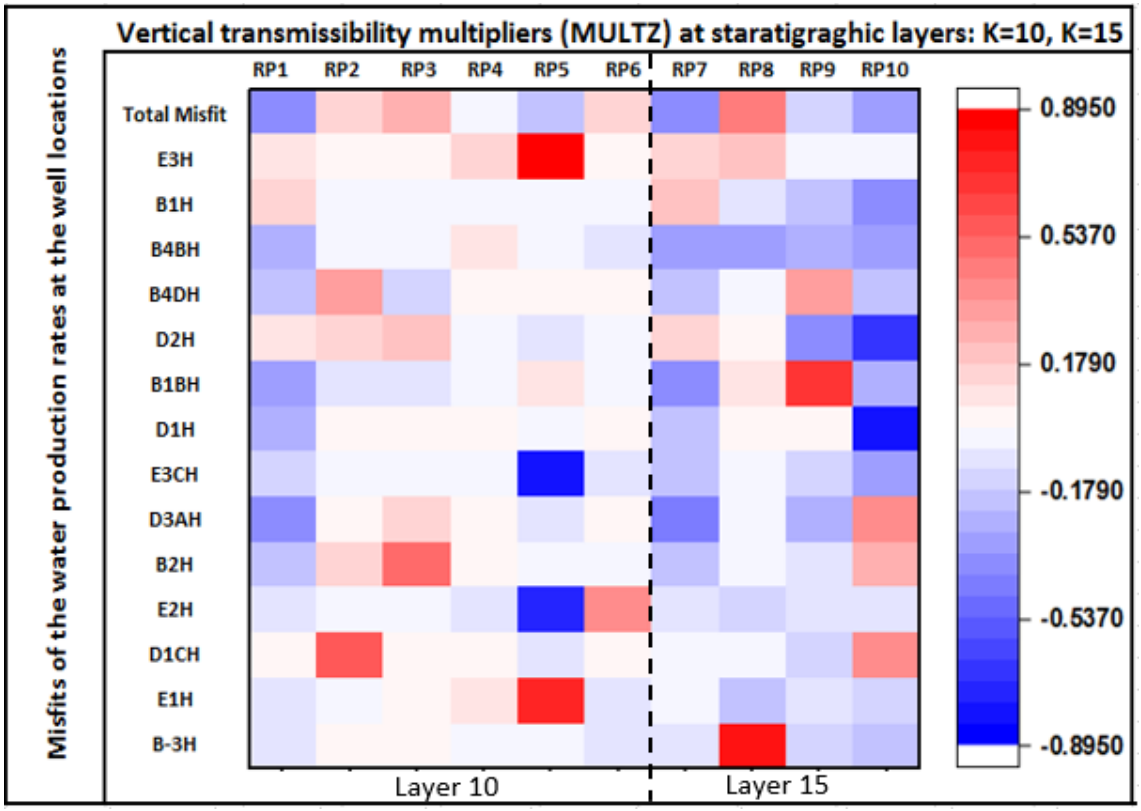

Figure 8.12 Sensitivity of well water production rates to changes in vertical transmissibility multipliers (Pearson's Coefficents)

If we consider the misfit between the predicted and measured water rates at the 14 wells, we would have 14 conflicting objectives to match. The number of objectives is increased further if we consider seismic misfits in the history matching. To improve the convergence rate and achieve better match, we need to reduce the number of objective functions. We want to achieve this by methodically grouping the wells. Our method of grouping the objective components depends on the conflicting information provided by the Pearson's Coefficents of the wells. The coefficients provide information on the rank correlations of the wells. Zero or near zero values indicate independent objectives. The magnitude of the positive coefficients between any two wells indicates the level of agreement between the wells while the magnitude of negative coefficients is a measure of the level of conflict. In basic terms, two objectives are said to agree if an improvement in one of the objectives leads to an improvement in the other objective. On the other hand, two objectives are in conflict when an improvement in one leads to the deterioration of the other. We aim to place any two objectives into one objective group if the objectives have high level of agreement and less conflict. We also consider the positions of the wells in the simulation grid. For instance, grouping is favoured when two wells with high positive coefficients are producing from the same region or the well are completed in the same vicinity (see Figure 8.8 for the positions of the wells). Using a cut off value of ± 0.3

for the pearson's coefficients, the wells are placed in 6 groups as shown in Table 8.3. The misfits in the three time-lapse seismic surveys are also grouped into one objective.

Table 8.3 Well and seismic objective groups for history matching

Group Name	Wells	Remarks
GRP_1	E-1H, E-3H	Strongly in agreement
GRP_2	E-2H, E-3CH	Strongly in agreement
GRP_3	B-4BH, D-3AH	In agreement
GRP_4	D-1H, D-2H	In agreement
GRP_5	B-1H, B-3H	In agreement
GRP_6	B-4DH, D-1CH, B-1BH, B-2H	In agreement
Seismic	2001-2006 AI, 2001-2006 AI, 2003-2006 AI	Strongly in agreement

AI in the above table is the Difference in AI

The well correlation and group dependency on parameters are highlighted as follows:

- GRP1: E-1H and E-3H are in strong agreement and are both positively correlated to parameter RP5
- GRP2: E-2H and E-3CH are in strong agreement and are both in negative correlation to parameter RP5. E-2H is also in weak positive correlation to RP6
- GRP3: B-4BH and D-3AH are in agreement and are both in negative correlation to parameter RP7.
- GRP4: D-1H and D-2H are in agreement and are both in negative correlation to parameter RP10.
- GRP5: B-1H and B-3H are in relatively independent. B-1H is weakly influenced by the parameters R7 and R10 while B-3H is highly sensitive to parameter R8.
- GRP6: B-4DH, D-1CH, B-1BH, B-2H are all in agreement to one another and are all influenced by parameter RP10. However, B-4DH and D1-CH are also dependent on RP2; B-IBH is strongly influenced by RP9 while B-2H is highly sensitive to RP3

8.5 Searching for better data-fitting models

We aim to improve the match of well water production rates at the wells using different approaches (Table 8.4). The approaches differ in the way the objectives in the form of misfits between the predicted and observed are utilised as match metric during optimisation.

Table 8.4 Well and seismic objective groups for history matching

Approach	Description
Single Objective Seismic (SOS)	The three time lapse seismic data are used as the only constraint during history matching
Single Objective Production (SOP)	The 14 individual misfits evaluated for the water rates at the 14 producers are summed into one single misfit which becomes the match criterion
Single Objective Production and Seismic (SOPS)	Sum-objective optimisation in which production misfit is added to seismic misfit. The 14 individual misfits evaluated for the water rates at the 14 producers are added to the 3 misfits predicted for each of the seismic surveys to form one single misfit. This single misfit becomes the criterion for selecting the best models in a generation for the next iteration
Dual Objective Production and Seismic (DOPS)	Dual-objective optimisation in which production misfit and seismic misfit are treated seperately and handled in multi-objective fashion. The 14 individual misfits evaluated for the water rates at the 14 producers are added together to become a single production misfit, while the 3 misfits predicted for each of the seismic surveys are summed to become one single seismic misfit. The problem then reduces to a multiobjective problem with two objectives.
Multi-Objective Production and Seismic (MOPS)	Multiple-objective optimisation in which each of the objectives are treated as a separate function. With MOPS, the 17 objectives (comprised of the 14 individual production misfits and the 3 seismic misfits) can be handled in a multi-objective function fashion. However, for the reasons given in the next section, the 17 objectives are reduced to 8 objectives (comprising of 8 group-objective). Seven out of the eight groups are made up of two individual well misfits each, while the 3 seismic misfits are lumped into a single misfit. The 8 objective groups are handled in multi-objective fashion

We will compare the results of the above approaches to determine which approach is most suitable for the history matching of the Norne Field.

We search for better-data fitting models by perturbing the transmissibility multipliers (MULTZ maps) at layers 10 and 15 of the basecase model. A genetic algorithm (described under section 3.7.2 in Chapter 3 for single objective optimisation and under section 7.3.2 in Chapter 7 for multi-objective optimisation) is used in all cases, initialised with quasi random number generator using the parameter limit ranges shown in Table 8.5. The RP-parameters correspond to the 10 reparameterised MULTZ regions. Log_{10} values of the parameters are sampled to avoid bias.

Table 8.5 MULTZ regions and transmissibility perturbation range

MULTZ Region	Basecase Log10 Transmissibility Multiplier value	Log_{10}Transmissibility Multiplier Perturbation Range [Minimum, Maximum]
RP1	-1.5	[-4.3, 0.00]
RP2	-1.3	[-3.3, 0.00]
RP3	-0.6	[-2.6, 0.00]
RP4	-1.3	[-4.0, 0.00]
RP5	-2.3	[-3.3, 0.00]
RP6	-2.3	[-4.3, 0.00]
RP7	-3.1	[-5.1, 0.00]
RP8	-2.5	[-4.4, 0.00]
RP9	-4.5	[-6.5, 0.00]
RP10	-4.5	[-6.5, 0.00]

Optimisation was initialised using 128 models. A total of 59 iterations was performed for each approach, and at each iteration 32 new models are generated. This gives an ensemble of 2016 models in each case.

8.5.1 Single objective history matching

The results of three cases of single objective history matching, in which all misfits are summed to form a single match metric, are presented and include:

i. Seismic history matching using only the time lapse seismic
ii. Production history matching using well water rates as match data
iii. Seismic and production history matching using all the time lapse seismic and well water rates as the match data

Figure 8.13 shows that the misfit evolution in the three cases followed a similar trend. There are some substantial misfit reductions in each of the three cases by a factor of about: 1/8 in seismic misfit (Figure 8.13a), 1/6 in the total production misfit (Figure 8.13b) and 1/6 in the total production and seismic misfit (Figure 8.13c). Also, convergence in each of the three cases was achieved in just about 27 iterations (1000 models) after which there was no further misfit reduction.

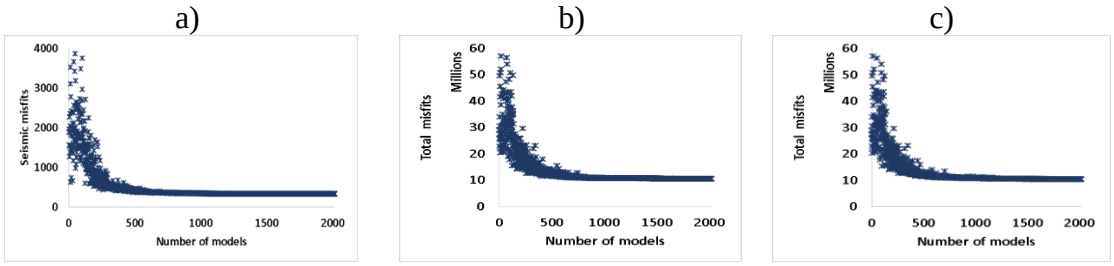

Figure 8.13 The evolution of misfits of Norne Field models during single-objective a)seismic history matching, b) production history matching, and c) seismic and production history matching

Figure 8.14 compares the parameter evolution for seismic history matching and production history matching. Each of the model parameters in the two cases converged. However, the solutions suggested by the seismic data differs from those suggested by the production data especially in parameters RP3, RP5, RP7, RP8, RP9 and RP10 which coverged to different values.

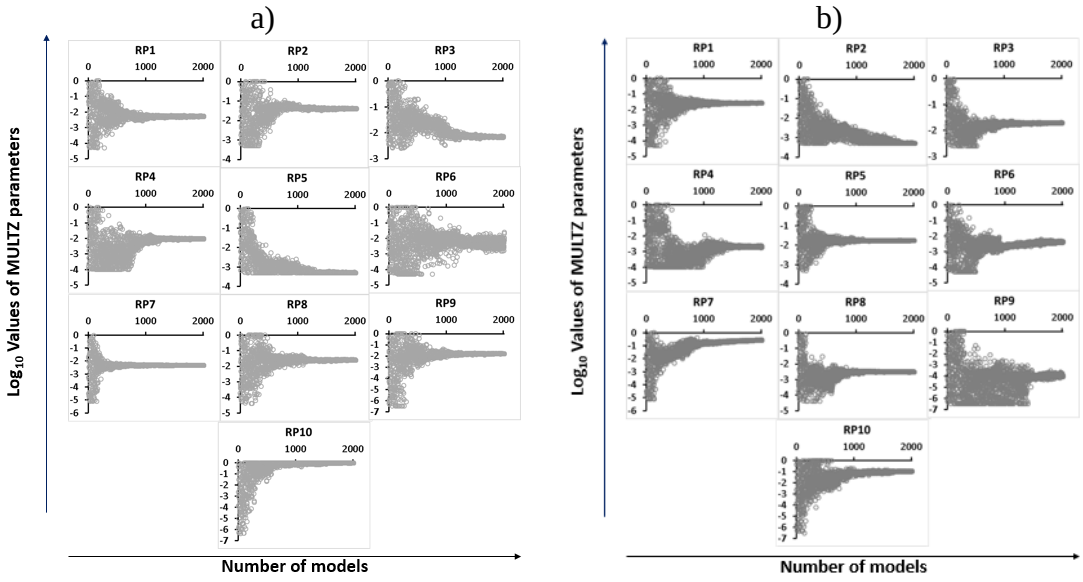

Figure 8.14 The evolution of model parameters in single-objective history matching using a) seismic data, and b) production data

The parameter evolution in history matching using both seismic and production data (Figure 8.15) shows that the production data dominated the process. The trend in Figure 8.15 is very similar to Figure 8.13b (the production only case). The data assimilation in this case is skewed against the seismic data

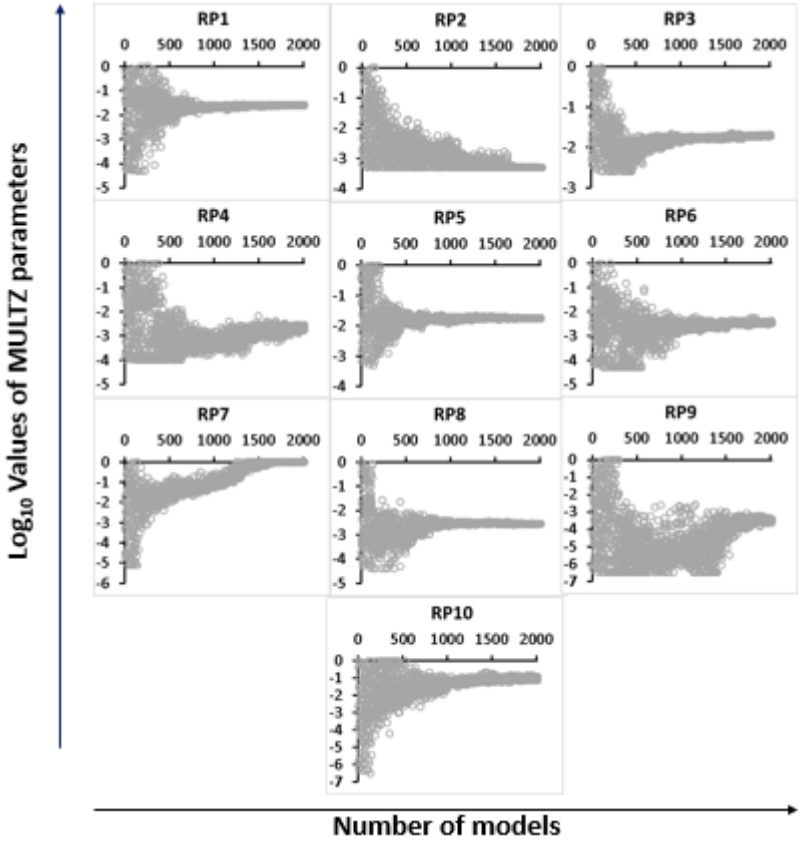

Figure 8.15 The evolution of model parameters in single sum-objective history matching using both seismic and production data

Next, we look at how the individual component of the misfits evolved during the single sum-objective seismic and production history matching (Figure 8.16). We note particularly that the match in seismic data, and the water rates in wells E-3H, E-3CH and D-1H started deteriorating after some iterations as the single objective optimisation favours the minimisation of the misfits in some other wells.

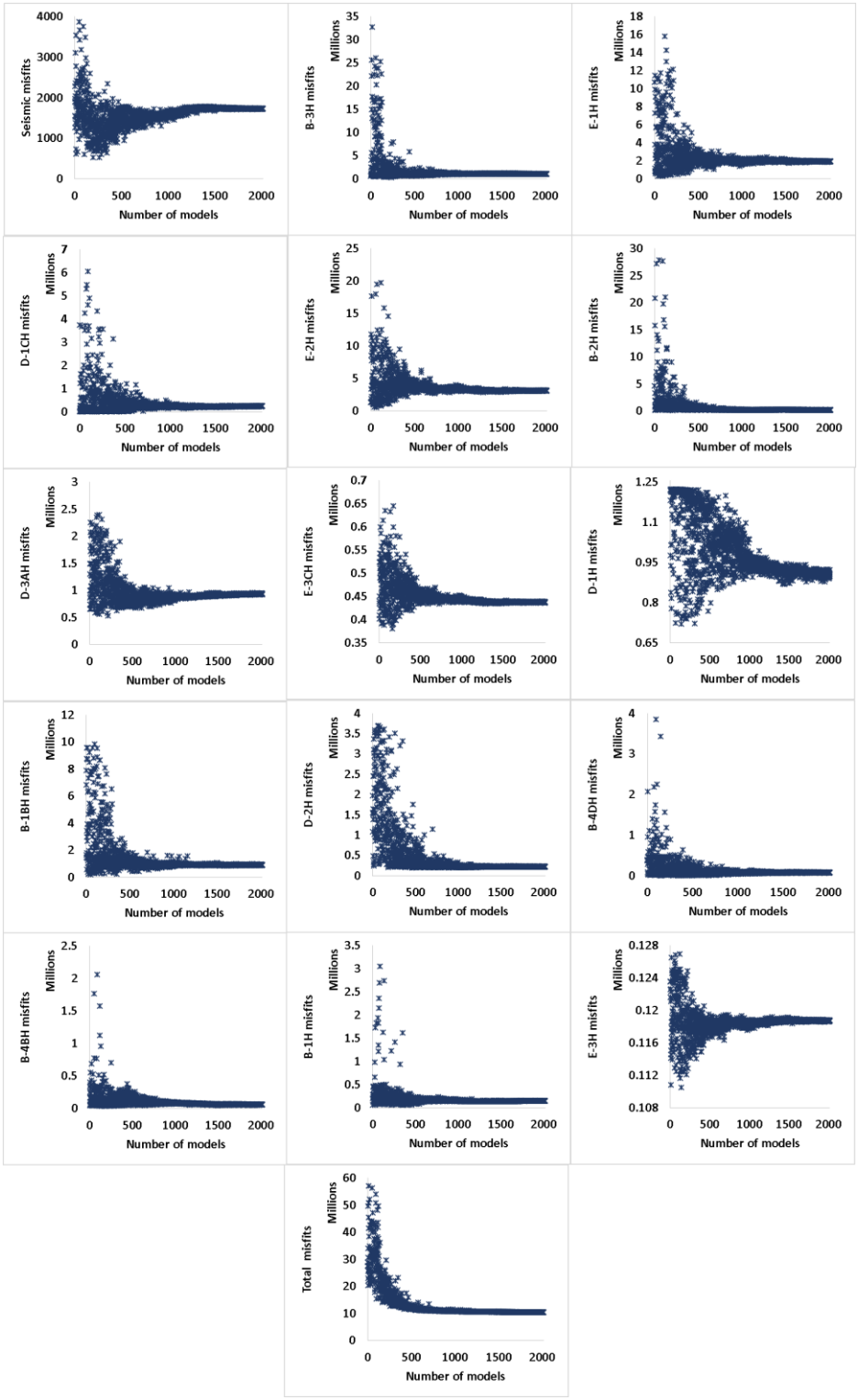

Figure 8.16 The evolution of individual components of misfits in single sum-objective history matching using both seismic and production data.

The objectives are conflicting and although we observed progressive reduction in the total misfits, some individual misfits were not getting better.

8.5.2 Dual multi-objective history matching

Next, we look at the results of optimisation for the DOPS project in which the production and seismic data are treated as separate functions (two separate misfits) and handled in multi-objective fashion. The evolution of the fronts is shown in Figure 8.17

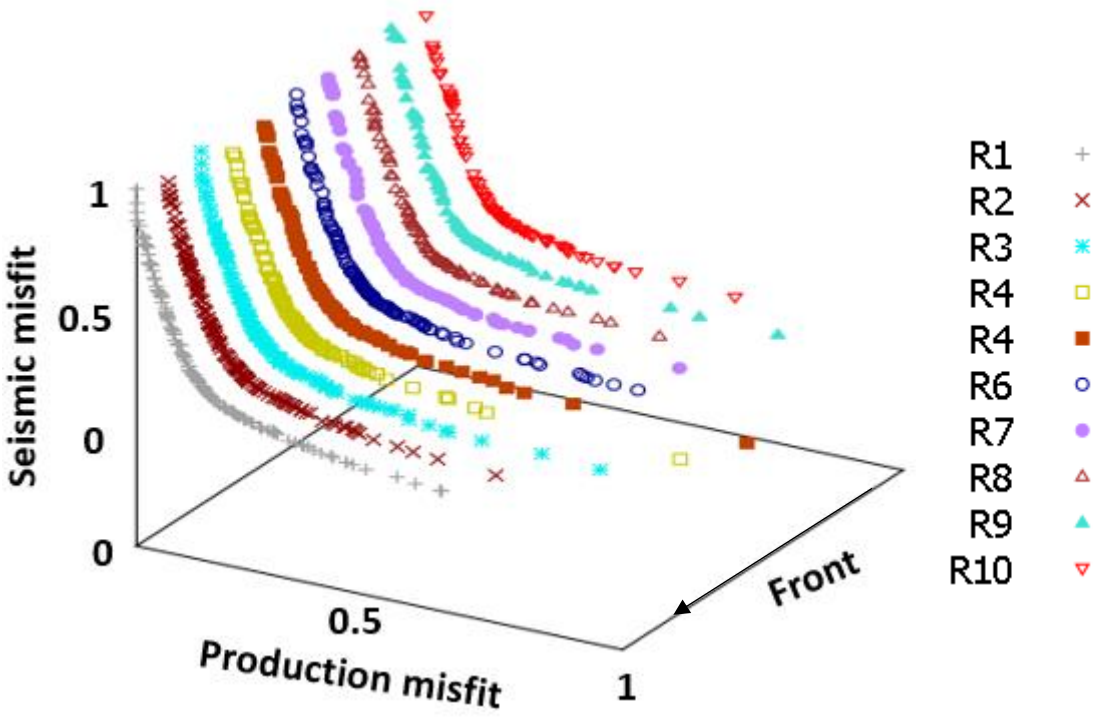

Figure 8.17 The evolution of fronts in multi-objective history matching of seismic and production data (DOPS approach). The misfit values are normalised.

In the plots of the evolution of individual misfits (Figure 8.18), we observe that the optimisation is no longer skewed against the seismic data. This is an improvement over the single-objective approach. However, some individual production misfits are still reduced at the expense of the others. The optimisation is still skewed against the reduction of misfits in water rates of wells E-3H, E-3CH and D-1H. The trends of the individual and total misfits also show better exploration of the objective space in DOPS than in the single objective case. The model parameters evolution plots in Figure 8.19 suggest solutions that are in some cases different from those suggested by either the SOS, SOP or SOPS approach. The DOPS approach also resulted in better exploration of the model space in search of parameters combinations that give optimal trade-off between the seismic and production data.

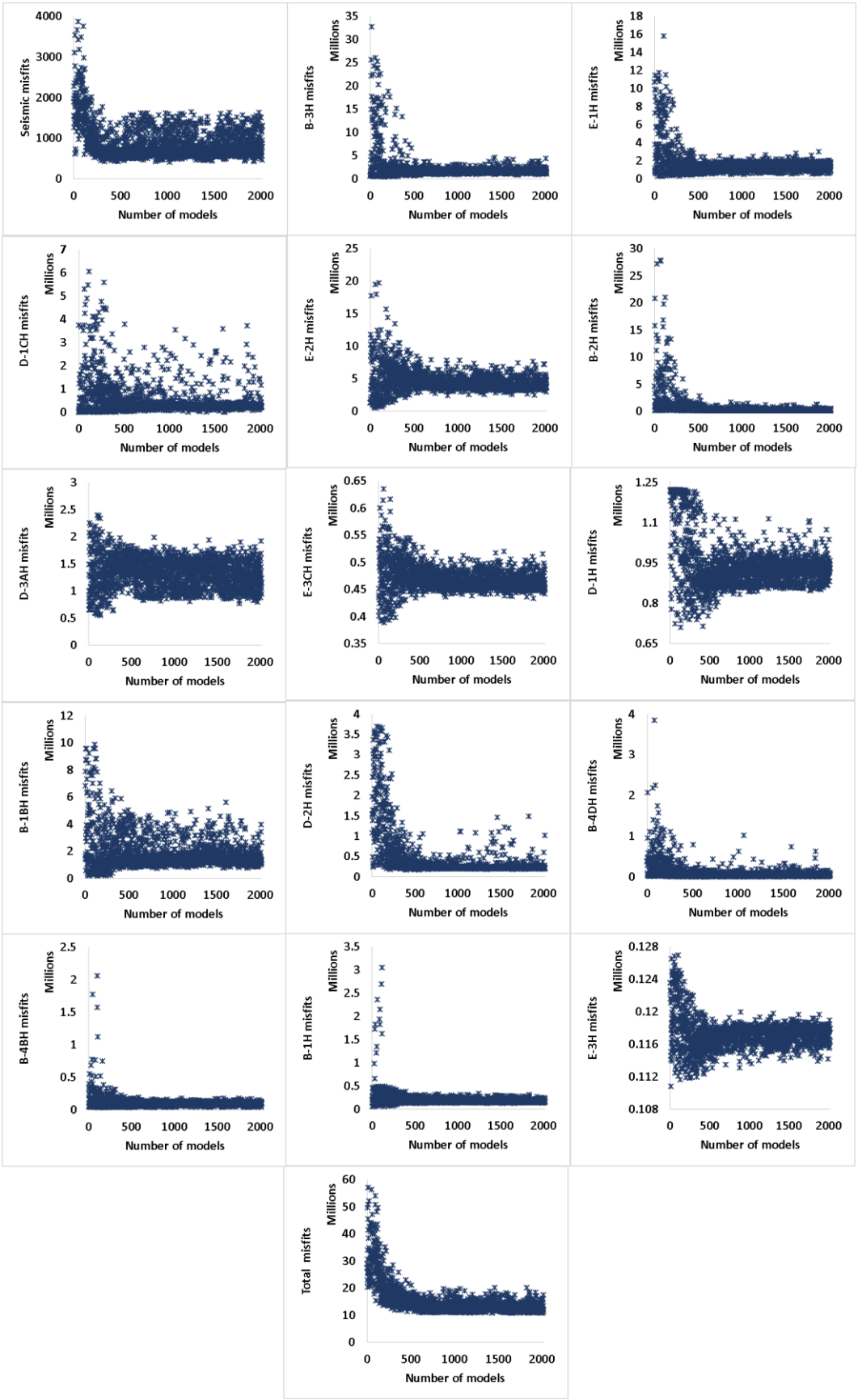

Figure 8.18 The evolution of individual components of misfits in multi-objective history matching using both seismic and production data (DOPS approach).

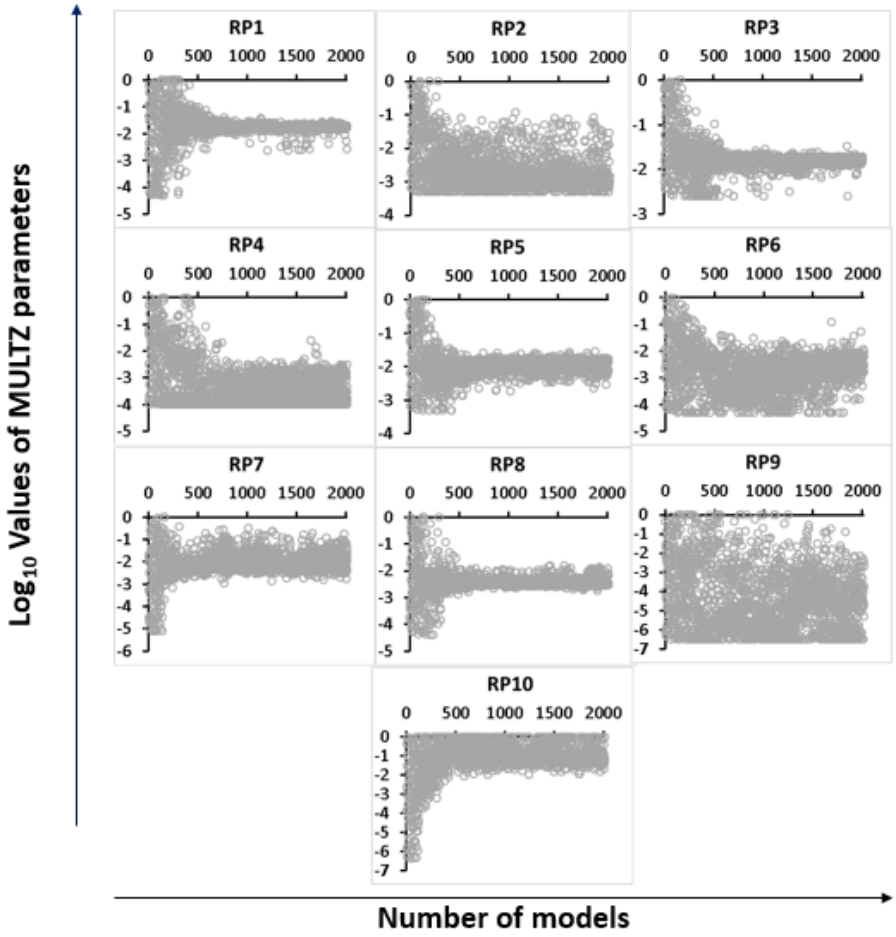

Figure 8.19 The evolution of model parameters in DOPS using seismic and production data as separate functions

8.5.2 Many objectives history matching

We have seen that the DOPS approach removed the bias against the match of the seismic data but failed to remove the bias against the match of the water rates at some wells. We want to improve on the match of the individual well water rates by handling the well misfits as separate functions. We can do this for all the 14 wells but we previously mentioned that by grouping the wells the number of objectives is reduced and the optimisation becomes more effective.

We used the well groupings in Table 8.3 of section 8.4 to identify the separate objectives. The misfits of the six well groups (GRP1 to GRP6) together with the seismic misfits give a total of seven objectives. We used those for history matching using the MOPS approach. The evolution of fronts in the group objective pairs show the trade-off in misfits' reduction for the various pairs (Figure 8.20). The downward trend of the ranks from right to left indicates the reduction in the misfits of the objective pairs. As were the cases in Chapter 7, the parameter evolution plots (Figure 8.21) show more exploration of the model space than in the case of DOPS.

The evolution of misfits in Figure 8.22 shows that the misfits of all the individual objective groups were reduced progressively and the bias noticed in SOPS and DOPS may have been eliminated.

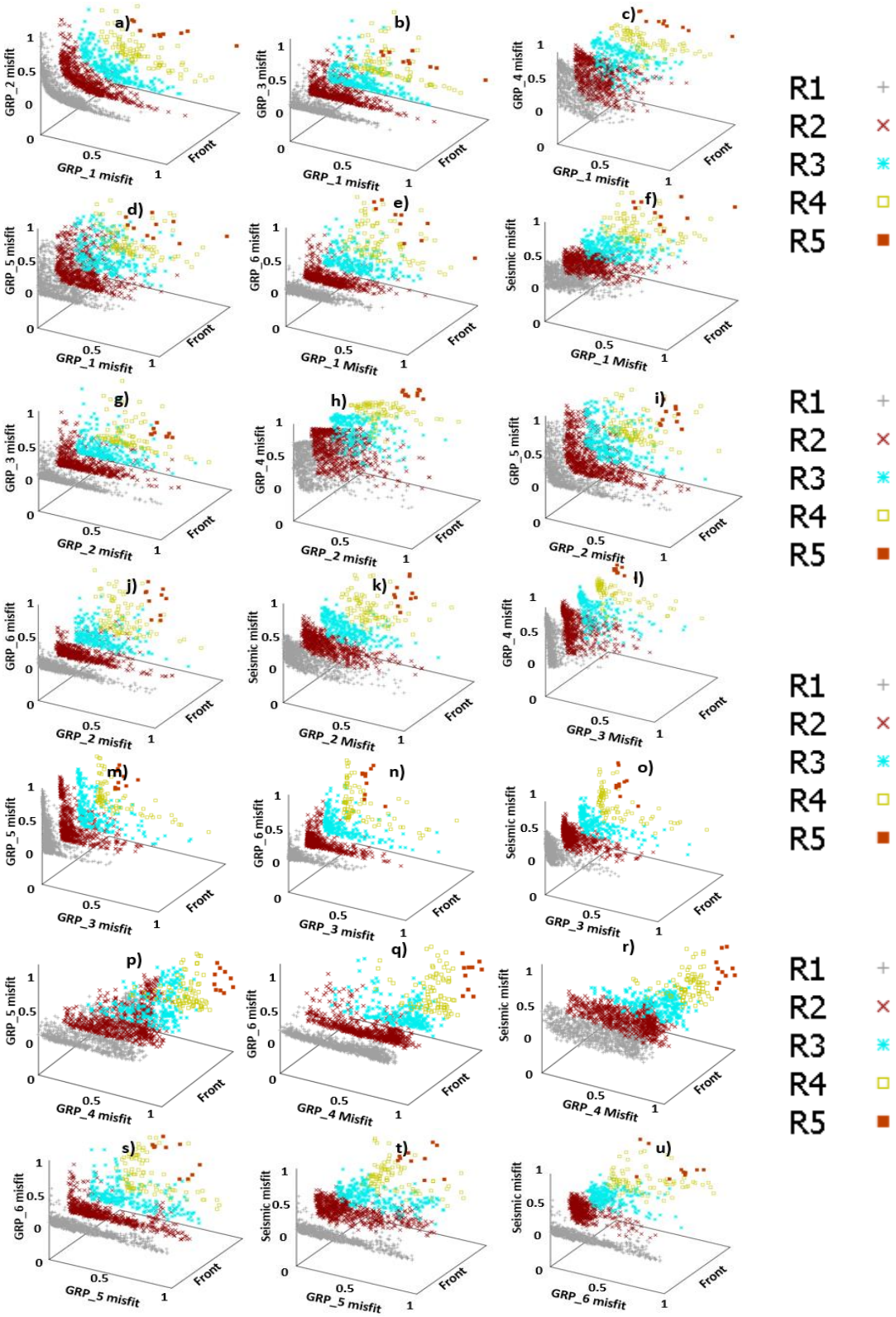

Figure 8.20 The evolution of fronts in multi-objective history matching of seismic and production data (MOPS approach). The misfit values are normalised.

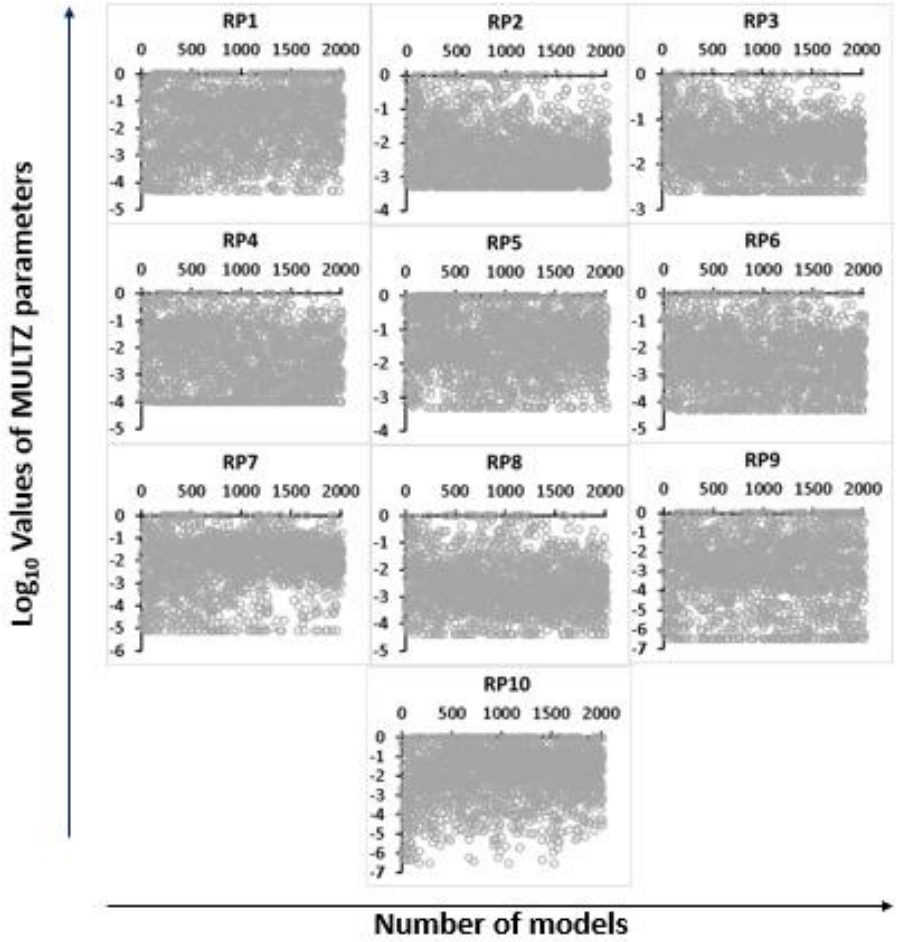

Figure 8.21 The evolution of model parameters in MOPS using 7 objective groups as separate functions

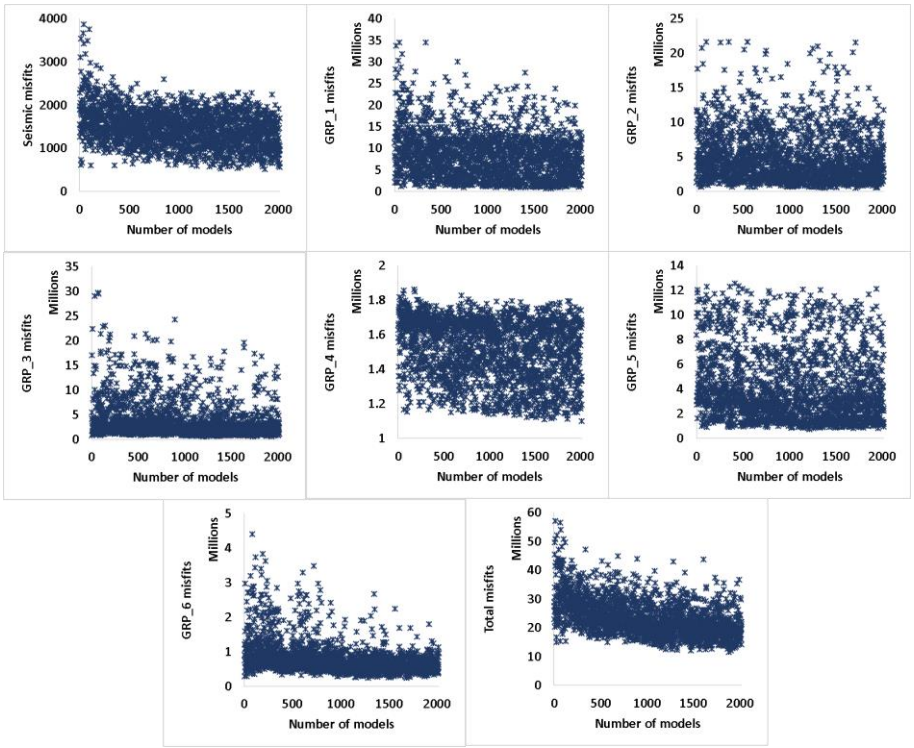

Figure 8.22 The evolution of objective group misfits in multi-objective history matching using both seismic and production data (MOPS approach).

The MOPS approach explores the model space much better in search of trade off solutions that minimises all the objectives. The many objectives problem has been handled by MOPS removing as much bias as possible. The seismic misfit is reduced as well as the other objective groups of the production misfits.

8.6 Posterior analysis and predictions

In the case of SOPS, we perform posterior analysis on the ensemble of 2016 models using NABayes analysis (discussed in section 5.9 in Chapter 5). The analysis shows that a total of 69 models were visited at least once during the posterior walk. Weights, proportional to the frequency of visits, were assigned to the models. The 20 models shown in Figure 8.23 account for 94% of the total weights. We observed that the parametric make up of these 20 models are all similar, and the variance in their predictions is negligible. With Gaussian statistics, the differences in the P10, P50 and P90 values of the reservoir quantities are also negligible.

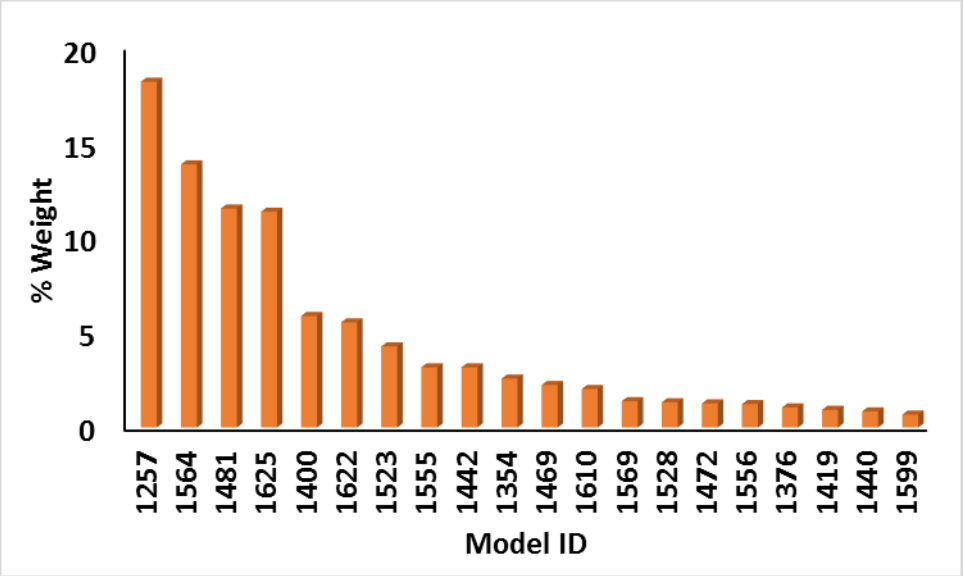

Figure 8.23 Weight of posterior models in Norne Field seismic and production history matching

Within the defined parameters' limits, we are not able to define the uncertainty envelope in predictions using posterior models from the SOPS approach. Figure 8.24 compares the P50 profiles of the predicted water production rates with the observed water production rates.

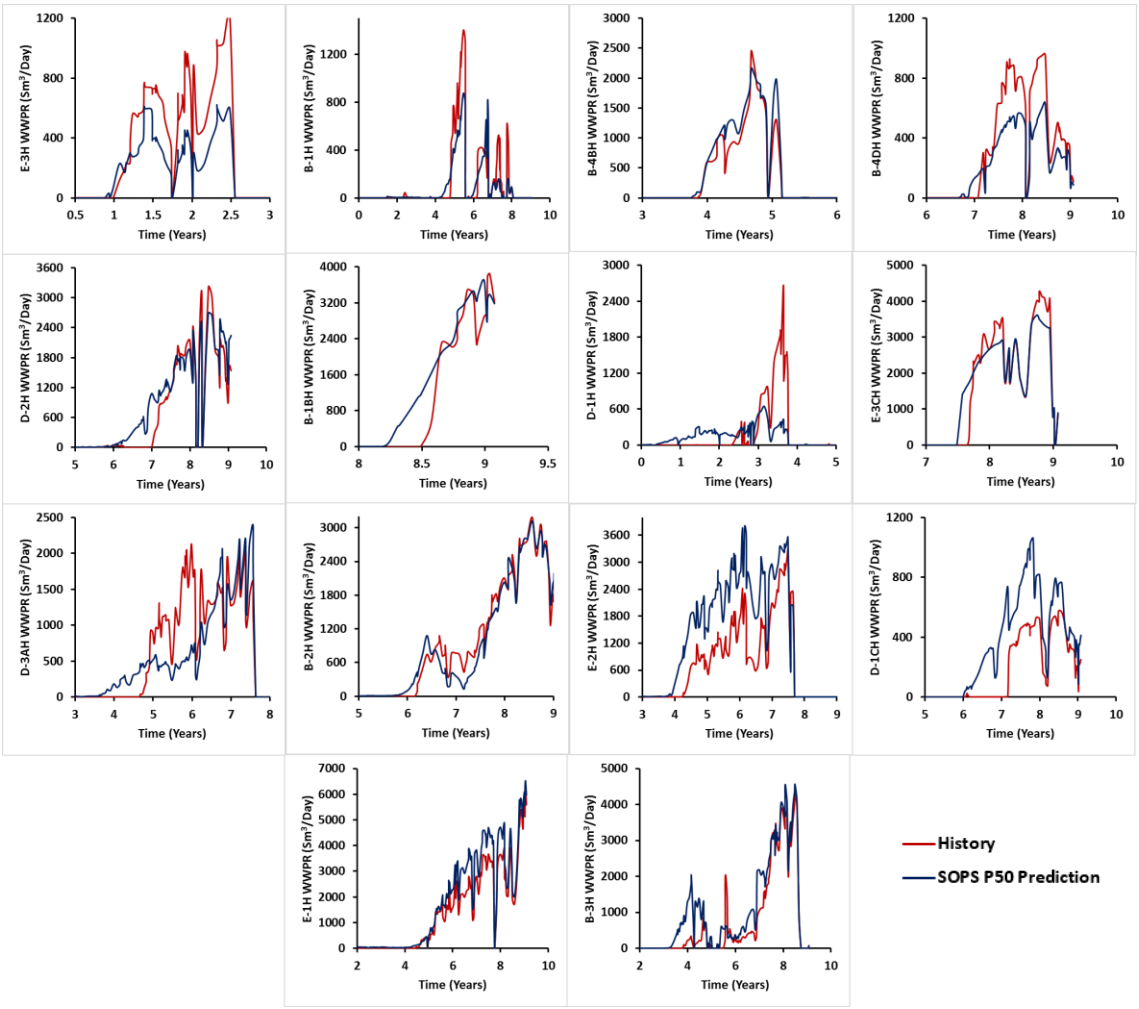

Figure 8.24 P50 water production profiles predicted with seismic history matched posterior models versus history.

On the other hand, we can predict the uncertainty envelopes using the Pareto Front (PF) models generated from MOPS approach. In Figure 8.25, the uncertainty envelopes defined by the predictions of the prior models are presented for comparison with the uncertainty in the predictions of the MOPS PF models in Figure 8.26. The large uncertainties in the predictions of the prior models have been reduced through history matching using the MOPS approach.

Also, the predictions of the field quantities including Field Gas Oil Ratio (FGOR), Field Oil Production Total (FOPT) and the Field Water Production Total (FWPT) are made in Figure 8.27 using the 30 models selected at random from the 1st Rank models.

Comparing the profiles defined by the predictions of the PF models to the historical/measured quantities (the red lines) in Figures 8.26 and 8.27, we see that the MOPS approach was able to generate models which define the correct uncertainty envelopes in most cases. This is consistent with the observations made in Chapter 7 where the use of PF models for predictions and uncertainty quantification was demonstrated.

The spread in the predictions of the models differ from well to well depending on the extent to which the history data constrains the regional model parameters.

Just as in the case of the synthetic reservoir handled under section 7.5.2 in Chapter 7, the history matching of Norne Field presented some difficulties due to the conflicting objective functions. In many cases, a better match in the water rate of one well resulted in worse match in another. The MOPS approach could resolve the conflict by searching the model space more widely, and yielded pareto model solutions as trade-off between the various objectives through the non-domination ranking and screening of fronts described in Chapter 7. The method of well grouping and reparameterization adopted also helped the multi-objective algorithm in finding better data fitting models in the highly compartmentalised Norne Field. The SOPS approach on the other hand was easily trapped in some local minina giving a set of similar models with less satisfactory fit to the history data. With NABayes analysis, the SOPS models could not define the uncertainty in the Norne Field predictions.

Figure 8.28 shows some of the 2001-2006 seismic difference maps predicted with the PF models, and Figure 8.29 shows the mean predictions of the models. The maps are AI averaged over layers 5-22 of Norne Field simulation model. The predicted seiasmic matches the observed seismic closely. Therefore, we have obtained solution models which gives prediction that fits the seismic data and give reasonable uncertainty estimates of reservoir quatities. The spread in the predictions of the AI about the mean is represented by the uncertainty maps in Figure 8.30. The uncertainty maps were estimated as standard deviations using the method predicted spatial quantities described under section 5.10 in Chapter 5. The estimated uncertainty margin is low (maximum variance, $\sigma^2 = 0.0025$) because the predictions of most of the PF models honour the observed seismic data. The maximum spread occurred mostly around the injector areas (especially F-2H, and C-4AH) where the complex effects of pressure, gas exsolution and gas dissolution make the interpretation of seismic data very difficult.

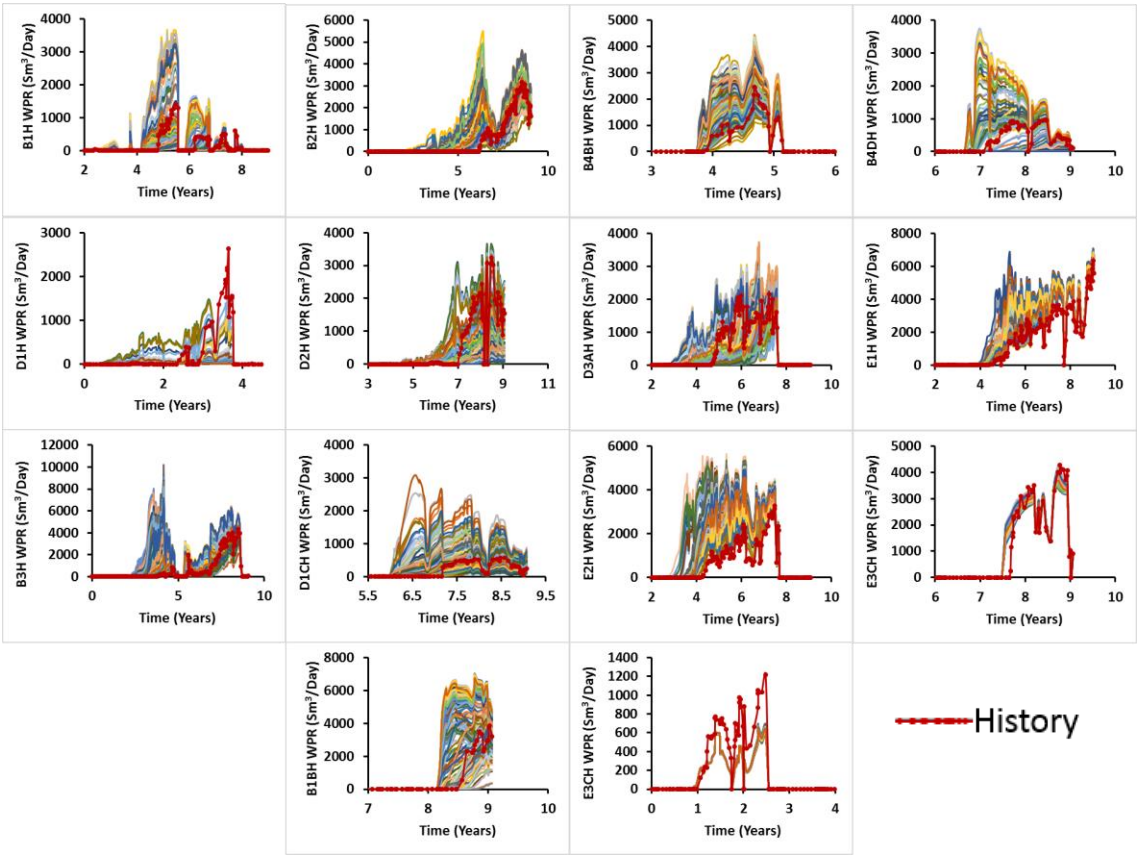

Figure 8.25 Predictions of well water production rates using the prior models.

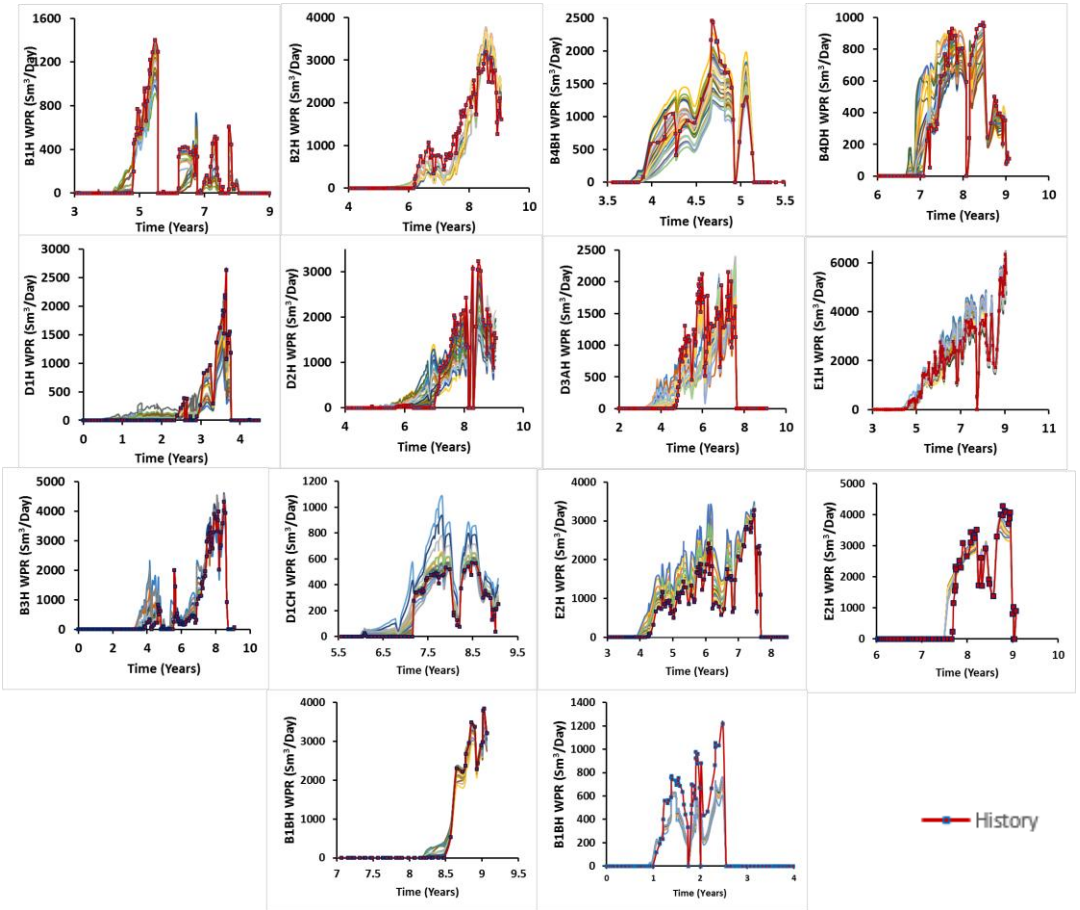

Figure 8.26 Uncertainty envelopes in predicted water rates using Pareto Front models from MOPS.

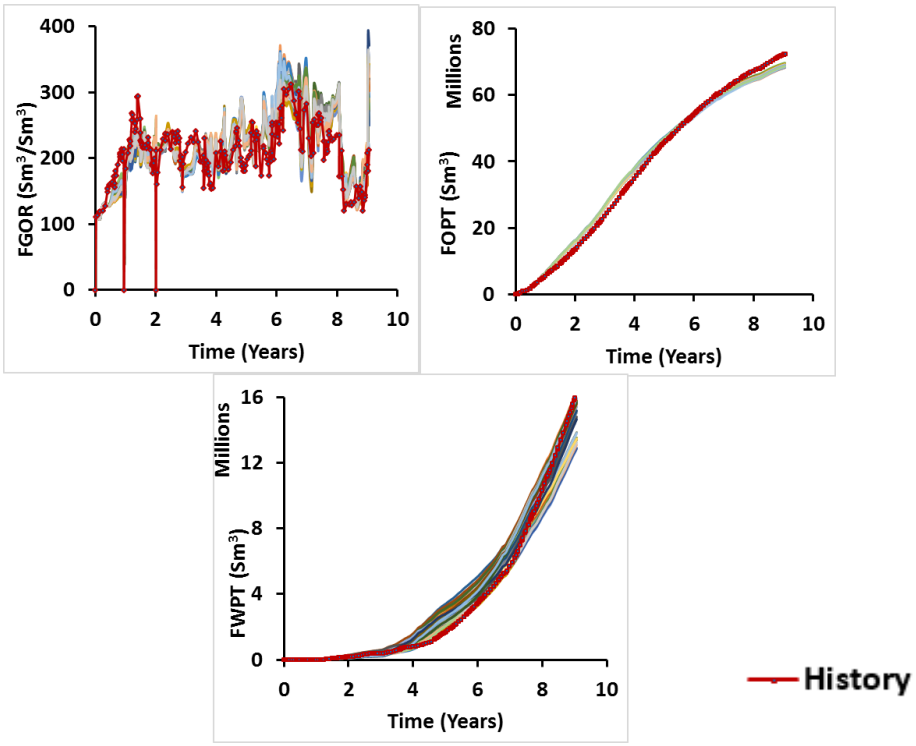

Figure 8.27 Predictions of Norne Field quantities using Pareto Front models from MOPS.

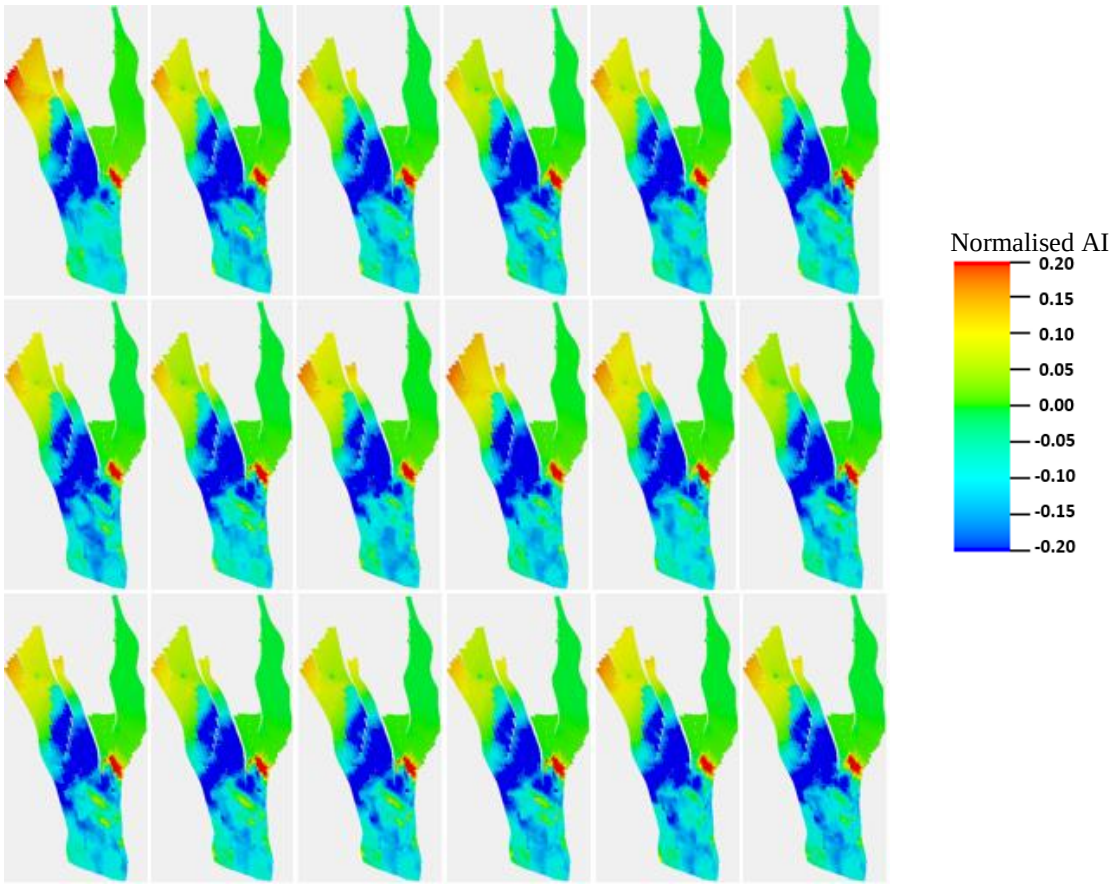

Figure 8.28 Predictions of Year 2001-2006 Norne Field AI maps using Pareto Front models from MOPS. The AI maps are normalised.

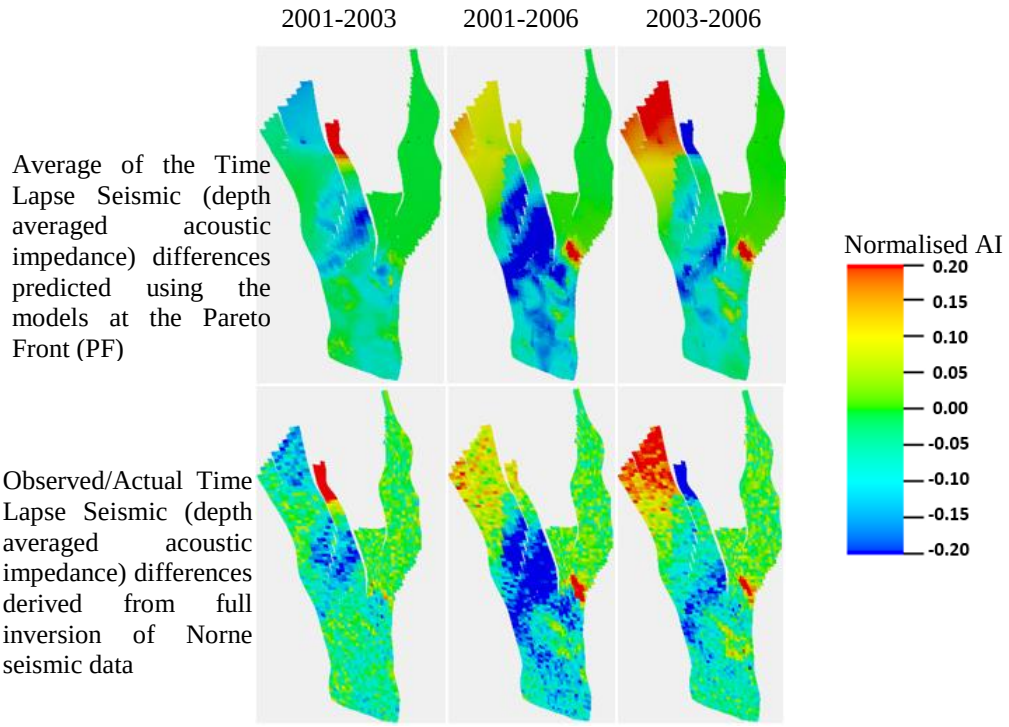

Figure 8.29 Comparing the averaged PF models predictions of AI with the the observed AI

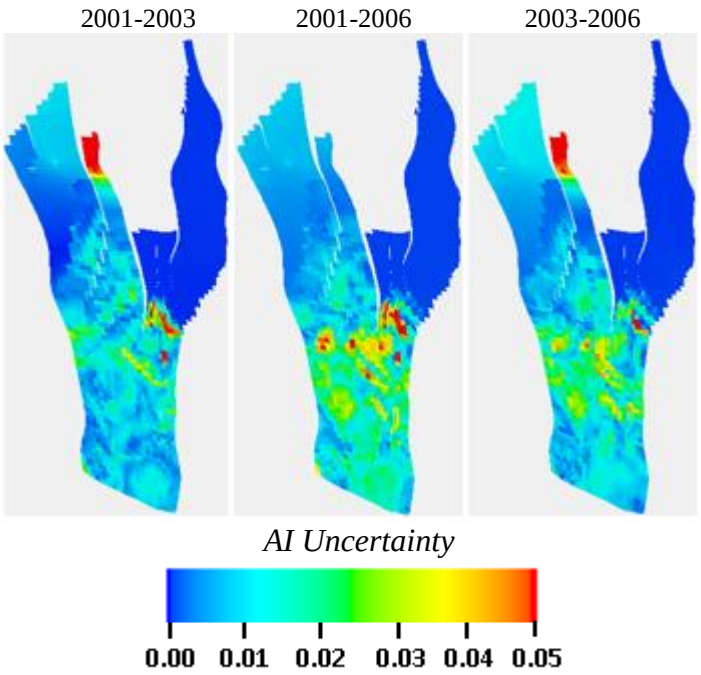

Figure 8.30 The uncertainty in the AI maps predicted using the PF models.

8.7 Summary

The difficult problem of history matching the Norne Field was handled using multi-objective optimisation approach. The Norne Field reservoir model was updated to match the flooding pattern observed in the reservoir through several measurements including the time lapse seismic data and water rates measured in 14 producing wells. Both the seismic data (in the form of three AI differences) and the water rate measurements were integrated in the automatic history matching loop to constrain the model realisations generated.

Several of the optimisations methods studied in the previous chapter were adopted in the automatic update of the Norne Field reservoir model, including: single objective history matching using only seismic data, single objective history matching using only production data, single sum-objective history matching using both seismic data and production data, Pareto-based multi-objective history matching with production and seismic data as two separate functions, Pareto-based history matching using the seismic data and 6 groups of well objectives handled in multi-objective fashion.

Each of the techniques could reduce the total misfits between the predicted and historical quantities. However, we found that some objectives are reduced at the expense of the others. The seismic and the well objectives were shown to be conflicting and some strong correlations between the wells made history matching of Norne Field reservoir very challenging.

It was demonstrated that the best approach to handling the conflicting objectives was by treating the wells as separate objectives and handling them in multi-objectiv fashion. The 14 wells were placed into 6 groups considering their correlations and the agreements in their respective intearctions. The Norne Field MULTZ maps were also reparameterised. The problem was then reduced to to 7 objectives and 10 model parameters handled with the MOPS approach to generate pareto optimal models. The pareto models were then used in defining the uncertainty envelopes for the Norne Field model predictions.

Chapter 9–Summary, Conclusions and Recommendations

9.1 Summary

This thesis adopted several approaches for integrating seismic and production data in the assisted history matching workflow to update the simulation model. Seismic and production data are data of different sources and may often carry conflicting information on reservoir model properties. Both data carry useful information and the process of reservoir characterisation should consider both. History matching requires that comparison is made of observed and predicted data. In automatic history matching method, predictions are quantitatively compared to observed seismic and production data in such a way to allow the reservoir model to be updated objectively. Without proper calibration, seismic and production data may not represent the same physical properties that are modelled. The process of integration may favour the assimilation of one data more than the other. The overall aim of the thesis was to identify suitable metrics for comparing the predicted and observed quantities especially given conflicting data in history matching.

In finding the process for integrating both data in the most objective way, this thesis examined alternative approaches to history matching. The study focused on using multiple-objective methods in history matching to identify those that are most appropriate for the data available. A set of algorithms called Dynamic Screening of Fronts in Multi-Objective Optimisation (DSFMO) was set up to work with the neighbourhood algorithm (NA) and the genetic algorithm (GA) in a dominance based optimisation method. These enabled the investigation of different options for making the choice of models during the selection process as optimisation progresses. DSFMO is a novel approach in which the concept of oversampling and undersampling are combined with non-domination sorting of models for the optimisation of problems formulated with many objectives The algorithms were tested in some synthetic benchmark cases and were found to be robust in handling several problems of conflicting objectives. Investigation of the options also revealed the approach that is most suitable for problems of many model parameters and many conflicting objectives. This option was implemented in resolving the very challenging problem of multi-objective optimisation using production and seismic data (MOPS) of the highly compartmentalised Statoil Norne Field. MOPS with the DSFMO leads to an improved set of pareto reservoir models which can be used for better

uncertainty quantification and more effective reservoir management The recommended approach for the integration of seismic and production data is shown in Figure 9.1.

.

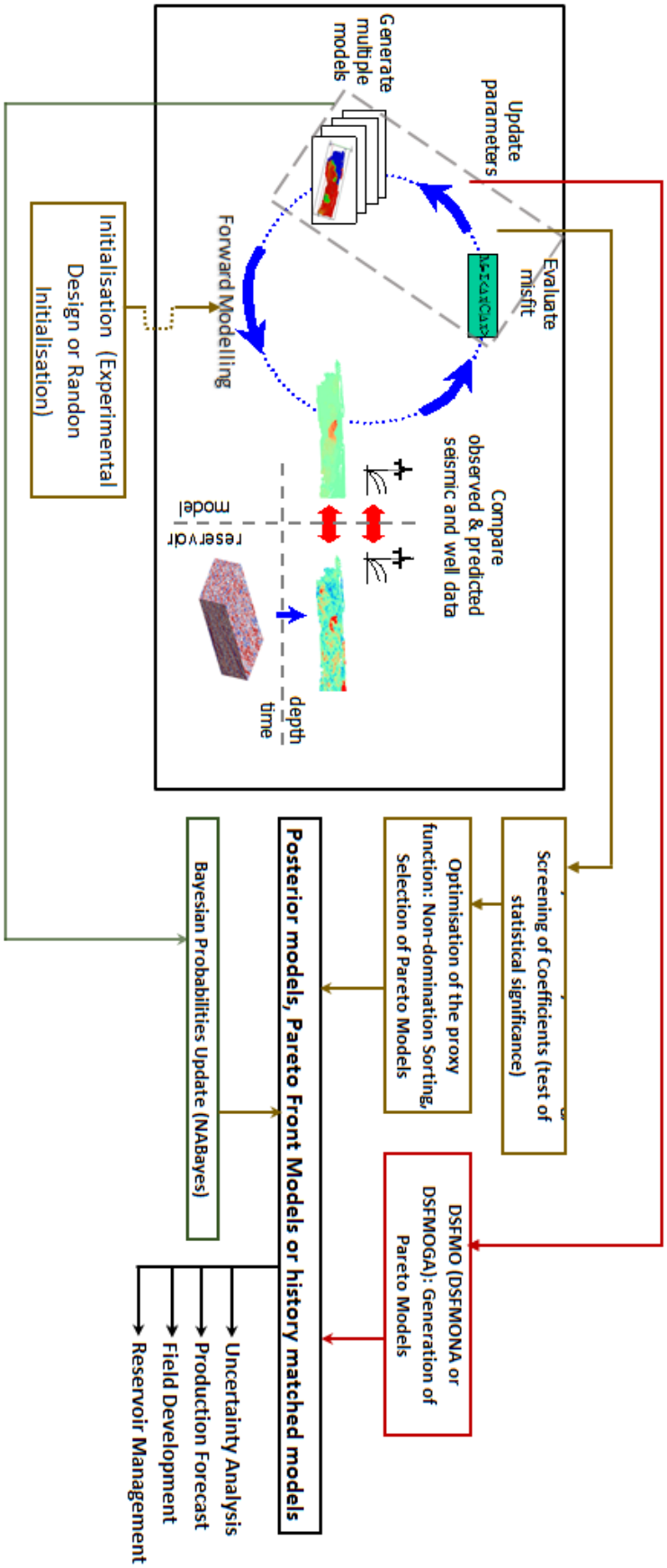

Figure 9.1 The Recommended Approach

In other related works in this thesis, the use of proxy models to speed up history matching was investigated and the recommended approach is also shown in Figure 9.1 above. The strengths and weaknesses of proxy method were investigated. Proxy model was also shown to be effective in model appraisal in Bayesian viewpoint. The use of proxy was tested in three different optimisation methods including neighbourhood algorithm, genetic algorithm and particle swarm optimisation. The use of different experimental design methods was investigated and ways of improving the quality of proxy models for history matching were tested in a synthetic reservoir model for which the true solution is known.

9.2 Conclusions

The dominace-based NA and GA method with the options for dynamic screening of fronts in multi-objective optimisation has been shown to be successful in resolving history matching problems in which there are many conflicting objectives. Proxy methods have also been shown to be valid in history matching and appraisal applications. The following conclusions are drawn from applying the methods developed in this thesis on synthetic equations, synthetic reservoir models and Norne Field.

History matching with proxy models

With the use of proxy models derived from different calibration data based on experimental design and optimisation on a synthetic reservoir simulation model for which we know the solution, we found the following:

i. Calibration of proxy models with design points derived from conventional experiment design (ED) is insufficient to give a high-quality surrogate of the reservoir response
ii. Addition of some converging models from actual history matching ED models improved the quality of quadratic proxy for better representation of the reservoir response
iii. Proxies derived from space filling ED methods such as Latin Hypercube Design and Sobol-Antonov-Saleev (SAS) yield better predictive models than other conventional design methods.

iv. The regression coefficients in the quadratic proxy function are related to the convergence of models, and can therefore be a measure of convergence during

Ensemble Appraisal and Probabilistic Forecasting

By using proxy models to approximate the posterior probability distribution of the ensemble of models generated during the optimisation of a synthetic reservoir model, we make the following conclusions on proxy-assisted appraisal and forecasting of reservoir performance:

i. Proxy models has shown to be a fast and reliable alternative to the existing approaches for ensemble appraisal within Bayesian framework.
ii. The results from proxy approach were comparable to those obtained using NABayes
iii. It was possible to include all models in the ensemble in obtaining the Bayesian indicators of model resolution and trade-off in the various model parameters.
iv. Predictions and uncertainty quantifications using the posterior models gave similar results irrespective of the optimisation algorithm used to generate the input ensemble:
v. The level of confidence that should be placed on the models can be asseses through the appraisal approach for more realistic and accurate predictions
vi. Unbiased sampling method gives a systematic probabilistic forecasting that can be relied on for reservoir development strategies and planning.

Options for multi-objective integration of seismic and production data

A suite of algorithms for dynamic screening of fronts in multi-objective (DSFMO) history matching was tested using several analytical functions, synthetic reservoir models and the real Norne Field. The findings are highlighted as follows:

i. DSFMO is good at finding good data fitting models that satisfy all the individual objectives and provides a more diverse global ensemble of history matched models than single-objective methods
ii. DSFMO was demonstrated to have other benefits in reducing the chance of convergence into a false optimum point, improving the chance of finding global best fitting models, improving the diversity in the history matched models, and improving the quality of forecasts and uncertainty quantification.
iii. The multi-objective method showed superiority to single-objective method in handling the conflicting objectives in the very challenging Norne Field history matching.

iv. With optimal pareto models representing the trade off among 7 objectives groups in Norne Field history matching, it was possible to define the correct uncertainty envelope in the reservoir model predictions.

The outcome in using DSFMO approach is several solutions that match both seismic and production data. This will be used for development planning scenarios for P50- best estimate and for uncertainty estimate in the form of P90, P50 and P10 reserve ranges. The value of this work therefore is in producing models that can be used for planning and reserves/resources estimates.

9.4 Recommendations for Future work

Sensitivity studies on the Norne Field reservoir model reveals that local effects of some parameters on the responses of the reservoir. These effects were considered in grouping the wells for more effective multi-objective optimisation of the conflicting objectives. A more effective approach would be a decoupling parameterisation approach presented in Sedighi and Stephen (2010). This requires a more detailed knowledge of the localization effects so that appropriate spatial relationships between the parameters and the reservoir responses can be developed and utilised. With this approach the local effects of parameters on the well and time lapse responses can enable the grouping of the various objectives such that each objective group will be associated with a sub-volume in the model space. This may be a potential parameterisation scheme to further improve the effectiveness of the multi-objective optimisation and should be investigated in future studies.

In addition, the problem of history matching the Norne Field was handled in multi-objective fashion in a parameterising scheme which considered only the vertical transmissibility multipliers as the barriers to flow. A more complete study should include the fault transmissibility multipliers also.

In all parts of the work where seismic was used as observed data, the data was integrated into the workflow as depth-averaged data. Future work may consider comparing the observed and seismic data on cell by cell bases so that the seismic misfit becomes the sum of all the individual cell misfits.

In the part of the thesis where proxy model was used, quadratic polynomial was considered sufficient to represent the reservoir response. Further studies may consider comparing this approach to other methods including the free-form mathematical models,

multivariate kriging model and artificial neural network to determine the proxy approach that best represents the reservoir response. Also, the proxy-methods should be tested in a problem of higher model dimensions. One of the findings of this work is that misfits are correlated with the regression coefficients. It is therefore possible to develop a worklow in which the regression coefficients are used to determine the level of convergence and specify the stopping criteria.

References

Aanonsen, S. I., Aavatsmark, I., Barkve, T., Cominelli, A., Gonard, R., Gosselin, O., Kolasinski, M., Reme, H. (2003). Effect of scale dependent data correlations in an integrated history matching loop combining production data and 4D seismic data. Paper presented at the SPE Reservoir Simulation Symposium. Society of Petroleum Engineers.

Aanonsen, S. I., Eide, A. L., Holden, L., & Aasen, J. O. (1995). Optimizing reservoir performance under uncertainty with application to well location. Paper presented at the SPE Annual Technical Conference and Exhibition. Society of Petroleum Engineers.

Aanonsen, S. I., Nævdal, G., Oliver, D. S., Reynolds, A. C., & Vallès, B. (2009). The ensemble Kalman filter in reservoir engineering--a review. SPE Journal, 14(03), 393-412.

Abdollahzadeh, A., Reynolds, A., Christie, M., Corne, D. W., Williams, G. J., & Davies, B. J. (2013). Estimation of distribution algorithms applied to history matching. SPE Journal, 18(03), 508-517.

Adeyanju, O. A., & Oyekunle, L. O. (2015, August). Optimizationof Wax Deposition in Sub-Cooled Pipeline Using Response Surface Methodology. In SPE Nigeria Annual International Conference and Exhibition. Society of Petroleum Engineers.

Agarwal, B., & Blunt, M. (2003). A streamline-based method for assisted history matching applied to an Arabian Gulf field. Paper presented at the SPE Annual Technical Conference and Exhibition. Society of Petroleum Engineers.

Ahmadloo, F., Asghari, K., & Araghi, M. M. (2009). Heavy Oil Viscosity Prediction Using Surface Response Methodology. Paper presented at the Canadian International Petroleum Conference.

Ajibola, J., Orodu, O., & Onyeukwu, C. (2013). Sidetrack/Recompletion Time Evaluation by Proxy Model. Paper presented at the SPE Nigeria Annual International Conference and Exhibition. Society of Petroleum Engineers.

Akshay, S. (2003). Case studies of uncertainty analysis in the seismic to reservoir simulation workflow. Paper presented at the SPE Annual Technical Conference and Exhibition. Society of Petroleum Engineers.

Alessio, L. D., Bourdon, L. M., & Coca, S. (2005). Experimental design as a framework for multiple realisation history matching: F6 further development studies. Paper presented at the SPE Asia Pacific Oil and Gas Conference and Exhibition. Society of Petroleum Engineers.

Al-Kasim, F. T., Synøve, T., Jakobsen, K. A., Tang, Y., & Jalali, Y. (2002). Remotely controlled in-situ gas lift on the Norne subsea field. Paper presented at the SPE Annual technical conference and exhibition. Society of Petroleum Engineers.

Al-Najem, A., Siddiqui, S., Soliman, M., & Yuen, B. (2012). Streamline simulation technology: evolution and recent trends. Paper presented at the SPE Saudi Arabia Section Technical Symposium and Exhibition. Society of Petroleum Engineers.

Amudo, C., Graf, T., Harris, N. R., Dandekar, R., Amor, F. B., & May, R. S. (2008, December). Experimental design and response surface models as a basis for stochastic

history match-a Niger delta experience. In IPTC 2008: International Petroleum Technology Conference.

Antonov, I. A., & Saleev, V. M. (1979). An economic method of computing LP _τ-sequences. Zhurnal Vychislitel'noi Matematiki i Matematicheskoi Fiziki, 19(1), 243-245.

Archer, R. A., Zakeri, G., & Vaudrey, T. (2005). Splines as an Optimization Tool in Petroleum Engineering. Paper presented at the SPE Annual Technical Conference and Exhibition. Society of Petroleum Engineers.

Arenas, E., van Kruijsdijk, C., & Oldenziel, T. (2001). Semi-automatic history matching using the pilot point method including time-lapse seismic data. Paper presented at the SPE Annual Technical Conference and Exhibition. Society of Petroleum Engineers.

Arwini, S., & Stephen, K. D. (2010). A New Method to Improve Convergence Rates with Seismic History Matching. Paper presented at the SPE EUROPEC/EAGE Annual Conference and Exhibition. Society of Petroleum Engineers.

Arwini, S. G., & Stephen, K. D. (2011). Combining Experimental Design with Proxy Derived Sensitivities to Improve Convergence Rates in Seismic History Matching. Paper presented at the SPE EUROPEC/EAGE Annual Conference and Exhibition. Society of Petroleum Engineers.

Asafuddoula, M., Singh, H. K., & Ray, T. (2017). An Enhanced Decomposition-Based Evolutionary Algorithm With Adaptive Reference Vectors. IEEE transactions on cybernetics.

Atherton, R. W., Schainker, R. B., & Ducot, E. R. (1975). On the statistical sensitivity analysis of models for chemical kinetics. AIChE Journal, 21(3), 441-448.

Aulia, A., Jeong, D., Saaid, I. M., Shuker, M. T., & El-Khatib, N. A. (2017, November). A New History Matching Sensitivity Analysis Framework with Random Forests and Plackett-Burman Design. In SPE Symposium: Production Enhancement and Cost Optimisation. Society of Petroleum Engineers.

Badru, O., & Kabir, C. (2003). Well placement optimization in field development. Paper presented at the SPE Annual Technical Conference and Exhibition. Society of Petroleum Engineers.

Baker, R. (2001). Streamline technology: reservoir history matching and forecasting= its success, limitations, and future. Journal of Canadian Petroleum Technology, 40(04).

Batzle, M., & Wang, Z. (1992). Seismic properties of pore fluids. Geophysics, 57(11), 1396-1408.

Bellman, R. E. (1957). Dynamic programming. Princeton University Press. Viewed on October 7th, 2018 in https://en.wikipedia.org/wiki/Curse_of_dimensionality

Bevillon, D., & Mohagerani, S. (2015). a Miscible EOR Project in a Mature, Offshore, Carbonate Middle East Reservoir–Uncertainty analysis With Proxy Models Based on Experimental Design of Reservoir Simulations. Paper presented at the SPE Reservoir Characterisation and Simulation Conference and Exhibition. Society of Petroleum Engineers.

Biot, M. A. (1956). Theory of propagation of elastic waves in a fluid-saturated porous solid. II. Higher frequency range. The Journal of the acoustical Society of america, 28(2), 179-191.

Bissell, R. (1994). Calculating optimal parameters for history matching. Paper presented at the ECMOR IV-4th European Conference on the Mathematics of Oil Recovery.

Bissell, R., Dubrule, O., Lamy, P., Swaby, P., & Lepine, O. (1997). Combining geostatistical modelling with gradient information for history matching: The pilot point method. Paper presented at the SPE Annual Technical Conference and Exhibition. Society of Petroleum Engineers.

Blonk, B., Calvert, R., Koster, J., & van der Zee, G. (1998). Assessing the Feasibility of a 4D Seismic Reservoir Monitoring Project. Paper presented at the European Petroleum Conference. Society of Petroleum Engineers.

Bogatkov, D. S., & Babadagli, T. (2009). Integrated modeling of the fractured carbonate Midale field and sensitivity analysis through experimental design. SPE reservoir evaluation & engineering, 12(06), 951-962.

Bonet-Cunha, L., Oliver, D. S., Redner, R., & Reynolds, A. (1996). A hybrid Markov chain Monte Carlo method for generating permeability fields conditioned to multiwell pressure data and prior information. Paper presented at the SPE Annual Technical Conference and Exhibition. Society of Petroleum Engineers.

Box, E., George, H., Stuart, J., & Hunter William, G. (2005). Statistics for Experiments. New Jersey: John Willey and Sons. In: Inc.

Box, G. E. P., & Wilson, K. B. (1951). On the Experimental Attainment of Optimum Conditions. Journal of the Royal Statistical Society. Series B (Methodological), 13(1), 1-45.

Box, G. E., & Behnken, D. W. (1960). Some new three level designs for the study of quantitative variables. Technometrics, 2(4), 455-475.

Brefort, B. & Pelce, V. (1990). Inverse modelling for incompressible flow. Applications to gas reservoirs. Paper presented at the 2nd European Conference on the Mathematics of Oil Recovery.

Buland, A., & Omre, H. (2003). Bayesian linearized AVO inversion. Geophysics, 68(1), 185-198.

Cai, X., Mei, Z., & Fan, Z. (2017). A decomposition-based many-objective evolutionary algorithm with two types of adjustments for direction vectors. IEEE transactions on cybernetics, (99), 1-14.

Calvert, R. (2005). Insights and methods for 4D reservoir monitoring and characterization: Society of Exploration Geophysicists and European Association of Geoscientists and Engineers.

Campana, E. F., Fasano, G., & Pinto, A. (2006). Dynamic system analysis and initial particles position in particle swarm optimization. Paper presented at the IEEE Swarm Intelligence Symposium.

Carlin, B. P. (1994). Tools for Statistical Inference: Methods for the Exploration of Posterior Distributions and Likelihood Functions. Journal of the American Statistical Association, 89(427), 1142-1144.

Castellini, A., Vahedi, A., Singh, U., Sawiris, R. S., & Roach, T. (2008, January). Reconciling History Matching and Assessment of Uncertainty in Production Forecasts: A Study Combining Experimental Design, Proxy Models and Genetic Algorithms. In International Petroleum Technology Conference. International Petroleum Technology Conference.

Castro, S. A., Caers, J., Otterlei, C., Meisingset, H., Hoye, T., Gomel, P., & Zachariassen, E. (2009). Incorporating 4D seismic data into reservoir models while honoring production and geologic data: A case study. The Leading Edge, 28(12), 1498-1505.

Castro, S., Caers, J., & Durlofsky, L. (2006, September). Improved modeling of 4D seismic response using flow-based downscaling of coarse grid saturations. In ECMOR X-10th European Conference on the Mathematics of Oil Recovery.

Chankong, V., & Haimes, Y. Y. (2008). Multiobjective decision making: theory and methodology: Courier Dover Publications.

Chavent, G., Dupuy, M., & Lemmonier, P. (1975). History matching by use of optimal theory. Society of Petroleum Engineers Journal, 15(01), 74-86.

Chen, C., Gao, G., Honorio, J., Gelderblom, P., Jimenez, E., & Jaakkola, T. (2014). Integration of principal-component-analysis and streamline information for the history matching of channelized reservoirs. Paper presented at the SPE Annual Technical Conference and Exhibition. Society of Petroleum Engineers.

Chen, C., Gao, G., Li, R., Cao, R., Chen, T., Vink, J. C., & Gelderblom, P. (2017). Integration of Distributed Gauss-Newton with Randomized Maximum Likelihood Method for Uncertainty Quantification of Reservoir Performance. Paper presented at the SPE Reservoir Simulation Conference. Society of Petroleum Engineers.

Chen, W. H., Gavalas, G. R., Seinfeld, J. H., & Wasserman, M. L. (1974). A new algorithm for automatic history matching. Society of Petroleum Engineers Journal, 14(6), 593-608.

Chen, Y., Oliver, D. S., & Zhang, D. (2009). Data assimilation for nonlinear problems by ensemble Kalman filter with reparameterization. Journal of Petroleum Science and Engineering, 66(1-2), 1-14.

Cheng N. and Osdal B (2008). Updating the Norne Reservoir Model Using 4D Seismic Data. IO Workshop. Paper presented at the IO Workshop, Trondheim.

Cheng, R., Jin, Y., & Narukawa, K. (2015, March). Adaptive reference vector generation for inverse model based evolutionary multiobjective optimization with degenerate and disconnected pareto fronts. In International Conference on Evolutionary Multi-Criterion Optimization (pp. 127-140). Springer, Cham.

Chewaroungroaj, J., Varela, O. J., & Lake, L. W. (2000). An evaluation of procedures to estimate uncertainty in hydrocarbon recovery predictions. Paper presented at the SPE Asia Pacific Conference on Integrated Modelling for Asset Management. Society of Petroleum Engineers.

Christie, M., Eydinov, D., Demyanov, V., Talbot, J., Arnold, D., & Shelkov, V. (2013). Use of multi-objective algorithms in history matching of a real field. Paper presented at the SPE reservoir simulation symposium. Society of Petroleum Engineers.

Christie, M., MacBeth, C., & Subbey, S. (2002). Multiple history-matched models for Teal South. The Leading Edge, 21(3), 286-289.

Chu, C. (1990). Prediction of Steamflood Performance in Heavy Oil Reservoirs Using Correlations Developed by Factorial Design Method. Paper SPE 20020 presented at the SPE California Regional Meeting, Ventura, California, USA, 4–6 April. Ventura, California. Society of Petroleum Engineers.

Clerc, M., & Kennedy, J. (2002). The particle swarm-explosion, stability, and convergence in a multidimensional complex space. IEEE transactions on Evolutionary Computation, 6(1), 58-73.

Coello, C. A. C., Lamont, G. B., & Van Veldhuizen, D. A. (2007). Evolutionary algorithms for solving multi-objective problems (Vol. 5). New York: Springer.

Cooke, D., & Cant, J. (2010). Model-based seismic inversion: Comparing deterministic and probabilistic approaches. CSEG Recorder, 35(4), 29-39.

Corre, B., Thore, P., De Feraudy, V., & Vincent, G. (2000). Integrated uncertainty assessment for project evaluation and risk analysis. Paper presented at the SPE European Petroleum Conference. Society of Petroleum Engineers.

Correia, G. G., & Schiozer, D. J. (2016). Reservoir characterization using electrofacies analysis in the sandstone reservoir of the Norne Field (offshore Norway). Petroleum Geoscience, 2015-056.

Cullick, A. S., Johnson, W. D., & Shi, G. (2006). Improved and more rapid history matching with a nonlinear proxy and global optimization. Paper presented at the SPE Annual Technical Conference and Exhibition. Society of Petroleum Engineers.

Curia, D. (2009). Seismic Inversion Methods. Retrieved from http://davidcuria.blogspot.com/2009/07/seismic-inversion-methods.html

Dadashpour, M., Kleppe, J., & Landro, M. (2007). Porosity and permeability estimation by gradient based history matching using time-lapse seismic data. Paper presented at the SPE Middle East Oil and Gas Show and Conference. Society of Petroleum Engineers.

de Marsily, G., Lavedan, G., Boucher, M., & Fasanino, G. (1984). Interpretation of interference tests in a well field using geostatistical techniques to fit the permeability distribution in a reservoir model. Geostatistics for natural resources characterization, Part, 2, 831-849.

Deb, K. (2001). Multi-Objective Optimization Using Evolutionary Algorithms. John Wiley& Sons. Inc., New York, NY.

Deb, K., Agrawal, S., Pratap, A., & Meyarivan, T. (2000, September). A fast elitist non-dominated sorting genetic algorithm for multi-objective optimization: NSGA-II. In International Conference on Parallel Problem Solving From Nature (pp. 849-858). Springer, Berlin, Heidelberg.

Deb, K., Pratap, A., Agarwal, S., & Meyarivan, T. A. M. T. (2002). A fast and elitist multiobjective genetic algorithm: NSGA-II. IEEE transactions on evolutionary computation, 6(2), 182-197.

Deb, K., & Saxena, D. K. (2005). On finding pareto-optimal solutions through dimensionality reduction for certain large-dimensional multi-objective optimization problems. Kangal report, 2005011.

Dejean, J., & Blanc, G. (1999). Managing uncertainties on production predictions using integrated statistical methods. Paper presented at the SPE Annual Technical Conference and Exhibition. Society of Petroleum Engineers.

Denney, D. (2007). Improved and More-Rapid History Matching with a Nonlinear Proxy and Global Optimization. Journal of Petroleum Technology, 59(06), 68-71.

Dong, Y., & Oliver, D. S. (2005). Quantitative use of 4D seismic data for reservoir description. SPE Journal, 10(01), 91-99.

Doyen, P. (2007). Seismic reservoir characterization: An earth modelling perspective (Vol. 2): EAGE publications Houten.

Dvorkin, J., & Nur, A. (1996). Elasticity of high-porosity sandstones: Theory for two North Sea data sets. Geophysics, 61(5), 1363-1370.

Eberhart, R., & Kennedy, J. (1995, October). A new optimizer using particle swarm theory. In Micro Machine and Human Science, 1995. MHS'95., Proceedings of the Sixth International Symposium on (pp. 39-43). IEEE.

Eberhart-Phillips, D., Han, D.-H., & Zoback, M. D. (1989). Empirical relationships among seismic velocity, effective pressure, porosity, and clay content in sandstone. Geophysics, 54(1), 82-89.

El Ouair, Y., Lygren, M., Osdal, B., Husby, O., & Springer, M. (2005). Integrated reservoir management approach: From time-lapse acquisition to reservoir model update at the Norne Field. Paper presented at the International Petroleum Technology Conference. International Petroleum Technology Conference.

Elabed, S. (2003). Analysis of the Neighbourhood Algorithm Applied to History Matching Under Uncertainty. Unpublished Technical Report., Heriot-Watt University,

Elvind, D., Asmund, H., & Rolf, V. (1992). Maximum information at minimum cost: a North Sea field development study with an experimental design. Journal of Petroleum Technology, 44(12), 1,350-351,356.

Enchery, G., Ravalec-Dupin, L., & Roggero, F. (2007). An improved pressure and saturation downscaling process for a better integration of 4D seismic data together with production history. Paper presented at the EUROPEC/EAGE Conference and Exhibition. Society of Petroleum Engineers.

England, W. A., & Townsend, C. (1998). The Effects of faulting on production form a shallow marine reservoir-A study of the relative importance of fault parameters. Paper presented at the SPE Annual Technical Conference and Exhibition. Society of Petroleum Engineers.

Erbas, D., & Christie, M. A. (2007). Effect of sampling strategies on prediction uncertainty estimation. Paper presented at the SPE Reservoir Simulation Symposium. Society of Petroleum Engineers.

Escobar, I., Williamson, P., Cherrett, A., Doyen, P., Bornard, R., Moyen, R., & Crozat, T. (2007). Fast geostatistical stochastic inversion in a stratigraphic grid. In SEG Technical Program Expanded Abstracts 2006 (pp. 2067-2071): Society of Exploration Geophysicists.

Eshelman, L. J., & Schaffer, J. D. (1993). Real-coded genetic algorithms and interval-schemata. In Foundations of genetic algorithms (Vol. 2, pp. 187-202): Elsevier.

Esmaiel, T. E., Fallah Bolandtaba, S., & van Kruijsdijk, C. (2005). Reservoir screening and sensitivity analysis of waterflooding with smart wells through the application of experimental design. Paper presented at the SPE Middle East Oil and Gas Show and Conference. Society of Petroleum Engineers.

Fahimuddin, A., Aanonsen, S. I., & Skjervheim, J.-A. (2010). Ensemble based 4D seismic history matching: Integration of different levels and types of seismic data. Paper presented at the SPE EUROPEC/EAGE Annual Conference and Exhibition. Society of Petroleum Engineers.

Fan, Z., Zhang, Y., & Yang, D. (2017). Estimation of Three-Phase Relative Permeabilities for A WAG Process Using An Improved Ensemble Randomized Maximum Likelihood Algorithm. Paper presented at the SPE Reservoir Characterisation and Simulation Conference and Exhibition. Society of Petroleum Engineers.

Fedutenko, E., Yang, C., CaRD, C., & Nghiem, L. (2013). Time-dependent proxy modeling of SAGD process. Paper presented at the SPE Heavy Oil Conference-Canada. Society of Petroleum Engineers.

Ferraro, P., & Verga, F. (2009, January). Use of evolutionary algorithms in single and multi-objective optimization techniques for assisted history matching. In Offshore Mediterranean Conference and Exhibition. Offshore Mediterranean Conference.

Floricich, M., MacBeth, C., & Staples, R. (2005). An engineering-driven approach for separating pressure and saturation using 4D seismic: Application to a Jurassic reservoir in the UK North Sea. In SEG Technical Program Expanded Abstracts 2005 (pp. 2464-2467): Society of Exploration Geophysicists.

Floris, F. J. T., Bush, M. D., Cuypers, M., Roggero, F., & Syversveen, A. R. (2001). Methods for quantifying the uncertainty of production forecasts: a comparative study. Petroleum Geoscience, 7(Supp), 87-96.

Francis, A. (2002). Deterministic inversion: Overdue for retirement. Paper presented at the PETEX 2002 Conference and Exhibition.

Friedmann, F., Chawathe, A., & Larue, D. (2001). Assessing uncertainty in channelized reservoirs using experimental designs. Paper presented at the SPE Annual Technical Conference and Exhibition. Society of Petroleum Engineers.

Gao, G., Zafari, M., & Reynolds, A. C. (2005). Quantifying uncertainty for the PUNQ-S3 problem in a Bayesian setting with RML and EnKF. Paper presented at the SPE reservoir simulation symposium. Society of Petroleum Engineers.

Gardner, R. H., O'neill, R. V., Mankin, J. B., & Carney, J. H. (1981). A comparison of sensitivity analysis and error analysis based on a stream ecosystem model. Ecological Modelling, 12(3), 173-190.

Gassmann, F. (1951). Elastic waves through a packing of spheres. Geophysics, 16(4), 673-685.

Gavalas, G. R., Shah, P. C., & Seinfeld, J. H. (1976). Reservoir history matching by Bayesian estimation. Society of Petroleum Engineers Journal, 16(06), 337-350.

Geman, S., & Geman, D. (1984). Stochastic relaxation, Gibbs distributions, and the Bayesian restoration of images. IEEE Transactions on pattern analysis and machine intelligence, (6), 721-741.

Geoview. (2014). HRS-9 Reference Manual.

Glimm, J., Hou, S., Lee, Y. H., Sharp, D. H., & Ye, K. (2004). Sources of uncertainty and error in the simulation of flow in porous media. Computational & Applied Mathematics, 23(2-3), 109-120.

Gómez-Hernánez, J. J., Sahuquillo, A., & Capilla, J. (1997). Stochastic simulation of transmissivity fields conditional to both transmissivity and piezometric data—I. Theory. Journal of Hydrology, 203(1-4), 162-174.

Gosselin, O., Aanonsen, S., Aavatsmark, I., Cominelli, A., Gonard, R., Kolasinski, M., Ferdinandi, F, Kovacic, L., & Neylon, K. (2003). History matching using time-lapse seismic (HUTS). Paper presented at the SPE Annual Technical Conference and Exhibition. Society of Petroleum Engineers.

Gouveia, W. P., Johnston, D. H., Solberg, A., & Lauritzen, M. (2004). Jotun 4D: Characterization of fluid contact movement from time-lapse seismic and production logging tool data. The Leading edge, 23(11), 1187-1194.

Greaves, R. J., & Fulp, T. J. (1987). Three-dimensional seismic monitoring of an enhanced oil recovery process. Geophysics, 52(9), 1175-1187.

Grechka, V. (2009). Fluid-solid substitution in rocks with disconnected and partially connected porosity. Geophysics, 74(5), WB89-WB95.

Grimstad, A. A., Mannseth, T., Nævdal, G., & Urkedal, H. (2003). Adaptive multiscale permeability estimation. Computational Geosciences, 7(1), 1-25.

Gu, Y., & Oliver, D. S. (2005). History matching of the PUNQ-S3 reservoir model using the ensemble Kalman filter. SPE journal, 10(02), 217-224.

Gu, Y., & Oliver, D. S. (2007). An iterative ensemble Kalman filter for multiphase fluid flow data assimilation. Spe Journal, 12(04), 438-446.

Guerrero, H. J., Osorio, J. G., & Teufel, L. W. (2000). A parametric study of variables affecting the coupled of fluid-flow/geomechanical processes in stress-sensitive oil and gas reservoirs. Paper presented at the SPE Asia Pacific Oil and Gas Conference and Exhibition. Society of Petroleum Engineers.

Guyaguler, B., Horne, R. N., Rogers, L., & Rosenzweig, J. J. (2000). Optimization of Well Placement in a Gulf of Mexico Waterflooding Project. Paper presented at the SPE Annual Technical Conference and Exhibition. Society of Petroleum Engineers.

Haas, A., & Dubrule, O. (1994). Geostatistical inversion-a sequential method of stochastic reservoir modelling constrained by seismic data. First break, 12(11), 561-569.

Hajizadeh, Y. (2010). Ants can do history matching. Paper presented at the SPE Annual Technical Conference and Exhibition. Society of Petroleum Engineers.

Hajizadeh, Y., Christie, M. A., & Demyanov, V. (2011). Towards multiobjective history matching: faster convergence and uncertainty quantification. Paper presented at the SPE reservoir simulation symposium. Society of Petroleum Engineers.

Hamdi, H., Hajizadeh, Y., & Sousa, M. C. (2015). Gaussian Process for Uncertainty Quantification of Reservoir Models. Paper presented at the SPE/IATMI Asia Pacific Oil & Gas Conference and Exhibition. Society of Petroleum Engineers.

Russell, B., & Hampson, D. (2006). The old and the new in seismic inversion. CSEG Recorder, 31(10), 5-11.

Hampson, D. P., Schuelke, J. S., & Quirein, J. A. (2001). Use of multiattribute transforms to predict log properties from seismic data. Geophysics, 66(1), 220-236.

Han, D., & Batzle, M. (2000). Velocity, density and modulus of hydrocarbon fluids—Data measurement. In SEG Technical Program Expanded Abstracts 2000 (pp. 1862-1866): Society of Exploration Geophysicists.

Han, Y., Park, C., & Kang, J. M. (2010). Estimation of Future Production Performance Based on Multi-objective History Matching in a Waterflooding Project. Paper presented at the SPE EUROPEC/EAGE Annual Conference and Exhibition. Society of Petroleum Engineers.

Haugen, V. E. J., Natvik, L.-J., Evensen, G., Berg, A. M., Flornes, K. M., & Naevdal, G. (2006). History matching using the ensemble Kalman filter on a North Sea field case. Paper presented at the SPE Annual Technical Conference and Exhibition. Society of Petroleum Engineers.

He, J., Xie, J., Wen, X.-H., & Chen, W. (2015). Improved proxy for history matching using proxy-for-data approach and reduced order modeling. Paper presented at the SPE Western Regional Meeting. Society of Petroleum Engineers.

Hoffman, B. T., & Caers, J. (2005). Regional probability perturbations for history matching. Journal of Petroleum Science and Engineering, 46(1-2), 53-71.

Hu, L. Y., Blanc, G., & Noetinger, B. (2001). Gradual deformation and iterative calibration of sequential stochastic simulations. Mathematical Geology, 33(4), 475-489.

Huang, X., Meister, L., & Workman, R. (1997). Production history matching with time lapse seismic data. In SEG Technical Program Expanded Abstracts 1997 (pp. 862-865): Society of Exploration Geophysicists.

Huang, Y., Alsos, T., Sørensen, H. M., & Tian, S. (2013). Proving the value of 4D seismic data in the late-life field–Case study of the Norne main field. First Break, 31(9), 57-67.

Hughes, E. J. (2005, September). Evolutionary many-objective optimisation: many once or one many?. In Evolutionary Computation, 2005. The 2005 IEEE Congress on (Vol. 1, pp. 222-227). IEEE.

Hutahaean, J., Demyanow, V., & Christie, M. (2015). Impact of model parameterisation and objective choices on assisted history matching and reservoir forecasting. Paper presented at the SPE/IATMI Asia Pacific Oil & Gas Conference and Exhibition. Society of Petroleum Engineers.

Hutahaean, J., Demyanov, V., & Christie, M. A. (2017). On Optimal Selection of Objective Grouping for Multiobjective History Matching. SPE Journal, 22(04), 1-296.

Iman, R. L., Helton, J. C., & Campbell, J. E. (1981). An approach to sensitivity analysis of computer models: Part I—Introduction, input variable selection and preliminary variable assessment. Journal of quality technology, 13(3), 174-183.

Ishibuchi, H., Tsukamoto, N., & Nojima, Y. (2008, March). Evolutionary many-objective optimization. In Genetic and Evolving Systems, 2008. GEFS 2008. 3rd International Workshop on (pp. 47-52). IEEE.

Jack, I. (1997). Time-lapse seismic in reservoir management: Society of Exploration Geophysicists.

Jafarpour, B., Goyal, V. K., McLaughlin, D. B., & Freeman, W. T. (2010). Compressed history matching: exploiting transform-domain sparsity for regularization of nonlinear dynamic data integration problems. Mathematical Geosciences, 42(1), 1-27.

Jahns, H. O. (1966). A rapid method for obtaining a two-dimensional reservoir description from well pressure response data. Society of Petroleum Engineers Journal, 6(04), 315-327.

Jian, F. X., Larue, D. K., Castellini, A., & Toldi, J. (2004). Reservoir Modeling Methods and Characterization Parameters for a Shoreface Reservoir: What Is Important for Fluid-Flow Performance?. SPE Reservoir Evaluation & Engineering, 7(02), 89-104. Society of Petroleum Engineers.

Jiang, M., Luo, Y. P., & Yang, S. Y. (2007). Particle swarm optimization-stochastic trajectory analysis and parameter selection. In Swarm intelligence, Focus on ant and particle swarm optimization: InTech.

Jiang, M., Luo, Y. P., & Yang, S. Y. (2007). Stochastic convergence analysis and parameter selection of the standard particle swarm optimization algorithm. Information Processing Letters, 102(1), 8-16.

Jin, L., Alpak, F. O., van den Hoek, P., Pirmez, C., Fehintola, T., Tendo, F., & Olaniyan, E. E. (2011). A Comparison of Stochastic Data-Integration Algorithms for the Joint History Matching of Production and Time-Lapse Seismic Data. Paper presented at the SPE Annual Technical Conference and Exhibition. Society of Petroleum Engineers.

Johnston, D. H. (2013). Practical applications of time-lapse seismic data: Society of Exploration Geophysicists.

Jones, A., Al-Qabandi, S., Reddick, C., & Anderson, S. (1997). Rapid assessment of pattern waterflooding uncertainty in a giant oil reservoir. Paper presented at the SPE Annual Technical Conference and Exhibition. Society of Petroleum Engineers.

Junker, H., Dose, T., Plas, L., & Little, A. J. H. (2006). Modern approach to estimation of uncertainty of predictions with dynamic reservoir simulation-a case study of a German Rotliegend gasfield. Paper presented at the SPE Annual Technical Conference and Exhibition. Society of Petroleum Engineers.

Kabir, C., Chawathe, A., Jenkins, S., Olayomi, A., Aigbe, C., & Faparusi, D. (2002). Developing New Fields Using Probabilistic Reservoir Forecasting. Paper presented at the SPE Annual Technical Conference and Exhibition. Society of Petroleum Engineers.

Kabir, C., Chien, M., & Landa, J. (2003). Experiences with automated history matching. Paper presented at the SPE Reservoir Simulation Symposium. Society of Petroleum Engineers.

Kabir, C., & Young, N. (2001). Handling Production-Data Uncertainty in History Matching: The Meren Reservoir Case Study. Paper presented at the SPE Annual Technical Conference and Exhibition. Society of Petroleum Engineers.

Kazemi, A., Stephen, K., & Shams, A. (2011). Seismic history matching of nelson using time-lapse seismic data: An investigation of 4d signature normalization. SPE Reservoir Evaluation & Engineering, 14(05), 621-633.

Kazemi, A., & Stephen, K. D. (2011). Automatic production and seismic history matching by updating locally and by geological environment in the Nelson field. Paper presented at the SPE EUROPEC/EAGE Annual Conference and Exhibition. Society of Petroleum Engineers.

Khaninezhad, M., & Jafarpour, B. (2013). Bayesian history matching and uncertainty quantification under sparse priors: a randomized maximum likelihood approach. Paper presented at the SPE Reservoir Simulation Symposium. Society of Petroleum Engineers.

King, G., Lee, S., Alexandre, P., Miguel, M., Blevens, M., Pillow, M., & Christie, G. (2005). Probabilistic forecasting for mature fields with significant production history: a Nemba field case study. Paper presented at the SPE Annual Technical Conference and Exhibition. Society of Petroleum Engineers.

King, M., Park, H.-Y., & Datta-Gupta, A. (2013). Handling conflicting multiple objectives using Pareto-based evolutionary algorithm for history matching of reservoir performance. Paper presented at the 2013 SPE Reservoir Simulation Symposium. Society of Petroleum Engineers.

Kitayama, S., & Yamazaki, K. (2012). Compromise point incorporating trade-off ratio in multi-objective optimization. Applied Soft Computing, 12(8), 1959-1964.

Kjonsvik, D., Doyle, J., Jacobsen, T., & Jones, A. (1994). The effects of sedimentary heterogeneities on production from a shallow marine reservoir-what really matters? Paper presented at the SPE Annual Technical Conference and Exhibition. Society of Petroleum Engineers.

Kloosterman, H. J., Kelly, R. S., Stammeijer, J., Hartung, M., Van Waarde, J., & Chajecki, C. (2003). Successful application of time-lapse seismic data in Shell Expro's Gannet Fields, Central North Sea, UKCS. Petroleum Geoscience, 9(1), 25-34.

Kragh, E. D., & Christie, P. (2002). Seismic repeatability, normalized rms, and predictability. The Leading Edge, 21(7), 640-647.

Kretz, V., Valles, B., & Sonneland, L. (2004). Fluid front history matching using 4D seismic and streamline simulation. Paper presented at the SPE Annual Technical Conference and Exhibition. Society of Petroleum Engineers.

Kuster, G. T., & Toksöz, M. N. (1974). Velocity and attenuation of seismic waves in two-phase media: Part I. Theoretical formulations. Geophysics, 39(5), 587-606.

Lancaster, S., & Whitcombe, D. (2000). Fast-track 'coloured'inversion. In SEG Technical Program Expanded Abstracts 2000 (pp. 1572-1575): Society of Exploration Geophysicists.

Landa, J. L., & Güyagüler, B. (2003). A methodology for history matching and the assessment of uncertainties associated with flow prediction. Paper presented at the SPE Annual Technical Conference and Exhibition. Society of Petroleum Engineers.

Landa, J. L., & Horne, R. N. (1997). A procedure to integrate well test data, reservoir performance history and 4-D seismic information into a reservoir description. Paper presented at the SPE Annual Technical Conference and Exhibition. Society of Petroleum Engineers.

Landrø, M., Digranes, P., & Strønen, L. K. (2001). Mapping reservoir pressure and saturation changes using seismic methods-possibilities and limitations. First break, 19(12), 671-684.

LaVenue, A. M., & Pickens, J. F. (1992). Application of a coupled adjoint sensitivity and kriging approach to calibrate a groundwater flow model. Water Resources Research, 28(6), 1543-1569.

Le Ravalec, M., Da Veiga, S., Derfoul, R., Enchéry, G., Gervais, V., & Roggero, F. (2012). Integrating data of different types and different supports into reservoir models. Oil & Gas Science and Technology – Rev. IFP Energies Nouvelles, 67(5), 823-839.

Le Ravalec, M., Noetinger, B., & Hu, L. Y. (2000). The FFT moving average (FFT-MA) generator: An efficient numerical method for generating and conditioning Gaussian simulations. Mathematical Geology, 32(6), 701-723.

Li, B., & Friedmann, F. (2005). Novel multiple resolutions design of experiment/response surface methodology for uncertainty analysis of reservoir simulation forecasts. Paper presented at the SPE Reservoir Simulation Symposium. Society of Petroleum Engineers.

Li, G., & Reynolds, A. C. (2007). An iterative ensemble Kalman filter for data assimilation. Paper presented at the SPE annual technical conference and exhibition. Society of Petroleum Engineers.

Li, Q. (2001). LP sparse spike inversion. Strata Technique Document, Hampson-Russell Software Services Ltd.

Lindseth, R. O. (1979). Synthetic sonic logs—A process for stratigraphic interpretation. Geophysics, 44(1), 3-26.

Liu, H. L., Chen, L., Zhang, Q., & Deb, K. (2016, November). An evolutionary many-objective optimisation algorithm with adaptive region decomposition. In CEC (pp. 4763-4769).

Liu, N., Oliver, D. S. (2005). Ensemble Kalman filter for automatic history matching of geologic facies. Journal of Petroleum Science and Engineering, 47(3-4), 147-161.

Lumley, D., Nur, A., Strandenes, S., Hydro, N., Dvorkin, J., & Packwood, J. (1994). Seismic monitoring of oil production: A feasibility study. In SEG Technical Program Expanded Abstracts 1994 (pp. 319-322): Society of Exploration Geophysicists.

Lygren, M., Husby, O., Osdal, B., El Ouair, Y., & Springer, M. (2005). History matching using 4D seismic and pressure data on the Norne field. Paper presented at the 67th EAGE Conference & Exhibition.

MacBeth, C. (1995). How can anisotropy be used for reservoir characterization?. First Break, 13(1), 31-37.

MacBeth, C. (2004). A classification for the pressure-sensitivity properties of a sandstone rock frame. Geophysics, 69(2), 497-510.

Manceau, E., Mezghani, M., Zabalza-Mezghani, I., & Roggero, F. (2001). Combination of experimental design and joint modeling methods for quantifying the risk associated with deterministic and stochastic uncertainties-An integrated test study. Paper presented at the SPE Annual Technical Conference and Exhibition. Society of Petroleum Engineers.

Margrave, G., & Manning, P. (2004). Seismic modeling: An essential interpreter's tool: Presented at the CSEG National Convention.

Martinez, F., and Gonzalo, E. (2008). "The Generalized PSO: A New Door to PSO Evolution", Journal of Artificial Evolution and Applications, Article ID: 861275, 15 pages. doi:10.1155/2008/861275

Maschio, C., & Schiozer, D. J. (2004). Integration of Streamline Simulation and Automatic History Matching. Paper presented at the SPE Annual Technical Conference and Exhibition. Society of Petroleum Engineers.

Matheron, G. F. (1971). The theory of regionalized variables and its applications, volume 5 of Les cahiers du Centre de Morhologie Mathématique de Fontainebleau. École Nationale Supérieure des Mines de Paris.

Matthew, L. W., Pullin, N. E., & Hirscha, W. K. (1987, January). Techniques Applied To Obtain Very High Resolution 3-D Seismic Imaging At An Athabasca Tar Sands Thermal Pilot. In Annual Technical Meeting. Petroleum Society of Canada.

Maurya, S., Sarkar, P. (2016). Comparison of Post stack Seismic Inversion Methods: A case study from Blackfoot Field, Canada. International Journal of Scientific & Engineering Research, Volume 7, Issue 8, August - 2016.

Mavko, G., Mukerji, T., & Dvorkin, J. (2009). The rock physics handbook: Tools for seismic analysis of porous media: Cambridge university press.

McKay, M. D., Beckman, R. J., & Conover, W. J. (1979). Comparison of three methods for selecting values of input variables in the analysis of output from a computer code. Technometrics, 21(2), 239-245.

Mezghani, M., Fornel, A., Langlais, V., & Lucet, N. (2004). History matching and quantitative use of 4D seismic data for an improved reservoir characterization. Paper presented at the SPE Annual Technical Conference and Exhibition. Society of Petroleum Engineers.

Milliken, W., Emanuel, A., Chakravarty, A. (2001). Applications of 3D streamline simulation to assist history matching. Society of Petroleum Engineers. Doi:10.2118/74712-PA

Min, B., Kang, J. M., Chung, S., Park, C., Jang, I. (2014). Pareto-based multi-objective history matching with respect to individual production performance in a heterogeneous reservoir. Journal of Petroleum Science and Engineering, 122, 551-566.

Mohamed, L., Christie, M. A., & Demyanov, V. (2011). History matching and uncertainty quantification: multiobjective particle swarm optimisation approach. Paper presented at the SPE EUROPEC/EAGE annual conference and exhibition. Society of Petroleum Engineers.

Mohamed, L., Christie, M. A., & Demyanov, V. (2010). Comparison of stochastic sampling algorithms for uncertainty quantification. Proceedings of the SPE EUROPEC/EAGE Annual Conference and Exhibition, 23-26 May 2011, Vienna, Austria. Society of Petroleum Engineers.

Montgomery, D. C. (2017). Design and analysis of experiments: John wiley & sons.

Morell, E. (2010). History matching of the Norne field. Master Master thesis, Norwegian Uni. of Science and Technology.

Moreno, J., Kazemi, H., & Gilman, J. (2004). Streamline simulation of countercurrent water-oil and gas-oil flow in naturally fractured dual-porosity reservoirs. Paper presented at the SPE Annual Technical Conference and Exhibition. Society of Petroleum Engineers.

Morokoff, W. J., & Caflisch, R. E. (1994). Quasi-random sequences and their discrepancies. SIAM Journal on Scientific Computing, 15(6), 1251-1279.

Mosegaard, K., & Tarantola, A. (1995). Monte Carlo sampling of solutions to inverse problems. Journal of Geophysical Research: Solid Earth, 100(B7), 12431-12447.

Myers, R. H., & Montgomery, D. C. (1995). Response surface methodology: process and product optimization using designed experiments (Vol. 4): Wiley New York.

Naevdal, G., Johnsen, L. M., Aanonsen, S. I., & Vefring, E. (2005). Reservoir Monitoring and Continuous Model Updating Using Ensemble Kalman Filter. SPE Journal 10(01), 66-74.

Nørgård, J.-P. (2006). Revolutionising History Matching and Uncertainty Assessment. Retrieved from http://archives.datapages.com/data/geo-expro-magazine/003/003004/pdfs/34.htm

Nur, A. M. (1982). Seismic imaging in enhanced recovery. Paper presented at the SPE Enhanced Oil Recovery Symposium. Society of Petroleum Engineers.

Obidegwu, D., Chassagne, R., & MacBeth, C. (2015). Seismic assisted history matching using binary image matching. Paper presented at the EUROPEC 2015. Society of Petroleum Engineers.

Okano, H. (2013). Reservoir Model History-Matching and Uncertainty Quantification in Reservoir Performance Forecast Using Bayesian Framework. Paper presented at the SPE Reservoir Characterization and Simulation Conference and Exhibition. Society of Petroleum Engineers.

Olalotiti-Lawal, F., & Datta-Gupta, A. (2015). A multi-objective Markov chain Monte Carlo approach for history matching and uncertainty quantification. Paper presented at the SPE Annual Technical Conference and Exhibition. Society of Petroleum Engineers.

Oldenburg, D., Scheuer, T., & Levy, S. (1983). Recovery of the acoustic impedance from reflection seismograms. Geophysics 48(10), 1318-1337.

Oliver, D. S., & Chen, Y. (2011). Recent progress on reservoir history matching: a review. Computational Geosciences, 15(1), 185-221.

Oliver, D. S., Reynolds, A. C., & Liu, N. (2008). Inverse theory for petroleum reservoir characterization and history matching: Cambridge University Press.

Onwunyili, C., & Stephen, K. (2018). A Fast Approach to Ensemble Appraisal and Reservoir Performance Predictions. Paper presented at the 80th EAGE Conference and Exhibition 2018.

Osdal, B. (2004). Using high quality and repeatable Q-marine data in reservoir monitoring on the norne field. Paper presented at the 66th EAGE Conference & Exhibition.

Osdal, B., & Alsos, T. (2002). Seismic Modelling of Eclipse Simulations and Comparsion with Real 4D Data at the Norne Field. Paper presented at the 64th EAGE Conference & Exhibition.

Osdal, B., Husby, O., Aronsen, H. A., Chen, N., & Alsos, T. (2006). Mapping the fluid front and pressure buildup using 4D data on Norne Field. The Leading Edge, 25(9), 1134-1141.

Osterloh, W. T. (2008). Use of multiple-response optimization to assist reservoir simulation probabilistic forecasting and history matching. Paper presented at the SPE Annual Technical Conference and Exhibition. Society of Petroleum Engineers.

O'Sullivan, A., & Christie, M. (2005). Solution error models: a new approach for coarse grid history matching. Paper presented at the SPE Reservoir Simulation Symposium. Society of Petroleum Engineers.

Ozdogan, U., Sahni, A., Yeten, B., Guyaguler, B., & Chen, W. H. (2005). Efficient assessment and optimization of a deepwater asset using fixed pattern approach. Paper presented at the SPE Annual Technical Conference and Exhibition. Society of Petroleum Engineers.

Pan, Y., & Horne, R. N. (1998). Improved methods for multivariate optimization of field development scheduling and well placement design. Paper presented at the SPE Annual Technical Conference and Exhibition. Society of Petroleum Engineers.

Peake, W., Abadah, M., & Skander, L. (2005). Uncertainty assessment using experimental design: Minagish oolite reservoir. Paper presented at the SPE Reservoir Simulation Symposium. Society of Petroleum Engineers.

Peng, C. Y., & Gupta, R. (2003). Experimental design in deterministic modelling: assessing significant uncertainties. Paper presented at the SPE Asia Pacific Oil and Gas Conference and Exhibition. Society of Petroleum Engineers.

Peng, C. Y., & Gupta, R. (2004). Experimental design and analysis methods in multiple deterministic modelling for quantifying hydrocarbon in-place probability distribution curve. Paper presented at the SPE Asia Pacific Conference on Integrated Modelling for Asset Management. Society of Petroleum Engineers.

Plackett, R. L., & Burman, J. (1946). The design of optimum multifactorial experiments. Biometrika, 33 (4), 305-325.

Poli, R., & Broomhead, D. (2007). Exact analysis of the sampling distribution for the canonical particle swarm optimiser and its convergence during stagnation. Paper presented at the Proceedings of the 9th annual conference on Genetic and evolutionary computation.

Portella, R., Salomao, M., Blauth, M., & Duarte, R. (2003). Uncertainty quantification to evaluate the value of information in a deepwater reservoir. Paper presented at the SPE Reservoir Simulation Symposium. Society of Petroleum Engineers.

Purwar, S., Jablonowski, C. J., & Nguyen, Q. P. (2010). A Method For Integrating Response Surfaces Into Optimization Models With Real Options: A Case in Gas Flooding. Paper presented at the SPE Hydrocarbon Economics and Evaluation Symposium. Society of Petroleum Engineers.

Queipo, N. V., Pintos, S., Rincon, N., Contreras, N., & Colmenares, J. (2000, January). Surrogate Modeling-Based Optimization for the Integration of Static and Dynamic Data into a Reservoir Description. In SPE Annual Technical Conference and Exhibition. Society of Petroleum Engineers.

Quinao, J. J., & Zarrouk, S. J. (2015). Application of Experimental Design and Response Surface Methods in Probabilistic Geothermal Resource Assessment: numerical simulation and volumetric methods. Proceedings World Geothermal Congress 2015 Melbourne, Australia.

RamaRao, B. S., LaVenue, A. M., De Marsily, G., & Marietta, M. G. (1995). Pilot point methodology for automated calibration of an ensemble of conditionally simulated transmissivity fields: 1. Theory and computational experiments. Water Resour. Res., 31(3), 475-493.

Reis, L. C. (2006). Risk analysis with history matching using experimental design or artificial neural networks. Paper presented at the SPE Europec/EAGE Annual Conference and Exhibition. Society of Petroleum Engineers.

Rey, A., & Landa, J. L. . (2017). A Practical Approach to Incorporate Data-Driven 4D Seismic Inversion into Flow Simulation History Matching. Paper presented at the SPE Annual Technical Conference and Exhibition, Texas, USA. Society of Petroleum Engineers.

Rodrigues, J. (2006). Calculating derivatives for automatic history matching. Computational Geoscience, 10(1), 2006, p. 119-136.

Roggero, F. (1997). Direct selection of stochastic model realizations constrained to historical data. Paper presented at the SPE Annual Technical Conference and Exhibition. Society of Petroleum Engineers.

Roggero, F., Ding, D. Y., Berthet, P., Lerat, O., Cap, J., & Schreiber, P. E. (2007). Matching of Production History and 4D Seismic Data--Application to the Girassol Field, Offshore Angola. Paper presented at the SPE Annual Technical Conference and Exhibition. Society of Petroleum Engineers.

Roggero, F., & Hu, L. (1998). Gradual deformation of continuous geostatistical models for history matching. Paper presented at the SPE annual technical conference and exhibition. Society of Petroleum Engineers.

Roggero, F., Lerat, O., Ding, D. Y., Berthet, P., Bordenave, C., Lefeuvre, F., & Perfetti, P. (2012). History matching of production and 4D seismic data: application to the Girassol Field, Offshore Angola. Oil & Gas Science and Technology–Revue d'IFP Energies nouvelles, 67(2), 237-262.

Rotondi, M., Nicotra, G., Godi, A., Contento, F. M., Blunt, M. J., & Christie, M. (2006). Hydrocarbon production forecast and uncertainty quantification: A field application. Paper presented at the SPE Annual Technical Conference and Exhibition. Society of Petroleum Engineers.

Russell, B., & Hampson, D. (1991). Comparison of poststack seismic inversion methods. In SEG Technical Program Expanded Abstracts 1991 (pp. 876-878): Society of Exploration Geophysicists.

Rwechungura, R. W., Dadashpour, M., & Kleppe, J. (2011). Advanced history matching techniques reviewed. Paper presented at the SPE Middle East Oil and Gas Show and Conference. Society of Petroleum Engineers.

Rwechungura, R. W., Suwartadi, E., Dadashpour, M., Kleppe, J., & Foss, B. A. (2010). The Norne Field case-a unique comparative case study. Paper presented at the SPE Intelligent Energy Conference and Exhibition. Society of Petroleum Engineers.

Sagitov, I., & Stephen, K. (2012). Assisted Seismic History Matching in Different Domains-What Seismic Data Should We Compare?(SPE 154503). Paper presented at the 74th EAGE Conference and Exhibition incorporating EUROPEC 2012. Society of Petroleum Engineers.

Sagitov, I., & Stephen, K. D. (2013). Optimizing the Integration of 4D Seismic Data in History Matching: Which Data Should We Compare? Paper presented at the EAGE Annual Conference & Exhibition incorporating SPE Europec. Society of Petroleum Engineers.

Sambridge, M., & Mosegaard, K. (2002). Monte Carlo methods in geophysical inverse problems. Rev. Geophysiscs, 40(3), 3-1-3-29.

Sambridge, M. S. (1999a). Geophysical Inversion with a Neighbourhood Algorithm–I. Searching a Parameter Space. Geophys.J.Int., 138, 479-494.

Sambridge, M. S. (1999b). Geophysical inversion with a neighbourhood algorithm—II. Appraising the ensemble. Geophys.J.Int., 138(3), 727-746.

Sandsdalen, C., Barbieri, M., Tyler, K., & Aasen, J. O. . (1996). Applied Uncertainty Analysis Using Stochastic Modelling. Society of Petroleum Engineers. doi:doi:10.2118/35533-MS

Santos, J., Davolio, A., MacBeth, C., & Schiozer, D. (2017). 4D seismic interpretation of the Norne Field-a semi-quantitative approach. Paper presented at the 15th International Congress of the Brazilian Geophysical Society & EXPOGEF, Rio de Janeiro, Brazil, 31 July-3 August 2017.

Sarkar, S., Gouveia, W. P., & Johnston, D. H. (2003). On the inversion of time-lapse seismic data. In SEG Technical Program Expanded Abstracts 2003 (pp. 1489-1492): Society of Exploration Geophysicists.

Sawyer, D., Cobb, W., Stalkup, F., & Braun, P. H. (1974). Factorial design analysis of wet-combustion drive. Society of Petroleum Engineers, 14(01), 25-34.

Saxena, D. K., Duro, J. A., Tiwari, A., Deb, K., & Zhang, Q. (2013). Objective reduction in many-objective optimization: Linear and nonlinear algorithms. IEEE Transactions on Evolutionary Computation, 17(1), 77-99.

Saxena, U., & Vjekoslav, P. (1971). Factorial designs as an effective tool in mining and petroleum engineering. Society of Petroleum Engineers

Sayyafzadeh, M., & Haghighi, M. (2012). Regularization in History Matching Using Multi-objective Genetic Algorithm and Bayesian Framework (SPE 154544). Paper presented at the 74th EAGE Conference and Exhibition incorporating EUROPEC 2012. Society of Petroleum Engineers.

Schlumberger. (2017). Eclipse 100 Reference Manual.

Schulze-Riegert, R. W., Krosche, M., Fahimuddin, A., & Ghedan, S. G. (2007). Multi-objective optimization with application to model validation and uncertainty quantification. Paper presented at the SPE Middle East oil and gas show and conference. Society of Petroleum Engineers.

Sedighi-Dehkordi, F., & Stephen, K. D. (2009). Faster Convergence in Seismic History Matching by Efficient Parameter Searching. Paper presented at the EUROPEC/EAGE Conference and Exhibition. Society of Petroleum Engineers.

Sedighi-Dehkordi, F., & Stephen, K. D. (2010). Faster convergence in seismic history matching by dividing and conquering the unknowns. Society of Petroleum Engineers. Doi:10.2118/121210-MS.

Seldal, M., Reime, A., & Arnesen, D. (2009). Improving Reservoir Simulation Models using 4D data at the Snorre Field. Paper presented at the EUROPEC/EAGE Conference and Exhibition. Society of Petroleum Engineers.

Selle, O. M., Springer, M., Auflem, I. H., Chen, P., Matheson, R., Mebratu, A. A., & Glasbergen, G. (2008). Gelled scale inhibitor treatment for improved placement in long horizontal wells at norne and heidrun fields. Paper presented at the SPE International Symposium and Exhibition on Formation Damage Control. Society of Petroleum Engineers.

Sengupta, M., Mavko, G., & Mukerji, T. (2003). Quantifying subresolution saturation scales from time-lapse seismic data: A reservoir monitoring case study. Geophysics, 68(3), 803-814.

Shi, Y., & Eberhart, R. (1998, May). A modified particle swarm optimizer. In Evolutionary Computation Proceedings, 1998. IEEE World Congress on Computational Intelligence., The 1998 IEEE International Conference on (pp. 69-73). IEEE.

Simpson, T., Mistree, F., Korte, J., & Mauery, T. (1998). Comparison of response surface and kriging models for multidisciplinary design optimization. Paper presented at the 7th AIAA/USAF/NASA/ISSMO Symposium on Multidisciplinary Analysis and Optimization.

Singh, A. P., Maucec, M., & Knabe, S. P. (2014). History Matching Using Streamline Trajectories. Paper presented at the Abu Dhabi International Petroleum Exhibition and Conference. Society of Petroleum Engineers.

Skjervheim, J.-A., Evensen, G., Aanonsen, S. I., Ruud, B. O., & Johansen, T. A. (2005). Incorporating 4D seismic data in reservoir simulation models using ensemble Kalman filter. Paper presented at the SPE Annual Technical Conference and Exhibition. Society of Petroleum Engineers.

Slotte, P. A., & Smorgrav, E. (2008). Response surface methodology approach for history matching and uncertainty assessment of reservoir simulation models. Paper presented at the Europec/EAGE Conference and Exhibition. Society of Petroleum Engineers.

Sobol', I. M. (1967). On the distribution of points in a cube and the approximate evaluation of integrals. USSR Comput. Maths. Math. Phys.7: 86 – 112.

Solorzano, L. N., Arredondo, S., & Sergio, E. (1973). Method for Automatic History Matching of Reservoir Simulation Models. Paper presented at the Fall Meeting of the Society of Petroleum Engineers of AIME. Society of Petroleum Engineers.

Srinivas, N., & Deb, K. J. E. c. (1994). Muiltiobjective optimization using nondominated sorting in genetic algorithms. Evolutionary Computation Journal 2(3), pp. 221-248.

Staples, R., Stammeijer, J., Jones, S., Brain, J., Smit, F., & Hatchell, P. (2006). Time-Lapse (4D) Seismic Monitoring-Expanding Applications. Paper presented at the Joint Convention, What's Next. Retrieved from http://www.searchanddiscovery.com/pdfz/documents/2015/41601staples/ndx_staples.pdf.html

Statoil. (1999). Geological Report Norne Field PL 128 Well 6608/10-C-3 H.

Statoil. (2001). PL128-Norne Field Reservoir Management Plan.

Statoil. (2004). Geological and Petrophysical Report Norne Field PL 128, Well 6608/10-C-4.

Statoil. (2005). Norne Reservoir Simulation Model. Updated Reference Case 2005.

Statoil. (2006). Annual Reservoir Development Plan Norne and Urd Field 2006.

Steffensen, I., & Karstadt, P. I. (1996). Norne field development-fast track from discovery to production. Journal of Petroleum Technology, 48(04), 296-339.

Stephen, K. D. (2009). A comparison of GA and NA approaches in SHM. Presented at the 2nd Steering Meeting of Phase III of the SHM project. Edinburgh.

Stephen, K. D. (2013). Seismic History Matching with Saturation Indicators Combined With Multiple Objective Function Optimization. Paper presented at the EAGE Annual Conference & Exhibition incorporating SPE Europec. Society of Petroleum Engineers.

Stephen, K. D., & Macbeth, C. (2006). Reducing Reservoir Prediction Uncertainty Using Seismic History Matching. Paper presented at the SPE Europec/EAGE Annual Conference and Exhibition. Society of Petroleum Engineers.

Stephen, K. D., Soldo, J., Macbeth, C., & Christie, M. A. J. S. J. (2006). Multiple model seismic and production history matching: A case study. SPE-94173-PA, SPEJ 11(04), 418-430.

Stephen, K. D. (2007). Scale and process dependent model errors in seismic history matching. Quantitative Methods in Reservoir Characterization. Oil & Gas Science and Technology – Rev. IFP, Vol. 62 (2007), No. 2, pp. 123-135

Subbey, S., Christie, M., & Sambridge, M. (2004). Prediction under uncertainty in reservoir modeling. Journal of Petroleum Science and Engineering, 44(1-2), 143-153.

Subbey, S., Christie, M., & Sambridge, M. J. C. M. (2002). Uncertainty reduction in reservoir modeling. Fluid Flow and Transport in Porous Media: Mathematical and Numerical Treatment, Vol. 295 of Contemporary Mathematics, pp. 1-10. American Mathematical Society, Providence, Rhode Island.

Suzuki, S., & Caers, J. K. (2006). History matching with an uncertain geological scenario. Paper presented at the SPE Annual Technical Conference and Exhibition. Society of Petroleum Engineers.

Tanaka, S., Kam, D., Datta-Gupta, A., & King, M. J. (2015). Streamline-Based History Matching of Arrival Times and Bottomhole Pressure Data for Multicomponent Compositional Systems. Paper presented at the SPE Annual Technical Conference and Exhibition. Society of Petroleum Engineers.

Tang, R., Behrens, R., & Emanuel, A. (1991). Reservoir studies with geostatistics to forecast performance. Society of Petroleum Engineers. doi:10.2118/18432-PA

Tarantola, A. (2005). Inverse problem theory and methods for model parameter estimation (Vol. 89): SIAM.

Tarantola, A. (1987). Inverse problem theory: Method for data fitting and model parameter estimation. Elsevier Science Publishers, Amsterdam 1987.

Thiele, M. R., Batycky, R., & Fenwick, D. J. J. o. P. T. (2010). Streamline simulation for modern reservoir-engineering workflows. Society of Petroleum Engineers. doi:10.2118/118608-JPT.

Thore, P. (2006). Accuracy and limitations in seismic modeling of reservoir. In SEG Technical Program Expanded Abstracts 2006 (pp. 1674-1677): Society of Exploration Geophysicists.

Tian, Y., Cheng, R., Zhang, X., Cheng, F., & Jin, Y. (2017). An indicator based multi-objective evolutionary algorithm with reference point adaptation for better versatility. IEEE Transactions on Evolutionary Computation, 2017, in press.

Tillier, E., Le Ravalec, M., Da Veiga, S. (2012). Simultaneous inversion of production data and seismic attributes: Application to a synthetic SAGD produced field case. Oil Gas Sci. Technol. 67, 2, 289-301.

Trani, M., Wojnar, K., Moncorgé, A., & Philippe, B. . (2017). Ensemble-Based Assisted History Matching Using 4D Seismic Fluid Front Parameterization. Paper presented at the SPE Middle East Oil & Gas Show and Conference, Manama, Kingdom of Bahrain. Society of Petroleum Engineers.

Trelea, I. C. (2003). The particle swarm optimization algorithm: convergence analysis and parameter selection. Information processing letters, 85(6), 317-325.

Tikhonov, A. N., & Arsenin, V. Y. (1977). Solution of III-posed Problems. VH Winston & Sons, Washington, DC.

Ullmann De Brito, D., Caletti, L., & Moraes, R. (2011). Incorporation of 4D Seismic in the Re-construction and History Matching of Marlim Sul Deep Water Field Flow Simulation Model. Paper presented at the SPE EUROPEC/EAGE Annual Conference and Exhibition. Society of Petroleum Engineers.

Van den Bergh, F., & Engelbrecht, A. (2006). A study of particle swarm optimization particle trajectories. ”, Information Sciences 176, 937-971

Veeken, P. C., Priezzhev, I. I., Shmaryan, L. E., Shteyn, Y. I., Barkov, A. Y., & Ampilov, Y. P. (2009). Nonlinear multitrace genetic inversion applied on seismic data across the Shtokman field, offshore northern Russia. Geophysics Special Issue, 2009

Venkataraman, R. (2000). Application of the method of experimental design to quantify uncertainty in production profiles. Paper presented at the SPE Asia Pacific Conference on Integrated Modelling for Asset Management. Society of Petroleum Engineers.

Verlo, S. B., & Hetland, M. (2008). Development of a field case with real production and 4D data from the Norne Field as a benchmark case for future reservoir simulation model testing. Master's thesis, Norwegian University of Science and Technology.

Vetterling, W. T., Press, W. H., Teukolsky, S. A., & Flannery, B. P. (1992). Numerical recipes: example book C (The Art of Scientific Computing). In: Press Syndicate of the University of Cambridge.

Vincent, G., Corre, B., Pascal, L., & Charles, T. (2002). Optimisation of the incremental development policy for a mature waterflood project. Paper presented at the Abu Dhabi International Petroleum Exhibition and Conference. Society of Petroleum Engineers.

Vincent, G., Corre, B., Thore, P. (1999). Managing structural uncertainty in a mature field for optimal well placement. Society of Petroleum Engineers. doi:10.2118/48953-MS

Waggoner, J., Cominelli, A., & Seymour, R. (2002). Improved reservoir modeling with time-lapse seismic in a Gulf of Mexico gas condensate reservoir. Paper presented at the SPE Annual Technical Conference and Exhibition. Society of Petroleum Engineers.

Walden, A. T., White, R. E. J. I. t. o. G., & Sensing, R. (1998). Seismic wavelet estimation: A frequency domain solution to a geophysical noisy input-output problem. IEEE Transactions on Geoscience and Remote Sensing, Vol. 36, No. 1, January 1998.

Walker, G., Allan, P., Trythall, R., Parr, R., Marsh, M., Kjelstadli, R., Olav, B., Johnson, D., & Lane, S. (2006). Three case studies of progress in quantitative seismic-engineering integration. The Leading Edge, 25(9), 1161-1166.

Walker, G., & Pettigrew, S. (2006). Measures of Efficiency for Assisted History Matching. Paper presented at the ECMOR X-10th European Conference on the Mathematics of Oil Recovery.

Wang, F., & White, C. D. (2002). Designed simulation for a detailed 3D turbidite reservoir model. Paper presented at the SPE Gas Technology Symposium. Society of Petroleum Engineers.

Wang, G. (2003). Adaptive response surface method using inherited latin hypercube design points. Transactions of the ASME, Journal of Mechanical Design, Vol. 125, pp. 210-220, June 2003.

Wang, R., Purshouse, R. C., & Fleming, P. J. (2013). On finding well-spread Pareto optimal solutions by preference-inspired co-evolutionary algorithm. Paper presented at the Proceedings of the 15th annual conference on Genetic and evolutionary computation.

Wang, Z., & Nur, A. (1990). Dispersion analysis of acoustic velocities in rocks. The Journal of the Acoustical Society of America, 87(6), 2384-2395.

Wang, Z., Zhang, Q., Li, H., Ishibuchi, H., Jiao, L. (2017). On the use of two reference points in decomposition based multiobjective evolutionary algorithms. Swarm and Evolutionary Computation, vol. 34, pp. 89–102, 2017.

Wang, Z. (2001). Fundamentals of seismic rock physics. Geophysics, 66(2), 398-412.

Wang, Z. (2000). The Gassmann equation revisited: Comparing laboratory data with Gassmann's predictions. Seismic and acoustic velocities in reservoir rocks, 3, 8-23.

Watts, G. (2011). Permanent reservoir monitoring still facing challenges in bod for industry acceptance. First Break, 29, no. 5, p. 13-15.

White, C. D., & Royer, S. A. (2003). Experimental design as a framework for reservoir studies. Paper presented at the SPE Reservoir Simulation Symposium. Society of Petroleum Engineers.

White, C. D., Willis, B. J., Narayanan, K., & Dutton, S. P. J. S. J. (2001). Identifying and estimating significant geologic parameters with experimental design. Society of Petroleum Engineers. doi:10.2118/74140-PA.

Winkler, K. W. (1985). Dispersion analysis of velocity and attenuation in Berea sandstone. J. Geophys. Res., 90: 6793–6800.

Xiang, Y., Zhou, Y., Li, M., & Chen, Z. (2017). A vector angle-based evolutionary algorithm for unconstrained many-objective optimization. IEEE Transactions on Evolutionary Computation, vol. 21, no. 1, pp. 131–152, 2017.

Yeten, B., Castellini, A., Guyaguler, B., & Chen, W. (2005). A comparison study on experimental design and response surface methodologies. Paper presented at the SPE Reservoir Simulation Symposium. Society of Petroleum Engineers.

Yilmaz, Ö. (2001). Seismic data analysis: Processing, inversion, and interpretation of seismic data. Society of exploration geophysicists.

Yoon, S., Malallah, A. H., Datta-Gupta, A., Vasco, D. W., & Behrens, R. A. (1999). A multiscale approach to production data integration using streamline models. Paper presented at the SPE Annual Technical Conference and Exhibition. Society of Petroleum Engineers.

Zachariassen, E., Meisingset, H., Otterlei, C., Andersen, T., Hatland, K., Hoye, T., Mangeroy, G., Liestol, F. (2006). Method for Conditioning the Reservoir Model on 3D and 4D Elastic Inversion Data Applied to a Fluvial Reservoir in the North Sea. Paper presented at the SPE Europec/EAGE Annual Conference and Exhibition. Society of Petroleum Engineers.

Zangl, G., Graf, T., & Al-Kinani, A. (2006). Proxy modeling in production optimization. Paper presented at the SPE Europec/EAGE Annual Conference and Exhibition. Society of Petroleum Engineers.

Zerpa, L. E., Queipo, N. V., Pintos, S., Tillero, E., & Alter, D. (2007). An efficient response surface approach for the optimization of ASP flooding processes: ASP pilot project LL-03 reservoir. Paper presented at the Latin American & Caribbean Petroleum Engineering Conference.

Zhang, C., Tan, K. C., Lee, L. H., & Gao, L. J. S. C. (2018). Adjust weight vectors in MOEA/D for bi-objective optimization problems with discontinuous Pareto fronts. Soft Computing, pp. 1–16, 2017.

Zhang, Y., Bansal, N., Fujita, Y., Datta-gupta, A., King, M. J., & Sankaran, S. (2014). From Streamlines to Fast Marching: Rapid Simulation and Performance Assessment of Shale Gas Reservoirs Using Diffusive Time of Flight as a Spatial Coordinate. Paper presented at the SPE Unconventional Resources Conference. Society of Petroleum Engineers.

Zhang, Y., Wang, S., & Ji, G. (2015). A comprehensive survey on particle swarm optimization algorithm and its applications. Mathematical Problems in Engineering, 2015.

Zitzler, E., & Thiele, L. (1999). Multiobjective evolutionary algorithms: a comparative case study and the strength Pareto approach. IEEE Transactions on Evolutionary Computation. 3(4), 257-271.

Zou, Y., Li, J., Huang, G., & Li, H. (2002). An inexact air quality model for petroleum pollutants based on techniques of factorial analysis and stochastic simulation. Paper

presented at the SPE International Thermal Operations and Heavy Oil Symposium and International Horizontal Well Technology Conference. Society of Petroleum Engineers.

Zubarev, D. I. (2009). Pros and cons of applying proxy-models as a substitute for full reservoir simulations. Paper presented at the SPE Annual Technical Conference and Exhibition. Society of Petroleum Engineers.